Biological and Medical Physics, Biomedical Engineering

Eric Hanssen Editor

# Cellular Imaging

Electron Tomography and Related Techniques



# BIOLOGICAL AND MEDICAL PHYSICS, BIOMEDICAL ENGINEERING

#### BIOLOGICAL AND MEDICAL PHYSICS, BIOMEDICAL ENGINEERING

The fields of biological and medical physics and biomedical engineering are broad, multidisciplinary and dynamic. They lie at the crossroads of frontier research in physics, biology, chemistry, and medicine. The Biological and Medical Physics, Biomedical Engineering Series is intended to be comprehensive, covering a broad range of topics important to the study of the physical, chemical and biological sciences. Its goal is to provide scientists and engineers with textbooks, monographs, and reference works to address the growing need for information.

Books in the series emphasize established and emergent areas of science including molecular, membrane, and mathematical biophysics; photosynthetic energy harvesting and conversion; information processing; physical principles of genetics; sensory communications; automata networks, neural networks, and cellular automata. Equally important will be coverage of applied aspects of biological and medical physics and biomedical engineering such as molecular electronic components and devices, biosensors, medicine, imaging, physical principles of renewable energy production, advanced prostheses, and environmental control and engineering.

#### Editor-in-Chief:

Bernard S. Gerstman, Department of Physics, Florida International University, Miami, Florida, USA

#### Editorial Board:

Masuo Aizawa, Department of Bioengineering, Tokyo Institute of Technology, Yokohama, Japan

Olaf S. Andersen, Department of Physiology,

Biophysics and Molecular Medicine, Cornell University, New York, USA

Robert H. Austin, Department of Physics, Princeton University, Princeton, New Jersey, USA

James Barber, Department of Biochemistry, Imperial College of Science, Technology and Medicine, London, England

Howard C. Berg, Department of Molecular and Cellular Biology, Harvard University,

and Cellular Biology, Harvard University, Cambridge, Massachusetts, USA

Victor Bloomfield, Department of Biochemistry, University of Minnesota, St. Paul, Minnesota, USA

Robert Callender, Department of Biochemistry, Albert Einstein College of Medicine,

Bronx, New York, USA

Steven Chu, Lawrence Berkeley National Laboratory, Berkeley, California, USA Johann Deisenhofer, Howard Hughes Medical

Institute, The University of Texas, Dallas,

Texas, USA

George Feher, Department of Physics, University of California, San Diego, La Jolla, California, USA

Hans Frauenfelder,

Los Alamos National Laboratory, Los Alamos, New Mexico, USA

Ivar Giaever, Rensselaer Polytechnic Institute,

Troy, NewYork, USA

Sol M. Gruner, Cornell University,

Ithaca, New York, USA

Judith Herzfeld, Department of Chemistry, Brandeis University, Waltham, Massachusetts, USA

Mark S. Humayun, Doheny Eye Institute, Los Angeles, California, USA

Pierre Joliot, Institute de Biologie Physico-Chimique, Fondation Edmond

de Rothschild, Paris, France

Lajos Keszthelyi, Institute of Biophysics, Hungarian Academy of Sciences, Szeged, Hungary

Paul W. King, Biosciences Center

and Photobiology Group, National Renewable Energy Laboratory, Golden, Colorado, USA

Robert S. Knox, Department of Physics and Astronomy, University of Rochester, Rochester, New York, USA

Gianluca Lazzi, University of Utah, Salt Lake City, Utah, USA

Aaron Lewis, Department of Applied Physics, Hebrew University, Jerusalem, Israel

Stuart M. Lindsay, Department of Physics and Astronomy, Arizona State University,

Tempe, Arizona, USA

David Mauzerall, Rockefeller University,

New York, New York, USA

Eugenie V. Mielczarek, Department of Physics and Astronomy, George Mason University,

Fairfax, Virginia, USA

Markolf Niemz, Medical Faculty Mannheim, University of Heidelberg, Mannheim, Germany

V. Adrian Parsegian, Physical Science Laboratory, National Institutes of Health,

Bethesda, Maryland, USA

Linda S. Powers, University of Arizona,

Tucson, Arizona, USA

Earl W. Prohofsky, Department of Physics, Purdue University, West Lafayette, Indiana, USA

Tatiana K. Rostovtseva,

NICHD, National Institutes of Health, Bethesda, Maryland, USA

Andrew Rubin, Department of Biophysics, Moscow State University, Moscow, Russia Michael Seibert, National Renewable Energy

Laboratory, Golden, Colorado, USA

David Thomas, Department of Biochemistry, University of Minnesota Medical School, Minneapolis, Minnesota, USA

More information about this series at http://www.springer.com/series/3740

Eric Hanssen Editor

## Cellular Imaging

Electron Tomography and Related Techniques



Editor
Eric Hanssen
Bio21 Institute Advanced Microscopy
Facility
University of Melbourne
Melbourne, VIC
Australia

ISSN 1618-7210 ISSN 2197-5647 (electronic) Biological and Medical Physics, Biomedical Engineering ISBN 978-3-319-68995-1 ISBN 978-3-319-68997-5 (eBook) https://doi.org/10.1007/978-3-319-68997-5

Library of Congress Control Number: 2017955245

#### © Springer International Publishing AG 2018

This work is subject to copyright. All rights are reserved by the Publisher, whether the whole or part of the material is concerned, specifically the rights of translation, reprinting, reuse of illustrations, recitation, broadcasting, reproduction on microfilms or in any other physical way, and transmission or information storage and retrieval, electronic adaptation, computer software, or by similar or dissimilar methodology now known or hereafter developed.

The use of general descriptive names, registered names, trademarks, service marks, etc. in this publication does not imply, even in the absence of a specific statement, that such names are exempt from the relevant protective laws and regulations and therefore free for general use.

The publisher, the authors and the editors are safe to assume that the advice and information in this book are believed to be true and accurate at the date of publication. Neither the publisher nor the authors or the editors give a warranty, express or implied, with respect to the material contained herein or for any errors or omissions that may have been made. The publisher remains neutral with regard to jurisdictional claims in published maps and institutional affiliations.

Printed on acid-free paper

This Springer imprint is published by Springer Nature
The registered company is Springer International Publishing AG
The registered company address is: Gewerbestrasse 11, 6330 Cham, Switzerland

#### **Preface**

Like most microscopists, I didn't fall in the mould as an undergraduate student. At the time I was certain I was destined to be a molecular biologist, never visualizing the actual samples I would be working on. I told myself that my research career would never involve any form of imaging, since I did not think it was interesting. A couple of years down the track I started my postgraduate studies and found myself, within 2 weeks of starting, in front of my first transmission electron microscope.

Almost immediately, I loved it, it must have been my inner artist shaping my future. However, I was frustrated by the fact that I was looking at a three-dimensional world in only two dimensions, so I set myself a challenge that I would one day progress to three-dimensional electron microscopy despite the fact that at that time it appeared to be nothing more than a good science fiction novel. Indeed, only a few specialized laboratories had the expertise to obtain three-dimensional datasets with an electron microscope. So instead, I spent the first decade of my research career honing my sectioning skills, as well as a few diamond knives, eventually progressing from single sections to a large number of serial sections. Since then a few years, along with a few laboratories and core facilities, have gone by, and the technologies permitting visualization of the "real" three-dimensional nanoworld have evolved and are now accessible to most researchers around the world.

Overall, it has been an interesting journey since the first book on electron tomography, edited by Joachim Frank, appeared in 1992. Even though no major new concepts have emerged in the last twenty years, the technology has evolved steadily. From stacks of thin serial sections to acquisition of tilt series in a transmission electron microscope, to even tilt series of serial sections, we have increased the resolution in the third dimension by an order of magnitude. While the microscopes have moved back from 400–1000 kV to 300 kV with the dissemination of field emission guns, the sample thickness of 300–500 nm has remained constant. Now it seems that the field is slowly moving towards scanning transmission electron tomography, which permits an increase in the thickness of the sample by at

vi Preface

least threefold to the micron range. Both techniques can be used on plastic sections or cryosections, but the latter avoids all the pitfalls and artefacts of chemical fixation. However, cryo-ultramicrotomy is not for the faint hearted and remains the "Holy Grail" for most of us. It also introduces a major artefact in the compression of sections and formation of crevasses. Yet new developments in the last 5 years will make this an artefact from the past with the preparation of focused ion beam cryo-lamellas instead of the cryosections. Though this is, for now, still only applied in a few laboratories that have the resources and more importantly the rare skill sets required. Dual beam microscopes have also seen an increased usage in biological sciences with the introduction of serial block face imaging where the microscope sequentially section and image the surface of the sample therefore creating a three-dimensional dataset at intermediate resolution between optical and transmission electron microscopy. The same techniques can be applied using a microtome inside the scanning electron microscope chamber creating virtual sections. Indeed the sections are actually accumulating on the surface of the knife and cannot be recovered.

So we have now moved full circle and are back to serial sections using the slightly less complicated tool that is the scanning electron microscope. Will this practice be the future of electron microscopy for the masses?

For now, all these techniques are complementary and one cannot replace fully the others. While plastic electron tomography is often seen as the poor parent of cryo-electron tomography, it is indisputable that the output in terms of number of samples per unit of time is far greater. In turn, cryo-ultramicrotomy is far faster than lamella preparation using focused ion beams, while block face imaging is for large samples at slightly lower resolution.

At the fringe of these three-dimensional techniques are applications that link them to the world of fluorescence microscopy and structural biology. On one side is array tomography, still using serial sections but with fluorescently labelled probes that let the scientist identify the otherwise grey blob. Or what used to be blobs, as subtomogram averaging is progressing fast, thanks to the direct electron detectors. This permits to do structural biology at a resolution not quite as high as single particle, but still below the 10 Å mark. The main advantage of this technique is to be able to place the structure in the context of the whole cell.

Furthermore, the acquisition of images is one thing, but the annotation and segmentation require some additional processing in order to be able to handle data with low signal-to-noise ratio (e.g. cryo-electron tomography).

Finally, the propagation of these techniques, their automation, and therefore the amount of data generated, have led to what are probably some of the biggest challenges the field has encountered and will have to face for the next few years: data storage and management. With these techniques going towards full automation some skills are likely to be lost, i.e. with the introduction of kits in molecular biology how many students still know what diatomaceous earth looks likes and

Preface vii

what it is used for? Electron microscopy is one of the remaining technologies where skill is everything. Will we survive the new era of automation?

Putting together this book was an interesting and challenging adventure. I was lucky enough to find academic and technical experts willing to spend a large amount of time writing these chapters. For this and their dedication and patience, I would like to thank all of the authors.

Melbourne, Australia

Eric Hanssen

### Contents

1	Elect	ron Tomography: A Primer	1			
	Andre	ew Leis				
	1.1	An Introduction to Electron Tomography	1			
	1.2	Principles of Electron Tomography	4			
	1.3	Sample Preparation for Electron Tomography	6			
		1.3.1 Scenario 1: Plastic sections	7			
		1.3.2 Scenario 2: Frozen-hydrated specimens	8			
	1.4	Radiation Damage	9			
	1.5	Acquisition of Projections	9			
	1.6	Special Acquisition Case: Block-Face SEM	12			
	1.7	Alignment of Projections	13			
	1.8	Reconstruction of an Aligned Tilt Series	15			
	1.9	Resolution	17			
	1.10	Post-reconstruction Image Processing	18			
		1.10.1 Segmentation and denoising	19			
		1.10.2 Template matching	20			
		1.10.3 Subtomogram averaging	21			
	1.11	Recommendations and Future Perspectives	22			
	1.12	The Importance of Sample Geometry	23			
	1.13	Conclusion	25			
	1.14	Protocol	26			
	Refer	ences	27			
2	STE	M Tomography in Biology	33			
		on Grayer Wolf, Eyal Shimoni, Michael Elbaum				
		and Lothar Houben				
	2.1	Introduction	33			
	2.2	Basics of STEM Imaging of Biological Material	35			
		2.2.1 Electron-Sample Interactions	35			
		2.2.2 STEM Contrast of Biological Samples	38			

x Contents

		2.2.3	Resolution and Thick Sample Effects	39
		2.2.4	Elemental Analysis	42
	2.3	STEM	Tomography	43
		2.3.1	Historical Background	43
		2.3.2	STEM Tomography of Thick Plastic-Embedded	
			Sections	45
		2.3.3	Cryo-STEM Tomography for Vitrified, Unstained	
			Cells	46
		2.3.4	CSTET and Elemental Analysis of Bacteria	47
		2.3.5	CSTET and Elemental Analysis	
			of Eukaryotic Cells	48
	2.4	Conclu	asions and Future Prospects	50
	2.5	STEM	Tomography Experimental Setup at the Weizmann	
		Institut	te	53
		2.5.1	CSTET data collection protocol	53
		2.5.2	Plastic section data collection	54
	Refe	rences		55
3	Elect	ron Cry	vo-Tomography	61
,			eira, Teige R. S. Matthews-Palmer and Morgan Beeby	01
	3.1		action	61
	3.2		Overview and Key Concepts	64
	3.3		nen Preparation for ECT	65
	5.5	3.3.1	Vitrifying Thin Specimens: Plunge-Freezing	66
		3.3.2	Vitrifying Thick Specimens: Strategies Towards	00
		2.2.2	Tractability	67
	3.4	Tilt Se	ries Acquisition	68
		3.4.1	Hardware Configuration	68
		3.4.2	Data Acquisition Software	71
		3.4.3	Data Collection: Electron Dose Considerations	73
		3.4.4	Data Collection: Choosing Microscope Defocus	74
		3.4.5	Data Collection: Magnification	74
		3.4.6	Data Collection: Tilt Scheme Considerations	74
		3.4.7	Data Collection: Energy Filters and Phase Plates	77
	3.5	Tomog	gram Reconstruction: From Tilt Series Data to	
			ical Insights	77
		3.5.1	Alignment	77
		3.5.2	Reconstruction	78
		3.5.3	Post-processing to Maximize Signal in Tomograms	79
		3.5.4	Visualization and Interpretation of Denoised	
			Tomograms	80
	3.6	Examp	oles of ECT	81
		3.6.1	Bacterial Cell Shape Maintenance	81
		3.6.2	The Eukaryotic Nuclear Pore Complex	84

Contents xi

	3.7	Future Challenges: What Do We Need from ECI	0.5
	2.0	E 23	85
	3.8	6	87
	3.9		87
	Bibli	ography	88
4	Larg	ge-Scale Electron Tomography of Cells Using SerialEM	
	and 1	IMOD	95
	Eilee	n O'Toole, Peter van der Heide, J. Richard McIntosh	
	and I	David Mastronarde	
	4.1		96
	4.2		99
	4.3	Using SerialEM for Automated Single Frame or Montaged	
		Serial Tilt Series Acquisition	99
	4.4	Using IMOD's Etomo Interface to Compute Basic Single	
		C	02
	4.5	The Etomo Batch Tomogram Interface	03
	4.6	Using IMOD's Join Interface to Stack Serial	
			04
	4.7	Using IMOD's 3dmod for Modeling Features in Serial	
		Reconstructions	06
	4.8	Special Topics: Increasing Area for 'Supermontage'	
			08
		4.8.1 Using SerialEM to Acquire Supermontage	
			08
		4.8.2 Using IMOD's Etomo Interface to Compute	
		$\mathcal{E}$	10
			10
		1	10
		8.1	11
			12
		$\epsilon$	12
			12
	4.9		13
	Refer	rences	14
5	Volu	me Scanning Electron Microscopy: Serial Block-Face	
		ning Electron Microscopy Focussed Ion Beam Scanning	
	Elect	tron Microscopy	17
		ard I. Webb and Nicole L. Schieber	
	5.1	Introduction	17
	5.2	Volume Scanning Electron Microscopy—SBEM	
		and FIB-SEM	18

xii Contents

		5.2.1 Sample Processing	122
		5.2.2 Imaging	124
	5.3	Serial Block-Face Scanning Electron Microscopy	
		(SBF-SEM or SBEM).	126
		5.3.1 Sample Processing	126
		5.3.2 Sample Setup and Mounting	129
		5.3.3 SBEM Operation	130
	5.4	Focused Ion Beam Scanning Electron Microscopy	134
		5.4.1 Sample Processing	135
		5.4.2 Sample Setup and Mounting	137
		5.4.3 FIB-SEM Operation	139
	5.5	Discussion	141
	Refer	ences	143
6	Conj	ugate Immunofluorescence—SEM Array Tomography	
	for S	tudying Mammalian Synapses and Axons	149
	Kristi	na D. Micheva and Kristen D. Phend	
	6.1	Introduction/Background	149
	6.2	Approaches to Large-Scale Molecular and Ultrastructural	
		Imaging	150
	6.3	Array Tomography: A Different Kind of Tomography	153
	6.4	Array Tomography Sample Preparation: Workflow and	
		General Considerations	155
	6.5	Array Tomography: Computer Assisted Imaging of Serial	
		Sections on Rigid Substrates	159
	6.6	Application of Conjugate IF-SEM Array Tomography	
		for the Study of Mammalian Synapses and Axons	161
	6.7	Variations of the Method	164
	6.8	Detailed Protocol for Conjugate IF-EM AT Using Freeze	
		Substitution and Embedding in Lowicryl HM-20	166
	6.9	Conclusions	179
	Refer	ences	179
7		ment of Tilt Series	183
1		erguet, C. Messaoudi, C. O. S. Sorzano and S. Marco	103
	7.1	Why Do We Need to Align Tilt Series?	102
	7.1		183 185
	1.2	Standard Alignment Process	
		7.2.1 Precentering the Tilt Series	186
	7.2	7.2.2 Determining the Orientation of the Tilt Axis	190
	7.3	Advanced Alignment Methods	194
		7.3.1 Multiscale Registration	194
	<i>a .</i>	7.3.2 Invariant Feature Recognition	197
	7.4	Extension to Data Other than Tilt Series	203
		7.4.1 Data Alignment in Multiple-Axis Tomography	203

Contents xiii

		7.4.2	Serial Images Alignment	204
	7.5	Conclus	sion	205
	Refere			205
8			Reconstruction from Electron Micrographs	209
		nard He	•	
	8.1	_	les of Reconstruction	209
	8.2	_	tive Reconstruction	211
		8.2.1	Weighted Back-Projection (WBP)	213
		8.2.2	Frequency Space Reconstruction (FSR)	213
	8.3		e Reconstruction	214
		8.3.1	The Starting Volume	216
		8.3.2	Calculating the Projection Difference	216
		8.3.3	Updating the 3D Map Volume	218
		8.3.4	The Number of Iterations	218
	8.4	Real Sp	pace Pre-processing	219
		8.4.1	Normalizing Images	220
		8.4.2	Removing High Contrast Features	220
		8.4.3	Removing Extraneous Areas	220
		8.4.4	Denoising	221
	8.5	Contras	t Transfer Function (CTF) Correction	221
		8.5.1	CTF Theory	221
		8.5.2	Determining CTF Parameters	222
		8.5.3	Correcting for the CTF	223
	8.6	Denoisi	ing	223
		8.6.1	Low-Pass Filter	224
		8.6.2	Iterative Median Filter	224
		8.6.3	Bilateral Filter	224
		8.6.4	Mean Shift Filtering	225
		8.6.5	Non-local Means Filter	225
		8.6.6	Beltrami Flow: Isotropic Diffusion	226
		8.6.7	Non-linear Anistropic Diffusion (NAD)	226
	8.7	Informa	ation Recovery	226
		8.7.1	Missing Information	226
		8.7.2	Recovering Missing Information	227
		8.7.3	Visual Assessment	227
		8.7.4	Resolution Estimation	227
	8.8	Subtom	nogram Reconstruction	230
		8.8.1	3D Alignment and Averaging	230
		8.8.2	2D Alignment, Reconstruction and Averaging	230
		8.8.3	Model-Based Averaging	230
	8.9	Conclus	sion	231
	Refere			231

xiv Contents

9			iology in Situ Using Cryo-Electron Subtomogram	225
			177 111 777	237
			and Friedrich Förster	205
	9.1		action	237
	9.2		ing the Resolution of Volumetric Data by Averaging	238
	9.3		E Localization	238
		9.3.1	Template-Free Approaches	238
		9.3.2	Template Matching	239
		9.3.3	Peak Selection After Template Matching	240
		9.3.4	Example Dataset	240
	9.4		nogram Alignment	242
		9.4.1	Scoring Strategies	242
		9.4.2	Sampling Strategies	243
		9.4.3	Example Dataset	244
	9.5	Subton	nogram Classification	246
		9.5.1	Uncoupled Alignment and Classification	246
		9.5.2	Simultaneous Alignment and Classification	246
		9.5.3	Example Dataset	247
	9.6	Availal	ble Software	248
	9.7	Selecte	ed Recent Applications of Subtomogram Averaging	248
		9.7.1	Ribosomes	248
		9.7.2	Other Cytosolic Complexes	249
		9.7.3	Membrane Protein Complexes	250
	9.8	Practic	al Section: Step-by-Step Guide for Subtomogram	
			is Using av3 and PyTom	251
		9.8.1	Template Matching and Peak Selection	251
		9.8.2	Extraction and Alignment of Subtomograms	253
		9.8.3	Classification of Subtomograms Using CPCA	
			and Kmeans Clustering	254
	Refer	ences		255
10	Resol	lution in	Electron Tomography	261
		ail Kudr		
	10.1	Introdu	iction	261
	10.2		Imposed by Sample Preparation	263
		10.2.1	Sectioning- and SEM-Based Methods	263
		10.2.2	Imaging Cryo Preserved Samples	265
	10.3	Resolu	tion of Tomographic Reconstructions	266
		10.3.1	Geometric Limits	266
		10.3.2	TEM Electron Optical Limits	269
		10.3.3	STEM Tomography	272
		10.3.4	Measuring the Resolution of Tomograms	272
	10.4		of Subtomogram Averaging	273
		10.4.1	Alignment of Subtomograms to the Average	

Contents xv

		10.4.2 Limited Number of Particles	276
		10.4.3 Structural Heterogeneity	277
		10.4.4 Data Collection Strategy	277
		10.4.5 Image Processing	278
	10.5	Conclusion and Overview	278
	Refer	ences	279
11	Signa	l Optimization in Electron Tomography	283
	Maur	o Maiorca and Peter B. Rosenthal	
	11.1	Introduction	283
	11.2	Signal Optimisation in the Fourier Domain	285
		11.2.1 Fourier Transforms	285
		11.2.2 Bandpass Filters	286
		11.2.3 Gaussian Filter	288
	11.3	Signal Optimization in Real Space	288
		11.3.1 Median Filter	289
		11.3.2 Physical Model of Linear Diffusion	290
		11.3.3 Non-Linear Diffusion.	291
		11.3.4 Edge Enhancing Diffusion (EED)	292
		11.3.5 Bilateral Filter	294
	11.4	Pre-Reconstruction Approaches	295
	11.5	Conclusion	298
	Refer	ences	299
12	Segm	entation of Features in Electron Tomographic	
	Reco	nstructions	301
	Niels	Volkmann	
	12.1	Introduction	301
	12.2	Membrane Segmentation	303
	12.3	Segmentation of Large Macromolecular Assemblies	306
	12.4	Segmentation of Filamentous Structures	308
	12.5	Outlook and Conclusions	311
	Refer	ences	313
Ind	OV		210

#### **List of Contributors**

Morgan Beeby Department of Life Sciences, Imperial College London, London, UK

**J. Bernard Heymann** National Institute of Arthritis, Musculoskeletal and Skin Diseases, National Institutes of Health, Bethesda, MD, USA

Michael Elbaum Department of Materials and Interfaces, Weizmann Institute of Science, Rehovot, Israel

**Josie L. Ferreira** Department of Life Sciences, Imperial College London, London, UK

**Friedrich Förster** Department of Molecular Structural Biology, Max-Planck Institute of Biochemistry, Martinsried, Germany; Cryo-Electron Microscopy, Bijvoet Center for Biomolecular Research, Utrecht University, Utrecht, The Netherlands

**Peter van der Heide** Institute for Molecular Bioscience, Queensland Bioscience Precinct, The University of Queensland, Brisbane, Australia

**Lothar Houben** Electron Microscopy Unit, Department of Chemical Research Support, Weizmann Institute of Science, Rehovot, Israel

**Mikhail Kudryashev** Max Planck Institute for Biophysics, Frankfurt am Main, Germany; Buchmann Institute for Molecular Life Sciences, Goethe University of Frankfurt am Main, Frankfurt am Main, Germany

**Andrew Leis** CSIRO Australian Animal Health Laboratory, Geelong, VIC, Australia

Mauro Maiorca Francis Crick Institute, London, UK

**S. Marco** Institut Curie, Centre de Recherche, Centre Universitaire, Orsay Cedex, France

xviii List of Contributors

**David Mastronarde** Department of MCD Biology, University of Colorado, Boulder, CO, USA

**Teige R. S. Matthews-Palmer** Department of Life Sciences, Imperial College London, London, UK

C. Messaoudi CNRS UMR9187, Centre Universitaire, Orsay Cedex, France

**Kristina D. Micheva** Department of Molecular and Cellular Physiology, Stanford University School of Medicine, Stanford, CA, USA

**Eileen O'Toole** Department of MCD Biology, University of Colorado, Boulder, CO, USA

**Stefan Pfeffer** Department of Molecular Structural Biology, Max-Planck Institute of Biochemistry, Martinsried, Germany

**Kristen D. Phend** Department of Cell Biology and Physiology, University of North Carolina, Chapel Hill, NC, USA

**J. Richard McIntosh** Department of MCD Biology, University of Colorado, Boulder. CO, USA

Peter B. Rosenthal Francis Crick Institute, London, UK

**Nicole L. Schieber** Cell Biology and Biophysics Unit, European Molecular Biology Laboratory (EMBL), Heidelberg, Germany

**Eyal Shimoni** Electron Microscopy Unit, Department of Chemical Research Support, Weizmann Institute of Science, Rehovot, Israel

**C. O. S. Sorzano** Biocomputing Unit, National Center of Biotechnology (CSIC). C/Darwin, Madrid, Spain

A. Verguet INSERM U1196, Centre Universitaire, Orsay Cedex, France

**Niels Volkmann** Sanford Burnham Prebys Medical Discovery Institute, La Jolla, CA, USA

**Richard I. Webb** Centre for Microscopy and Microanalysis, The University of Queensland, Brisbane, QLD, Australia

**Sharon Grayer Wolf** Electron Microscopy Unit, Department of Chemical Research Support, Weizmann Institute of Science, Rehovot, Israel

#### **About the Editor**

Eric HanssenEric Hanssen studied molecular biology at the Université Blaise Pascal in France. He then spent four years at the Université Claude Bernard in Lyon, France, where he worked on his Ph.D. titled: "Molecular and ultrastructural studies of fibrillin containing microfibrils in elastic tissues. Evolution of fibrillin during ageing". This work involved the development of molecular tools, antibodies and RNA probes, to study extracellular matrix by electron microscopy. He then acquired his first postdoctoral experience as a "Fondation pour la Recherche Medicale" Fellow and Australian Research Council IREX Fellow at the University of Adelaide in South Australia. His main research field remained in extracellular matrix and elastic tissue, applying molecular biology tools and immuno-electron microscopy. He then moved on to La Trobe University to develop new imaging technique involving x-rays and electrons with a strong emphasis on three-dimensional imaging of red blood cells infected with the malaria parasite, Plasmodium falciparum. He is now an Associate Professor at the Bio21 Molecular Science and Biotechnology Institute where he heads the Advanced Microscopy Facility and focusses on cellular three-dimensional imaging.

## **Chapter 1 Electron Tomography: A Primer**

**Andrew Leis** 

**Abstract** This chapter is an introduction to the theory and practise of electron tomography. It identifies the areas in need of most attention to maximise the efficiency of descriptive studies of morphology, and in the case of structural biology, to enable the transition from a reductionist approach to in-depth systems biology. The chapter concludes with a step-by-step guide to acquiring tomograms.

#### 1.1 An Introduction to Electron Tomography

Electron tomography provides the unique possibility to view three-dimensional (3D), nanometre-scale detail within the cellular context (for detailed reviews, see [1–3]). It is one of a small group of bioimaging technologies that utilise electrons or photons to deliver 3D information about structural complexity spanning macromolecules, viruses, cells and tissues. These techniques include confocal microscopy, some forms of super-resolution microscopy, and soft X-ray tomography, albeit with differing means of generating contrast, and overlapping resolution. With proper attention to structural preservation, these techniques are capable of capturing and deciphering cellular events such as the workings of protein machines in healthy cells [4] and in disease, a special case being the morphogenesis of infectious agents [5–8]. The common feature of these techniques is the ability to image hydrated (or frozen-hydrated) specimens. Confocal and super-resolution microscopy techniques visualise fluorescent 'spots' rather than actual densities but they also provide unambiguous identification and possibly some temporal resolution. Furthermore, the spatial information can be decisive, as is the case for fluorescence ('Förster') resonance energy transfer (FRET) analysis of protein-protein interactions [9]. Cryo- electron tomography captures snapshots of true densities within the cellular landscape but given the prospects for macromolecular crowding, especially in prokaryotes [10, 11]

1

A. Leis (\subseteq)

CSIRO Australian Animal Health Laboratory, Private Bag 24, Geelong, VIC 3222, Australia

e-mail: leisandrew@gmail.com

and the similarities of many complexes at the best, attainable resolution, it can be more difficult to assign structure or determine interactions without explicit, *a priori* information. Therefore, this group of techniques should be considered together as a complementary and powerful means of determining structure-function relationships in cells [12]. Correlative light and electron microscopy (CLEM, [13–17]) seeks to apply such technologies in combination for the elucidation of structure-function relationships.

From an instrumentation perspective, electron tomography belongs to the group of electron microscope -based technologies capable of generating 3D structures, collectively referred to as '3D electron microscopy' (3DEM, [18]). 3DEM comprises four, independent strategies (Fig. 1.1). Three of these utilise a transmission electron microscope (TEM) as a projection device, while a third uses a scanning electron microscope (SEM). The first of the TEM strategies—electron tomography—constitutes the main theme of this book. The second TEM technique employs a scanning transmission electron microscope (STEM, Wolf, Chap. 2). This technique has the advantage of being able to analyse thicker specimens and with enhanced contrast

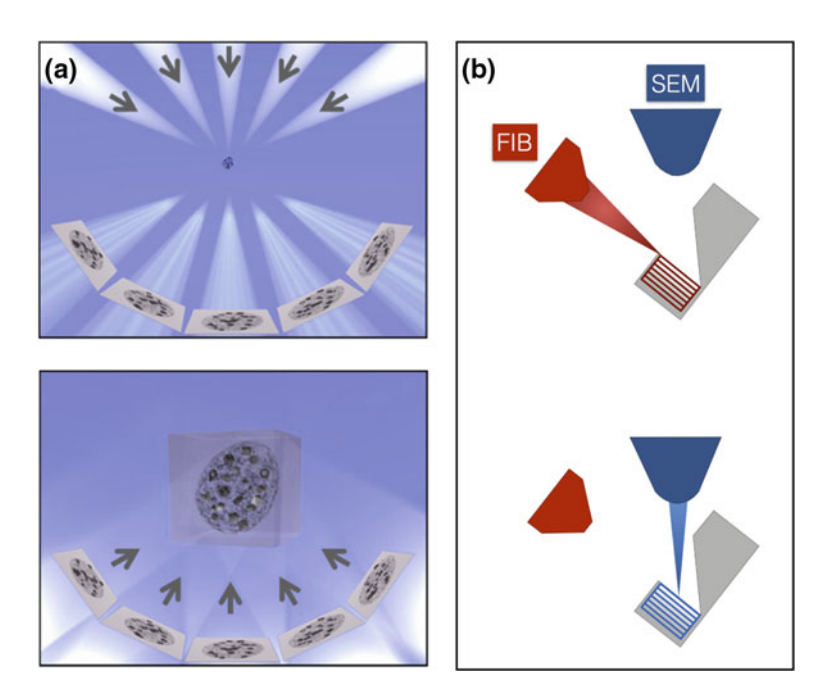


**Fig. 1.1** Imaging geometries for electron tomography. **a** TEM and STEM tomography. 2D projections acquired from a 3D object (upper panel) are back-projected to provide the solution to the structure (reproduced from [1], with permission from Nature Publishing Group); **b** serial-block-face SEM tomography. Fresh layers of the specimen are removed (sputtered) sequentially using a focussed gallium ion beam (FIB). As each layer is removed, the freshly revealed block surface is imaged by a scanning electron microscope (SEM) to build up a 3D volume

compared to bright-field TEM [19, 20], noting that phase plates now offer a solution for the latter. A third TEM technique—single-particle analysis (SPA)—should be considered separately as a powerful means of determining the structures of identical or nearly identical copies of macromolecules or symmetrical (principally, icosahedral) viruses. SPA will be discussed briefly to introduce certain concepts, and for the sake of completeness. The SEM tomography technique, serial block-face imaging, utilises a scanning electron microscope in conjunction with a sectioning device. either a diamond knife [21] or an ion beam [22–26], to build up a three-dimensional volume, layer by layer, analogous to the operating principle of a confocal microscope. At present, this technique is practised on plastic-embedded specimens. It is covered in detail in Chap. 5. To complete this short overview of tomography strategies, it is worth mentioning the technique known as 'array tomography'. Although best known from fluorescence microscopy, it is equally applicable to the serial-block-face technique or indeed, in combination (Chap. 6). It allows large-scale surveys of classical ultrastructure afforded by serial block-face imaging but in combination with the mapping of fluorescent epitopes. Like serial block-face imaging, however, it is not suited to studies of molecular structural biology.

Finally, we can define a category of biophysical techniques that provide superior resolution to electron tomography but with the caveat that the structures are generated from isolated and purified entities that are thus removed from the cellular context. The resulting structures can be used for visual proteomics interrogations of cellular interaction networks. These techniques are the standard techniques of structural biology, and include X-ray crystallography as well as single-particle analysis (cryo-) electron microscopy. As mentioned above, SPA is a reductionist approach to solving structure that takes advantage of statistical sampling ex vivo. The term 'single-particle' is a misnomer because the technique takes into account as many particles as can be sampled efficiently, typically tens of thousands, rather than a unique occurrence of a molecule within its native context. SPA is related to crvoelectron tomography in terms of common sample preparation and bright-field, low-dose imaging conditions. It may begin with air-dried and stained preparations because these structures serve as useful starting models for computational refinement of frozen-hydrated data. Unlike X-ray crystallography, SPA does not have a requirement for crystals, and it can cope with large, multi-unit complexes as well as some heterogeneity. For comprehensive reviews of SPA in structural biology and virology, the reader is referred to detailed reviews [27–33]. Modern structural biology increasingly aims to harness the synergies of these techniques when used in combination ('hybrid techniques', [34]). In particular, the high-resolution structures can be used to populate tomograms of cells via the process of pattern recognition in real space (see 'Template Matching'). Thus, it is important to consider tomograms generated by electron tomography as complete maps of a cell's proteome, where (dose-) limited resolution can be circumvented to produce a 'pseudo-atomic atlas' of the macromolecular machinery that underlies cellular function [1].

The definition of electron tomography used in this book includes TEM/STEM tomography as well as the newer SEM strategies. It therefore expands upon the

4 A. Leis

definition provided in the most recent textbook on electron tomography [18], which suggests that it should loosely incorporate strategies where the specimen is tilted. The revised definition reflects the recent success of approaches for building up 3D volumes by SEM, which was previously regarded almost exclusively as a 'surface' technique. This chapter will introduce the principles of TEM- and SEM-based electron tomography, recent technological developments, and selected contributions to cell and structural biology. It cannot possibly do justice to the published applications of electron tomography. For recent, general reviews, the reader is referred to references [3, 35]. Other recent reviews cover application of electron tomography to viruses [30, 36] and prokaryotes [37], while newer publications enabled by low-temperature nanofabrication showcase novel insights and possibilities for the biology of 'higher' organisms [38–41].

#### 1.2 Principles of Electron Tomography

The TEM strategy for electron tomography is analogous to medical X-ray imaging (computed tomography—'CT' or 'CAT' scans) in that it uses projections of a specimen recorded from different viewing angles and back-projects them into Fourier Space (syn. frequency domain) to calculate a real-space (syn. position space) reconstruction of the 'specimen' (Fig. 1.2). The main difference to computed tomography in terms of image acquisition is the tilting of the specimen in electron tomography compared to tilting of the imaging gantry during computed tomography, although a concept for a tilting electron microscope has been published [42]. Note also that 'soft' X-ray tomography of cells utilises a fixed X-ray source or synchrotron beamline and either a rotating or tilting sample holder. A TEM goniometer and sample holder are used for the latter. TEM tomography is used routinely for specimens that have undergone a substitution process to replace the sample's water with a plastic resin, which in turn can be sectioned and introduced into the microscope using a standard sample holder. This technique is useful for studies of ultrastructure, such as the arrangements of organelles [43] or studies of e.g. membranes during virus morphogenesis [44, 45]. A variation of this protocol with additional contrast agent is used for serial-block-face SEM tomography [46] (see Chap. 5 and below). Cryo- electron tomography (or electron cryotomography, Chap. 3) is the method of choice for appropriately thin, frozen-hydrated specimens, where structural accuracy is paramount, i.e. the density map reflects the true nature of the feature rather than added contrast agent, the accumulation of which depends on its relative affinity for the different regions of a molecule.

So-called 'single-particle analysis' 3D electron microscopy uses projections of many copies of identical or nearly identical, frozen-hydrated macromolecules or viruses to build up a 3D reconstruction. This powerful, biochemical reductionist approach combines computational averaging of many copies of identical or nearly identical, randomly orientated molecules with statistical suppression of noise to generate a composite structure of the molecule at a resolution typically better than

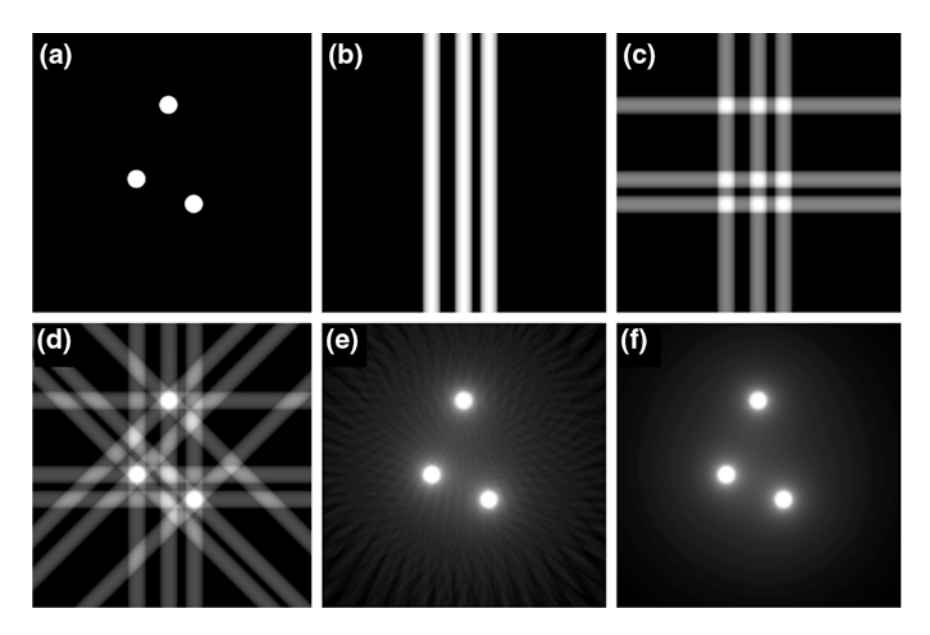


**Fig. 1.2** Application of the Radon Transform to mock, 2D data (adapted from Linaroudis [47]). **a** Original 'features'; **b** one projection; **c** 2 projections; **d** 4 projections; **e** 45 projections; **f** 180 projections. In each case, the projections are equidistant and span the full angular range

10 Å (reviewed in [31, 33, 48]). The sample is usually not tilted; exceptions are the random conical tilt and related orthogonal tilt methods [49]. Instead, the typically reasonable assumption is made that the macromolecules or viruses lie in random orientations with respect to the beam. These different views of the 'same' structure contribute more or less equally to the structure solution, and deviations from similarity become apparent in the 'class averages' representing the different orientations. Apart from its similar requirements for a TEM and image processing, single-particle analysis bears little relationship to the subject of this book, electron tomography, except that the structures it generates can be used to populate tomograms of cells in the strategy known as 'visual proteomics' [1, 38, 50–53]. As such, it belongs to a separate category of nominally 'high-resolution' techniques that includes X-ray crystallography but also NMR spectroscopy. Another reason for mentioning it here is that similar computational approaches can be applied to symmetrical and/or repetitive structures in tomograms to enhance local resolution. This is known as subtomogram averaging [54], and forms the subject of Chap. 9.

The structure of the Herpes simplex virus (Fig. 1.3) provides an elegant demonstration of this approach because each mature virus contains both pleomorphic and symmetrical components [55]. The resolution for the symmetrical components can be enhanced post-acquisition. Thus, even though electron tomography produces a comparatively modest resolution compared to single-particle analysis of wholly symmetrical viruses [56], it is unique in its ability

6 A. Leis

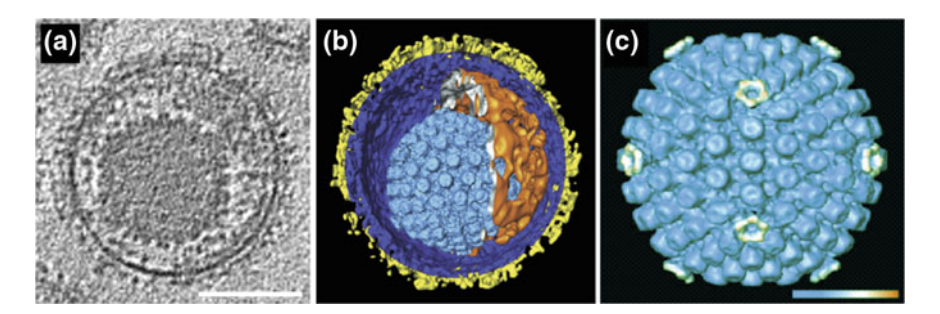


**Fig. 1.3** Electron tomography samples pleomorphic and symmetrical structures. The three-dimensional structure of individual herpesviruses at modest resolution was sufficient to visualise individual glycoprotein spikes (yellow) on the virus surface. Computational extraction of a modest number of nucleocapsids (n = 11) followed by averaging and applying icosahedral symmetry resulted in a substantial improvement in local resolution [55]. Scale bar = 100 nm. Reproduced with permission from the American Association for the Advancement of Science

to generate structures for pleomorphic specimens at a resolution of better than 10 nm. Furthermore, tomograms of cells can be archived and refined locally when improved structures become available. In the context of cell biology and virology, this is extremely important: all cells are pleomorphic, and they are subject to stochastic variability. They may contain symmetrical or repetitive structures, *e.g.* icosahedral viruses but tomography is needed to visualise the cellular landscape. On the other hand, the use of single-particle averaging for determining the structure of wholly symmetrical viruses is well established and represents a mature technology [57].

#### 1.3 Sample Preparation for Electron Tomography

The ability of electron tomography to generate authentic structures at a resolution of better than 10 nm emphasises the requirement for suitable, resolution-preserving sample preparation procedures. All forms of sample preparation require a fixation (immobilisation) step to stabilise the structures and maintain their spatial relationships when introduced into the vacuum environment of the electron microscope. The classical approach is chemical fixation using aldehyde-based cross-linkers, which are easily criticised as artefacts. Physical immobilisation by rapid freezing can be used instead, and it is used exclusively for cryo- electron tomography, as well as for single-particle analysis. In brief, vitrification means that with sufficiently fast cooling rates, water is transformed into an amorphous solid that is thought to resemble liquid water, and which is (meta) stable during controlled image acquisition. This is referred to as the 'frozen-hydrated' state.

Before discussing the different methods for acquiring, aligning, reconstructing and segmenting tomograms (see following sections), it is first necessary to mention the characteristics of the specimens that determine the imaging conditions and image-processing strategies. For example, beam-sensitive, frozen-hydrated specimens require a dedicated, low-dose acquisition scheme, and the resultant noisy reconstructions benefit from denoising to aid in surface rendering ('segmentation', see later). Stained plastic sections of membrane-rich cells, on the other hand, are more amenable to automated segmentation routines; these are suitable for characterising ultrastructure rather than studying molecular arrangements and interactions.

#### 1.3.1 Scenario 1: Plastic sections

The classical TEM protocol developed for biological samples comprises aldehyde fixation, dehydration in a graded alcohol series, infiltration with resin, heat-induced polymerisation and sectioning using an ultramicrotome. This procedure was the mainstay of biological electron microscopy in the second half of the twentieth century [58], and with mostly subtle variations, it continues to be the most widely used strategy for studies of cell ultrastructure. Refined versions of this protocol bypass chemical fixation in favour of rapid freezing and progressive solvent substitution at low temperature, culminating in a UV-polymerised resin block that can also be sectioned by ultramicrotomy. This improvement avoids the artefacts of chemical fixation, although it is difficult to study alterations that occur after freezing. As for any vitrification process, with or without added cryoprotectant, it depends critically on specimen thickness. Nevertheless, the freeze-substitution process has been studied systematically from a process perspective, and it was shown that the processing time can be reduced from days to as little as 3 h [59]. Structural preservation after freeze-substitution is clearly superior to structure visualised after the use of chemical fixatives. In either case, sections need to be cut as thin as possible without eliminating the feature of interest. In practical terms, this is dictated by the accelerating voltage of the microscope. Sections of nominal thickness 80-90 nm are suitable for electron tomography using a 120 kV TEM, whilst thicknesses up to 300 nm represent the maximum thickness for use in 300 kV instruments whilst still avoiding the possibility of multiple scattering events [52] that degrade resolution.

Although freeze substitution is superior to classical fixation and embedding, it is highly informative to revisit the use of powerful (1 MV) transmission electron microscopes as projection devices but without the benefits of adequate structural preservation. This led to the flawed 'microtrabecular lattice' concept of cell structure [60]. Here, removal of solvent and/or fixation with glutaraldehyde caused the soluble components of the cytosol to be deposited on elements of the cytoskeleton, portraying mammalian cells erroneously [61] as an irregular network of cross-linked 'microtrabeculae' (Fig. 1.4). Porter interpreted these observations as the fundamental organisation of the cytoplasm, the physical basis for cytoplasmic motility, and the determinants of cell shape [61]. In the absence of tomography, he made use of stereo pairs to demonstrate his results.

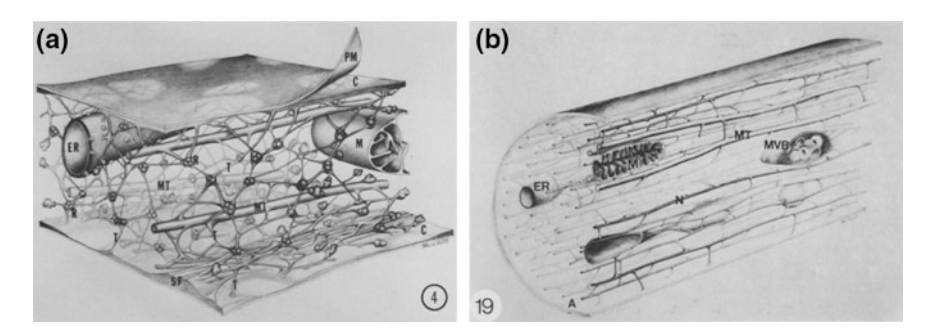


**Fig. 1.4** Models of Porter's microtrabecular lattice [60] and axonal lattice [62]. The decorated cytoskeleton is largely the result of soluble components of the cytosol having 'nowhere to go', and agglomerating onto the cytoskeleton. Crosslinks are also difficult to reconcile. Reproduced with permission of The Rockefeller University Press

Porter's rather exhaustive efforts to corroborate his findings preceded cryo-EM, and they did not survive scrutiny when it was shown that similar features could be induced in homogeneous solutions of serum albumin [63]. The methods that led to the erroneous microtrabecular lattice concept have been superseded by cryofixation followed by freeze-substitution, or by cryo-EM. At present, only cryo-EM of a sufficiently thin, vitreous specimen can guarantee a faithful reproduction of the cell interior. New technical developments in cryo-EM are beginning to allow the study of eukaryotic cells [39, 40, 64, 65].

#### 1.3.2 Scenario 2: Frozen-hydrated specimens

Electron tomography of frozen-hydrated specimens is detailed in Chap. 2. Most commonly, the specimens (isolated macromolecules, viruses, organelles; intact cells) are vitrified by plunging into liquefied ethane. If sufficiently thin—as dictated by the accelerating voltage—tomograms can be recorded directly. Thicker, frozen-hydrated cells can be thinned on the sample support grid using a cryogenically-cooled focussed ion beam setup prior to transfer to the TEM (see [66] for details). Alternatively, a cellular sample can be vitrified by high-pressure freezing and then vitreously sectioned using e.g. a cryo-ultramicrotome. For all manipulations that follow the vitrification step, it is essential to maintain the specimen at a temperature colder than the devitrification temperature (-137 °C/136 K) to avoid a phase transition from an amorphous state to cubic crystalline ice. Focussed ion beam (FIB) sample fabrication at cryogenic temperatures is an emerging technology that is still practised by a handful of specialist cryo-tomography laboratories but its benefits have been realised recently [67–69], and they are highly convincing. The major breakthrough is that it enables studies of plant and animal cells by cryo- electron tomography where previously, the technique was restricted to isolated macromolecules, viruses and small cells such as bacteria that could be plunge frozen from suspensions and visualised directly [66]. Where available,

cryo-FIB followed by TEM tomography essentially supersedes cryo- electron microscopy/tomography of vitreous sections (CEMOVIS/CETOVIS) because it does not suffer from the unavoidable artefacts that plague knife-cut sections. These include significant compression (>30%), and further deformations that occur during cutting or attachment to a support grid. Nevertheless, tomography of vitreous sections led to key breakthroughs including the first demonstration of ATP synthases in mammalian cells [64], and the discovery of the mycobacterial outer membrane [70, 71].

#### 1.4 Radiation Damage

An electron beam represents a form of ionising radiation, collimated into a small area such that all specimens, whether frozen or plastic-embedded, are prone to significant and irreversible damage. In TEM tomography, the need to acquire all of the projections from the identical region of interest places an ultimate limit on the amount of information that can be acquired. It is therefore critical to know how to measure and control the electron dose, and to keep this dose at subcritical levels. In frozen-hydrated specimens, radiation (colloq., 'beam') damage can be seen in the form of gas bubbles that are generated as a result of radiolysis. Perhaps more critically, this is preceded by more subtle damage that can erase fine detail. The consequence of an upper limit to the cumulative electron dose is that it must be estimated before exposure of the specimen. Too little dose may lead to difficulty in acquisition (failed position tracking, for example) but more importantly, it results in a poor yield of information. The cumulative dose during tilt-series acquisition should not exceed 100 e<sup>-</sup>/Å<sup>2</sup> [3].

For plastic sections, deformations in the form of shrinkage and mass loss are profound [72]. It is common practice to pre-irradiate the specimen, which allows it to undergo a rapid shrinkage phase before acquisition of the tilt series. Here, successful alignment of tomograms is dependent on comparatively minor changes between subsequent projections. This practise is addressed systematically in Chap. 4. In the author's experience, a tomographic reconstruction of an Epon section with nominal (microtome) section thickness of 150 nm will approximate 110 nm, even when using low-dose acquisition techniques and cooling the specimen in a cryo- sample holder. The final thickness also appears to be quite variable. Quantitation from plastic sections is not possible without bold assumptions concerning distortions. Furthermore, these distortions are not isotropic. Even for pre-irradiated plastic sections, it is advisable to use low-dose acquisition techniques as described below. This helps to facilitate subsequent alignment.

#### 1.5 Acquisition of Projections

We have already noted that tomograms comprise multiple views of the same object. We will first discuss the considerations for acquisition of cryo tomograms. Gordon *et al.* [73] summarise the electron tomography problem as the necessity to "reconstruct

10 A. Leis

a picture from a finite subset of its projections taken at distinct angles." Completeness of information, however, depends on sampling statistics. For cryo- electron tomography, this is an apparent paradox. The requirement for as many projections as possible while covering the full angular range conflicts with the need to keep the electron dose at subcritical levels to avoid erasing details. This means that a finite electron dose is typically fractionated over the available tilt range. The "dose fractionation theorem" [74, 75] states that the dose tolerated by the specimen can be divided by the number of contributing projections to provide the maximum permissible dose for any one projection image of the tilt series. A negligible proportion of the dose is expended on secondary tasks such as searching, tracking, and focussing, and ideally, tracking and focussing are performed at adjacent positions along the tilt-axis (Fig. 1.5) so that all of the available dose is used for acquiring structural information. Projection images obtained with a low-dose collection strategy have poor signal-to-noise (SNR) characteristics; however, contrast is restored by tomographic reconstruction and subsequent visualisation of each "virtual" slice. Energy filters operating in "zero-loss"

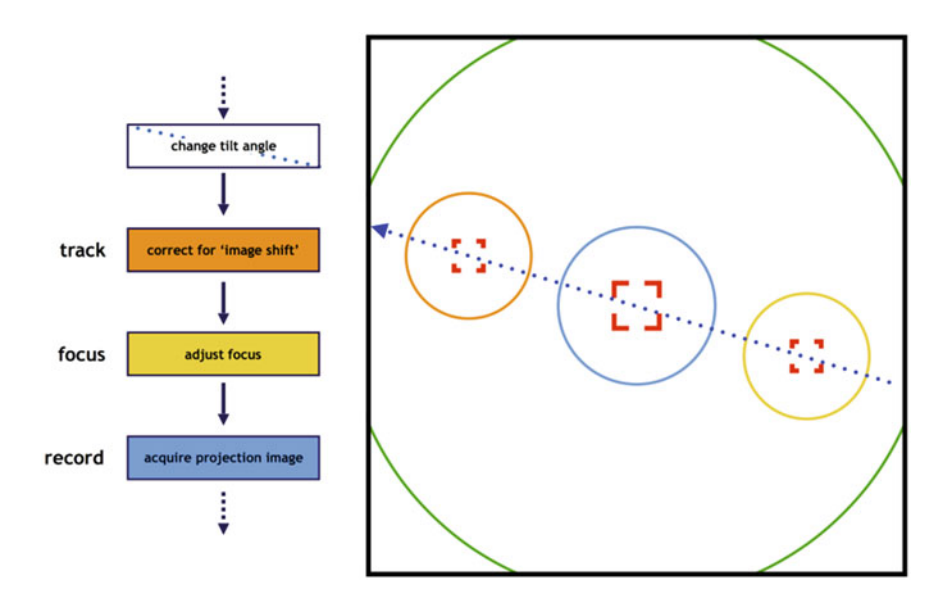


Fig. 1.5 Schematic of simplified acquisition scheme for low-dose electron tomography. After searching for the region of interest (outer circle indicating spread beam and low flux), the beam position and other parameters for the exposure are copied to focus and tracking states, which are positioned along the tilt axis using the image shift function. The beam is then re-directed to the detector for these 'off-axis' states. This restricts all secondary tasks to areas adjacent to the target region, meaning that exposure of the target is solely for the purposes of collecting data. The beam blank function is used to ensure that exposure is limited to the times specified (while reading out the data, for example). The areas captured by the detector are shown by photo corners, and the tilt axis is indicated by a blue dotted line. To expedite the process, modifications such as comparatively higher dose and partial detector readout are commonly made to the tracking and focus states. Also, it is possible to identify multiple targets and automate serial tomogram collection

mode remove contributions from inelastically scattered electrons [76] that cause image blur. The combination of moderate accelerating voltage (300 kV) and an energy filter therefore compensate for the poor SNR characteristics inherent in frozen specimens. They also facilitate tomography on slightly thicker specimens but with a concomitant trade-off in resolution. Note that, for unstained (cryo) specimens, SNR is discussed in preference to contrast, the latter of which can be enhanced artificially. Contrast enhancement does not suppress noise.

In cryo- electron tomography, the radiation sensitivity of the frozen-hydrated specimen means that tomograms comprise only about half as many projections as for plastic sections, collected at increments of 1.5 or 2 degrees. Further complications arise from the increase in apparent thickness of the slab-shaped sample during tilting and ultimately, the limited range of the tilt holder/sample grid combination. This gives rise to the so-called "missing (information) wedge", which describes the unsampled region in Fourier space. The information deficit results in a real-space artefact whereby features parallel to the electron beam appear to be smeared, while features orthogonal to the beam are unresolved. A  $\pm$  70° tilt range provides 78% of the available information but with an anisotropic, i.e. biased, representation of information. A dual-axis acquisition scheme [77, 78] addresses the fundamental geometric bias. In this acquisition scheme, a complementary series of projections is acquired from the orthogonal axis and merged with the initial tilt series. If the second tilt series covers a similar angular range, dual-axis tomography improves sampling to 93% of the corresponding Fourier space [79], and the resolution is more isotropic. Long, filamentous structures such as microtubules are resolved equally well, regardless of whether they are parallel to the tilt axis or perpendicular.

Much of the preceding discussion is applicable to plastic sections, although the beam damage experienced is more subtle in the sense that it is deceptively gradual and to the novice, might go unnoticed. It is not less important. For plastic-embedded sections, a tomographic tilt-series may comprise more than 150 separate projections collected at 1° increments. If we assume that the sample thickness remains constant, 150 similar exposures corresponds to 150 times the electron dose for a single projection. In practise, it is much higher due to the increased beam cross-section at progressively higher tilt, where thickness is related to the cosine of the tilt angle. Thus, although the specimen might not appear to be distorting, it is in fact undergoing continuous mass loss and shrinkage. Comparison of projections 1 and 150 will show marked differences attributed to non-uniform shrinkage alone. Apart from inadequately representing the specimen, alignment of the projections will be difficult unless the projections are modified after acquisition by applying stretching factors, and by accounting for non-linear movements of gold particles. Prior to acquisition, the beam is spread for 10-15 min to expose the region of interest and the surrounding area to a higher flux of electrons. This allows the region of interest to undergo gross changes prior to recording the tilt-series. Even so, further changes cannot be halted entirely—only the *rate* of change slows. To minimise further changes during data acquisition, the low-dose acquisition

procedures detailed above for cryogenic specimens may be used. Additionally, the plastic section may be introduced into the microscope via a cryo sample holder. After pre-irradiation, the sample holder dewar is filled with liquid nitrogen, and once the temperature has equilibrated to, say, -175 °C, the tilt-series can be acquired with the least possible variation from start to finish [80, 81]. This approach results in further changes of only a few percent, making it more feasible to align the set of projections. Cooling a plastic-embedded specimen does not eliminate beam-induced shrinkage. Pre-irradiation of the specimen at room temperature is mandatory, and as a consequence, profound changes (anisotropic shrinkage and mass loss) take place prior to the acquisition of the first projection of the tilt series. The cooling serves only to minimise further changes during acquisition. As noted by Luther [82], the take-up of this cooled plastic-section technique has been low, and the "ultimate goal" should be to use vitreous specimens exclusively. In practise, however, this strategy is convenient, and its success rate in terms of yielding a 'result' from cellular specimens or tissues is very high. Use of this strategy should be considered in the light of the question being posed, and whether conclusions are likely to be the result of changes induced by sample processing.

The ability to record so many projections from a plastic section has resulted in a further misconception about the attainable resolution explained in terms of the Crowther criterion, which simplifies the achievable resolution by considering the number of projections and (related to this), the angular spacing of the projections. This will be discussed under the heading 'Resolution', suffice to say that the concept is subject to limits, and ultimately, it is meaningless in the absence of adequate sample preservation.

#### 1.6 Special Acquisition Case: Block-Face SEM

The name 'serial block-face scanning electron microscopy, SBFSEM' was coined by Denk for a technique in which a specimen block is imaged during precise removal of sections, each of constant thickness, one layer at a time [21]. The name describes a newer focussed ion beam sectioning approach [66] equally well.

Serial block face SEM uses plastic-embedded specimens exclusively. The ability to image the face of a planed, frozen-hydrated block using cryo-SEM had been demonstrated previously [83]. This might not seem obvious, as SEM is usually thought of as a technique to visualise topography. A surface that is planed with a diamond knife is essentially flat, except for knife marks. Contrast in a cryo-SEM is typically achieved by brief etching of the surface to expose features. Etching is achieved by sublimation, which in turn is effected by raising the temperature to approximately -90 °C, well above the devitrification temperature. Thus, devitrification has occurred, and this is likely to be the case in freeze-substitution as well. Furthermore, due to heat-transfer considerations, it is doubtful whether larger specimens (>200  $\mu$ m) can be vitrified in the first place. On the other hand, freeze-substitution and plastic-embedding provides specimen blocks that are readily

amenable to large-volume imaging. It is beyond the scope of this introductory chapter to outline the theory of scanning electron microscopy and focussed ion beam technology, suffice to say that the sample preparation closely resembles that of plastic blocks used for TEM tomography but with the further incorporation of/doping with heavy metals to aid in contrast and to obviate specimen charging [24, 25, 46]. The appearance of the resulting micrographs also resembles bright-field TEM micrographs. This familiar appearance means that interpretation and segmentation tasks are similar to TEM tomography of plastic sections [84] but the strategy is applicable to a much larger scale, such as whole cells. The approach is described in detail in Chap. 5

It is also worth noting at this point that scanning electron microscopes using an in-built ultramicrotome, the so-called 'Denk technique' [21], require a variable pressure or 'environmental' SEM (VP-SEM, ESEM, respectively). This is to cope with outgassing from each newly exposed resin surface, which has been discussed above in relation to mass loss. Ablation with a focussed ion beam requires a dedicated 'dual-beam' or 'cross-beam' FIB-SEM instrument. This is a scanning EM instrument with an ion beam column fitted at a fixed angle to the electron gun (the stage, however, can typically be tilted and possibly also rotated to provide maximum freedom for nanofabrication). Finally, the FIB-SEM with its highly flexible milling capabilities can be used to nanofabricate specimens for cryo- electron tomography [39, 40, 66, 67], provided that the vitrification cold-chain is uninterrupted, and that the specimen is protected from the formation of frost during transfer to the TEM. Electron diffraction studies by Marko and colleagues [85] show convincingly that the milling process does not compromise vitrification. Areas adjacent to FIB-milled lamellae are sputtered destructively, which highlights the importance of preserving target structures such that they are located within the remaining volume.

#### 1.7 Alignment of Projections

A TEM projection micrograph from a thin specimen contains a wealth of 3D information, yet in the classical 2D depiction, features from multiple planes are superimposed, and the ability to determine relative depth and thereby distinguish between interconnected and discrete features is lost. For example, features may appear to be contiguous when they are in fact separate, unconnected entities lying in close proximity. The true nature of the sample densities and their spatial relationships become apparent when an aligned tilt series of projections is viewed as an image sequence. The current discussion refers almost exclusively to alignment of projections acquired by TEM tomography, where alignment is a mandatory step of the workflow. (N.B. The term 'alignment' is essentially synonymous with the term 'registration' used commonly in medical imaging.)

Unlike some related imaging techniques that operate in Fourier space, e.g. magnetic resonance imaging (MRI), individual projections from a TEM tilt series

require alignment to a common frame of reference prior to reconstruction. As a consequence, electron tomography reconstructions are not available in real-time. Misalignment of projections is due to the fact that cross-correlation-based tracking attempts to re-centre the region of interest at each tilt angle but in the case of low-dose tomography, this function depends on the tracking region behaving in exactly the same manner as the recording region. Even when microscope settings are optimised, unreliable tracking or cumulative translational shifts (*cf.* drift/blurring) might be due to a slight unevenness in the grid, for example.

Alignment of projections has traditionally relied on the presence of fiducial markers to create a coordinate system for mutual alignment of the projections. In this method, colloidal gold particles are added to the specimen before plunge-freezing (cryo-tomography) or to one or both surfaces of sections (plastic or cryo, see below). The spatial coordinates of each electron-dense marker are selected in every projection to establish a common coordinate system. This requires at least 3 particles to be visible in all projections, and preferably at least 5 to account for rotations that result from variations in lens current (a nominal magnification of 20,000X might actually be 20,002X in one projection followed by, say, 19,997X in the next, an so on). Adsorbed gold colloids on plastic sections are typically numerous and distributed randomly. This allows for considerable manipulation of the aligned image stack prior to reconstruction, such that the reconstruction represents a globally corrected solution. For cryo- tomography, gold colloids are typically titrated into a suspension sample prior to vitrification. Therefore, cryo specimens typically have fewer markers per field of view, and the gold may bind preferentially to certain components. The lack of shrinkage and mass loss experienced by these samples, however, means that this is usually sufficient. For cellular samples grown on TEM sample grids, the markers can be deposited on the carbon film support prior to incubation with the cells. Alternatively, colloidal gold can be deposited onto vitreous specimens using an adaptation of the ingenious quantum dot method demonstrated by Masich et al. [86]. Briefly, gold colloids are functionalised with triphenylphosphine to render them soluble in toluene. The stabilised particles are dried in batches, and when required, the stabilised powder is resuspended in isopropane, which remains liquid at -150 °C. The vitrified sample grid is dipped in the gold suspension, blotted with filter paper, and then transferred to a cryo sample holder for tomography [64]. Gold colloids are preferred to quantum dots for alignment because they offer constant contrast at all tilt angles. Quantum dots are perfect crystals. During tilting, their contrast is minimal when the plane of the crystal lattice coincides with the direction of the electron beam. They thus tend to 'blink' on and off, and often blend in with (low contrast) electron-dense sample features when the markers' contrast is not at its maximum. It may be preferable to use mixtures of 10 nm and 20 nm gold colloids, in the event that the 10 nm particles become difficult to track in highly tilted projections.

Marker-free alignment, usually of the feature-tracking variety, is essential when fiducial markers are scarce or absent, when the markers are poorly distributed (*e.g.* all near the tilt axis) or when the sample does not behave as a rigid body [87, 88], such as a poorly attached cryosection. Of course, gold colloids can be selected as

features. These approaches are computationally more advanced but variants are now implemented in some commercial as well as freely available software packages. The reader is referred to the review by Amat *et al.* [89] for an in-depth discussion.

After alignment, reconstruction (see following section) is a comparatively simple task that can be executed via command line, provided that the alignment meets (user-defined) acceptable standards. For example, the operator might specify a given tolerance corresponding to sub-pixel alignment. If the pixel size at the detector corresponds to 1 nm, then sub-pixel alignment corresponds to sub-nanometre accuracy. This should not be confused with resolution in the final reconstruction. It simply means that if the alignment accuracy is better than 1 or 2 nm, then it will do justice to the expected resolution of, say, 4 nm in the final reconstruction. In other words, it does not degrade resolution.

By definition, the principle of SEM 'slice and view' tomography (Chap. 5) would indicate that individual slices do not require further alignment: the block is not tilted during acquisition, and the detector-block geometry is maintained throughout the process, such that sequential images should be in perfect registration as they are acquired. Specimen drift or other factors such as stage movement can lead to a translational (*xy*) shift between one or more slices. These image shifts are easily corrected during or after acquisition, however, and the process can be automated. This is done most easily via a cross-correlation function, and it would make sense to include this in the workflow, even if the unaligned stack passes visual inspection. Typically, the first step in such a workflow would be to deal with the massive file size via an initial *xy* scaling ('binning') factor. Alignment could be done after this step. If dedicated functions are not provided by the system, suitable scripts/macros for this task are freely available for software such as ImageJ, although they may have been written for other techniques (*e.g.* Turboreg).

#### 1.8 Reconstruction of an Aligned Tilt Series

As discussed in the preceding section, sequential micrographs acquired by slice and view SEM are by definition already registered, and as such, represent *xy* slices of the reconstructed volume. The remainder of this section applies to reconstruction of tilt series acquired by TEM tomography. For a more detailed discussion, see Chap. 5.

After achieving a satisfactory alignment (preferably according to some quantitative criterion), the practical execution of a reconstruction algorithm using modern software packages can be as simple as a one-step operation using default settings. This will generate a mathematically valid solution to the reconstruction problem, which can be output as an xy image stack and/or animation. The defaults would typically comprise a reconstruction of the entire volume corresponding to equal xyz dimensions. Since a slab geometry is typically characterised by z dimensions that are a small fraction of the xy area, reconstruction of equal xyz dimensions results in

a reconstruction with a huge amount of redundant space above and below the actual specimen. This can be cropped from the 3D volume to save disk space. More sophisticated software allows the user to specify the z dimensions to be reconstructed as well as any centre offset, which saves computation time, especially in the case of more intensive algorithms.

For many years, radioastronomers, medical X-ray (CT) tomographers and, more recently, electron tomographers have used reliable reconstruction algorithms based on the Radon Transform. The standard reconstruction algorithm for this purpose is the weighted back projection (syn. filtered back projection) algorithm [90]. This algorithm is based on the theorem proved mathematically by Radon in the early 1900s [91] and which was rediscovered by radioastronomers in the 1960s [92]. Typically, each image of a single-axis tilt series corresponds to a projection of the object onto a plane perpendicular to the tilt axis. In electron tomography, the intensities arise from electrons that pass through the specimen, essentially along a straight line or 'ray' perpendicular to the plane. The number and type of electrons reaching the detector depends on their interactions with the specimen and the electrostatic densities along a given path through the specimen [93]. Radon's theorem explains that each real-space image corresponds to a 2D plane in Fourier space that intersects the origin and is perpendicular to the viewing axis. Back-projection algorithms make use of this theorem by repopulating the planes according to the angular projections acquired at the microscope. In real space, this is equivalent to an inverse projection operation, with the observed densities being distributed equally along the ray onto all volume elements that contribute to the projection (Fig. 1.1 (lower panel), 2, 9). Thus, back-projection algorithms are regarded as a first-order approximation to an underdetermined system of linear equations given by the projection images. Prior to summation, appropriate filtering ('weighting') is used to reduce artefacts caused by uneven sampling in Fourier Space ('discretisation artefacts'), which effectively bias the distribution towards low frequencies [94].

Post-reconstruction image processing can be applied to reduce the size of the calculated volume or to make an arbitrary correction for X-axis tilt. Due to the speed and robust nature of the weighted backprojection algorithm, it is common practise to perform this calculation even if the intention is to proceed to more time-consuming, iterative reconstruction algorithms such as the algebraic reconstruction technique (ART) or simultaneous iterative reconstruction technique (SIRT). Both of these algorithms involve repeated back-projection steps [95]. ART compares the differences between the reprojections of the reconstructed volume and the measured data and corrects the volume accordingly [96, 97]. It then takes the respective difference images and multiplies them by appropriate weighting factors and adds them to the original back-projection model, and the projections are recalculated until such time as a certain stopping criterion is met. ART is computationally efficient and contains all frequency information but tends to be relatively unstable with respect to noise. The SIRT algorithm is similar to ART, but performs the update of the reconstruction volume only after all corrections have been calculated as opposed to one at a time [90, 98]. SIRT converges more slowly but it is regarded as superior with respect to noise and artificial edge enhancements. Thus, SIRT reconstructions perform well with noisy data typical of cryo-EM and generally tend to look 'smoother' than the corresponding weighted backprojection. Ultimately, the choice may come down to user preference and perceived aesthetic qualities of the final result but both represent mathematically correct solutions to the backprojection problem. More importantly, the choice of reconstruction algorithm may influence the efficacy of subsequent denoising and segmentation routines. Electron tomography may yet benefit from alternative reconstruction algorithms that were abandoned originally due to (then) unrealistic computational requirements.

#### 1.9 Resolution

We have already defined electron tomography as a technique capable of 4 nm resolution. Resolution is discussed in detail in Chap. 10, and in relation to subtomogram averaging below. Resolution in 3D space is not a trivial concept, and misleading claims of resolution are sometimes made due to a fundamental misunderstanding of the Crowther criterion, which relates resolution to sampling efficiency. Assuming that the object is sampled isotropically, i.e. the angular range is sampled evenly (which is usual for some forms of tomography but does not usually apply to electron tomography), the Crowther criterion simply states that the resolution is a function of the number of unique projections. This seems logical but it represents a theoretical or 'best-case' scenario. For plastic-embedded samples that seem to tolerate many projections without obvious radiation damage, it is tempting to record projections with an increment of 1 degree or less, which generates more than 150 projections. Inserting this number into the formula for the Crowther criterion produces an impressive number that certainly cannot withstand scrutiny. The obvious test of this claim is to be able to identify a feature in the tomogram that demonstrates such resolution. Resolution of better than 0.8 nm should be able to resolve alpha helices in proteins. The best resolution achieved using cryo- electron tomography does not exceed 4 nm, nor is it likely to exceed 2 nm in raw data. Information and resolution are related but information is more important than unproductive debates [4]. In practice, resolution is degraded by specimen thickness, interpolation artefacts that occur as a result of the reconstruction algorithm, and in the case of unstained specimens that require phase contrast via imposed underfocus, the contrast transfer function (CTF) determined by the chosen defocus value. The latter is of course addressed by the use of phase plate technology [99]. Perhaps more obviously, resolution is a function of the magnification, which implies that it cannot surpass the Nyquist Frequency. For a more thorough treatment of resolution in electron tomography, the reader is referred to the work of Steven [100] and the chapter by Penczek [101], as well as Chap. 9. Subtomogram averaging (see below) is a means of increasing resolution locally where structures are amenable to averaging.

18 A. Leis

#### 1.10 Post-reconstruction Image Processing

This section introduces the strategies for mining the complexity of tomograms, which are covered in detail in subsequent chapters (Chaps. 8, 11 and 12). These optional techniques are segmentation, which is often aided by prior denoising, and subtomogram averaging. Template matching can be used to select subtomographic volumes for subtomogram averaging; this can be regarded as a special form of segmentation.

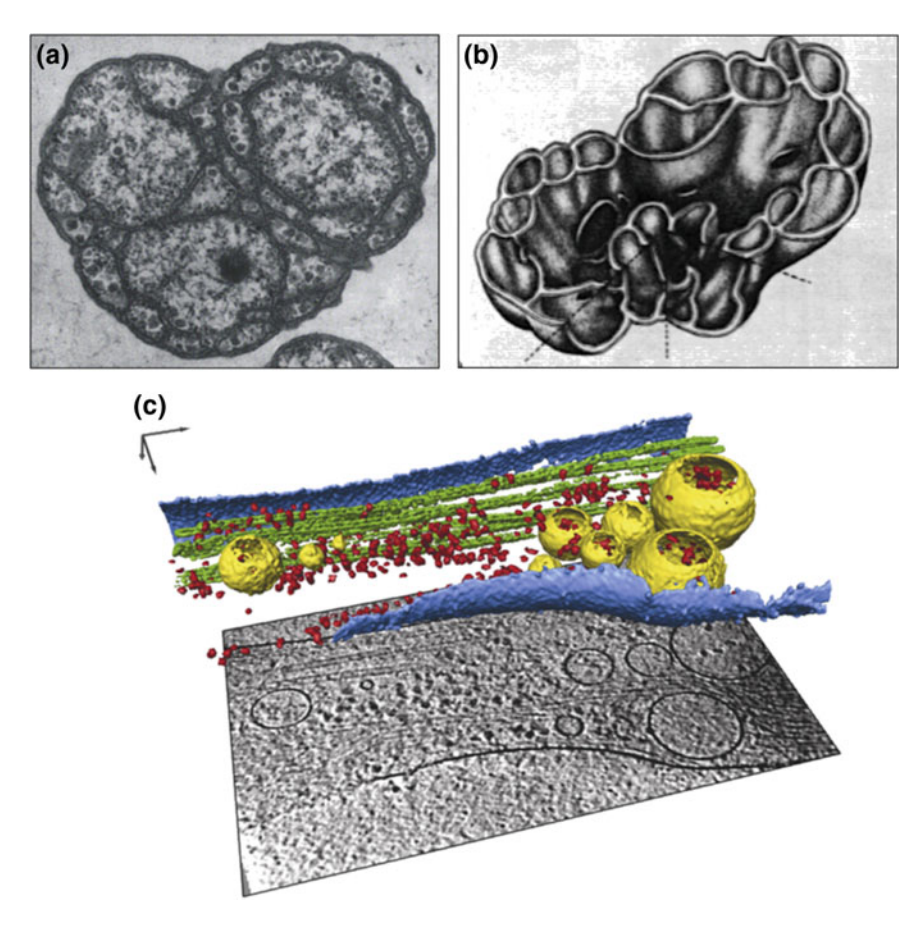


**Fig. 1.6** Progress in segmentation. Early 1970's. **a** Thin section electron micrograph of a compartmentalised bacterium and **b** 'artist's impression' of internal structure based on the micrograph and a clay model [104]; **c** surface-rendering of an appendage from a mammalian cell grown in tissue culture

#### 1.10.1 Segmentation and denoising

Segmentation can be defined as the process by which electron-dense features in a tomogram are ascribed identities and highlighted relative to other features (Fig. 1.6; Chap. 12; [18]). This decomposition into structural components, e.g. membranes or filaments is essential to understanding function [35]. Early examples of segmentation were actual models made with, for example, ping pong balls, corks [102], balsa wood [103], and even clay [104]. Given that segmentation still tends to be time-consuming, even for a specialist, the reasons for doing so are to give clarity to the features of interest (via the use of colour and shading but also by purposefully omitting distracting features), and to present the data in a way that does justice to 3D spatial representation. Here, the benefits of tomography are finally realised. Judicious use of colour, lighting and perspective provides an intuitive representation of features in real space. There is no convention for colour-coding of features, and colours can be chosen to emphasise distinct structures and even their functional relationships. Segmentation of a 2D micrograph is certainly possible but it makes assumptions about whether features are interconnected or merely in close proximity. 2D snapshots from any plane of the reconstruction can reveal details that were not apparent from the original 2D perspective.

Computerised segmentation can be an entirely objective approach [105, 106], not to mention the least tedious. Semiautomated (semi-objective) approaches can also be highly efficient [84]. Nonetheless, tomograms are often segmented manually because the available segmentation algorithms are often inferior to human anticipation, which can infer incomplete and/or anisotropic data. Examples of features that can be delineated without *a priori* information (such as an electron-dense label) include membranes, components of the cytoskeleton, and distinctive molecular complexes such as the 26S proteasome [38]. In this case, structural signature alone is sufficient for reliable identification [107].

Stained plastic sections are dominated by amplitude contrast and a correspondingly high signal-to-noise ratio. In the simplest case, manual thresholding of intensities and removal of spurious (outlying) features may yield an acceptable result for less complex tomograms. The 'Watershed' algorithm and other useful segmentation methods are discussed in Chap. 12. Projections of unstained cryo specimens are dominated by (weaker) phase contrast and noise. Bilateral filtering and nonlinear anisotropic diffusion (NAD) [108] are examples of real-space, nonlinear denoising algorithms that are relatively stable with respect to noise; however, they remove some signal component selectively, resulting in data with higher SNR but suboptimal preservation of information (see Chap. 8). Therefore, denoising is suitable as an aid to segmentation but not for further quantitative analysis or subtomogram averaging.

#### 1.10.2 Template matching

A special subset of segmentation is 'motif search' or 'template matching', a form of pattern recognition. This is the basis for 'visual proteomics' [53]. Like subtomogram averaging, it can only be performed on cryo datasets because these faithfully represent the native structure. Briefly, a tomogram of a cell contains densities corresponding to the expressed portion of the genome, the proteome. If a template structure generated by an independent technique is modified to suit the characteristics of the tomogram (CTF, resolution), then the tomogram can be searched exhaustively using this structure as a template, and cross-correlation peaks indicate the spatial coordinates of the 'hits' as well as the statistical likelihood of it being true (Fig. 1.7). Of course, templates can be obtained from the tomogram too. A complete set of templates allows the tomogram to be repopulated with the structures positioned at their respective 3D coordinates and correct spatial orientations.

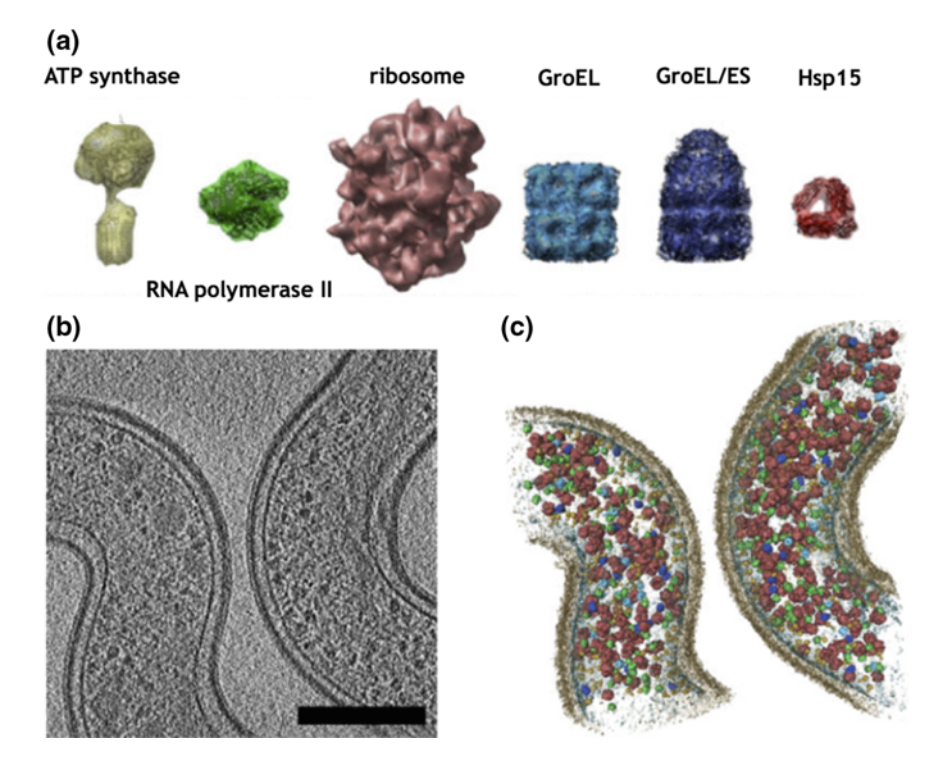


Fig. 1.7 Visual proteomics [1, 3, 51, 52] is an approach that takes 'high-resolution' structures generated by single-particle analysis, X-ray crystallography and/or NMR spectroscopy, and docks these densities into the 3D space of a cell via 'template matching', a form of pattern recognition. The approach uses the available catalogue of possible structures, taking into account the available resolution in the tomogram. Reproduced from [51] with permission from Nature Publishing Group. Scale bar = 200 nm

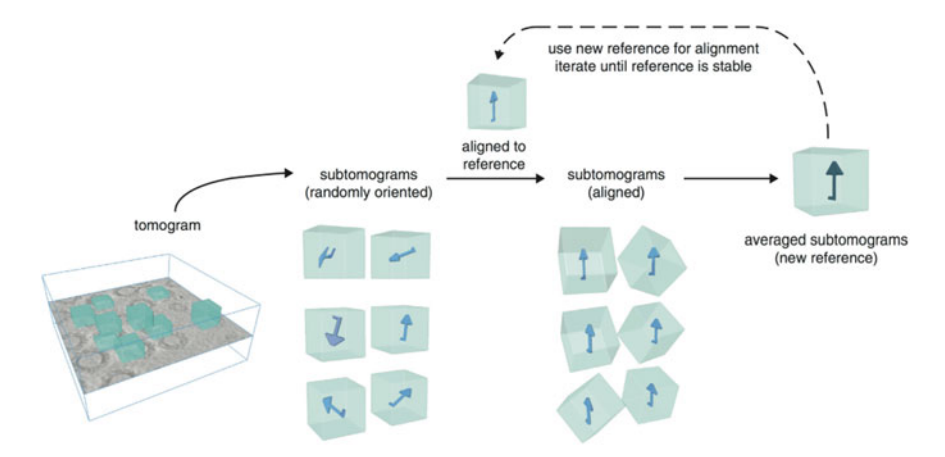


Fig. 1.8 Strategy for subtomogram averaging (reproduced from [54], with permission from Elsevier)

#### 1.10.3 Subtomogram averaging

Resolution of 4 nm must be improved upon to realise the full potential of molecular cartography, and to decipher molecular function. The best resolution that can be expected in electron tomography raw data, i.e. without interpolation artefacts and signal loss at the detector, might never surpass 2 nm [109]; however, this would suffice for the unambiguous structural determination of many intermediate-sized molecular complexes. The improvements required for this are now being realised via the use of phase plates [110] and direct electron detectors that account for all electrons incident on the detector [111]. Considerable information is present beyond (2 nm)<sup>-1</sup>, buried in noise [52]. This information can only be extracted using filtering techniques in conjunction with a priori knowledge of expected structure. Another possibility is provided by subtomogram averaging. A requirement of subtomogram averaging is that the features be recognisable in the tomograms. After localising the repetitive features manually or via template matching, they are extracted in silico, after which the subtomograms are subjected to classification, alignment and averaging [54, 112] (Fig. 1.8). The original features in the tomograms can be replaced with the relevant averages to generate 'synthetic' tomograms with a superior local SNR ratio (Chap. 9). For reasons discussed previously, this is only possible using cryo- electron tomography. For example, a resolution of 7.7 Å was achieved by applying this technique to the Gag polyprotein, the major structural component of retroviruses including HIV [113]. Importantly, the technique has been quite successful for membrane-associated complexes where other structural biology techniques struggle. The reader is referred to Chap. 9 and references, e.g. [54], for further information.

#### 1.11 Recommendations and Future Perspectives

Electron microscopes and tomography software have become very user-friendly, and they often incorporate automated column alignments that assist the acquisition process to run to completion. Alignment is now comparatively easy thanks to optimised SNR collection, smoother tracking, and flexible tilt series alignment software that automates identification and tracking of fiducial markers or other features in 3D space, perhaps by combining both strategies (treating adsorbed gold beads as 'features'). These procedures are non-invasive—gold particles do not need to be injected destructively into the specimen prior to fixation via a gene guntype approach.

Nevertheless, it is just as useful to identify current bottlenecks and impediments to progress. Most tomography reviews over the past 10-15 years have highlighted the need for optimised detectors, phase plates, and artefact-free specimen thinning. Efforts in these areas have led to significant improvements. The ability to make use of every (elastically scattered) electron incident on the detector surface means that information yield can be truly optimised. Of course, nothing can be done about the inelastically scattered electrons, apart from removing their collective contribution to blurring via an zero-loss energy filter [76]. Depending on the question, STEM tomography (Chap. 2) provides further flexibility for thicker specimens. The use of phase plates allows projections to be recorded close to focus, circumventing the need for CTF correction. Several studies demonstrate the success of this technology [110, 114–117]. Previously, a defined level of underfocus was required to provide optimal contrast for features of interest with a given size but at the expense of high-frequency information [118]. Volta phase plates do not suffer from fringing artefacts inherent in Zernike-type plates. They are also highly practical, allowing routine use [99, 119].

These breakthroughs in combination with true advances in sample preparation mean that single-particle cryo-EM and electron tomography have entered a new era. Vitrification is now common to both plastic and cryo workflows. Therefore, apart from the necessity to render infectious agents inactive, the artefacts of chemical fixation should no longer play a role. It is tempting to conclude that the major challenges (images acquired in focus, suitable specimen thinning procedures, close to 100% information yield from calibrated electron dose) have been addressed satisfactorily, and although there is always room for improvement, perhaps the most important point to note is that these solutions are costly in terms of instrumentation and highly-trained, dedicated personnel.

Finally, the success of standard sample collection geometries for numerous high-impact publications belies the fact that cylindrical samples have numerous advantages, including constant focus and thickness during tilting. For the last part of this chapter, I will explain why this is problematic and how this setup could help electron tomography data collection to be even more efficient, and to realise its true potential in terms of information yield.

#### 1.12 The Importance of Sample Geometry

The 'slab' geometry common to microtome sections and vitreous thin films is suboptimal for a number of reasons. The missing (unsampled) wedge in Fourier space corresponds to information content that is substantially incomplete, and the sampled 2D planes are not sampled evenly due to the increase in apparent thickness at progressively higher tilt angles: every projection of the tilted sample is inferior to the sole projection of the untilted sample where the sample is thinnest. At progressively higher tilt, and using the same electron dose or greater for the 'thicker' beam cross-sections, the specimen suffers from a concomitant increase in radiation damage and degradation in resolution. In terms of all-important information yield, the reliance on a slab geometry is simply inefficient. Attempts to deal with imperfect data (reviewed in [120]) take up considerable resources [121] and makes interpretation of tomograms difficult [122]. The dual-axis acquisition scheme deals with anisotropy but only partly addresses the completeness of information. The ideal sample geometry is in fact a cylinder used in conjunction with an on-axis, rotating sample holder. With this setup, the following benefits would become apparent:

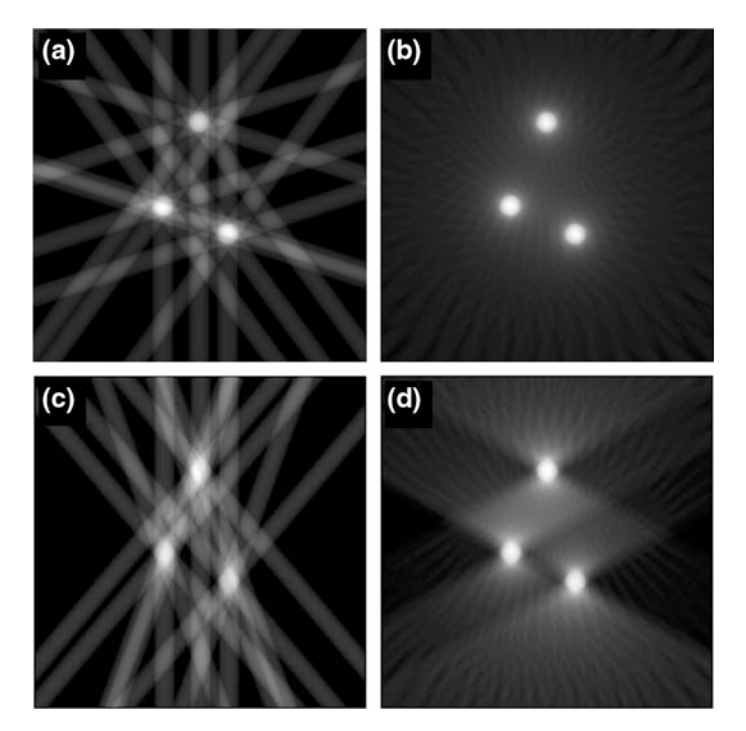


**Fig. 1.9** Effect of the missing wedge on mock 2D data. The upper panels  $\bf a$ ,  $\bf b$  represent sampling of the full angular range (180°) achieved with an on-axis rotation holder, while the lower panels  $\bf c$ ,  $\bf d$  represent a missing wedge of  $\pm$  30°, corresponding to a tilt range of 120° common to a slab geometry.  $\bf a$ ,  $\bf c$  5 projections;  $\bf b$ ,  $\bf d$  25 projections

(1) the full angular range would be sampled. There would be no missing wedge or missing pyramid, leading to (a) simplified interpretation and (b) easier segmentation due to the fact that information is substantially complete and isotropic (Fig. 1.9);

- (2) unlike the case for slabs, there would be a negligible focus gradient across the specimen during 'rotation'. An imposed defocus of, say, −5 μm would be valid for all areas, which would simplify CTF correction and would also allow the use of large-format detectors. Where phase plates are used to provide in-focus contrast, this benefit would be realised fully;
- (3) the thickness would remain constant during rotation, meaning that every projection would have identical SNR characteristics. Each projection would contribute equally to the reconstructed volume. As a corollary, radiation damage would be uniform, simplifying the dose fractionation task. For example, some acquisition schemes for plastic sections attempt to compensate for the increased beam cross-section at higher tilt by calculating the exposure time necessary to keep the brightness constant for all projections, and increase the exposure time accordingly. This leads to highly irregular distortions;
- (4) constant thickness means that fiducial markers would be equally apparent in every projection. An inability to track markers precisely or at all sometimes leads to projections of highly-tilted specimens being discarded;
- (5) larger volumes could be reconstructed: if desired, the cylindrical specimen could be slightly thicker than an untilted slab because all projections will have the same quality. Proportionally more dose could be expended on each projection. Therefore, for the same nominal resolution, the cylinder allows for a larger reconstructed volume.

In principle, cylinders of vitreous material can be manufactured by lathe using a modified cryo- ultramicrotome setup, or by focussed ion beam. Rotation sample holders for room-temperature tomography have been available for some time but an equivalent cryo- sample holder has not. The use of a vitreous cylinder was proposed in 2009 [4] and adapted for proof of principle studies of ribosomes, vesicles and bacteria [123]. Specimens that were plunge-frozen in carbon nanotubes were imaged with moderate success using a standard (tilting) goniometer, which allowed tilting to  $\pm 79^{\circ}$  but as noted above, with equivalent SNR in all projections. In the absence of a dedicated cryo- rotation holder, the main limit to quality seemed to be the thickness of between 400 and 800 nm, and not the carbon nanotube wall thickness of 10–20 nm, which corresponded to the thickness of amorphous carbon films used for plunge freezing. Nanotubes with an internal diameter of <1  $\mu$ m impose restrictions on the size of specimen that can be introduced, which must be in the form of a suspension.

Although progress has been made towards nanofabrication of suitable sample geometries, targeted milling (preserving the target whilst sputtering less relevant features above and/or below the target) has only been addressed in part. Methods for localising features prior to electron tomography have been demonstrated [15, 124, 125]. These methods establish the *xy* coordinates of features of interest but they seldom take into account the fact that thinning (as in the case of FIB) can

inadvertently eliminate the feature of interest due to an inability to determine the position of the feature relative to the z axis.

#### 1.13 Conclusion

The functions of viruses and cells are linked inextricably with structure. Electron tomography is therefore pivotal to an enhanced understanding of biology. This chapter hopefully makes clear that the practise of electron tomography has matured to the point of being useful to specialist biologists who have minimal training in physics and computer programming. A capable microscopist, however, will be able to troubleshoot effectively and adjust suboptimal beam conditions that would otherwise lead to the collection of inferior data. They will also be more wary of the numerous traps of image analysis [126].

Visualisation using electron tomography must always be considered in the light of structural preservation. Tomograms of plastic-embedded, stained samples provide information about the architecture and arrangements of organelles: ultrastructure. These amplitude contrast -dominated (stained) specimens are easier to segment, and all other factors considered, they supplant the need for stereological techniques and their assumptions. Importantly, quantitation of *e.g.* the volume fraction of mitochondria must take into account anisotropic (and frequently disregarded) shrinkage and mass loss that occurs during pre-irradiation and tilt-series acquisition. These considerations do not attempt to take into account the shrinkage, swelling, extraction, or redistribution of components that *precedes* image acquisition.

Tomograms of frozen-hydrated cells are effectively low-resolution snapshots of a cell's proteome. They are mandatory for studies of structural biology. Studies of function depend on the maintenance of spatial relationships between macromolecular assemblies. This is afforded by vitrification, which is routine for viruses and small cells [127, 128], and has become feasible for mammalian cells thanks to cryo- electron tomography of vitreous sections furnished by focussed ion beam milling [67, 129]. The majority of organelles are easily recognisable, and we have now entered an era of being able to make this claim for many large molecular assemblies *in situ*, where unambiguous structural signatures allow tomograms to be searched via sophisticated 3D cross-correlation functions. In the absence of improved resolution, smaller and/or less distinctive structures require correlative techniques for meaningful localisation. Thankfully, fluorescent and/or electron-dense markers for this purpose have been identified that are compatible with vitrification and even freeze-substitution strategies [17]. Also, photobleaching is less problematic at vitreous temperatures [130, 131].

The importance of recent developments in phase plate technology and nanofabrication cannot be understated. The next major technical advances in electron tomography are likely to emerge as a result of improvements to sample fabrication that will in turn facilitate faster and more objective 3D segmentation. Applications will benefit most from cryo-correlative microscopy, particularly sub-diffraction-limit

cryo- fluorescence microscopy [132–136], and time-resolved electron tomography of cellular events [137].

#### 1.14 Protocol

This protocol is universal in the sense that low-dose acquisition schemes should be used for plastic sections as well as for beam-sensitive cryo samples. The reader should consult several such protocols, including those published by the Boulder, CO, group and the cryo protocol of Sun and Li [138].

- (1) Prepare sample according to data acquisition strategy (plastic or cryo). For detailed instructions on plunge freezing, refer to one of the numerous protocols, *e.g.*: [139–141]. Carbon-coating of plastic sections is recommended [82].
- (2) Perform all microscope column alignments, and in particular, beam tilt pivot points, tomo rotation centre, beam tilt calibrations, image (beam) calibrations, image shift pivot points, and image shift for the working magnification range.
- (3) Record a gain reference and check that it is valid via integration and/or auto-correlation (*e.g.* Digital Micrograph, Gatan, Pleasanton, CA). Determine the electron dose.
- (4) Load the sample. Plastic sections can be mounted in a cryo sample holder where available. In this case, the holder is inserted, filled with liquid nitrogen, and allowed to reach a stable temperature before continuing.
- (5) Locate the region of interest. This might be done manually or via input of coordinates obtained via fluorescence microscopy on a Finder-style sample grid, for example. Use the lowest practical magnification and enhance phase contrast by underfocussing.
- (6) Adjust the eucentric height, and focus on the specimen.
- (7) Centre the condenser aperture and adjust the gain conditions.
- (8) Align the rotation centre, preferably using gold markers.
- (9) Correct for objective astigmatism, and focus on the specimen.
- (10) Determine the possible tilt range, *i.e.* until a grid bar obscures the detector or image quality is too degraded.
- (11) Set the acquisition states for a minimum of tracking, focus and recording positions. Set the focus and tracking positions adjacent to the recording position but further along the tilt axis where the illuminated areas do not overlap.
- (12) Set the defocus value to correspond to the resolution of the target structure (not applicable for phase plate -equipped instruments).
- (13) If necessary, burn a hole in the tracking and/or focus areas by condensing the beam for a few seconds. For stained plastic sections, specify focus close to zero (say, -200 nm) to ensure that the autofocus function attempts to calculate a target focus value. For plastic sections, focussing and tracking can be done on the target (recording) area but this is not recommended.

- (14) Specify the tilt series parameters including file name, tilt range, tilt increment. Also, take care to specify the image file format, and whether you wish to save individual projections or an image stack (this is not critical, as it is easy to convert between the two later).
- (15) Record the tilt series and align and reconstruct using *e.g.* IMOD [142]. Usually, a tilt log of metadata will be saved along with the image stack, specifying all acquisition conditions including tilt angles.
- (16) Save aligned image stack (optional) and reconstructed volume.
- (17) Optional steps: denoising\*, segmentation, template matching\*, subtomogram averaging\*
  - \* applicable to cryo data only

#### References

- S. Nickell et al., A visual approach to proteomics. Nat. Rev. Mol. Cell. Biol. 7(3), 225–230 (2006)
- A. Hoenger, High-resolution cryo-electron microscopy on macromolecular complexes and cell organelles. Protoplasma 251(2), 417–427 (2014)
- Asano, S., B.D. Engel, and W. Baumeister, In Situ Cryo-Electron Tomography: A Post-Reductionist Approach to Structural Biology. J. Mol. Biol. (2016). 428(2 Pt A): p. 332– 43
- 4. A. Leis et al., Visualizing cells at the nanoscale. Trends Biochem. Sci. 34(2), 60–70 (2009)
- U.E. Maurer, B. Sodeik, K. Grunewald, Native 3D intermediates of membrane fusion in herpes simplex virus 1 entry. Proc. Natl. Acad. Sci. U. S. A. 105(30), 10559–64 (2008)
- K. Iwasaki, T. Omura, Electron tomography of the supramolecular structure of virus-infected cells. Curr. Opin. Struct. Biol. 20(5), 632–9 (2010)
- I. Ibiricu et al., Cryo electron tomography of herpes simplex virus during axonal transport and secondary envelopment in primary neurons. PLoS Pathog. 7(12), e1002406 (2011)
- C. Risco et al., Three-Dimensional Imaging of Viral Infections. Annu. Rev. Virol. 1(1), 453– 73 (2014)
- 9. S. Padilla-Parra, M. Tramier, FRET microscopy in the living cell: different approaches, strengths and weaknesses. BioEssays. **34**(5), 369–76 (2012)
- K. Grunewald et al., Prospects of electron cryotomography to visualize macromolecular complexes inside cellular compartments: implications of crowding. Biophys. Chem. 100(1– 3), 577–91 (2003)
- G. Foffi et al., Macromolecular crowding: chemistry and physics meet biology (Ascona, Switzerland, 10-14 June 2012). Phys. Biol. 10(4), 040301 (2013)
- 12. V. Lucic, A. Leis, W. Baumeister, Cryo-electron tomography of cells: connecting structure and function. Histochem. Cell. Biol. **130**(2), 185–96 (2008)
- A.V. Agronskaia et al., Integrated fluorescence and transmission electron microscopy.
   J. Struct. Biol. 164(2), 183–189 (2008)
- K. Cortese, A. Diaspro, C. Tacchetti, Advanced correlative light/electron microscopy: current methods and new developments using Tokuyasu cryosections. J. Histochem. Cytochem. 57(12), 1103–12 (2009)
- 15. W. Kukulski et al., Correlated fluorescence and 3D electron microscopy with high sensitivity and spatial precision. J. Cell. Biol. **192**(1), 111–9 (2011)
- R.I. Koning et al., Correlative cryo-fluorescence light microscopy and cryo-electron tomography of Streptomyces. Methods Cell. Biol. 124, 217–39 (2014)

 C. Loussert Fonta, B.M. Humbel, Correlative microscopy. Arch. Biochem. Biophys. 581, 98–110 (2015)

- 18. Frank, J., ed. Electron tomography: methods for visualization of structures in the Cell. 2nd ed. (Springer: New York, 2006) p. 464
- A.E. Yakushevska et al., STEM tomography in cell biology. J. Struct. Biol. 159(3), 381–91 (2007)
- S.G. Wolf, L. Houben, M. Elbaum, Cryo-scanning transmission electron tomography of vitrified cells. Nat. Methods 11(4), 423–8 (2014)
- 21. W. Denk, H. Horstmann, Serial block-face scanning electron microscopy to reconstruct three-dimensional tissue nanostructure. PLoS Biol. 2(11), e329 (2004)
- 22. M. Ballerini et al., Life science applications of focused ion beams (FIB). Eur. J. Histochem. **41**(Suppl 2), 89–90 (1997)
- 23. J.A. Heymann et al., Site-specific 3D imaging of cells and tissues with a dual beam microscope. J. Struct. Biol. **155**(1), 63–73 (2006)
- G. Knott et al., Serial section scanning electron microscopy of adult brain tissue using focused ion beam milling. J. Neurosci. 28(12), 2959–64 (2008)
- G. Knott, S. Rosset, M. Cantoni, Focussed ion beam milling and scanning electron microscopy of brain tissue. J. Vis. Exp. 53, e2588 (2011)
- C. Kizilyaprak, J. Daraspe, B.M. Humbel, Focused ion beam scanning electron microscopy in biology. J. Microsc. 254(3), 109–14 (2014)
- W. Chiu et al., Electron cryomicroscopy of biological machines at subnanometer resolution. Structure 13(3), 363–72 (2005)
- J. Frank, Single-particle reconstruction of biological macromolecules in electron microscopy–30 years. Q. Rev. Biophys. 42(3), 139–58 (2009)
- C.F. Hryc, D.H. Chen, W. Chiu, Near-atomic-resolution cryo-EM for molecular virology. Curr. Opin. Virol. 1(2), 110–7 (2011)
- J. Chang et al., Reconstructing virus structures from nanometer to near-atomic resolutions with cryo-electron microscopy and tomography. Adv. Exp. Med. Biol. 726, 49–90 (2012)
- 31. X.C. Bai, G. McMullan, S.H. Scheres, How cryo-EM is revolutionizing structural biology. Trends Biochem. Sci. **40**(1), 49–57 (2015)
- 32. E. Binshtein, M.D. Ohi, Cryo-electron microscopy and the amazing race to atomic resolution. Biochemistry **54**(20), 3133–41 (2015)
- 33. D. Elmlund, H. Elmlund, Cryogenic electron microscopy and single-particle analysis. Annu. Rev. Biochem. **84**, 499–517 (2015)
- 34. A.C. Steven, W. Baumeister, The future is hybrid. J. Struct. Biol. 163(3), 186–195 (2008)
- 35. Plitzko, J.M. W. Baumeister, in *Cryoelectron Tomography (CET)*, in *Science of Microscopy*, ed. by P.W. Hawkes, J.C.H. Spence (Springer: New York, 2007)
- 36. M.G. Rossmann, Structure of viruses: a short history. Q. Rev. Biophys. **46**(2), 133–80 (2013)
- 37. C.M. Oikonomou, G.J. Jensen, A new view into prokaryotic cell biology from electron cryotomography. Nat. Rev. Microbiol. **14**(4), 205–20 (2016)
- S. Asano et al., Proteasomes. A molecular census of 26S proteasomes in intact neurons. Science 347(6220), 439–42 (2015)
- B.D. Engel et al., In situ structural analysis of Golgi intracisternal protein arrays. Proc. Natl. Acad. Sci. U. S. A. 112(36), 11264–9 (2015)
- Engel, B.D., et al., Native architecture of the Chlamydomonaschloroplast revealed by in situ cryo-electron tomography. Elife 4 (2015)
- 41. J. Mahamid et al., Visualizing the molecular sociology at the HeLa cell nuclear periphery. Science **351**(6276), 969–72 (2016)
- 42. W. Hoppe et al., Three-dimensional reconstruction of individual negatively stained yeast fatty-acid synthetase molecules from tilt series in the electron microscope. Hoppe Seylers Z. Physiol. Chem. **355**(11), 1483–7 (1974)
- B.J. Marsh, M. Pavelka, Viewing Golgi structure and function from a different perspective insights from electron tomography. Methods Cell. Biol. 118, 259–79 (2013)

- 44. C. Suarez et al., Open membranes are the precursors for assembly of large DNA viruses. Cell. Microbiol. **15**(11), 1883–95 (2013)
- 45. C. Suarez et al., African swine fever virus assembles a single membrane derived from rupture of the endoplasmic reticulum. Cell. Microbiol. 17(11), 1683–98 (2015)
- 46. R.L. Felts et al., 3D visualization of HIV transfer at the virological synapse between dendritic cells and T cells. Proc. Natl. Acad. Sc.i U. S. A. 107(30), 13336–41 (2010)
- 47. A.A. Linaroudis, Interpretation of electron tomograms of biological specimens by means of the Scaling Index Method, in Faculty of Chemistry. Technische Universität München (2006)
- 48. Y. Cheng et al., A primer to single-particle cryo-electron microscopy. Cell **161**(3), 438–49 (2015)
- A. Leschziner, The orthogonal tilt reconstruction method. Methods Enzymol. 482, 237–62 (2010)
- 50. J.O. Ortiz et al., Mapping 70S ribosomes in intact cells by cryoelectron tomography and pattern recognition. J. Struct. Biol. **156**(2), 334–41 (2006)
- 51. M. Beck et al., Visual proteomics of the human pathogenLeptospira interrogans. Nat. Methods **6**(11), 817–U55 (2009)
- 52. F. Forster, B.G. Han, M. Beck, Visual proteomics. Methods Enzymol. 483, 215–43 (2010)
- 53. M. Beck et al., Exploring the spatial and temporal organization of a cell's proteome. J. Struct. Biol. **173**(3), 483–96 (2011)
- J.A. Briggs, Structural biology in situ—the potential of subtomogram averaging. Curr. Opin. Struct. Biol. 23(2), 261–7 (2013)
- 55. K. Grunewald et al., Three-dimensional structure of herpes simplex virus from cryo-electron tomography. Science **302**(5649), 1396–8 (2003)
- 56. N. Grigorieff, S.C. Harrison, Near-atomic resolution reconstructions of icosahedral viruses from electron cryo-microscopy. Curr. Opin. Struct. Biol. **21**(2), 265–73 (2011)
- 57. Baker, T.S., N.H. Olson, S.D. Fuller, Adding the third dimension to virus life cycles: three-dimensional reconstruction of icosahedral viruses from cryo-electron micrographs. Microbiol. Mol. Biol. Rev. **63**(4), 862–922 (1999) table of contents
- B.A. Afzelius, A.B. Maunsbach, Biological ultrastructure research; the first 50 years. Tissue Cell 36(2), 83–94 (2004)
- K.L. McDonald, R.I. Webb, Freeze substitution in 3 hours or less. J. Microsc. 243(3), 227– 233 (2011)
- J.J. Wolosewick, K.R. Porter, Microtrabecular lattice of the cytoplasmic ground substance. Artifact or reality. J. Cell. Biol. 82(1), 114–39 (1979)
- J. Heuser, Whatever happened to the 'microtrabecular concept'? Biol. Cell 94(9), 561–96 (2002)
- M.H. Ellisman, K.R. Porter, Microtrabecular structure of the axoplasmic matrix: visualization of cross-linking structures and their distribution. J. Cell. Biol. 87(2 Pt 1), 464–79 (1980)
- 63. H. Kondo, On the real structure of the cytoplasmic matrix: learning from the embedment-free electron microscopy. Arch. Histol. Cytol. **58**(4), 397–415 (1995)
- M. Gruska et al., Electron tomography of vitreous sections from cultured mammalian cells.
   J. Struct. Biol. 161(3), 384–392 (2008)
- T. Wagenknecht, C. Hsieh, M. Marko, Skeletal muscle triad junction ultrastructure by focused-ion-beam milling of muscle and cryo-electron tomography. Eur. J. Transl. Myol. 25 (1), 4823 (2015)
- Y. Fukuda, A. Leis, A. Rigort, Preparation of vitrified cells for TEM by Cryo-FIB Microscopy, in *Biological Field Emission Scanning Electron Microscopy*, ed. by B. Humbel, R. Fleck (2016)
- 67. M. Marko et al., Focused-ion-beam thinning of frozen-hydrated biological specimens for cryo-electron microscopy. Nat. Methods 4(3), 215–217 (2007)
- 68. A. Schertel et al., Cryo FIB-SEM: volume imaging of cellular ultrastructure in native frozen specimens. J. Struct. Biol. **184**(2), 355–360 (2013)
- 69. B.D. Engel, et al., Native architecture of the Chlamydomonas chloroplast revealed by in situ cryo-electron tomography. Elife **4** (2015)

 C. Hoffmann et al., Disclosure of the mycobacterial outer membrane: Cryo-electron tomography and vitreous sections reveal the lipid bilayer structure. Proc. Natl. Acad. Sci. U. S.A. 105(10), 3963–3967 (2008)

- 71. B. Zuber et al., Direct visualization of the outer membrane of mycobacteria and corynebacteria in their native state. J. Bacteriol. **190**(16), 5672–5680 (2008)
- 72. P.K. Luther, Sample shrinkage and radiation damage of plastic sections, in *Electron Tomography: Methods for Three-Dimensional Visualization of Structures in the Cell*, ed. by J. Frank (Springer, 2006)
- 73. Gordon, R., G.T. Herman, S.A. Johnson, Image reconstruction from projections. Sci. Am. **233**(4), 56–61, 64–8 (1975)
- R. Hegerl, W. Hoppe, Influence of electron noise on three-dimensional image reconstruction. Zeitschrift Naturforsch. A 314(12), 1717–1721 (1976)
- 75. B.F. McEwen, K.H. Downing, R.M. Glaeser, The relevance of dose-fractionation in tomography of radiation-sensitive specimens. Ultramicroscopy **60**(3), 357–73 (1995)
- 76. R. Grimm et al., Zero-loss energy filtering under low-dose conditions using a post-column energy filter. J. Microsc. **183**(1), 60–68 (1996)
- 77. D.N. Mastronarde, Dual-axis tomography: an approach with alignment methods that preserve resolution. J. Struct. Biol. **120**(3), 343–52 (1997)
- 78. S. Nickell et al., Pyrodictium cannulae enter the periplasmic space but do not enter the cytoplasm, as revealed by cryo-electron tomography. J. Struct. Biol. 141(1), 34–42 (2003)
- 79. V. Lucic, F. Forster, W. Baumeister, Structural studies by electron tomography: from cells to molecules. Annu. Rev. Biochem. **74**, 833–65 (2005)
- 80. M.B. Braunfeld et al., Cryo automated electron tomography: towards high-resolution reconstructions of plastic-embedded structures. J. Microsc. **174**(Pt 2), 75–84 (1994)
- 81. M.L. Harlow et al., The architecture of active zone material at the frog's neuromuscular junction. Nature **409**, 479–484 (2001)
- 82. P.K. Luther, Sample shrinkage and radiation damage of plastic sections, in *Electron Tomography: Methods for Three-Dimensional Visualization of Structuresin the Cell*, ed. by J. Frank (Springer, 2006)
- P. Walther, M. Muller, Biological ultrastructure as revealed by high resolution cryo-SEM of block faces after cryo-sectioning. J. Microsc. 196(Pt 3), 279–87 (1999)
- A. Kreshuk et al., Automated detection and segmentation of synaptic contacts in nearly isotropic serial electron microscopy images. PLoS ONE 6(10), e24899 (2011)
- M. Marko et al., Focused ion beam milling of vitreous water: prospects for an alternative to cryo-ultramicrotomy of frozen-hydrated biological samples. Journal of Microscopy-Oxford 222, 42–47 (2006)
- S. Masich et al., A procedure to deposit fiducial markers on vitreous cryo-sections for cellular tomography. J. Struct. Biol. 156(3), 461–8 (2006)
- D. Castano-Diez et al., Fiducial-less alignment of cryo-sections. J. Struct. Biol. 159(3), 413–423 (2007)
- C.O. Sorzano et al., Marker-free image registration of electron tomography tilt-series. BMC Bioinformatics 10, 124 (2009)
- 89. F. Amat et al., Alignment of cryo-electron tomography datasets. Methods Enzymol. **482**, 343–67 (2010)
- P.F.C. Gilbert, Reconstruction of a 3-dimensional structure from projections and its application to electron-microscopy.
   Direct methods. Proc. Roy. Soc. London B, 182 (1066), 89–102 (1972)
- 91. J. Radon, Über die Bestimmung von Funktionen durch ihre Integralwerte längs gewisser Mannigfaltigkeiten. Berichte über die Verhandlungen der Königlich Sächsischen Gesellschaft der Wissenschaften zu Leipzig. Math. Phys. Klasse. **69**, 262–277 (1917)
- R.N. Bracewell, A.C. Riddle, Inversion of fan-beam scans in radio astronomy. Astrophys. J. 150, 427–434 (1967)
- 93. R. Gordon, G.T. Herman, Reconstruction of pictures from their projections. Graph. Image Proc. **14**(12), 759–768 (1971)

- 94. G. Harauz, M. van Heel, Exact filters for general three-dimensional reconstruction. Optik 73, 146–156 (1986)
- 95. A.P. Leis et al., Cryo- electron tomography of biological specimens: the essential role of digital signal processing. IEEE Signal Process. Mag. 23(3), 95–103 (2006)
- 96. G.T. Herman, S. Rowland, Resolution in ART. An experimental investigation of the resolving power of an algebraic picture reconstruction technique. J. Theor. Biol. **33**(1), 213–23 (1971)
- 97. G.T. Herman, A. Lent, S.W. Rowland, ART: mathematics and applications. A report on the mathematical foundations and on the applicability to real data of the algebraic reconstruction techniques. J. Theor. Biol. **42**(1), 1–32 (1973)
- 98. P. Gilbert, Iterative methods for 3-dimensional reconstruction of an object from projections. J. Theoret. Biol. **36**(1), 105–117 (1972)
- 99. R. Danev et al., Volta potential phase plate for in-focus phase contrast transmission electron microscopy. Proc. Natl. Acad. Sci. U. S. A. 111(44), 15635–40 (2014)
- G. Cardone, K. Grunewald, A.C. Steven, A resolution criterion for electron tomography based on cross-validation. J. Struct. Biol. 151(2), 117–29 (2005)
- P.A. Penczek, Resolution measures in molecular electron microscopy. Methods Enzymol. 482, 73–100 (2010)
- 102. D. Derosier, 3D reconstruction from electron micrographs a personal account of its development. Methods Enzymol. 481, 1–24 (2010)
- A.B. Maunsbach, B.A. Afzelius, Biomedical Electron Microscopy: Illustrated Methods and Interpretations (San Diego: Academic Press, 1999), p. 548
- 104. S.W. Watson et al., A lobular, ammonia-oxidizing bacterium, Nitrosolobus multiformis nov.gen.nov.sp. Arch. Mikrobiol. **76**(3), 183–203 (1971)
- 105. A. Rigort et al., Automated segmentation of electron tomograms for a quantitative description of actin filament networks. J. Struct. Biol. 177(1), 135–44 (2012)
- M. Rusu et al., Automated tracing of filaments in 3D electron tomography reconstructions using Sculptor and Situs. J. Struct. Biol. 178(2), 121–8 (2012)
- O. Medalia et al., Macromolecular architecture in eukaryotic cells visualized by cryoelectron tomography. Science 298(5596), 1209–13 (2002)
- A.S. Frangakis, R. Hegerl, Noise reduction in electron tomographic reconstructions using nonlinear anisotropic diffusion. J. Struct. Biol. 135(3), 239–50 (2001)
- 109. R. Henderson, Realizing the potential of electron cryo-microscopy. Q. Rev. Biophys. **37**(1), 3–13 (2004)
- Y. Fukuda et al., Electron cryotomography of vitrified cells with a Volta phase plate.
   J. Struct. Biol. 190(2), 143–54 (2015)
- 111. G. McMullan et al., Enhanced imaging in low dose electron microscopy using electron counting. Ultramicroscopy **109**, 1411–1416 (2009)
- 112. F. Forster et al., Retrovirus envelope protein complex structure in situ studied by cryo-electron tomography. Proc. Natl. Acad.Sci. U. S. A. **102**(13), 4729–34 (2005)
- 113. F.K. Schur et al., Structure of the immature HIV-1 capsid in intact virus particles at 8.8 A resolution. Nature **517**(7535), 505–8 (2015)
- K. Murata et al., Zernike phase contrast cryo-electron microscopy and tomography for structure determination at nanometer and subnanometer resolutions. Structure 18(8), 903–12 (2010)
- K. Nagayama, Biological applications of phase-contrast electron microscopy. Methods Mol. Biol. 1117, 385–99 (2014)
- G.P. Kishchenko et al., Effect of fringe-artifact correction on sub-tomogram averaging from Zernike phase-plate cryo-TEM. J. Struct. Biol. 191(3), 299–305 (2015)
- T.H. Sharp, A.J. Koster, P. Gros, Heterogeneous MAC Initiator and Pore Structures in a Lipid Bilayer by Phase-Plate Cryo-electron Tomography. Cell. Rep. 15(1), 1–8 (2016)
- J. Dubochet, et al., CEMOVIS: Cryo-electron microscopy of vitreous sections, in Handbook of Cryo-Preparation Methods for Electron Microscopy, ed. by B. Humbel D. Spehner (CRC Press: Boca Raton, 2009) pp. 259–289

119. R. Danev, W. Baumeister, Cryo-EM single particle analysis with the Volta phase plate. Elife **5** (2016)

- 120. M.F. Schmid, C.R. Booth, Methods for aligning and for averaging 3D volumes with missing data. J. Struct. Biol. **161**(3), 243–8 (2008)
- L. Kovacik et al., A simple Fourier filter for suppression of the missing wedge ray artefacts in single-axis electron tomographic reconstructions. J. Struct. Biol. 186(1), 141–52 (2014)
- 122. B. Turonova, L. Marsalek, P. Slusallek, On geometric artifacts in cryo electron tomography. Ultramicroscopy **163**, 48–61 (2016)
- 123. C.M. Palmer, J. Lowe, A cylindrical specimen holder for electron cryo-tomography. Ultramicroscopy 137, 20–9 (2014)
- 124. W. Kukulski et al., Precise, correlated fluorescence microscopy and electron tomography of lowicryl sections using fluorescent fiducial markers. Methods Cell. Biol. 111, 235–57 (2012)
- 125. J. Arnold et al., Site-specific cryo-focused ion beam sample preparation guided by 3d correlative microscopy. Biophys. J. **110**(4), 860–9 (2016)
- 126. R. Henderson, Avoiding the pitfalls of single particle cryo-electron microscopy: einstein from noise. Proc. Natl. Acad. Sci. U.S.A. 110(45), 18037–18041 (2013)
- 127. G.P. Henderson, L. Gan, G.J. Jensen, 3-D ultrastructure of O. tauri: electron cryotomography of an entire eukaryotic cell. PLoS ONE 2(8), e749 (2007)
- 128. M.M. Farley et al., Minicells. Back in Fashion. J. Bacteriol. 198(8), 1186-95 (2016)
- 129. A. Rigort et al., Focused ion beam micromachining of eukaryotic cells for cryoelectron tomography. Proc. Natl. Acad. Sci. U.S.A. 109(12), 4449–4454 (2012)
- W.E. Moerner, M. Orrit, Illuminating single molecules in condensed matter. Science 283 (5408), 1670–6 (1999)
- C.L. Schwartz et al., Cryo-fluorescence microscopy facilitates correlations between light and cryo-electron microscopy and reduces the rate of photobleaching. J. Microsc. 227(Pt 2), 98– 109 (2007)
- 132. E. Betzig et al., Imaging intracellular fluorescent proteins at nanometer resolution. Science **313**(5793), 1642–1645 (2006)
- 133. Y.W. Chang et al., Correlated cryogenic photoactivated localization microscopy and cryo-electron tomography. Nat. Methods 11(7), 737–9 (2014)
- R. Kaufmann, C. Hagen, K. Grunewald, Fluorescence cryo-microscopy: current challenges and prospects. Curr. Opin. Chem. Biol. 20, 86–91 (2014)
- 135. R. Kaufmann et al., Super-resolution microscopy using standard fluorescent proteins in intact cells under cryo-conditions. Nano. Lett. **14**(7), 4171–5 (2014)
- 136. G. Wolff, et al., Towards correlative super-resolution fluorescence and electron cryo-microscopy. Biol. Cell. (2016)
- 137. W. Kukulski et al., Plasma membrane reshaping during endocytosis is revealed by time-resolved electron tomography. Cell **150**(3), 508–20 (2012)
- J. Sun, H. Li, How to operate a cryo-electron microscope. Methods Enzymol. 481, 231–49 (2010)
- 139. C.V. Iancu et al., Electron cryotomography sample preparation using the Vitrobot. Nat. Protoc. 1(6), 2813–2819 (2006)
- R.A. Grassucci, D.J. Taylor, J. Frank, Preparation of macromolecular complexes for cryo-electron microscopy. Nat. Protoc. 2(12), 3239–3246 (2007)
- 141. G.P. Resch et al., Immersion freezing of cell monolayers for cryo-electron tomography. Cold. Spring. Harb. Protoc. **2011**(7), 815–23 (2011)
- 142. J.R. Kremer, D.N. Mastronarde, J.R. McIntosh, Computer visualization of three-dimensional image data using IMOD. J. Struct. Biol. **116**(1), 71–6 (1996)

# **Chapter 2 STEM Tomography in Biology**

Sharon Grayer Wolf, Eyal Shimoni, Michael Elbaum and Lothar Houben

**Abstract** STEM modality provides major advantages for electron tomography of thicker (>300 nm) biological specimens, both for plastic-embedded, heavy-metal stained samples, and for vitrified, unstained cells. With the proliferation of modern TEM microscopes that allow for switching between TEM and STEM modes with relative ease, we expect the use of STEM tomography to increase. The concepts for STEM imaging are significantly different than for TEM, and therefore we will describe in detail the STEM imaging modality, followed by STEM tomography concepts and applications.

#### 2.1 Introduction

The foundations for atomic-scale scanning-transmission electron microscope (STEM) imaging were developed by Albert Crewe's team in the 1960s [1–3]. Ironically, though subsequent dominance of STEM imaging has been in the materials sciences, Crewe's keen interest at the time was in analysis and imaging of biological specimens [4, 5]. It was recognized that favorable and quantifiable contrast could be obtained with STEM for unstained biological cells, and indeed the elemental composition of such specimens could be probed by electron energy-loss spectroscopy

S. G. Wolf ( ) · E. Shimoni · L. Houben

Electron Microscopy Unit, Department of Chemical Research Support,

Weizmann Institute of Science, Rehovot, Israel

e-mail: Sharon.Wolf@weizmann.ac.il

E. Shimoni

e-mail: eyal.shimoni@weizmann.ac.il

L. Houben

e-mail: lothar.houben@weizmann.ac.il

M. Elbaum

Department of Materials and Interfaces, Weizmann Institute of Science,

Rehovot, Israel

e-mail: michael.elbaum@weizmann.ac.il

© Springer International Publishing AG 2018

E. Hanssen (ed.), *Cellular Imaging*, Biological and Medical Physics, Biomedical Engineering, https://doi.org/10.1007/978-3-319-68997-5\_2

(EELS) [6–8] and energy-dispersive X-ray spectroscopy (EDS). However, these early results were not readily adopted by the community of biological electron microscopists. Until recently, biological applications of STEM were not mostly focused on the cellular context [9], but rather on other applications, such as precise mass measurements for proteins [10–14], and even demonstrations for sequencing DNA [15]. Today, STEM is again being explored for imaging and analysis of biological cells, including imaging of wet cells using special vacuum-tight chambers [16], low-voltage STEM in SEM instruments [17], and chemical composition [18, 19]. In particular, STEM imaging is increasingly appreciated as an important method for obtaining tomograms of thick biological specimens whether they are fixed, embedded sections, or cryo-preserved vitrified samples.

The advantages lie with the method of STEM imaging, where the electron beam is finely focused at the plane of the specimen (Fig. 2.1), and is rastered across the sample, point by point, line after line, similarly to scanning electron microscopes (SEMs), atomic force microscopes or laser scanning confocal fluorescence microscopes. Transmitted electrons are counted for each point by a series of detectors that collect the electrons at different scattering angles.

Figure 2.1 shows that the role of the microscope optics in STEM is to focus the electron beam to a small probe, which is actually a demagnified image of the electron emitter. It is particularly important to appreciate that the beam encounters no image-forming lenses after passing through the sample. Instead, an image is formed in the computer by mapping the detector counts, point-by-point, with the scan position.

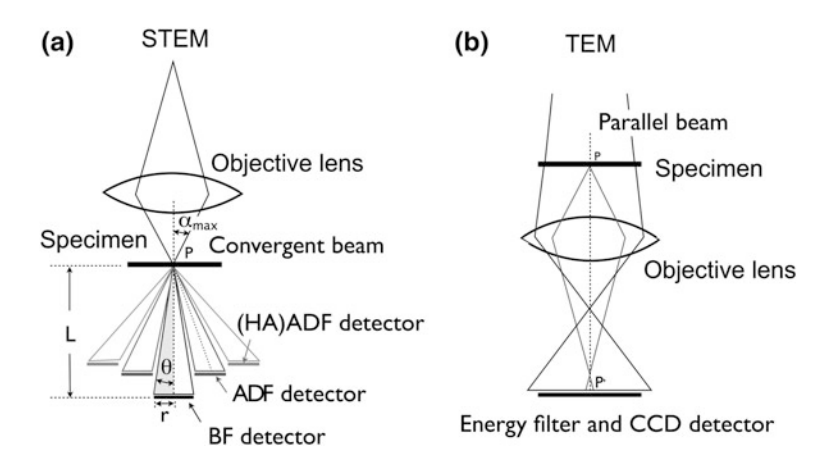


**Fig. 2.1** Schematic ray diagrams of convergent probe STEM and TEM wide-field imaging for tomography. **a** In STEM imaging a convergent, finely focused electron probe with semi-convergence angle  $\alpha_{max}$  rasters across the sample, and electrons are counted for each object position P on detectors that span a range of detection angles  $\Theta$ . The bright-field (BF) detector collects electrons with angles  $\Theta < \alpha_{max}$ , and annular dark-field (ADF) and high-angle annular DF (HAADF) detectors collect electrons with scattering angles  $\Theta > \alpha_{max}$ . **b** For wide-field TEM imaging, the specimen is illuminated by a parallel beam. Waves emerging from point P are focused by the objective to P'. The sketch shows the configuration for phase contrast used in cryogenic imaging. The unscattered beam serves as a reference wave to generate contrast by interference when the specimen is taken out of focus. (Adapted from Wolf et al. [20])

STEM image-formation is an incoherent process, and the much-discussed issue of chromatic aberration in TEM imaging is irrelevant. For phase-contrast TEM imaging, only elastically scattered coherent electrons provide a useful signal. Inelastically scattered electrons cause damage to the sample and add blur to the image. For tomography they are often removed with an energy filter. Incoherent STEM imaging is less affected by inelastic scattering and thus STEM imaging can be very efficient, especially for thick samples where phase coherence is lost. Finally, because the beam is rastered, dynamic focusing at high tilt is naturally available for tilt series recording in tomography. Dynamic focusing is simply achieved by adjusting the focus for each line during the scan, <sup>1</sup> according to its geometric location on the tilted sample.

In the following sections, we will describe STEM image formation and complementary analytical tools, and provide a framework for understanding the advantages of STEM imaging for tomography. Afterwards, we will discuss applications of STEM in tomography of thick biological specimens, first for plastic-embedded samples, and then for cryo-preserved specimens.

#### 2.2 Basics of STEM Imaging of Biological Material

#### 2.2.1 Electron-Sample Interactions

Contrast and resolution of STEM and TEM images are affected by the interaction of the electron beam with the sample. The primary interactions between the fast electron and the atoms in the sample are due to electrostatic Coulomb forces. Elastic and inelastic, as well as coherent and incoherent processes occur in the scattering of electrons [18, 21]. Elastic scattering can result in a rather large deflection of the incident electron but does not change the state of a target atom; specifically, no energy is lost by the electron. Quasi-elastic scattering is connected with oscillations in molecules or phonon excitations that attenuates the coherence and leads to thermal diffuse scattering. Inelastic events (wherein electrons do lose energy after interaction with the specimen) originate from interaction between the incident electron and the target electrons by excitation of collective oscillations (plasmons), valence electrons, or the ionization of inner atomic shells. Inelastically scattered electrons appear as a new source within the specimen and attenuate or destroy coherent interference effects. In addition the deposited energy causes damage to the sample.

Both the angular scattering and the total scattering amplitude depend strongly on the nuclear charge and thus on the atomic number Z of the atoms in the sample. This dependence is utilized in the various methods associated with electron microscopy imaging and spectroscopy. In a crystalline solid, diffraction effects change the angular dependence of scattering dramatically, but in amorphous solids,

<sup>&</sup>lt;sup>1</sup>The focus is adjusted per line, assuming that the scan lines are parallel to the tilt axis.

as for most of the biological materials, diffraction effects are weak and to a good approximation the magnitude and angular distribution of the scattering reflect simply the number and sort of scattering atoms. This approximation holds at least in thin samples where multiple scattering effects are small. We therefore start our discussion of the electron-specimen interaction with the single-scattering approximation for independent atoms (i.e., the "thin specimen limit").

The differential scattering cross-section conveniently describes the angular distribution of scattering from a target atom. For elastic scattering, the differential cross-section follows the Rutherford formula for the screened Coulomb potential of the nuclear charge [21]. For fast electrons, the largest contribution to the total elastic scattering cross-section  $\sigma_{el}$  stems from forward scattering and depends on the screening of the nuclear charge by shell electrons. In the Wentzel approximation, the nuclear charge is screened by an exponential term with the shielding parameter R. The statistical Thomas-Fermi model yields  $R = a_H Z^{-1/3}$  with the Bohr radius  $a_H = 0.0529$  nm. In this shielding approximation the differential cross-section for elastic scattering in first order Born approximation becomes:

$$\frac{\mathrm{d}\sigma_{\mathrm{el}}}{\mathrm{d}\Omega} \cong \left[ \frac{2ZR^2}{a_H} \frac{1 + E/E_0}{1 + (\theta/\theta_0)^2} \right]^2, \quad \theta_0 = \frac{\lambda}{2\pi R}$$
 (2.1)

where E denotes the electron energy, E<sub>0</sub> the rest energy of the electron and

 $\theta_0 = \lambda/2\pi R$  is the characteristic scattering angle. Fifty percent of the electrons are scattered into angles smaller than  $\theta_0$ . As an example, the characteristic scattering angle for oxygen is 15 mrad for 200 keV electrons.

Integration of (2.1) yields an approximate of:

$$\sigma_{\rm el} \cong \frac{h}{\pi E_0^2 \beta^2} Z^{4/3} \tag{2.2}$$

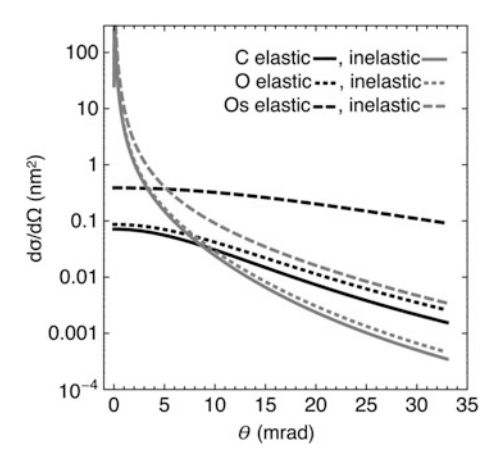
with  $\beta$  equal to the velocity v divided by the speed of light c. Equation 2.2 gives the total elastic scattering cross-section, which increases monotonically with the atomic number.

The angular dependence and the total cross-section of inelastic scattering can be reasonably approximated with a Bethe-model for a single mean energy transfer  $\Delta E$  for the inelastic event. The differential cross-section takes the form [21]:

$$\frac{d\sigma_{\text{inel}}}{d\Omega} \cong \frac{Z\lambda^4 (1 + E/E_0)^2}{4\pi^4 a_H^2} \frac{\left[1 - (1 + \theta^2/\theta_0^2)^{-2}\right]}{(\theta^2 + \theta_E^2)^2}, \quad \theta_E = \frac{\Delta E}{E} \frac{E + E_0}{E + 2E_0}$$
(2.3)

where  $\theta_E$  is the characteristic angle that is responsible for the decay of the inelastic scattering. An inelastic scattering process is less localized than the elastic one,

Fig. 2.2 Angular dependence of elastic and inelastic scattering for carbon (Z = 6), oxygen (Z = 8) and Osmium (Z = 76)



therefore inelastic scattering is concentrated within much smaller angles than elastic scattering. The characteristic angle for an elastic scattering event  $\theta_0$  is increasing with Z but is on the order of 10 mrad, while the characteristic angle  $\theta_E$  is typically of the order 0.1 mrad. For STEM tomography, this means that unscattered and inelastically scattered electrons will be collected by the BF disc detector (Fig. 2.1).

Figure 2.2 shows exemplary differential scattering cross-section data following (2.3) for the light elements C and O and for the heavier element Os. The former are major constituents in biological material and the latter is often used as a stain reagent. The difference in the characteristic scattering angles for inelastic and elastic scattering is obvious, as is the increase of the high angle elastic scattering with increase in the atomic number Z. At lower angles and in particular for the low Z, the contribution of the inelastic scattering can be substantial.

Integration of the differential inelastic cross-sections to all scattering angles yields a total cross-section that is proportional to  $Z^{1/3}$  [18]. The ratio of the total inelastic scattering cross-section and the total elastic scattering cross-section is therefore an inverse function of the atomic number, the relation is approximately:

$$\sigma_{inel}/\sigma_{el} = \gamma/Z$$
 (2.4)

with a coefficient  $\gamma$  that is close to 20 and hardly dependent on the atomic number or electron energy. The relation holds for small sample thicknesses where multiple scattering is negligible (i.e., the thin-specimen limit), and essentially all the high angle elastic scattering is collected [22].

<sup>&</sup>lt;sup>2</sup>This is essentially a statement of Heisenberg's uncertainty principle. To the extent that the electron is localized in space during the scattering process, its momentum, and therefore emission angle, carries a finite uncertainty. Elastic scattering from the atomic nuclei involves a precise localization and therefore a large uncertainty in momentum; inelastic scattering from the much larger electron cloud invokes a correspondingly smaller uncertainty in momentum, hence a small characteristic scattering angle.

For biological samples the effective atomic number is low, therefore inelastic scattering events are more probable than elastic events (2.4). Since inelastic scattering generally involves the ionization of atoms, and since this often destroys the local atomic configuration, the relation between the inelastic and elastic scattering cross-section immediately reveals that specimens with light elements are more likely to suffer from radiolysis. This radiation damage is a significant impediment to electron microscopy of biological specimens.

The inverse of the cross section  $\sigma_{el}$  multiplied by the number density of atoms per unit volume  $n_a$  is interpreted as the mean distance or mean free path (MFP) between elastic collisions. The MFP is an excellent guideline for understanding the limit of sample thickness for electron microscopy imaging.

The MFP for inelastic scattering by vitreous ice has been estimated to be 200 nm for 120 kV electrons [3, 23]. The ratio of MFP for elastic to inelastic scattering depends approximately as 20/Z, where Z is the atomic number. Thus for biological material dominated by the light elements carbon, nitrogen, and oxygen (Z = 6, 7,8), for an electron traversing one elastic MFP, there would be three inelastically scattered electrons (2.4). The inelastic MFP also sets a limit for optimal TEM tomography conditions.<sup>3</sup> This is because for TEM tomographic imaging of biological specimens, the interpretable signal originates in the elastic scattering. The inelastically scattered electrons contribute an unfocused haze and so should be blocked in an energy filter that sits before the camera. For thicknesses equal to one inelastic MFP, the signal is reduced by 1/e. When tilted to 60 degrees the projected thickness doubles, so only a fraction  $1/e^2$  of the signal remains. For STEM imaging, on the other hand, the practical thickness limit is the elastic MFP, because there is a deleterious effect on the signal from multiple elastic scattering. This still allows for imaging by STEM tomography of specimens that are at least three times thicker than by TEM. With some compromise in resolution the thickness range can be extended further.

# 2.2.2 STEM Contrast of Biological Samples

As described in the introduction, a STEM image is formed pixel by pixel by scanning a focused electron probe over the sample; transmitted electrons are counted at each point by a series of detectors. Most commonly used are annular DF (ADF) and high-angle annular DF (HAADF) detectors to collect electrons that are scattered out of the primary electron beam (Fig. 2.1). These detectors record

<sup>&</sup>lt;sup>3</sup>It should be stressed that we consider here thick samples for which STEM imaging offers advantages over TEM. For the opposite extreme, that is for thin unstained samples up to a few 100s of nanometers, TEM proves superior. For such samples that are considerably thinner than the inelastic MFP, and for which the weak phase approximation holds, TEM phase contrast offers superior contrast and signal-to-noise-ratio compared with the STEM dark field [24].

variations in the scattering of electrons that are produced by spatial modulations in density and differential scattering cross-sections, integrated over a range from inner to outer cutoff angles of the detector. Note that when the specimen is removed the ADF signal is zero. A bright field (BF) detector is configured to match, more or less, the illuminating cone that diverges from the focus at the specimen. Scattering to angles beyond this cone causes a loss in signal and therefore dark contrast on a brighter background. Since the BF detector collects only those electrons that deviate little from direct transmission, the BF image ideally reflects the variation in total scattering from point to point. For a given chemical composition, the DF signal is directly proportional to the number of scattering atoms, i.e., the mass density. Mass measurement by STEM [9, 10, 11, 14, 25] have therefore frequently been used to access information not directly accessible by other techniques.

The DF signal at larger scattering angles is comprised of elastically scattered electrons. These may undergo additional inelastic scattering, but inelastic scattering alone will not produce a signal at high angles. The differential scattering cross-section for elastic scattering (2.1, 2.2) follows the simple Rutherford dependence of  $Z^2$  at high scattering angles where screening effects are negligible. Because heavy atom stains scatter electrons elastically, several orders of magnitude more strongly than the light atoms of biological matter, the stain in plastic sections provides most of the signal in DF images that only collect the high-angle scattering. According to Fig. 2.2, an inner collection angle of several 10s of mrad is typically enough to suppress the scattering of the matrix of light elements and to provide a good signal-to-noise-ratio for dark-field images of stained samples.

For plastic sections, the BF contrast peaks at stained areas where electrons are scattered away from the forward direction, i.e., these electrons are not collected by the BF detector. The ADF detects primarily these stained areas but without the background of transmitted or forward scattered electrons that are present in the BF. For cryo-preserved specimens, objects in the cells that have higher concentrations of heavy atoms will be preferentially detected by ADF, while a combination of mass/thickness contrast and variations in atomic composition provide the BF signal. As will be discussed in the following Sect. 2.2.3, for thick specimens in tomography applications, these advantages of background-free DF imaging are offset due to beam divergence and multiple scattering through the long sample path, and therefore BF images are often used for plastic thick samples.

# 2.2.3 Resolution and Thick Sample Effects

Inelastic and plural scattering in a thick specimen lowers the tomographic resolution [26]. In most biological specimens the interest is in structural details much larger than a single atom (except for the case of single-particle reconstructions of purified macromolecules). In such a case plural electron scattering in thick samples may be tolerated to an extent that preserves the three-dimensional structure, even if atomic

resolution and sensitivity are lost. However, energy loss and plural scattering in the specimen affects the image quality differently in STEM and TEM. A STEM detector records angular variations in the scattering of electrons rather than changes in their energy. Hence chromatic effects do not severely affect the image quality. In the case of TEM, phase coherence is strongly affected by chromatic effects, because electrons have to pass through the objective lens and its chromatic aberration causes energy-loss electrons to be imaged imperfectly onto the camera, causing blurring of the image.

The resolution of a STEM image is related to the angular broadening of the beam upon propagation through the sample. The spreading of a STEM probe in thick biological samples is, to first approximation, governed by two effects: the geometrical beam divergence and the broadening due to plural elastic scattering in the specimen [20, 27, 28]. Beam profile calculations for a STEM beam that penetrates a thick slab of ice are shown in Fig. 2.3. The calculations are based on a wave optical multislice algorithm that accounts for the incident probe wavefunction and the elastic scattering of electrons using a "frozen lattice" approximation for high-angle scattering from an atomistic structure, including the effects of thermal vibrations [29]. A realistic atomistic model of amorphous ice was obtained from molecular dynamics simulations [20]. Figure 2.3 displays the electron probe propagation and broadening in vacuum and ice for two different semi-convergence angles  $\alpha$  of the STEM probe, 2.9 and 9.7 mrad. The minimal 'geometrical' broadening of the probe in vacuum is attained for a focus roughly at the center plane of the sample. Profile spreading caused by scattering dominates for both semi-convergence angles at the

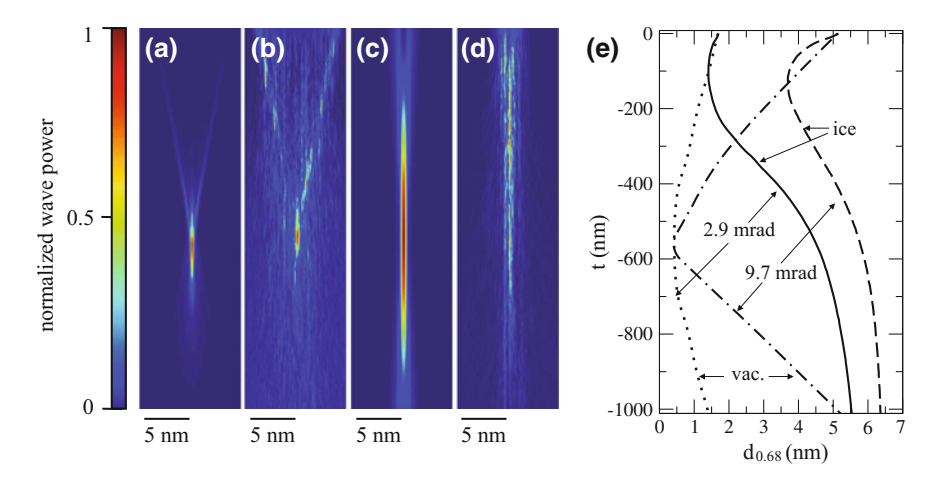


**Fig. 2.3** Calculated longitudinal beam profiles and broadening for a 200 keV electron probe in vacuum and ice. The beam semi-convergence angle is  $\bf a, b$  10 mrad and  $\bf c, d$  2.9 mrad, the spherical aberration is 2 mm and the probe is focused at the center of the sample. The profiles are plotted for a depth t up to 1  $\mu$ m. Note the aspect ratio in the profile images is expanded in the horizontal dimension.  $\bf e$  Probe diameter  $d_{0.68}$  that contains 68% of the electrons as a function of depth t

large specimen thickness, so that the beam diameter at the exit face is roughly the same for both semi-convergence angles. Although incident beam convergence of 9.7 mrad produces a smaller probe focus in vacuum, a smaller semi-convergence angle should be used for tomographic experiments, in order to utilize the larger depth of focus that is proportional to  $1/\alpha^2$ , and to reduce the electron dose for radiation-sensitive material that scales with  $\alpha^2$ .

Figure 2.3e shows the beam diameter defined as the area that contains 68% of the electrons as a function of the specimen depth for  $\alpha = 9.7$  mrad and  $\alpha = 2.9$ mrad. The figure indicates that a resolution in the range of a few nanometers can be obtained with an electron probe of small convergence angle in biological samples even if they are a micrometer thick. In agreement with the previous discussion, the smaller semi-convergence angle is the better compromise for the resolution throughout the sample. A refined calculation would take into account multiple inelastic scattering, which leads to an additional broadening of the STEM beam in thicker specimens [30], but does not change this major conclusion. The quantitative broadening displayed in Fig. 2.3e will be slightly worse when multiple inelastic scattering is to be included. In fact, nanometer-resolution has been demonstrated in STEM for micrometer-thick plastic sections [31], stained samples [32], and liquid-cells [16]. It should be stressed that a similar resolution cannot be obtained in phase contrast TEM unless zero-loss filtering is applied [26], upon which the majority of electrons that suffer from one or more inelastic scattering events will not contribute to the image, but do heavily contribute to radiation damage.

In the presence of multiple scattering, object details will be imaged with better resolution when they are located on the surface facing the probe forming lens in STEM, and facing the objective lens in TEM [26, 33, 34]. In STEM mode this top-bottom effect results in a poorer resolution for specimen details at the bottom of a thick layer, whereas details at the top are imaged with a resolution given by the diameter of the scanning beam. In TEM-mode, details at the bottom are imaged with additional chromatic error, whereas details at the top show the additional influence of multiple scattering [34]. In STEM mode the resolution throughout the sample thickness can be optimized by an appropriate focus which reduces the resolution at the top surface but improves the resolution at the bottom surface by balancing with the geometrical broadening. This situation is shown in Fig. 2.4, where the probe is focused roughly at the center of the sample. In practice, this is hard to achieve because the depth of the area of focus is unknown during standard tomographic experimental protocols. However it is possible to combine a series of acquisitions at multiple focus values in order to extend the depth of field [35, 36].

With increasing thickness, the resolution in STEM ADF or HAADF images tends to degrade more than in a BF image because the dark field detectors collect an increasing fraction of multiply scattered electrons, while a small BF detector ideally does not distinguish between events that take electrons out of the direction of transmission. It was therefore suggested that STEM tomography tilt series of thick stained sections is optimally performed with a BF detector [28, 31, 37]. Care must be taken because multiple (in)elastic scattering can lead to contrast inversion in the

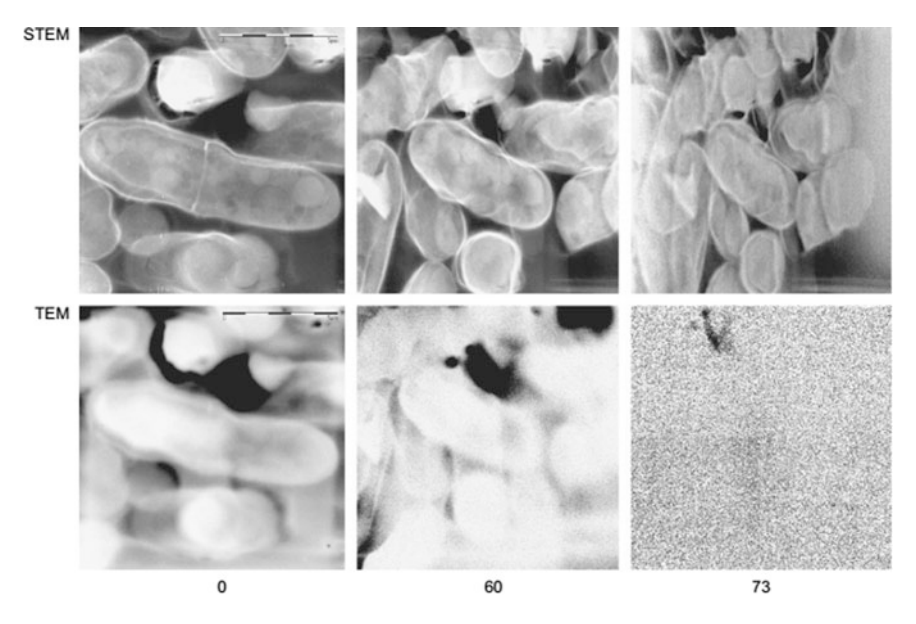


Fig. 2.4 Comparison of TEM and HAADF-STEM tomograms of micrometer-thick sections of yeast cells, at 0, 60, and 73° tilt. (Reprinted from [32])

DF image when the outer collection angle is not sufficiently large. In such a case, a considerable fraction of the scattering ends up beyond the DF detector, e.g. when the scattering distribution broadens upon increase of thickness with specimen tilt. Then the contrast of inclusions in a thick matrix, such as clusters of stain reagents, could be inverted. These effects are even more pronounced when energy-selected images are used to amplify the effect of inelastic scattering from the lighter matrix with respect to the scattering of a heavily stained reagent [7].

# 2.2.4 Elemental Analysis

The ability to perform both multimodal imaging and spectroscopy makes STEM a truly powerful analytical technique for studying biological materials [8, 9, 19]. DF STEM collects electrons scattered at pre-defined high angles for image formation, while simultaneously allowing small-angle scattered electrons to pass through the opening in the detector into an electron energy-loss spectrometer (EELS). STEM is ideally suited for elemental analysis of biological samples when beam damage is the limiting factor, since the entire spectrum is collected in parallel. This is in contrast to energy filtered TEM where images from successive energy-loss windows are recorded sequentially. In STEM, the electron dose is applied only to the volume that is analyzed, and the dose rate can be controlled

conveniently with the pixel dimensions and the pixel dwell time. In parallel, EDS can be used to analyze characteristic X-rays generated in the interaction volume on the nano-scale.

In principle, STEM EELS and EDS signals can be recorded with a similar resolution to the bright-field STEM signal; the ultimate spatial resolution is limited by the broadening of the beam. For EDS, multiple inelastic scattering also degrades the spatial resolution, since it results in the production of fast secondary electrons that generate characteristic x-rays, particularly from light elements. However, the cross-sections for inner-shell excitation ("core-loss") and a subsequent X-ray emission are typically 4–6 orders of magnitude smaller than a cross-section for elastic scattering or plasmon scattering [21]. As a result, the practically meaningful resolution for elemental analysis becomes dose-limited and considerably worse than the attainable resolution in a bright-field image.

Despite the fact that the resolution becomes dose limited, analytical signals observed in STEM have clear and compelling applications for biological samples. Whole-cell elemental mapping has demonstrated compositional distribution in freeze-dried biological cells via EDS in STEM [38]. Recent advancement in the collection angle of EDS detectors enhances the possibilities of chemical analysis and mapping of biological specimens [39]. The complementary approach of EELS was employed to identify light atoms (e.g., C, N, O, P, S) and light or transition metals (e.g., Ca, Mg, Zn, Cu, Fe) in thin sections [8, 19, 38, 39].

#### 2.3 STEM Tomography

# 2.3.1 Historical Background

During the first decades since the invention of the electron microscope, most of the information in structural cell biology at submicron dimensions was derived from bright field TEM observations of thin-sectioned plastic-embedded specimens. The thickness limitation was partially circumvented by the imaging of consecutive (serial) sections, which allowed for 3D reconstruction from many 2D slices [40].

High acceleration voltage TEMs (HVTEM), which became available towards the end of the 1960s, are superior to low voltage TEMs with respect to penetration power, lens aberrations and electron-beam damage, see (2.1, 2.2). They were thus used for the observation of sections between 0.5 to several microns in thickness [41, 42]. Micrographs of such observations were difficult or impossible to interpret, since much information was lost when the complex 3D structure contained in the section was projected onto a 2D negative. Thus stereo pairs were obtained in order to regain and analyze some 3D information [41, 43–45], and later electron tomography was developed in order to obtain 3D reconstructions [46]. While HVTEM instruments have higher penetration power than conventional TEM, they still suffer from lens

aberrations as well as from small depth of focus, resulting in blurred images especially at high tilt angles when tilt series are acquired for electron tomography reconstruction [47, 48].

The notion that STEM imaging is more suitable for the observation of thick biological sections than conventional TEM (CTEM) was known already in 1938 when von Ardenne built the first STEM: "At that time this type (i.e. STEM) had priority for us because there was a chance that, even in investigations of relatively thick specimens, such as standard microtome sections, chromatic aberration could be kept low" [49]. After a long gap in the advance of STEM technology, Crewe and his colleagues revived the field and constructed the modern STEM in the 1960s. Crewe & Groves stated that the penetration power of a microscope is not only the ability of a microscope to penetrate through the sample, but also "the ability of a given microscope to produce a high quality image of a thick object" [50]. In this respect the STEM performs better than CTEM as "For a carbon specimen one micron thick a STEM operating in bright field at 90 keV produces an image which is roughly equivalent to that of a CEM operating in bright field at 1 MeV" [50]. It is therefore intriguing to note that the advantage of STEM in the observation of thick biological sections was only picked up for further development decades later, thanks to a small community that optimized STEM biological imaging [8]. STEM was used in a biological context mainly as an analytical tool—for spectroscopy and elemental mapping using EDS or EELS [7, 8, 18, 19, 51, 52], for mass measurements of proteins [10, 12, 13], or for the detection of heavy atom particles which were either naturally occurring in the sample or added as probes or labels [14, 53– 55]. Much work was conducted over the years to characterize and optimize imaging conditions of thick samples in the STEM, which paved the way to STEM tomography of such samples. Gentsch et al. [56] investigated the "top bottom" effect (see Sect. 2.2.3). Smith and Cowley investigated the calculated dependence of image contrast on the collection angle of the STEM detector [57]. They corroborated their calculations with measured contrast of sections up to 2 µm in thickness. They also advocated the use of energy filters for contrast enhancement of thick sections. Indeed, Colliex et al. [7] used a dedicated STEM equipped with an energy loss spectrometer to find optimal conditions for visualizing thick sections with selected inelastically scattered electrons.

Beorchia et al. [58] used a 300 kV STEM explicitly with the aim of optimizing STEM imaging of thick sections for tomographic reconstruction. To that end they used plastic sections with thickness ranging between 0.5 and 8  $\mu m$ . They calculated the rate and degree of section shrinkage upon electron irradiation by measuring the distance between gold beads adhered to both sides of the sections and found that sections shrink between 45% for a 1  $\mu m$  thick section to 30% for an 8  $\mu m$  thick sections. They obtained tilt series ranging between  $\pm$  50° with images having sharp contrast and good focus.

# 2.3.2 STEM Tomography of Thick Plastic-Embedded Sections

STEM tomography was first developed for materials science applications, mainly using the HAADF detector, because it was appreciated that DF contrast provides "true-projections" of the sample (Sects. 2.2.1, 2.2.2) [59]. HAADF STEM tomography was used also for biological applications to localize ultra-small immuno-gold labels adsorbed to plastic sections [54, 55] and to localize membranes [60].

A major advantage of performing tomography in STEM mode is the ability to raster the beam in lines parallel to the tilt axis of the tilted sample, while focusing the beam according to the height of each line. Thus, by using dynamic focusing mode [61, 62], focus gradients across highly tilted samples are avoided and all regions of the resulting image remain in-focus. Dynamic focusing is implemented in currently available STEM tomography software packages such as SerialEM [63], Xplore3D [64] (FEI Company, The Netherlands), and others [65, 66]. This is in contrast to CTEM tomography, in which only a narrow region of the tilted sample close to the tilt axis is in focus, while the rest of the sample is blurred. This effect is aggravated as thicker samples are observed due to changes of the contrast transfer function.

The work of Aoyama et al. [32] demonstrated the unequivocal advantage of STEM over zero-loss energy-filtered TEM tomography of thick (1  $\mu$ m) sections observed with 300 kV STEM. The quality of TEM images was low even at zero tilt (Fig. 2.4). STEM images showed much more information throughout the tilt series, and due to dynamic focusing images remained sharp even at high tilt angles (up to 73°). It was found that radiation damage in the STEM mode was considerably lower than during TEM tilt series acquisition even when the average electron dose was carefully equalized between the two modes. This is in agreement with our findings with cryo-STEM tomography [20] (see Sect. 2.4), and could be explained as a result of the short dwell time of the beam at each scanned point, which probably allows for energy dissipation, hence to less damage. Images were significantly improved when the semi-convergence angle was reduced from 30 to 3 mrad.

Interestingly, the authors claimed that due to the thickness of the sample "the distinct advantages of HAADF imaging could unfortunately not be observed". Indeed, the group of Richard Leapman at the NIH optimized conditions for STEM tomographic acquisition by advocating use of the BF detector instead [31]. The BF detector was less sensitive to the deleterious effects of multiply-scattered electrons (see 2.2.3). Thus, BF STEM was found to be more suitable for the imaging of thick samples as the degradation of resolution due to the top-bottom effect was much reduced compared to HAADF STEM. In addition, using a small semi-convergence angle, while increasing the probe size at focus, resulted in less divergence of the beam through the thick sample (see Sect. 2.2.3), as has been demonstrated elsewhere [27, 32, 58, 67–69].

Further development of STEM tomography for plastic sections include using microprobe mode (i.e., very small semi-convergent angles) [69], dual-axis data

collection [70], and through-focal tilt-series approach for keeping thick volume entirely in focus, ameliorating the beam-spreading phenomenon [35, 36].

#### 2.3.3 Cryo-STEM Tomography for Vitrified, Unstained Cells

The advantages of STEM tomography for stained, embedded thick sections leads to the obvious question of whether there is an advantage for vitrified, unstained samples as well. Until recently, there was a commonly held belief that STEM imaging for cryo-preserved, unstained biological specimens would not be possible due to insufficient scattering contrast from the light elements of biological specimens, given the dose limits for sample damage by the focused scanning probe beam. We recently showed that these concerns can be overcome [20].

As discussed in Sect. 2.2.3, cells and tissue consist almost entirely of organic material and water, which constitute small atoms with low atomic number Z: hydrogen, carbon, nitrogen, oxygen. Specific objects in the cells are enriched in heavier atoms. Examples include ribosomes and poly-phosphate bodies, with enriched phosphorus content, and mineralization precursors based on calcium deposits [71, 72]. In addition, the cell has varying mass density due to inherent density differences in specific organelles macromolecules (lipids vs proteins, for example). The contrast observed in cryo-STEM tomography (CSTET) images will depend on the detector used. The DF image represents the elastic scattering, with an extra sensitivity to heavier atoms. The BF contrast shows the missing signal, i.e., the scattering to all angles beyond the detector outer cutoff. BF contrast represents mainly the mass density variation in different parts of the cell, as projected down the path of the electron probe beam. Choosing a sufficiently large upper collection angle for the BF signal, similar or larger than the probe convergence angle, will suppress phase contrast.

Damage to vitrified biological material is a major concern, and much literature has documented the dose (usually measured in electrons/Ų) that is tolerable in order to prevent loss of detail and resolution [19, 73–75]. Dose tolerance is based on the effect of specific interactions between the electron and the specimen (as described in Sect. 2.2.1). Indeed, Dose tolerance of vitrified specimens was shown to actually be improved in cryo-STEM with respect to cryo-TEM imaging (as measured by observation of bubbling in the sample) [20]. Beam scanning was recognized long ago as a means to reduce sample damage in electron crystallography, and the STEM probe can be considered an extreme form of this approach [62]. As for preservation of high resolution information, it was shown that with judicious selection of scan rate and electron flux, resolution reaching 2 Å could be obtained for STEM images of SrTiO<sub>3</sub> at 15 electron/Ų electron doses, similar to those used for single particle macromolecular TEM imaging [76]. Due to the

extended dose tolerance exhibited by CSTET, dual-axis tomography schemes can be considered using judicious dose-fractionation.

#### 2.3.4 CSTET and Elemental Analysis of Bacteria

Much cryoTEM tomography (CET) has been performed on vitrified bacterial cells, resulting in a wealth of information about bacterial cellular structure and function (recent reviews: [77–80]). However, because of the limitations on specimen thickness, most wildtype bacteria are too thick to study by CET. Lately, the use of bacterial mini-cells [81] and ghosts [82] has become popular, because they are of sufficiently thin dimensions to provide high-quality CET reconstructions. Since CSTET allows for tomography of specimens around three times thicker than for CET (Sect. 2.2.1), a wide variety of cells can be observed without the need for sectioning or use of mini-cells.

Comparison of CSTET and CET reconstructions of *Agrobacteria tumefaciens* revealed that similar features could be found with CSTET, but with much improved contrast over noise (Fig. 2.5).

As was shown previously for thick plastic sections [32] (Fig. 2.4), we found that useful data could be collected up to very high tilts with the CSTET mode, while for TEM imaging, the data collected at high tilts did not provide information that improved the reconstructions. This was measured by comparing cross-correlations of odd-even divided datasets. Only for the CSTET data did addition of high-tilt data increase the coefficient value (supplementary Fig. 5 in [20]), indicating a contribution of added information above noise.

T-phage attack on an E coli cell is observable in three dimensions by CSTET, even though the overall thickness of the sample exceeds 1 micron (Fig. 2.6). The phages can be observed in early stages of attachment and cargo delivery (unpublished results).

As described in Sect. 2.2.4, analytical measurements by EDS or EELS are straightforward in STEM mode. Unlike the approach of freeze-drying the entire grid, the area of interest can be targeted exclusively in STEM while preserving the vitrified state of the rest of the sample. Thus, for instance, sample thickness can be directly calculated with EELS measurements [83]. In addition, elemental analysis was performed by EDS on the dense bodies found in vitrified *Agrobacteria tumefaciens*, and found to contain excess phosphorus (see Fig. 2.7), identifying them as polyphosphate bodies (PPBs) [84]. Because elastic scattering is directly related to atomic number (Fig. 2.2), it was also possible, by judicious choice of collection angle, to map and quantify the distribution of phosphorus in the DF image [84]. Such Z contrast can of course be generalized to other situations where the elemental composition is known.

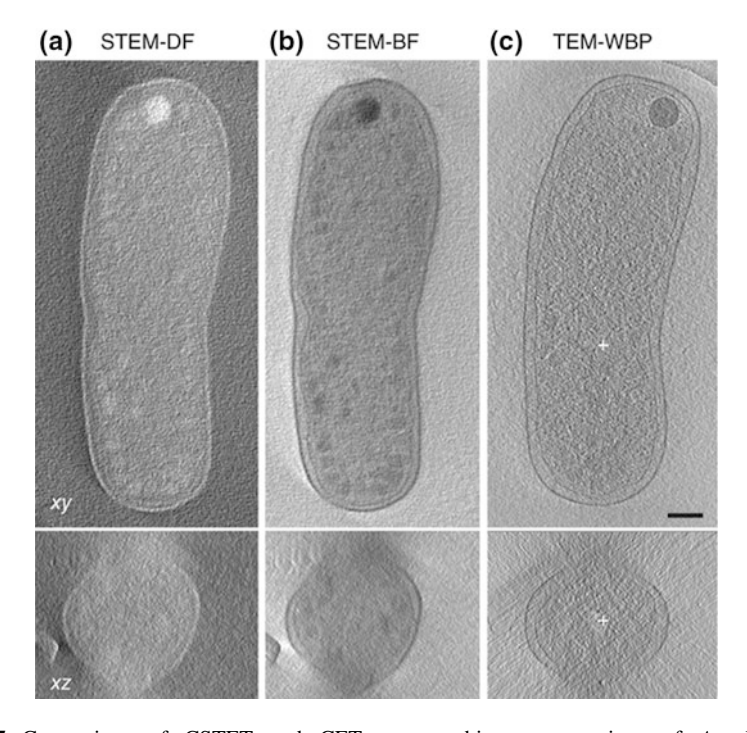


**Fig. 2.5** Comparison of CSTET and CET tomographic reconstructions of *Agrobacteria tumefaciens*. **a, b** 20-nm-thick reconstructed xy and xz sections of a CSTET tilt series of 84 images taken to  $\pm$  65° with intervals of 2° for tilt angles below 50° and of 1° at tilts higher than 50°, using the signals collected from DF (**a**) and BF (**b**) detectors. Total cumulative exposure was 115 electrons/Ų. **c** 20-nm-thick sections of an energy-filtered CET reconstruction from a tilt series of 81 images over a range of  $\pm$ 62° with similar sampling geometries. The defocus was -25  $\mu$ m, and a cumulative exposure of 80 electrons/Ų. Reconstructions were done by weighted back projection. Scale bars, 200 nm. (Adapted from [20])

# 2.3.5 CSTET and Elemental Analysis of Eukaryotic Cells

Eukaryotic cells have been studied extensively by CET tomography (recent reviews: [85–87]), primarily at the very thin edges. Cell adhesion and cytoskeleton structure can often be studied in detail. In order to access thicker regions, it is necessary to produce thin lamellae by cryo-sectioning, either by the CEMOVIS technique [88–90], or cryo-Focused Ion Beam (FIB) milling [91–93]. These methods can produce spectacular results but the methodology for producing the thin sections is highly challenging. In addition, the lamellae are removed from their whole-cell context. By just being able to access three-fold thicker regions of spreading vitrified cells, CSTET allows for access to far more cellular processes and organelles, as schematically illustrated in Fig. 2.8.

Results with CSTET on eukaryotic cells have shown excellent visibility in the reconstructions, even for regions as thick as one micron. In contrast to bacteria,

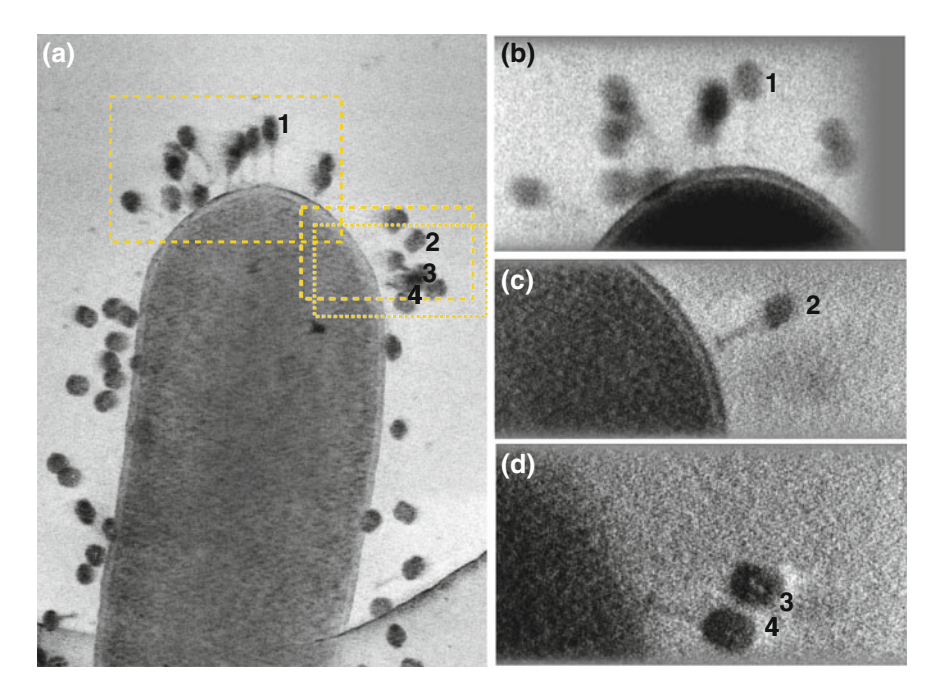


**Fig. 2.6** T-phage attack on an E coli cell. Volumetric rendering of the BF CSTET reconstruction. The image is a projection (minimum intensity) through the entire reconstruction volume. Most of the phage have not yet injected DNA so the capsids appear full. Such reconstructions are difficult to obtain by TEM because the phage are shadowed by the bacterium during much of the tilt series

where the macromolecular crowding is very high, and lack of compartmentalization renders the cell density very similar in most parts of the cell, the eukaryotic cell organelles and compartments have dramatically different mass densities, allowing for highly detailed visualization of lipid droplets, mitochondria, endoplasmic reticulum (ER), actin filaments, microtubules and other cellular components [94]. Examples in Fig. 2.9 depict areas from CSTET reconstructions of breast epithelial and lung fibroblast cells. The resolution in these tomograms is sufficient to observe the mitochondrial cristae. Details of data collection are provided in Sect. 2.5. The DF reconstructions (Fig. 2.9b, d) highlight the areas enriched in higher Z elements, such as ribosomes (labeled "rib"). Deposits displaying strong contrast within the mitochondrial matrices of the fibroblast cells were analyzed by EDS and found to contain Ca and P atoms (labeled "CaP" in panels a, b). Such deposits are not present in the mitochondria of the breast epithelial cell shown here. Unlike most other cellular features whose contrast inverts from BF to DF, lipid droplets ("ld" in panels c, d) appear darker in both images. The high lipid density creates a strong BF signal, but the high concentration of carbon, as opposed to oxygen in the aqueous background, results in weaker scattering to high angles and a low contrast in the DF. Even such a small difference in atomic number has a strong effect on the contrast.

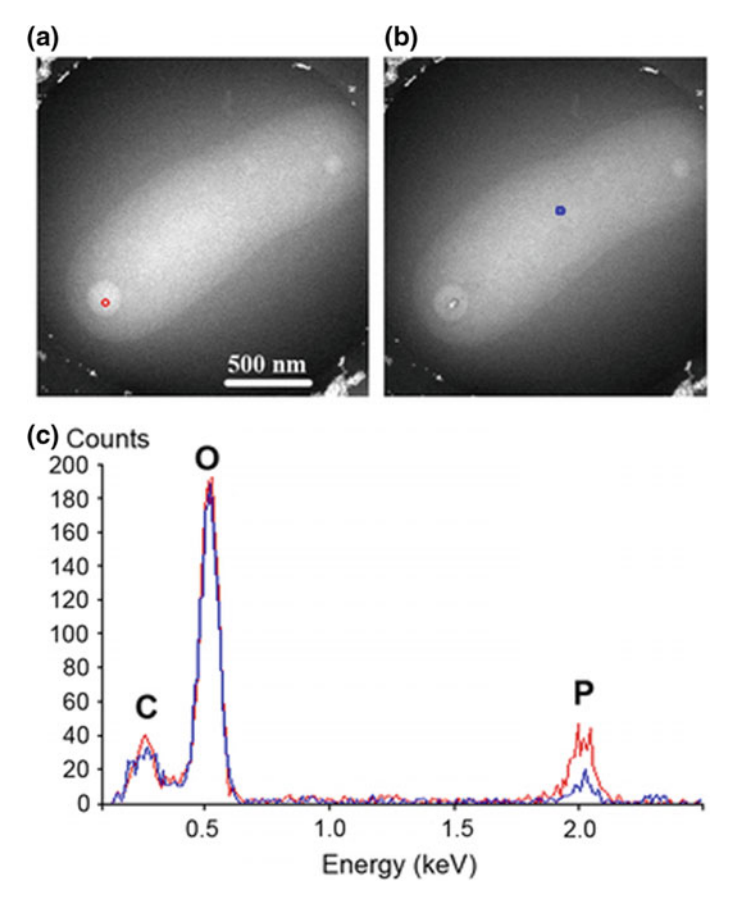


**Fig. 2.7** EDS analysis of a bacterium. **a**, **b** Cryo-STEM images of a bacterium for which EDS spectra were measured. The red and blue circles show the areas for EDS analysis of the PPB (red) and the cellular background (blue). In (**b**), there is evidence of damage from EDS measurement of the PPB, which was measured first. **c** The PPB EDS spectrum (red) superimposed on that of the cellular background (blue). (Adapted from [84])

# 2.4 Conclusions and Future Prospects

It is recognized that STEM tomography holds enormous promise for thicker biological sections. Despite this, the method has not been widely applied. With the development of computer controlled TEM/STEM instruments in the last two decades, high-performance STEM has became routine in a regular TEM column and many more researchers now have the opportunity to apply STEM to biological materials. At the Weizmann Institute, we have used exclusively STEM (rather than TEM) for tomography of plastic sections (details of the experimental setup in Sect. 2.5) since obtaining our Tecnai F20 TEM/STEM [95–99], and we believe that

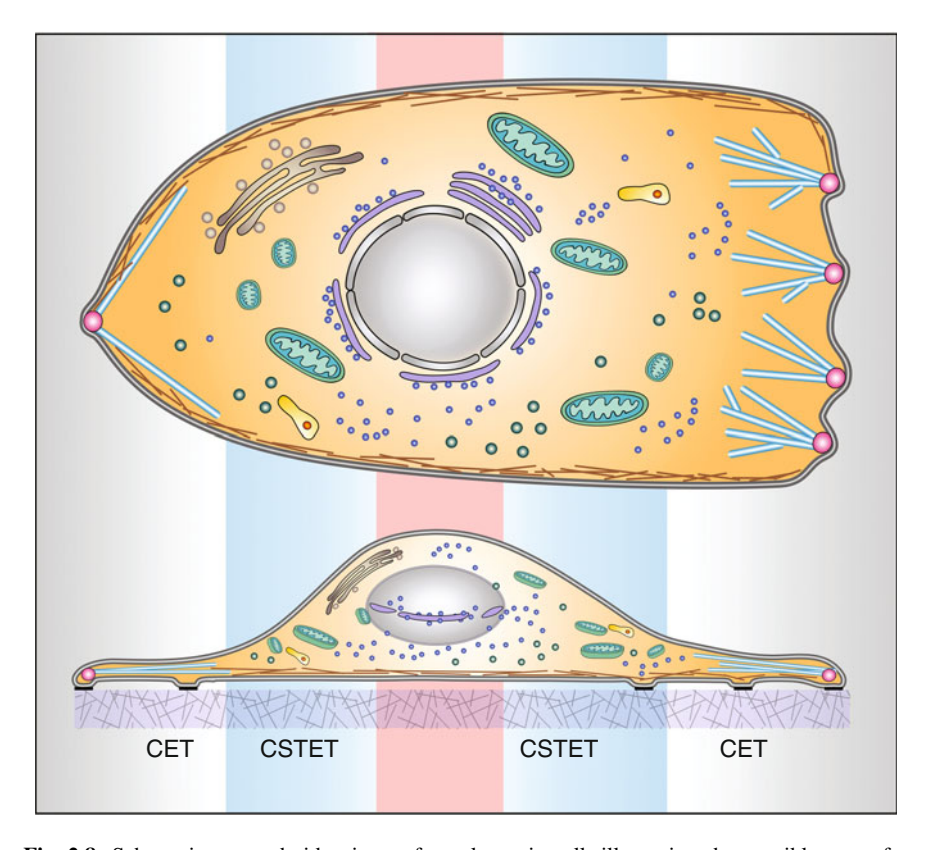


**Fig. 2.8** Schematic top and side views of a eukaryotic cell, illustrating the possible areas for investigation by CET or CSTET. The red region remains too thick, and can be observed only after thinning

as these dual-mode instruments become more available, the method will also be more popular. Instruments with 3-condenser lens systems, which allow for flexible control of semi-convergence angle and probe size, are increasingly available. Complementary methods of "serial surface" imaging by SEM combined with microtomy or FIB milling of plastic sections (covered in other chapters of this book) are excellent techniques that have their own advantages including wide field of view (FOV), lack of missing-wedge artifacts, etc. But the inherently lower resolution of the SEM means that if it is desired to obtain all the detail that the stain distribution provides, then STEM tomography is still the application of choice.

Because STEM is superior for identifying ultra-small gold labels and other fiducial markers [54, 55], it also holds high promise for multiplex-immunolabeling studies, where several sizes of fiducial or alternatively, fiducials of different metal compositions, could be discriminated and identified.

For vitrified samples, CSTET is a brand new method, and we anticipate it will meet a need for observing biological organelles within the context of their cellular

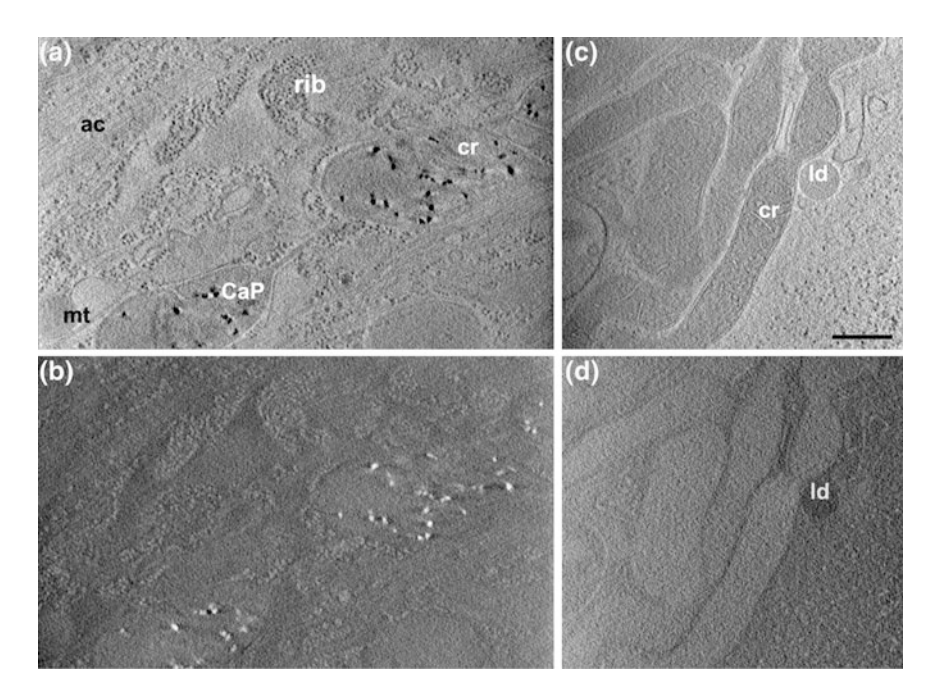


**Fig. 2.9** CSTET reconstructions of vitrified human cells, from cryoSTEM tilt series of vitrified cells with simultaneous collection of BF and HAADF signals. Panels a,b: The BF (a) and HAADF (b) reconstructions of a 50-nm thick portion of a human lung fibroblast WI-38 cell (this region of the cell is 500 nm thick in total). Panels c,d: The BF (c) and HAADF (d) reconstructions of a 50-nm thick portion of a human epithelial breast MCF10A cell (this region of the cell is 780 nm thick in total). Scalebar = 400 nm for all panels. Abbreviations: ac = actin filaments, mt = microtubule, lb = lipid droplet, rib = ribosomes, cr = mitochondrial cristae, CaP = mitochondrial matrix deposits containing calcium and phosphorus

environment, without the need for cryo-microtomy or FIB milling. Recent results demonstrating "live" STEM imaging of lightly-stained bacteria in a liquid cell [100] were obtained with a DF detector. It would be interesting to see if BF imaging would allow for observation of samples without addition of contrasting agents, and if dynamic processes could be observed in the liquid environment [101].

Because of the ability to penetrate thicker areas, the use of correlative methods based on fluorescent markers is sorely needed for CSTET. Specific areas of interest can be difficult to identify when scanning thick cells, because of the superimposition of details in the projected images.

Other emerging techniques for obtaining 3D data on whole vitrified cells are cryo X-ray tomography [96, 103, 104], and cryoFIB/SEM slice & view [105–107]. They both hold promise for wider FOV than CSTET could provide, but at the expense of resolution compared to CSTET.

The CSTET technique could be optimized by working at higher voltage (300 kV or higher), and by improving control over the illuminating probe beam. Another area for optimization is on the detection side. A multi-ring annular detector that would allow for multiple detection on a controllable range of acceptance angles would allow for fine-tuning of contrast in the DF reconstructions. With improved detectors, scan generators and electron optics, it may be possible to obtain excellent results even from the thickest regions close to the nuclei of intact vitrified cells [93].

# 2.5 STEM Tomography Experimental Setup at the Weizmann Institute

STEM tomography of plastic sections and CSTET are conducted on a Tecnai F20 microscope operated at 200 kV, equipped with a HAADF detector at the 35 mm port, and a Gatan BF/DF detector located under the fluorescent screen. Details of the microscope configuration can be found online at <a href="http://www.weizmann.ac.il/ChemicalResearchSupport/electron-microscopy/instrumentation">http://www.weizmann.ac.il/ChemicalResearchSupport/electron-microscopy/instrumentation</a>. Switching between TEM and STEM is done in a straightforward manner, by choosing the appropriate "FEG Control" registers. Alignment after switching modes takes less than 15 min for an experienced practitioner. The workflow, in brief is as follows:

#### 2.5.1 CSTET data collection protocol

- 1. The protocol for sample vitrification of cells is identical to that for cryo-TEM.
- The Gatan TAC100 retractable cryoblades and cold finger are cooled down at least 20 min before inserting the sample. The EDS equipment on this instrument precludes use of an FEI cryobox. The sample is inserted using standard routine for side-entry holders.
- 3. In TEM or STEM imaging mode, at very low magnifications, appropriate areas for study are selected, and those positions are saved.
- 4. The appropriate FEG register for STEM imaging is chosen, and a large condenser aperture is inserted for alignment. After basic alignments, an appropriate small aperture is selected (10 or 20-micron apertures usually).
- 5. The dose is measured by imaging the beam (over vacuum) onto the Gatan US4000 camera, situated under the fluorescent screen, and converting integrated counts to electrons according to the calibrated value. The dose can be controlled by the condenser aperture size, the spot size value, the extraction voltage, the gun lens value, and scan rates. Typical dose values are 0.5–3 electrons/Ų/tilt.
- 6. CSTET datasets have been obtained with the FEI tomography software, but in our current configuration, SerialEM [63] is used for data collection. The software is installed on a separate computer from the FEI microscope computer.

7. In SerialEM, the "Low Dose" function is used such that search mode is done at very low "magnification" (i.e., extreme undersampling over a large field of view). Focussing is done at a distance away from the site of interest, along the tilt axis, at very high magnification over a small field of view so that fiducial gold particles are easily brought into focus by the autofocus module in SerialEM.

- Exposure conditions are typically 2048X2048 arrays, sampled at 2–5 μs per dwell spot. This means that for each tilt, the acquisition time is about 8–20 s per frame.
- 9. Datasets are reconstructed using a variety of software, including IMOD [108], Tomo3D [109] and TomoJ [110].

#### 2.5.2 Plastic section data collection

- Sections are mounted on Formvar coated 50–200 mesh grids. For STEM tomography, slot grids are avoided; while grids mounted on slot grids may be stable during TEM tilt series acquisition, they tend to move during STEM acquisition and the resulting images may be distorted.
- 2. Grids are coated with carbon on both sides, and then floated on poly lysine solution (1 mg/ml), washed with bidistilled water, floated on colloidal gold solution and washed again. The procedure is repeated for the other side of the grid. Incubation time and concentration of solutions can be adjusted for optimal distribution of colloidal gold. Grids can be plasma cleaned or glow discharged prior to incubation with poly lysine if the distribution of gold particles is too sparse.
- 3. Grids are double stained with 2% uranyl acetate in 50% ethanol and Reynolds lead citrate for 10 min each step. Ethanolic uranyl acetate solution is preferred in order to enhance the infiltration of uranyl into the thick section. Note that while stain provides contrast it also adds to the beam broadening effect. Hence, heavy stain of thick sections may in principle be counterproductive and the staining procedure may need to be optimized accordingly.
- 4. Gently plasma-clean the grid in the side-entry holder before insertion. This is mandatory for STEM acquisition for two reasons: a. Dirt on the holder may deflect the beam due to charging effects. b. Contamination on the surface of the sample builds-up during scanning, which results in darkening and blurring of the image.
- 5. After inserting into the microscope, irradiate the sample with a bright wide-field electron beam at very low magnification for 30 min.
- 6. In TEM imaging mode, appropriate areas for study are selected, and those positions are saved.

- 7. Choose appropriate FEG register for STEM imaging and insert a large condenser aperture for alignment. After basic alignments, insert an appropriate small aperture (10 or 20-micron apertures usually).
- 8. Dose for plastic sections is about 100 times larger than for CSTET.

#### References

- A.V. Crewe, J. Wall, L.M. Welter, A high-resolution scanning electron microscope. J. Appl. Phys. 39(13), 5861–5868 (1968). doi:10.1063/1.1656079
- J. Wall, J. Langmore, M. Isaacson, A.V. Crewe, Scanning-transmission electron microscopy at high resolution. Proc. Natl. Acad. Sci. 71(1), 1–5 (1974). doi:10.1073/pnas.71.1.1
- 3. R. Grimm, D. Typke, M. Barmann, W. Baumeister, Determination of the inelastic mean free path in ice by examination of tilted vesicles and automated most probable loss imaging. Ultramicroscopy **63**(3–4), 169–179 (1996). doi:10.1016/0304-3991(96)00035-6
- A.N. Stroud, L.M. Welter, D.A. Resh, D.A. Habeck, A.V. Crewe, J. Wall, Scanning electron microscopy of cells. Science 164(3881), 830–832 (1969). doi:10.1126/science.164.3881.830
- A.V. Crewe, J. Wall, A scanning microscope with 5 Å resolution. J. Mol. Biol. 48(3), 375–393 (1970). doi:http://dx.doi.org/10.1016/0022-2836(70)90052-5
- E. Kellenberger, E. Carlemalm, W. Villiger, M. Wurtz, C. Mory, C. Colliex, Z-Contrast in biology—a comparison with other imaging modes. Ann. Ny. Acad. Sci. 483, 202–228 (1986). doi:10.1111/j.1749-6632.1986.tb34522.x
- C. Colliex, C. Mory, A.L. Olins, D.E. Olins, M. Tencé, Energy filtered STEM imaging of thick biological sections. J. Microsc. 153(Pt 1), 1–21 (1989). doi:10.1111/j.1365-2818.1989. tb00588.x
- 8. C. Colliex, C. Mory, Scanning transmission electron microscopy of biological structures. Biol. Cell **80**(2–3), 175–180 (1994)
- A. Engel, in Scanning Transmission Electron Microscopy: Biological Applications, ed. by P. W. Hawkes, Advances in Imaging and Electron Physics, vol 159. Cold Field Emission and the Scanning Transmission Electron Microscope. Elsevier, pp 357–386 (2009). doi:10.1016/ s1076-5670(09)59009-x
- A. Engel, Molecular weight determination by scanning transmission electron microscopy. Ultramicroscopy 3, 273–281 (1978). doi:http://dx.doi.org/10.1016/S0304-3991(78)80037-0
- 11. R. Freeman, K.R. Leonard, Comparative mass measurement of biological macromolecules by scanning transmission electron microscopy. J. Microsc. **122**(3), 275–286 (1981)
- 12. J.S. Wall, J.F. Hainfeld, Mass mapping with the scanning transmission electron microscope. Annu. Rev. Biophys. Biophys. Chem. **15**(1), 355–376 (1986). doi:10.1146/annurev.bb.15. 060186.002035
- 13. S.A. Muller, A. Engel, Structure and mass analysis by scanning transmission electron microscopy. Micron (Oxford, England: 1993) **32**(1), 21–31 (2001). doi:10.1016/S0968-4328 (00)00022-6
- 14. A.A. Sousa, R.D. Leapman, Development and application of STEM for the biological sciences. Ultramicroscopy **123**, 38–49 (2012). doi:10.1016/j.ultramic.2012.04.005
- D.C. Bell, W.K. Thomas, K.M. Murtagh, C.A. Dionne, A.C. Graham, J.E. Anderson, W.R. Glover, DNA base identification by electron microscopy. Microsc. Microanal. 18(5), 1049–1053 (2012). doi:10.1017/S1431927612012615
- N. de Jonge, F.M. Ross, Electron microscopy of specimens in liquid. Nat. Nanotechnol. 6 (11), 695–704 (2011). doi:10.1038/nnano.2011.161
- 17. T. Klein, E. Buhr, G.C. Frase, in Chapter 6—TSEM: A Review of Scanning Electron Microscopy in Transmission Mode and Its Applications, ed by W.H. Peter. Advances in

- Imaging and Electron Physics, vol 171. Elsevier, pp 297–356 (2012). doi:http://dx.doi.org/10.1016/B978-0-12-394297-5.00006-4
- 18. R. Egerton, Electron energy-loss spectroscopy in the electron microscope. 3 edn. Springer US (2011), doi:10.1007/978-1-4419-9583-4
- 19. M.A. Aronova, R.D. Leapman, Development of electron energy-loss spectroscopy in the biological sciences. MRS Bull. 37(1), 53–62 (2012). doi:10.1557/mrs.2011.329
- S.G. Wolf, L. Houben, M. Elbaum, Cryo-scanning transmission electron tomography of vitrified cells. Nat. Methods 11(4), 423–428 (2014). doi:10.1038/nmeth.2842
- L. Reimer, H. Kohl, Transmission electron microscopy: physics of image formation (2008). doi:10.1007/978-0-387-40093-8
- L. Reimer, M. Ross-Messemer, Contrast in the electron spectroscopic imaging mode of a TEM. J. Microsc. 159(2), 143–160 (1990). doi:10.1111/j.1365-2818.1990.tb04772.x
- S. Sun, S. Shi, R. Leapman, Water distributions of hydrated biological specimens by valence electron energy loss spectroscopy. Ultramicroscopy 50(2), 127–139 (1993). doi:http://dx. doi.org/10.1016/0304-3991(93)90003-G
- P. Rez, Comparison of phase contrast transmission electron microscopy with optimized scanning transmission annular dark field imaging for protein imaging. Ultramicroscopy 96 (1), 117–124 (2003). doi:10.1016/S0304-3991(02)00436-9
- J.S. Wall, J.F. Hainfeld, M.N. Simon, Scanning transmission electron microscopy of nuclear structures. Methods Cell Biol. 53, 139–164 (1998)
- H. Rose, Influence of plural scattering on the image quality of thick amorphous objects in transmission electron microscopy. in 9th International Congress on Electron Microscopy, Toronto, 1978. pp 230–243
- 27. J.K. Hyun, P. Ercius, D.A. Muller, Beam spreading and spatial resolution in thick organic specimens. Ultramicroscopy **109**(1), 1–7 (2008). doi:10.1016/j.ultramic.2008.07.003
- A.A. Sousa, M.F. Hohmann-Marriott, G. Zhang, R.D. Leapman, Monte Carlo electron-trajectory simulations in bright-field and dark-field STEM: implications for tomography of thick biological sections. Ultramicroscopy 109(3), 213–221 (2009)
- J. Barthel, Time-efficient frozen phonon multislice calculations for image simulations in high-resolution STEM, in *Proceedings of the 15th European Microscopy Congress*, Manchester, 2012
- 30. R. Reichelt, A. Engel, Contrast and resolution of scanning transmission electron microscope imaging modes. Ultramicroscopy **19**(1), 43–56 (1986)
- 31. M.F. Hohmann-Marriott, A.A. Sousa, A.A. Azari, S. Glushakova, G. Zhang, J. Zimmerberg, R.D. Leapman, Nanoscale 3D cellular imaging by axial scanning transmission electron tomography. Nat. Methods **6**(10), 729–731 (2009). doi:10.1038/nmeth.1367
- 32. K. Aoyama, T. Takagi, A. Hirase, A. Miyazawa, STEM tomography for thick biological specimens. Ultramicroscopy 109, 70–80 (2008). doi:10.1016/j.ultramic.2008.08.005
- 33. H. Hashimoto, in *Proceedings. AMU-ANL Workshop on High Voltage Electron Microscopy*, Argonne National Laboratory, 1966, pp. 68–70
- 34. L. Reimer, P. Gentsch, Superposition of chromatic error and beam broadening in transmission electron microscopy of thick carbon and organic specimens. Ultramicroscopy 1(1), 1–5 (1975)
- S. Trepout, C. Messaoudi, S. Perrot, P. Bastin, S. Marco, Scanning transmission electron microscopy through-focal tilt-series on biological specimens. Micron (Oxford, England: 1993) 77, 9–15 (2015). doi:http://dx.doi.org/10.1016/j.micron.2015.05.015
- T. Dahmen, H. Kohr, N. de Jonge, P. Slusallek, Matched backprojection operator for combined scanning transmission electron microscopy tilt- and focal series. Microsc. Microanal. 21(03), 725–738 (2015)
- 37. P. Rez, T. Larsen, M. Elbaum, Exploring the theoretical basis and limitations of cryo-STEM tomography for thick biological specimens. J. Struct. Biol. **196**(3), 466–478 (2016)
- 38. J.S. Wu, A.M. Kim, R. Bleher, B.D. Myers, R.G. Marvin, H. Inada, K. Nakamura, X.F. Zhang, E. Roth, S.Y. Li, T.K. Woodruff, T.V. O'Halloran, V.P. Dravid, Imaging and

- elemental mapping of biological specimens with a dual-EDS dedicated scanning transmission electron. Ultramicroscopy **128**, 24–31 (2013). doi:10.1016/j.ultramic.2013.01.004
- 39. Y.H. Pan, K. Sader, J.J. Powell, A. Bleloch, M. Gass, J. Trinick, A. Warley, A. Li, R. Brydson, A. Brown, 3D morphology of the human hepatic ferritin mineral core: new evidence for a subunit structure revealed by single particle analysis of HAADF-STEM images. J. Struct. Biol. **166**(1), 22–31 (2009). doi:10.1016/j.jsb.2008.12.001
- F.S. Sjostrand, Ultrastructure of retinal rod synapses of the guinea pig eye as revealed by three-dimensional reconstructions from serial sections. J. Ultrastruct. Res. 2(1), 122–170 (1958)
- 41. F. Nagata, K. Hama, K.R. Porter, Three dimensional observation of biological specimen with high voltage electron microscope. J. Electron. Microsc. (Tokyo) 18(2), 106–109 (1969)
- 42. A.M. Glauert, The high voltage electron microscope in biology. J. Cell Biol. **63**(3), 717–748 (1974)
- 43. P. Favard, N. Carasso, The preparation and observation of thick biological sections in the high voltage electron microscope. J. Microsc. **97**(1), 59–81 (1973)
- 44. G.L. Scott, R.W. Guillery, Studies with the high voltage electron microscope of normal, degenerating, and Golgi impregnated neuronal processes. J. Neurocytol. **3**(5), 567–590 (1974)
- T. Arii, K. Hama, Method of extracting three-dimensional information from HVTEM stereo images of biological materials. J. Electron. Microsc. (Tokyo) 36(4), 177–195 (1987)
- 46. J. Frank, Electron tomography: methods for three-dimensional visualization of structures in the cell, 2nd edn. (Springer, New York, London, 2006)
- A. Takaoka, T. Hasegawa, K. Yoshida, H. Mori, Microscopic tomography with ultra-HVEM and applications. Ultramicroscopy 108(3), 230–238 (2008). doi:10.1016/j.ultramic.2007.06. 008
- K. Murata, M. Esaki, T. Ogura, S. Arai, Y. Yamamoto, N. Tanaka, Whole-cell imaging of the budding yeast Saccharomyces cerevisiae by high-voltage scanning transmission electron tomography. Ultramicroscopy 146, 39–45 (2014). doi:10.1016/j.ultramic.2014.05.008
- 49. M. vonArdenne, Personal recollections about the development of the electron microscope and its technology. Optik **105**(4), 139–153 (1997)
- 50. T. Groves, Thick specimens in the CEM and STEM resolution and image formation. Ultramicroscopy 1(15–31) (1975)
- 51. K. Zierold, X-ray microanalysis of freeze-dried and frozen-hydrated cryosections. J Electron Microsc. Tech. 9(1), 65–82 (1988). doi:10.1002/jemt.1060090107
- R.D. Leapman, Detecting single atoms of calcium and iron in biological structures by electron energy-loss spectrum-imaging. J. Microsc. 210(1), 5–15 (2003). doi:10.1046/j. 1365-2818.2003.01173.x
- M.T. Otten, D.J. Stenzel, D.R. Cousens, B.M. Humbel, J.L.M. Leunissen, Y.D. Stierhof, W. M. Busing, High-angle annular dark-field STEM imaging of immunogold labels. Scanning 14(5), 282–289 (1992). doi:10.1002/sca.4950140507
- 54. U. Ziese, C. Kubel, A. Verkleij, A.J. Koster, Three-dimensional localization of ultrasmall immuno-gold labels by HAADF-STEM tomography. J. Struct. Biol. **138**(1–2), 58–62 (2002). doi:10.1016/S1047-8477(02)00018-7
- A.A. Sousa, M.A. Aronova, Y.C. Kim, L.M. Dorward, G. Zhang, R.D. Leapman, On the feasibility of visualizing ultrasmall gold labels in biological specimens by STEM tomography. J. Struct. Biol. 159(3), 507–522 (2007). doi:10.1016/j.jsb.2007.06.006
- P. Gentsch, H. Gilde, L. Reimer, Measurement of the top bottom effect in scanning transmission electron microscopy of thick amorphous specimens. J. Microsc. 100(1), 81–92 (1974). doi:10.1111/j.1365-2818.1974.tb03915.x
- D.J. Smith, J.M. Cowley, Aperture contrast in thick amorphous specimens using scanning transmission electron microscopy. Ultramicroscopy 1(2), 127–136 (1975). doi:10.1111/epi. 12023

- 58. A. Beorchia, L. Heliot, M. Menager, H. Kaplan, D. Ploton, Applications of medium-voltage STEM for the 3-D study of organelles within very thick sections. J. Microsc. **170**(Pt 3), 247–258 (1993)
- P.A. Midgley, M. Weyland, J.M. Thomas, B.F.G. Johnson, Z-Contrast tomography: a technique in three-dimensional nanostructural analysis based on Rutherford scattering. Chem. Comm. 16(10), 907–908 (2001). doi:10.1039/b101819c
- A.E. Yakushevska, M.N. Lebbink, W.J.C. Geerts, L. Spek, E.G. van Donselaar, K.A. Jansen, B.M. Humbel, J.A. Post, A.J. Verkleij, A.J. Koster, STEM tomography in cell biology. J. Struct. Biol. 159(3), 381–391 (2007). doi:http://dx.doi.org/10.1016/j.jsb.2007.04. 006
- F. Zemlin, Dynamic focussing for recording images from tilted samples in small-spot scanning with a transmission electron microscope. J. Electron Microsc. Tech. 11(4), 251– 257 (1989). doi:10.1002/jemt.1060110404
- 62. K.H. Downing, Automatic focus correction for spot-scan imaging of tilted specimens. Ultramicroscopy **46**(1–4), 199–206 (1992)
- 63. D.N. Mastronarde, Automated electron microscope tomography using robust prediction of specimen movements. J. Struct. Biol. **152**(1), 36–51 (2005). doi:10.1016/j.jsb.2005.07.007
- 64. C. Kübel, A. Voigt, R. Schoenmakers, M. Otten, D. Su, T.-C. Lee, A. Carlsson, J. Bradley, Recent advances in electron tomography: TEM and HAADF-STEM tomography for materials science and semiconductor applications. Microsc. Microanal. 11(5), 378–400 (2005). doi:10.1017/S1431927605050361
- 65. J. Feng, A.P. Somlyo, A.V. Somlyo, Z. Shao, Automated electron tomography with scanning transmission electron microscopy. J. Microsc. **228**(Pt 3), 406–412 (2007). doi:10. 1111/j.1365-2818.2007.01859.x
- L. Bonetta, Zooming in on electron tomography. Nat. Meth. 2(2), 139–145 (2005). doi:10. 1038/nmeth0205-139
- 67. P.A. Midgley, M. Weyland, 3D electron microscopy in the physical sciences: The development of Z-contrast and EFTEM tomography. Ultramicroscopy **96**(3–4), 413–431 (2003). doi:10.1016/S0304-3991(03)00105-0
- J. Loos, E. Sourty, K. Lu, B. Freitag, D. Tang, D. Wall, Electron tomography on micrometer-thick specimens with nanometer resolution. Nano. Lett. 9(4), 1704–1708 (2009). doi:10.1021/nl900395g
- 69. J. Biskupek, J. Leschner, P. Walther, U. Kaiser, Optimization of STEM tomography acquisition-a comparison of convergent beam and parallel beam STEM tomography. Ultramicroscopy **110**(9), 1231–1237 (2010). doi:10.1016/j.ultramic.2010.05.008
- A.A. Sousa, A.A. Azari, G.F. Zhang, R.D. Leapman, Dual-axis electron electron tomography of biological specimens: extending the limits of specimen thickness with bright-field STEM imaging. J. Struct. Biol. 174(1), 107–114 (2011). doi:10.1016/j.jsb.2010.
- S. Boonrungsiman, E. Gentleman, R. Carzaniga, N.D. Evans, D.W. McComb, A.E. Porter, M.M. Stevens, The role of intracellular calcium phosphate in osteoblast-mediated bone apatite formation. Proc. Natl. Acad. Sci. U S A 109(35), 14170–14175 (2012). doi:10.1073/ pnas.1208916109
- G.M. Khalifa, D. Kirchenbuechler, N. Koifman, O. Kleinerman, Y. Talmon, M. Elbaum, L. Addadi, S. Weiner, J. Erez, Biomineralization pathways in a foraminifer revealed using a novel correlative cryo-fluorescence–SEM–EDS technique. J. Struct. Biol. doi:http://dx.doi.org/10.1016/j.jsb.2016.01.015
- R.D. Leapman, S.Q. Sun, Cryoelectron energy-loss spectroscopy—observations on vitrified hydrated specimens and radiation damage. Ultramicroscopy 59(1–4), 71–79 (1995). doi:10. 1016/0304-3991(95)00019-w
- L.R. Comolli, K.H. Downing, Dose tolerance at helium and nitrogen temperatures for whole cell electron tomography. J. Struct. Biol. 152(3), 149–156 (2005). doi:10.1016/j.jsb.2005.08. 004

- L.A. Baker, J.L. Rubinstein, Radiation damage in electron cryomicroscopy. Methods Enzymol. 481, 371–388 (2010). doi:10.1016/S0076-6879(10)81015-8
- J.P. Buban, Q. Ramasse, B. Gipson, N.D. Browning, H. Stahlberg, High-resolution low-dose scanning transmission electron microscopy. J. Electron. Microsc. (Tokyo) 59(2), 103–112 (2010). doi:10.1093/jmicro/dfp052
- 77. R.C. Guerrero-Ferreira, E.R. Wright, Cryo-electron tomography of bacterial viruses. Virology 435(1), 179–186 (2013). doi:http://dx.doi.org/10.1016/j.virol.2012.08.022
- 78. K. Celler, R.I. Koning, A.J. Koster, G.P. van Wezel, Multidimensional view of the bacterial cytoskeleton. J. Bacteriol. **195**(8), 1627–1636 (2013). doi:10.1128/jb.02194-12
- 79. C.M. Oikonomou, G.J. Jensen, A new view into prokaryotic cell biology from electron cryotomography. Nat. Rev. Micro. 14(4), 205–220 (2016). doi:10.1038/nrmicro.2016.7
- V. Gold, M. Kudryashev, Recent progress in structure and dynamics of dual-membrane-spanning bacterial nanomachines. Curr. Opin. Struct. Biol. 39, 1–7 (2016). doi:http://dx.doi.org/10.1016/j.sbi.2016.03.001
- M.M. Farley, B. Hu, W. Margolin, J. Liu, Minicells, back in fashion. J. Bacteriol. 198(8), 1186–1195 (2016). doi:10.1128/jb.00901-15
- X. Fu, B.A. Himes, D. Ke, W.J. Rice, J. Ning, P. Zhang, Controlled bacterial lysis for electron tomography of native cell membranes. Structure 22(12), 1875–1882 (2014). doi: http://dx.doi.org/10.1016/j.str.2014.09.017
- 83. P. Rez, W. Chiu, J.K. Weiss, J. Brink, The thickness determination of organic crystals under low dose conditions using electron energy loss spectroscopy. Microsc. Res. Tech. **21**(2), 166–170 (1992). doi:10.1002/jemt.1070210208
- S.G. Wolf, P. Rez, M. Elbaum, Phosphorus detection in vitrified bacteria by cryo-STEM annular dark-field analysis. J. Microsc. 260(2), 227–233 (2015). doi:10.1111/jmi.12289
- 85. S. Asano, B.D. Engel, W. Baumeister, In Situ Cryo-Electron Tomography: A Post-Reductionist Approach to Structural Biology. J. Mol. Biol. **428**(2, Part A), 332–343 (2016). doi:http://dx.doi.org/10.1016/j.jmb.2015.09.030
- R. Fernández-Busnadiego, Supramolecular architecture of endoplasmic reticulum–plasma membrane contact sites. Biochem. Soc. Trans. 44(2), 534–540 (2016). doi:10.1042/ bst20150279
- 87. R.N. Irobalieva, B. Martins, O. Medalia, Cellular structural biology as revealed by cryo-electron tomography. J. Cell Sci. **129**(3), 469–476 (2016). doi:10.1242/jcs.171967
- 88. C. Bouchet-Marquis, A. Hoenger, Cryo-electron tomography on vitrified sections: a critical analysis of benefits and limitations for structural cell biology. Micron (Oxford, England: 1993) 42(2), 152–162 (2011). doi:http://dx.doi.org/10.1016/j.micron.2010.07.003
- 89. A. Al-Amoudi, A.S. Frangakis, in *Three-Dimensional Visualization of the Molecular Architecture of Cell–Cell Junctions In Situ by Cryo-Electron Tomography of Vitreous Sections*, ed. by C. Has, C. Sitaru. Molecular Dermatology: Methods and Protocols. Humana Press, Totowa, NJ, pp. 97–117 (2013). doi:10.1007/978-1-62703-227-8\_4
- L. Norlén, O. Öktem, U. Skoglund, Molecular cryo-electron tomography of vitreous tissue sections: current challenges. J. Microsc. 235(3), 293–307 (2009). doi:10.1111/j.1365-2818. 2009.03219.x
- T. Wagenknecht, C. Hsieh, M. Marko, Skeletal Muscle Triad Junction Ultrastructure by Focused-Ion-Beam Milling of Muscle and Cryo-Electron Tomography. European journal of translational myology 25(1), 4823 (2015). doi:10.4081/ejtm.2015.4823
- J. Arnold, J. Mahamid, V. Lucic, A. de Marco, J.J. Fernandez, T. Laugks, T. Mayer, A.A. Hyman, W. Baumeister, J.M. Plitzko, Site-Specific Cryo-focused ion beam sample preparation guided by 3D correlative microscopy. Biophys. J. 110(4), 860–869 (2016). doi:10.1016/j.bpj.2015.10.053
- 93. J. Mahamid, S. Pfeffer, M. Schaffer, E. Villa, R. Danev, L. Kuhn Cuellar, F. Förster, A.A. Hyman, J.M. Plitzko, W. Baumeister, Visualizing the molecular sociology at the HeLa cell nuclear periphery. Science **351**(6276), 969–972 (2016). doi:10.1126/science.aad8857

- 94. D. Kirchenbuechler, Y. Mutsafi, B. Horowitz, D. Fass, S.G. Wolf, M. Elbaum, Cryo-STEM tomography of intact vitrified fibroblasts. AIMS Biophys. **2**(3), 259–273 (2015). doi:10. 3934/biophy.2015.3.259
- D. Charuvi, V. Kiss, R. Nevo, E. Shimoni, Z. Adam, Z. Reich, Gain and loss of photosynthetic membranes during plastid differentiation in the shoot apex of Arabidopsis. Plant Cell 24(3), 1143–1157 (2012). doi:10.1105/tpc.111.094458
- S. Kapishnikov, A. Weiner, E. Shimoni, P. Guttmann, G. Schneider, N. Dahan-Pasternak, R. Dzikowski, L. Leiserowitz, M. Elbaum, Oriented nucleation of hemozoin at the digestive vacuole membrane in Plasmodium falciparum. Proc. Natl. Acad. Sci. U S A 109(28), 11188–11193 (2012). doi:10.1073/pnas.1118120109
- Y. Mutsafi, E. Shimoni, A. Shimoni, A. Minsky, Membrane assembly during the infection cycle of the giant mimivirus. PLoS Pathog. 9(5), e1003367 (2013). doi:10.1371/journal.ppat. 1003367
- 98. O. Tsabari, R. Nevo, S. Meir, L.R. Carrillo, D.M. Kramer, Z. Reich, Differential effects of ambient or diminished CO2 and O2 levels on thylakoid membrane structure in light-stressed plants. Plant J. **81**(6), 884–894 (2015). doi:10.1111/tpj.12774
- E. Milrot, Y. Mutsafi, Y. Fridmann-Sirkis, E. Shimoni, K. Rechav, J.R. Gurnon, J.L. Van Etten, A. Minsky, Virus-host interactions: insights from the replication cycle of the large Paramecium bursaria chlorella virus. Cell. Microbiol. 18(1), 3–16 (2016). doi:10.1111/cmi. 12486
- E. Kennedy, E.M. Nelson, T. Tanaka, J. Damiano, G. Timp, Live bacterial physiology visualized with 5 nm resolution using scanning transmission electron microscopy. ACS Nano 10(2), 2669–2677 (2016). doi:10.1021/acsnano.5b07697
- Nd Jonge, D.B. Peckys, G.J. Kremers, D.W. Piston, Electron microscopy of whole cells in liquid with nanometer resolution. Proc. Natl. Acad. Sci. 106(7), 2159–2164 (2009). doi:10. 1073/pnas.0809567106
- 102. S. Kapishnikov, A. Weiner, E. Shimoni, G. Schneider, M. Elbaum, L. Leiserowitz, Digestive vacuole membrane in Plasmodium falciparum-infected erythrocytes: relevance to templated nucleation of hemozoin. Langmuir: ACS J. Surf. Colloids 29(47), 14595–14602 (2013). doi:10.1021/la402545c
- E.A. Smith, B.P. Cinquin, M. Do, G. McDermott, M.A. Le Gros, C.A. Larabell, Correlative cryogenic tomography of cells using light and soft x-rays. Ultramicroscopy 143, 33–40 (2014). doi:10.1016/j.ultramic.2013.10.013
- E. Duke, K. Dent, M. Razi, L.M. Collinson, Biological applications of cryo-soft X-ray tomography. J. Microsc. 255(2), 65–70 (2014). doi:10.1111/jmi.12139
- 105. A. Schertel, N. Snaidero, H.M. Han, T. Ruhwedel, M. Laue, M. Grabenbauer, W. Mobius, Cryo FIB-SEM: volume imaging of cellular ultrastructure in native frozen specimens. J. Struct. Biol. 184(2), 355–360 (2013). doi:10.1016/j.jsb.2013.09.024
- N. Vidavsky, A. Masic, A. Schertel, S. Weiner, L. Addadi, Mineral-bearing vesicle transport in sea urchin embryos. J. Struct. Biol. 192(3), 358–365 (2015). doi:10.1016/j.jsb.2015.09. 017
- 107. S. Sviben, A. Gal, M.A. Hood, L. Bertinetti, Y. Politi, M. Bennet, P. Krishnamoorthy, A. Schertel, R. Wirth, A. Sorrentino, E. Pereiro, D. Faivre, A. Scheffel, A vacuole-like compartment concentrates a disordered calcium phase in a key coccolithophorid alga. Nat. Commun. 7 (2016). doi:10.1038/ncomms11228
- J.R. Kremer, D.N. Mastronarde, J.R. McIntosh, Computer visualization of three-dimensional image data using IMOD. J. Struct. Biol. 116(1), 71–76 (1996). doi:10.1006/jsbi.1996.0013
- J.-I. Agulleiro, J.-J. Fernandez, Tomo3D 2.0—Exploitation of Advanced Vector eXtensions (AVX) for 3D reconstruction. J. Struct. Biol. 189(2), 147–152 (2015). doi:http://dx.doi.org/10.1016/j.jsb.2014.11.009
- C. MessaoudiI, T. Boudier, C.O.S. Sorzano, S. Marco, TomoJ: tomography software for three-dimensional reconstruction in transmission electron microscopy. BMC Bioinformatics 8(1), 1–9 (2007). doi:10.1186/1471-2105-8-288

# **Chapter 3 Electron Cryo-Tomography**

Josie L. Ferreira, Teige R. S. Matthews-Palmer and Morgan Beeby

**Abstract** Electron cryo-tomography is an integrative imaging technique that produces high-resolution 3-D images of cells and purified complexes. These images can uniquely provide mechanistic insights into in situ biology at molecular and cellular scales. To produce these images, specimens are preserved by flash-freezing without stains or fixatives; these flash-frozen specimens are imaged over a range of angles in an electron microscope and this data used to reconstruct 3-D images of the specimen in near-native state to 'macromolecular' resolution. In this introductory chapter we take the perspective of the workflow of a cryo-tomography project to outline the technique, and important underlying concepts.

#### 3.1 Introduction

Advances in biological sciences have been critically dependent upon the imaging techniques available at the time. It follows that understanding the mechanistic underpinnings of biology in the 21st century relies upon techniques capable of visualizing the components of entire biological processes in situ, and the emergent properties of their interactions.

A technique capable of providing such holistic biological insights is electron cryo-tomography (ECT), an electron microscopy approach that images flash-frozen specimens in three-dimensions, over scales from molecular to cellular, to resolutions capable of discerning individual macromolecular complexes. Because the specimen is cryo-preserved without stains, tomographic images are derived from phase-contrast with the biological material itself and therefore reveal the molecular

J. L. Ferreira  $\cdot$  T. R. S. Matthews-Palmer  $\cdot$  M. Beeby ( $\boxtimes$ ) Department of Life Sciences, Imperial College London, SW7 2AZ London, UK e-mail: mbeeby@imperial.ac.uk

J. L. Ferreira

e-mail: j.ferreira14@imperial.ac.uk

T. R. S. Matthews-Palmer

e-mail: t.matthews-palmer14@imperial.ac.uk

architecture of intact cells in a near-native state. As a result, ECT has made significant and previously unobtainable biological insights into cell biology [1–4]; we illustrate this with examples at the end of this chapter.

ECT is not restricted to imaging unique individual cells and other specimens, however: if multiple cryo-tomograms of identical structures are collected, these identical single particles can be computationally extracted, aligned, and averaged, an approach known as *subtomogram averaging*, *subvolume averaging*, or *single-particle electron tomography*. This approach 'averages out' noise and reinforces signal, greatly improving the signal-to-noise ratio, with the potential for boosting resolution from nanometres to Ångstroms. Because cryo-tomograms are in 3-D, particles can be extracted even from cryo-tomograms of crowded environments such as the cytoplasm, enabling in situ structure determination [5]. Advances in hardware and software have increasingly seen subtomogram averaging applied to structural biology problems, and a growing number of subtomogram averages have been determined to sub-nanometre resolutions, enabling fitting of crystal structures into densities of macromolecular complexes in situ. The boundaries continue to blur between ECT and more traditional single-particle cryo-EM approaches to structure determination, particularly in light of the considerable advances in contemporary cryo-EM [6].

This chapter focuses on the workflow of a biological ECT research project, discussing each step consecutively with emphasis on choices faced by the researcher, and the rationale behind the decision. We start with an overview of the process and underlying concepts, followed by in-depth discussion of specimen choice, preparation, and vitrification; background on microscope hardware setup; software and data collection parameters; and tomogram reconstruction, processing, and interpretation. We intend this chapter to provide an overview and introduction for those training in ECT and many topics are covered in greater depth in subsequent chapters of this book.

Fig. 3.1 An overview of the electron tomography workflow. ECT can be used to image a wide ▶ range of biological specimens from purified protein complexes to large eukaryotic cells and tissues. The sample preparation and vitrification method is primarily dictated by the size of the specimen being imaged. Small specimens (up to a few µm thick) can be plunged into a liquid cryogen, causing rapid vitrification before the formation of crystalline ice can occur. Large specimens (more than a few µm thick) must be high pressure frozen. As imaging of specimens thicker than  $\sim 500$  nm is greatly hindered by excessive inelastic scattering, a method of thinning must be chosen for thicker samples. FIB-milling can be used to mill away part of the specimen, leaving a thin lamellae to be imaged, or cryo-sectioning can be used to produce thin slices of a high pressure-frozen sample. Grid preparation remains a major bottleneck in ECT and the process of sample preparation and vitrification may need to be repeated multiple times before data-collection can begin. When ready, the grids are loaded into the microscope and data-collection parameters are setup according to the type of specimen and biological question. Areas of interest are targeted and tilt series' are collected. Images are then processed and tomograms reconstructed. Finally, single tomograms can be analysed (segmented tomogram from [131]) or multiple sub-volumes can be picked and averaged, producing a higher resolution sub-tomogram average

#### 3.2 ECT: Overview and Key Concepts

In essence, ECT involves calculating the 3-D structure of a flash-frozen specimen to nanometre-resolution (for an overview workflow, see Fig. 3.1). A well-chosen specimen is first flash-frozen, vitrifying it to preclude the formation of ice crystals. The specimen is then inserted into an appropriately configured microscope, and a 'tilt series' of 2-D projection images of the specimen are acquired over a range of angles. Although in 2-D projection images the 3-D information is collapsed along the Z-axis, the full tilt series can be used to computationally extrapolate this 3-D information. Identical subvolumes within the tomogram(s) can additionally be subjected to subtomogram averaging. To design imaging sessions and interpret images it is critical to understand a number of key concepts outlined below.

It is important to understand aspects of electron scattering relevant to ECT. ECT's ability to image biological material without stains or fixatives is facilitated by the strong scattering of electrons by matter, enabling discernible imaging contrast from individual molecules [7]. The flipside of this strong interaction is that many electrons deposit energy into the biological material. When an electron is scattered by the specimen it may be scattered *elastically* or *inelastically* [7]; inelastically scattered electrons break bonds and lose energy, as a result contributing incoherently to the image as noise. Additionally, minimizing the damage caused by inelastically scattered electrons necessitates deliberately keeping electron exposure of the specimen to a minimum, resulting in very low signal-to-noise ratios, and making interpretation of cryo-tomograms challenging. Furthermore the strong interaction with matter means that samples thicker than a few hundreds of nanometres become intractable to imaging due to the uninterpretable inelastic (or multiple) electron scattering.

Another aspect of electron scattering important to interpretation of electron microscopy images is the effect of the considerable spherical aberration in conventional electron lenses. This aberration alters the phase of scattered electrons; the phase alteration is a function of the angle of scatter—i.e., the resolution of the image component. This unintuitively leads to oscillation of the contrast of the image as a function of resolution, a function referred to as the Contrast Transfer Function, or CTF. As a result, features of certain resolutions have zero contrast, while others have negative contrast—obviously a hindrance to interpretation of the image. A positive aspect of the CTF is that it is a function of the focus of the lens (together with the electron acceleration voltage and the spherical aberration coefficient of the objective lens), conveniently meaning that appropriate, deliberate defocusing of the lens can be used to produce phase contrast in specimens, and until recently this was the only method to achieve phase contrast because phase plates (as used in conventional visible light microscopy) had not been developed sufficiently (and still remain rare). The resolution at which the first contrast inversion occurs in the oscillating CTF is colloquially referred to as the "first zero", a particularly important concept in ECT. It is possible to mathematically correct for the CTF contrast inversions in the image past this "first zero", although some data is lost, and some attenuated, as a result.

To understand and interpret a cryo-tomogram it is also important to understand digital image processing concepts. Centrally important is to have an intuitive understanding of Fourier transforms, 3-D Fourier space, and how Fourier concepts can be used to reconstruct a 3-D volume from 2-D projection images taken from different angles [8–10] (the *central projection theorem* and its real space equivalent, the *inverse Radon transform*), and describing images in terms of their constituent spatial frequencies. Of critical importance to interpretation is the fact that cryo-tomograms are invariably 'missing' parts of data in Fourier space due to the fact that the grid cannot be rotated through a full  $\pm$  90° during imaging. This missing data, often referred to as the 'missing wedge' (because the missing data is wedge-shaped in 3-D Fourier space) results in artefacts in the tomogram, manifesting as greatly reduced resolution along the axis parallel to the electron beam, which can only be overcome using averaging techniques.

Another important digital imaging concept is the number of pixels required to capture desired details in an image. At low magnifications the image of a structure of interest covers only a few pixels, but as magnification increases, the image expands to cover a larger array of pixels. To capture the details that you are interested in, therefore, your sampling must be sufficiently fine-grained; the highest resolution (or *spatial frequency*, in Fourier terms) that can be sampled by a given pixel size is described by the *Nyquist frequency*: two objects cannot be resolved if their separation is smaller than a single pixel; the size of a pixel must therefore be no more than half that of the desired highest resolution.

### 3.3 Specimen Preparation for ECT

Vitrification as a preservation method means a specimen can be inserted into the high vacuum of the electron microscopy column for imaging without artefact-associated fixatives [11]. The first cryo-tomographic studies were performed in the mid-1990s [12–14], building on successes in single particle analysis of vitrified specimens [15] stemming from work on vitrification of water in 1981 [16].

Specimen choice and experimental design is critical in ECT. Unsurprisingly, ECT adheres to the GIGO principle—"Garbage In, Garbage Out"—i.e., to obtain good tomography data, an appropriate specimen must be prepared sufficiently well. Before vitrification, therefore, the specimen that best answers the biological question must be selected. If imaging intact cells, is a wild-type organism sufficient, or would another strain or species have cells better suited for tomography, or produce more copies of a specific structure of interest? Should key genes be deleted, truncated, or otherwise manipulated to perturb cellular or molecular structure? If dynamic information is important, can these insights be gained from vitrified specimens, and if so, how could this be achieved?

The most important factor behind image quality is that the specimen and its envelope of vitreous ice are thin enough to avoid excessive electron scattering, meaning it is important to consider strategies to image the thinnest possible

specimen. While sectioning is possible (see below), a number of other options should first be considered. It may be possible to choose an alternative, thinner, species such as imaging *Ostreococcus tauri* (the smallest known eukaryote) to study the eukaryotic spindle [17]. If the organism is genetically manipulable it may be possible to make it thinner, as has recently been done successfully with bacterial 'minicells' [18] or thinner cells [19, 20]. Different media may also lead cells to grow thinner than in standard media [21]. If these non-disruptive approaches fail, thick cells can be gently deflated without full lysis. For example, the bacterial cell wall can be punctured using lysozyme or penicillin to reduce the thickness of the still quasi-intact cell [22]. Partial purification of intact organelles can be achieved as illustrated by purification of eukaryotic mitochondria [23], nuclei [24], or bacterial chemoreceptor arrays [25].

#### 3.3.1 Vitrifying Thin Specimens: Plunge-Freezing

Thin specimens (up to a few microns) can be vitrified by direct plunging into a liquid cryogen. The cooling rate is lower for thicker specimens, which increases the incidence of crystalline ice that damages biological material and diffracts electrons. Specimens are typically mixed with 5–20 nm-diameter gold fiducial markers for tilt series alignment, and applied to a standard 3 mm-diameter electron microscopy grid overlayed with a thin support film. The support film is commonly carbon, although gold support provides stability advantages [26]. Support films are typically glow discharged to make them hydrophilic for specimen adhesion.

A number of cryogens can be used for vitrification. The low heat of vaporization and low boiling point (77 K) of nitrogen means it vaporizes to form an insulating gaseous envelope around the specimen, rendering it unsuitable as a cryogen. More appropriate cryogens with higher boiling points and greater heat capacities can be cooled in a metal cup within an outer reservoir of liquid nitrogen. Ethane's greater heat capacity and high boiling point (184.5 K) make it widely-used. Ethane cooled by liquid nitrogen freezes at 90 K, however, requiring the user to supply heat occasionally to keep the ethane liquid yet cold enough to vitrify. A mixture of ethane with propane conveniently avoids this problem since the mixture remains liquid down to 77 K [27].

To achieve suspension of the specimen in a very thin aqueous envelope for vitrification, specimen suspension is conventionally applied to the grid with a pipette, although it is also possible to dip the grid into the suspension. The specimen accumulates in holes in the grid support film, and excess liquid is removed by blotting with filter paper to leave a thin envelope. Blotting is achieved either manually by carefully touching a piece of filter paper to the grid held by a homemade 'gravity plunger' device that can be triggered to plunge into cryogen (the grid held in tweezers on the end of a vertical rod), or by using a commercial device that uses motorized blotting pads inside a humidity- and temperature-controlled chamber, together with motorized or pneumatic plunging. Such commercial devices allow for

increased reproducibility; blotting parameters typically tuned are blot time and position of blotting paper to control wicking of excess liquid from the grid, and chamber temperature and humidity to regulate evaporation between blotting and plunge-freezing (evaporation rapidly increases the osmotic pressure in a thin film, so can dehydrate cells and disrupt proteins). After vitrification, grids can be immediately transferred to the microscope, placed in long-term storage under liquid nitrogen, or shipped in a dry-shipper to another facility.

Vitrification remains as much an art as a science, however, with ice quality depending on subtleties of the specimen, liquid medium, grid manufacturer and hydrophilicity of the support. Reliably reproducing good grids remains a bottleneck for many projects, and future developments will enable routine and reproducible grid preparation. As such, it is important to screen vitrification conditions for each new specimen type. Screening is best performed on a screening microscope with the ability to rapidly load single grids via a side-entry cryoholder; the speed of such a system enables the user to shuttle between the microscope and vitrification apparatus, iteratively refining vitrification parameters.

# 3.3.2 Vitrifying Thick Specimens: Strategies Towards Tractability

Although specimens as thick as a few microns can be vitrified without formation of crystalline ice, specimens thicker than  $\sim 500$  nm suffer from excessive inelastic and multiple scattering that progressively degrade the image signal-to-noise ratio, requiring thinning approaches even in high-powered microscopes. There are currently two techniques to thin a specimen after freezing: the relatively well-developed cryo-sectioning of specimens using a diamond blade cooled to cryo temperatures (CEMOVIS), and milling techniques to slice through the specimen using a focused ion beam.

Specimens too thick for vitrification by plunge-freezing can fortunately be vitrified under high-pressures (2100 bar) to lower the freezing point of water and slow the formation of ice [28]. A cryo-microtome can subsequently be used to cut the pellet into thin slices (typically 50–200 nm thick) to be manipulated onto a grid for ECT [29]. Cryo-sectioning is technically challenging and can be hindered by artefacts such as compression crevasses caused by the action of the sectioning blade.

An approach suitable for specimens thin enough for freezing at ambient temperatures on a grid, yet too thick for imaging whole, is to use a focused ion beam (FIB) to mill away biological material above and below the part of the specimen of interest. An ion beam—typically of Gallium ions [30]—is directed to mill a plane through the specimen nearly parallel to the grid plane, leaving a thin lamellum supported by unmilled specimen edges, allowing for tilt series acquisition. FIB-milling is a multi-step process, involving ablating the bulk of the specimen first with a high current, followed by a low-current polishing step, minimizing radiation damage to the surface of the lamella [31]. The approach is not currently high-throughput, although is undergoing rapid development [32].

#### 3.4 Tilt Series Acquisition

When suitable grids have been obtained, tilt series can be collected. The ease of collection, quality, and characteristics of the data collected depends on the hardware configuration of the microscope and selection of parameters. In this section we step through the implications of hardware configuration, software configuration, and highlight the rationale behind choice of various data collection parameters.

#### 3.4.1 Hardware Configuration

The user is likely to have a choice of microscopes to collect data on, either at a local facility, or by traveling to collect data at a remote facility. This section provides an overview of contemporary electron microscope hardware to enable the user to assess the suitability of a microscope for a given project.

The first step is loading the specimen into the microscope itself. Loading into the microscope needs to be rapid and controlled so as to avoid warming or exposure to moisture in the atmosphere that might condense onto the specimen during transfer; if vitreous ice warms above  $-160~^{\circ}\text{C}$  [33] it may undergo a phase transition to cubic ice. Loading and transfer of grids focuses, therefore, on maintaining the grid either in liquid nitrogen or in the supercooled gaseous nitrogen immediately above the liquid nitrogen surface which excludes atmospheric water.

Two main types of specimen loading options are available in commercial microscopes: side-entry cryoholder systems enable insertion of a single grid into the microscope at once, while cryocartridge systems allow the user to insert multiple grids simultaneously into a holding area in the column. With cryoholder systems, grids are mounted on the end of a cooled metal rod inserted through an airlock in the side of the microscope, necessitating brief exposure to the surrounding atmosphere protected only by a thin retractable shutter. This is generally seen as less stable and lower throughput than cartridge entry because the sample is in direct physical contact with a large liquid nitrogen dewar with the possibility of vibrations from boiling nitrogen. Nevertheless acquisition of high quality data is possible on side entry microscopes given a well-maintained stage. With a cryocartridge system grids are cooled by thermocoupling to the microscope cryogen via flexible braids instead of physical attachment to the cryoholder dewar itself. With these systems, vibrations are reduced, and data collection is considered to be more stable. After insertion, the cryoholder's dewar must be refilled every few hours, whereas with cartridge-based systems the cryogen dewar is not directly attached to the specimen holder and can therefore be considerably larger, facilitating longer data collection sessions between cryogen refills, which can be automated. High throughput can also be devised for cryoholder-based systems by building automated robotic refilling strategies controlled by data collection software [34, 35]. It was thought that using liquid helium as a microscope cryogen might provide some benefits by reducing radiation damage, but tests revealed that liquid nitrogen actually provides superior results [36].

Electron microscopes perform analogously to visible light microscopes: a radiation source is projected through a specimen, and scattered radiation is focused by lenses to form an image. The electron microscope uses electrons for illumination, and the more coherent the beam is, the more coherent the scattered electrons that are refocused to form a higher resolution image [7]. Contemporary electron microscopes use tungsten filaments, lanthanum hexaboride crystals, or field emission guns (FEGs). The latter two sources are sufficiently coherent for ECT; however when aiming for a high resolution subtomogram average, a FEG is the best source, and will always be fitted to 300kV microscopes which are optimal for ECT. The electrons can be accelerated from the electron gun with various energies, which dictate the mean penetration depth before the first scattering event. Appropriate settings are discussed below.

Image data can be recorded in a number of ways: film, charge coupled detectors (CCDs), or direct detection devices (DDDs). Performance of these three detector types is assessed in terms of the Modulation Transfer Function (MTF) which describes the attenuation of spatial frequency approaching Nyquist frequency as a result of pixel cross-talk; and the Detective Quantum Efficiency (DQE) which describes the fraction of input signal captured by the detector. A camera with a DQE value half that of another camera would require double the electron dose to achieve an image of the same quality. Although film allows for large images to be recorded at relatively high resolutions, the time required to repeatedly load and develop it is a huge bottleneck for cryo-tomographic data collection, rendering it unfeasible for high-throughput imaging [37]. CCD cameras detect photons produced by electrons hitting the detector and offer a large improvement in output time as compared to film. However, although CCDs are efficient in making data acquisition high-throughput, the random interactions of the electrons with the scintillator comes with a resolution cost and near Nyquist frequency the performance of CCDs is lower than that of film in terms of both DOE and MTF [37].

The recent development of DDDs based on Complementary Metal–Oxide–Semiconductor (CMOS) technology has revolutionized the field of cryo-microscopy because by directly detecting electrons, a considerably superior MTF is achieved. Some DDDs have a number of additional critical innovations that further their abilities. One of the major resolution limitations in cryo-microscopy has been specimen movement due to instability of the specimen holder, exposure to the electron beam, or specimen charging that deflects electrons. New DDDs can be used to correct for the blurring caused by this movement by acquiring many 'subframes' with sufficient signal for subsequent subframe alignment and averaging, producing a sharper composite image. In tomography this is particularly important at high tilts (particularly for relatively unstable specimen cryoholders) where the specimen is thickest, giving an improved signal-to-noise ratio and providing higher resolution images. Another major DDD innovation is to use a *superresolution* approach to locate where individual electrons hit the camera by determining the peak's centroid to subpixel accuracy—effectively halving the pixel size and quadrupling number of

pixels, i.e., doubling the Nyquist frequency [38]. This means that if the electron flux is kept slow relative to image acquisition rate, detections events can be interpreted as having come from a single electron, enabling equal weighting of each electron collision with the detector, resulting in lowered noise, a strategy referred to as *counting mode*. The very high DQEs of new DDDs enables acquisition of images with superior quality to CCD camera images with considerably lower electron dose resulting in less electron damage to the specimen. The DQEs of current DDDs are superior to both film and CCDs at all spatial frequencies [39]. Each camera has different imaging properties which may be optimal for different specimens and techniques. If DDDs continue to improve on frame-rate and precision of the detection of individual electron events, their DQEs are expected to approach 100%, even at spatial frequencies approaching Nyquist. The problem then becomes storage of the large volumes of data that is generated!

Because inelastically scattered electrons are incoherent due to reduced energy, they contribute only noise to the image, and some contemporary microscopes are equipped with an energy filter that can remove them—a crucial advantage for thicker tomography specimens. Energy filterered TEM (EFTEM) allows the selection of only electrons within a specific range of energy-loss to hit the detector, greatly increasing the signal-to-noise ratio of images of thicker specimens. Energy filters are composed of magnetic prisms that bend the electron beam, altering electron trajectories as a function of their energy loss, enabling filtering of all but a narrow window of energies by inserting a physical 'slit' in the beam path; slit size and centre can be altered according to user needs.

An alternative approach to generating phase contrast is to use the still relatively new technology of phase plates which function by altering the phase difference between the scattered and unscattered electron beam [40]. In recent years, two types of phase plates have become commercially available. The Zernike phase plate [41] provides a uniform spectral transfer with a flat CTF for frequencies important for tomography. The Zernike phase plate is made of a metal aperture supporting a thin amorphous carbon film with a small hole ( $\sim 1$ um) in the centre positioned at the back focal plane of the objective lens that unscattered electrons pass through. Scattered electrons are further scattered by the carbon film increasing their path length, hence producing a phase shift. At the desired phase shift of 90° the sine component of the CTF shifts to cosine, which maximises contrast for low spatial frequencies. The more recently developed Volta Phase plate has demonstrated useful improvements in contrast for ECT [42]. This phase plate is a heated continuous film of amorphous carbon that builds a potential when irradiated by the focused electron beam. This potential confers a phase shift on the unscattered beam, resulting in phase contrast. In addition to improved contrast, use of a phase plate allows for at- or near-focus imaging and reduction in electron dose [43], not only decreasing specimen damage but reducing specimen movement and allowing for improved tilt series alignments and improved reconstructions.

#### 3.4.2 Data Acquisition Software

The user has a choice in data collection software packages, and the needs of the project will dictate which is used. As it is critically important to minimize exposure of the specimen to the electron beam prior to data collection, data collection is performed under the 'low dose' philosophy. This means that an area of the grid is imaged once and stored digitally together with metadata about which part of the grid the image corresponds to, and its magnification. The user can then perform additional targeting 'offline' by referring back to this image instead of re-exposing the area to the electron beam. In general the software will use a number of preset magnifications to first take an overview grid 'atlas'. Favourable squares can be identified on the grid atlas and imaged at higher magnification, and targets selected from the stored square images. Because electron dosages per unit area are lower for low magnification images, the total dose before data collection is essentially negligible.

A variety of sophisticated data collection software packages integrate this philosophy into their design. In practice, tilt series collection is not straightforwards, as optic stability, stage accuracy and reproducibility, and specimen stability may not be ideal, requiring constant monitoring and compensation. Data acquisition software therefore utilizes a low dose philosophy and controls microscope optics, stage movement, and imaging, automatically applying entire sets of presets to simultaneously change parameters such as image shifts and beam intensity together with magnification changes while tilt series images are being collected. Although the end goal is the same—one or more tilt series of the specimen—there is an array of software to acquire data (at the time of writing the "Software Tools for Molecular Microscopy" Wikibook provided an up-to-date list). Proprietary solutions exist; at the time of writing JEOL produces TEMography™ for JEOL microscopes; FEI Company produces the Xplore3D<sup>TM</sup> Tomography Suite and its successor, Tomography 4.0<sup>TM</sup>, for FEI microscopes; TVIPS GmbH produces EM-Tomo for TVIPS cameras attached to a variety of microscopes; and Gatan Inc. produces a tomography module for their GMS imaging suite for microscopes fitted with Gatan cameras.

The user, however, also has a number of free software options, the choice resting upon the desired balance between interactivity and automation, and ease of installation. At one end of the spectrum, tilt series can be collected manually by the user without dedicated software, ensuring the specimen remains at eucentric height. In practice this approach is rarely followed, except in exceptional circumstances where user intervention is essential, for example with manual alignment of phase plates [44]. Arguably the most widely used package is SerialEM [45] (a sister package to the IMOD suite of programs for tomographic reconstruction, manipulation, and analysis), best known for its flexibility, customizability, and platform-agnosticism, and batch tilt series acquisition mode. Another free solution to tilt series acquisition is UCSF Tomo [46] which is considerably simpler in presentation than SerialEM and employs a prediction-based scheme to maintain specimen focus and centring in the viewing window for batch tomography mode that is sufficiently robust in terms of targeting and tracking for routine overnight tilt

series acquisition. The most complex data collection software is Leginon, developed to fully automate data collection across various electron cryo-microscopy modalities [47] and microscope manufacturers, and can be installed across multiple computers controlling all microscopes in a facility [48]. To achieve automated tilt series acquisition, the predictive codebase of UCSF Tomo has been incorporated into Leginon [49].

The user must identify parameters for data collection optimal to answering the biological question. For frozen-hydrated biological specimens the main limitation to resolution is radiation damage. This means that data collection parameters need to be carefully optimised to reduce the extent of this damage while simultaneously optimizing the signal-to-noise ratio of images collected (see Table 3.1 for an overview of parameters to consider).

**Table 3.1** Multiple data-collection parameters can be altered depending on the type of sample being imaged and the required result. Outlined here are general rules-of-thumb that can be followed when dealing with thick samples, when high contrast tomograms are desired, or when attempting to generate sub-tomogram averages of high resolution

	Strategy to increase contrast	Strategy to increase resolution	Strategy to deal with thick samples
Voltage	Low (200 keV) as thickness allows	High (300 keV)	High (300 keV)
Total electron dose	High (>100e-/A2)	Low (<50e-/A2)	High (>100e-/A2)
Defocus	High (-5um to -15um)	Low (-2um to -4um)	High (-5um to -15um)
Magnification	Low (more e- per pixel)	High (pixel size half Nyquist)	Low (more e- per pixel)
Tilt range	Low (maximise e- dose per projection image)	Higher (decrease missing wedge)	Low (extreme tilts will be even thicker)
Tilt increment	Large (more e- per image)	Small (sample fine details but not important for subtomogram averaging)	Large (facilitates higher SNR, enabling alignment of tilt series)
Tilt scheme	Not relevant	Dose symmetric	Dose symmetric
Phase plates	Always use if possible	Always use if possible	Always use if possible
Energy filter	Always use if possible	Always use if possible	Always use if possible

#### 3.4.3 Data Collection: Electron Dose Considerations

The acceleration voltage of the electron beam can be selected, and dictates the penetrance and contrast of the electron beam, with higher energies being capable of penetrating thicker samples due to statistically longer electron path-lengths before being inelastically or multiply scattered. Voltage can be selected up to a given maximum for the microscope model. Higher voltages (300 kV) are invariably better suited to the thicker samples used in ECT and therefore the user will usually select the highest voltage the microscope is capable of delivering; higher voltage microscopes also tend to be better equipped for tomographic data collection. In practical terms, 200 kV is the lowest voltage useful for tomography of samples thicker than a couple of hundred nanometres.

Cumulative electron dose over the tilt series is a critical consideration for ECT. Unfortunately, for every elastically scattered electron that contributes to image formation, there are approximately three inelastically scattered electrons that damage the specimen and contribute noise to the image [50]. This problem is particularly acute for ECT where multiple images need to be acquired of a single specimen, with each successive image progressively damaging the specimen. If a high resolution subtomogram average is desired, the user must ensure that the cumulative electron dose across the tilt series must be kept low enough to avoid excessive damage at the molecular level, typically to <50 e<sup>-</sup>/Å<sup>2</sup> levels used for single particle analysis [51, 52]. Optimal electron dose for subtomogram averaging can be determined by using only a subset of early frames from the tilt series to make the final reconstruction. Here, a reconstruction based on the full tilt series can be used for alignment, but the average can be made using only the first few—relatively undamaged—images, leading to increased resolution [53]. This process could be followed using different subsets of early frames to determine the optimal dose before electron damage becomes detrimental to the average. Medium-resolution subtomogram averages from whole cells may benefit from trading higher-resolution information for higher contrast by increasing the electron dose to  $>60 \text{ e}^{-1}/\text{Å}^2$  [54] while collection of very large datasets for multiple lower-resolution averages may benefit from reduced data quantity requirements by trading medium-resolution information for higher contrast by using higher electron doses of greater than 120 e<sup>-</sup>/Å<sup>2</sup> [35]. Finally, whole-cell tomography projects, in which noise obscures signal below ~4 nm resolution can be collected at even higher electron doses from  $\sim 120 \text{ e}^{-1}/\text{Å}^2$  to  $\sim 300 \text{ e}^{-1}/\text{Å}^2$ , depending upon the radiation tolerance of the specimen, the principal consideration being to avoid large-scale warping or 'bubbling' of the specimen that will lead to poor tomographic reconstruction [55]. Because total cumulative dose is distributed between the frames of the tilt series, but sample thickness increases with tilt angle, exposure times (or electron flux) can be increased as a function of tilt angle.

#### 3.4.4 Data Collection: Choosing Microscope Defocus

Defocusing the microscope's objective lens is a convenient and conventional approach to attaining phase contrast of the specimen by manipulating the CTF to provide contrast at desired spatial frequencies. As a rough approximation, the higher the defocus, the higher the low-resolution contrast, but the lower the contrast at high resolution. The user must therefore carefully choose the optimal defocus for the biological question and sample thickness (thicker samples will require higher defocus to compensate for lower signal-to-noise ratio). For whole-cell tomography projects, defocus is set relatively high (on a 300 kV microscope, typically between -5 μm and -15 μm, to provide a first zero of  $\sim 1/3 \text{ nm}^{-1} - \sim 1/5 \text{ nm}^{-1}$ ). Because the signal-to-noise ratio beyond the first zero is very low, the image is usually filtered beyond the first zero, as discussed further below. For averaging projects, defocus tends to be set closer to focus (on a 300 kV microscope, typically between -2 μm and -8 μm, which provides a first zero around  $\sim 1/2 \text{ nm}^{-1}$  to  $\sim 1/4 \text{ nm}^{-1}$ ) so as to extend the resolution up to the first zero, and reduce attenuation of signal past the first zero due to rapid CTF oscillation; this data can subsequently be recovered by CTF correction and averaging because averaging can boost the signal-to-noise ratio above negligible values.

#### 3.4.5 Data Collection: Magnification

Having determined the optimal electron dose and defocus it is important to consider the best magnification for data collection. In the digital era it is perhaps more appropriate to think in terms of *pixel size* rather than *magnification* to set Nyquist frequency to a suitable value. Oversampling by using pixel sizes considerably smaller than necessary for a required Nyquist frequency is often important because DQE is optimal at frequencies considerably lower than Nyquist frequency. If magnification is set too high, however, the field of view will decrease—as will the electron dose per pixel. This results in decreased signal-to-noise ratio, and fewer particles in the field of view, necesitating collection of more data to compensate if performing subtomogram averaging. In cameras with relatively poor MTFs, *binning* can be used to increase the electron dose per pixel and improve the MTF [56]: the signal from a cluster of adjacent pixels (typically four pixels in a  $2 \times 2$  block) are averaged into a single pixel, doubling the effective pixel size, increasing the signal to noise ratio, but decreasing spatial resolution by quartering the number of pixels.

#### 3.4.6 Data Collection: Tilt Scheme Considerations

After configuring microscope settings for data collection, the data acquisition tilt scheme must be determined. The number of projection images, their tilt angle

distribution, and their order of collection will all impact the qualities of data in the tomogram's 3D Fourier space, and therefore of the tomogram itself.

Tilt range effectively dictates Z-axis resolution and resolution anisotropy. Because the grid bars of the electron microscope are electron opaque, the specimen cannot be tilted a full  $\pm 90^{\circ}$ , resulting in incomplete data on the 3D structure of the specimen, the so-called "missing wedge" of data in Fourier space. In practical terms this effectively reduces resolution along the Z-axis, which must be considered during interpretation of results. The missing wedge in Fourier space manifests in real space tomograms as a 'smearing' of object parallel to the direction of the beam, making spherical objects appear ellipsoidal, and planar structures such as cell membranes becoming invisible when perpendicular to the beam [57]. The amount of missing data depends on the tilt range parameter; the user's choice of this depends upon the desired resolution, stage stability at high tilt, desired speed of acquisition, microscope voltage, and specimen thickness. In a 300 kV microscope it may be possible to tilt to  $\pm 70^{\circ}$  for thin samples, less so in lower-voltage microscopes, except with very thin samples. To reduce the amount of unsampled data in Fourier space, dual-axis tilt series can be collected. Here, after collecting the first tilt series the grid is turned 90° around the axis parallel to the beam, either manually, or mechanically within the microscope [55]. With the grid rotated, a second, orthogonal tilt series can be collected. The electron dose is split evenly between the two tilt series and both tilt series used to calculate a single tomogram with decreased anisotropy due to shrinking the missing wedge to a smaller "missing pyramid". For example, with a  $\pm 67^{\circ}$  tilt range, a dual-axis dataset shrinks the unsampled data from 26% to 10%. Some filamentous structures have been shown to only become visible in dual-axis tomograms [58]. As the total dose tolerated by the biological specimen remains constant, however, and the number of projection images collected doubles, the electron dose per image is halved, leading to less accurate tilt series alignment. The large amount of time needed to collect a dual-axis tilt-series as well as the errors in alignment associated with it diminish the benefits, and in practice dual-axis tomography is rarely performed. It is noteworthy that the maximum achievable resolution remains unchanged but the data improves by becoming more isotropic [59].

The resolution of a reconstructed tomogram is dependent upon the tilt increment between successive projection images (i.e., the size of gaps in data in Fourier space) [60]. The Crowther criterion states that  $d \simeq \pi D/N$ , where d is the smallest resolvable distance, D is the diameter of a cylindrical specimen, and N is the number of projection images over a  $\pm 90^{\circ}$  range. Theoretically, therefore, the finer the tilt increment, the higher the achievable resolution. It is important to note that the final signal-to-noise ratio of a tomogram is independent of the number of images in the tilt series, given constant electron dose; higher tilt increments are therefore used only to speed up the process and increase the signal-to-noise ratio of individual tilt frames to facilitate accurate tilt series alignment. The tilt increment must therefore be set to enable acquisition of spatial frequencies of interest, while

maximising the electron dose per image for a good signal-to-noise ratio for alignment, and to increase the acquisition time. Because specimens are on planar grids and are thicker when tilted, it is possible to compensate for this by sampling higher tilt angles at finer increments. The Saxton tilt scheme [61] where the tilt increment is proportional to the cosine of the tilt angle provides even sampling in Fourier space and optimally divides the electron dose into the minimum number of images, although in practice is not generally performed, particularly as the most information-rich images are those taken of the thinnest sample at lower tilt [55]. It is important to note that the Crowther criterion does not apply to subtomogram averaging projects, as data missing from one subtomogram will be filled in by another, the only limitation being the requirement to accurately align particles, which is dependent mainly upon high-contrast, low spatial frequency data.

The structural information in an image depends on tilt angle (a shallow tilt angle provides a thinner sample, and thus less inelastic or multiple scattering) and cumulative electron dose (the less pre-exposure the sample has seen, the less damaged it will be)—so at which tilt angle should the user collect their first projection image—the image with the least electron damage? While more traditional unidirectional strategies start at one extreme of the tilt range and collect the entire tilt series in a single sweep tilt over to the other extreme, bidirectional schemes start at 0°, seeking to expend the first electrons on the thinnest view of the sample by collecting one half of the tilt series, before returning to  $0^{\circ}$  to collect the other side. Both schemes, however, have problems. Unidirectional schemes use the first electrons at high tilts when the specimen is thickest, losing high resolution features. While the bidirectional scheme uses its first electrons when the undamaged specimen is thinnest, artefacts can be introduced into the reconstruction as a result of the large structural differences due to damage from cumulative electron exposure between corresponding negative and positive angles. The specimen will have undergone structural changes due to electron damage and will not be the same in the first set of low angle images as in the second set. Recently a dose symmetric scheme has been developed with the goal of preserving the high-resolution data, producing near-symmetric information in Fourier space and evenly distributing electron damage throughout the tilt series [62]. The dose symmetric scheme starts at zero and oscillates in tilt direction (for example, 0°, -3°, 3°, 6°, -6°, -9°, 9°...). When using an unstable side-entry holder, an intermediate scheme, the asymmetric scheme, can be used. Here, the tilt scheme starts at an intermediary angle (say 24°), sweeps through to one end  $(-60^{\circ})$  and then returns to collect the remaining images (+24° to +60°) [63]. This is a good compromise and expends the 'best' electrons across the entirety of the relatively low-tilt range, with higher tilts (with thicker specimen and therefore lower signal) being collected only after the specimen has received much of the electron dose [52]. It is also possible to collect two tilt series of the same specimen at different defoci with the intention of CTF correcting the data, with the higher spatial frequency components being derived from the first tilt series [64].

#### 3.4.7 Data Collection: Energy Filters and Phase Plates

Finally, if the microscope is equipped with an energy filter or phase plate, the user should decide whether to use them. An energy filter will invariably improve image quality; the only user-tunable parameter is filter width. In ECT the typical size of a filter slit is around 20 eV (centered at the 'zero loss' energy, or incident energy of the electron beam) as inelastic scattering events are known to remove more than 10 eVs worth of energy (typically 100-1000 eV) [65] and the temporal coherence of current FEGs is extremely good. With a phase plate the only consideration that the user will have is whether its use will impede throughput.

# 3.5 Tomogram Reconstruction: From Tilt Series Data to Biological Insights

Having acquired one or more tilt series, the user must reconstruct a 3-D tomogram, a process divided into the two steps of alignment and reconstruction. Many software packages exist for this, and it is usually possible to perform different stages with different packages. Widely-used packages include IMOD [66], protomo [67], SPIDER [68], TOM Toolbox [69], and TomoJ [70]. Dedicated programs have also been developed to tackle individual steps such as automated fiducial alignment [71], multicore tomographic reconstruction [72], CTF-correction [73] and processor-intensive filtering [74].

### 3.5.1 Alignment

Alignment of the tilt series is the process of precisely determining the relative orientations of each frame of the tilt series to others so as to be able to accurately compute a 3-D tomogram, and is comprehensively covered in Chap. 7. In brief, relative rotations and translations must be determined, as must subtle magnification and rotation changes. To best deduce these transformations it is conventional to add high-density gold fiducial markers for ease of tracking.

After tilt series acquisition, if images are collected on a DDD camera in movie mode, motion correction is performed prior to any alignment. Next, tilt series frames are coarsely aligned by cross-correlation, then fiducial markers are picked and tracked in 2-D either manually, semi-automatically, or fully-automatically to determine a 3-D model of fiducial locations. This 3-D model provides the transformations required to accurately align individual frames in the tilt series for reconstruction. Alternatively, a number of fiducial-less alignment strategies can track high-contrast landmark features instead of exogenous fiducial markers [75, 76].

The aligned tilt series is next processed to maximize signal, as described fully in Chap. 11. Optionally binning is performed to further improve signal-to-noise, avoid unnecessary oversampling, and reduce file size. Typically tilt series are low-pass filtered to remove data past the first zero of the CTF, or CTF-corrected if the tomogram will be used for subtomogram averaging. Tilt series may also be pre-processed by masking the intense signal from gold fiducial markers or contaminants to avoid reconstruction artefacts associated with such very dense materials [66, 77, 78].

Tilt series CTF correction must account for low signal-to-noise ratio (resulting from the low electron dose per frame) and a defocus gradient (instead of uniform defocus across the entire image) if the image being processed is not the zero-tilt image. To boost this low signal-to-noise ratio, power spectra of multiple parts of multiple images corresponding to the same nominal defocus are usually calculated [73]. CTF correction may alternatively be deferred until averaging [51].

Tilt images may also be "exposure filtered" as developed for single particle analysis [79]. This essentially acts as a series of low-pass filters with the frequency cut-off dependant on the cumulative dose each image has received. Exposure filtering leads to an increase in the SNR, giving higher contrast tomograms, and easier subtomogram alignment. However, as it results in the dampening of thon rings it should be performed after CTF correction.

#### 3.5.2 Reconstruction

Tomographic reconstruction involves calculating a single 3-D reconstruction from the multiple aligned 2-D projection images in the tilt series and is covered in-depth in Chap. 8. Reconstruction can be performed using a variety of algorithms although in practice the weighted back-projection (WBP) algorithm is most often used [66], or a family of iterative algorithms typified by the SIRT algorithm [72]. WBP involves "back projecting" the densities from each tilt series image back through a volume; these projections reinforce in areas of the volume corresponding to the specimen structure, with down-weighting of the disproportionately high contribution of the low spatial frequencies. WBP is fast but produces low signal-to-noise ratio reconstructions. Recent increases in computational power has enabled routine use of the SIRT algorithm; SIRT iteratively minimizes discrepancies between the input tilt series and calculated projected tilt series from the tomogram to produce higher contrast reconstructions, although may attenuate signal at high spatial frequencies. If the dataset collected was dual-axis, the conventional approach is to calculate and merge two single-axis tomograms; in the absence of significant specimen warping however, it is possible to attain higher quality reconstructions by aligning both axes simultaneously using a fiducial-less approach [67, 80].

#### 3.5.3 Post-processing to Maximize Signal in Tomograms

Post-processing of the tomogram depends upon the biological question: cell biological questions tend to have the tomogram as the final product for interpretation, while more structural biological questions will involve an additional, subtomogram averaging step. In both cases, however, the aim of post-processing is the same: maximization of relevant signal for accurate interpretation of the dataset to shed light on the biological question. Interpretation often involves visualization of the tomogram in 3-D (instead of 2-D slices through the tomographic data) via volume rendering or, more often, 3-D surface representations using segmentation or isosurfaces. To get to such a 3-D representation a number of noise-reduction approaches can be taken.

If the final image is a tomogram of a unique specimen, signal at resolutions lower than a few nanometres is overwhelmed by noise, and filtering is therefore crucial to optimize more relevant medium- and low-resolution signal for interpretation or segmentation. Filtering is fully treated in Chaps. 7 and 11; as an overview, filters take various forms: linear, non-linear, and anisotropic, and the choice of which to use depends on the problem and available resources [81]. Linear filters act uniformly across the tomogram independent of the local voxel values; non-linear filters modulate their effect depending upon local voxel values (therefore, for example, filtering strongly in areas lacking sharp edges, but less strongly in the presence of edges); while anisotropic filters apply an anisotropic 3D filter that acts to filter parallel, but not perpendicular, to edges (therefore retaining edge information, but still removing noise). The simplest linear filter is a low-pass filter (or Gaussian filter) to remove data beyond the first zero of the CTF. The median filter is a simple nonlinear filter that takes the middle-ranked voxel value of a kernel of voxels around the current voxel [82]. Nonlinear anisotropic diffusion is a nonlinear anisotropic technique that takes into account local structure within the tomogram to locally and anisotropically filter the tomogram, in effect enhancing edges (by not applying perpendicular to the edge) while removing noise (by filtering in other directions) [83]. Nonlinear anisotropic diffusion is generally accepted as the most effective denoising algorithm for individual tomograms [84], although requires considerable computational power.

How can the resolution of a tomogram be assessed? The resolution of a unique tomogram can be cited using a number of criteria [80, 85] as described in Chap. 10. In essence, a part of the tilt series is excluded from reconstruction and subsequently used to determine consistency at different spatial frequencies to quantify the point at which signal-to-noise ratio drops below a threshold. It is important to note that these numbers are relative values for comparison as opposed to technical 'resolution', and tomogram resolution is invariably highly anisotropic due to missing data [86]. Often resolutions of individual tomograms are expressed informally in terms of discernible features such as ability to resolve leaflets of phospholipid bilayers.

If the object of interest is present in many identical copies in tomograms, the very low signal at high resolution can be recovered by averaging the identical

particles. Particles are superimposed, classified, and averaged, reinforcing signal, averaging-out noise, and—provided the specimen is present in a diversity of orientations—producing a complete dataset without a missing wedge of data in Fourier space, as described fully in Chap. 9. Alignment of subtomograms is the crucial first step in subtomogram averaging, typically using a global or restrained six-dimensional rotational and translational search. Optimal alignments are typically deterministic [87, 88], although a maximum likelihood approach has also now been implemented [51]. Alignment algorithms must take into account the missing data from the tomogram for optimal alignment, usually achieved by downweighting missing Fourier components. Intimately interdependent with alignment is classification of heterogeneity, and typically these two processes are performed simultaneously. Because the alignment step is the critical step to determine the highest possible quality subtomogram average, DDD cameras offer considerable advantage by enabling better alignment (in addition to the better data for averaging). Determining the resolution of a subtomogram average is achieved using the 'Gold standard' approach to calculate the FSC as used in single particle analysis [89], fully described in Chap. 10.

## 3.5.4 Visualization and Interpretation of Denoised Tomograms

Subsequent to denoising via filtering or averaging, the tomographic volume is now ready for visualization and interpretation. Visualization may simply involve analysis of slices of the tomogram, or volumetric representation in which the tomogram is viewed as a 3-D box, with density represented by opacity of voxels (3-D pixels). Another common approach is segmentation, described in Chap. 12, in which boundaries of structures are represented as 3-D surfaces. Although many automatic and semi-automatic segmentation algorithms have been described [81], due to the low signal-to-noise ratio, segmentation is usually a manual task despite being inherently slow and subjective. In contrast, the signal-to-noise ratio of subtomogram averages is generally high enough to render boundaries of structures automatically using a density threshold to generate an isosurface.

How can the user identify structures in a tomogram? A number of approaches can be used. "Visual proteomics" is an approach to determining the composition of the cytoplasm using tomography. The dense, heterogenous mixture of hundreds of types of macromolecular complexes in the cytoplasm is intractable to visualize and assign manually, necessitating automated assignment approaches. Template matching uses a template macromolecular complex (such as a ribosome or chaperone) to search a tomographic volume for significant matches. Template matching performs well for large structures above approximately one megadalton [90]. Where the identity of structure is unclear, imaging mutants with removed or enriched components provides evidence on the identity of a structure [91]. Although a

one-size-fits-all tomography tag akin to GFP has not yet been developed, fluorescent proteins can be used by correlating light and electron cryo-microscopies (Correlated Light and Electron Microscopy, or CLEM) in which the location of a fluorescent protein in a cryo-preserved specimen is determined using light cryo-microscopy, followed by ECT and correlation of the two. This technique works best with high resolution imaging such as cryo-PALM (PhotoActivated Light Microscopy) [92]. Alternative work towards a general-purpose tag for ECT has been to develop a ferritin-based fusion tag, although because ferritin is an oligomer, aggregative artefacts are associated with this approach [93]. In the case of identifying objects in subtomogram averages, contrast is sufficiently high to obviate the need for a particularly dense metal tag and densities may be identified by removing components and monitoring resulting subtomogram averages for density losses [94, 35, 95], or by fusing additional domains to components and monitoring for additional densities in the subtomogram average of these mutants [96].

The final stage of the project workflow is the backup and archival of data. Local data should be robustly backed up. Published data can be deposited in the EMDB, which serves as a repository for published electron cryo-microscopy data [97], while raw images used to generate published data can be deposited in the EMPIAR public repository [98].

#### 3.6 Examples of ECT

ECT's unique ability to span cellular and structural biology has lead to important insights in a number of areas. Many of these successes have been in biological systems that are integral to, or associated with, cells and membranes. The reason for this is clear: the pleomorphic nature of membranes makes traditional structural biology techniques difficult or intractable, but poses no such problems for tomographic imaging and analysis. Here we illustrate ECT's unique abilities to provide mechanistic insights into large macromolecular complexes and dynamic cellular processes by highlighting its contributions to two fields: bacterial cell shape maintenance, and the eukaryotic nuclear pore complex. ECT has also provided pivotal advances in a number of other fields such as bacterial pathogenesis [54, 99, 100], proteasome structure [101], membrane trafficking and remodelling [100, 103], and virus infection [102–104, 105, 106] beyond the scope of this chapter.

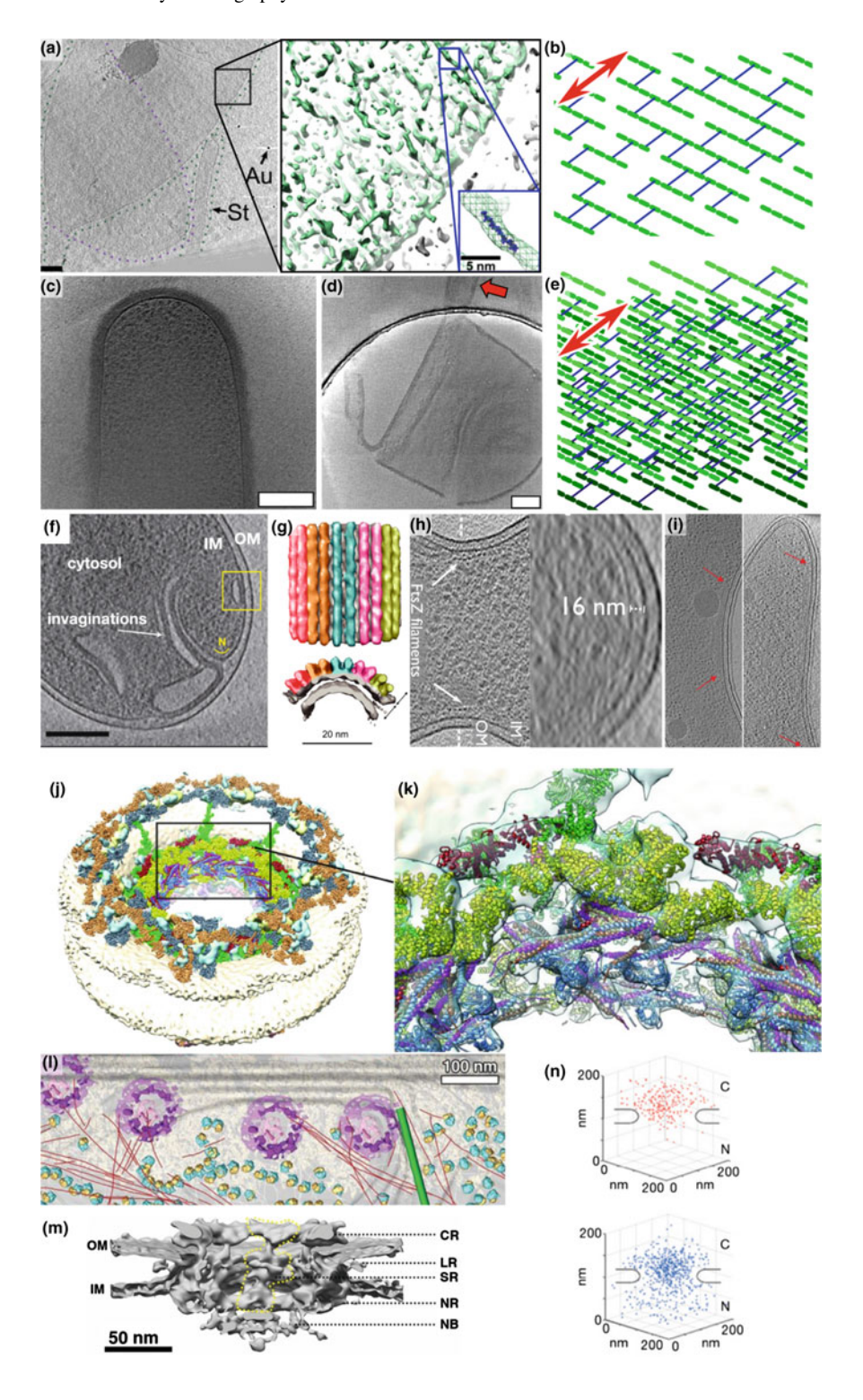
### 3.6.1 Bacterial Cell Shape Maintenance

Bacteria shape themselves, grow, and divide in a deterministic and orchestrated manner. What mechanisms underly these fundamental processes of bacterial cell biology? ECT has made a number of crucial contributions in this area (Fig. 3.2a–i).

Fundamental to cell shape is peptidoglycan, a single giant molecule of interlinked glycans and peptides that confers bacterial shape and mechanical protection, and serves as a scaffold for cell division. Understanding the architecture of peptidoglycan is therefore crucial to understanding these processes, but its size and lack of crystalline structure proved challenging for structural study by traditional techniques. ECT was uniquely able, therefore, to determine the architecture of both Gram-negative [107] and Gram-positive [108] peptidoglycan (Fig. 3.2a–e), and visualize its remodelling during growth and sporulation [19, 109]. These insights have proved foundational to our thinking of how peptidoglycan remodelling confers deterministic cell shape during constant growth [110, 111].

In parallel, ECT provided a series of mechanistic insights into peptidoglycan remodeling [112] by directly visualizing a number of bacterial cytoskeletal elements central to cell shape determination. MreB, a bacterial actin homolog, is core to a multiprotein complex that co-ordinates peptidoglycan biosynthesis (Fig. 3.2f, g). Subtomogram averaging supported by X-ray crystallography revealed that MreB directly binds the membrane [113], the first example of a membrane-binding actin homolog, as an anti-parallel filament [114]. Intriguingly, cryo-tomographic studies revealed that MreB does not form elongated filaments as eukaryotic actins do and as previous light microscopy studies suggested, rationalizing more recent studies that suggested shorter, mobile MreB oligomers [115–117]. ECT also visualized the machinery underlying peptidoglycan remodelling for cell division, the Z-ring, comprised of a number of proteins including the tubulin homolog FtsZ (Fig. 3.2h). FtsZ forms filaments at the division plane with connections spanning the inner membrane [91, 115], and connecting FtsA filaments intermediate between the FtsZ ring and the membrane [118]. Finally, while many bacteria form canonical rod shapes using MreB, others form more elaborate curved or helical shapes. ECT has

Fig. 3.2 Cell shape determination by bacteria and the eukaryotic nuclear pore complex as ▶ examples of the use of ECT. (a-i): ECT has revealed mechanisms behind how bacterial cell shape is determined by peptidoglycan architecture, whose synthesis is coordinated by cytoskeletal elements. ECT discerned densities consistent with being individual glycan strands in isolated Gram-negative peptidoglycan (a, from [107]), confirming that glycans run circumferentially around the long-axis of the cell. Red arrow denotes long-axis of the cell (b). Gram-positive peptidoglycan is considerably thicker and denser (c, from [108]), but distinct breaking and curling in isolated peptidoglycan, highlighted with a red arrow (d, from [108]) can only be rationalized by circumferential glycans also in Gram-positive peptidoglycan. Red arrow denotes long-axis of the cell (e). Cytoskeletal element MreB has been visualized in situ by ECT (f, from [113]), and subtomogram averages of lipid tubes coated with MreB reveal its likely physiological binding mode in situ (g, from [114]). FtsZ filaments have been visualized during cell division (h, from [118]), and Caulobacter crescentus cells have many distinct cytoplasmic filaments, including the metabolic enzyme CTP synthase (i, from [120]). (j-n): The nuclear pore complex is a multimegadalton protein complex whose structure and function is being dissected using ECT. ECT has determined structures to sufficient resolution ( $\sim 20\text{Å}$ ) to fit crystal structures (j, k, from [122]); FIB-milling and ECT has enabled visualization of the nuclear pore complex in situ (L, from [32]), and subtomogram averaging has revealed the in situ structure (m, from [32]). Gold labeling has enabled visualization of the pore transit in situ (n, from [121]). All figures reproduced with permission where appropriate



further implicated other bacterial cytoskeletal proteins in shape determination. For example, in *Caulobacter crescentus*, cryo-tomographic imaging revealed multiple classes of cytoplasmic filamentous bundles involved in cell shape determination [119]. Further work established the major filament bundle to be composed of CTP synthase which together with crescentin (an intermediate filament-like protein) dictates *C. crescentus's* distinctive curved shape [120] (Fig. 3.2i).

In imaging peptidoglycan and the bacterial cytoskeleton, ECT was uniquely able to provide insights into the architecture of large macromolecular complexes that were intractable to traditional structural biology techniques, yet too small for accurate insights from AFM, and too dynamic, have too many components, and too finely-structured to study using super-resolution light microscopy.

#### 3.6.2 The Eukaryotic Nuclear Pore Complex

The  $\sim 100$  Mda,  $\sim 450$ -protein eukaryotic nuclear pore regulates high-speed, bidirectional and highly selective transport of a wide range of molecules in and out of the nucleus. Its size, complexity, its location deep within the eukaryotic cell, and membrane association make it a formidable specimen to study structurally. ECT, therefore, has been uniquely able to contextualize results from more reductionist approaches, providing considerable insights into the structure and mechanism of the nuclear pore from a range of species, and enabling construction of comprehensive pseudoatomic models [121, 122] (Fig. 3.2j-n).

The power of cryo-FIB milling was first demonstrated on whole *Dictyostelium discoideum* cells, providing a subtomogram average of nuclear pore complexes in situ [123]. With cryo-FIB milling, structures can be observed in their native environment, yet with a specimen thickness as thin as (or thinner than) isolated organelles. Using cryo-tomographic data collected from a thin cryo-FIB-milled lamellum, 67 protomers from the ten octameric nuclear pore complexes were extracted and used to generate a subtomogram average to 79 Å resolution. A follow-up study to this involved cryo-FIB milling human cells to visualize the nuclear envelope using a Volta phase plate, enabling a lower electron dosage on the specimen due to higher contrast (Fig. 3.21, m) [32]. Here, specimen charging was minimized by sputtering the specimen with platinum both before and after cryo-FIB milling. The resulting high signal-to-noise ratio in individual particles enabled the authors to observe differences in nuclear pore complex diameters between nuclear pore complexes from different nuclei, suggesting that different conformations are related to the physiological state of the cell.

High resolution subtomogram averages of the *Xenopus laevis* oocyte nuclear pore complex to 20 Å resolution have directly visualized the structure in situ. One insight enabled by this was the visualization of two possible transport routes through the complex [124, 125]. This was consistent with ECT snapshots of the positions of hundreds of gold-labelled proteins with nuclear localization signals providing information on the dynamics of pathways followed by proteins during

nuclear import (an import-defective control revealed accumulation on the cytoplasmic face and in the pore only) (Fig. 3.2n) [121]. In addition to being a strikingly direct proof-of-principle of visualization of molecular function in situ, this suggested an important possible mechanistic insight: nuclear import is through an off-axis channel, while export passes through the centre of the nuclear pore channel.

ECT has also provided mechanistic insights into disassembly of nuclear pore complexes triggered at mitosis to enable chromosomal segregation. By purifying nuclei from human cells, structures have been determined to resolutions as high as 23 Å [24, 126], enabling fitting of a structure of the Y complex and identification of protein interfaces. These protein interfaces are enriched for phosphorylation sites pivotal in controlling nuclear pore complex disassembly, an insight not possible without an overview of the entire intact structure provided by ECT.

# 3.7 Future Challenges: What Do We Need from ECT for Better Mechanistic Insights into Biology?

ECT is uniquely capable of making in situ insights into biological mechanisms. What advances will further push its capabilities? We finish this chapter by covering two broad areas: higher resolution tomograms, and methods to interpret them.

Higher resolution tomograms and subtomogram averages will clearly enable exciting biological insights at molecular and cellular scales. Many areas of ECT can be developed towards higher resolution tomograms, and advances will be synergistic: higher quality images are needed; better processing is needed, and more data is needed.

Higher quality images from the electron microscope will provide higher resolution tomograms and subtomogram averages. The key advantage of higher signal will be the ability to perform better tilt series alignments during tomogram reconstruction and better alignment of subtomograms for averaging. Better cameras with improved DOEs combined with robust and comprehensively characterized phase plates would provide the most obvious single resolution improvement, enable imaging specimens with lowered electron damage yet higher contrast. This would be further augmented by higher coherence electron optics: ultra-high coherence electron sources, monochromators, and spherical aberration correctors. To take full advantage of improved imaging systems, improved specimen stability will reduce attenuation of higher resolutions in high-quality images. This could be achieved with a combination of further improved ultra-stable supports [26], additional approaches to reduce specimen charging such as paraxial charge compensators [127] or routine platinum sputtering [32], development of as-yet-unforeseen approaches to stabilize the specimen analogous to graphene supports for single particle analysis [128, 129], or more stable stages capable of faster and more stable data collection. Finally, sample thickness remains a primary problem toward

high-resolution. Higher throughput, faster FIB milling together with streamlined workflows will facilitate high-resolution subtomogram averaging in situ, as will development of additional genetic techniques to acquire thinner cells.

Improved algorithms will be needed that capitalize upon higher resultant signal-to-noise ratios to provide higher quality reconstructions. One approach will be to develop tomogram reconstruction algorithms that compensate for specimen movement or warping over the tilt series, and mosaic reconstructions based on detection of 'tectonic plates' of structure within the specimen that move synchronously; combinations of multiple individual localized reconstructions of such areas will avoid the 'one size fits all' global fiducial model approach. Algorithms to correct for CTF and phase plate CTF will also be enabled by better quality images. CTF correction of phase plate images requires fitting to two unknowns, defocus and phase plate phase shift, as opposed to solely defocus.

Given higher quality images from hardware and software advances it will be important to increase the throughput of cryo-tomographic imaging. Higher throughput imaging will be enabled by a number of developments. Camera frame-rate and stage speed and stability would enable continuous data collection from a continuously moving stage on timescales of seconds as opposed to minutes, facilitating collection of datasets as large as used in single particle analysis projects, and cutting dataset acquisition times from weeks to hours [35, 54]. Continued algorithm development to use the full tilt series for initial alignment but only the relatively undamaged initial frames for final reconstruction will capitalize on the wealth of data. Increased data acquisition speeds will make specimen availability and targeting the new bottlenecks. Greater availability of sample will avoid having insufficient sample to image; this could be facilitated by automated switching of grids in automated cartridge-based systems, ability to load larger numbers of grids, or more reliable production of grids with optimal specimen density such as the SpotItOn [130] or microfluidics approaches. Fully automated tomography targeting, reconstruction, and annotation will also need to be developed in light of increased throughput, incorporating automated sophisticated target recognition (e.g., automated recognition of cells or holes in carbon), followed by fully automated tomogram reconstruction and automated segmentation of features. Higher quality data will spur advances in global template matching and automated segmentation.

It will be important to be able to interpret higher quality tomograms. Higher signal-to-noise ratio tomograms will lend themselves to easier template matching strategies. It will also be necessary to further develop tagging strategies to identify structures in tomograms. Integrated streamlined workflows incorporating CLEM and cryo-FIB milling in which all metadata is tracked on behalf of the user will remove the overhead of tracking targets by the user are essential. Development of streamlined workflows for super-resolution CLEM is needed to enable fluorescent tags to be used as standard tools for identifying components of tomograms, but it will also be critical to develop a general-purpose tag to be used solely for ECT visualization of protein localization. The recent proof-of-principle study employing ferritin suggests the way forwards [93]. Tagging advances are also needed for

subtomogram analysis. Dissection of macromolecular machinery in situ has met with success by imaging deletion and truncation mutants and imaging the resulting assembly intermediates [35, 95]. Recent developments suggest a powerful complementary approach in which proteins are tagged for localization. A generic framework to rapidly design such tags would facilitate easy interpretation of densities in subtomograms [96].

Finally, these methods may provide a platform for integration of ECT imaging with systems-perspective and cell-level simulations and promises to extract a wealth of information from cryo-tomograms.

#### 3.8 Concluding Remarks

In summary, ECT has become a fully-fledged technique capable of unique insights into biological systems, bridging scales and perspectives from molecular to cellular. Most exciting is the fact that the technique has clearly not yet reached its prime. The future is bright for ECT.

#### 3.9 Practical Guide

Technically, ECT currently requires considerable training. To competently carry out all steps without supervision will typically require multiple months of exposure, training, and experience, and years of additional experience will continue to expand the user's knowledge and abilities. Nevertheless, the fact that the initial stages of ECT do not rely upon in-depth knowledge of Fourier transforms means that an intuitive grasp of the basics of the technique is relatively easy to acquire, and the learning curve to becoming a tomographer, though long, is rarely steep.

The workflow for a ECT project starts when the user identifies a biological question that can be answered by ECT:

- 1. Identify the ECT experiment(s) required to address the question. Identify the resources required. This may involve data-collection at a remote facility, depending on local facility availability.
- 2. Identify optimal specimen: optimize genetics, growth conditions, species, purification procedures, as appropriate. This is often the most challenging step.
- 3. Iteratively optimize vitrification of the specimen, a process that will take one or more days for normal specimens. This process typically involves freezing using a vitrification device starting with parameters and conditions that have been used successfully in a previous project.

- 1. Prepare sample and transport to electron microscopy facility on ice.
- 2. Select and glow-discharge electron microscopy grids.
- 3. Add fiducial markers to sample and vitrify immediately.
- 4. Screen grids on a screening electron cryo-microscope until desirable conditions are found. As there is inevitable variability between vitrified grids, typically three or more identical grids will be frozen for subsequent data collection.
- 4. Load specimen into microscope and collect tilt series:
  - 1. Align and configure microscope (1 h).
  - 2. Load grids into the aligned microscope suitable for data collection (1–2 h).
  - 3. Configure data collection software with parameters appropriate to the question (1 h).
  - 4. Identify targets (1–5 h).
  - 5. Acquire tilt series (15–120 min per tilt series, depending on data collection parameters and acquisition software).
- 5. Reconstruct tomograms:
  - 1. Transfer tilt series to a processing computer for reconstruction.
  - 2. Reconstruct tomograms manually, semi-automatically, or fully-automatically.
- 6. Post-process tomogram
  - 1. Filter and segment, or subtomogram average and generate isosurface.
- 7. Interpret data
- 8. Publish!
  - 1. Write paper, submit, and manage peer review.
  - 2. Archive data in EMDB and EMPIAR.

**Acknowledgements** The authors would like to thank Bonnie Chaban, Peter Rosenthal, and Louie Henderson for insightful comments. This work has been supported by BBSRC grant BB/L023091/1 to MB.

### **Bibliography**

- C.M. Oikonomou, G.J. Jensen, A new view into prokaryotic cell biology from electron cryotomography. Nat. Rev. Microbiol. (2016)
- 2. L. Gan, G.J. Jensen, Electron tomography of cells. Q. Rev. Biophys. 45(01), 27-56 (2012)
- J.L.S. Milne, S. Subramaniam, Cryo-electron tomography of bacteria: progress, challenges and future prospects. Nat. Rev. Microbiol. 7(9), 666–675 (2009)
- V. Lučić, A. Rigort, W. Baumeister, Cryo-electron tomography: the challenge of doing structural biology in situ. J. Cell Biol. 202(3), 407–419 (2013)

- J.A.G. Briggs, Structural biology in situ—the potential of subtomogram averaging. Curr. Opin. Struct. Biol. 23(2), 261–267 (2013)
- 6. W. Kühlbrandt, The resolution revolution. Science 343(6178), 1443–1444 (2014)
- 7. D.B. Williams, C.B. Carter, Transmission Electron Microscopy: A Textbook for Materials Science. (Springer, 2009)
- 8. G. Rhodes, Crystallography made crystal clear a guide for users of macromolecular models (Elsevier/Academic Press, Amsterdam; Boston, 2006)
- 9. E. Hecht, Optics (Fourth edition, Pearson new international edition, 2014)
- 10. J.C. Russ, The image processing handbook, 6th edn. (CRC; London, Boca Raton, Fla, 2010)
- 11. J. Dubochet, Cryo-EM—the first thirty years. J. Microsc. 245(3), 221–224 (2012)
- 12. K. Dierksen, D. Typke, R. Hegerl, J. Walz, E. Sackmann, W. Baumeister, Three-dimensional structure of lipid vesicles embedded in vitreous ice and investigated by automated electron tomography. Biophys. J. **68**(4), 1416–1422 (1995)
- R. Grimm, M. Bärmann, W. Häckl, D. Typke, E. Sackmann, W. Baumeister, Energy filtered electron tomography of ice-embedded actin and vesicles. Biophys. J. 72(1), 482–489 (1997)
- 14. R. Grimm, H. Singh, R. Rachel, D. Typke, W. Zillig, W. Baumeister, Electron tomography of ice-embedded prokaryotic cells. Biophys. J. 74(2), 1031–1042 (1998)
- 15. P.N.T. Unwin, P.D. Ennis, Two configurations of a channel-forming membrane protein. Nature **307**(5952), 609–613 (1984)
- J. Dubochet, Aw McDowall, Vitrification of pure water for electron microscopy. J. Microsc. 124(3), 3–4 (1981)
- L. Gan, M.S. Ladinsky, G.J. Jensen, Organization of the smallest eukaryotic spindle. Curr. Biol. 21(18), 1578–1583 (2011)
- M.M. Farley, B. Hu, W. Margolin, J. Liu, Minicells, Back in Fashion. J. Bacteriol. JB. 00901–15 (2016)
- E.I. Tocheva et al., Peptidoglycan transformations during Bacillus subtilis sporulation. Mol. Microbiol. 88(4), 673–686 (2013)
- T. Murray, D.L. Popham, P. Setlow, Bacillus subtilis cells lacking penicillin-binding protein 1 require increased levels of divalent cations for growth. J. Bacteriol. 180(17), 4555–4563 (1998)
- M. Schaechter, O. Maaloe, N. Kjeldgaard, Dependency on medium and temperature of cell size and chemical composition during balanced grown of Salmonella typhimurium. J. Gen. Microbiol. 19(3), 592–606 (1958)
- S. Chen et al., Structural diversity of bacterial flagellar motors. EMBO J. 30(14), 2972–2981 (2011)
- K.M. Davies et al., Macromolecular organization of ATP synthase and complex I in whole mitochondria. Proc. Natl. Acad. Sci. 108(34), 14121–14126 (2011)
- K.H. Bui et al., Integrated structural analysis of the human nuclear pore complex scaffold. Cell 155(6), 1233–1243 (2013)
- A. Briegel, et al., Structure of bacterial cytoplasmic chemoreceptor arrays and implications for chemotactic signaling. eLife 3, e02151 (2014)
- C.J. Russo, L.A. Passmore, Ultrastable gold substrates: properties of a support for high-resolution electron cryomicroscopy of biological specimens. J. Struct. Biol. 193(1), 33–44 (2016)
- W.F. Tivol, A. Briegel, G.J. Jensen, An improved cryogen for plunge freezing. Microsc. Microanal. 14(05), 375–379 (2008)
- D. Studer, B.M. Humbel, M. Chiquet, Electron microscopy of high pressure frozen samples: bridging the gap between cellular ultrastructure and atomic resolution. Histochem. Cell Biol. 130(5), 877–889 (2008)
- K.L. McDonald, M. Auer, High-pressure freezing, cellular tomography, and structural cell biology, BioTechniques, 41(2), 137, 139, 141 passim, (Aug. 2006)
- M. Marko, C. Hsieh, W. Moberlychan, C.A. Mannella, J. Frank, Focused ion beam milling of vitreous water: prospects for an alternative to cryo-ultramicrotomy of frozen-hydrated biological samples. J. Microsc. 222(1), 42–47 (2006)

31. E. Villa, M. Schaffer, J.M. Plitzko, W. Baumeister, Opening windows into the cell: focused-ion-beam milling for cryo-electron tomography. Curr. Opin. Struct. Biol. 23(5), 771–777 (2013)

- 32. J. Mahamid et al., Visualizing the molecular sociology at the HeLa cell nuclear periphery. Science **351**(6276), 969–972 (2016)
- 33. L.G. Dowell, A.P. Rinfret, Low-temperature forms of ice as studied by X-Ray diffraction. Nature **188**(4757), 1144–1148 (1960)
- W.V. Nicholson, H. White, J. Trinick, An approach to automated acquisition of cryoEM images from lacey carbon grids. J. Struct. Biol. 172(3), 395–399 (2010)
- 35. M. Beeby, D.A. Ribardo, C.A. Brennan, E.G. Ruby, G.J. Jensen, D.R. Hendrixson, Diverse high-torque bacterial flagellar motors assemble wider stator rings using a conserved protein scaffold. Proc. Natl. Acad. Sci. 113(13), E1917–E1926 (2016)
- C.V. Iancu, E.R. Wright, J.B. Heymann, G.J. Jensen, A comparison of liquid nitrogen and liquid helium as cryogens for electron cryotomography. J. Struct. Biol. 153(3), 231–240 (2006)
- 37. G. McMullan, S. Chen, R. Henderson, A.R. Faruqi, Detective quantum efficiency of electron area detectors in electron microscopy. Ultramicroscopy 109(9), 1126–1143 (2009)
- 38. X. Li et al., Electron counting and beam-induced motion correction enable near atomic resolution single particle cryoEM. Nat. Methods 10(6), 584–590 (2013)
- 39. M. Kuijper et al., FEI's direct electron detector developments: Embarking on a revolution in cryo-TEM. J. Struct. Biol. **192**(2), 179–187 (2015)
- Danev, R., Nagayama, K.: Chapter Fourteen—Phase Plates for Transmission Electron Microscopy, in *Cryo-EM Part A Sample Preparation and Data Collection*, vol. 481 (Academic Press, 2010), pp. 343–369
- 41. R. Danev, S. Kanamaru, M. Marko, K. Nagayama, Zernike phase contrast cryo-electron tomography. J. Struct. Biol. **171**(2), 174–181 (2010)
- 42. Y. Fukuda, U. Laugks, V. Lučić, W. Baumeister, R. Danev, Electron cryotomography of vitrified cells with a Volta phase plate. J. Struct. Biol. (2015)
- 43. R.C. Guerrero-Ferreira, E.R. Wright, Cryo-electron tomography of bacterial viruses. Virology 435(1), 179–186 (2013)
- 44. W. Dai et al., Visualizing virus assembly intermediates inside marine cyanobacteria. Nature **502**(7473), 707–710 (2013)
- 45. D.N. Mastronarde, Automated electron microscope tomography using robust prediction of specimen movements. J. Struct. Biol. **152**(1), 36–51 (2005)
- 46. Q.S. Zheng, M.B. Braunfeld, J.W. Sedat, D.A. Agard, An improved strategy for automated electron microscopic tomography. J. Struct. Biol. **147**(2), 91–101 (2004)
- 47. C. Suloway et al., Automated molecular microscopy: the new Leginon system. J. Struct. Biol. **151**(1), 41–60 (2005)
- 48. G.C. Lander et al., Appion: an integrated, database-driven pipeline to facilitate EM image processing. J. Struct. Biol. **166**(1), 95–102 (2009)
- 49. C. Suloway et al., Fully automated, sequential tilt-series acquisition with Leginon. J. Struct. Biol. **167**(1), 11–18 (2009)
- R. Henderson, The potential and limitations of neutrons, electrons and X-rays for atomic resolution microscopy of unstained biological molecules. Q. Rev. Biophys. 28(2), 171–193 (1995)
- T.A.M. Bharat, C.J. Russo, J. Löwe, L.A. Passmore, S.H.W. Scheres, Advances in single-particle electron cryomicroscopy structure determination applied to sub-tomogram averaging. Structure 23(9), 1743–1753 (2015)
- F.K.M. Schur, W.J.H. Hagen, A. de Marco, J.A.G. Briggs, Determination of protein structure at 8.5 Å resolution using cryo-electron tomography and sub-tomogram averaging. J. Struct. Biol. 184(3), 394–400 (2013)
- A. Bartesaghi, F. Lecumberry, G. Sapiro, S. Subramaniam, Protein secondary structure determination by constrained single-particle cryo-electron tomography. Structure 20(12), 2003–2013 (2012)

- B. Hu, et al.: Visualization of the type III secretion sorting platform of Shigella flexneri. Proc. Natl. Acad. Sci. 201411610 (2015)
- 55. D. Stokes, G. Owen, An introduction to low dose electron tomography—from specimen preparation to data collection. Mod. Res. Educ. Top. Microsc 939–950 (2007)
- 56. R. Erni, Abberation-corrected Imaging in Transmission Electron Microscopy: An introduction. World Scientific (2010)
- 57. G.E. Murphy, G.J. Jensen, Electron cryotomography. BioTechniques, **43**(4), 413, 415, 417 passim, (2007)
- 58. C.V. Iancu et al., A 'flip-flop' rotation stage for routine dual-axis electron cryotomography. J. Struct. Biol. **151**(3), 288–297 (2005)
- V. Lucić, F. Förster, W. Baumeister, Structural studies by electron tomography: from cells to molecules. Annu. Rev. Biochem. 74, 833–865 (2005)
- R.A. Crowther, D.J. DeRosier, A. Klug, The reconstruction of a three-dimensional structure from projections and its application to electron microscopy. Proc. R. Soc. Lond. Math. Phys. Eng. Sci. 317(1530), 319–340 (1970)
- 61. W.O. Saxton, W. Baumeister, M. Hahn, Three-dimensional reconstruction of imperfect two-dimensional crystals. Ultramicroscopy **13**(1–2), 57–70 (1984)
- 62. W.J.H. Hagen, W. Wan, J.A.G. Briggs, Implementation of a cryo-electron tomography tilt-scheme optimized for high resolution subtomogram averaging. J. Struct. Biol. **197**(2), 191–198 (2017)
- 63. W. Wan, J.A.G. Briggs, Chapter thirteen—cryo-electron tomography and subtomogram averaging, in Methods in Enzymology, vol. 579, ed. by R.A. Crowther (Academic Press, 2016), pp. 329–367
- 64. M. Kudryashev, H. Stahlberg, D. Castaño-Díez, Assessing the benefits of focal pair cryo-electron tomography. J. Struct. Biol. (2011)
- R.D. Leapman, Novel techniques in electron microscopy. Curr. Opin. Neurobiol. 14(5), 591–598 (2004)
- J. Kremer, D. Mastronarde, J. McIntosh, Computer visualization of three-dimensional image data using IMOD. J. Struct. Biol. 116(1), 71–76 (1996)
- H. Winkler, K.A. Taylor, Marker-free dual-axis tilt series alignment. J. Struct. Biol. 182(2), 117–124 (2013)
- 68. T.R. Shaikh et al., SPIDER image processing for single-particle reconstruction of biological macromolecules from electron micrographs. Nat. Protoc. **3**(12), 1941–1974 (2008)
- S. Nickell et al., TOM software toolbox: acquisition and analysis for electron tomography.
   J. Struct. Biol. 149(3), 227–234 (2005)
- C. Messaoudil, T. Boudier, C.O.S. Sorzano, S. Marco, TomoJ: tomography software for three-dimensional reconstruction in transmission electron microscopy. BMC Bioinformatics 8, 288 (2007)
- F. Amat, F. Moussavi, L.R. Comolli, G. Elidan, K.H. Downing, M. Horowitz, Markov random field based automatic image alignment for electron tomography. J. Struct. Biol. 161 (3), 260–275 (2008)
- 72. J.I. Agulleiro, J.J. Fernandez, Fast tomographic reconstruction on multicore computers. Bioinforma. Oxf. Engl. **27**(4), 582–583 (2011)
- J.J. Fernández, S. Li, R.A. Crowther, CTF determination and correction in electron cryotomography. Ultramicroscopy 106(7), 587–596 (2006)
- J.-J. Fernández, S. Li, An improved algorithm for anisotropic nonlinear diffusion for denoising cryo-tomograms. J. Struct. Biol. 144(1-2), 152-161 (2003)
- 75. C.O.S. Sorzano et al., Marker-free image registration of electron tomography tilt-series. BMC Bioinformatics **10**, 124 (2009)
- D. Castaño-Díez, M. Scheffer, A. Al-Amoudi, A.S. Frangakis, Alignator: a GPU powered software package for robust fiducial-less alignment of cryo tilt-series. J. Struct. Biol. 170(1), 117–126 (2010)
- J.-J. Fernandez et al., Removing contamination-induced reconstruction artifacts from cryo-electron tomograms. Biophys. J. 110(4), 850–859 (2016)

 K. Song, L.R. Comolli, M. Horowitz, Removing high contrast artifacts via digital inpainting in cryo-electron tomography: an application of compressed sensing. J. Struct. Biol. 178(2), 108–120 (2012)

- T. Grant, N. Grigorieff, Measuring the optimal exposure for single particle cryo-EM using a 2.6 Å reconstruction of rotavirus VP6. eLife e06980 (2015)
- 80. C.A. Diebolder, F.G.A. Faas, A.J. Koster, R.I. Koning, Conical Fourier shell correlation applied to electron tomograms. J. Struct. Biol. **190**(2), 215–223 (2015)
- 81. J.-J. Fernandez, Computational methods for electron tomography. Micron **43**(10), 1010–1030 (2012)
- P. van der Heide, X.-P. Xu, B.J. Marsh, D. Hanein, N. Volkmann, Efficient automatic noise reduction of electron tomographic reconstructions based on iterative median filtering. J. Struct. Biol. 158(2), 196–204 (2007)
- A.S. Frangakis, R. Hegerl, Noise reduction in electron tomographic reconstructions using nonlinear anisotropic diffusion. J. Struct. Biol. 135(3), 239–250 (2001)
- R. Narasimha et al., Evaluation of denoising algorithms for biological electron tomography.
   J. Struct. Biol. 164(1), 7–17 (2008)
- G. Cardone, K. Grünewald, A.C. Steven, A resolution criterion for electron tomography based on cross-validation. J. Struct. Biol. 151(2), 117–129 (2005)
- 86. P.A. Penczek, Chapter Three—Resolution Measures in Molecular Electron Microscopy, in *Cryo-EM, Part B: 3-D Reconstruction*, vol. 482 (Academic Press, 2010), pp. 73–100
- 87. D. Castaño-Díez, M. Kudryashev, M. Arheit, H. Stahlberg, Dynamo: a flexible, user-friendly development tool for subtomogram averaging of cryo-EM data in high-performance computing environments. J. Struct. Biol. **178**(2), 139–151 (2012)
- 88. D. Nicastro, C. Schwartz, J. Pierson, R. Gaudette, M.E. Porter, J.R. McIntosh, The molecular architecture of axonemes revealed by cryoelectron tomography. Science **313**(5789), 944–948 (2006)
- S.H.W. Scheres, S. Chen, Prevention of overfitting in cryo-EM structure determination. Nat. Methods 9(9), 853–854 (2012)
- F. Förster, B.-G. Han, and M. Beck, "Chapter Eleven—Visual Proteomics, in *Cryo-EM, Part C: Analyses, Interpretation, and Case studies*, vol. 483, (Academic Press, 2010), pp. 215–243
- 91. Z. Li, M. Trimble, Y. Brun, G. Jensen, The structure of FtsZ filaments in vivo suggests a force-generating role in cell division. EMBO J. 26, 4694–4708 (2007)
- 92. Y.-W. Chang, *et al.*, Correlated cryogenic photoactivated localization microscopy and cryo-electron tomography. Nat. Methods, vol. advance online publication, (2014)
- 93. Q. Wang, C.P. Mercogliano, J. Löwe, A ferritin-based label for cellular electron cryotomography. Struct. Lond. Engl. 1993 **19**(2), 147–154 (2011)
- M. Beeby, structural diversity of bacterial flagellar motors. Presented at the MicroMorning, Caltech, (14-Jul-2011)
- 95. P. Abrusci et al., Architecture of the major component of the type III secretion system export apparatus. Nat. Struct. Mol. Biol. **20**(1), 99–104 (2013)
- K. Song et al., In situ localization of N and C termini of subunits of the flagellar nexin-dynein regulatory complex (N-DRC) using SNAP tag and cryo-electron tomography. J. Biol. Chem. 290(9), 5341–5353 (2015)
- 97. S. Velankar et al., PDBe: improved accessibility of macromolecular structure data from PDB and EMDB. Nucleic Acids Res. **44**(D1), D385–D395 (2016)
- 98. A. Iudin, P.K. Korir, J. Salavert-Torres, G.J. Kleywegt, A. Patwardhan, EMPIAR: a public archive for raw electron microscopy image data. Nat. Methods 13(5), 387–388 (2016)
- 99. A. Nans, H.R. Saibil, R.D. Hayward, Pathogen-host reorganisation during Chlamydia invasion revealed by cryo-electron tomography. Cell. Microbiol. p. n/a-n/a, (2014)
- A. Kawamoto et al., Common and distinct structural features of Salmonella injectisome and flagellar basal body. Sci. Rep. 3, 3369 (2013)
- 101. S. Asano et al., A molecular census of 26S proteasomes in intact neurons. Science 347 (6220), 439-442 (2015)

- B.D. Engel, M. Schaffer, S. Albert, S. Asano, J.M. Plitzko, W. Baumeister, In situ structural analysis of Golgi intracisternal protein arrays. Proc. Natl. Acad. Sci. 112(36), 11264–11269 (2015)
- C. Hagen et al., Structural basis of vesicle formation at the inner nuclear membrane. Cell 163 (7), 1692–1701 (2015)
- 104. T.A.M. Bharat et al., Cryo-electron tomography of Marburg virus particles and their morphogenesis within infected cells. PLoS Biol. 9(11), e1001196 (2011)
- F.K.M. Schur, R.A. Dick, W.J.H. Hagen, V.M. Vogt, J.A.G. Briggs, The structure of immature virus-like rous sarcoma virus gag particles reveals a structural role for the p10 domain in assembly. J. Virol. 89(20), 10294–10302 (2015)
- 106. W. Dai, C. Fu, H.A. Khant, S.J. Ludtke, M.F. Schmid, W. Chiu, Zernike phase-contrast electron cryotomography applied to marine cyanobacteria infected with cyanophages. Nat. Protoc. 9(11), 2630–2642 (2014)
- L. Gan, S. Chen, G.J. Jensen, Molecular organization of Gram-negative peptidoglycan. Proc. Natl. Acad. Sci. 105(48), 18953–18957 (2008)
- 108. M. Beeby, J.C. Gumbart, B. Roux, G.J. Jensen, Architecture and assembly of the Gram-positive cell wall. Mol. Microbiol. **44**(4), 664–672 (2013)
- E.I. Tocheva, E.G. Matson, D.M. Morris, F. Moussavi, J.R. Leadbetter, G.J. Jensen, Peptidoglycan remodeling and conversion of an inner membrane into an outer membrane during sporulation. Cell 146(5), 799–812 (2011)
- K.C. Huang, R. Mukhopadhyay, B. Wen, Z. Gitai, N.S. Wingreen, Cell shape and cell-wall organization in Gram-negative bacteria. Proc. Natl. Acad. Sci., p. pnas.0805309105 (2008)
- L.T. Nguyen, J.C. Gumbart, M. Beeby, G.J. Jensen, Coarse-grained simulations of bacterial cell wall growth reveal that local coordination alone can be sufficient to maintain rod shape. Proc. Natl. Acad. Sci. 112(28), E3689–E3698 (2015)
- 112. M. Pilhofer, G.J. Jensen, The bacterial cytoskeleton: more than twisted filaments. Curr. Opin. Cell Biol
- 113. J. Salje, F. van den Ent, P. de Boer, J. Löwe, Direct membrane binding by bacterial actin MreB. Mol. Cell **43**(3), 478–487 (2011)
- 114. F. van den Ent, T. Izoré, T.A. Bharat, C.M. Johnson, J. Löwe, Bacterial actin MreB forms antiparallel double filaments. eLife 3, e02634, (2014)
- E.C. Garner, R. Bernard, W. Wang, X. Zhuang, D. Z. Rudner, T. Mitchison, Coupled, circumferential motions of the cell wall synthesis machinery and MreB filaments in B. subtilis. Science (2011)
- J. Domínguez-Escobar, A. Chastanet, A.H. Crevenna, V. Fromion, R. Wedlich-Söldner, R. Carballido-López, Processive movement of MreB-associated cell wall biosynthetic complexes in Bacteria. Science 333(6039), 225–228 (2011)
- S. van Teeffelen et al., The bacterial actin MreB rotates, and rotation depends on cell-wall assembly. Proc. Natl. Acad. Sci. 108(38), 15822–15827 (2011)
- 118. P. Szwedziak, Q. Wang, T.A.M. Bharat, M. Tsim, J. Löwe, Architecture of the ring formed by the tubulin homologue FtsZ in bacterial cell division. eLife 3, e04601 (2014)
- A. Briegel, D. Dias, Z. Li, R. Jensen, A. Frangakis, G. Jensen, Multiple large filament bundles observed in Caulobacter crescentus by electron cryotomography. Mol. Microbiol. 62, 5–14 (2006)
- 120. M. Ingerson-Mahar, A. Briegel, J.N. Werner, G.J. Jensen, Z. Gitai, The metabolic enzyme CTP synthase forms cytoskeletal filaments. Nat. Cell Biol. **12**(8), 739–746 (2010)
- M. Beck, V. Lučić, F. Förster, W. Baumeister, O. Medalia, Snapshots of nuclear pore complexes in action captured by cryo-electron tomography. Nature 449(7162), 611–615 (2007)
- 122. J. Kosinski et al., Molecular architecture of the inner ring scaffold of the human nuclear pore complex. Science **352**(6283), 363–365 (2016)
- 123. A. Rigort et al., Focused ion beam micromachining of eukaryotic cells for cryoelectron tomography. Proc. Natl. Acad. Sci. **109**(12), 4449–4454 (2012)

94 J. L. Ferreira et al.

124. M. Eibauer, M. Pellanda, Y. Turgay, A. Dubrovsky, A. Wild, O. Medalia, Structure and gating of the nuclear pore complex. Nat. Commun. 6, 7532 (2015)

- 125. M. Zwerger, M. Eibauer, O. Medalia, Insights into the gate of the nuclear pore complex. Nucl. Austin Tex **7**(1), 1–7 (2016)
- 126. A. von Appen et al., In situ structural analysis of the human nuclear pore complex. Nature **526**(7571), 140–143 (2015)
- 127. J.A. Berriman, P.B. Rosenthal, Paraxial charge compensator for electron cryomicroscopy. Ultramicroscopy **116**, 106–114 (2012)
- 128. C.J. Russo, L.A. Passmore, Controlling protein adsorption on graphene for cryo-EM using low-energy hydrogen plasmas. Nat. Methods 11(6), 649–652 (2014)
- 129. R.S. Pantelic, J.C. Meyer, U. Kaiser, W. Baumeister, J.M. Plitzko, Graphene oxide: a substrate for optimizing preparations of frozen-hydrated samples. J. Struct. Biol. **170**(1), 152–156 (2010)
- 130. T. Jain, SpotItOn: a new approach to EM specimen preparation. Presented at the NRAMM, Scripps, San Diego, California, USA (11-Dec-2012)
- 131. A. Müller, M. Beeby, A.W. McDowall, J. Chow, G. J. Jensen, W.M. Clemons, Ultrastructure and complex polar architecture of the human pathogen Campylobacter jejuni. MicrobiologyOpen, p. n/a-n/a, (2014)

## Chapter 4 Large-Scale Electron Tomography of Cells Using SerialEM and IMOD

Eileen O'Toole, Peter van der Heide, J. Richard McIntosh and David Mastronarde

**Abstract** We have developed methods to compute tomographic reconstructions of relatively large areas and volumes of sectioned cells using SerialEM and IMOD. The SerialEM program has emerged as a major tool for automated acquisition of tilt series for electron tomography [1]. This program contains a number of unique features, including a prediction algorithm that allows rapid image acquisition, and it can also routinely acquire tilt series from montaged images. The IMOD package contains alignment methods that correct for the non-uniform changes that occur over a large specimen area during data collection [1, 2]. In addition, the IMOD package offers tools for aligning and stacking tomograms from serial sections, allowing larger volumes to be reconstructed. Until recently practical considerations, such as constraints on electronic image shift, have limited the size of the area that could be reconstructed using ordinary montaging to  $\sim 10 \times 10$  µm. The desire to study areas larger than this has spurred the development of methods for stitching together laterally adjacent tomograms, referred to as super-montaging. In this chapter, we describe the steps involved in performing large-scale tomography including super-montaging, using the human mitotic spindle as an example.

E. O'Toole () J. Richard McIntosh · D. Mastronarde
Department of MCD Biology, University of Colorado, Boulder, CO, USA

e-mail: Eileen.otoole@colorado.edu

J. Richard McIntosh

e-mail: richard.mcintosh@colorado.edu

D. Mastronarde

e-mail: mast@Colorado.EDU

P. van der Heide

Institute for Molecular Bioscience, Queensland Bioscience Precinct, The University of Queensland, Brisbane, Australia

© Springer International Publishing AG 2018
E. Hanssen (ed.), *Cellular Imaging*, Biological and Medical Physics,
Biomedical Engineering, https://doi.org/10.1007/978-3-319-68997-5\_4

#### 4.1 Introduction

Studying and understanding cells in their entirety has long been a major goal of the cell biology community. Despite advances in light microscopy, this method cannot deliver the resolution necessary to describe some of the cell's essential working parts. Electron microscopes (EMs) solve the resolution problem, yet most cells are too thick to image directly and must be sectioned into thinner slices to view in the EM. In addition, most cells are so large that the field of view in a single image, recorded at useful resolution, is not wide enough to capture some structures of interest. Therefore, to visualize large areas and volumes of cells in three dimensions (3D), it is necessary to expand the field of view and to increase the thickness of the observed volume. This has led to the evolution of new imaging technologies termed 'Volume-EM'; methods that use either a transmission electron microscope (TEM) or scanning electron microscope (SEM) to reconstruct large areas and volumes of cells in 3D [3, 4].

There are several approaches to performing large-scale 3D reconstructions by EM. The first, serial section TEM (ssTEM) involves the use of serial, thin (50–80 nm) sections to reconstruct larger volumes of cells. This method requires considerable technical skill to manually cut and collect the serial sections for imaging. Although large areas can be imaged using montage strategies, the z resolution of any 3D reconstruction is limited by the thickness of the slices. Nevertheless, ssTEM has been used for many years to address questions in cell biology, such as the 3D organization of mitotic spindles [5], and to study structural aspects of neurobiology [6–8]. An analogous approach, array tomography, uses a SEM to image large numbers of serial sections collected onto tape, silicon or glass discs [9]. Again, array tomography is limited in z resolution but has the advantage of imaging very large areas of material in any given section. This technique is now contributing to the field of neuroscience where a significant volume of the mouse neocortex has been reconstructed ([10, 11]; see Chap. 6).

SEM has also been used to image a face on a block of embedded material (BF-SEM), employing either a microtome mounted in the chamber of an SEM (SBF-SEM; Gatan 3View) or a focused beam of ions (FIB-SEM) to remove thin slices of material from the block after each image is recorded (see Chap. 5). SBF-SEM and FIB-SEM can efficiently gather large quantities of data from a single specimen with minimal human intervention. SBF-SEM uses surface images at intervals of 10–50 nm [12], implying a resolution in that direction of at least twice the section thickness. FIB-SEM is closer to isotropic resolution with a sampling interval said to be as little as 3 nm under the best conditions [13]. Unlike TEM based techniques, the majority of the specimen is simply disposed of in both these methods, but they are very useful for imaging large ultrastructural features, such as whole plasma membranes and neuron axonal networks. On the other hand, features whose size is on the same order as the slice interval are poorly reproduced or even omitted completely if they do lie at an appropriate position relative to the Z slices. Further details on SBF-SEM and FIB-SEM can be found in Chap. 5.

EM tomography (ET) enables 3D reconstructions of parts of cells or of whole cells, in the case of bacteria, at 4–6 nm resolution in 3D and thus has been a popular method for studying structure-function relationships among organelles [14, 15]. This method involves the use of a TEM to collect tilted views of a thick (200–400 nm) section over a wide angular range (typically  $\pm 60$  or  $70^{\circ}$ ). The tilted views are then aligned, and a reconstruction is computed. ET is best suited for reconstructing objects that change significantly within a small volume, such as the twisting contours of intracellular membranes or complex networks of cytoskeletal elements (e.g., the mitotic spindle). Cryo-electron tomography (cryoET) is a specialized form of ET in which frozen-hydrated material is imaged, allowing material to be imaged in a near-native state [16]. In CryoET, the specimen suffers from damage during exposure to the electron beam, and this limits imaging large areas and volumes. For this reason, this chapter focuses on the large area and volume reconstruction from plastic-embedded sections. A separate chapter describing the utility of using cryoET is included in Chap. 3.

For plastic section tomography, larger volumes have been generated by stacking tomograms of serial thick (250–400 nm) sections along the Z axis (ssET), a logical extension of the more established serial section microscopy with thin sections [17, 18]. In this way, one can progress through the sample in successive 3D slabs to generate what amounts to a column of tomographic data. In the first study that used tools in IMOD for ssET, serial sections of  $\sim$ 250 nm thickness were imaged with 1.5° of angular change between tilted views and digitized at a pixel size of 2.3 nm. This study achieved a resolution of  $\sim$ 7 nm revealing the complex membranes of the Golgi complex in considerable detail (Fig. 4.1a, [18]). The first reconstruction of an entire mammalian cell was done with a murine pancreatic  $\beta$  cell (Fig. 4.1b, [19]). By reducing the magnification to a nominal  $\sim$ 4700×, such that the entire cell cross section could be visualized in a single field of view, and capturing tomograms through  $\sim$ 40 serial sections, an entire mammalian cell was imaged in 3D with  $\sim$ 5 nm voxels, providing a resolution of 10–15 nm.

Areas larger than the frame size of the CCD camera at a given magnification can be captured by montaging. The use of montaging in the plane of each section at higher magnification, combined with serial section tomography was used to reconstruct whole cells from the yeast, *Schizosaccharomyces pombe*, allowing the details of the interphase microtubule cytoskeleton to be visualized with unprecedented resolution. Details such as the morphology of microtubule ends could then be analyzed in the natural cellular context (Fig. 4.1c, [20]). To increase the area of the reconstructed volume even further, we have developed methods for stitching together laterally adjacent tomograms, which we refer to as supermontages (Fig. 4.1d, [21]. Stacking supermontage tomograms allows the reconstruction of significant cell volumes, such as the mitotic spindle of *C. elegans* (Fig. 4.1d). An alternative approach using TxBR montage reconstruction has also been described [22].

In this chapter, we describe the use of SerialEM and IMOD to enable reconstructions of relatively large volumes of sectioned material with an emphasis on recent advances in automation for both image acquisition and tomographic

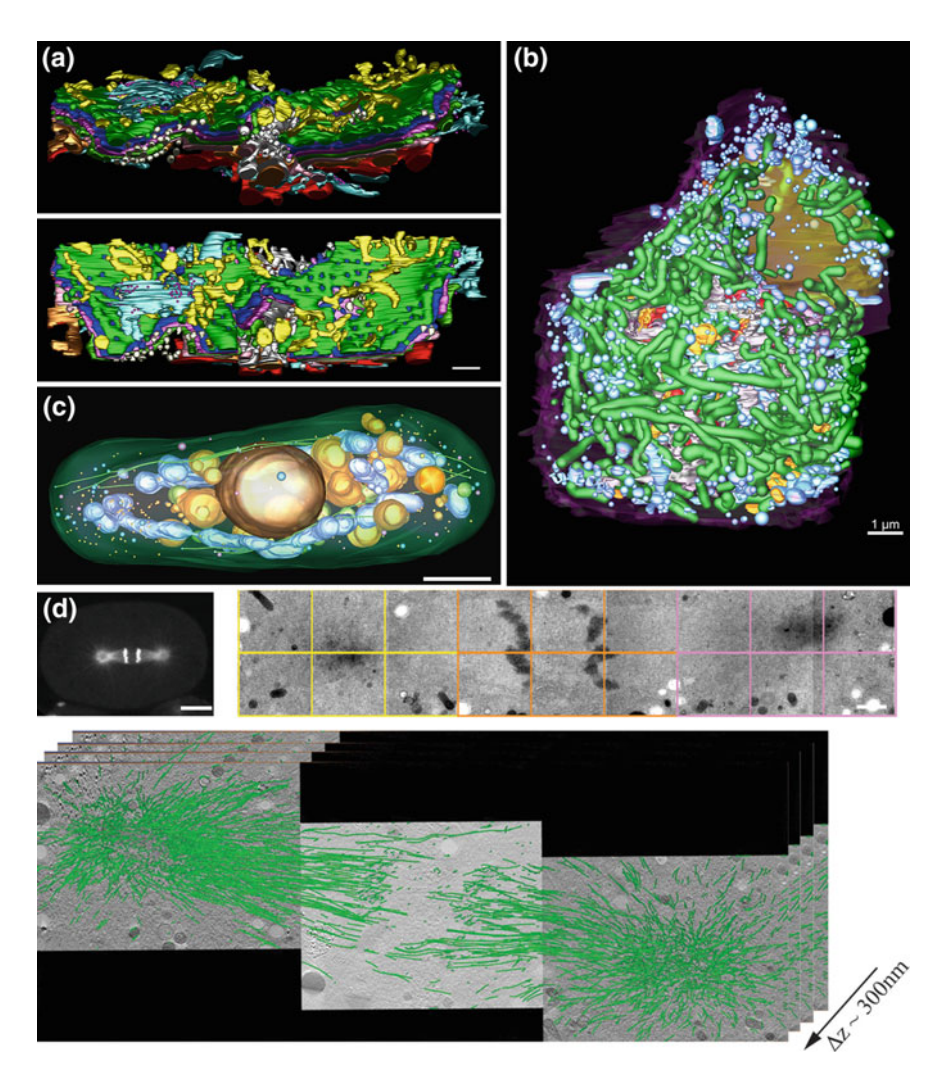


**Fig. 4.1** The use of SerialEM and IMOD to reconstruct increasing areas and volumes of cells. **a** Serial section tomography allows the reconstruction of the Golgi apparatus in mammalian tissue culture cells at 2.3 nm pixel size (volume 1 μm × 1 μm; [18]) Scale bar = 250 nm. **b** Reconstruction of the first mammalian cell at 5 nm voxel size and 40 serial tomograms (volume  $10 \ \mu m \times 10 \ \mu m \times 20 \ \mu m$ ; [19]) Scale bar = 1 μm. **c** Complete yeast cell reconstructed using montaging to capture the entire area of the cell at 1.5 nm voxels through 15 serial sections (volume 3 μm × 6 μm × 4 μm [20]) Scale bar = 1 μm. **d** Significant portion of a *C. elegans* anaphase spindle was reconstructed using supermontaging at 1.2 nm voxels through 4 serial sections (volume  $22 \ \mu m \times 5 \ \mu m \times 1 \ \mu m$ ; [21]). Scale bar =  $10 \ \mu m$ , 1 μm. Figures reprinted with permission

reconstruction. Recent advances in the SerialEM program provide automated acquisition from multiple positions, including automated serial section tilt series and supermontage acquisition. The IMOD package provides alignment methods

that correct for the non-uniform changes that occur over the area of a large specimen during collection of images for single-axis and dual-axis tilt series [1, 2, 23]. In addition, tools for aligning and stacking tomograms from serial sections have made this procedure routine. Finally, we describe the programs for stitching together laterally adjacent tomograms, creating a "supermontage" of tomograms themselves based on montaged images.

#### 4.2 Specimen Preparation for Large-Scale Tomography

Large scale ET uses samples that are resin-embedded, stained with heavy metals, and cut into sections of appropriate thickness for the microscope's operating voltage (200-300 nm thick). The use of high-pressure freezing followed by freeze substitution results in excellent preservation of cell ultrastructure and is therefore the sample preparation method of choice for study of mammalian cell ultrastructure by ET. Methods for preparing cell monolayers for serial tomography have been developed [24, 25] and an overview of the process is illustrated in Fig. 4.2. Cells are grown on sapphire discs that have been carbon-shadowed with a grid pattern, high pressure frozen and freeze substituted in 1% osmium and 0.1% uranyl acetate in acetone at low temperature and subsequently embedded in a thin wafer of epon resin [25]. Samples can be imaged in the LM and cells of interest identified, excised and remounted for microtomy (Fig. 4.2a; arrow, inset). Serial 300 nm sections of the cell are collected onto formyar-coated slot grids and post stained with 2% uranyl acetate followed by lead citrate (Fig. 4.2b). Colloidal gold particles (15 nm) are then affixed to each side of the grid to serve as fiducial markers for tilt series alignment.

# **4.3** Using SerialEM for Automated Single Frame or Montaged Serial Tilt Series Acquisition

Efficient, automated data collection for ET has been an important goal for large area and volume reconstruction. A number of programs are available for automated image acquisition for ET (e.g., commercial programs from Gatan and FEI; academic software from UCSF tomography [26] and the TOM toolbox [27]), but our freely available SerialEM program has emerged as the tool of choice for many laboratories (http://bio3d.colorado.edu/SerialEM). It contains a number of unique features, including a prediction algorithm that allows rapid image acquisition. As a result, it can routinely acquire tilt series from montaged images [1]. In addition, the Navigator module in SerialEM assists with identifying and moving to areas of interest to allow tilt series to be taken from multiple areas automatically, thus increasing throughput. Figure 4.3 shows an example of a Navigator window that

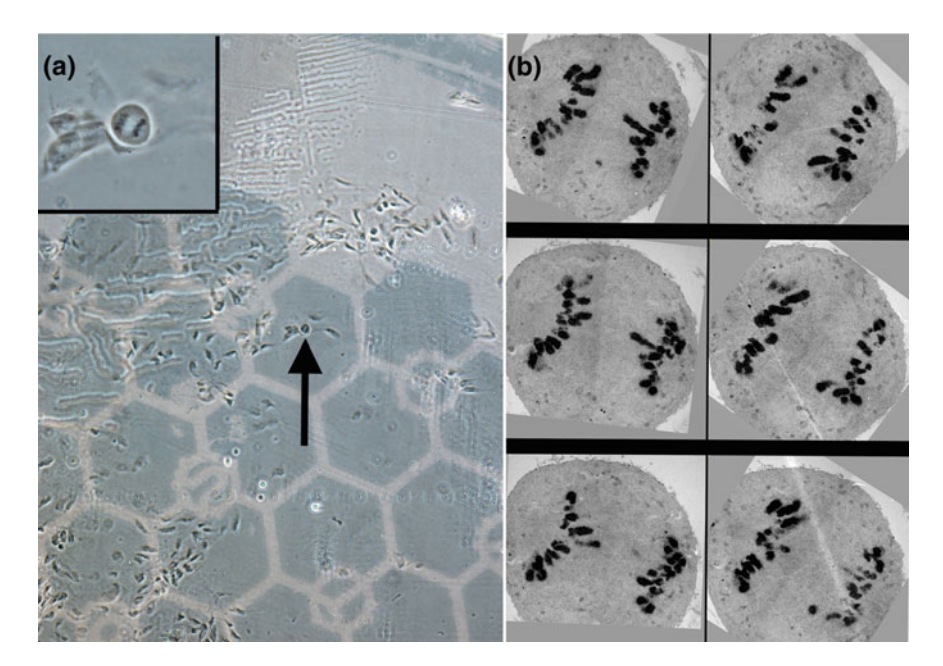
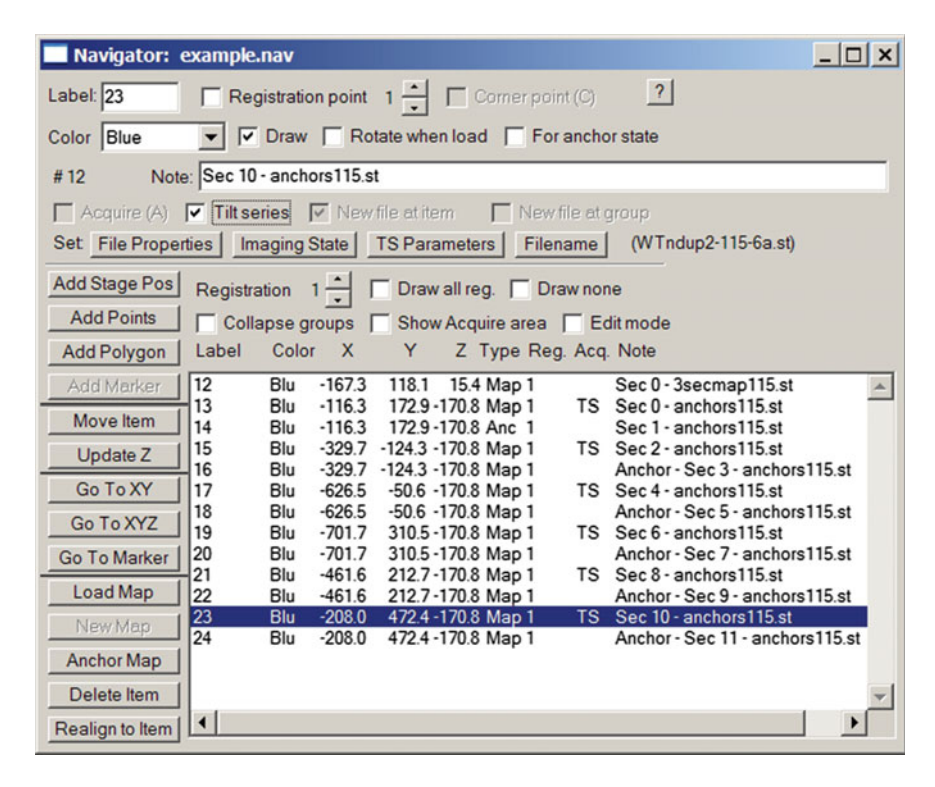


Fig. 4.2 Preparation of U2OS monolayers for LM and EM. a LM of fixed, embedded cells grown on a marked sapphire disk; insert shows the selected cell. b Serial 300 nm sections imaged in the EM

has been set up to acquire images from 6 serial sections. The Navigator works with images called maps, about which it stores all the information needed to move to a specific point on the sample. A key to success in the automatic acquisition of tilt series from multiple positions is to make a map of the desired area at the final magnification for recording data and then drop the magnification to a take a medium magnification map that will be used for realigning reliably to the specimen position after the stage is moved to its nominal coordinates. Described below is a sequence of steps used to automatically acquire tilt series of single or montaged images from serial sections.

Steps to auto-acquire tilt series from multiple positions:

- 1. Insert grid and run the rough eucentricity operation, which can find the eucentric height even if it is 200 μm away.
- 2. Open the Navigator window from the top SerialEM menu bar.
- 3. Find an area/cell of interest and preirradiate the area to  $\sim 2000e-A^2$ .
- 4. Take a Record (full-resolution) image at the tilt series magnification.
  - if montage images are used, calibrate image shift, open montage file and set the number of pieces and overlap in x and y.
- 5. Save the image.



**Fig. 4.3** Automatic acquisition of tilt series from multiple positions across serial sections using the Navigator feature of SerialEM. The Navigator window has various controls and a table listing all the recorded locations, in this case images that are saved as maps. The maps marked as "TS" are high-magnification images where tilt series are to be acquired. For each one, there is an "anchor" image at lower magnification that is aligned to after returning to the stage position. Various parameters, and the filename, can be set independently for the currently selected item with the four buttons on the line starting with "Set:"

- 6. Make that image a new map by pressing the New Map button in the Navigator window dialogue.
- 7. Go to a lower magnification where the field of view is at least 10  $\mu$ m (typically  $\sim 4000 \times$ ) and take a Record image without moving the stage.
- 8. Save the image in the same file.
- 9. Make that image a New Map.
- Check "For anchor state" on the lower magnification image in the Navigator window.
- 11. Go to a new area of interest or find the area/cell on an adjacent section.
- 12. Take a Record image at the tilt series magnification.
- 13. Save the image.

14. Press 'Anchor Map'. The program automatically makes that image a map and acquires the medium-magnification map.

- 15. Repeat steps 12-14 until you have found all of your areas of interest.
- 16. Select the first tilt series map and check 'Tilt series' in the Navigator window.
  - this will prompt to name the file and set up the tilt series parameters.
- 19. Make each subsequent tilt series area a TS.
  - it is possible to change individual tilt series parameters if they differ from the original. The file names will automatically be chosen.
- 20. In Navigator drop down menu, select "Acquire at Points".
- 21. Select 'Autocenter beam' to invoke a beam-centering procedure; 'Cook specimen' if the area has not been pre-irradiated, and 'Fine eucentricity' if this operation is not selected in the tilt series parameters for each series. Set 'Close valves at end' and 'Send email' as desired, then press the GO button. Both 'Autocenter beam' and 'Cook specimen' require setting up conditions for the operation in advance.

# **4.4** Using IMOD's Etomo Interface to Compute Basic Single Frame or Montage Tilt Series

The IMOD package is a suite of programs used to compute tomographic reconstructions and to model cellular features. It is freely available on our website (http:// bio3d.colorado.edu/imod) and there are tutorials and guides for its use. IMOD runs on several platforms (Linux, Mac OS X, Windows) making this a flexible and powerful option for tomographic studies. The basic flow of operation is shown in the flow chart in Fig. 4.4 and is similar to the process control buttons in the Etomo graphical user interface that is used to create tomograms. The basic steps are: (1) preprocess the tilt series data to remove the extreme pixel intensities generated by x-rays, (2) create an approximately aligned stack and a fiducial model for alignment, (3) refine the alignment, (4) set angular and position parameters to reconstruct the specimen in the smallest volume, (5) create a final aligned stack and generate the tomogram, (6) combine tomograms from tilt series taken around two orthogonal axes; and, (7) trim the final tomogram and warp it if necessary so that the specimen is flat. We encourage users first to familiarize themselves with the steps involved in building dual axis tomograms through use of a tutorial before building their own tomograms: http://bio3d.colorado.edu/imod/doc/etomoTutorial.html.

Virtually all of these steps can run automatically, and the Etomo interface allows the user to take advantage of this automation for many of the steps (Fig. 4.4). For example, the fiducial model can be generated automatically [28], and tomograms can be positioned and combined automatically, which can greatly reduce the effort required to go through the process.

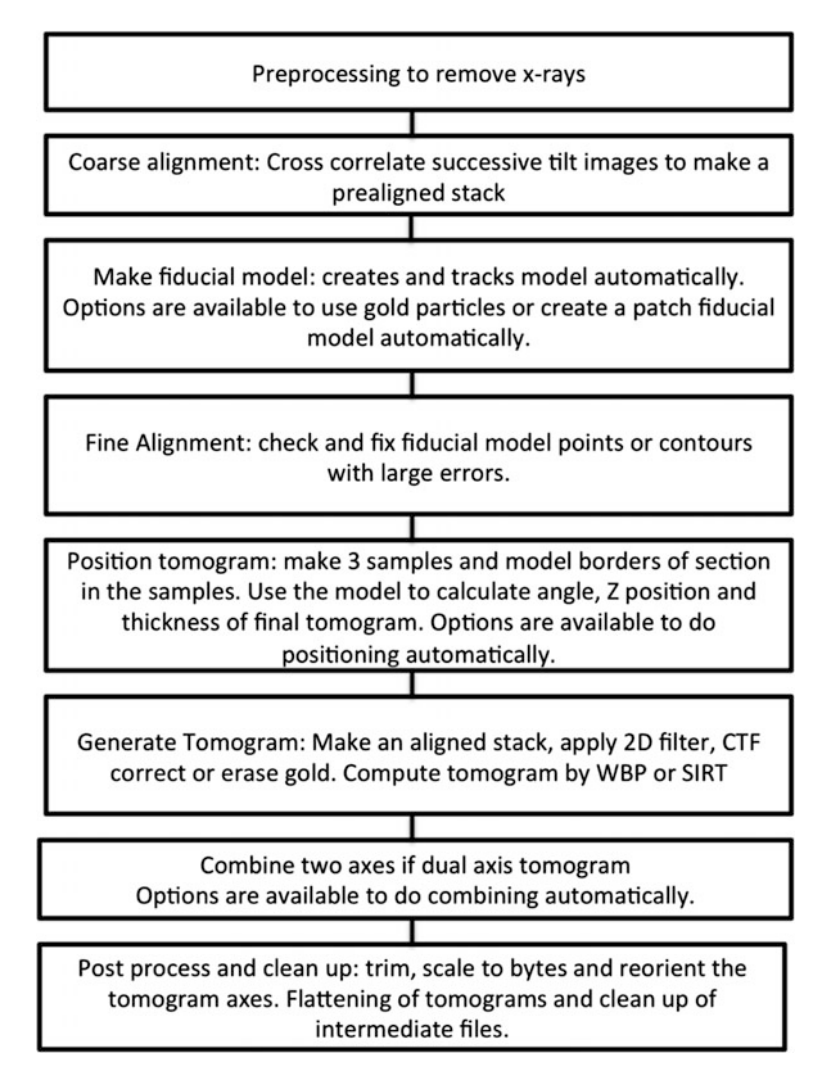


**Fig. 4.4** Basic work flow involved in tomographic reconstruction using IMOD's Etomo graphical user interface. Several steps have options that provide automation

## 4.5 The Etomo Batch Tomogram Interface

IMOD includes a program, Batchruntomo, that can run the reconstruction steps automatically, as well as an interface in Etomo for batch processing of tilt series that have stereotyped parameters [29]. Use of these features can greatly increase the ease and speed with which tomographic reconstructions can be computed. Batchruntomo is controlled by text files containing "directives" that allow great flexibility in the operations run and the parameters used. Many directives that set parameters for

individual operations can also be provided to Etomo when starting to process a data set interactively, in files referred to as templates. More than one template can be used; for example, one file could specify parameters for a particular microscope, and another could set parameters appropriate for cryoET.

The batch tomogram interface in Etomo has several components, on different tabbed pages, for selecting the tilt series to process, setting parameters, and controlling and monitoring Batchruntomo as it runs. A detailed guide for its use can be found at <a href="http://bio3d.colorado.edu/imod/betaDoc/batchGuide.html">http://bio3d.colorado.edu/imod/betaDoc/batchGuide.html</a>. Parameters and operations are selected on a single page that presents a carefully chosen subset of options. Less commonly needed options not exposed there can be entered through a template file.

Processing through Batchruntomo is fully compatible with the interactive processing through Etomo. At the end of a batch run, the user can open any data set in the reconstruction interface and examine the results, such as to see whether steps such as fiducial tracking, alignment, or gold erasing were done correctly. The user can also post-process the data (trim, scale or flatten the volume) and clean up intermediate files. If a step is anticipated to need manual intervention in advance, it is possible to run all sets through that step, check the results, and resume batch processing. In general, very large reconstructions will require intervention more often, but the batch interface is still useful for handling routine operations and minimizing manual operations.

# 4.6 Using IMOD's Join Interface to Stack Serial Reconstructions

A limitation to ET is the section thickness one can image in the EM. The use of higher voltage EMs (200-300 kV) allows significantly thicker sections to be imaged (200-400 nm), depending on the density of material. However, at thicknesses greater than this, plural scattering and inelastic scattering events seriously reduce image resolution. This is particularly a problem because the specimen thickness doubles when the section is tilted to  $\pm 60^{\circ}$ , and triples at  $70^{\circ}$  [14]. However, this limitation can be overcome by stacking, or joining tomograms computed from serial sections, thus increasing the reconstructed sample volume. The basic step in joining serial tomograms is to align a computed slice from the top of one tomogram with a computed slice from the bottom of the adjacent tomogram. Thanks to beam-induced distortions of each section, this alignment usually requires more than a simple shift and rotation. A general linear transformation is typically sufficient for smaller areas, but tomograms computed from larger, montaged areas often contain non-linear differences between successive sections that must be corrected with a warping transformation (see below). Once a transformation is found for each section interface, these section-to-section transformations are converted into ones that bring all sections into alignment with each other with the

minimum overall shift. These transforms are then applied, and all slices are combined into one joined tomogram. The IMOD package has a useful interface for joining serial section tomograms. A detailed tutorial for its use and a sample data set can be found at http://bio3d.colorado.edu/imod/doc/JoinTutorial.html.

Similar to most Etomo interfaces, the join interface is divided into tabbed panels: Setup, Align, Join, Model, Rejoin. The Setup tab contains a table to add tomograms, assign the order with which they will be joined, and identify a range of sample slices at each surface that will be used for alignment. A range of slices to include in the final volume is also set here, as well as large or small rotations that may be needed for stacking volumes properly.

Sample slices are usually aligned with the manual alignment program, Midas. Although automated alignment is available, sample slices (particularly of smaller areas) often do not have enough corresponding features for an automated approach because some material is lost at the surface of the section. Midas allows one to pick out features that do match and align them. When a linear transformation is inadequate, one can add warping points and drag corresponding features into alignment at those points, as illustrated in Fig. 4.5. An overview of the best linear alignment is shown in Fig. 4.5a–c. The center of the images are aligned well, but as shown in

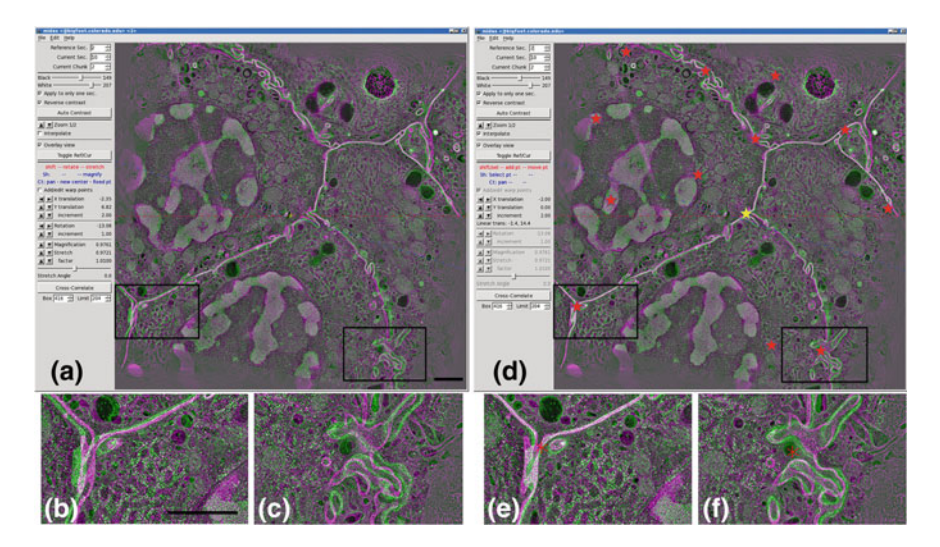


Fig. 4.5 Illustration of warping in the Midas program for manual image alignment. The images are green/magenta overlays of two slices near the top and bottom of successive serial sections of a pancreatic beta cell. Each tomogram is a  $2 \times 2$  supermontage of reconstructions from  $3 \times 3$  montages, reconstructed by Peter van der Heide. **a**, **b**, **c**: The best alignment that can be achieved by adjusting a single linear transformation. The boxed areas in **a** are expanded in **b** and **c** to show the misalignments. **d**, **e**, **f**: Alignment after turning on "Add/edit warp points" and adjusting the alignment at the points marked by stars (the currently active point is in yellow; others are in red). It is impossible to align all structures in such overlapping views because the slices are many nanometers apart, but an average misalignment has been corrected at each warping point. Scale bar is  $1 \mu m$ 

higher zoom of the boxed areas in Fig. 4.5a, misalignments are evident in other areas of the images. Warping points were added (Fig. 4.5d, red stars) and warping alignments were applied at these local regions, greatly improving the overall alignment across the entire area (Fig. 4.5e, f). The alignment transforms are then applied to the serial tomograms creating a final, joined volume.

# **4.7** Using IMOD's 3dmod for Modeling Features in Serial Reconstructions

Tomographic volumes can be viewed and structures of interest modeled using IMOD's 3dmod program. A detailed guide on its use can be found at http://bio3d.colorado.edu/ imod/doc/3dmodguide.html. 3dmod contains useful features for modeling membranes, vesicles, and trajectories such as microtubules and filaments. One tool, the slicer window, allows the user to rotate the position of a slice cut for display from the image data to get the best view of a particular object. This slicer window is particularly useful for tracking complex networks of microtubules in the mitotic spindle (Fig. 4.6). Tomograms were computed from  $3 \times 3$  montage tilt series (Fig. 4.6a) from five, serial, 300 nm sections. Individual microtubules were tracked throughout the volume (Fig. 4.6b). The complete models shown in Fig. 4.6c, d are based on a reconstructed volume of  $7 \times 7 \times 1.5 \ \mu\text{m}^3$ . A total of 1402 microtubules were modeled in this volume. The left panel shows kinetochore-associated microtubules (KMTs, yellow), non-KMTs (red or white, depending on their likely pole association), and centrioles (blue). Light blue and green dots mark pole-distal and pole-proximal microtubule ends. The right panel shows only the microtubules that were situated with both ends in the reconstructed volume. The differences between the left and right panels demonstrate the value of working towards complete spindle reconstructions: when many microtubules leave the reconstructed volume, the information about microtubule lengths and end locations is compromised.

Quantitative measurements of spindle characteristics, such as microtubule lengths and 3D microtubule end positions, can then be measured from model contour data, using programs in the IMOD software package. An initial quantitative analysis of the spindle microtubules in these reconstructions shows the differences in KMT and non-KMT lengths and end distributions (Fig. 4.6e). Analysis of these differences is sure to be informative about the dynamics of different microtubule classes.

3dmod has image caching capabilities that allow one to work with volumes that are too large to fit into memory. The most advanced caching feature provides rapid access to very large volumes at a full range of zooms by working with an "image pyramid", which consists of copies of the volume at different resolutions. Such a pyramid can be built with a simple IMOD command.

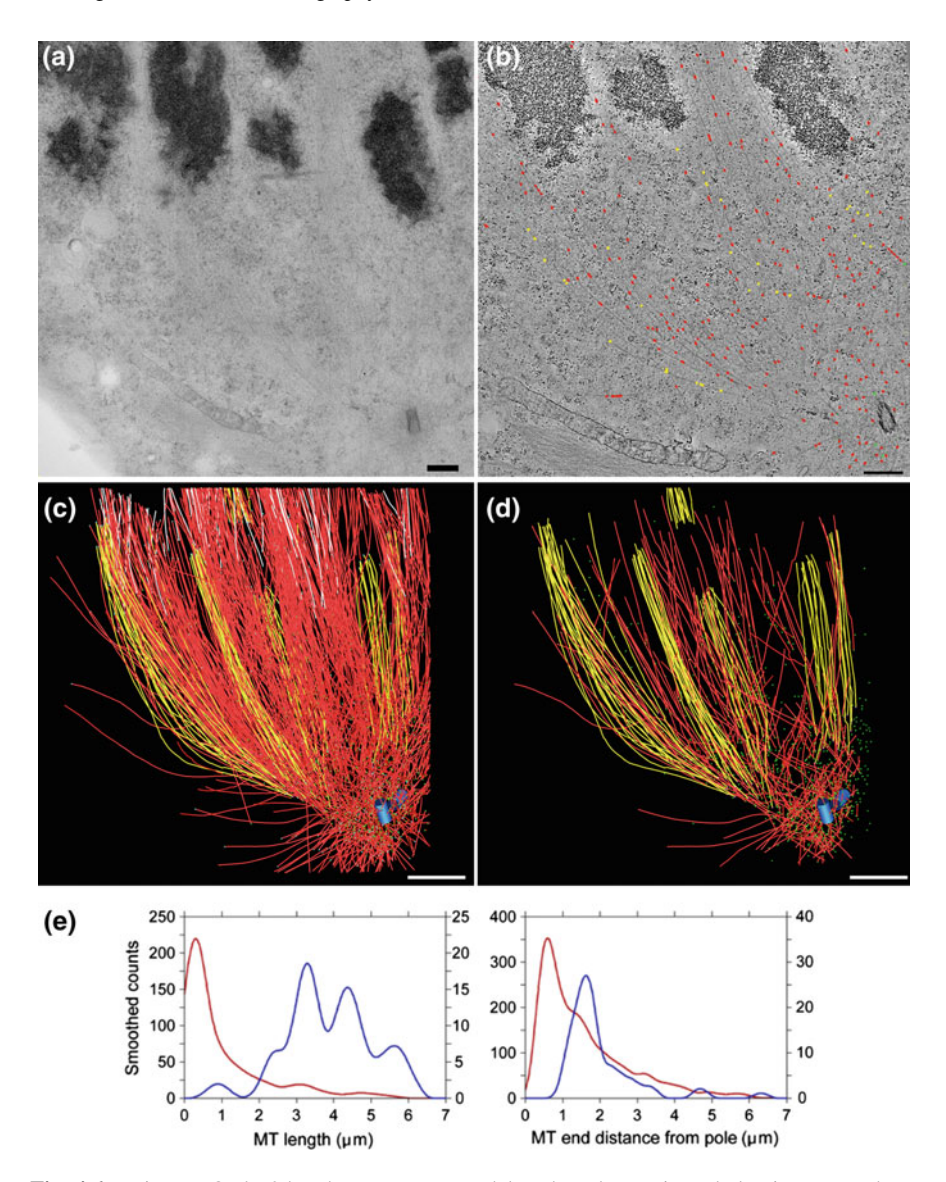


**Fig. 4.6** Using IMOD's 3dmod program to model and analyze microtubules in a metaphase mammalian tissue culture cell. **a**  $3 \times 3$  montage tilt series were imaged at 1.2 nm pixel. Tilt series were collected over five serial, 300 nm sections. **b** Example of a selected tomographic slice with model points tracing microtubules (red, yellow dots). **c** This subvolume of the spindle contains 76 KMTs (Yellow), 60 of which are complete, and 1248 non-KMTs (Red), 383 of which are complete. 62 of the non-KMTs (white) and 16 KMTs appear to associate with the opposite pole. **d** Shows only microtubules that have both ends in within the reconstructed volume. **e** Quantitative analysis of microtubule distributions in the reconstructed volume. Left are the distributions of lengths for complete non-KMTs (red) and KMTs (blue) with scales on left and right ordinates, respectively. Right are the distributions of axial distances of the MT pole-proximal ends from the mother centriole: Again, non-KMTs (red) and KMTs (blue) are markedly different. Bars = 500 nm for **a**, **b**; 1 μm for **c**, **d** 

# 4.8 Special Topics: Increasing Area for 'Supermontage' Reconstructions

## 4.8.1 Using SerialEM to Acquire Supermontage Tilt Series

Single or dual axis tilt series are acquired from large area domains of each section, using tools within the Navigator control and the user interface of the SerialEM image acquisition software. The Navigator allows one to set up super-montage maps with appropriate overlap, from which montage tilt series are automatically acquired (Fig. 4.7a, b). It is important to name the montaged tilt series from the individual panels with information in the file name that refers to the position of the panel in the supermontage. For example, the panel in Fig. 4.7b would have a name ending in \_x2y1z1.mrc to indicate that this panel of the supermontage is the right most panel in x and from the first section in z.

Steps to set up a supermontage tilt series acquisition using an example of a  $2 \times 1$  supermontage of  $3 \times 3$  montages.

- 1. Insert grid, adjust eucentricity
- 2. Find cell/area of interest and pre-irradiate entire cell to  $\sim 2000 \text{ e-/A}^2$
- 3. Create an overview map at medium magnification ( $\sim$ 4700×) by opening a new montage, typically 2 × 2 pieces. Check 'stage montage' and acquire.
- 4. Open a Navigator window and make the image a new map.
- 5. Go to the desired tilt series magnification and open a montage file with  $3 \times 3$  pieces.
- 6. Double click on the overview map line in the Navigator table to read in the map. Using the left mouse button, click in the center of the image area that you want to acquire.
- 7. From the top SerialEM menu, select Navigator—Montaging & Grids—Setup Supermontage and define as a  $2 \times 1$  supermontage.
- 8. Turn on Acquire for the new entries in the Navigator table
- 9. From the top SerialEM menu, select Navigator—Acquire at Points, checking Realign and Acquire map image options in the popup window. Hit go.
- 10. Setup beam autocentering.
- 11. In the main Navigator window, highlight the line of the first acquire map and check Tilt Series. This will bring up a file properties window. Select a montage, set it up as  $3 \times 3$ , name the file and set the increment and total angular range.
- 12. Select the other lines as Tilt series. The files will automatically be named sequentially but final names can be set at this time by the operator.
- 13. From the top SerialEM menu, select Navigator—Acquire at Points.
  - Choose Autocenter beam, Realign to item, Close column valves at the end
    of the tilt series and Send email, Acquire tilt series.

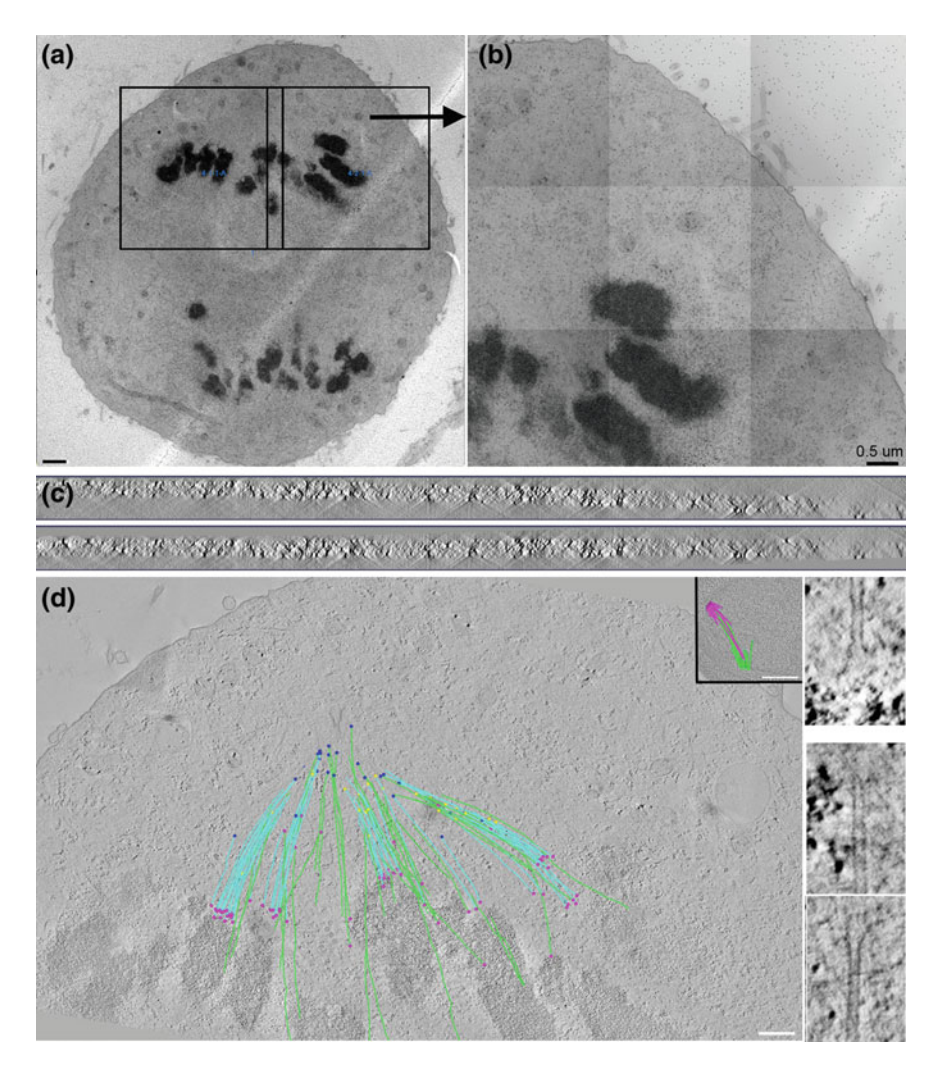


Fig. 4.7 Example of how supermontaging is used to reconstruct portions of an anaphase half spindle from a mammalian tissue culture cell. a Overview of a  $2 \times 1$  supermontage map used to define the areas of tilt series acquisition. b  $3 \times 3$  montage tilt series were acquired from each of the supermontage panels in a. c Reconstructions from montaged tilt series are often bent or dome shaped making lateral stitching of the supermontage panels difficult (top). IMOD program, flattenwarp, provides flattening of the reconstructed volume (bottom). d Slice from a super-montage with a subset of spindle MTs modeled. KMTs in blue, others in green. Closed minus ends, blue dot; open, yellow. Plus ends, purple. Insert show a metaphase yeast spindle at the same magnification for comparison. At right, the end of a KMT (top) and the pole-proximal ends of 2 non-KMTs. Flared vs. capped ends are clear. Bars =  $0.5 \mu m$ 

# 4.8.2 Using IMOD's Etomo Interface to Compute Individual Montage Panels

Imod's Etomo interface is used to compute tomograms from the individual montage tilt series panels of the supermontage. Two practices can be important for facilitating the lateral stitching. First, if the tilt axis is rotated more than  $\sim 5^{\circ}$  from vertical or horizontal, it is necessary to create oversized aligned stacks (where the tilt axis has been rotated to be vertical) so that each tomogram includes all of the volume that can be reconstructed with high quality. For the example in Fig. 4.7b, a final size of 7000, 7000 pixels was used. If using the reconstruction interface, one can increase this size using the advanced button in the final alignment page. To use automated processing with Batchruntomo, the size would have to be set with a directive in a template file. The second practice is to flatten the tomograms. Montaged tomograms often have a dome-like or bent shape after reconstruction (Fig. 4.7c, top), possibly caused by the gradients in lateral shrinkage between the area from which data was acquired, the larger pre-irradiated area, and the surrounding unirradiated area. Tools for flattening volumes are available in IMOD, where a model of the tomogram's top and bottom surfaces is generated and transformations are produced to flatten the material in the tomogram (Fig. 4.7c, bottom). Flattening is useful for joining serial section tomograms, but we have found it essential to do this step before lateral stitching of supermontage panels.

#### 4.8.3 Using IMOD to Stitch Supermontages Laterally

The lateral edges of the resulting individual montages are stitched together to create a super-montage using a series of programs that are run from a command line (Fig. 4.8). The supermontage pipeline consists of five separate programs—Setupstitch, Edgepatches, Fitpatches, Stitchalign, and Tomostitch—four of which are Python scripts that run several other programs in IMOD [30]. Before beginning the process, it is useful to make binned tomograms to test parameters and expedite the process of creating the supermontage volume.

## 4.8.4 Setupstitch

The first tool in the pipeline is Setupstitch, which sets up the initial configuration file. This file starts with information about the tomograms and their overlap; it is used and added to by each program in the sequence. Details of the many options for this program can be found at <a href="http://bio3d.colorado.edu/imod/doc/man/setupstitch.html">http://bio3d.colorado.edu/imod/doc/man/setupstitch.html</a>. Since oversized tomograms include regions that are empty of image contrast, and areas reconstructed from incomplete data, a simple "patch region model" is created to define the area containing useful data. An overlap between volumes at their edges

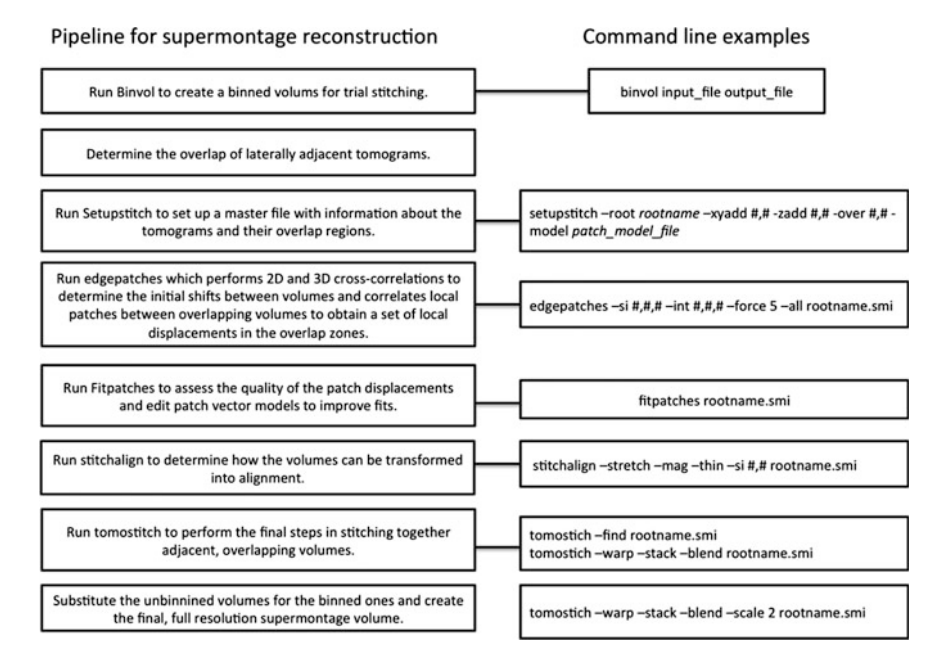


**Fig. 4.8** The basic workflow for stitching tomograms that overlap laterally to create a supermontage. Five programs are involved in the supermontage reconstruction pipeline (left). Programs are run at the command line and examples of their usage is shown on the right

is measured based on relative locations of matching features in neighboring volumes.

Options for running this program include: root, to define the root name of all files; -xyadd and -zadd, to give information about the pieces of the panels and z section of the supermontage; -overlap, to specify how much the files overlap in pixels in x and y; and -model, to identify the useful region of oversized tomograms.

## 4.8.5 Edgepatches

Edgepatches is then run to analyze the shifts between pieces at each edge, based on differences detected by cross correlation. Details of the program can be found at <a href="http://bio3d.colorado.edu/imod/doc/man/edgepatches.html">http://bio3d.colorado.edu/imod/doc/man/edgepatches.html</a>. First the shifts in XYZ required to bring the volumes into alignment in the center of their overlap regions are calculated, then a set of local patches is correlated between the pairs to determine a set of local displacements that would align volumes accurately throughout the overlap zones.

Options for running this program include: size, to specify the patch size in x, y, z;—int, to specify the interval between the patches;—force, for thin volumes, to set the number of patches in Z, regardless of the intervals between patches; and—all, to tell the program to analyze overlap zones for all frames, useful when the analysis needs to be redone.

### 4.8.6 Fitpatches

The Fitpatches tool assesses the quality of the patch displacements, and creates a set of vector models that allow the user to manually correct aberrant vectors. Details about this program can be found at <a href="http://bio3d.colorado.edu/imod/doc/man/fitpatches.html">http://bio3d.colorado.edu/imod/doc/man/fitpatches.html</a>. The program creates a number of vector models that can be opened and aberrant vectors or ones with large residual values can be deleted. A description of the editing process can be found in Sect. 12.5 of the IMOD Tomography Guide (<a href="http://bio3d.colorado.edu/imod/doc/tomoguide.html">http://bio3d.colorado.edu/imod/doc/tomoguide.html</a>). If models are edited, Fitpatches is run again to convert the corrected vector models back into text files with displacements.

#### 4.8.7 Stitchalign

The Stitchalign tool takes the edge vectors from Edgepatches or Fitpatches and calculates two components needed for the final alignment. One is a set of linear transforms appropriate to bring all the volumes into best alignment. The other is a new set of displacement vectors for each volume, so that when each volume is independently warped with these vectors, adjacent volumes will be locally aligned in their overlap zones. Further details about this program can be found at <a href="http://bio3d.colorado.edu/imod/doc/man/stitchalign.html">http://bio3d.colorado.edu/imod/doc/man/stitchalign.html</a>.

Options to this program include: stretch, to find in-plane stretch parameters;—mag, to find overall magnification;—thin, to find factors by which to change the thickness of the volumes;—size, to set the size in X and Y of transformed files to be created by the volume warping program, Warpvol. The default is the size of the largest input volume.

#### 4.8.8 Tomostitch

Tomostitch is run to perform the final steps in stitching together the overlapping volumes. Further details about this program can be found at <a href="http://bio3d.colorado.edu/imod/doc/man/tomostitch.html">http://bio3d.colorado.edu/imod/doc/man/tomostitch.html</a>. It is usually used in two stages, first to run Findwarp on the warping vector fields produced by Stitchalign. If there are large errors, the program will stop and the user will need to go back and edit more vectors to improve the model. Then Tomostitch is run again to warp the volumes individually, stack them into a single montage volume with appropriate overlap, and blend the pieces together to form the final supermontage volume.

This last step produces a binned supermontage that the user can open to evaluate the quality of the lateral edge stitching. If the results are satisfactory, a full resolution supermontage can then be created; the result is a seamless, lateral stitching of the individual montage panels to create the super-montage volume (Fig. 4.7d).

Joining of super-montages from adjacent serial sections is then performed using non-linear alignments of the adjacent serial sections. Such non-linear alignments are essential for aligning super-montage tomograms because the effects of non-uniform changes in the specimen during data collection are amplified over such large areas. This is done using warping transforms, as illustrated in Fig. 4.5, along with the help of segmented objects that span from one section to the next, providing registration points for the alignment of the successive reconstructions. In this example, half of an anaphase spindle was reconstructed from 3 serial sections with a total size of 14.75  $\mu m \times 6.14$   $\mu m \times 900$  nm. A complete 1  $\mu m$  mitotic spindle from budding yeast is shown for comparison (Fig. 4.7d; inset). Individual microtubules can be modeled and tracked in the volume and different classes of microtubules can be defined, such as those that connect to the chromosomes (Fig. 4.7, light blue). Even in these large volumes, details of the morphology of open and closed MT ends in the spindle can be resolved (Fig. 4.7d, right).

#### 4.9 Conclusions and Future Directions

Large-scale EM tomography makes it possible to study the 3D organization of complex cellular assemblies, such as the mitotic spindle, with an almost isotropic resolution that is not attainable by other methods. Automation of image acquisition using SerialEM and options for complete automation of tomographic reconstruction using IMOD greatly facilitate the various operations and reduce the time it takes to collect the necessary data and compute the 3D volumes. A major advantage of large-scale tomography over other volume EM methods is its ability to image fine structure details at  $\sim 4$  nm resolution in their cellular context following optimal fixation procedures, such as rapid freezing/freeze-substitution, and without excessive staining. The time intensive nature of large-scale tomography and its expense are limitations to the method, but it is currently the best approach for visualizing fine structural details, such as membrane coats, microtubule end morphologies, and very slender filaments over larger cellular volumes.

A major goal for future 3-D EM studies is the development of electron-dense labels that can be used for the localization of specific proteins in well-preserved samples. In the past, studies coupling ssTEM with immunocytochemistry have been used to document the spatial distribution of cellular antigens [31]. This approach has been used to study the localization of specific proteins throughout the yeast mitotic spindle as well as the yeast centrosome [32, 33]. Similarly, immunoelectron tomography has been used to identify antigens directly below the section surface to confirm the identity of proteins associated with the Golgi membranes in plant cells [34]. However, these methods have limitations in that only those antigens present at the surface of the section are labeled, reducing the z-resolution. Several groups have employed small, clonable polypeptide to tag proteins with a label that can use either catalysis [35] or photo-activation [36] to oxidize diaminobenzidine and produce a polymer that becomes electron dense upon fixation with OsO<sub>4</sub>. These methods have

provided effective EM labels, although they are not yet useable with samples that have been fixed by rapid freezing and freeze-substitution. An electron dense label that was usable in the volume of a well-preserved cell would therefore be a significant advance.

The use of fluorescent, clonable labels, such as GFP, has revolutionized light microscopy where tagged proteins of interest can be observed in a living cell. Methods to preserve GFP signal after sample processing for electron microscopy have been used for correlative light and electron microscopy [37, 38]. The fluorescent signal present in sections of embedded material is correlated to a structure in the EM through the use of alignment markers, although the label itself is not visible. Recently, metallothionein (MTH) has been successfully used as a clonable tag for protein localization in the EM [39]. Heavy metals that bind to MTH are quite toxic to living cells but their addition can be accomplished during freeze-substitution or by soaking sections of material embedded in a hydrophilic resin, such as Lowicryl K4 M. The method works best with proteins that are present in high copy number. With this approach, a MTH-tagged component of the yeast spindle pole body (SPC42) was successfully labeled and localized with impressive signal-to-noise and resolution. However, the method was not successful with protein components in the yeast nuclear pore complex. Therefore, coupling protein localization with 3-D structure studies of optimally-preserved cells remains a goal for future structural cell biologists; the availability of such a method would certainly enhance our understanding of structure-function relationships in cell biology.

**Acknowledgements** The authors would like to dedicate this chapter to the life and memory of Peter van der Heide who was instrumental in the early development of these methods. We would like to thank Mary Morphew for specimen preparation. This work was supported by and NIH RR00592 and P41GM103431 to A. Hoenger and by NIH/NIBIB grant R01-EB005027 to D. N. Mastronarde

#### References

- D.N. Mastronarde, Automated electron microscope tomography using robust prediction of specimen movements. J. Struct. Biol. 152(1), 36–51 (2005)
- J.R. Kremer, D.N. Mastronarde, J.R. McIntosh, Computer visualization of three-dimensional image data using IMOD. J. Struct. Biol. 116(1), 71–76 (1995)
- 3. C.J. Peddie, L.M. Collinson, Exploring the third dimension: volume electron microscopy comes of age. Micron **61**, 9–19 (2014)
- A. Kremer, S. Lippens, S. Bartunkova, B. Asselbergh, C. Blanpain, M. Fendrych, A. Goossens, M. Holt, S. Janssens, M. Krols, J.-C. Larsimont, C. Mc Guire, M.K. Nowack, X. Saelens, A. Schertel, B. Schepens, M. Slezak, V. Timmerman, C. Theunis, R. VAN Brempt, Y. Visser, C.J. Guérin, Developing 3D SEM in a broad biological context. J. Microsc. 259(2), 80–96 (2015)
- J.R. McIntosh, K.L. McDonald, M.K. Edwards, B.M. Ross, Three-dimensional structure of the central mitotic spindle of Diatoma vulgare. J. Cell Biol. 83(2 Pt 1), 428–442 (1979)

- J.G. White, E. Southgate, J.N. Thomson, S. Brenner, The structure of the nervous system of the nematode Caenorhabditis elegans. Philos. Trans. R. Soc. Lond. B Biol. Sci. 314(1165), 1– 340 (1986)
- S. Takemura, Connectome of the fly visual circuitry. Reprod. Syst. Sex. Disord. 64(1), 37–44 (2015)
- 8. J.R. Anderson, B.W. Jones, C.B. Watt, M.V. Shaw, J.-H. Yang, D. Demill, J.S. Lauritzen, Y. Lin, K.D. Rapp, D. Mastronarde, P. Koshevoy, B. Grimm, T. Tasdizen, R. Whitaker, R.E. Marc, Exploring the retinal connectome. Mol. Vis. 17, 355–379 (2011)
- K.J. Hayworth, J.L. Morgan, R. Schalek, D.R. Berger, D.G.C. Hildebrand, J.W. Lichtman, Imaging ATUM ultrathin section libraries with WaferMapper: a multi-scale approach to EM reconstruction of neural circuits. Front. Neural Circuits 8, 68 (2014)
- K.D. Micheva, S.J. Smith, Array tomography: a new tool for imaging the molecular architecture and ultrastructure of neural circuits. Neuron 55(1), 25–36 (2007)
- N. Kasthuri, K.J. Hayworth, D.R. Berger, R.L. Schalek, J.A. Conchello, S. Knowles-Barley, D. Lee, A. Vázquez-Reina, V. Kaynig, T.R. Jones, M. Roberts, J.L. Morgan, J.C. Tapia, H.S. Seung, W.G. Roncal, J.T. Vogelstein, R. Burns, D.L. Sussman, C.E. Priebe, H. Pfister, J.W. Lichtman, Saturated reconstruction of a volume of neocortex. Cell 162(3), 648–661 (2015)
- 12. W. Denk, H. Horstmann, Serial block-face scanning electron microscopy to reconstruct three-dimensional tissue nanostructure. PLoS Biol. 2(11), e329 (2004)
- 13. D. Wei, S. Jacobs, S. Modla, S. Zhang, C.L. Young, R. Cirino, J. Caplan, K. Czymmek, High-resolution three-dimensional reconstruction of a whole yeast cell using focused-ion beam scanning electron microscopy. Biotechniques **53**(1), 41–48 (2012)
- 14. R. McIntosh, D. Nicastro, D. Mastronarde, New views of cells in 3D: an introduction to electron tomography. Trends Cell Biol. **15**(1), 43–51 (2005)
- 15. A. Hoenger, J.R. McIntosh, Probing the macromolecular organization of cells by electron tomography. Curr. Opin. Cell Biol. **21**(1), 89–96 (2009)
- V. Lučič, A. Rigort, W. Baumeister, Cryo-electron tomography: the challenge of doing structural biology in situ. J. Cell Biol. 202(3), 407–419 (2013)
- G.E. Soto, S.J. Young, M.E. Martone, T.J. Deerinck, S. Lamont, B.O. Carragher, K. Hama, M.H. Ellisman, Serial section electron tomography: a method for three-dimensional reconstruction of large structures. Neuroimage 1(3), 230–243 (1994)
- M.S. Ladinsky, D.N. Mastronarde, J.R. McIntosh, K.E. Howell, L.A. Staehelin, Golgi structure in three dimensions: functional insights from the normal rat kidney cell. J. Cell Biol. 144(6), 1135–1149 (1999)
- A.B. Noske, A.J. Costin, G.P. Morgan, B.J. Marsh, Expedited approaches to whole cell electron tomography and organelle mark-up in situ in high-pressure frozen pancreatic islets. J. Struct. Biol. 161(3), 298–313 (2008)
- J.L. Höög, C. Schwartz, A.T. Noon, E.T. O'Toole, D.N. Mastronarde, J.R. McIntosh, C. Antony, Organization of interphase microtubules in fission yeast analyzed by electron tomography. Dev. Cell 12(3), 349–361 (2007)
- 21. S. Redemann, T. Müller-Reichert, Correlative light and electron microscopy for the analysis of cell division. J. Microsc. **251**(2), 109–112 (2013)
- S. Phan, A. Lawrence, T. Molina, J. Lanman, M. Berlanga, M. Terada, A. Kulungowski, J. Obayashi, M. Ellisman, TxBR montage reconstruction for large field electron tomography. J. Struct. Biol. 180, 154–164 (2012)
- D.N. Mastronarde, Dual-axis tomography: an approach with alignment methods that preserve resolution. J. Struct. Biol. 120(3), 343–352 (1997)
- K.L. McDonald, M. Morphew, P. Verkade, T. Müller-Reichert, Recent advances in high-pressure freezing: equipment- and specimen-loading methods. Methods Mol. Biol. 369, 143–173 (2007)
- K. McDonald, H. Schwarz, T. Müller-Reichert, R. Webb, C. Buser, M. Morphew, 'Tips and tricks' for high-pressure freezing of model systems. Methods Cell Biol. 96, 671–693 (2010)
- Q.S. Zheng, M.B. Braunfeld, J.W. Sedat, D.A. Agard, An improved strategy for automated electron microscopic tomography. J. Struct. Biol. 147(2), 91–101 (2004)

S. Nickell, F. Förster, A. Linaroudis, W. Del Net, F. Beck, R. Hegerl, W. Baumeister, J.M. Plitzko, TOM software toolbox: acquisition and analysis for electron tomography. J. Struct. Biol. 149(3), 227–234 (2005)

- 28. D. Mastronarde, Automated tomographic reconstruction in the IMOD software package. Microsc. Micronal. **19**(Suppl. 2), 544–545 (2013)
- 29. D.N. Mastronarde, S.R. Held, Automated tilt series alignment and tomographic reconstruction in IMOD. J. Struct. Biol. **197**(2), 102–113 (2017)
- 30. D.N. Mastronarde, P.A. van der Heide, G.P. Morgan, B.J. Marsh, Supermontaging: Reconstructing large cellular volumes by stitching together laterally adjacent tomograms. Microsc. Microanal. **14**(Suppl2), 106–107 (2008)
- M.K. Morphew, 3D immunolocalization with plastic sections. Methods Cell Biol. 79, 493– 513 (2007)
- T. Müller-Reichert, I. Sassoon, E. O'Toole, M. Romao, A.J. Ashford, A.A. Hyman, C. Antony, Analysis of the distribution of the kinetochore protein Ndc10p in Saccharomyces cerevisiae using 3-D modeling of mitotic spindles. Chromosoma 111(7), 417–428 (2003)
- 33. A.J. Bridge, M. Morphew, R. Bartlett, I.M. Hagan, The fission yeast SPB component Cut12 links bipolar spindle formation to mitotic control. Genes Dev. **12**(7), 927–942 (1998)
- 34. B.-H. Kang, E. Nielsen, M.L. Preuss, D. Mastronarde, L.A. Staehelin, Electron tomography of RabA4b- and PI-4 Kβ1-labeled trans Golgi network compartments in Arabidopsis. Traffic **12**(3), 313–329 (2011)
- 35. X. Shu, V. Lev-Ram, T.J. Deerinck, Y. Qi, E.B. Ramko, M.W. Davidson, Y. Jin, M.H. Ellisman, R.Y. Tsien, A genetically encoded tag for correlated light and electron microscopy of intact cells, tissues, and organisms. PLoS Biol. 9(4), e1001041 (2011)
- J.D. Martell, T.J. Deerinck, Y. Sancak, T.L. Poulos, V.K. Mootha, G.E. Sosinsky, M.H. Ellisman, A.Y. Ting, Engineered ascorbate peroxidase as a genetically encoded reporter for electron microscopy. Nat. Biotechnol. 30(11), 1143–1148 (2012)
- 37. W. Kukulski, M. Schorb, M. Kaksonen, J.A.G. Briggs, Plasma membrane reshaping during endocytosis is revealed by time-resolved electron tomography. Cell **150**(3), 508–520 (2012)
- W. Kukulski, M. Schorb, S. Welsch, A. Picco, M. Kaksonen, J.A.G. Briggs, Precise, correlated fluorescence microscopy and electron tomography of lowicryl sections using fluorescent fiducial markers. Methods Cell Biol. 111, 235–257 (2012)
- M.K. Morphew, E.T. O'Toole, C.L. Page, M. Pagratis, J. Meehl, T. Giddings, J.M. Gardner, C. Ackerson, S.L. Jaspersen, M. Winey, A. Hoenger, J.R. McIntosh, Metallothionein as a clonable tag for protein localization by electron microscopy of cells. J. Microsc. 260(1), 20– 29 (2015)

# Chapter 5 Volume Scanning Electron Microscopy: Serial Block-Face Scanning Electron Microscopy Focussed Ion Beam Scanning Electron Microscopy

Richard I. Webb and Nicole L. Schieber

**Abstract** Volume scanning electron microscopy is renewing interest in electron microscopy by offering three dimensional visualisation of biological systems. Two main contributors to this are the Serial Block-Face SEM (SBEM) and Focused Ion Beam SEM (FIB-SEM). The resolution offered by the FIB-SEM makes it the go-to tool for studies at higher resolution over smaller areas, particularly for subcellular studies. Compared to FIB-SEM, SBEM gives a much larger field of view (FOV) with a reduced resolution and anisotropic data. These methods require specific considerations as compared to the more traditional transmission electron microscopy. One major consideration is the sample preparation which is an integral part of the entire process for volume SEM. In this chapter we discuss the two techniques from a more practical approach.

#### 5.1 Introduction

Gaining three-dimensional (3D) information about a biological system at the cellular level allows a better understanding of both its structure and function. In biology, early electron microscopy relied on gaining ultrastructural information by observing flat two dimensional ultrathin sections (50–60 nm) and trying to infer the three dimensional structure from them. However, each section supplies only a snapshot of an extremely small part of the cell, thus many things are overlooked and wrong interpretations can be made.

R. I. Webb (⊠)

Centre for Microscopy and Microanalysis, The University of Queensland, Brisbane, QLD 4072, Australia

e-mail: r.webb@uq.edu.au

N. L. Schieber

Cell Biology and Biophysics Unit, European Molecular Biology Laboratory (EMBL),

69117 Heidelberg, Germany e-mail: nicole.schieber@embl.de

<sup>©</sup> Springer International Publishing AG 2018

<sup>117</sup> 

For many years the only way to gain 3D data on biological systems was to use serial section transmission electron microscopy (ssTEM). While this technique has been used almost since ultramicrotomy was invented [1, 2], it has never been widely accepted because of the technical challenges. It requires cutting large numbers of serial sections that are transferred to a grid and taken to the transmission electron microscope (TEM) as a full intact series. The individual imaging of each section and the consequent realigning is also a bottleneck since it is generally done manually. The most complete example of ssTEM was performed on *Caenorhabditis elegans* where the entire nervous system was reconstructed [3].

Technological advances have moved the field beyond ssTEM in terms of throughput and automation with volume scanning electron microscopy (SEM). Two forms of this are microtome based Serial Block-Face SEM (SBEM, also named SBF-SEM in some reports), and Focused Ion Beam SEM (FIB-SEM). These methods both sequentially image the sample surface by SEM after the removal of material by either cutting or milling. They have sped up and automated a process, which previously required skilled personnel plus a lot of slow, tedious work (ssTEM).

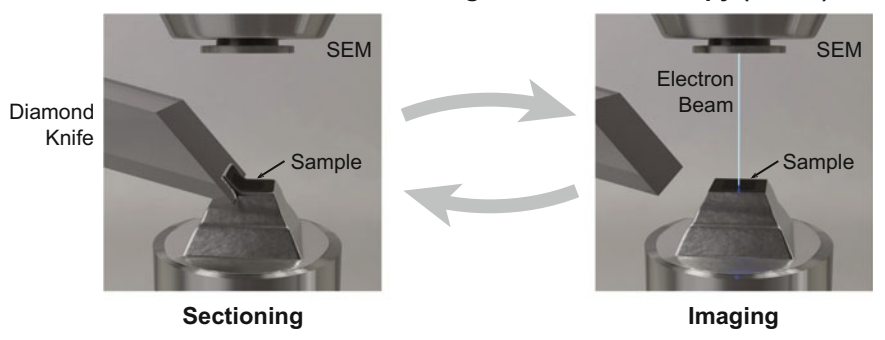
In this chapter we will focus on two versions of volume-SEM, SBEM and FIB-SEM. The specific sample preparation is a fundamental part of these techniques, so here our aim is to provide a more practical approach to both preparing biological samples for such microscopes and to discuss the operation of the systems.

# 5.2 Volume Scanning Electron Microscopy—SBEM and FIB-SEM

SBEM and FIB-SEM technologies have successfully opened up possibilities to visualize biological samples in three dimensions [4–9]. From resin embedded biological material the SBEM, uses an integrated ultramicrotome to cut away material and FIB-SEM, uses a gallium focused ion beam to mill it away (Fig. 5.1 schematic). In an iterative process, the SEM then images the newly generated surface and the collection of these 2D images can be converted to a 3D ultrastructural volume. Both techniques are destructive, so it is important to consider exactly what is wanted from a SBEM or FIB-SEM project before it begins. FIB-SEM and SBEM give similar results but each has their limitations. Titze and Genoud [10] and Briggman and Bock [11] give comprehensive overviews of these 3D EM techniques, as well as others.

Volume SEM gives access to similar information to that typically acquired in a TEM. Indeed, they both rely on the interaction of the electron beam with heavy metal stained cellular components. However, the lateral resolution of TEM is higher than in SEM (due to many factors including the higher acceleration voltage in TEM and the probe size in SEM). Furthermore, TEM is a wide-field technique,

#### Serial Block-Face Scanning Electron Microscopy (SBEM)



#### Focused Ion Beam Scanning Electron Microscopy (FIB-SEM)

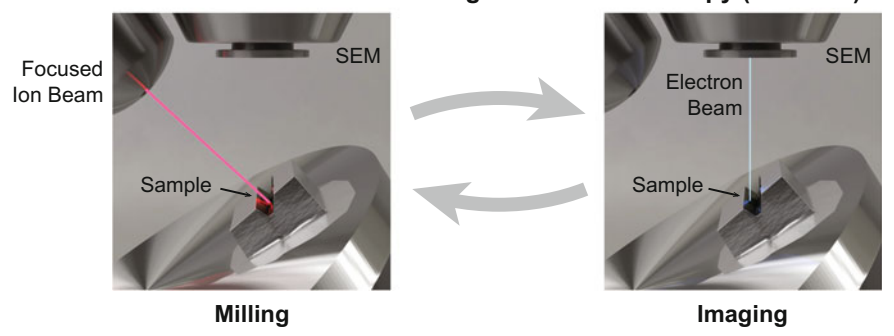
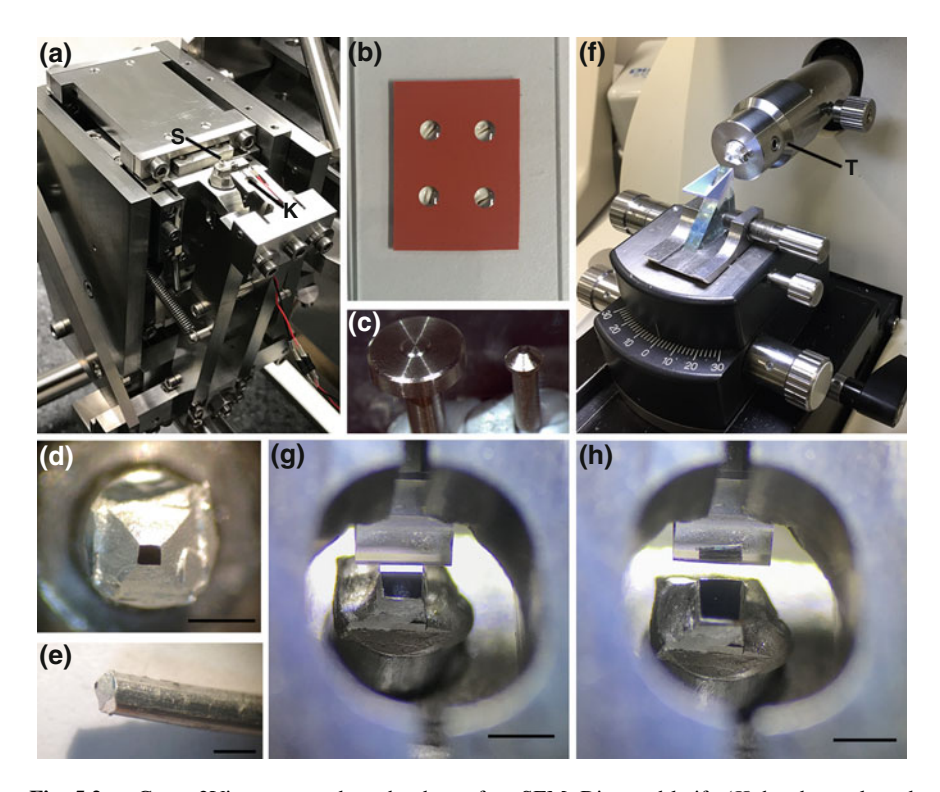


Fig. 5.1 Workflow schematics of Serial Block-Face Scanning Electron Microscopy and the Focused Ion Beam Scanning Electron Microscopy

while SEM relies on a raster scan of the sample, which can also limit the resolution. In the TEM, images are formed from 2D projected information coming from the full depth of the section (50 nm) resulting in the overlaping of structures. Volume SEMs collect backscattered electrons coming from a limited depth within the sample (dependent on the voltage but usually only a few nanometres), resulting in a better Z resolved image.

The concept of placing a microtome into an SEM so that the sample could be imaged sequentially as pieces of it were removed was first conceived by Leighton in 1981 [12]. It was then fully developed by Denk and Horstmann [5] and Gatan released a commercialised version (3View) years later [5]. The 3View (Fig. 5.2a), can be installed onto an SEM from several manufacturers: FEI, Zeiss, JEOL, Hitachi and Tescan. In 2015, FEI released their own version, the VolumeScope, on their Teneo SEM as a fully integrated package. Along with this they released a deconvolution system [13–15], which captures images using different landing energies after each section. By deconvolving the information from multiple images it is possible to obtain 10 nm isotropic resolution using this SBEM. Initially the SBEM technology was widely used in neurobiological studies in order to piece



**Fig. 5.2** a Gatan 3View mounted on the door of an SEM. Diamond knife (*K*) has been cleared away from the sample (*S*), **b** Polymerised resin with zebrafish embryo tail samples in holes punched in Silicone Insulator sheet, **c** Sample mounts from the FEI VolumeScope (left) and Gatan 3View (right), **d** and **e** Sample mounts for the 3View made from aluminium jewellers wire, 12 g. The sample has been trimmed so there is no excess resin and surrounded by conductive silver paint but not yet sputter coated with platinum (**d** scale 1 mm; **e** scale 2 mm), **f** Sample being prepared on an ultramicrotome. The sample has been mounted in the conical shaped holder supplied with the 3View and then placed into the trimming adapter of the ultramicrotome (*T*), **g** Lining up the sample with the diamond knife using the reflections on the block-face (scale 1 mm) **h** Sample sectioning in the 3View. The knife is at the beginning of its travel ready for the cutting stroke. Previously cut sections can be seen mounted up on the edge of the knife (scale 1 mm)

together the connectome, but has since moved to working on an extensive range of biological samples (see [16–18]). The technique has also been used in material science research [19, 20] though its uptake there has been slower.

In contrast to SBEM, the FIB-SEM was developed for use in materials science and nano-technology applications [21]. The first use of a liquid metal ion source (LMIS) was documented by Krohn [22], who was trying to develop thrusters for use in space. In the 1980's, FIB systems based on high-brightness gallium LMISs became commercially available [23]. One of the first FIB applications in life sciences was Yonehara et al. [24], where they used an argon ion beam to mill biological specimens then observed with a low accelerating voltage SEM in the same

instrument. FIB-SEM as we know it today (sometimes called FIB-SEM tomography), started to be used in materials science at the end of the 1990s [25, 26]. Since this time, there are continual improvements to this powerful tool as it spreads into all aspects of biological research for imaging in 3D at nanoscale resolutions [6].

There are several additional factors to be considered for the serial block-face techniques that are not an issue when performing standard ultrathin section TEM. Importantly, the interaction between the electron beam and the sample leads to an accumulation of charges at the sample surface, which are deleterious to the imaging quality. While high voltages allow higher resolutions, charge formation is normally inversely proportional to the acceleration voltage. Hence, the balance between image quality and sample damage is critical. SEM has always suffered from charging problems since samples are extremely susceptible to damage from the electron beam and have to be imaged at low voltages. A factor that is rarely considered in normal TEM work where ultrathin sections with little mass are held on a highly conductive metal grid. Coating the entire surface of a sample with metal alleviates the issue for normal SEM, however having a sample embedded in a non-conductive resin with its surface fully exposed to the electron beam becomes an issue of real concern to the serial block-face techniques, especially SBEM [27, 28]. The beam damage can take several forms, such as charging, image distortions forming lines or shifting images, uneven sectioning thickness, or poor sectioning resulting in a damaged surface. In SBEM, charging is the most limiting factor to the technique. In FIB-SEM, whether imaging or milling, the ion beam introduces Ga<sup>+</sup> ions on/into the sample as well as destroying its surface [29]. These positive gallium ions reduce the charging affect of biological samples, having a similar effect as gas in variable pressure-SEM, to neutralise the charge at the sample surface [29, 30].

The SBEM, while it does not give as good of a lateral and axial resolution as FIB-SEM, still has many advantages. The removal of material by a diamond knife means the process is very fast, taking only a few seconds to remove a section from the entire block-face. Nevertheless, this is a limiting factor, since the size of the sample is restricted to the width of the diamond knife (typically 1.2–1.5 mm) and should be as thin as possible to reduce the charging volume. The FIB only allows milling of a relatively small area (in the range of  $50 \times 50 \, \mu m$ ) at any one time and the area of this exposed face dictates the speed at which the cutting can take place. Thus, this technique is well suited to smaller volumes and achieving high resolutions. Titze and Genoud [10] give a comparison of the best voxel sizes achieved (x, y, z):  $10 \times 10 \times 25 \, nm$  in SBEM, [31] and  $5 \times 5 \times 5 \, nm$  for FIB-SEM [32, 33]. However, Russell et al. [9] have shown that they could produce a large dataset cutting slices at 10 nm and thus giving isotropic resolution for the SBEM of  $10 \times 10 \times 10 \, nm$ .

The interplay between resolution and size is a problem common to all imaging techniques [34]. The best image quality from the region of interest (ROI) would be achieved by a small pixel size, high dwell time (the amount of time that the beam will collect data at each pixel) and often a large FOV. However, this is rarely achievable at the same time. The stability of the sample and the system in use will

ultimately set the limits. In general, for all imaging techniques small areas can be viewed at the highest possible resolution but larger fields of view must be imaged with a lower resolution or with other procedures such as tiling [34, 35]. This interplay is particularly notable in FIB-SEM and SBEM where there is a need to balance imaging conditions with the mechanism to remove sections. In both technologies, imaging conditions that are too harsh for the sample will result in inconsistent removal of material and poor image quality. The best way to manage this is to narrow down what is required from the microscope to answer the biological question and how much data is necessary to achieve this. At the FIB-SEM, improved hardware and intelligent software such as Atlas3D part of Atlas5 (Zeiss) helps to extend these limitations [34]. In the SBEM, the ability to section an entire block-face alongside the implementation of montaging or working with regions of interest allows acquisition from very large areas. In both cases, this leads to the production of gigabyte or even terabyte sized datasets, which could be too unwieldy to handle (especially from SBEM). Big datasets are very slow to move from one place to another and need big capacity storage and significant computing power in order to analyse them. It also takes considerable time to acquire large datasets, this can be on the order of days, and the instrument is then not available for other projects. It is important to be realistic about what is to be achieved from the work [10, 36].

Where possible, correlative light and electron microscopy (CLEM) is extremely useful for volume SEM. It has been utilised to bridge the gap between many scales and forms of microscopy. Recently the combination of microscopic X-ray computed tomography (microCT) with FIB-SEM [37, 38] and SBEM [39] is receiving a lot of attention. For volume SEM, CLEM will help to target the specific region of interest, thereby reducing the area that needs to be acquired [9, 37, 38]. It will also help (when possible) to give a broader context of the sample since it will likely look very different in the SEM. This can similarly be achieved by simply documenting well the mounting and preparation of the sample prior to loading it into the instrument.

## 5.2.1 Sample Processing

Sample processing for electron microscopy aims for excellent preservation of structures. The steps to achieve this have not changed significantly throughout the years, they are variations of a similar format: primary fixation, contrasting, dehydration and infiltration [40]. The same is true for volume-SEM techniques. However, these samples need enhanced contrast relative to standard TEM samples where it is possible to post stain the ultrathin sections (Fig. 5.3). Instead, all of the heavy metals must be infiltrated into the sample during the initial processing. These heavy metals will be responsible for the production of the backscattered electrons (even at low voltages) and thus the actual imaging of the sample and at the same time make the sample conductive to alleviate the effects of charging.

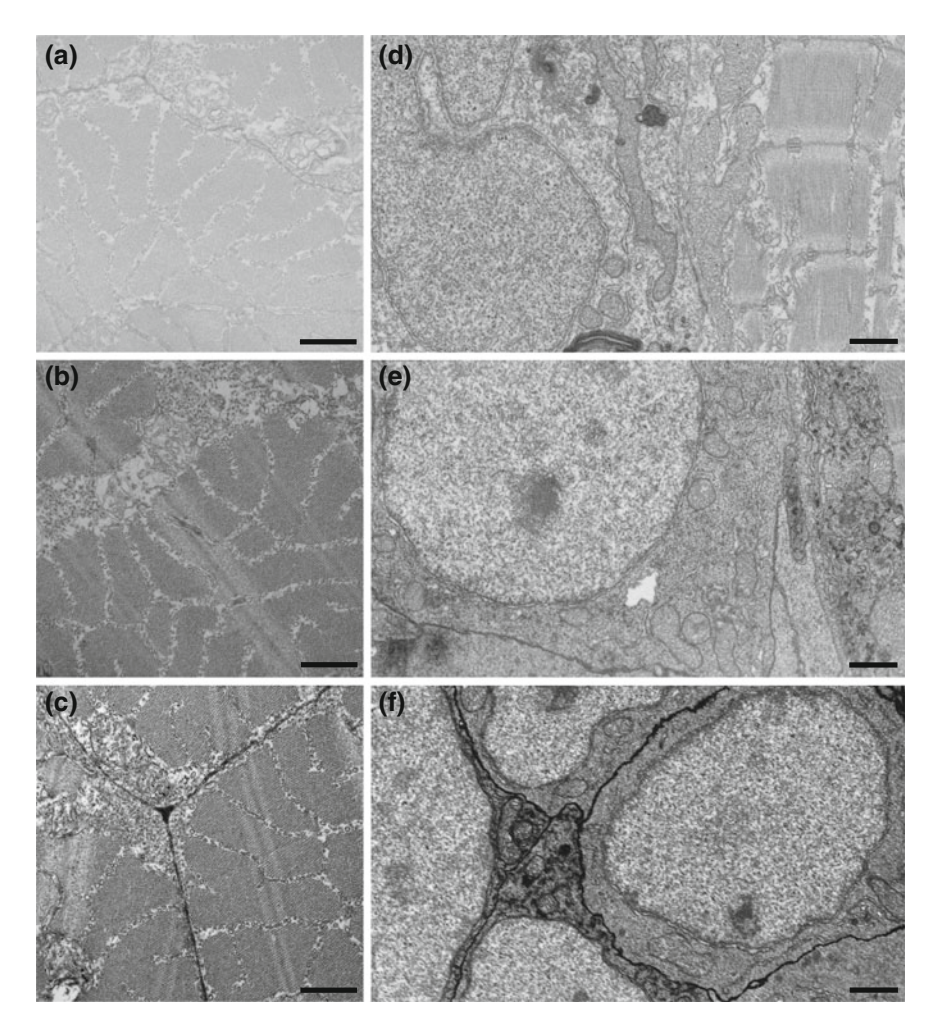


**Fig. 5.3** a–c TEM images of thin sections of muscle in a zebrafish larvae taken with comparable imaging conditions, **a** Unstained section processed by standard TEM processing protocol of glutaraldehyde and osmium tetroxide, **b** Section of the same sample as in (a) that was post-stained with uranyl acetate and lead citrate, **c** Section of sample processed using the NCMIR SBEM protocol with no post-staining, **d**–e SEM images from 3 different zebrafish larvae taken with a FIB-SEM, the imaging surface for each was exposed with the FIB and imaged by SEM at 1.5 kV by back scatter detector (EsB). **d** Sample processed with a TEM protocol of glutaraldehyde, osmium tetroxide and *en bloc* uranyl acetate, **e** Sample processed with 2 steps of osmium tetroxide (reduced and aqueous), **f** Sample processed with the NCMIR SBEM protocol (scale for all 1 μm)

Particularly for SBEM, sample processing is an integral part of the technique largely to avoid charging problems. The development of a processing protocol that gave more consistent results [41, 42] helped to project SBEM into becoming a routine technique. This protocol has been designed to deposit large amounts of

heavy metals (such as osmium, uranium and lead) into the samples allowing their attachment to structures to give the sample conductivity. The work of JoAnn Buchanan has also been invaluable in designing SBEM protocols and she discusses many useful protocols for SBEM [43]. On the other hand, preparations for FIB-SEM do not require as many heavy metal steps as for SBEM since the ion beam introduces positive Ga<sup>+</sup> ions on/into the sample that help to neutralize surface charging [29, 30]. Thus the conductivity of a FIB-SEM sample itself is less critical and it is possible to image samples with a large variety of preparations (Fig. 5.3).

Utilizing a microwave oven for sample processing has been around for some time. The microwaves aid in the processing by enhancing certain reactions and increasing the diffusion of chemicals into the sample. It can speed up processing substantially by reducing processing protocols from days to hours [44]. The wattage of the microwave energy is kept low and is cycled so that the specimens do not overheat and until now no changes to the ultrastructure have been attributed to using this method. In addition, a low vacuum is applied during the processing to enhance diffusion. It has even been shown that microwave processing can reduce artefacts induced during standard processing [45]. Later sections, 5.3.1.2 and 5.4.1.2 give examples of microwave assisted processing protocols showing their usefulness for SBEM and FIB-SEM.

As with TEM, biological samples need to be embedded in resins. Unfortunately, these resins are not at all conductive which is a serious issue particularly for SBEM [18, 46]. Standard formulas for resins used in TEM work will not work well in SBEM or FIB-SEM because they need to be more resistant to beam damage. As a result, resins that are more highly cross-linked have been used. The epoxy resin Durcupan ACM gives the most reliable results with greater stability in the beam. However, other resins such as hard formulas of Epon and Spurrs have also been successfully used.

Specific to SBEM, attempts have been made to improve the conductivity by including conductive material in the resins. Wanner et al. [31], removed the pre-polymerised resin from around the sample and re-embedded the sample in Epo-Tek EE129-4, an epoxy glue that contains silver particles. Nguyen et al. [47] have used a fine conductive carbon powder, Ketjenblack EC600JD, and included it in the final embedding resin to reduce charging. In both of these cases the conductive material in the resin does not penetrate the sample but sits around the outside. There is a critical need for a truly conductive resin that could be used in SBEM as the benefits would be enormous.

## 5.2.2 Imaging

As with SEM imaging in general, the parameters responsible for good image quality are the voltage, the probe current and the dwell time. The aim is to get a

high signal-to-noise ratio (SNR) by producing high numbers of backscattered electrons from the heavy metal stained structures. Lateral resolution is also important and this is a factor of voltage and probe size. However, when deciding on the imaging conditions, it is a balance between image quality, acquisition speed, sample damage and the desired results.

During a 3D acquisition, in both SBEM and FIB-SEM, the images are acquired using a backscattered electron detector that sits above the sample. Using this form of imaging, contrast is given by light elements producing dark coloured pixels and heavy elements producing bright pixels. As images of this type are foreign to most biologists they are inverted to produce an image that looks similar to a TEM image.

In order to reduce charging in the sample, the SEM is operated at low voltages (usually lower than 3 kV) for imaging during 3D acquisitions. Lower kVs also ensure the signal is coming from the surface or only a short distance below. The signal should be limited to the depth of removed material. Using Monte Carlo simulations it can be shown that the use of higher kVs will produce a backscatter signal at a greater depth (Fig. 5.4). Though it is difficult to simulate accurately the depth of this signal due to the complex mixture of metals (Fig. 5.4) that are introduced into a biological sample during processing it is still accepted that the signal will only come from depths within the section thickness if lower voltages are used.

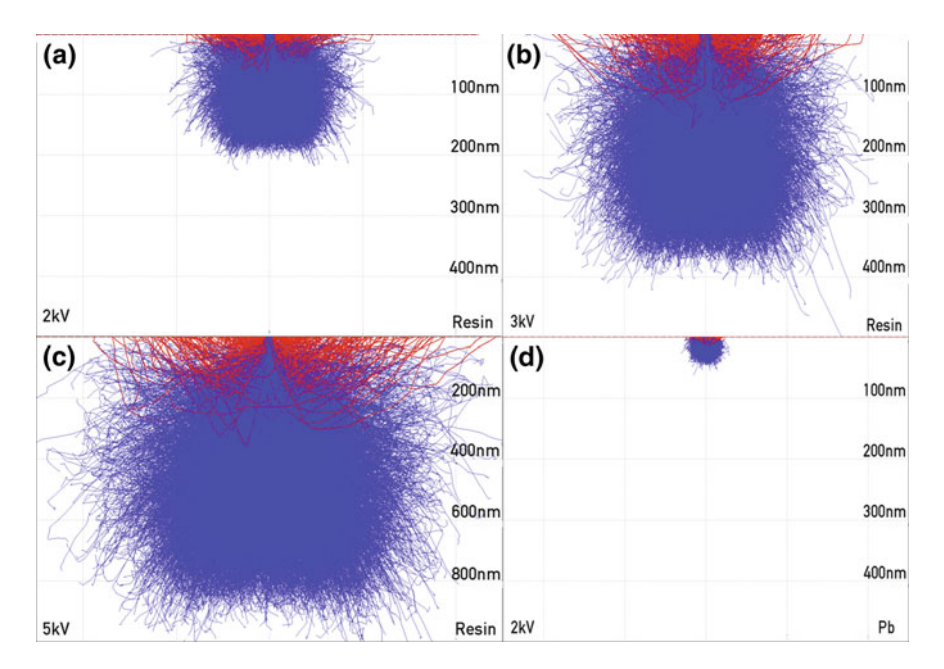


**Fig. 5.4** Monte Carlo simulations of epoxy resin and lead (to illustrate heavy metal staining) showing the production of both secondary (*blue*) and backscattered (red) electrons caused by the incident beam at different voltages. The depths within the sample are shown at right. Resin **a** 2 kV **b** 3 kV **c** 5 kV Lead **d** 2 kV. Monte Carlo simulations are produced using the software Casino [97]

# 5.3 Serial Block-Face Scanning Electron Microscopy (SBF-SEM or SBEM)

Serial Block-Face Scanning Electron Microscopy (SBEM) is essentially an ultramicrotome built inside an SEM, and works on the same principle of removing thin sections of material from the surface of the resin embedded sample. The sample is then moved forward by a small increment and another section can be removed. Images of the block-face are acquired between each section. This technology is capable of providing detailed 3D data but has a restricted resolution along the z-axis and is limited by sample charging and can have artefacts from sectioning [28, 34].

Cutting sections of 50 nm is routine in SBEM and it is possible to cut thinner. Russell et al. [9] demonstrated that they could cut at 10 nm sections with the right sample. The 3View uses an oscillating diamond knife. Studer [48] and Hashimoto et al. [20] show that the oscillation does cause less damage while sectioning and could be useful particularly for very thin sections. During the sectioning process the sections tend to stick together and mount up as a group on the knife edge. These can then be cleaned from the knife edge using compressed air at the end of the process.

In SBEM beam damage is particularly an issue. This means that it is not possible to work at high magnifications in SBEM as when doing so the electron beam dose is high in a small region of the sample. As a result, most SBEM work is done at relatively low magnifications (generally below x10K). However, in an SEM it is easy to change the pixel density of the image to gain large amounts of information by enlarging the images taken at low magnifications. The Gatan 3View system allows acquisition of images at up to  $32k \times 24k$  and with the Maps software available in the FEI VolumeScope it is possible to collect images at  $40k \times 40k$  pixels.

## 5.3.1 Sample Processing

SBEM is highly dependent on the processing of the sample. For a dedicated SBEM project the samples should be processed with protocols using large amounts of heavy metals as discussed below.

#### **5.3.1.1** Conventional Bench Processing

A protocol designed in the NCMIR laboratory in San Diego has now become widely used in the processing of samples for SBEM and is used with some slight modifications in most laboratories [41, 42]. This standard protocol has an initial osmium tetroxide step containing potassium ferrocyanide, which is known to give

good membrane contrast [49], followed by a double osmium step with thiocarbohydrazide as a linker, allowing the deposition of the second osmium [50]. Lastly, an *en bloc* aqueous uranyl acetate step is performed followed by an *en bloc* lead aspartate [51] at 60 °C.

The NCMIR processing protocol is as follows:

- 1. Primary fixation in aldehydes and washing in buffer
- 2. 2% osmium tetroxide 1.5% potassium ferrocyanide 1 h
- 3. Water washes,  $5 \times 3$  min
- 4. 1% thiocarbohydrazide 20 min at room temperature
- 5. Water washes,  $5 \times 3$  min
- 6. 2% osmium tetroxide 30 min at room temperature
- 7. Water washes,  $5 \times 3$  min
- 8. 1% uranyl acetate (aqueous) overnight at 4 °C
- 9. Water washes,  $5 \times 3$  min
- 10. Lead aspartate at 60 °C 30 min at room temperature
- 11. Water washes,  $5 \times 3$  min
- 12. Dehydrate through graded acetone series
- 13. Infiltrate with Durcupan resin
- 14. Polymerise 48 h in 60° oven

The washes in this protocol must be thorough to ensure full removal of the solutions and the use of high quality water and agitation is essential. Glass containers also prevent precipitation onto the wall of the container. Fresh chemicals ensure the best staining so the purchase of new chemicals on a regular basis can be valuable. The working solutions should be prepared fresh just before use though some solutions (potassium ferrocyanide and aspartic acid) can be stored as stocks at 4 °C for up to a month. While this protocol uses potassium ferrocyanide, potassium ferricyanide has also been shown to work successfully [9].

Samples produced by this and other similar protocols become extremely brittle and so must be handled with great care or they will easily shatter into pieces. In addition, cracks are often seen in these samples [52, 53]. The staining achieved by these protocols can be inconsistent due to problems with the infiltration of the reagents. To give consistent staining throughout the sample Hua et al. [52] have modified the protocol so that they separate the osmium and the ferrocyanide, putting the sample first in osmium alone and then without washing, placing it into the ferrocyanide. They have also shown that a two-step uranyl acetate protocol helps. They allow the uranyl acetate to penetrate overnight at 4 °C then heat the solution to 50 °C.

Embedding into small moulds is useful, since after polymerization the sample will have to be cut away from all the surrounding resin. Silicone Isolator Sheets from Electron Microscopy Supplies (Cat # 70338) make a good mould when a small hole is punched in them. These are 0.5 mm in thickness and can be stuck to a glass slide (Fig. 5.2b).

#### **5.3.1.2** Microwave Processing

The sample protocol listed above is quite long lasting 5 days. To speed up the process and aid with the diffusion of chemicals the Pelco Biowave microwave (Ted Pella Inc.) can also be used for all electron microscopy processing [44]. A protocol utilising a Ted Pella Biowave processing microwave oven is given below.

- 1. 2% osmium tetroxide 1.5% potassium ferricyanide 4 cycles of 2 min at 80 W with vacuum
- 2. Ouick bench water wash, then  $2 \times 40$  s 80 W with vacuum
- 3. 1% thiocarbohydrazide 6 alternating cycles of 2 min at 80 W with vacuum
- 4. Quick bench water wash, then  $2\times40~\text{s}~80~\text{W}$  with vacuum 2% osmium tetroxide 6 alternating cycles of 2 min at 80 W with vacuum
- 5. Quick bench water wash, then  $2 \times 40$  s 80 W with vacuum
- 6. 1% uranyl acetate (aqueous) 6 alternating cycles of 2 min at 80 W with vacuum
- 7. Quick bench water wash, then  $2 \times 40 \text{ s} 80 \text{ W}$  with vacuum
- 8. Lead aspartate at 50 °C 6 alternating cycles of 2 min at 80 W with vacuum
- 9. Quick bench water wash, then 2 × 40 s 80 W with vacuum
- 10. Dehydration and infiltration at 250 W with vacuum
- 11. Polymerisation at 60 °C in a normal oven for 2 days.

For the lead staining the temperature of the Steady Temp is turned up to 50 °C and the sample processing vials or cell culture dishes are placed directly onto the Cold Spot inside the chamber of the Biowave. This will allow warming of the samples during the en bloc staining with Walton's lead aspartate. Kremer et al. [16] also list a slightly different microwave protocol for SBEM sample processing.

#### 5.3.1.3 High Pressure Freezing and Freeze Substitution

High pressure freezing and freeze substitution give superior structural preservation to standard room temperature processing [40]. Standard freeze substitution protocols do not impregnate sufficient metals into the sample to allow their use with SBEM. Webb and Webb [54] have introduced an extended freeze substitution protocol that is suitable for SBEM. Below is their protocol based on the quick freeze substitution protocol of McDonald and Webb [55]. Thiocarbohydrazide is not particularly soluble in acetone but enough becomes available in solution to be used for this work. It is dissolved at 0.05 g in 5 ml of acetone. After mixing thoroughly and heating at 60 °C for an hour this stock solution is diluted 1:10 with acetone (personal communication Shigeki Watanabe). Lead acetate at 5% is made by dissolving it in methanol [56]. Once the freeze substitution has reached room temperature and the samples are washed in acetone, the remainder of the process is performed at room temperature. Agitation for all steps is important in enhancing diffusion of the solutions and also helps with the acetone washes. When this technique is combined with quick processing following McDonald [40] samples

can be fully processed from frozen sample to fully polymerised block in under one working day.

- 1. Quick freeze substitution process in 1% imidazole 1% osmium tetroxide 1.5–3 h, warm to room temperature
- 2. Wash in acetone,  $3 \times 5$  min
- 3. Thiocarbohydrazide 30 min
- 4. Wash in acetone,  $3 \times 5$  min
- 5. 2% osmium tetroxide 30 min
- 6. Wash in acetone,  $3 \times 5$  min
- 7. 2% uranyl acetate in acetone 30 min
- 8. Wash in acetone,  $3 \times 5$  min
- 9. 5% lead acetate in methanol 30 min
- 10. Wash in acetone,  $3 \times 5$  min
- 11. Infiltrate with Durcupan resin using microcentrifuge
- 12. Polymerise for 2 h at 90 °C

## 5.3.2 Sample Setup and Mounting

To prepare the embedded sample for the SBEM all excess resin must be removed to the minimum amount possible without losing information. If the sample is stuck down to the adherent surface of sticky tape it is relatively easy to trim with a razor blade without losing the sample. Exposing the sample on all sides of the block is important where possible, especially on the back side of the sample, so when it is glued to the stub the sample itself is in contact with the metal. For cell cultures embedded on a culture dish it is necessary to peel the polymerised resin off the dish and cut out a very small region which is then trimmed as close as possible to the cells. These samples can be mounted in two orientations on the stub, to achieve either longitudinal or transverse sections. For CLEM projects it is important to consider specific sample set ups for SBEM. Russell et al. [9] describe this process in great detail for its application to cell monolayers that are grown in a dish with a photo-etched grid pattern, making it possible to overlay 3D light microscopy onto the 3D electron microscopy.

The sample stubs used in the 3View system, called rivets, are small pins with two different head sizes (Fig. 5.2c). It is also possible to make rivets easily from jeweller's aluminium wire of 12 g (personal communication Graham Kidd) (Fig. 5.2d, e). A roll of this wire can produce large numbers of rivets and costs very little. For the VolumeScope it is necessary to use specific sample stubs that consist of a shaft with an 8 mm head. In the middle of the head is a 2 mm raised section for attachment of the sample (Fig. 5.2c).

The sample is glued to the sample stub using a 2 part conductive epoxy glue (CircuitWorks Conductive Epoxy CW2400). Placing it in a 60 °C oven can aid in the setting of the glue. The sample is positioned according to the orientation needed

for sectioning in the SBEM. If the sample already has a smoothened surface ready for sectioning (for example, cultured cells grown on a dish) it is important to try to make the block-face almost but not quite perpendicular to the shaft of the mount. In this way it will be almost parallel to the cutting action of the diamond knife in the SBEM.

Further trimming of the sample can be performed on an ultramicrotome stage. Using the trimming adapter (Fig. 5.2f) or the segment arc set on 0° is useful so that the sample will be aligned for the SBEM. The cutting window in the 3View is only 1.2 mm and 2 mm in the VolumeScope, so the block-face should be smaller than this window. Semi-thin or even ultrathin sections can be taken from the block to find the ROI and to check the quality of preservation of the sample.

Conductive silver paint (Colloidal Silver Liquid, Ted Pella, Inc.) is then put around the sample on all sides making a layer that is continuous around the entire sample and that also connects it to the sample stub (Fig. 5.2d, e). Placing the sample in a 60 °C oven will completely dry this paint. Finally, the mounted sample is sputter coated with a thin layer of platinum to make a continuous coat over the entire surface. Altogether, the conductive epoxy glue, the silver paint and the sputter coating will give conductivity to the sample in an attempt to reduce charging.

Samples ready for SBEM can be stored inside the chamber so they are kept under vacuum. This helps to outgas the resin and stabilize the samples. The sample is inserted into the stage of the SBEM and aligned with the SEM door opened. This alignment involves setting up the sample so it is in the correct position relative to the diamond knife. As in an ultramicrotome, the sample positioning is done watching reflections that are seen on the sample block-face. The reflections (Fig. 5.2g) are used to judge the distance between the sample block-face and the diamond knife and the sample is raised until this reflection almost vanishes so that the sample and knife are almost touching. For most samples the initial sectioning is still part of the alignment and is done while the door is still open. The sectioning can be performed at a greater section thickness (200 nm) and a faster cutting speed (1.2 mm/sec). Once the entire block-face has been sectioned the process is stopped, the sections are removed from the knife edge with compressed air (Fig. 5.2h), the door of the SEM is closed and the chamber is pumped down. For cultured cells being sectioned longitudinally it is important to stop this coarse approach as soon as the first sections come off.

After the chamber has reached vacuum wait for the sample to stabilise and outgas fully. At least an hour is advisable.

# 5.3.3 SBEM Operation

Once the SEM is pumped down and the sample is stable the electron beam can be turned on and the sample imaged. Some prior knowledge of the system and its operation on similar samples will give a starting point (for example, the voltage or

the vacuum). At low magnification the sample is searched to find the ROI. It is advisable to work at low voltage, though sometimes a higher voltage can be useful for revealing the sample anatomy below the block-face. When working with cell cultures that were embedded on the culture plate, a voltage of 5 kV will make it possible to view the cells below the surface of the resin, although this will cause some charging. Once more detailed viewing is needed and the magnification is increased, the microscope and SBEM will need to be setup so as not to damage the sample.

The structure of interest may not be in view immediately and it may take some sectioning and continuous checking until the region is reached. In order to find the ROI and capture a data set of the entire structure it is necessary to use neighbouring markers to locate it before sectioning commences.

In the Sect. 5.3.2, it was explained that a sample of a monolayer of cells should be mounted with a slight tilt of the face so that it will not be completely aligned with the knife. The tilt means that in the SBEM only one corner will be sectioned initially and then sectioning can be tracked until it gets close to the cell of interest (Fig. 5.5a). At this point alignment is done on a neighbouring cell and then the acquisition can be commenced on the correct region so that a data set of the complete cell is captured.

Imaging in the SBEM is a compromise between sufficient image quality to achieve the resolution necessary that will discern the structures being studied and the effects of charging and beam damage. The number of parameters that can be varied is high: voltage, probe current, vacuum, dwell time, magnification, pixel size, pixel density and section thickness. All of these will have an effect on how well the sectioning and imaging will work. Different microscope systems have

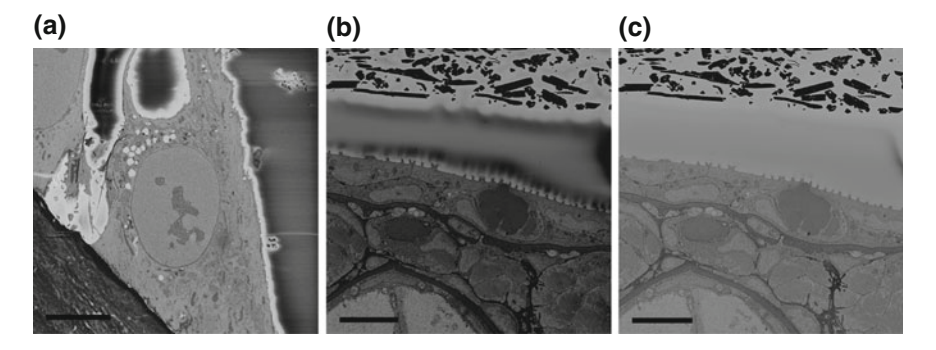


Fig. 5.5 a The block-face of the cultured cells (primary human fibroblasts) is not perfectly parallel to the knife so it is cut at an angle and cells appear as it sections further across the sample. The dark area at the lower left is the platinum on the sample surface which has not yet been sectioned away,  $\bf b$  1.8 kV and  $\bf c$  1.5 kV used to image a zebrafish embryo in high vacuum showing the difference in image quality and charging (seen as the black region in the resin outside the sample) with only a small change in voltage. All other microscope and 3View operating parameters were kept constant. The silver paint around the sample can be seen at the top of the image (scale in all 10  $\mu$ m)

many more microscope parameters, which will again be important here (e.g. apertures, spot size and use of high current modes). It is difficult to give figures for which parameters should be used with particular sample types as this varies based on the processing protocol and the microscope used. With such variability it is necessary to do a lot of testing with a system to gain knowledge of what will work with a particular sample type. However, it is important to have a place to start and reviewing literature can provide this (see Table 5.1 for a summary of examples). The figures in this table also show the variability in parameters that can be used to achieve results.

As mentioned previously, it is important to use low voltages and as a standard this is in the range of 1–3 kV, although voltages as high as 4 kV have been used [57]. This lowers the interaction volume so it is less than the section thickness but also lessens the charging. Of course hand-in-hand with this is lower backscatter signal production from the sample and so deterioration of SNR. Small changes in voltage can make substantial changes in the image quality and the beam damage on the sample. Figure 5.5 shows that with only a change in voltage from 1.5 to 1.8 kV there is a considerable increase in signal but also an increase in the effects of charging (Fig. 5.5b, c).

Vacuum conditions can help and many groups use low vacuum mode in order to dissipate the charges. However, this also leads to a drop in image quality with a lower SNR: the poorer the vacuum, the poorer the image. To compensate, it may be necessary to use a higher voltage or a longer dwell time. While high vacuum has been used successfully [9, 58], a wide range in low vacuum conditions have also been found to be useful from 5 Pa [9] to 40–50 Pa [57, 59, 60]. An increase in dwell time can improve the SNR, but the compromise here is that this can lead to sample damage and will of course extend the acquisition time. The figures in the literature show an incredibly varied range from 2  $\mu$ s [9] to 15–20  $\mu$ s [61].

The section thickness dictates the resolution in the z direction and cutting as thin as 10 nm can be achieved on some biological samples [9]. However, this is not usually possible. If high resolution is not the object of the study then sections of 100 nm may be enough and allow acquisition of more data in z in a shorter time, for example by Starborg et al. and Scheuring et al. [57, 60].

When setting up a SBEM run it must also be taken into consideration how long to dedicate the instrument to this one data collection. It is a relatively time-consuming process. It can take 11 h to section and then capture 500 images at 4 k  $\times$  4 k pixel resolution with a 4  $\mu s$  dwell time, a full volume size of 46  $\times$  46  $\times$  25  $\mu m$ . This would give 500 images with a resolution of 11  $\times$  11  $\times$  50 nm. By many standards this is a small amount of data. A SBEM is a big investment of money and to tie it up for many hours or days for one data collection is possibly false economy. Montages make it possible to collect information over a large area but with no drop off in resolution. For example, Helmstaedter et al. [62] collected images at 16.5  $\times$  23 nm with a 4  $\times$  4 montage to acquire a total volume of 1,200,000 mm³, while Briggman et al. [63] using similar resolutions and a 1  $\times$  7 mosaic acquired 6,300,000 mm³ of data, both from the mouse retina.

Table 5.1 Co	mparison of SB	EM operating paran	Fable 5.1 Comparison of SBEM operating parameters for examples of a range of samples taken from the literature	range of samples	taken from the litera	ıture	
Voltage	Vacuum (Pa)	Vacuum (Pa)   Spot size (SS) or   Pixel dwell time	Pixel dwell time	Pixel size	Section thickness   Reference	Reference	Sample
(kV)		aperture (A)	(msec)	(mm)	(nm)		
5	09	SS 2.5	5	6-6.2	100	Hughes et al. [98]	Trypanosome
4	50		7–8	9–15	100	Scheuring et al. [57] Arabidopsis	Arabidopsis
3.8	40–53	SS 3.5	10	10	100	Starborg et al. [60]   Collagen fibrils	Collagen fibrils
2.8	High	SS 3-3.5	2	10	30	Mikula et al. [58]	Mouse brain
	vacuum						
2.5	26-40	SS 3	15–20	20	40	Anttonen et al. [61]   Cochlea	Cochlea
2	5	A 30	3	10	10	Russell et al. [9]	Vero cells
2	High	A 30	2	15	15	Russell et al. [9]	MD4 cells
	vacuum						
1.8	High	A 30	4	10	50	Unpublished results   Zebrafish	Zebrafish
	vacuum						embyros

It is a lot of trial and error in setting up a SBEM to acquire a dataset. For similar samples it is quite often possible to use the same settings thus simplifying the process. As a guide this is always a good place to start and then to adjust the system as necessary. Once it appears that the sectioning and imaging will be stable the run can be commenced. However, it good to keep checking the SBEM during the run to ensure that it is still working well. All of this testing on a sample can mean that a reasonable amount of material is removed before the run is started, so it's important to take this into consideration when setting up the sample.

## 5.4 Focused Ion Beam Scanning Electron Microscopy

Focused Ion Beam Scanning Electron Microscopy (FIB-SEM) was also previously known as Ion Abrasion Scanning Electron Microscopy (IA-SEM) [64]. It uses a focused ion beam (typically gallium, Ga<sup>+</sup>) to mill away slices from resin-embedded (or cryo-fixed) samples and then images the newly generated surface by the SEM in an iterative process in order to build a 3D dataset [6, 65]. The FIB operates similar to the SEM whereby a beam of charged particles is rastered across a specimen, and the resultant signals at each raster position are plotted to form an image. However, it uses ions instead of electrons to form the beam. The ions are massive relative to electrons, and they interact with the sample and cause sputtering. At low beam currents, the FIB gallium ions are used for imaging while high beam currents are used for site-specific sputtering [29].

The FIB coupled with an SEM, has proven to be a versatile and powerful tool in material and biological research alike. A basic FIB-SEM instrument consists of a LMIS, an ion column, a sample stage, an electron column and gas inlets. Commercial instruments have an SEM column that is usually oriented vertically and a FIB column that is oriented in the range of 45°–55° relative to the electron column. Both beams can access a sample in the FIB-SEM chamber simultaneously when they are at the coincidence point. 3D acquisitions are normally done with the sample tilted so that its surface is orthogonal to the FIB and the SEM is viewing the sample at an angle (Fig. 5.1). Section 5.4.3 describes an example of this method of FIB-SEM operation drawing predominately from the Zeiss systems. This arrangement is preferred as it is efficient and stable with only minor compromises to the resolution and signal [6].

The ion and electron beams complement each other in charge reduction, protective depositions and imaging information. The electron beam can be used to monitor the ion beam milling to target precisely the feature of interest, while allowing non-destructive imaging of the sample. FIB-SEM allows sample preparation, imaging and analysis to be accomplished in one tool. It is used to obtain isotropic datasets from biological samples so that the resolution in z is equal to the lateral pixel resolution in xy. Reports have been made of consistent slice thickness around 3 nm, with the Atlas 3D software [34]. More routine collection over FOVs

that are tens of microns are at 5 nm isotropic voxel size [10]. FIB-SEM has been applied to numerous samples and its use has extended into many different fields [7, 64, 66–73]. The diversity of applications is evidence of a successful system which has significantly contributed to answering fundamental cell biology questions [69]. It also permits direct analysis of cell-substrate interfaces which is not possible with traditional ultramicrotomy [74] as the ion beam can cut both hard and soft materials.

## 5.4.1 Sample Processing

Processing of biological material for FIB-SEM has been successful with many different protocols (Fig. 5.3d–f). One such example is a dissected piece of mouse brain that was processed according to Knott et al. [7]. Here the primary fixation was by perfusion (2.5% glutaraldehyde, 2% paraformaldehyde in phosphate buffer), followed by 1.5% potassium ferrocyanide with 1% osmium tetroxide, 1% osmium tetroxide and then 1% uranyl acetate in water [7]. This is in stark contrast to the extensive heavy metals necessary for SBEM. The following Sects. (5.4.1.1, 5.4.1.2, 5.4.1.3) outline processing protocols for cell monolayers by conventional bench, microwave and high-pressure freezing/freeze substitution.

#### **5.4.1.1** Conventional Bench Processing

Tissue culture cells are grown on a MatTek dish (MatTek Corp., USA,# P35G-2-14-CGRD) or P35G-2/1.5-14-CGRD) with coordinate pattern to facilitate finding back cells at the FIB-SEM and processed with the following protocol.

- 1. Primary fixation with 2x concentration of fixative in equal proportions to the cell media—final concentration 2.5% glutaraldehyde 0.05% malachite green oxalate in 0.1 M PHEM buffer left 1 min
- 2. Immediately followed by same 1x fixative 20 min on ice.
- 3. Buffer rinses,  $5 \times 3$  min
- 4. 1% osmium tetroxide and 0.8% potassium ferricyanide (in water on ice for 1 h)
- 5. Water rinses,  $5 \times 3$  min
- 6. Aqueous 1% tannic acid 20 min on ice
- 7. Water rinses,  $5 \times 3$  min
- 8. 0.5% uranyl acetate in water 1 h room temperature
- 9. Dehydration in a series of ethanol solutions on ice
- 10. Resin infiltration was done by adding 100% Durcupan resin to the dish and leaving the dishes overnight in the fumehood
- 11. The following day, the resin was reduced and a coverslip was placed over the top of the well
- 12. Dish was polymerized at 60 °C for 3 days

After polymerisation the coverslips and plastic are removed to reveal a flat resin disc containing the cell monolayer and imprinted co-ordinate pattern on one surface. The outer plastic walls of the dish are carefully removed by a hacksaw with the dish held in a clamp. The dish needs to be supported while sawing to end up with a complete, unbroken disc. After the outer plastic walls are removed, the resin disc and parts of the petri dish remain. This is then moved between liquid nitrogen and warm water several times until the glass starts to separate from the resin. At this point a thumb is placed over the central part where the resin disc is and pressure is applied. The disc is broken out with the other hand. The glass should separate from both sides so that all that remains is the resin disc that can be mounted on an SEM stub.

#### 5.4.1.2 Microwave Processing

Here again the MatTek dish is used to process cell monolayers, however in this method, all steps are carried out right through to polymerisation in a Pelco Biowave Microwave (Ted Pella, Inc.) [69].

- 1. Primary fixation with 2x concentration in equal proportions to the cell media—final concentration is 2.5% glutaraldehyde 0.05% malachite green oxalate in 0.1 M PHEM buffer left 1 min
- 2. Immediately followed by same 1x fixative in microwave for 7 alternating cycles of 2 min at 100 W with vacuum
- 3. Two quick buffer bench rinses
- 4. Two 40 s buffer rinses in the microwave at 250 W without vacuum
- 5. 1% osmium tetroxide and 0.8% potassium ferricyanide in water 7 alternating cycles of 2 min at 100 W with vacuum
- 6. Two quick water bench rinses
- 7. Two 40 s buffer rinses in the microwave at 250 W without vacuum
- 8. Aqueous 1% tannic acid 7 alternating cycles of 1 min at 150 W under vacuum
- 9. Two quick water bench rinses
- 10. Two 40 s buffer rinses in the microwave at 250 W without vacuum
- 11. 0.5% uranyl acetate in water 7 alternating cycles of 1 min at 150 W under vacuum
- 12. Dehydration in a series of ethanol solutions each for 40 s at 250 W without vacuum
- 13. Resin infiltration with Durcupan in a 2 step graded series for 3 min at 250 W under vacuum for each step
- 14. Repeat steps 11-13 from Sect. 5.4.1.1

#### 5.4.1.3 High Pressure Freezing and Freeze Substitution

Cell monolayers can also be observed in the FIB-SEM that are grown on sapphire discs, high pressure frozen (HPF) and freeze substituted (FS) as in Villinger et al. [66]. Below is a slight adaptation from this papers FS protocol.

- 1. Substituted in 1% osmium tetroxide 0.5% uranyl acetate 5% water in acetone
- 2. -90-20 °C with a 5 °C/hour slope
- 3. Kept at 20 °C for up to one hour
- 4.  $3 \times 40$  s acetone rinses at 250 W without vacuum in the microwave
- 5. Resin infiltration with Durcupan in a two step graded series for 3 minutes at 250 W under vacuum for each step
- 6. Processed sapphire discs are place into an eppendorf tube, see Villinger et al. [66]
- 7. Polymerized at 60 °C for 3 days.

## 5.4.2 Sample Setup and Mounting

Before embarking on FIB-SEM, check the quality of samples via routine TEM inspection to look for good preservation and sufficient sample contrast. When imaging monolayers prepared as described above (both chemically fixed and HPF), the cells are directly exposed to FIB-SEM imaging after removal of the coverslip (or sapphire disc). They are mounted cell side up onto an SEM stub (for illustration of chemically fixed cell sample see Fig. 5.6g–i) with carbon conductive cement (Plano) or 2 part conductive epoxy glue (CircuitWorks Conductive Epoxy CW2400). The mounting of HPF cell samples is described by Villinger et al. [66].

The region of interest needs to be positioned as close as possible to the upper edge of the block surface in relation to the FIB beam (surface *I* in Fig. 5.6e). The top of the cross section will have the best imaging surface since it is where the ion beam is most focused. The focus of the beam is decreased the deeper it penetrates, therefore reducing the milling effect and decreasing the chance that ions will be able to sputter molecules away from the block [7].

For tissues, it is necessary to trim the sample. Strategies for exposing specific targets within bulk specimens have been developed and described previously (see Karreman et al. [37] and Maco et al. [75]). If this is not required, they need to be trimmed to expose the sample surface at two faces at the microtome (Fig. 5.6a–f). One of these surfaces will become the imaging surface (surface 2 in Fig. 5.6e), the other will be perpendicular to the FIB and the deposition will be placed here over your ROI (surface 1 in Fig. 5.6e). Processed blocks are first trimmed with a razor blade and then with a 90° diamond knife to get smooth surfaces (Fig. 5.6a). This can then be removed from the block with a sharp razor blade using double sided or masking tape to stop the piece being lost (Fig. 5.6b). The very small block will remain attached to the double sided tape (Fig. 5.6c) and can be trimmed to give a flat surface to mount directly onto the SEM stub (Fig. 5.6d, white arrow head).

For all samples, once mounted on an SEM stub with a conductive cement or glue, each are carefully surrounded with silver paint (Colloidal Silver Liquid, Ted Pella, Inc.), so as to not cover any regions of interest but to ensure it is well grounded to the specimen stub (Fig. 5.6d, g). Then the samples are sputter coated with a thin layer of gold, or carbon. These applications help to dampen charge accumulation in the sample [34].

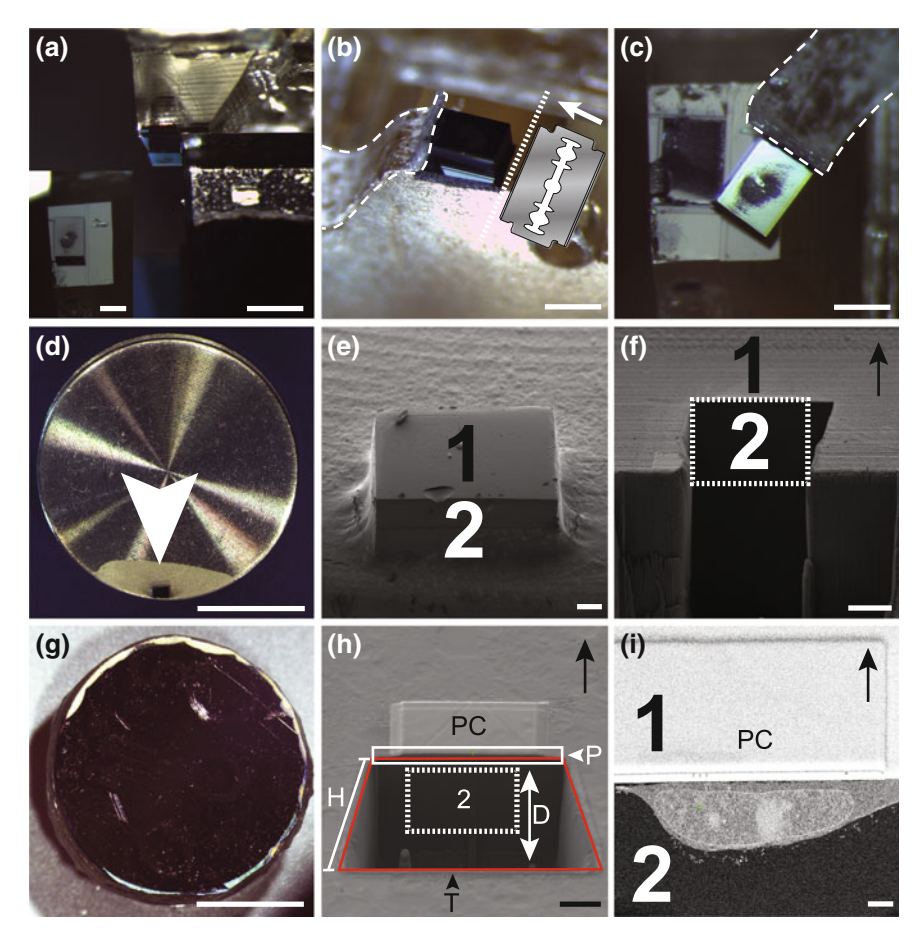


Fig. 5.6 Preparation and mounting of samples for FIB-SEM. a-f Processed and polymerised mouse brain sample that is trimmed and mounted for FIB-SEM, a In an ultramicrotome, processed blocks are trimmed with a 90° diamond knife so that the biological material is exposed for at least 2 smooth surfaces (scale 1 mm), inset—trimmed block from a top view (scale 500 μm), b Double-sided tape (dashed line) is then attached to keep the trimmed region secured when it is cut it off with a razor blade (cutting towards tape as indicated by white arrow) (scale 1 mm), c After it is cut off, the block is very small (it will remain attached to the double sided tape, dashed line) (scale 1 mm), d Finally the sample (white arrow head) is attached to the SEM stub and silver paint is added to all sides of the sample (scale 5 mm), e The finished block in the SEM with two smoothened surfaces (for all panels: I—block surface where protective coat is deposited, 2 imaging surface) (scale 100 µm). When the targeted ROI is found, the sample preparation within the FIB-SEM is performed. f A trench after an acquisition (scale 20 µm), g For comparison to a trimmed piece of tissue in (a-f) this is a full MatTek dish as prepared for FIB-SEM (scale 5 mm), **h** An example of a trench at the beginning of an acquisition to expose the imaging surface (2, dotted line) with the secondary electron detector at 5 kV; PC—protective coat, T—trench P polish, H—height, D—depth, (scale 10 μm), i A low resolution example of a back scattered detector image at 1.5 kV showing the exposed cell (scale 2.5 µm) (In f, h, and i-black arrow indicates milling direction)

## 5.4.3 FIB-SEM Operation

For efficient use of the FIB-SEM, there are some considerations aside from proper mounting that will give the best possible results. Make sure those of the gas injection systems (GIS) that will be used are turned on with enough time to warm up. This keeps them heated, stable and ready to use. Perform FIB alignments using a Faraday cup and silicon mat to ensure the best possible beam profile. Give the sample time to stabilise by loading them at least one day before starting the acquisition so that it can out gas and after the final polish wait for at least 1 h to allow the sample holder and sample to reach thermal equilibrium with the microscope stage and chamber [75]. The process of sample preparation should be documented very well since the sample will likely look very different in the SEM. If possible, build a map either with CLEM or by overlaying different imaging modalities to outline exactly where to image.

There are many papers explaining the intricacies of acquiring data with a FIB-SEM [6, 7, 21, 32, 64, 65, 72, 75–80]. In general, the approach is similar for all biological samples, although there are many things to optimise depending on your requirements and the system you are operating. The following description of microscope operation is based on the Zeiss systems with the aim to outline details that can be utilised from any FIB-SEM instrument.

When the sample is in the FIB-SEM, before the column valves are opened, outgas the GIS so that the lines are clear before use and to be sure there is no contamination in the reservoir. Turn on the SEM and FIB. For SEM, an electron high tension (EHT) of 5 kV is a good starting point for biological samples. HPF samples may need higher values to see the material, which is deeper below the resin surface. Position the specimen stub under the SEM beam and at low magnification find the sample. Set the eucentric height by centring a feature on the specimen surface when tilted to a few different angles between 0° and 54°. Set the working distance and optimise SEM imaging conditions with crisp focus and astigmatism. With a FIB imaging current of 50 pA make a good image. Even at low currents such as this, the FIB will damage the sample surface so do not image unnecessarily. Set the coincidence so that both the SEM and FIB beams are looking at the same point.

Once the microscope is aligned to the sample, locate the region of interest and begin the sample preparation. Regardless of the instrument in use, the first step is to deposit a protective coat by ionising the precursor gas with the FIB (Fig. 5.6h, *PC*). This coat will protect the surface of the sample and ensure even milling that is parallel to the direction of the ion beam [34, 75]. This is particularly important if the surface of the sample has some topography or when imaging surfaces of heterogeneous material composition [7]. Without it, there may be streaking or vertical stripes down the block face, known as curtaining artefact [81]. After inserting the GIS nozzle, note that it acts as an antenna and creates a small beam shift, check that the assigned position of the deposition still corresponds to the targeted ROI. The size of this deposition will depend on the ROI to be imaged. As a starting point,

a protective coat of  $30 \times 30 \,\mu m$  with a thickness of 1  $\mu m$  would take 15–20 min with 1 nA FIB current. The thickness of deposition with the same FIB current will be less over a larger area. If while performing the protection coat, the FIB is milling rather than depositing, lower the current and/or reduce the size of the area.

Create a rough trench to expose the cross-section imaging surface (Fig. 5.6f and h, T). The imaging surface will be perpendicular to the sample top surface as illustrated in Fig. 5.6f, h. Generally the trench is created with 15-30 nA milling currents using a trapezium shape (Fig. 5.6h, T). Draw a trapezium for the first rough mill so that there is some distance between the protective coat and trench (Fig. 5.6h, T). The depth of the trench (Fig. 5.6h, D) is dependent on the size of the imaging FOV. The rule of thumb is to create a trench that is three times deeper than the aimed imaging depth. For example, a cell that is 10 µm in depth, would need a milled trench that is 30 µm deep. The height of the trench (Fig. 5.6h, H), which together with the depth determines the slope of the trench, should not shadow the imaging surface. In this example, this would be roughly 40  $\mu$ m high (Fig. 5.6h, H). When working with complex tissue it may be possible to avoid the trench by trimming the sample at the microtome so that the imaging surface is already exposed (Fig. 5.6a-e) [37, 75, 79, 80]. The last stage of sample preparation is the final polish (Fig. 5.6h, P, outlined in white) of the imaging cross section. Typically the polished volume has the same width and depth as the rough trench, but only 1-3 µm in height and uses a smaller current (2-7 nA). There should be some overlap with the trench so that a wall is not created between the trench and newly polished surface.

Make the final adjustments to the SEM (lower keV, EsB detector, brightness and contrast, focus, astigmatism and wobbler) and check the coincidence point. SEM imaging parameters and FOV are chosen to optimize for the best SNR and resolution. Select the area for the acquisition, where the FIB will mill thin slices at the chosen thickness. For an isotropic resolution of 8 nm then each slice would be 8 nm in z over the 30  $\mu m$  ROI and the pixel size would also be 8 nm. FIB currents in the range of 600 pA-2 nA are used for this step. The sample is now prepared for the final mill and image acquisition.

Allow any thermal or mechanical drift to dissipate by leaving the room for around 2 h [75]. Further operations are managed remotely. Check the positioning of the milling area, and ensure there is a small overlap with the previous mill (polishing) so that a wall is not created. Start mill and image with a low dwell time (1–3  $\mu$ s) over the chosen FOV and when it is milling uniformly slowly increase the dwell time until the required image quality is achieved with consistent milling. This should occur provided that the sample is mounted securely and time has been given to stabilise. If it is not, then first adjust the image acquisition time. The best results are obtained when the imaging time is similar to milling time [34]. Data collection is limited by the slow speed of SEM image acquisition and to a lesser extent the ion beam milling [34]. Imaging a 10  $\mu$ m (in the milling direction indicated by *black arrow* in Fig. 5.6f, h, and i) portion of a cell with xy FOV of 20  $\times$  20  $\mu$ m, dwell time 10–12  $\mu$ s per pixel at 3D isotropic resolution of 8 nm takes approximately 24 h using Atlas 3D [34]. For FIB-SEM, the balance between the two beams and

the sample is a limiting factor. During the first few hours of the run, the stability needs to be monitored but with as minimal disturbance to the microscope as possible. If the dwell time necessary to achieve uniform milling is too low to achieve a good SNR, reduce the FOV or increase the pixel size. It may also be necessary to increase the FIB beam current or adjust the milling time by correcting the milling rates and/or increasing the milling depth. Image acquisition and milling times should be defined in relation to specimen drift [34]. There is always a balance between these factors since the series of SEM images is collected automatically. If the acquisition time is too long, the sample may either drift into the FIB beam thus increasing the slice thickness or drift away from the FIB beam so that the surface is burned by the imaging SEM beam and not milled away. As Maco et al. [75] instructs, "any interruption to the imaging procedure will cause irregular thicknesses to be removed by the milling beam". When parameters that produce quality data with uniform milling are found it is crucial to minimise disturbances, with only brief checks of focus and astigmatism [75].

#### 5.5 Discussion

Volume SEM utilising the SBEM and FIB-SEM enables better appreciation of the complexity of biological systems, which by nature are in three dimensions. They produce a series of 2D images that are combined to create a 3D volume at the nanoscale. This new generation of techniques has taken serial sectioning into a new realm. It is now possible to understand the relative relationship between different structures in a full volume rather than as individual two-dimensional images that are obtained from routine TEM of ultrathin sections. Despite the existence of ssTEM for more than 60 years, this method is limited by its laborious nature. With the availability of commercial instruments that allow for automation, SBEM and FIB-SEM have received wide acceptance in the scientific community and have now made volume EM a routine technique.

While SBEM and FIB-SEM lack the ultimate resolution of a TEM, they fill a major gap in resolution between light microscopy and the high end TEM. Many biological studies do not require the highest resolution in order to answer the scientific question being asked. A resolution of  $5\times5\times5$  nm for the FIB-SEM and  $10\times10\times10$  nm for the SBEM, is quite sufficient for many of studies. However, the FIB-SEM can produce 3D data at nanoscale resolutions sufficient to visualise all organelles and large macromolecular complexes [10] and it is well suited to smaller areas and achieving high resolutions. The SBEM on the other hand can be an incredibly valuable tool when trying to gain structural data about a biological system because it offers the opportunity to gain 3D data over a relatively large area. With the SBEM an analysis of studies published have shown that typical volumes can range from  $5000-500,000~\mu m^3$  and yet for the FIB-SEM it is only  $20,000-100,000~\mu m^3$  [18] highlighting the fact that the SBEM is a tool for capturing large volumes relative to the FIB-SEM.

There are many considerations to be made prior to embarking on EM in general, but even more so the volume SEM techniques. Both SBEM and FIB-SEM have their own limitations and rely heavily on the sample preparation. The sample must produce sufficient signal to allow imaging in backscatter mode with low accelerating voltages and withstand the effects of the electron beam to allow imaging and sectioning/milling. These affects are amplified in SBEM, where charging is an especially large hurdle. The interplay between resolution and imaging size is another consideration in FIB-SEM and SBEM where there is a need to balance imaging conditions with the mechanism to remove sections. Optimising the data quality requires strict assessment of what is to be achieved from the data. SBEM and FIB-SEM while overlapping in their applicability do have their own niches and can be and used as complimentary techniques. It is not uncommon for laboratories to have both systems and to direct to either depending on the needs of the projects.

CLEM has been utilised by both SBEM and FIB-SEM to facilitate targeting the ROI and optimise the acquired volume [9, 37, 75, 79]. Recently Brama et al. [82] have designed an integrated LM/SBEM in which a miniature fluorescence light microscope is built into the stage of the SBEM allowing sequential imaging of the same region using both modalities. At present the instrument they have built, the miniLM, is just a proof of principle as the resolution in the images needs to be improved.

There have been many applications of the FIB-SEM. Schertel et al. [83] were able to apply a typical mill and image approach in a cryo-FIB-SEM on natively frozen mouse optic nerve and *Bacillus subtilis* spores. Recently, cryo-FIB-SEM is also receiving attention for its ability to prepare thin lamella for cryo-electron tomography. This has been successful in not only cells [84, 85] but also nematodes [71]. The benefit here is that thicker sections can be prepared (500 nm) with less artefacts as compared to those achieved by cryo-electron microscopy of vitreous sections (CEMOVIS), 100 nm [65].

With tools that can capture data in an automated way, the bottleneck becomes handling this 3D volume once it is collected [86]. The datasets can be enormous making the handling and analysis a major undertaking. Even data movement from the instrument can be a difficult exercise. In saying this, the data collected is simply a 3D volume and there are many softwares available for its analysis. The volume is made up of a series of 2D images that first need to be aligned before analysis. This is a simple problem that can be taken care of by IMOD, plugins within FIJI (for [87], BigWarp http://fiji.sc/BigWarp; harnessing example BigDataViewer system [88], StackReg [89]), or in house custom made scripts. Segmentation is the best method for 3D visualisation of specific structures within the context of the volume and can be performed with software such as Amira and IMOD, which is a time consuming process. Programs such as Ilastik [90, 91] and MIB [92] house tools to help with the segmentation in an attempt to make it semi-automated.

The broad application of SBEM and FIB-SEM pushes forward the methods alongside technological advances. Moreover, there are continual improvements to instruments and detectors. An example of this is the multi-beam SEM with 61 [93],

91 beams [94], and most recently even 196 beams [95]. These have been developed to improve image acquisition times by several orders of magnitude and could revolutionise the speed at which SBEM work could be done. Eberle et al. [96] demonstrate the potential of the 61 beam to image the block-face of a resin embedded mouse brain sample.

While volume SEM, particularly SBEM and FIB-SEM, have now made it possible to achieve true 3D structural data of biological systems in an automated fashion there is still a need for considerable developments in these techniques. Advances in speed, resolution and sample preparation are important to make these techniques more routine. Speed and resolution will be achieved as a result of new instrumentation, both in microscopes and detectors. The production of a truly conductive and beam stable resin will revolutionise SBEM as it will relieve the many problems associated with cutting and imaging that are now inherent with this technique. Improvements to automated segmentation, which is the stumbling block of analysing these large data sets will lessen the workload and allow production of results in a more timely fashion. Volume SEM is technically challenging and so improvements to the entire workflow will assist in an even wider adoption by biological researchers.

Acknowledgements Thanks to the staff from both the EMBL Electron Microscopy Core Facility and the University of Queensland Centre for Microscopy and Microanalysis. The constant support from Yannick Schwab cannot be surpassed. We are also thankful to Anna Steyer and Rachel Mellwig for their helpful discussions and suggestions to the manuscript. A special mention to Matthia Karreman and José Miguel Serra Lleti. Without the work of Robyn Chapman we wouldn't have a SBEM system and it's her untiring efforts that have led to its development in our facilities. I thank her for all her determination to make this technique a success. Rob Parton has always been a source of encouragement for this work and has been willing to supply samples for us to work with when developing new ideas. Rachel Templin has been a wonderful backup helping us to process large numbers of samples as we have sought to develop new processing for this technology.

#### References

- 1. A. Birch-Andersen, Reconstruction of the nuclear sites of *Salmonella typhimurium* from electron micrographs of serial sections. J. Gen. Microbiol. **13**(2), 327–329 (1955)
- B.G. Bang, F.B. Bang, Graphic reconstruction of the third dimension from serial electron microphotographs. J. Ultrastruct. Res. 1, 138–146 (1957). doi:10.1016/S0022-5320(57) 80002-1
- 3. J.G. White, E. Southgate, J.N. Thomson, S. Brenner, The structure of the nervous system of the nematode Caenorhabditis elegans: the mind of a worm. Phil. Trans. R. Soc. London **314**, 1–341 (1986)
- K.L. Briggman, M. Helmstaedter, W. Denk, Wiring specificity in the direction-selectivity circuit of the retina. Nature 471, 183–188 (2012). doi:10.1038/nature09818
- W. Denk, H. Horstmann, Serial block-face scanning electron microscopy to reconstruct three-dimensional tissue nanostructure. PLoS 2(11), e329–10 (2004). doi:10.1371/journal. pbio.0020329

- K. Narayan, S. Subramaniam, Focused ion beams in biology. Nat. Publishing Group 12, 1021–1031 (2015). doi:10.1038/nmeth.3623
- G. Knott, H. Marchman, D. Wall, B. Lich, Serial section scanning electron microscopy of adult brain tissue using focused ion beam milling. J. Neurosci. 28, 2959–2964 (2008). doi:10. 1523/JNEUROSCI.3189-07.2008
- K.L. Briggman, W. Denk, Towards neural circuit reconstruction with volume electron microscopy techniques. Curr. Opin. Neurobiol. 16, 562–570 (2006). doi:10.1016/j.conb.2006. 08.010
- M.R. Russell, T.R. Lerner, J.J. Burden, D.O. Nkwe, A. Pelchen-Matthews, M.C. Domart, J. Durgan, A. Weston, M.L. Jones, C.J. Peddie, R. Carzaniga, O. Florey, M. Marsh, M.G. Gutierrez, L.M. Collinson, 3D correlative light and electron microscopy of cultured cells using serial blockface scanning electron microscopy. J. Cell Sci. JCS 130(1), 188433–14 (2016). doi:10.1242/jcs.188433
- 10. B. Titze, C. Genoud, Volume scanning electron microscopy for imaging biological ultrastructure. Biol. Cell 1–29 (2016). doi:10.1111/boc.201600024
- 11. K.L. Briggman, D.D. Bock, Volume electron microscopy for neuronal circuit reconstruction. Curr. Opin. Neurobiol. 22, 154–161 (2012). doi:10.1016/j.conb.2011.10.022
- 12. S.B. Leighton, SEM images of block faces, cut by a miniature microtome within the SEM-a technical note. Scan. Electron. Microsc. **2**, 73–76 (1980)
- M. de Goede, E. Johlin, B. Sciacca, F. Boughorbel, E.C. Garnett, 3D multi-energy deconvolution electron microscopy. Nanoscale 9, 684–689 (2017). doi:10.1039/ C6NR07991A
- 14. F. Boughorbel, E.G.T. Bosch, V. Kooijman, B. Lich, F, de Jong, Charged particale microscopy imaging method. 1–15 (2013)
- 15. F. Boughorbel, X. Zhuge, P. Potocek, B. Lich, SEM 3D reconstruction of stained bulk samples using landing energy variation and deconvolution. Microsc. Microanal. 1–2 (2012). doi:10.1017/S1431927612004655
- A. Kremer, S. Lippens, S. Bartunkova, B. Asselbergh, C. Blanpain, M. Fendrych, A. Goosens, M. Holt, S. Janssens, M. Krols, J.C. Larsimont, C. McGuire, M.K. Nowack, X. Saelens, A. Schertel, B. Schepens, M. Slezak, V. Timmerman, C. Theunis, R. van Brempt, Y. Visser, C.J. Guerin, Developing 3D SEM in a broad biological context. J. Microsc. 259, 80–96 (2015). doi:10.1111/jmi.12211
- L. Hughes, C. Hawes, S. Monteith, S. Vaughan, Serial block face scanning electron microscopy—the future of cell ultrastructure imaging. Protoplasma 251, 395–401 (2014). doi:10.1007/s00709-013-0580-1
- 18. C.J. Peddie, L.M. Collinson, Exploring the third dimension: Volume electron microscopy comes of age. Micron 61, 9 (2014). doi:10.1016/j.micron.2014.01.009
- 19. A. Zankel, J. Wagner, P. Poelt, Serial sectioning methods for 3D investigations in materials science. Micron 62, 66–78 (2014). doi:10.1016/j.micron.2014.03.002
- T. Hashimoto, G.E. Thompson, X. Zhou, P.J. Withers, 3D imaging by serial block face scanning electron microscopy for materials science using ultramicrotomy. Ultramicroscopy 163, 6–18 (2016). doi:10.1016/j.ultramic.2016.01.005
- C. Has, C. Sitaru, Molecular dermatology comes of age. Mol. Dermatolo. 961, 1–408 (2013). doi:10.1007/978-1-62703-227-8
- V.E. Krohn, Liquid Metal Droplets for Heavy Particle Propulsion. Prog. Astronaut. Rocketry 5, 73–80 (1961). doi:10.2514/5.9781600864797.0073.0080
- 23. M.W. Phaneuf, Applications of focused ion beam microscopy to materials science specimens. Micron 30, 277–288 (1999). doi:10.1016/s0968-4328(99)00012-8
- K. Yonehara, N. Baba, K. Kanaya, Application of ion-beam etching techniques to the fine structure of biological specimens as examined with a field emission SEM at low voltage. J. Electron. Micrsc. Tech. 12, 71–77 (1989)
- M. Cantoni, L. Holzer, Advances in 3D focused ion beam tomography. MRS Bulletin 39, 354–360 (2014) doi:10.1557/mrs.2014.54

- V.G.M. Sivel, J. Van den Brand, W.R. Wang, H. Mohdadi, F.D. Tichelaar, P.F.A. Alkemade, H.W. Zandbergen, Application of the dual-beam FIB/SEM to metals research. J. Microsc. 214, 237–245 (2004). doi:10.1111/j.0022-2720.2004.01329.x
- B. Titze, Techniques to prevent sample surface charging and reduce beam damage effects for SBEM imaging. Dissertation. Heidelberg University. 1–112 (2013)
- S. Serrano-Zabaleta, A. Larrea, H. Stegmann, C. Waltenberg, Electron backscatter diffraction analysis of non-conductive samples using in-situ charge compensation. Microsc. Anal 9, 23– 26 (2013)
- D. Drobne, M. Milani, A. Zrimec, V. Leser, M. Berden Zrimec, Electron and ion imaging of gland cells using the FIB/SEM system. J. Microsc. 219, 29–35 (2005). doi:10.1111/j.1365-2818.2005.01490.x
- 30. K. Roberston, R. Gauvin, J. Finch, Application of charge contrast imaging in mineral characterization. Miner. Eng. 18, 343–352 (2005)
- A.A. Wanner, C. Genoud, T. Masudi, L. Siksou, R.W. Friedrich, Dense EM-based reconstruction of the interglomerular projectome in the zebrafish olfactory bulb. Nat. Neurosci. 19, 816–825 (2016). doi:10.1038/nn.4290
- 32. G. Knott, S. Rosset, M. Cantoni, Focussed ion beam milling and scanning electron microscopy of brain tissue. JoVE **53**, 1–4 (2011). doi:10.3791/2588
- 33. K.M. Boergens, W. Denk, Controlling FIB-SBEM slice thickness by monitoring the transmitted ion beam. J. Microsc. 252, 258–262 (2013). doi:10.1111/jmi.12086
- K. Narayan, C.M. Danielson, K. Lagarec, B.C. Lowekamp, P. Coffman, A. Laquerre, M.W. Phaneuf, T.J. Hope, S. Subramaniam, Multi-resolution correlative focused ion beam scanning electron microscopy: Applications to cell biology. J. Struct. Biol. 185, 278–284 (2014). doi:10.1016/j.jsb.2013.11.008
- J.L. Schroeder, M. Bakalar, T.J. Pohida, R.S. Balaban, Rapid overlapping-volume acquisition and reconstruction (ROVAR): automated 3D tiling for high-resolution, large field-of-view optical microscopy. J. Microsc. 243, 103–110 (2011). doi:10.1111/j.1365-2818.2011.03490.x
- N. Ohno, M. Katoh, Y. Saitoh, S. Saitoh, S. Ohno, Three-dimensional volume imaging with electron microscopy toward connectome. Microscopy 64, 17–26 (2015). doi:10.1093/jmicro/ dfu112
- M.A. Karreman, L. Mercier, N.L. Schieber, G. Solecki, G. Allio, F. Winkler, B. Ruthensteiner, J.G. Goetz, Y. Schwab, Fast and precise targeting of single tumor cells in vivo by multimodal correlative microscopy. J. Cell Sci. 129, 444–456 (2016). doi:10.1242/jcs.181842
- 38. A.P. Merkle, L. Lechner, S. Andy, J. Gelb, M. Kienle, M.W. Phaneuf, D. Unrau, S.S. singh, N. Chawla, Automated correlative tomography using XRM and FIB-SEM to span length scales and modalities in 3D materials. Microsc. Anal. 28, 1–4 (2014)
- E.A. Bushong, D.D. Johnson, K.-Y. Kim, M. Terada, M. Hatori, S.T. Peltier, S. Panda, A. Merkle, M.H. Ellisman, X-ray microscopy as an approach to increasing accuracy and efficiency of serial block-face imaging for correlated light and electron microscopy of biological specimens. Microsc. Microanal. 21(1), 231–238 (2015). doi:10.1017/S1431927614013579
- K.L. McDonald, Out with the old and in with the new: rapid specimen preparation procedures for electron microscopy of sectioned biological material. Protoplasma 251, 429–448 (2013). doi:10.1007/s00709-013-0575-y
- T.J. Deerinck, E.A. Bushong, A. Thor, M.H. Ellisman, SBEM Protocol v7\_01\_10. In: https://www.ncmir.ucsd.edu/sbem-protocol/. Accessed 18 Feb 2017
- T.J. Deerinck, E.A. Bushong, V. Lev-Ram, X. Shu, R.Y. Tsien, M.H. Ellisman, Enhancing Serial Block-Face Scanning Electron Microscopy to Enable High Resolution 3-D Nanohistology of Cells and Tissues. Microsc. Microanal. 16, 1138–1139 (2010). doi:10. 1017/S1431927610055170
- J.C. Tapia, N. Kasthuri, K.J. Hayworth, R. Schalek, J.W. Lichtman, S.J. Smith, J. Buchanan, High-contrast en bloc staining of neuronal tissue for field emission scanning electron microscopy. Nat. Protoc. 7, 193–206 (2012). doi:10.1038/nprot.2011.439

- R.T. Giberson, R.L. Austin, J. Charlesworth, G. Adamson, G.A. Herrera, Microwave and digital imaging technology reduce turnaround times for diagnostic electron microscopy. Ultrastruct. Pathol. 27, 187–196 (2003). doi:10.1080/01913120309937
- N.L. Schieber, S.J. Nixon, R.I. Webb, V.M.J. Oorschot, R.G. Parton, Modern approaches for ultrastructural analysis of the zebrafish embryo. Methods Cell Biol. 96, 425–442 (2010). doi:10.1016/S0091-679X(10)96018-4
- A.A. Wanner, M.A. Kirschmann, C. Genoud, Challenges of microtome-based serial block-face scanning electron microscopy in neuroscience. J. Microsc. 259, 137–142 (2015). doi:10.1111/jmi.12244
- 47. H.B. Nguyen, T.Q. Thai, S. Saitoh, B. Wu, Y. Saitoh, S. Shimo, H. Fujitani, H. Otobe, N. Ohno, Conductive resins improve charging and resolution of acquired images in electron microscopic volume imaging. Sci. Rep. 6, 1–10 (2016). doi:10.1038/srep23721
- 48. D. Studer, H. Gnaegi, Minimal compression of ultrathin sections with use of an oscillating diamond knife. J. Microsc. 197, 94–100 (2000)
- W.C. De Bruijn, Glycogen, its chemistry and morphologic appearance in the electron microscope: I. A modified OsO4 fixative which selectively contrasts glycogen. J. Ultrastruct. Res. 42(1-2), 1-22 (1973)
- A.M. Seligman, H.L. Wasserkrug, J.S. Hanker, A new staining method (OTO) for enhancing contrast of lipid-containing membranes and droplets in osmium tetroxide-fixed tissue with osmiophilic thiocarbohydrazide (TCH). J. Cell Biol. 30(2), 1–9 (1966)
- J. Walton, Lead asparate, an en bloc contrast stain particularly useful for ultrastructural enzymology. J. Histochem. Cytochem. 27, 1337–1342 (1979). doi:10.1177/27.10.512319
- 52. Y. Hua, P. Laserstein, M. Helmstaedter, Large-volume en-bloc staining for electron microscopy-based connectomics. Nat. Commun. 6, 1–7 (2015). doi:10.1038/ncomms8923
- 53. S. Mikula, J. Binding, W. Denk, Staining and embedding the whole mouse brain for electron microscopy. Nat. Meth. 9, 1198–1201 (2012). doi:10.1038/nmeth.2213
- R. Webb, R. Webb, Quick freeze substitution processing of biological samples for serial block-face scanning electron microscopy. Microsc. Microanal. 21, 1115–1116 (2015). doi:10. 1017/S1431927615006364
- 55. K.L. McDonald, R.I. Webb, Freeze substitution in 3 hours or less. J. Microsc. **243**, 227–233 (2011). doi:10.1111/j.1365-2818.2011.03526.x
- 56. H. Kushida, Block staining with lead acetate. J. Electron Microsc. 15, 90-92 (1966)
- D. Scheuring, C. Löfke, F. Krüger, M. Kittelmann, A. Eisa, L. Hughes, R.S. Smith, C. Hawes, K. Schumacher, J. Kleine-Vehn, Actin-dependent vacuolar occupancy of the cell determines auxin-induced growth repression. Proc. Natl. Acad. Sci. U.S.A. 113, 452–457 (2016). doi:10. 1073/pnas.1517445113
- S. Mikula, W. Denk, High-resolution whole-brain staining for electron microscopic circuit reconstruction. Nat Meth 12, 541–546 (2015). doi:10.1038/nmeth.3361
- 59. K.M. Furuta, S.R. Yadav, S. Lehesranta, I. Belevich, S. Miyashima, J. Heo, A. Vatén, O. Lindgren, B. de Rybel, G. van Isterdael, P. Somervuo, R. Lichtenberger, R. Rocha, S. Thitamadee, S. Tähtiharju, P. Auvinen, T. Beeckman, E. Jokitalo, Y. Helariutta, Arabidopsis NAC45/86 direct sieve element morphogenesis culminating in enucleation. Science 345, 933–937 (2014). doi:10.1126/science.1255097
- T. Starborg, N.S. Kalson, Y. Lu, A. Mironov, T.F. Cootes, D.F. Holmes, K.E. Kadler, Using transmission electron microscopy and 3View to determine collagen fibril size and three-dimensional organization. Nat. Protoc. 8, 1433–1448 (2013). doi:10.1038/nprot.2013.086
- 61. T. Anttonen, I. Belevich, A. Kirjavainen, M. Laos, C. Brakebusch, E. Jokitalo, U. Pirvola, How to bury the dead: elimination of apoptotic hair cells from the hearing organ of the mouse. JARO 15, 975–992 (2014). doi:10.1007/s10162-014-0480-x
- 62. M. Helmstaedter, Cellular-resolution connectomics: challenges of dense neural circuit reconstruction. Nat Meth 10, 501–507 (2013). doi:10.1038/nmeth.2476
- 63. K.L. Briggman, M. Helmstaedter, W. Denk, Wiring specificity in the direction-selectivity circuit of the retina. Nature 471, 183–188 (2011). doi:10.1038/nature09818

- 64. J.A.W. Heymann, D. Shi, S. Kim, D. Bliss, J.L.S. Milne, S. Subramaniam, 3D Imaging of mammalian cells with ion-abrasion scanning electron microscopy. J. Struct. Biol. **166**, 1–7 (2009). doi:10.1016/j.jsb.2008.11.005
- 65. C. Kizilyaprak, J. Daraspe, B.M. Humbel, Focused ion beam scanning electron microscopy in biology. J. Microsc. **254**, 109–114 (2014). doi:10.1111/jmi.12127
- C. Villinger, H. Gregorius, C. Kranz, K. Höhn, C. Münzberg, G. von Wichert, B. Mizaikoff, G. Wanner, P. Walther, FIB/SEM tomography with TEM-like resolution for 3D imaging of high-pressure frozen cells. Histochem. Cell Biol. 138, 549–556 (2012). doi:10.1007/s00418-012-1020-6
- 67. D.A.M. de Winter, C.T.W.M. Schneijdenberg, M.N. Lebbink, B. Lich, A.J. Verkleij, M.R. Drury, B.M. Humbel, Tomography of insulating biological and geological materials using focused ion beam (FIB) sectioning and low-kV BSE imaging. J. Microsc. 233, 372–383 (2009). doi:10.1111/j.1365-2818.2009.03139.x
- A. Rigort, F.J.B. Bäuerlein, E. Villa, M. Eibauer, T. Laugks, W. Baumeister, J.M. Plitzko, Focused ion beam micromachining of eukaryotic cells for cryoelectron tomography. Proc. Natl. Acad. Sci. U.S.A. 109, 4449–4454 (2012). doi:10.1073/pnas.1201333109
- L. Chatel-Chaix, M. Cortese, I. Romero-Brey, S. Bender, C.J. Neufeldt, W. Fischl,
   P. Scaturro, N. Schieber, Y. Schwab, B. Fischer, A. Ruggieri, Dengue virus perturbs mitochondrial morphodynamics to dampen innate immune responses. Cell Host Microbe 20 (3), 1–16 (2016). doi:10.1016/j.chom.2016.07.008
- G.E. Murphy, K. Narayan, B.C. Lowekamp, L.M. Hartnell, J.A.W. Heymann, J. Fu, S. Subramaniam, Correlative 3D imaging of whole mammalian cells with light and electron microscopy. J. Struct. Biol. 176, 268–278 (2011). doi:10.1016/j.jsb.2011.08.013
- J. Harapin, M. Börmel, K.T. Sapra, D. Brunner, A. Kaech, O. Medalia, Structural analysis of multicellular organisms with cryo-electron tomography. Nat. Publishing Group 12, 634–636 (2015). doi:10.1038/nmeth.3401
- L.H.P. Hekking, M.N. Lebbink, D.A.M. de Winter, C.T.W.M. Schneijdenberg, C.M. Brand, B.M. Humbel, A.J. Verkleij, J.A. Post, Focused ion beam-scanning electron microscope: exploring large volumes of atherosclerotic tissue. J. Microsc. 235, 336–347 (2009). doi:10. 1111/j.1365-2818.2009.03274.x
- S. Hirashima, K. Ohta, T. Kanazawa, S. Okayama, A. Togo, N. Uchimura, J. Kusukawa, K.-I. Nakamura, Three-dimensional ultrastructural analysis of cells in the periodontal ligament using focused ion beam/scanning electron microscope tomography. Sci Rep 6, 39435 (2016). doi:10.1038/srep39435
- F. Greve, S. Frerker, A.G. Bittermann, C. Burkhardt, A. Hierlemann, H. Hall, Molecular design and characterization of the neuron-microelectrode array interface. Biomaterials 28, 5246–5258 (2007)
- B. Maco, M. Cantoni, A. Holtmaat, A. Kreshuk, F.A. Hamprecht, G.W. Knott, Semiautomated correlative 3D electron microscopy of in vivo-imaged axons and dendrites. Nat. Protoc. 9, 1354–1366 (2014). doi:10.1038/nprot.2014.101
- 76. D. Drobne, 3D imaging of cells and tissues by focused ion beam/scanning electron microscopy (FIB/SEM), *Nanoimaging* (Humana Press, Totowa, NJ, 2013), pp. 275–292
- A.J. Bushby, K.M.Y. Png, R.D. Young, C. Pinali, C. Knupp, A.J. Quantock, Imaging three-dimensional tissue architectures by focused ion beam scanning electron microscopy. Nat. Protoc. 6, 845–858 (2011). doi:10.1038/nprot.2011.332
- 78. L.A. Giannuzzi, F.A. Stevie, Introduction to Focused Ion Beams (Springer, Boston, 2005)
- B. Maco, A. Holtmaat, M. Cantoni, A. Kreshuk, C.N. Straehle, F.A. Hamprecht, G.W. Knott, Correlative in Vivo 2 Photon and focused Ion Beam scanning electron microscopy of cortical Neurons. PLoS ONE 8, e57405 (2013). doi:10.1371/journal.pone.0057405.g003
- B. Maco, A. Holtmaat, M. Cantoni, A. Kreshuk, C.N. Straehle, F.A. Hamprecht, G.W. Knott, Correlative in vivo 2 photon and focused ion beam scanning electron microscopy of cortical neurons. Methods Cell Biol. 124, 339–361 (2013). doi:10.1016/B978-0-12-801075-4.00016-1

- 81. J.A.W. Heymann, M. Hayles, I. Gestmann, L.A. Giannuzzi, B. Lich, S. Subramaniam, Site-specific 3D imaging of cells and tissues with a dual beam microscope. J. Struct. Biol. **155**, 63–73 (2006). doi:10.1016/j.jsb.2006.03.006
- E. Brama, C.J. Peddie, G. Wilkes, Y. Gu, L.M. Collinson, M.L. Jones, ultraLM and miniLM: Locator tools for smart tracking of fluorescent cells in correlative light and electron microscopy. Wellcome Open Res. 1, 19–26 (2016). doi:10.12688/wellcomeopenres.10299.1
- A. Schertel, N. Snaidero, H.-M. Han, T. Ruhwedel, M. Laue, M. Grabenbauer, W. Möbius, Cryo FIB-SEM: Volume imaging of cellular ultrastructure in native frozen specimens. J. Struct. Biol. 184, 355–360 (2013). doi:10.1016/j.jsb.2013.09.024
- 84. J. Arnold, J. Mahamid, V. Lucic, A. de Marco, J.J. Fernandez, T. Laugks, T. Mayer, A.A. Hyman, W. Baumeister, J.M. Plitzko, Site-specific cryo-focused ion beam sample preparation guided by 3D correlative microscopy. Biophysj 110(4), 1–10 (2016). doi:10.1016/j.bpj.2015. 10.053
- J. Mahamid, S. Pfeffer, M. Schaffer, E. Villa, R. Danev, L.K. Cuellar, F. Förster, A.A. Hyman, J.M. Plitzko, W. Baumeister, Visualizing the molecular sociology at the HeLa cell nuclear periphery. Science 351, 969–972 (2016). doi:10.1126/science.aad8857
- S. Borrett, L. Hughes, Reporting methods for processing and analysis of data from serial block face scanning electron microscopy. J. Microsc. 263, 3–9 (2016). doi:10.1111/jmi.12377
- A. Cardona, S. Saalfeld, J. Schindelin, I. Arganda-Carreras, S. Preibisch, M. Longair,
   P. Tomancak, V. Hartenstein, R.J. Douglas, TrakEM2 software for neural circuit reconstruction.
   PLoS ONE 7, e38011 (2012). doi:10.1371/journal.pone.0038011
- T. Pietzsch, S. Saalfeld, S. Preibisch, P. Tomancak, BigDataViewer: visualization and processing for large image data sets. Nat. Publishing Group 12, 481–483 (2015). doi:10.1038/ nmeth.3392
- 89. P. Thévenaz, U.E. Ruttimann, M. Unser, A pyramid approach to subpixel registration based on intensity. IEEE Trans. Image Process. 7, 27–41 (1998). doi:10.1109/83.650848
- A. Kreshuk, C.N. Straehle, C. Sommer, U. Koethe, M. Cantoni, G. Knott, F.A. Hamprecht, Automated detection and segmentation of synaptic contacts in nearly isotropic serial electron microscopy images. PLoS ONE 6, e24899 (2011). doi:10.1371/journal.pone.0024899
- A. Kreshuk, R. Walecki, U. Koethe, M. Gierthmuehlen, D. Plachta, C. Genoud, K. Haastert-talini, F.A. Hamprecht, Automated tracing of myelinated axons and detection of the nodes of Ranvier in serial images of peripheral nerves. J. Microsc. 259, 143–154 (2015). doi:10.1111/jmi.12266
- 92. I. Belevich, M. Joensuu, D. Kumar, H. Vihinen, E. Jokitalo, Microscopy image browser: a platform for segmentation and analysis of multidimensional datasets. PLoS Biol. 14, e1002340 (2016). doi:10.1371/journal.pbio.1002340
- 93. A.L. Keller, D. Zeidler, T. Kemen, High-throughput data acquisition with a multi-beam SEM. Scan. Microscopies **9236** (2014)
- 94. T. Kemen, M. Malloy, B. Thiel, S. Mikula, W. Denk, G. Dellemann, D. Zeidler, Further advancing the throughput of a multi-beam SEM. Metrology, Inspection, and Process Control for Microlithography XXIX. (2015). doi:10.1117/12.2188560
- P. Kruit, Y. Ren, Multi-Beam Scanning Electron Microscope Design. Microsc. Microanal. 22, 574–575 (2016). doi:10.1017/S143192761600372X
- A.L. Eberle, S. Mikula, R. Schlek, J. Lichtman, M.L. Knothe Tate, D. Zeidler, High-resolution, high-throughput imaging with a multibeam scanning electron microscope. J. Microsc. 259, 114–120 (2015). doi:10.1111/jmi.12224
- 97. D. Drouin, A.R. Couture, D. Joly, X. Tastet, V. Aimez, R. Gauvin, CASINO V2.42: a fast and easy-to-use modeling tool for scanning electron microscopy and microanalysis users. Scanning 29, 92–101 (2007). doi:10.1002/sca.20000
- L. Hughes, K. Towers, T. Starborg, K. Gull, S. Vaughan, A cell-body groove housing the new flagellum tip suggests an adaption of cellular morphogenesis for parasitism in the bloodstream form of Trypanosoma brucei. J. Cell Sci. 126, 5748–5757 (2013). doi:10.1242/jcs.139139

# Chapter 6 Conjugate Immunofluorescence—SEM Array Tomography for Studying Mammalian Synapses and Axons

Kristina D. Micheva and Kristen D. Phend

**Abstract** Conjugate immunofluorescence—SEM array tomography enables the imaging of both the molecular content and the ultrastructure of tissues. The method is based on physical ultrathin serial sectioning, immunostaining and acquiring fluorescence and electron microscopy images of resin embedded tissues, followed by computational volume reconstruction and analysis. Conjugate immunofluorescence—SEM array tomography has been used for the study of brain tissue, and in particular for the characterization of diverse synapses and axons.

# 6.1 Introduction/Background

Electron microscopy is a powerful tool to study the ultrastructure of biological tissues; however, it can provide only limited molecular information. Immunoelectron microscopy uses antibody labelling to identify the presence of different molecular species, and secondary antibodies conjugated to colloidal gold of different sizes [1] are most commonly applied to differentiate between two or, rarely, three primary antibodies [2]. More recently, other probes of various sizes and shapes, such as colloidal metal particles with different shapes [3], quantum dots [4] and nanodiamonds [5], have been explored for increased multiplexing capabilities.

Multiplexing of antibodies is achieved much more easily with immunofluorescence, due to the availability of detector fluorophores of various wavelengths. One strategy in particular, the use of multiple rounds of immunofluorescent labelling, opens the possibility of high-level multiplexing. For example, multi-epitope-ligand

K. D. Micheva (⊠)

Department of Molecular and Cellular Physiology, Stanford University School of Medicine, Stanford, CA 94305, USA e-mail: kmicheva@stanford.edu

K. D. Phend

Department of Cell Biology and Physiology, University of North Carolina, Chapel Hill, NC 27599, USA

<sup>©</sup> Springer International Publishing AG 2018
E. Hanssen (ed.), *Cellular Imaging*, Biological and Medical Physics, Biomedical Engineering, https://doi.org/10.1007/978-3-319-68997-5\_6

cartography, or toponomics, enables the imaging of a hundred of antibodies with subcellular resolution [6–8]. Array tomography [9, 10] allows the imaging of dozens of different antibodies with even higher resolution ( $100 \times 100 \times 70$  nm using deconvolution, [11]). Super-resolution fluorescence imaging that can bring the resolution down to about 10–20 nm laterally is also becoming compatible with multiplexing (e.g. [12–14]).

Ultimately, the combination of light-level immunolabeling and electron microscopy can provide both the multiplexing capabilities needed to study the molecular architecture of biological tissues and the nanometer resolution to explore their ultrastructure. Efforts to achieve this have been hampered for many years by conflicting requirements of tissue preparation; procedures that preserve antigenicity are generally detrimental to ultrastructure, and vice versa. Furthermore, the computing power and tools required to register light-level and electron microscopic images were not available. Recently, several powerful approaches, such as automated TEM [15, 16], conjugate array tomography [17–19], and serial multiplex immunogold labeling [20], have succeeded in combining large-scale light level immunolabeling with electron microscopy.

# 6.2 Approaches to Large-Scale Molecular and Ultrastructural Imaging

An effective approach to obtain molecular information from ultrastructurally resolved tissue is automated TEM (ATEM) with computational molecular phenotyping [15, 16]. Designed and implemented by the Marc lab at the University of Utah, this approach uses serial ultrathin sections (50-70 nm) of plastic-embedded chemically fixed tissue to study the organization of the mammalian retina. A small subset of individual sections are taken from the series at regular intervals, processed for immunohistochemistry, and imaged at the light level. All the other sections are viewed by automated TEM with nanometer resolution. More than 1000 image tiles are obtained from each section to cover a large area for neuronal circuit reconstruction. The immunostained sections are then registered with the EM sections, allowing the molecular composition of cells to be established; this procedure is termed computational molecular phenotyping. Neuronal processes are traced and synapses ultrastructurally identified on the TEM sections. This method takes advantage of the fact that immunoreactivity for small molecules, such as GABA and glutamate, can be well preserved in tissue prepared with conventional methods for electron microscopy [21, 22]. Up to 11 different antibody labels have been used for computational molecular phenotyping, including the excitation marker AGB (1-amino-4-guanidobutane), a channel-permeant organic cation, used to probe prior in vivo activity. Typical ATEM image datasets range from several terabytes to more than a petabyte, and require exquisite new image processing, assembly, navigation and analysis algorithms, as well as new interpretive frameworks. This method has

allowed the imaging and full reconstruction of a retinal circular segment with a diameter of 0.22 mm and approximate thickness of 0.03 mm [16]. Ongoing exploration of the acquired retinal volume uncovers much greater complexity of the retinal synaptic network than previously recognized, and has demonstrated the existence of a number of new connection motifs and functions, as well as new contact architectures that challenge the classical ultrastructural definition of a chemical synapse [23].

A similar method based on conventional electron microscopy tissue preparation is serial multiplex immunogold labeling [20]. In this case, the tissue is also prepared using standard electron microscopy methods, embedded in plastic, and sectioned into long series of ultrathin sections. Small subsets of sections are labelled with antibodies to different neuropeptides using the immunogold technique where the secondary antibodies are conjugated to gold particles that can be conveniently observed under the electron microscope. As the case of small molecules like GABA and other neurotransmitters, the antigenicity of small neuropeptides withstands the tissue processing involved in EM sample preparation [24, 25]. The use of electron microscopy to image the immunolabel avoids potential problems of registration of light level and EM datasets. This approach was applied to serial sections spanning the entire body of the larva of the marine annelid *Platynereis dumerilii*. Eleven antibodies against neuropeptides were used and several molecularly identified neurons were fully reconstructed and their synaptic partners were identified, revealing a candidate chemotactic circuit in the larval head.

Unfortunately, the majority of antibodies cannot be used on conventionally prepared EM tissue. Many of the chemicals and treatments traditionally used to preserve good ultrastructure are detrimental to most antigens. The most notorious culprit is osmium tetroxide, which is used to protect the tissue from extraction during dehydration, as it binds to lipids and proteins. However, osmium also disrupts the tertiary structure of most proteins [26] preventing the binding of antibodies. Epoxy resins, which are typically the resin of choice for EM are also associated with decreased antigenicity and decreased access of antibodies, as they are known to covalently bind to the tissue components [27, 28]. Acrylic resins are preferred for immunolabeling studies [29], but they generally have lower stability in the electron beam and, especially, when osmium is omitted, can result in poor ultrastructural preservation. The cumulative effects of the treatments at different steps of tissue processing often result in an inverse relationship between the preservation of ultrastructure and antigenicity. As seen in Fig. 6.1, postfixation with osmium followed by Epon embedding provides the best ultrastructure and the worst immunoreactivity for the synaptic proteins synapsin and VGluT1, while omitting osmium and embedding in LRWhite gives the opposite results. Introducing a low concentration of osmium to the LRWhite embedding protocol only partially improves tissue integrity while reducing immunoreactivity.

One solution to this problem is offered by low-temperature methods for tissue processing. Sample dehydration, a necessary step preceding resin embedding, is much less damaging to tissue integrity at very low temperatures (<-70 °C), where lipid extraction by organic solvents is minimized [30]. Under these conditions, osmium is no

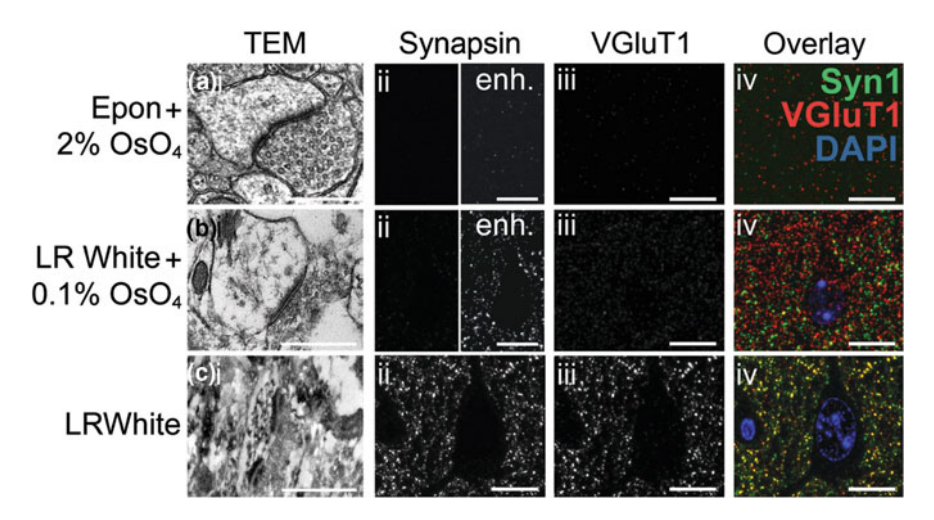


**Fig. 6.1** Tradeoff between ultrastructural integrity and immunoreactivity. Three different tissue preparation methods were compared using two different imaging modalities. **a** Formaldehyde/glutaraldehyde fixation, poststained with 2% OsO<sub>4</sub> and embedded in Epon resin. **b** Formaldehyde fixation, poststained with 0.1% OsO<sub>4</sub> and embedded in LR White. **c** Formaldehyde fixation, embedded in LR White without osmium. Images from layer 5 of mouse neocortex were acquired with TEM (*i*), or epifluorescence after immunostaining for synapsin (*ii*) and VGluT1 (*iii*). All IF was performed under identical conditions, constant exposure, and color map, except for the panels marked enhanced (enh.; *aii*, *bii*) where the maximally bright value was halved, and color images in *iv*, where channels were renormalized to 99.5% percentile. IF scale bars, 10 μm; EM scale bars, 500 nm. Modified from [18]

longer needed to stabilize the lipids, and can be omitted, thus greatly improving antigenicity without a parallel decline in ultrastructural preservation. To fully benefit from the low temperature dehydration, samples need also be infiltrated with resin and polymerized at low temperature, which is not possible with the conventional epoxy resins. Instead, other resins, such as the acrylic Lowicryl resins, can be used as they remain liquid and can polymerize at low temperatures. These so-called "freeze-substitution" methods have allowed the immmunodetection of a variety of antibodies with nanometer precision, using immunogold EM (for example, [31–36]). Because of the well preserved antigenicity and ultrastructure, freeze-substitution followed by embedding in Lowicryl produces tissue samples that are suitable not only for electron microscopy, but also for immunofluorescence, as recently achieved with the method of array tomography [18]. Conjugate array tomography, as this specific application is named, uses Lowicryl HM20 to ensure good preservation of tissue ultrastructure and antigenicity and thus enable imaging of both the molecular content and the ultrastructure of tissues (Fig. 6.2). This method is based on physical ultrathin serial sectioning, immunostaining and acquiring fluorescence and electron microscopy images of resin embedded tissues, followed by computational volume reconstruction and analysis.

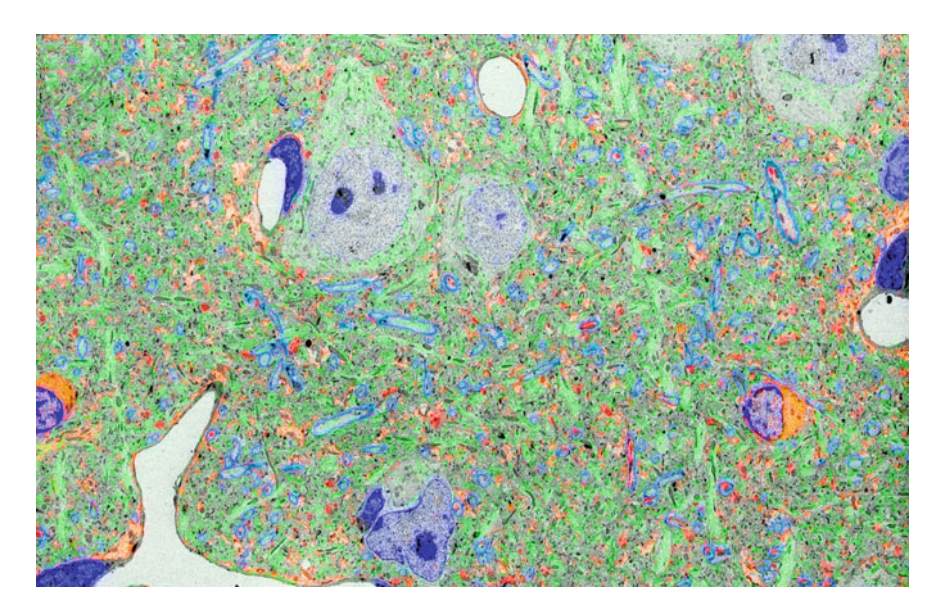


**Fig. 6.2** Conjugate immunofluorescence—SEM array tomography of mouse neocortex. The light and EM modes of imaging are computationally registered to obtain a 'multicolor' SEM image that contains ultrastructural and molecular information. MBP, light blue; α-tubulin, green; GABA, red; glutamine synthetase, orange, DAPI, dark blue. From [58]

# 6.3 Array Tomography: A Different Kind of Tomography

'Tomography' comes from the Greek word tomos, meaning a cut, slice or section, and refers to methods used for reconstructing the three-dimensional structure of an object from two-dimensional series of images. With electron tomography the slicing is achieved by tilting the stage and imaging the sample at different angles; with array tomography, the slicing is physical and involves actual cutting of ultrathin sections (Fig. 6.3). Both electron tomography and array tomography require sophisticated computational approaches for volume reconstruction.

The ultrathin physical sectioning of the sample used in AT offers a number of advantages. Of primary importance are the high resolution and depth independence of the immunofluorescence imaging (Fig. 6.4). The largest improvement in resolution comes from the physical section thickness (usually 70 nm), which is about 10 times thinner than the effective z-axis resolution of a confocal microscope [37]. The lateral resolution is also improved ( $\sim$ 200 nm) due to reduced light scatter in ultrathin sections, as well as the fact that imaging occurs at the design conditions for the high numerical-aperture objective used (i.e. the immediate contact between specimen and coverslip). Lateral resolution can be further improved to about 100 nm either by deconvolution [11], or by the use of structured illumination microscopy (SIM; [38, 39]; Fig. 6.4b). The high resolution of fluorescence imaging facilitates registration of the light and electron microscopic images and ensures the

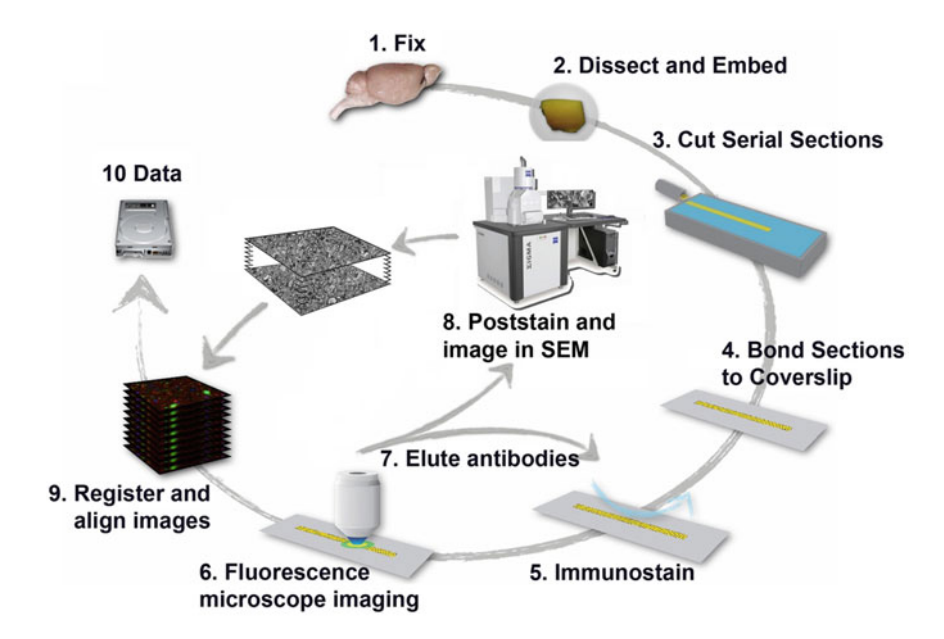


**Fig. 6.3** Array tomography method. Schematics of AT workflow. AT immunofluorescence achieves superlative depth-independent resolution and sensitivity based on planar arraying, staining and imaging of ultrathin serial sections. Iterative cycles of immunostaining, imaging and antibody elution enable acquisition of dozens of immunofluorescence channels, which can be computationally registered with the subsequently acquired SEM images

correct allocation of immunofluorescence to ultrastructural tissue compartments. Ultrathin sectioning also ensures that all sections from a tissue volume are stained and imaged under identical conditions, thus eliminating possible depth-related bias in working with thicker samples.

Another advantage of physical sectioning is that the use of such ultrathin sections facilitates the elution of antibodies off the section array, which enables multiple applications of different antibodies to the same serial sections. This greatly increases the number of proteins that can be visualized in one sample (more than 30 different antibodies per sample have been imaged by us) and therefore substantially expands the scope of research questions that can be addressed.

In array tomography, the serial sections are mounted on a hard substrate (coverslips) as opposed to grids. This allows the relatively easy collection of long uninterrupted series (hundreds to thousands of sections), because coverslips provide a much larger area and also a better support for the sections. Number 1.5 coverslips (0.17 mm thickness) provide the ideal substrate for high-performance microscope objectives and are preferred for section collection for array tomography. And while the section arrays on coverslips cannot be imaged in a TEM, recent technological advances enable excellent resolution with a field emission scanning electron

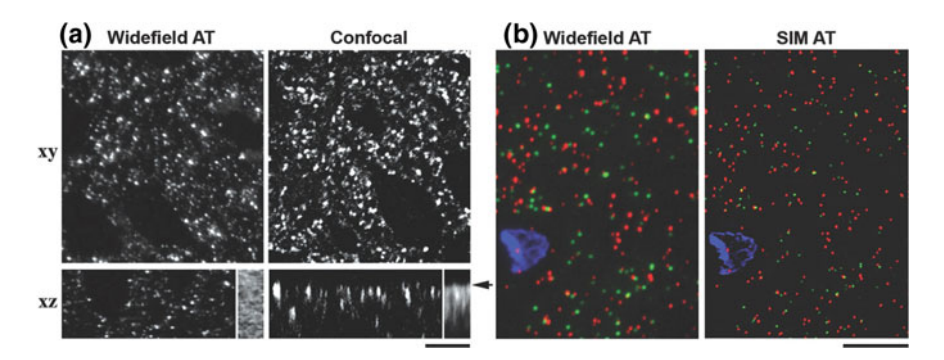


**Fig. 6.4** Improved resolution and depth independence of AT. **a** Synapsin I immunostaining for presynaptic boutons in mouse cerebral cortex, as imaged with AT (left, 40 serial sections, each 200 nm thick) and confocal whole mount immunofluorescence (right, 40 optical sections acquired at 200 nm intervals). Individual xy sections (top) and xz sections (bottom) resampled from the stacks of 40 sections. Inserts in the xz sections represent the sum of z sections from 20 μm of tissue and illustrate the depth-distribution of immunofluorescence. Scale bar, 5 μm. From [9]. **b** Comparison of VGluT1 (red), PSD95 (green) and DAPI staining of an ultrathin (70 nm) section from mouse cortex imaged with wide-field fluorescence (left) and structured illumination microscopes (right). Scale bar, 5 μm

microscope (FESEM). Furthermore, several commercial solutions to automate correlated light and SEM imaging now exist [40, 41].

The imaging of the same serial sections mounted on coverslips with both immunofluorescence and in the scanning electron microscope, is termed conjugate IF-SEM array tomography. This is a special case of correlative microscopy where exactly the same physical sample (array of serial ultrathin sections) is imaged in two different modalities, light and electron microscopy, and the resulting images are registered with voxel-to-voxel accuracy.

# 6.4 Array Tomography Sample Preparation: Workflow and General Considerations

Sample preparation for conjugate array tomography begins with chemical fixation that for many samples is best achieved through transcardial perfusion. When this is not possible, for example, for human surgical tissue or brain slices from electrophysiological experiments, immersion fixation is used. Good ultrastructural preservation is achieved using a combination of formaldehyde and glutaraldehyde. The use of glutaraldehyde offers the additional advantage of increasing the retention of small molecules, such as GABA and glutamate [42, 43]. And while glutaraldehyde significantly increases tissue autofluorescence and nonspecific antibody binding, this effect is much less pronounced in the case of the ultrathin sections used for AT, and can be further alleviated by preincubations with sodium

borohydride [44, 45]. In our experience, the majority of antibodies used in AT do not appear to be sensitive to glutaraldehyde, however, if such an effect is observed, glutaraldehyde concentration used for fixation can be decreased down to 0.1%.

The fixed tissue is then cut into  $100-200~\mu m$  slices using a Vibratome, and the region of interest is dissected out. To prevent the formation of ice crystals during low temperature processing, the tissue is cryoprotected with increasing concentrations of glycerol. It is then quick-frozen in a dry ice/ethanol bath and dehydration is performed through freeze-substitution using methanol at -90 °C. Under these milder conditions of dehydration, the stabilization of lipids and other tissue elements can be achieved with uranyl acetate, which is added to the methanol during the dehydration steps. Unlike osmium, uranyl acetate does not have major impact on the tertiary structure of proteins [46–48]. After the dehydration step, the sample is slowly warmed up to -45 °C and infiltrated with the resin Lowicryl HM20. Finally, the resin is polymerized using UV light at 0 °C. The polymerized block with tissue can be stored for many years before use.

To prepare serial sections, standard electron microscopy procedures are followed. The block is trimmed to a trapezoid block face shape and then sectioned with an ultramicrotome using a diamond knife. Typically 70 nm sections are collected, but depending on the needs, thickness can vary between 50 and 200 nm. Thinner sections provide the advantage of better resolution at the EM level, but have the drawbacks of lower contrast and increased effort for large volume reconstructions. Glue is applied to the sides of the block pyramid to ensure that the sections stick to each other and form a ribbon, which is then picked on a coverslip. Coverslips are coated with carbon, which greatly increases the adherence of the sections and also provides a conductive substrate required for the EM imaging. Conventional indirect immunostaining is used, usually with three different primary antibodies (Table 6.1) from different host species applied simultaneously, followed by the corresponding secondary antibodies conjugated to fluorophores with distinct excitation/emission spectra. While primary antibodies directly conjugated to fluorophores can also be used, the use of secondary antibodies provides considerable signal amplification, resulting in a much stronger and more robust immunofluorescence label. The coverslips are mounted on glass slides or custom-made chambers using non-hardening mounting medium that also contains the nuclear stain DAPI.

The immunolabeled samples are imaged using an automated epifluorescence microscope. No additional advantage is offered by using a confocal microscope, because there is no out of focus signal coming from the ultrathin sections used for AT. The final resolution of the immunofluorescent images is at the theoretical limit (~200 nm lateral resolution; z-resolution determined by section thickness) and can be further improved to  $\sim 100$  nm lateral resolution using deconvolution [11]. Alternatively, to achieve 100 nm lateral resolution, the samples can be imaged with structured illumination microscopy [38, 39]. The high resolution of immunofluorescent images facilitates the registration of the light and electron microscope images. Image acquisition begins with mapping of the ribbon of serial sections. This is done at a low magnification, typically with a  $10 \times$  objective, and a

 Table 6.1 Antibodies for conjugate IF-SEM array tomography

Antigen	Host	Antibody source	RRID
Neurotransmitters			
GABA	Guinea pig	Millipore AB175	RRID:AB_91011
GABA	Rabbit	Millipore AB131	RRID:AB_2278931
Glutamate	Rabbit	Millipore AB5018	RRID:AB_91640
Synaptic	•		•
Synapsin	Rabbit	Cell Signaling 5297	RRID:AB_2616578
Synaptophysin	Mouse	Abcam ab8049	RRID:AB_2198854
PSD95	Rabbit	Cell Signaling 3450	RRID:AB_2292883
PSD95	Mouse	NeuroMab 75-028	RRID:AB_2292909
VGluT1	Guinea pig	Millipore AB5905	RRID:AB_2301751
VGluT2	Rabbit	Synaptic systems 135 403	RRID:AB_887883
GAD2	Rabbit	Cell signaling 5843	RRID:AB_10835855
Gephyrin	Mouse	NeuroMab 73-465	RRID:AB_2632414
Clathrin	Rabbit	Cell signaling 4796	RRID:AB_10557412
Cell type markers			
Parvalbumin	Rabbit	SWANT PV28	RRID:AB_10013386
Calbindin	Rabbit	Millipore AB1778	RRID:AB_2068336
Calbindin	Mouse	NeuroMab 73-448	RRID:AB_2619740
NPY	Mouse	NeuroMab 73-456	RRID:AB_2629421
Tyrosine hydroxylase	Rabbit	Millipore AB152	RRID:AB_390204
Receptors			
GluA2/3	Rabbit	Millipore AB1506	RRID:AB_90710
GluN1	Mouse	Millipore MAB363	RRID:AB_94946
GluN2B	Mouse	NeuroMab 75-101	RRID:AB_2232584
GABA A Receptor β2/3	Mouse	Millipore MAB341	RRID:AB_2109419
Cytoskeletal			•
α Tubulin	Rabbit	Abcam ab18251	RRID:AB_2210057
Acetylated α tubulin	Mouse	Sigma T6793	RRID:AB_477585
βIII Tubulin	Chicken	Abcam ab41489	RRID:AB_727049
Detyrosinated tubulin	Rabbit	Millipore AB3201	RRID:AB_177350
δ2 Tubulin	Rabbit	Millipore AB3203	RRID:AB_177351
Neurofilament 200	Rabbit	Sigma N4142	RRID:AB_477272
Neurofilament, heavy chain	Chicken	AVES NF-H	RRID:AB_2313552
Neurofilament, medium chain	Chicken	AVES NF-M	RRID:AB_2313554
Neurofilament, light chain	Chicken	AVES NF-L	RRID:AB_2313553
γ actin	Mouse	Sigma A8481	RRID:AB_2289264
Synaptopodin	Rabbit	Synaptic Systems 163 002	RRID:AB_887825
Glial			·
Glutamine synthetase	Mouse	BD Biosciences 610517	RRID:AB_397879
GFAP	Chicken	AVES GFAP	RRID:AB_2313547
			(continued

<b>Table 6.1</b> (continued)
------------------------------

Antigen	Host	Antibody source	RRID		
Myelin					
MBP	Chicken	AVES MBP	RRID:AB_2313550		
PLP	Chicken	AVES PLP	RRID:AB_2313560		
CNPase	Chicken	AVES CNP	RRID:AB_2313538		
Ion channels					
Kv1.1	Mouse	NeuroMab 75-105	RRID:AB_2128566		
Kv1.2	Mouse	NeuroMab 75-008	RRID:AB_2296313		
Kv2.1	Mouse	NeuroMab 75-014	RRID:AB_10673392		
Other					
Laminin	Rabbit	Sigma L9393	RRID:AB_477163		
Caspr	Mouse	NeuroMab 75-001	RRID:AB_2083496		
GFP	Chicken	GeneTex GTX13970	RRID:AB_371416		

tiled image from the entire DAPI-stained ribbon is acquired. The DAPI labeled nuclei are a convenient bright label that can be used to localize the region of interest to be subsequently imaged at higher magnification. Other labels for low-magnification mapping that can be used depending on the experimental need, are tubulin, GABA, fluorescent proteins, or any other bright signal that labels larger structures (on the order of several microns) which persists on multiple serial sections. The desired region for imaging is chosen on a section from the low-magnification map, and software tools are used to map the same region on each serial section. The generated list of coordinates is used for automated imaging at high magnification (typically with a 63  $\times$  objective). After imaging, the antibodies are eluted from the sections using a high pH solution, and a new combination of antibodies is applied and imaged. This cycle can be repeated many times. The highest number of cycles achieved by us is 12; the number of cycles is limited by the number of available relevant antibodies, and, occasionally, by accidental damage to the coverslip. It should be noted that antibody elution somewhat decreases the ultrastructural quality of the tissue for the subsequent EM imaging [18]. This appears to be related to the high pH of the elution solution and occurs upon the first application of the elution solution. Subsequent rounds of staining and elution do not result in noticeable decrease of ultrastructure.

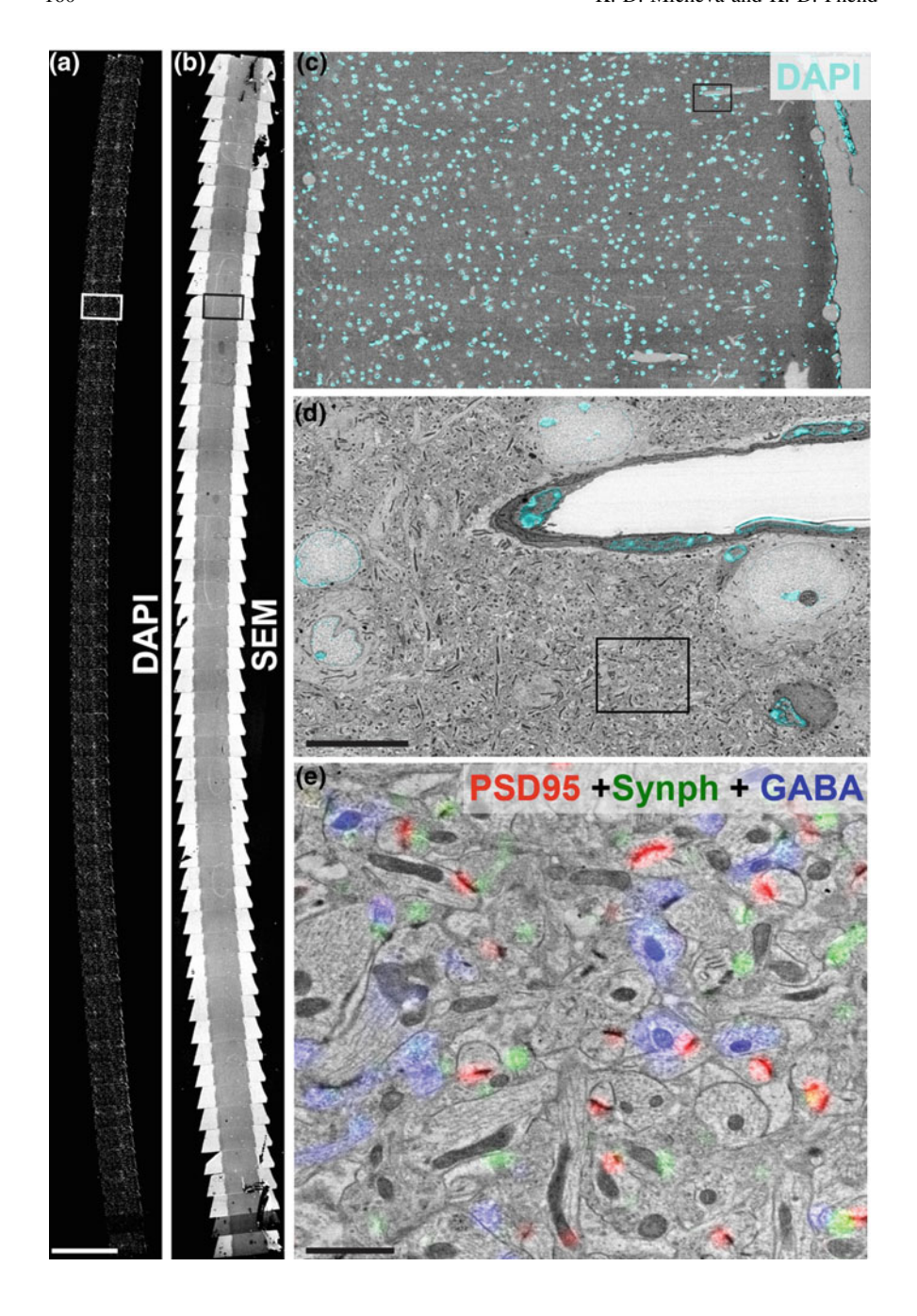
After completion of the immunofluorescent imaging, the antibodies are eluted again, the ribbon is washed well and poststained with heavy metals for electron microscopic imaging. The Lowicryl sections, and even more so the eluted Lowicryl sections, have much lower contrast compared to conventional Epon sections, which can be a problem for SEM imaging. Contrast can be improved by a pretreatment with 0.1% KMnO<sub>4</sub> dissolved in 0.1 N H<sub>2</sub>SO [49], followed by a longer application of uranyl acetate (30 min) and, finally, lead citrate. Ribbons are imaged in an FESEM microscope using the backscatter detector.

# 6.5 Array Tomography: Computer Assisted Imaging of Serial Sections on Rigid Substrates

The immunofluorescent and electron microscopic images obtained from the AT sample are at very different scales; these images have to be computationally registered to identify corresponding points (Fig. 6.5). Image registration is required at two different steps of the imaging process. First, low magnification IF and SEM images from the entire ribbon are registered in order to identify the positions for high magnification SEM imaging. And second, the high magnification IF and SEM images are registered to assign immunofluorescence from different channels to the underlying ultrastructure. Image registration is done by identifying corresponding points from the sample in the two modes of imaging, IF and SEM. For example, DAPI fluorescence from nuclei corresponds precisely to the darkly stained nuclear heterochromatin in the EM images; MBP immunofluorescence corresponds to the dark concentric circles of myelin in EM. Registration of light and EM images can be achieved in a variety of ways; below is a brief description of the workflow used in our lab which is described in more detail in [18].

To identify positions for high magnification SEM imaging, first a low-magnification SEM mosaic from the entire ribbon is obtained, and this mosaic is stitched together using the stitching algorithms available through FIJI [50]. MosaicPlanner, a custom Python-based graphical user interface, (available at <a href="http://code.google.com/p/smithlabsoftware">http://code.google.com/p/smithlabsoftware</a>), is then used to automatically find corresponding locations across sections and generate a position list which is used to acquire SEM images at an intermediate magnification. The series of acquired SEM images are aligned across the different sections using a translational transformation and an updated more precise position list is calculated, correcting for inaccuracies in the original position list. Finally, each serial section is reimaged at high resolution (2.23–3.7 nm/pixel) using this updated position list.

Image registration between the IF and SEM modalities is accomplished using the TrakEM2 plugin [51] within FIJI [50]. The registration procedure begins with electron micrographs taken at intermediate magnification, and then registration is refined using high magnification electron micrographs. DAPI images are histogramnormalized to make the spatial structure in both the dim autofluorescence and brighter DAPI fluorescence equally apparent. This is useful because variations in the dim autofluorescence correspond to ultrastructural features visible in the electron microscope, such as large dendrites with weak autofluorescence, and mitochondria with strong autofluorescence. Several corresponding features in the DAPI images and the medium magnification EM images are identified by eye, and used to fit a similarity transformation (rigid rotation plus uniform scaling). This transformation is automatically applied to the other light microscopy images. Once registered, identical alignment transformations that bring the images from section to section into correspondence can be calculated and applied to images from a set of sections. Alignment is based upon the EM images, using the elastic alignment algorithm in TrakEM2 [52], and these alignment transforms are then applied to IF data. These image reconstruction tools, including tools to assist in deconvolution, stitching, registration, and alignment, are available at http://code.google.com/p/smithlabsoftware.



**∢Fig. 6.5** Conjugate IF-SEM imaging. **a** Mosaic showing 55 sections of an array tomography ribbon, imaged for the fluorescent nuclear stain DAPI. Scale bar, 1 mm. **b** Mosaic of low magnification SEM images of the same ribbon shown in **a**. **c** A color overlay of the boxed region within **a** and **b** shows a single section from the ribbon. **d** A higher magnification SEM image from the boxed region in **c**. The DAPI signal (cyan) highlights the correspondence between the locations of nuclei within the field. Scale bar, 10 μm. **e** Higher magnification SEM image taken within the field of D (black box), overlaid with IF signals (PSD-95: red, synaptophysin: green, and GABA: blue). Scale bar, 1 μm. From [18]

# 6.6 Application of Conjugate IF-SEM Array Tomography for the Study of Mammalian Synapses and Axons

Mammalian synapses are small, usually submicron structures, which are highly diverse in their structure and molecular composition. This presents unique challenges for their imaging and requires the combination of different approaches to obtain a comprehensive view of individual synapses. The first glimpses of synapses were obtained using electron microscopy [53–55], and this remains the method of choice for identifying synapses and studying their ultrastructure. Conjugate IF-SEM array tomography adds an important facet to the study of the synaptic architecture of the brain by providing information on the molecular content of ultrastructurally identified individual synapses.

The great majority of mammalian neocortical synapses fall within two basic categories: excitatory glutamatergic ( $\sim 80\%$ ) and inhibitory GABAergic ( $\sim 15-20\%$ ). These two categories are characterized by the expression of distinct molecular markers, for example, the postsynaptic densities of excitatory synapses in cortex are enriched in PSD95, while the inhibitory postsynaptic densities generally express gephyrin (Fig. 6.6). On the presynaptic side, excitatory synapses express vesicular glutamate transporters (VGluTs), with the majority containing VGluT1, and a smaller population, mostly concentrated in layer 4, VGluT2 [56, 57]. Inhibitory synapses contain the vesicular GABA transporter (VGAT). Both types of synapses also contain synapsin, synaptophysin and other general synaptic markers. Various combinations of general synaptic markers and markers for specific synapse types can be used to identify synapses at the light level; while synapse detection in this case is not as conclusive due to resolution limitations, it allows a more efficient sampling of much larger numbers of synapses compared to electron microscopy. However, at the light level it is impossible to estimate how many synapses escape detection using this approach. This is where conjugate IF-SEM array tomography can be instrumental to assess the efficiency of synaptic markers and their combinations for synapse detection. For example, a recent study confirmed that immunofluorescence for PSD95 is present at the great majority of excitatory synapses (95%; [18]), and also found two populations of synapses that are likely to escape detection by PSD95 immunofluorescence: very small synapses and synapses onto GABA dendrites, both of which tend to be much more weakly labelled for PSD95. For inhibitory GABAergic synapses, the same study revealed that gephyrin is not as reliable a postsynaptic marker as PSD95, because approximately one quarter of inhibitory

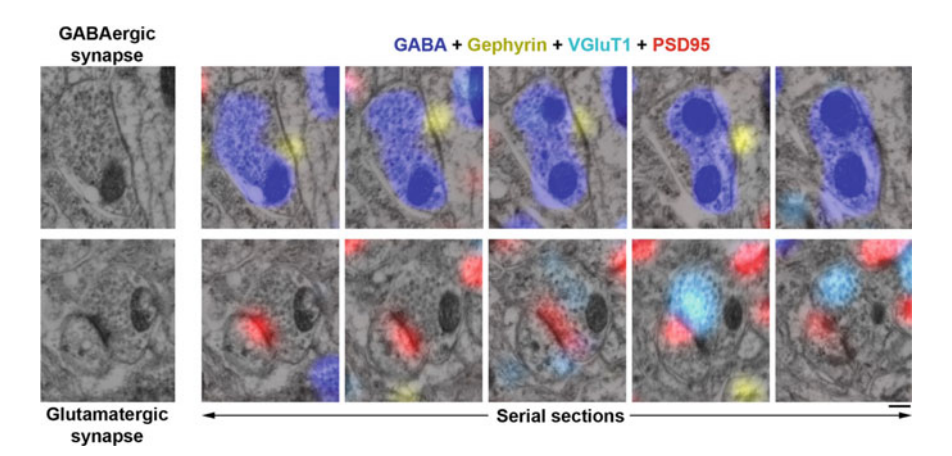


**Fig. 6.6** Examples of a GABAergic and glutamatergic synapse as identified by ultrastructural features and molecular immunolabels. Series of five consecutive sections from mouse neocortex overlaid with the corresponding immunofluorescence are shown. GABA, blue, gephyrin, yellow, VGlut1, cyan and PSD95, red. One section from the series that best displays the ultrastructural features of each type of synapse is shown to the left. Scale bar,  $0.2~\mu m$ 

synapses do not have immunodetectable levels of gephyrin. In order to improve light-level synapse detection, conjugate IF-SEM array tomography can be used in future studies to screen for markers that are specifically enriched on the postsynaptic side of excitatory synapses of very small size, or those contacting GABA dendrites, as well as of inhibitory synapses.

Another area where conjugate IF-SEM array tomography is finding successful application is the study of myelinated axons in the central nervous system (CNS) [58]. The size of myelinated axons (>200 nm in diameter), and the abundance of myelin proteins, such as myelin basic protein (MBP), make them an ideal target for immunofluorescence AT detection (Fig. 6.7). The ultrathin sections provide easy access for the antibodies against MBP and do not require lipid extraction. In addition, the use of ultrathin sections ensures that antigens can be detected equally well within myelinated and unmyelinated portions of the axon, which is in contrast to pre-embedding immunocytochemistry where myelinated portions of axons are much more weakly stained [59]. Even though myelinated axons can be easily resolved and traced using only immunofluorescence, the ability to use conjugate SEM adds important advantages. SEM imaging of small subvolumes selected from a much larger IF imaged volume, allows for quality control of tissue preservation and antibody performance, as well as for developing rules of correlation between immunofluorescence and ultrastructure. For example, conjugate light-electron AT confirms that immunofluorescence for MBP precisely outlines the myelinated sheaths of axons and can be used to estimate their thickness (Fig. 6.7f). Using these methods, together with an independently performed analysis of a publicly hosted EM dataset [60], we found that approximately half of all myelinated axons in layers 2/3 and a quarter in layer 4 in cortical gray matter arise from inhibitory interneurons with local

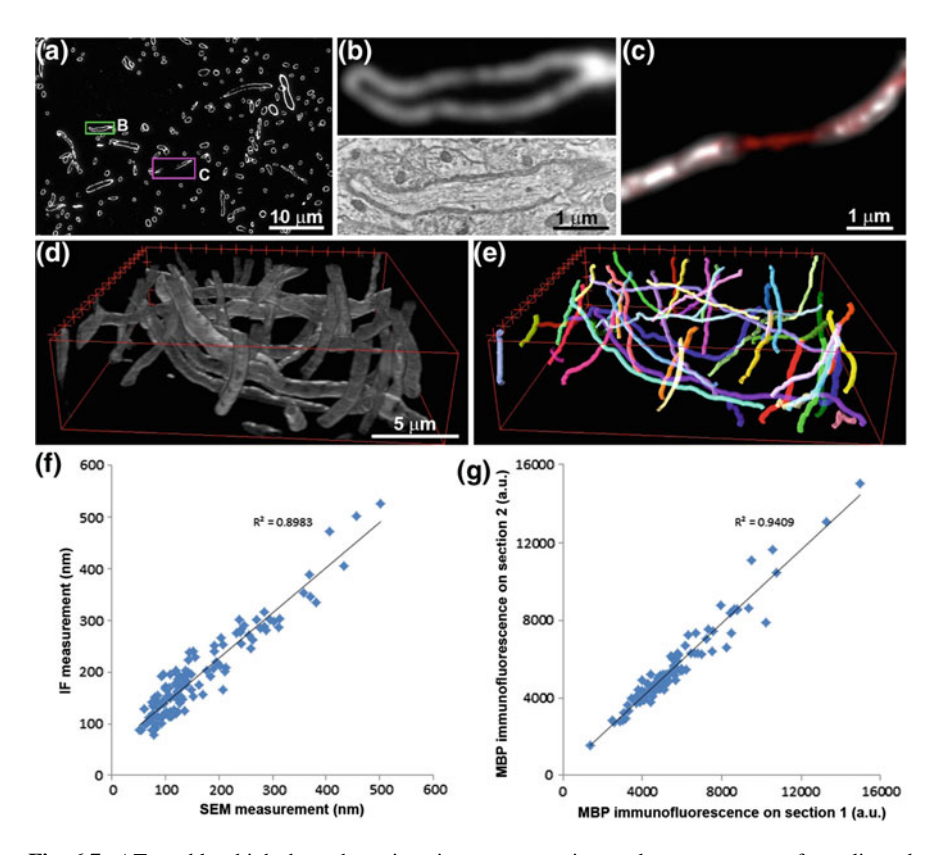


**Fig. 6.7** AT enables high-throughput imaging, segmentation and measurement of myelinated axons. **a** MBP immunofluorescence on a single ultrathin section (70 nm) from layer 5 of the adult mouse cortex. **b** MBP staining corresponds exactly to the myelin sheath as seen in the SEM of the axon boxed in green in **a**. **c** In the 3D reconstruction of the node of Ranvier (magenta box in **a**) the axonal path can be traced using cytoskeletal markers (tubulin, red). **d** Volume reconstruction of MBP immunofluorescence. **e** Segmented axons from the volume in **d**. **f** Myelin thickness as measured from IF data and SEM data. Myelin thickness was measured on the same sections using either immunofluorescence for MBP or ultrastructurally defined myelin on SEM images (N = 125 axonal profiles). **g** Consistency of MBP immunolabel. Correlation of MBP immunofluorescence of the same myelin sheath measured on two adjacent ultrathin sections (N = 100 axonal profiles). From [58]

axonal projections [58]. Despite the great variety of inhibitory interneurons in cortex, almost all of the inhibitory myelinated axons were found to belong to one interneuron type, the parvalbumin basket cells. In addition, immunofluorescent AT analysis shows that the myelin on these interneurons has a different organization (e.g. shorter nodes of Ranvier and internodes) and protein composition (higher MBP content) compared to excitatory axons. These findings challenge the notion that cortical myelin is mostly restricted to long-range excitatory axons in cortex and highlight the need to further explore the functional consequences of interneuron myelination.

# 6.7 Variations of the Method

Conjugate IF-SEM array tomography on freeze-substituted and Lowicryl embedded tissue enables the use of multiple antibodies against a variety of targets that can be applied, for example, to identify and distinguish between excitatory and inhibitory mammalian synapses, as well as to further explore synaptic diversity within these broad categories. However, specific research questions that require only a small subset of antibodies, may be more efficiently addressed using other tissue preparations. For example, as noted above, the antigenicity of GABA and other small molecules is well preserved in tissue prepared using standard electron microscopy procedures, including osmium postfixation and embedding in Epon. In fact, there is vast literature that has used GABA immunostaining and TEM to study the development, distribution and plasticity of the inhibitory GABA circuitry in a variety of animal species (for example, [61–64]). Therefore, when the focus of study is the brain GABA network, or another target with similarly preserved antigenicity (e.g. neuropeptides, [24]), conjugate IF-SEM array tomography can be performed on conventionally prepared tissue for electron microscopy (Fig. 6.8). Table 6.2 lists

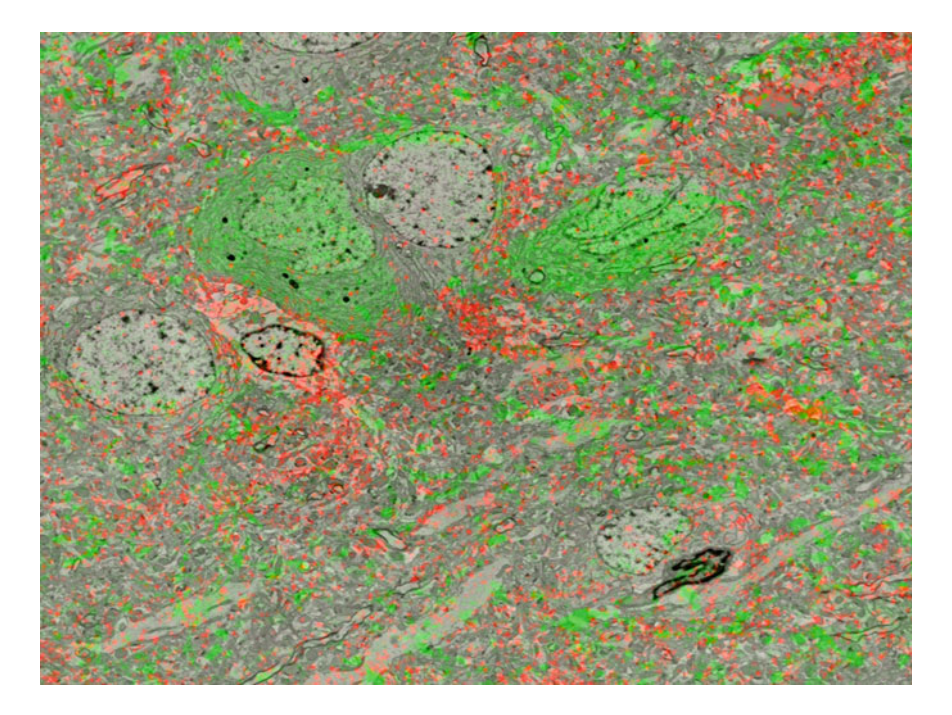
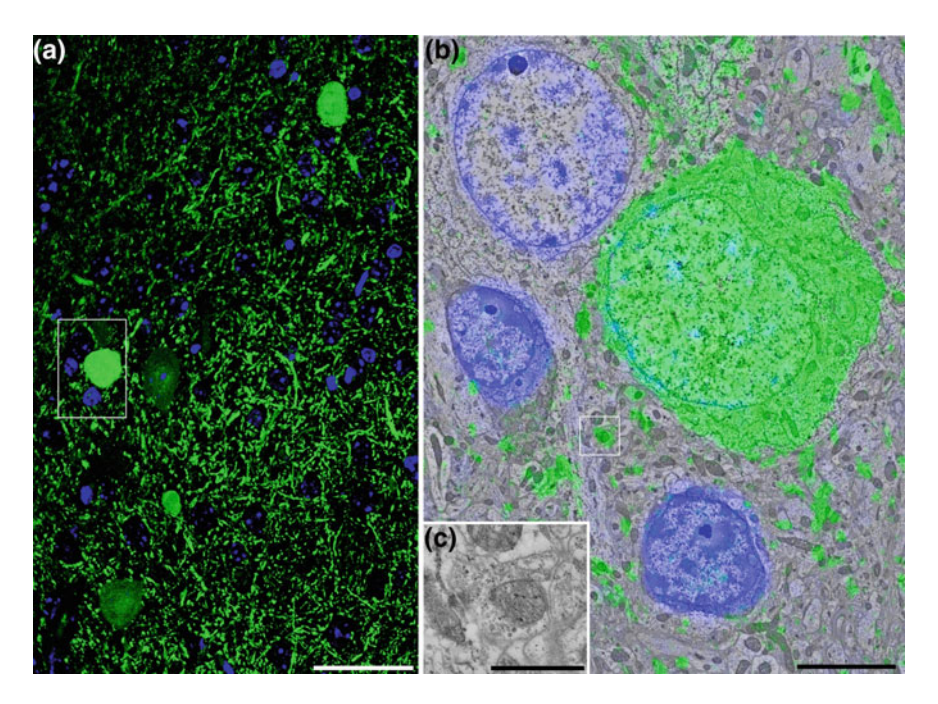


Fig. 6.8 Conjugate AT on conventionally prepared EM tissue. GABA (green) and glutamine synthetase (red) immunostaining of ultrathin sections from rat cortex fixed with 2% formaldehyde and 2.5% glutaraldehyde, postfixed with 1% OsO<sub>4</sub> and 1.5% K ferricyanide, and embedded in Epon. Two GABA cell bodies and one astrocyte (glutamine synthetase positive) are within the field of view. GABA antibody (Millipore AB131) was used at 1:300 dilution and the glutamine synthetase antibody (BD Biosciences 610517) at 1:25

Antigen	Host	Antibody source	RRID
GABA	Guinea pig	Millipore AB175	RRID:AB_91011
GABA	Rabbit	Millipore AB131	RRID:AB_2278931
Glutamate	Rabbit	Millipore AB5018	RRID:AB_91640
α Tubulin	Rabbit	Abcam ab18251	RRID:AB_2210057
Acetylated α tubulin	Mouse	Sigma T6793	RRID:AB_477585
Glutamine synthetase	Mouse	BD Biosciences 610517	RRID:AB 397879

**Table 6.2** Antibodies that can be used on conventionally prepared tissue for EM (including osmium postfixation and Epon embedding)



**Fig. 6.9** Conjugate AT on conventionally prepared EM tissue embedded in LRWhite. GABA (green) immunostaining and DAPI labeling of ultrathin sections from mouse cortex fixed with 2% formaldehyde and 2.5% glutaraldehyde, postfixed with 1% OsO<sub>4</sub> and 1.5% K ferricyanide, and embedded in LRWhite. GABA antibody (Millipore AB131) was used at 1:100 dilution followed by a goat anti-rabbit Alexa 488–10 nm colloidal gold conjugate at 1:50

several antibodies that can be used on such tissue. DAPI labelling of nuclei cannot be used on Epon embedded tissue; when this is required, embedding in LRWhite resin can be used instead (Fig. 6.9). Additionally, secondary antibodies conjugated to both a fluorophore and colloidal gold can be applied to further confirm the correspondence between immunofluorescence and ultrastructure (Fig. 6.9).

# 6.8 Detailed Protocol for Conjugate IF-EM AT Using Freeze Substitution and Embedding in Lowicryl HM-20

# 1. Tissue Fixation: Chemical fixation by perfusion

1A. Required materials and equipment:

Anesthetic

Paraformaldehyde (reagent grade, crystalline; Sigma-Aldrich #P6148)

Glutaraldehyde (50%, EM grade; Electron Microscopy Sciences #16310)

Sodium phosphate, monobasic, monohydrate

Sodium phosphate, dibasic, anhydrous (or dibasic heptahydrate)

Sodium chloride

Sodium heparin

Hazardous waste collection containers

Fume hood

Surgical tools

Gloves, safety glasses, coats (PPE)

Storage vials or tubes (20 ml scintillation vials or culture/centrifuge tubes)

# 1B. Preparations:

# **0.1M phosphate buffer, pH 6.8** (PB 6.8):

6.93 g sodium phosphate, monobasic, monohydrate

7.06 g sodium phosphate, dibasic, anhydrous (or 13.32 g dibasic heptahydrate)

Distilled or deionized water up to 1 L, titrate as needed

# **Fixative: 2% paraformaldehyde/2% glutaraldehyde in PB 6.8**. Prepare same day, keep at room temperature,

For 100 ml (per mouse):

2 g paraformaldehyde

Dissolve in warm, but not boiling:

100 ml PB 6.8

Cool solution to room temperature, add:

4 ml 50% glutaraldehyde

Filter (we use vacuum filtration with Whatman #40 filter paper)

# Heparinized normal saline

9 g sodium chloride

1 L distilled or deionized water

Add 1000 units/100 ml of sodium heparin

## 1C. Procedures:

Deeply anesthetize mice (e.g. sodium pentobarbital 80–100 mg/kg IP, no response to firm forepaw pinch), surgically open the chest to expose pericardial region, cut the right atrium, and insert a perfusion cannula into the left ventricle. We use gravity (i.e. pressure-based) flow, aiming for  $\sim 3$  ft hydrostatic pressure. A peristaltic pump also works; most important is technical success, getting fix to the brain reasonably quickly so the body and brain harden properly. After a brief ( $\sim 30$  s) flush with normal saline, run fixative for  $\sim 10$  min. Remove the brain, put it in the same fixative, store overnight at 4 °C, then replace with buffer and keep in the refrigerator. Fixed brains are stable in the refrigerator for >1 week. Collect fixative for hazardous waste disposal. Procedure should take place in a hood or with personnel-protecting ventilation, as fumes are hazardous.

# 2. Tissue blocking, mounting, sectioning

# 2A. Required materials and equipment:

Double-edged razor blades

Tweezers/forceps

Cyanoacrylate cement (we use "Crazy Glue")

70–95% ethanol in dispensing bottle (for cleaning blades and Vibratome)

Vibratome and mounting blocks

Saline and saline ice cubes

Paint brushes, or other section pickers

Collection trays (24-well cell culture trays work well)

Tray sealers (adhesive plastic film) minimize buffer loss and tissue dehydration 0.025% sodium azide in 0.01 M PBS (only for long storage, do not allow contact with metal, collect for disposal as hazardous waste)

Petri dish and/or dental wax

# 2B. Preparations:

# **0.01 M PBS** (store in refrigerator)

- 0.2 g sodium phosphate monobasic, monohydrate
- 2.6 g sodium phosphate dibasic, heptahydrate
- 8.8 g sodium chloride
- 1 L distilled or deionized water

# **Sodium azide storage solution** (collect used solutions as hazardous waste)

0.25 g sodium azide (use non-metal spatula)

1 L 0.01 M PBS

## 2C. Procedures:

Remove brain from storage vial and place in a petri dish containing buffer or PBS. Use tweezers or fine forceps under a dissecting microscope to peel and remove as much remaining vasculature and pial membrane as you can. Using a razor blade, make a block of tissue and glue it to a mounting block using Crazy Glue (not too much or it will rise into tissue gaps and cause sectioning problems). Avoid getting glue on fingers; if skin glues to block, remove glue with acetone. Re-immerse in buffer to keep tissue moist.

Set up Vibratome with saline and saline ice cubes or other chilling means. Have collection trays filled with buffer  $\pm$  azide on a chilled surface (we often use shipping cold packs, which we store in a freezer); mounted tissue blocks should be kept wet and cold until sectioned. For freeze-substitution processing, cut sections  $100\text{--}200~\mu m$  thick. We typically cut  $200~\mu m$  for capsule embedment of small pieces, but if processing an entire section it should be no more than  $100~\mu m$  to ensure proper resin cure. It is usually wise to cut some  $50~\mu m$  sections between sets of 200s for Nissl-stained reference or other LM/EM purposes. If possible, the block surface glued to base should be larger than the portion to be cut.

# 3. Freeze-substitution and embedment in Lowicryl HM-20

# 3A. Required materials and equipment:

Processing shell vials with caps (1 dram EMS/Fisher) and vial holders (aluminum, EMS #72640), and/or scintillation vials (20 ml)

Fine scalpel blades (#11 or #15)

Small, fine-tipped paint brush

Styrofoam box(es),  $\pm$  foil lining

Dry ice

100% ethanol (200 proof)

Cold packs

Disposable polyethylene transfer pipets (Fisher #13-711-9CM)

Glycerol

CaCl<sub>2</sub>

Sodium acetate trihydrate (ACS)

Uranyl acetate (depleted, available from EMS, Ted Pella, Fisher)

Methanol, (absolute, certified ACS, Fisher Scientific #A412-500)

Lowicryl HM-20 embedding kit (EMS #14340, or Ted Pella)

Freeze-substitution unit (Leica AFS or equivalent) with flow-through capsules and gelatin capsules for small chunks (1 mm  $\times$  1–2 mm  $\times$  200 µm)

For whole sections (100 µm thick), use baskets (Leica #G3314A)

For wafering and curing of sections: glass slides, scoring tool, ACLAR, and upside-down metal cans for wafer support

ACLAR embedding film (7.8 mil thickness, EMS #50425)

Oven capable of 60 °C for drying things before use

Independent temperature probe for AFS unit (Omega HH800A with Omega 5SC-TT-K-36-36 precision fine wire thermocouple, insulated, self-adhesive)

Acetone (can be used as substitution medium, but must be strictly anhydrous and doesn't work as well as methanol in humid climates or conditions); we use acetone mainly for cleaning.

# Day 1

# **Preparations:**

**0.1 M sodium acetate (NaA)**: 1.36 g sodium acetate trihydrate/100 ml distilled water, store at 4 °C

**0.1%** CaCl<sub>2</sub>: Make a 10% stock solution in water, store at 4 °C; dilute 1:100 with NaA as needed

**Glycerol Dilutions** (keep at 4 °C):

10% in NaA 20% in NaA 30% in NaA

**Substitution solution**: 1.5–4% (varies, depending on lot) uranyl acetate in anhydrous methanol, make day before needed, store tightly capped at 4  $^{\circ}$  C, filter (0.2  $\mu$ m PES 13 mm syringe filter); standard run uses 15 ml (5 ml/can)

Pre-clean Flo-through capsules (put capsules in a can with absolute ethanol or methanol, swirl, then remove one by one with forceps and force solvent through capsule with pipet before setting on Kimwipe to dry). Do the same for capsule holders, ACLAR spears (2 cm  $\times$  2 mm), and cans (for sections: baskets and ACLAR strips—2 cm  $\times$  6–8 mm), dry overnight in 60 °C oven.

# **Procedures:**

Select sections and put in labeled shell vials with 0.1 M NaA, keep all chilled, we set the vials in aluminum vial holders on shipping cold packs in a Styrofoam box on a gently rotating shaker.

## Pretreatment:

3 × 10 min changes of NaA 1 h in 0.1% CaCl<sub>2</sub>/NaA 3 × 5 min rinses in NaA

Cryoprotection, keep chilled throughout:

30~min in 10%~glycerol/NaA

30 min in 20% glycerol/NaA

30 min in 30% glycerol/NaA

Overnight in 30% glycerol/NaA

# Day 2

## **Procedures:**

Prepare AFS unit by filling with liquid nitrogen, insert black-topped tube, turn on and set the following program (can be modified):

 $T1 = -90 \, ^{\circ}\text{C} \text{ for } 32 \, \text{h}$ 

S1 = +4 °C/h

 $T2 = -45 \, ^{\circ}\text{C} \text{ for } 50 \, \text{h}$ 

S2 = +5 °C/h

T3 = 0 °C for 40 h

Hit "Start" and then immediately "Pause". Machine will go to T1 setting and hold. The instrument is subject to defective temperature monitoring; accordingly, when it displays the T1 temperature, the temperature should be independently verified using an independent probe or solutions of known freezing point. If necessary, adjust settings to achieve desired temperature. When all samples are in the machine, hit "Pause" again and program will start. Troubleshoot—things freezing when they shouldn't—if chamber temperature is verified, check that TF control knob isn't set too high (too far right).

Set up a freezing box (foil-lined Styrofoam box with about 1" 100% ethanol and dry ice bath), load capsules into labeled holders, fill each holder with about 5 ml absolute methanol and place in freezing bath to cool (cover when not transferring samples).

Under a dissecting microscope, place a section with a modest amount of cold 30% glycerol in a petri dish or on dental wax. Use a scalpel blade to excise desired areas of a size suitable for ultramicrotomy from cryoprotected sections (remainder of section can be returned to vial and stored for future use). Use a fine brush to transfer each sample to the tip of an ACLAR spear (2 cm  $\log \times 2$  mm wide tapered at one end), blot the brush and use it to wick off excess glycerol. Then transfer the loaded spear to the first capsule (refer to capsule numbering scheme in manual, #1 is marked by dots) and drop it in. As soon as one holder is loaded (8 samples), transfer it to the AFS chamber. Continue until all holders are loaded and transferred to AFS. Hit "Pause" to start the programmed run.

\*\* If using 100  $\mu$ m sections for flat embedding, mount the cryoprotected sections on 2 cm  $\times$  6–8 mm ACLAR strips (both sides if necessary), and insert upright into mesh-bottomed baskets in cans. Sections must be small enough to be immersed while upright. Baskets (4/can) can be notched to identify and cans tape-labeled. Sections can be wafer-embedded after substitution and infiltration and either cured in the AFS or removed to a chilled, external UV equipped chamber.

Once the program is started:

Chill any new solution in a separate can in the AFS for 5–10 min; also provide a can to receive waste solutions.

Briefly chill 2 disposable pipets (1 for removal of solutions, 1 to transfer new solutions).

 $2 \times 10$  min changes of anhydrous methanol (3 changes if there are moisture concerns).

After each change, use the new solution pipet to gently suck up and down in the central tube in each capsule holder, to mix the solution.

Replace the final methanol rinse with uranyl acetate/methanol. After mixing in each holder, close the machine, lower the glass plate, and detach it from the lifter.

Collect ethanol and methanol for hazardous waste disposal.

Clean used cans.

# Day 3

# Procedures (T1, S1):

Chill a pipet and gently mix solutions. Using a forceps carefully raise an ACLAR spear, if there is no sample attached to it, remove it to a rinsing container. If a sample is still attached, lower it back into its capsule and gently tap the spear against the bottom and flex it a bit, then check again to see if the sample has detached. Repeat if necessary, or move on and come back. Continue until all spears are removed. If desperate, chill a tool and use it to dislodge the sample. Do a final round of gentle solution mixing, then close lid, lower glass, and detach it from the lifter.

Day 4

# **Preparations:**

Lowicryl HM-20 (ml)	20	15	10
Crosslinker D (g)	2.98	2.24	1.49
Monomer E (g)	17.02	12.76	8.51
Mix gently, add			
Initiator C (g)	0.1	0.075	0.05

Mix by swirling gently, do not incorporate air bubbles.

5 ml of solution are needed for each holder. Dedicated 20 ml vials with caps for full strength Lowicryl and for mixtures with methanol are useful. Keep solutions in dark as much as possible.

For 1:1 Lowicryl/methanol—Make up 20 ml as above, take 8 ml and combine with 8 ml methanol in mixing bottle, swirl gently to mix.

For 2:1 Lowicryl/methanol—Take remaining 12 ml from the 20 ml above and combine with 6 ml methanol in mixing bottle.

Dry overnight at 60 °C:

The larger parts of 24 gelatin capsules (Leica 16702745) size 1 Spider covers (to pick up and transfer capsules)

Stem holders for spider covers

Bottom plate (spacer) for cans

4-5 universal cans

Chamber for gelatin capsules

# **Procedures (T2):**

Chill solutions and pipets as in beginning.

Remove uranyl acetate solution (collect for hazardous waste disposal).

 $3 \times 15$  min rinses in methanol, with gentle mixing as before (collect for disposal).

2 h 1:1 Lowicryl/methanol

2 h 2:1 Lowicryl/methanol
2 h Lowicryl (need 5 ml/capsule holder)
Overnight Lowicryl (need 5 ml/capsule holder)
Collect all for hazardous waste disposal.

# Day 5

# Required materials:

100% Ethanol

Oven-dried gelatin capsules, spider covers, stem holders, bottom spacer plates, cans, chamber for gelatin capsules

Cryomanipulator with M4 thread

Red temperature tube

# **Preparations:**

10 ml Lowicryl (see recipe above)

Set a stem holder in each of 3 curing containers (label cans) and place a bottom spacer plate on top of its base.

# Procedures (T2, S2, T3):

Chill Lowicryl, pipets and chamber for gelatin capsules.

Gently jiggle/tap capsule holders to encourage tissue to settle at the bottom of capsules.

Insert gelatin capsules in chamber.

Fill gelatin capsules with Lowicryl.

Screw cryomanipulator into socket of spider cover.

Align arrow of spider cover with position #1 of capsule holder (between 2 dots).

Push spider cover down into capsules, lift slightly and carefully check that all capsules are attached (you may have to try more than once; don't lose your alignment). When possible, move the spider cover with capsules to the gelatin capsule chamber and insert tissue capsules into gelatin capsules, pushing down to attach the gelatin capsules to the spider cover. Again, lift slightly and check for attachment. Unscrew the cryomanipulator, but leave the spider cover in place. Remove the empty capsule holder, mop up any spilled Lowicryl, and insert a labeled curing container (prepared as above) to which 10 ml 100% ethanol has been added. Chill. When chilled, use the insulated tweezers to transfer the loaded spider cover (again, lift slightly to check attachment and push down to re-engage if necessary) to the stem holder. The bottom spacer plate is used to help ensure that even if a gelatin/ tissue capsule detaches in the curing container it will remain in place and not fall over into the ethanol. Insert and fill the next set of gelatin capsules (transfer the Lowicryl within the gelatin chamber as needed). Then repeat as above until all spider cover/capsule sets are seated on their stem holders. Remove gelatin chamber and Lowicryl can. Mop the cryochamber floor and temperature tube top with a Kimwipe so no Lowicryl puddles remain.

Replace the black temperature tube with the red one.

Close cover, lower and release glass plate, re-open cover and insert UV lamp apparatus, connect to AFS and plug into power. Turn on the UV power switch. The UV indicator light on control panel should show a steady light. If it is flashing, the UV light is not lit. Check connections and seating of apparatus.

Days 6, 7: No procedures

# Day 8

# **Materials and Equipment:**

Acetone for cleaning

Styrofoam box, foil-lined, with UV lamp (BLAK-RAY Lamp, longwave UV366 nm, UVP, Upland, CA) embedded in lid to shine into box, and raised interior platform, or commercial chillable UV curing box

Dry ice

## **Procedures:**

To ensure that capsules are sufficiently cured, set up Styrofoam UV box with dry ice and platform at about 2" away from UV lamp (or use commercial box).

Remove curing cans from AFS, remove spider covers with attached capsules (labeling each set), blotting dry on paper towel, making sure capsules are stable.

Set the spider covers on the platform with the capsules facing up.

Replace the UV lid and turn on.

Let cure overnight.

When curing is complete, remove one capsule at a time, noting position, slit the gelatin and Flo-through capsule with a razor blade and peel them away from the Lowicryl block; label block if no label was inserted.

Repeat for remaining capsules.

Empty ethanol from curing cans (dispose as hazardous waste).

Place cans with stem holders and bottom spacer plates in acetone for cleaning, rinsing off residual resin debris, then air dry.

Spider covers should have cured resin residue gently removed with a dissecting needle, then clean in acetone and air dry.

# 4. Ultrathin sectioning and preparation of arrays

4A. Required materials and equipment:

Silanized coverslips ( $24 \times 65$  mm; Aratome, Menlo Park, USA), or High performance Schott Nexterion coverslips coated with Aminosilane (Schott, Jena, Germany)

Carbon rods (e.g. Ted Pella, #93010)

Carbon evaporator (e.g. Cressington Carbon Coater 308R)

Ultra Jumbo Diamond Knife or Histo Jumbo Diamond Knife (Diatome): The choice of knife depends on the size of the block to be cut. The Ultra Jumbo Knife has a 3 mm diamond edge. For larger block faces, the Histo Jumbo knife comes with 2 diamond size options—6 and 8 mm. Even though its cutting range is specified as 0.2–5  $\mu$ m, a new Histo Jumbo knife will cut ultrathin sections (70 nm).

Cryotrim 45 Diamond Knife (Diatome)—for trimming the block face

Ultramicrotome

Weldwood Contact Cement

Xylene

Thin paint brush

Slide warmer (Set at  $\sim 60$  °C)

Tween-20 (Electron Microscopy Sciences 25564)

# 4B. Preparations:

**Carbon coated coverslips**: Coat the coverslips with carbon (medium gray color). Follow the instructions for the particular carbon evaporator. Store in dust free boxes.

Note: If the coat is too light, this can cause problems with charging of the sample in the SEM. If the coat is too dark, the immunofluorescence signal will be significantly attenuated. The coverslip will be very hydrophobic, however we don't recommend glow discharge to increase hydrophilic properties, because this decreases the adhesion of sections to the coverslips.

**Glue**: Dilute contact cement with xylene ( $\sim 1:3$  until easily applicable with a paintbrush).

**Tween water**: 0.005% Tween 20 in water. Dissolve 10 µl Tween 20 in 200 ml distilled water.

#### 4C. Procedures:

Prepare the block for ultrathin sectioning: Trim the block around the tissue using a razor blade. A smaller blockface (2 mm or less width) with the width of the trapezoid greater than its height works best. Cut semithin sections until you reach the tissue. Trim the block again at this point, to ensure that the block face is not too big and the leading and trailing edge of the block face are parallel. The cryotrim 45 diamond knife can be used for precision trimming (Fig. 6.10a). Using a paint brush, apply the diluted glue to the leading and trailing sides of the block pyramid. Let dry (5 min) and apply again.

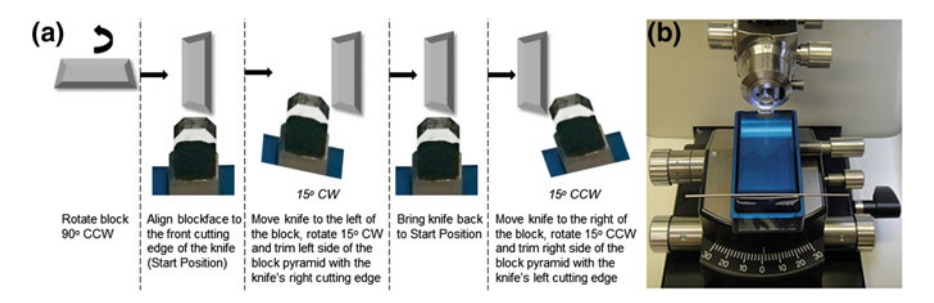


Fig. 6.10 Trimming of the block and ultrathin sectioning setup

Ultrathin sectioning: Fill the boat of the Jumbo Diamond knife with Tween water and insert a coverslip. The carbon coated coverslips are very hydrophobic and it is difficult to keep them submerged in pure water in the knife boat. The use of Tween water helps with wetting the coverslips and the stainless steel rod prevents the water from receding (Fig. 6.10b). The water level in the knife boat should be kept very low or water will jump onto the block face. After the glue has dried (up to 30 min), start cutting ribbons of serial sections (70 nm).

Picking up the sections on the coverslip: When the desired length of the ribbon is achieved, carefully detach it from the knife edge using an eyelash. Remove the rod and with the eyelash gently push the ribbon towards the coverslip, so that the edge of the ribbon touches the glass at the interface of the glass and the water. The edge of the ribbon will then stick to the coverslip. Using a syringe, slowly lower the water level in the knife boat until the entire ribbon sticks to the coverslip. Take out the coverslip. The coverslips have to be left flat to dry, because the sections may still move while wet with the Tween water. The position of the ribbon can be marked using a permanent marker on the coverslip side opposite of the sections. After the water has dried out, place the coverslip on the slide warmer ( $\sim 60$  °C) for 30 min. The coverslips can be stored at room temperature for at least 3 months.

Note: Slight variations in the Tween concentration can cause problems in sectioning and picking up of ribbons. If the sections sink or the ribbons start to break up easily, decrease the Tween concentration by adding several drops of water in the knife bath. If the water recedes abruptly or unevenly from the coverslip increase the Tween concentration by adding several drops of 0.01% Tween in water.

## 5. Immunostaining

# 5A. Required materials:

PAP pen (ImmmEdge Pen, Vector Laboratories) Tris Buffered Saline tablets (Sigma #T5030) Sodium borohydride (Sigma #S9125) Glycine Bovine serum albumin (e.g. AURION BSA-C, Electron Microscopy Sciences 25557)

Tween-20 (Electron Microscopy Sciences 25564)

Primary antibodies

Secondary antibodies: the appropriate species of Alexa Fluor 488, 594 and 647, IgG (H + L), highly cross-adsorbed (Invitrogen)

Transfer pipets, extra-fine tip polyethylene (Fisher Scientific 13-711-31) Mounting medium: SlowFade Gold antifade reagent with DAPI (Invitrogen)

Glass Slides, precleaned Gold Seal Rite-On micro slides (Fisher Scientific 12-518-103)

# 5B. Preparations:

Tris buffer: dissolve 1 tablet in 15 ml of ultrapure water

**1%** Na borohydride: 10 mg of Na borohydride in 1 ml of Tris. Prepare immediately before use. Do not close the Eppendorf tube or it may burst from the building pressure.

50 mM Glycine: 4 mg glycine in 1 ml of Tris

**Blocking solution**: Make a 1% stock of Tween-20 (10  $\mu$ l Tween in 1 ml of ultrapure water). Then add 50  $\mu$ l of the 1% Tween stock solution to 0.94 ml Tris. Add 10  $\mu$ l of Aurion BSA.

## 5C. Procedures:

Encircle the sections with a PAP pen leaving some extra space at the two ends of the ribbon. Put the coverslips in a Petri dish or box, and add wet KimWipes on the side to prevent evaporation of solutions. Keep closed during incubation times. All incubations except primary antibodies are done at room temperature.

Cover the sections with 1% Na borohydride for 3 min. Remove big bubbles that form during the incubation by gently tapping the box to the bench. Wash with Tris for a total of 20 min. Washing of the sections is done in several periods (3–4 periods of about 10–15 s) of continuous flow of buffer, by adding buffer with a plastic transfer pipet on one side of the sections and removing buffer with another pipet (or a pipet tip connected to a vacuum line) on the opposite side of the sections.

Remove Tris and add 50 mM glycine for  $\sim 5$  min.

Remove glycine and apply blocking solution for  $\sim 5$  min (no need to wash).

Remove blocking solution and apply primary antibody in Blocking Solution for 2 h at room temperature or overnight at 4 °C (no need to wash). Spin down the antibody solution at 13,000 rpm for 2 min before applying to sections.

Note: After this step, it is important not to let the sections dry at any point! Wash several times with Tris for a total of 15 min.

Apply secondary antibody (e.g. Alexa, 1:150) in blocking solution for 30 min. Spin down the antibody solution at 13,000 rpm for 2 min before applying to sections. Keep in the dark.

Wash with Tris several times for a total of 15 min.

Wash with filtered ultrapure water: wash the sections once, and then wash the whole coverslip. Note: At this point it is very easy for the sections to dry out, so be careful to always leave some water behind.

Mount with SlowFade Gold antifade reagent with DAPI (Invitrogen). The DAPI stain helps find the sections and focus. For mounting: remove some, but not all of the water from the array, then add a couple of drops of mounting medium and remove more of the water.

## 6. Elution

6A. Required materials:

NaOH (10 N)

SDS (20% w/v; Roche 1666924)

Tris buffer

6B. Preparations:

**Elution solution** (0.2 M NaOH and 0.02% SDS in ultrapure water): Add 200  $\mu$ l of NaOH (10 N) and 10  $\mu$ l SDS to 10 ml of ultrapure water. Store at room temperature for up to 6 months.

6C. Procedures:

Add water around the edge of the coverslip to help detach it from the microscope slide. Wait  $\sim 1$  min. The coverslip will float up. Pick it up with tweezers and wash away mounting medium with ultrapure water. Note: It is best to perform this step as soon as finished with imaging. Leaving the sections too long with the mounting medium will damage the sections.

Apply the elution solution for 20 min at room temperature (add the solution gently to the sections, do not wash with the elution solution). Elution time may vary for different antibodies; can be tested by applying only the secondary antibody after elution and checking for remaining fluorescence. Some antibodies cannot be sufficiently eluted, for example GABA, and such antibodies are best left for the last cycle of immunostaining.

Wash with Tris buffer (15 min). The initial wash should be slow.

A new immunostaining can be performed following the same procedure as described in Sect. 4.

Alternatively, to store the coverslip for possible staining at a later time, after the 15 min Tris wash briefly rinse with filtered ultrapure water. After the sections have dried, the coverslips can be stored for a long period of time.

# 7. Poststaining for electron microscopy

7A. Required materials:

KMnO<sub>4</sub> H<sub>2</sub>SO<sub>4</sub> 1N Uranyl acetate Lead citrate NaOH 2 N, carbonate free

# 7B. Preparations:

Acidified permanganate staining solution (0.1% KMnO<sub>4</sub> in 0.1 N H<sub>2</sub>SO<sub>4</sub> [49]): Prepare a stock solution of 1% KMnO<sub>4</sub> by adding 0.1 g KMnO<sub>4</sub> in 10 ml of distilled water. Immediately before staining, add 100  $\mu$ L of the KMnO<sub>4</sub> stock solution and 100  $\mu$ L of 1 N H<sub>2</sub>SO<sub>4</sub> to 800  $\mu$ L of distilled water. The KMnO<sub>4</sub> stock solution can be stored for several months at room temperature.

**5% aqueous uranyl acetate**: Weigh 5 g of uranyl acetate under the fume hood and add to 100 ml of ultrapure water. Cover the bottle with foil and dissolve overnight on a shaker in a warm room (37 °C). Can be stored for several months in the dark. Filter before use.

**Lead citrate solution**: Prepare fresh, during the uranyl acetate staining period. Under the fume hood weigh out 0.01–0.04 g lead citrate in a 10 ml tube. Add 1 ml of carbonate free 2 N NaOH to dissolve lead and then add 9 ml of water. Filter before using. The lead citrate powder can be weighed out in tubes ahead of time and stored at room temperature for convenience.

# 7C. Procedures:

Dip coverslip with sections in a Coplin jar filled with ultrapure water (wet sections stain better). Remove and put into petri dish with filter paper or gauze underneath. Cover the sections with freshly made acidified permanganate staining solution and leave for 1 min. Quickly remove stain and flood coverslip with ultrapure water. Wash extensively with water.

Put coverslip in a clean petri dish and add a small amount of filtered 5% aqueous uranyl acetate over the sections. Cover the petri dish and let stain for 30 min. While coverslip is staining, make up fresh lead solution.

Remove UA staining solution and flood coverslip with water. Wash extensively and then store in Coplin jar while getting lead stain ready. Add NaOH pellets to staining dish.

Add freshly made and filtered lead citrate over the sections. Immediately close the petri dish. Stain for 1 min ONLY! Remove lead and flood coverslip with water. Wash extensively with water.

Let dry, then mount with carbon paint onto SEM stub.

Ribbons are imaged in an FESEM microscope using the backscatter detector at 5-8 keV.

# 6.9 Conclusions

Cryoembedding in Lowicryl HM-20 preserves both antigenicity and ultrastructure of brain tissue, enabling conjugate array tomography. Using fluorescence microscopy, dozens of different antibodies and other fluorescent markers can be imaged at synaptic resolution within large volumes of tissue. The same arrays can also be viewed using field emission SEM, which allows for the classic benefits of electron microscopy. Such integration of different imaging modalities can substantially enrich our understanding of the brain.

# References

- J. Roth, The silver anniversary of gold: 25 years of the colloidal gold marker system for immunocytochemistry and histochemistry. Histochem. Cell Biol. 106(1), 1–8 (1996)
- B.L. Wang, L.I. Larsson, Simultaneous demonstration of multiple antigens by indirect immunofluorescence or immunogold staining. Novel light and electron microscopical double and triple staining method employing primary antibodies from the same species. Histochemistry 83(1), 47–56 (1985)
- 3. D.A. Meyer, J.A. Oliver, R.M. Albrecht, Colloidal palladium particles of different shapes for electron microscopy labeling. Microsc. Microanal. **16**(1), 33–42 (2010)
- B.N.G. Giepmans, T.J. Deerinck, B.L. Smarr, Y.Z. Jones, M.H. Ellisman, Correlated light and electron microscopic imaging of multiple endogenous proteins using quantum dots. Nat. Methods 2, 743–749 (2005)
- D.R. Glenn, H. Zhang, N. Kasthuri, R. Schalek, P.K. Lo, A.S. Trifonov, H. Park, J.W. Lichtman, R.L. Walsworth, Correlative light and electron microscopy using cathodoluminescence from nanoparticles with distinguishable colours. Sci. Rep. 2, 865 (2012)
- W. Schubert, B. Bonnekoh, A.J. Pommer, L. Philipsen, R. Böckelmann, Y. Malykh, H. Gollnick, M. Friedenberger, M. Bode, A.W. Dress, Analyzing proteome topology and function by automated multidimensional fluorescence microscopy. Nat. Biotechnol. 24(10), 1270–1278 (2006)
- M. Bode, M. Irmler, M. Friedenberger, C. May, K. Jung, C. Stephan, H.E. Meyer, C. Lach, R. Hillert, A. Krusche, J. Beckers, K. Marcus, W. Schubert, Interlocking transcriptomics, proteomics and toponomics technologies for brain tissue analysis in murine hippocampus. Proteomics 8(6), 1170–1178 (2008)
- 8. W. Schubert, Systematic, spatial imaging of large multimolecular assemblies and the emerging principles of supramolecular order in biological systems. J. Mol. Recognit. 27(1), 3–18 (2014)
- 9. K.D. Micheva, S.J. Smith, Array tomography: a new tool for imaging the molecular architecture and ultrastructure of neural circuits. Neuron **55**(1), 25–36 (2007)
- K.D. Micheva, B. Busse, N.C. Weiler, N. O'Rourke, S.J. Smith, Single-synapse analysis of a diverse synapse population: proteomic imaging methods and markers. Neuron 68(4), 639–653 (2010)
- G. Wang, S.J. Smith, Sub-diffraction limit localization of proteins in volumetric space using Bayesian restoration of fluorescence images from ultrathin specimens. PLoS Comput. Biol. 8 (8), e1002671 (2012)
- 12. A. Dani, B. Huang, J. Bergan, C. Dulac, X. Zhuang, Superresolution imaging of chemical synapses in the brain. Neuron **68**(5), 843–856 (2010)

- R. Jungmann, C. Steinhauer, M. Scheible, A. Kuzyk, P. Tinnefeld, F.C. Simmel, Single-molecule kinetics and super-resolution microscopy by fluorescence imaging of transient binding on DNA origami. NanoLett 10, 4756–4761 (2010)
- T. Kiuchi, M. Higuchi, A. Takamura, M. Maruoka, N. Watanabe, Multitarget super-resolution microscopy with high-density labeling by exchangeable probes. Nat. Methods 12, 743–746 (2015)
- J.R. Anderson, B.W. Jones, J.-H. Yang, M.V. Shaw, C.B. Watt, P. Koshevoy, J. Spaltenstein, E. Jurrus, U.V. Kannan, R. Whitaker, D. Mastronarde, T. Tasdizen, R. Marc, A computational framework for ultrastructural mapping of neural circuitry. PLoS Biol. 7(3), e1000074 (2009)
- J.R. Anderson, B.W. Jones, C.B. Watt, M.V. Shaw, J.H. Yang, D. Demill, J.S. Lauritzen, Y. Lin, K.D. Rapp, D. Mastronarde, P. Koshevoy, B. Grimm, T. Tasdizen, R. Whitaker, R.E. Marc, Exploring the retinal connectome. Mol. Vis. 17, 355–379 (2011)
- 17. D. Oberti, M.A. Kirschmann, R.H. Hahnloser, Projection neuron circuits resolved using correlative array tomography. Front Neurosci. 5, 50 (2011)
- F. Collman, J. Buchanan, K.D. Phend, K.D. Micheva, R.J. Weinberg, S.J. Smith, Mapping synapses by conjugate light-electron array tomography. J. Neurosci. 35(14), 5792–5807 (2015)
- E.B. Bloss, M.S. Cembrowski, B. Karsh, J. Colonell, R.D. Fetter, N. Spruston, Structured dendritic inhibition supports branch-selective integration in CA1 pyramidal cells. Neuron 89 (5), 1016–1030 (2016)
- R. Shahidi, E.A. Williams, M. Conzelmann, A. Asadulina, C. Verasztó, S. Jasek, L.A. Bezares-Calderón, G. Jékely, A serial multiplex immunogold labeling method for identifying peptidergic neurons in connectomes. Elife 4, e11147 (2015)
- J. Storm-Mathisen, A.K. Leknes, A.T. Bore, J.L. Vaaland, P. Edminson, F.M. Haug, O. P. Ottersen, First visualization of glutamate and GABA in neurones by immunocytochemistry. Nature 301(5900), 517–520 (1983)
- P. Somogyi, A.J. Hodgson, Antisera to gamma-aminobutyric acid. III. Demonstration of GABA in Golgi-impregnated neurons and in conventional electron microscopic sections of cat striate cortex. J. Histochem. Cytochem. 33(3), 249–257 (1985)
- R.E. Marc, B.W. Jones, C.B. Watt, J.R. Anderson, C. Sigulinsky, S. Lauritzen, Retinal connectomics: towards complete, accurate networks. Prog Retin Eye Res 37, 141–162 (2013)
- G. Pelletier, R. Puviani, O. Bosler, L. Descarries, Immunocytochemical detection of peptides in osmicated and plastic-embedded tissue. An electron microscopic study. J. Histochem. Cytochem. 29(6), 759–764 (1981)
- 25. A. Merighi, F. Cruz, A. Coimbra, Immunocytochemical staining of neuropeptides in terminal arborization of primary afferent fibers anterogradely labeled and identified at light and electron microscopic levels. J. Neurosci. Methods **42**(1–2), 105–113 (1992)
- A.J. Nielson, W.P. Griffith, Tissue fixation by osmium tetroxide. A possible role for proteins.
   J. Histochem. Cytochem. 27(5), 997–999 (1979)
- B.E. Causton, Does the embedding chemistry interact with tissue? in *The Science of Biological Specimen Preparation 1985*, ed. by M. Müller, R.P. Becker, A. Boyde, J. J. Wolosewick (SEM Inc, AMF O'Hare, Chicago), pp. 209–214
- 28. S.H. Brorson, F. Skjørten, The theoretical relationship of immunogold labeling on acrylic sections and epoxy sections. Micron 27(3–4), 193–201 (1996)
- G.R. Newman, J.A. Hobot, Modern acrylics for post-embedding immunostaining techniques.
   J. Histochem. Cytochem. 35(9), 971–981 (1987)
- E. Kellenberger, The Response of Biological Macromolecules and Supramolecular Structures to the Physics of Specimen Cryopreparation, in *Cryotechniques in Biological Electron Microscopy*, ed. by R.A. Steinbrecht, K. Zierold (Springer, Heidelberg, 1987), pp. 35–63
- A. Baude, Z. Nusser, E. Molnár, R.A. McIlhinney, P. Somogyi, High-resolution immunogold localization of AMPA type glutamate receptor subunits at synaptic and non-synaptic sites in rat hippocampus. Neuroscience 69, 1031–1055 (1995)
- 32. Z. Nusser, J.D. Roberts, A. Baude, J.G. Richards, W. Sieghart, P. Somogyi, Immunocytochemical localization of the alpha 1 and beta 2/3 subunits of the GABAA

- receptor in relation to specific GABAergic synapses in the dentate gyrus. Eur. J. Neurosci. 7, 630–646 (1995)
- A. Matsubara, J.H. Laake, S. Davanger, S. Usami, O.P. Ottersen, Organization of AMPA receptor subunits at a glutamate synapse: a quantitative immunogold analysis of hair cell synapses in the rat organ of Corti. J. Neurosci. 16, 4457–4467 (1996)
- K.W. Roche, C.D. Ly, R.S. Petralia, Y.X. Wang, A.W. McGee, D.S. Bredt, R.J. Wenthold, Postsynaptic density-93 interacts with the delta2 glutamate receptor subunit at parallel fiber synapses. J. Neurosci. 19, 3926–3934 (1999)
- 35. L.H. Bergersen, J. Storm-Mathisen, V. Gundersen, Immunogold quantification of amino acids and proteins in complex subcellular compartments. Nat. Protoc. 3, 144–152 (2008)
- A.L. Jacob, R.J. Weinberg, The organization of AMPA receptor subunits at the postsynaptic membrane. Hippocampus 25, 798–812 (2015)
- 37. J.B. Pawley, Handbook of Biological Confocal Microscopy (Plenum Press, New York, 1995)
- R. Heintzmann, C. Cremer, Lateral modulated excitation microscopy: improvement of resolution by using a diffraction grating. Proc. SPIE 3568, 185–196 (1999)
- M.G.L. Gustafsson, Surpassing the lateral resolution limit by a factor of two using structured illumination microscopy. J. Microsc. 198, 82–87 (2000)
- W.J. Wang, H.G. Tay, R. Soni, G.S. Perumal, M.G. Goll, F.P. Macaluso, J.M. Asara, J.D. Amack, M.F. Tsou, CEP162 is an axoneme-recognition protein promoting ciliary transition zone assembly at the cilia base. Nat. Cell Biol. 15(6), 591–601 (2013)
- C.J. Peddie, K. Blight, E. Wilson, C. Melia, J. Marrison, R. Carzaniga, M.C. Domart, P. O'Toole, B. Larijani, L.M. Collinson, Correlative and integrated light and electron microscopy of in-resin GFP fluorescence, used to localise diacylglycerol in mammalian cells. Ultramicroscopy 143, 3–14 (2014)
- P. Somogyi, A.J. Hodgson, I.W. Chubb, B. Penke, A. Erdei, Antisera to gamma-aminobutyric acid. II. Immunocytochemical application to the central nervous system. J. Histochem. Cytochem. 33, 240–248 (1985)
- 43. O.P. Ottersen, J. Storm-Mathiesen, Localization of amino acid neurotransmitters by immunocytochemistry. Trends Neurosci. 10, 250–255 (1987)
- 44. K. Weber, P.C. Rathke, M. Osborn, Cytoplasmic microtubular images in glutaraldehyde-fixed tissue culture cells by electron microscopy and by immunofluorescence microscopy. Proc. Natl. Acad. Sci. U S A 75(4), 1820–1824 (1978)
- 45. M.C. Willingham, An alternative fixation-processing method for preembedding ultrastructural immunocytochemistry of cytoplasmic antigens: the GBS (glutaraldehyde-borohydridesaponin) procedure. J. Histochem. Cytochem. 31(6), 791–798 (1983)
- 46. J.A. Terzakis, Uranyl acetate, a stain and a fixative. J. Ultrastruct. Res. 22, 168-184 (1968)
- 47. M.A. Berryman, R.D. Rodewald, An enhanced method for post-embedding immunocytochemical staining which preserves cell membranes. J. Histochem. Cytochem. **38**, 159–170 (1990)
- K.D. Phend, A. Rustioni, R.J. Weinberg, An osmium-free method of epon embedment that preserves both ultrastructure and antigenicity for post-embedding immunocytochemistry. J. Histochem. Cytochem. 43, 283–292 (1995)
- 49. A. Sawaguchi, S. Ide, Y. Goto, J. Kawano, T. Oinuma, T. Suganuma, A simple contrast enhancement by potassium permanganate oxidation for Lowicryl K4 M ultrathin sections prepared by high pressure freezing/freeze substitution. J. Microsc. 201, 77–83 (2001)
- J. Schindelin, I. Arganda-Carreras, E. Frise, V. Kaynig, M. Longair, T. Pietzsch, S. Preibisch,
   C. Rueden, S. Saalfeld, B. Schmid, J.Y. Tinevez, D.J. White, V. Hartenstein, K. Eliceiri,
   P. Tomancak, A. Cardona, Fiji: an open-source platform for biological-image analysis. Nat.
   Methods 9, 676–682 (2012)
- A. Cardona, S. Saalfeld, J. Schindelin, I. Arganda-Carreras, S. Preibisch, M. Longair, P. Tomancak, V. Hartenstein, R.J. Douglas, TrakEM2 software for neural circuit reconstruction. PLoS One 7(6), e38011 (2012)
- S. Saalfeld, R. Fetter, A. Cardona, P. Tomancak, Elastic volume reconstruction from series of ultra-thin microscopy sections. Nat. Methods 9, 717–720 (2012)

- J.D. Robertson, Ultrastructure of two invertebrate synapses. Proc. Soc. Exp. Biol. Med. 82, 219–223 (1953)
- 54. E.D. De Robertis, H.S. Bennett, Some features of the submicroscopic morphology of synapses in frog and earthworm. J. Biophys. Biochem. Cytol. 1(1), 47–58 (1955)
- S.L. Palay, Synapses in the central nervous system. J. Biophys. Biochem. Cytol. 2(4 Suppl), 193–202 (1956)
- R.T. Fremeau Jr., M.D. Troyer, I. Pahner, G.O. Nygaard, C.H. Tran, R.J. Reimer, E.E. Bellocchio, D. Fortin, J. Storm-Mathisen, R.H. Edwards, The expression of vesicular glutamate transporters defines two classes of excitatory synapse. Neuron 31, 247–260 (2001)
- 57. A. Graziano, X.B. Liu, K.D. Murray, E.G. Jones, Vesicular glutamate transporters define two sets of glutamatergic afferents to the somatosensory thalamus and two thalamocortical projections in the mouse. J. Comp. Neurol. **507**, 1258–1276 (2008)
- K.D. Micheva, D. Wolman, B.D. Mensh, E. Pax, J. Buchanan, S.J. Smith, D.D. Bock, A large fraction of neocortical myelin ensheathes axons of local inhibitory neurons. Elife 5. pii: e15784 (2016)
- H. Pawelzik, D.I. Hughes, A.M. Thomson, Physiological and morphological diversity of immunocytochemically defined parvalbumin- and cholecystokinin-positive interneurones in CA1 of the adult rat hippocampus. J. Comp. Neurol. 443, 346–336 (2002)
- D.D. Bock, W.C. Lee, A.M. Kerlin, M.L. Andermann, G. Hood, A.W. Wetzel, S. Yurgenson, E.R. Soucy, H.S. Kim, R.C. Reid, Network anatomy and in vivo physiology of visual cortical neurons. Nature 471(7337), 177–182 (2011)
- 61. C. Beaulieu, P. Somogyi, Targets and quantitative distribution of GABAergic synapses in the visual cortex of the Cat. Eur. J. Neurosci. 2, 296–303 (1990)
- 62. C. Beaulieu, Z. Kisvarday, P. Somogyi, M. Cynader, A. Cowey, Quantitative distribution of GABA-immunopositive and -immunonegative neurons and synapses in the monkey striate cortex (area 17). Cereb. Cortex. **2**, 295–309 (1992)
- 63. K.D. Micheva, C. Beaulieu, Quantitative aspects of synaptogenesis in the rat barrel field cortex with special reference to GABAcircuitry. J. Comp. Neurol. 373, 340–354 (1996)
- 64. R.R. Mize, R.H. Whitworth, B. Nunes-Cardozo, J. van der Want, Ultrastructural organization of GABA in the rabbit superior colliculus revealed by quantitative postembedding immunocytochemistry. J. Comp. Neurol. **341**, 273–287 (1994)

# **Chapter 7 Alignment of Tilt Series**

A. Verguet, C. Messaoudi, C. O. S. Sorzano and S. Marco

Abstract Computing of three-dimensional reconstructions from images obtained by transmission electron tomography needs three main steps: data acquisition, projection alignment, and 3D reconstruction. In this chapter we will focus on the process of alignment moving from the justification of its need to the study of the different classical approaches (cross-correlation, use of added fiducial markers) that have been commonly used in this alignment process. We will also discuss the most recent algorithms (multiscale registration, invariant feature recognition) as they have been adapted to Electron Tomography and improved to increase the accuracy and resolution of the final tomograms.

# 7.1 Why Do We Need to Align Tilt Series?

We may consider that tomography consists in determining a numerical representation in three dimensions of an object from their projections which requires the mathematical combination of the acquired projections by a process called reconstruction. In the case of transmission electron tomography (TET), these projections

A. Verguet

INSERM U1196, Centre Universitaire, Bat. 112, 91405 Orsay Cedex, France e-mail: amandine.verguet@ssji.net

C. Messaoudi

CNRS UMR9187, Centre Universitaire, Bat. 112, 91405 Orsay Cedex, France e-mail: cedric.messaoudi@curie.fr

C. O. S. Sorzano

Biocomputing Unit, National Center of Biotechnology (CSIC). C/Darwin, 3, Campus Universidad Autonoma (Cantoblanco), 28049 Madrid, Spain e-mail: coss@cnb.csic.es

S. Marco (\simeq)

Institut Curie, Centre de Recherche, Centre Universitaire, Bat. 112, 91405 Orsay Cedex, France

e-mail: sergio.marco@inserm.fr

© Springer International Publishing AG 2018
E. Hanssen (ed.), *Cellular Imaging*, Biological and Medical Physics,
Biomedical Engineering, https://doi.org/10.1007/978-3-319-68997-5\_7

are generated by tilting the object to be reconstructed around an axis. Therefore, the reconstruction process requires an accurate determination of the orientation of this axis, which is common to all projections, to combine them in a correct way. In addition, mathematical combination of projections needs that each one of the values on the 3D numerical representation of the reconstructed object has been estimated from data representing the same object at different tilt angles used during the acquisition process. In case that the orientation of the tilt axis is not precisely defined for each projection or that the values combined to compute the reconstruction do not correspond to an equivalent position in the original object, the mixed information will result into inaccurate results and artifacts. Some classical artifacts are blurred borders with small shifts or object deformation in "banana" or "star" shapes (see Fig. 7.1). A detailed explanation of geometrical artifacts can be found in [1].

In practice, as during the acquisition of the projection images the specimen is placed in a holder, which is physically tilted by a goniometer inside the imaging system, the precision and stability of motors to keep sample at the same exact position during acquisition is unattainable at the nanometer scale expected for TET. To compensate the lack of perfect tilting, automated acquisition tracks position and focus of sample. However, despite the high performance achieved, this compensation is still not enough and gives rise to shifts and rotations. In addition, the sample can be damaged during the acquisition process by suffering shrinkage or simply the compensation process can slightly modify the position of the focal plane.

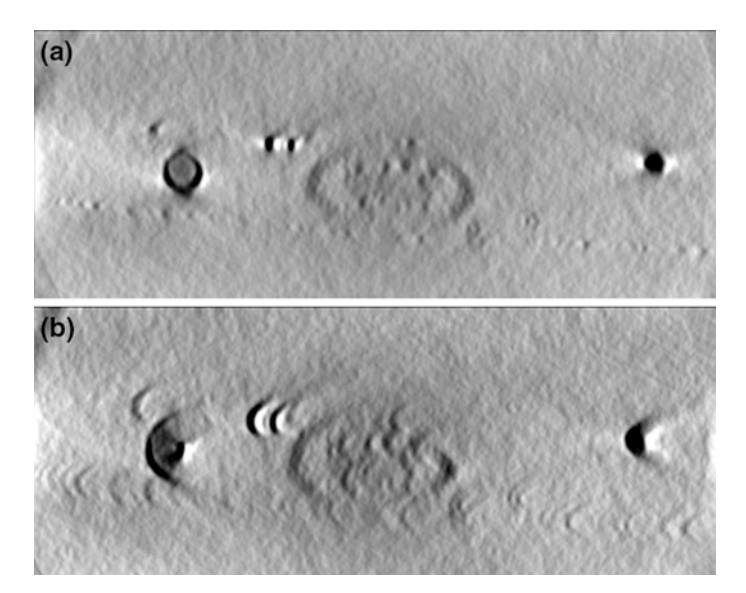


**Fig. 7.1** Reconstructions of *Pyrodictium abyssi*. **a** XZ from a reconstruction with correct alignment of tilt series images. **b** XZ from a reconstruction with incorrect alignment of tilt series images. It can be seen that spherical shape are elongated to the right in a shape similar to banana

This can lead to magnification changes or deformations in the recorded projections. The result is that the geometric relationships between the object and the obtained projections are not precisely known initially. Thus, a step of image alignment of these projection images is mandatory prior to compute accurate reconstructions. In this chapter, we will discuss different approaches to perform image alignment used with the aim of correcting most of the deviations from an ideal projection geometry. This means to describe methods to determine the geometrical relationships existing between the different projections of a tomographic tilt series.

Different approaches have been used to perform image alignment. The most classical one, frequently used to correct shifts between projections, is based on the maximisation of the cross-correlation existing between images [2-4]. However, this approach does not consider the existence of magnification changes or deformations cross-correlation, so that it is not good enough to align projections when shrinkage or change of focus occurs during the acquisition process which is not unusual in biological samples which are sensible to damages induced by the electron beam. A second way to perform image alignment, frequently used in biological samples, is to add fiducial gold colloidal markers to the sample. As gold beads can be localized very accurately, due to their spherical shape and high contrast, the alignments base on these markers are very accurate. In addition, if a large number of beads is used, the errors in their localization are averaged [5]. The marker-based methods have another advantage as it will generate a 3D model of their positions which guarantees a consistent alignment among the images from the full range of tilt angles. This 3D model can also be adapted to correct deformations induced in the sample during imaging. However, it is not always possible to use fiducial gold colloidal markers as they can interfere with reconstruction process (streak artifact for example [6]). Moreover, even if markers are added during sample preparation before observation, sometimes they are not uniformly distributed, being absent (or numbering not enough) in the region of interest for the reconstruction. To deal with this problem, approaches based on feature recognition have been developed. Thus, instead of adding external markers to the sample characteristic features are automatically extracted and tracked along the projection images of tilt-series before building 3D models prior to determine alignment parameters ().

# 7.2 Standard Alignment Process

As aforementioned, the acquisition of tilt series under the transmission electron microscope suffers from the goniometer and sample instabilities which main effects leads to shifts and in-plane rotations. To evaluate the accuracy of different alignment processes and algorithms it is frequent to use numerical phantoms which values are perfectly determined and which precisely simulate the different shifts, rotations or deformations to be corrected. Thus, it is possible to compare the parameters determined by algorithms or process to the simulated values included in

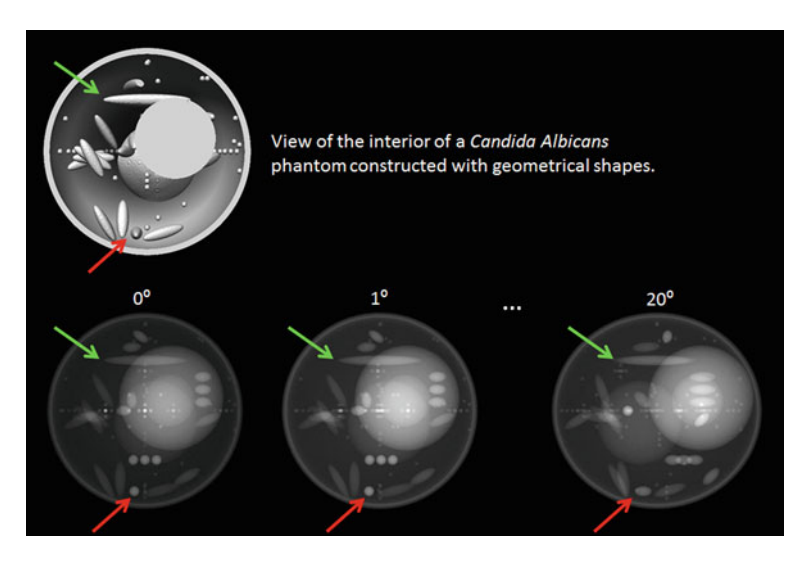


**Fig. 7.2** Phantom of a *Candida albicans* cell. In the top row, the cell has been virtually cut to show its interior. In the bottom row, projections at  $0^{\circ}$ ,  $1^{\circ}$  and  $20^{\circ}$  are shown. Typically, a tilt series go from  $-60^{\circ}$  to  $60^{\circ}$ 

the phantom. Therefore, we show in Fig. 7.2 the phantom of a *Candida albicans* cell and 3 of its projections at different angles  $(0^{\circ}, 1^{\circ}, \text{ and } 20^{\circ})$  that we will use for to illustrate how alignment approaches can identify the shift and rotation between two projection images and correct them as if they would have been acquired using a perfect goniometer.

As previously discussed, we can distinguish to main families of methods to align projections in a tomographic tilt series. The first family, which historically was the first used, considers all the information present in the projections, while the second family focus on a few confident points (points that can be precisely identified along the tilt series, see the arrows in Fig. 7.2). Since the first family of methods are frequently less accurate than those from the second family, they are usually used to precenter projections. This is done prior to the refinement of the alignment and to the determination of the orientation of the tilt axis, which is commonly performed by using methods based on 3D models of the positions of characteristic features.

# 7.2.1 Precentering the Tilt Series

Maybe, one of the first attempts to correct for the shifts was performed in 1982 by [4]. The idea was to exploit the similarity between projections at different tilts. Actually, if the difference between tilt angles is not large, the difference between the images is rather small (see tilt projections at 0° and 1° in Fig. 7.2) [4] performed a very detailed analysis of the modifications of the correlation function needed to

account for the fact that the two images being compared are coming from the same 3D object and are related by a single tilt operation. However, let us give one step back and introduce the correlation as a measure of similarity between two images.

Let us assume that we have two identical images whose relationship between both of them is a simple shift (see Figs. 7.1, 7.2 and 7.3). The cross-correlation function (called auto-correlation when only one image is used) between Figs. 7.1 and 7.2 may be defined as:

$$R_{1,2}(\Delta x, \Delta y) = \sum_{x,y} I_1(x - \Delta x, y - \Delta y)I_2(x,y)$$

This function is maximum when the two images maximally overlap. In this way, we may identify the shift  $\Delta_{1,2} = (\Delta x, \Delta y)$  required to go from Fig. 7.1 to Fig. 7.2, or viceversa  $\Delta_{2,1} = -\Delta_{1,2}$  (see Fig. 7.3). An interesting formula of this similarity estimator is that the location of the maximum is insensitive to linear transformations of the image intensities. Fortunately, this function can be calculated very quickly due to a property of the Fourier transform

$$R_{1,2}(\Delta x, \Delta y) = FT^{-1}\{FT\{I_1\}(FT\{I_2\})\}\$$

Therefore, all we have to do to determine the position that maximize the overlap between two images is to transform them to Fourier space, multiply the Fourier transform of one image by the complex conjugate of the other, and come back to real space. The simplicity of this operation has made that most packages to perform three-dimensional reconstructions from transmission electron microscopy

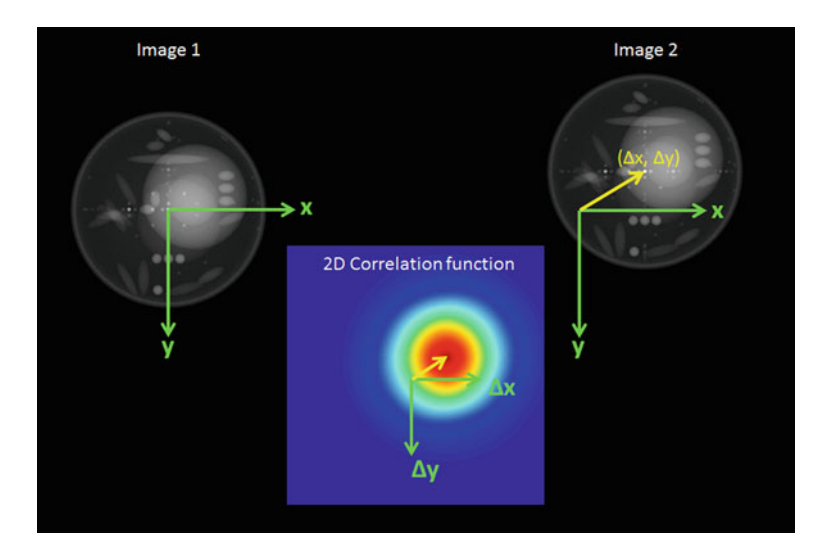


Fig. 7.3 Two identical images related by a shift, note that Image 2 is a shifted version [shifted by a vector displacement  $(\Delta x, \Delta y)$ ] of Image 1. The correlation function is maximum at the shifts required to go from Image 1 to Image 2

projections, include a tilt series alignment by cross correlation, as just described in this chapter and not in its modified version proposed by [4]. When this approach is applied to an experimental TET tilt series, the cross-correlation between two consecutive images,  $I_i$  and  $I_{i+1}$  is computed and the corresponding displacements  $(\Delta_{i,i+1})$  identified. This estimated displacement is a good estimation of the real shifts since in a tilt series, when the increment on the tilt angle is low, two consecutive images are almost the same (except for a shift, as illustrated in Fig. 7.2). Once the consecutive shifts are identified, we may find the relative shift between any two images i and j. For that, all images are translated to be centered with respect to the 0-tilt image. Let us illustrate this by representing a tilt series from  $-\theta_{\rm max}$  to  $\theta_{\rm max}$  degrees with increments of  $\Delta\theta$  degrees (e.g., from  $-60^{\circ}$  to  $60^{\circ}$  in steps of  $1^{\circ}$ ), with indexes from  $-i_{\rm max}$  to  $i_{\rm max}$  ( $i_{\rm max} = \theta_{\rm max}/\Delta\theta$ ). The shift needed to align an image with negative tilt to the 0-tilt image is just the accumulation from -i to 0 of all the consecutive shifts:

$$\mathbf{\Delta}_{-i,0} = \mathbf{\Delta}_{-i,-i+1} + \mathbf{\Delta}_{-i+1,-i+2} + \cdots + \mathbf{\Delta}_{-1,0} = \sum_{i=-1}^{-1} \mathbf{\Delta}_{-i,-j+1}$$

On the other side, for positive tilts, we need to accumulate the shifts in reverse order

$$m{\Delta}_{i,0} = -m{\Delta}_{i-1,i} - m{\Delta}_{i-2,i-1} - \dots - m{\Delta}_{0,1} = -\sum_{i=0}^{i-1} m{\Delta}_{j,j+1}$$

With these translations we may produce a new set of centered images  $\tilde{I}_i$ . Unfortunately, reality is not that easy for several reasons:

- Experimental images are extremely noisy, resulting in a noisy correlation function whose maximum may be spuriously misplaced (see Fig. 7.4).
- If one of the images is in-plane rotated with respect to the other, the correlation function is distorted with respect to the unrotated correlation function. This distortion may produce a totally incorrect estimation of the displacement vector (see Fig. 7.5).
- Local differences in the illumination conditions or the presence of a persistent illumination pattern totally distorts the correlation pattern (see Fig. 7.6).

Acknowledging these difficulties, we may try to robustly estimate the shifts between any two images. First, we can bandpass filter the images to remove any persistent illumination pattern, smooth local illumination variations (low frequency) as well as noise and small image details (high frequency) unnecessary to globally align two images. Once the images are bandpass filtered, they can be safely down-sampled, to reduce their size and speed-up calculations. Then, we may construct a polar 2D correlation function (the correlation function when the images are expressed in polar form). The location of the maximum in this polar correlation map indicates the optimal rotation [7]. In this way, we can identify both rotations and translations by alternating between looking for the best shift, then for the best rotation, and iterating several times this sequence till convergence.

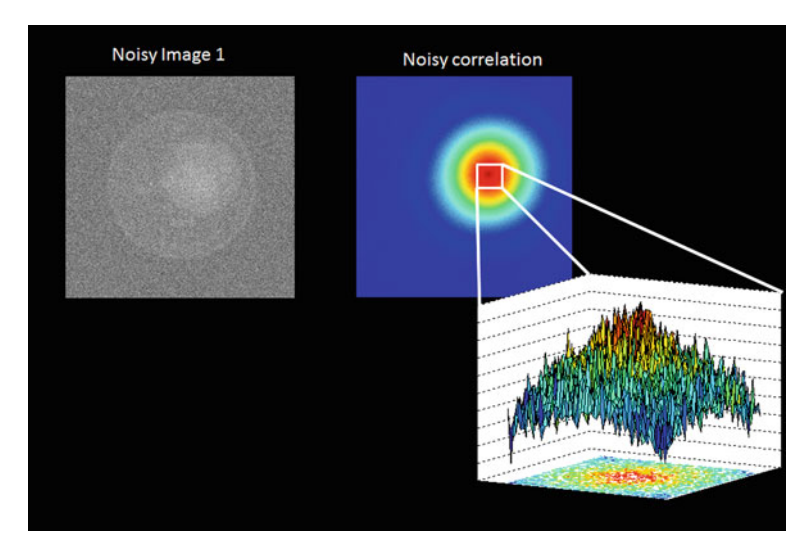


Fig. 7.4 Noisy Image 1, the corresponding correlation function with the Noisy Image 2, and a zoom of the summit of the correlation function

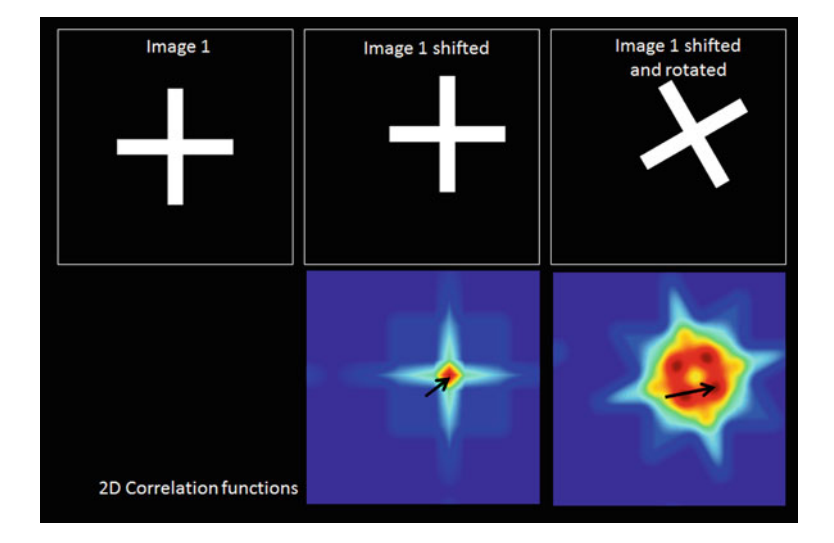


Fig. 7.5 Reference image (left), shifted image (middle) and shifted and rotated image (right), and their corresponding correlation functions. In the only shift case, the maximum of the correlation function correctly identifies the displacement vector, but this is not the case if there is also a rotation. Even small rotations of  $2^{\circ}-5^{\circ}$  may totally break the structure of the correlation function depending on the specific object being imaged

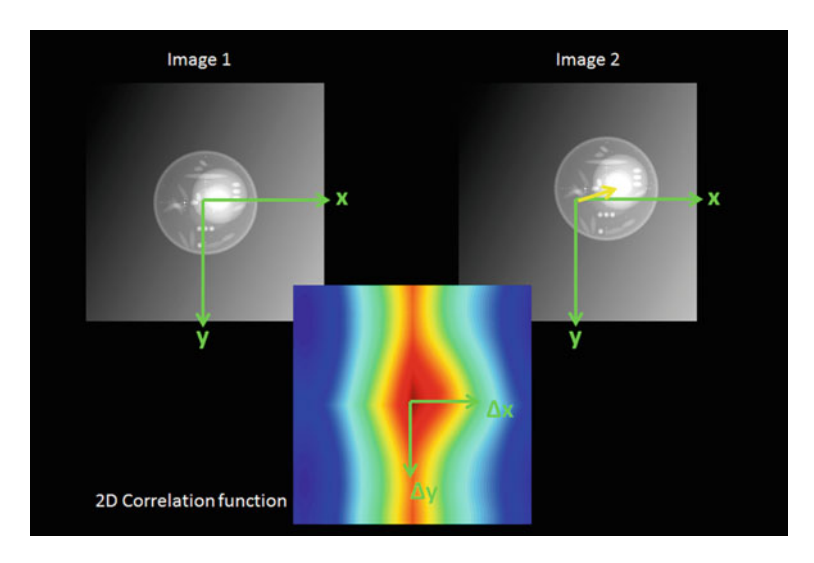


Fig. 7.6 The presence of a non-uniform illumination background, totally distorts the correlation structure

Correlations between images separated by small tilts  $(1^{\circ}-3^{\circ})$  are still good approximations to the hypothesis that the images being compared are the "same" simply related by an in-plane operation.

Combining all these strategies, we may safely calculate vector displacements between any two images i and j,  $\Delta_{i,j}$  (i < j and  $|j - i| \Delta \theta < \varepsilon$ , for a user selected  $\varepsilon$ ). Then, we can solve the overdetermined system of equations

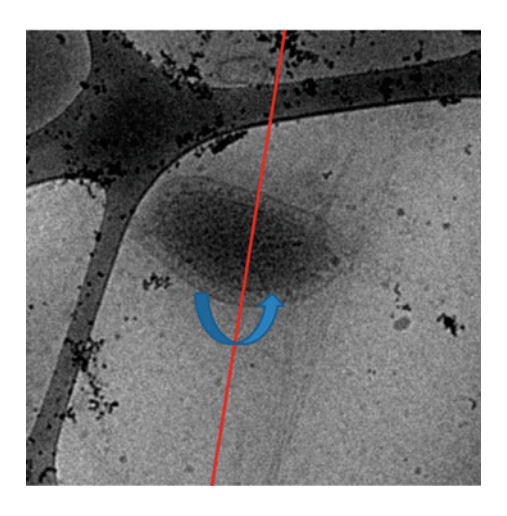
$$\Delta_{i,j} = \sum_{k=i}^{j-1} \Delta_{k,k+1}$$

as was done for Direct Detector frame alignment [8].

# 7.2.2 Determining the Orientation of the Tilt Axis

Once projection images on a tilt series are prealigned, they share a common orientation of the tilt axis. Thus the orientation of the tilt axis along the tilt series should not change and each projection in the tilt series should correspond to a different projection of the specimen at a given tilt angle. Therefore it is now possible to estimate the direction of this tilt axis used to generate the projections (see Fig. 7.7). Once identified, it is usually aligned with the vertical axis. Although this is not absolutely required to perform 3D reconstruction, it is convenient since it converts the 3D reconstruction problem into a 2D reconstruction problem conveying a speed-up of the reconstruction process by more than 1 order of magnitude.

Fig. 7.7 Tilt axis shown on a projection of *Pyrodictium abyssi* taken at the Electron Microscope. Ideally, the visualization of the whole tilt series should show a smooth transition from one image to the next in which the location and orientation of the tilt axis is fixed



The reason is that each slice can be reconstructed independently using the pixel values observed in each one of the rows of the aligned images.

Nevertheless, the accurate estimation of the direction of the tilt axis is not always possible from prealigned projections for different reasons: (1) the goniometer instabilities can induce some in-plane rotations which make the orientation of the tilt axis to be slightly different in each image; (2) our precentering of the images (previous section) is normally far from a perfect algorithm and although major movements have been corrected, there is still a non-negligible amount of shift between successive images; (3) more subtle, small errors during the centering of images may accumulate along the tilt series, so that there is an important accumulated drift from the beginning of the tilt series to its end. This latter error is the responsible of the "banana" shapes observed at the 3D reconstruction of misaligned tilt series.

Therefore, the accurate determination of the tilt axis direction in each one of the images is the most delicate process in the alignment process. For doing so, we need to identify corresponding points along the tilt series (see Fig. 7.8). These corresponding points in the projections are called 2D landmarks and they can be identified by different approaches:

- Manual, where markers are selected in each image of the tilt-series. The interest
  is the manual validation of corresponding points. However, the location of
  points are imprecise (a few pixels precision) and the process is not reproducible
  and time-consuming.
- Semi-automatic, where landmarks are manually selected on one image and the
  corresponding location on the other images is performed automatically. The
  interest is the manual selection of interesting points to track with an improvement of reproducibility and time consumption.
- Fully automatic, where the 2D landmarks are identified as any outstanding image feature like local maxima or minima [9] (Chap. 6), Harris corners [10], or any other feature detection algorithm could be employed (Fig. 7.8 show local

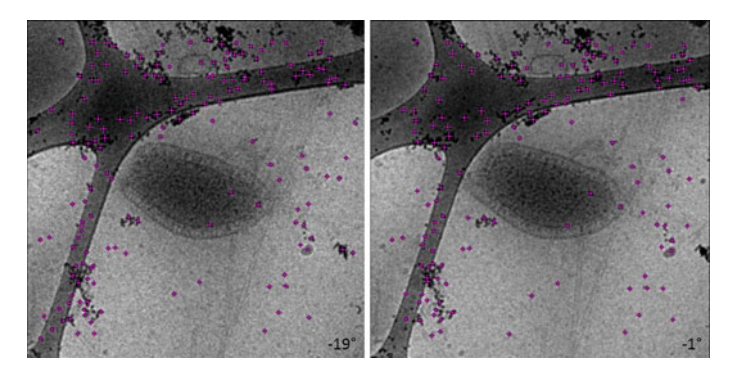


Fig. 7.8 Corresponding points between two projections at different tilt angles

minima features detected by TomoJ). Even small pieces of the image have been used once an initial alignment is manually provided by the user [11].

In many experiments, gold beads (seen as black dots in the images due to the high electron density of gold with respect to the biological material) are added to the sample. If case that they do not aggregate and that their distribution is good enough and uniform over the region of interest, they can be used as fiducial markers that can be easily tracked along the tilt series and so improve quality of alignment. However, adding gold beads is not strictly required for the alignment process because, even if gold beads are available, points that can be safely tracked along the tilt series can be frequently identified in the dataset. For instance, some of the points shown in Fig. 7.8 correspond to gold beads, but some others do not.

Once 2D landmarks (usually between 15 and 100) are identified on each image, the next step is to establish the correspondences between points in different images to obtain 2D landmark chains, i.e., tracking the same landmark along the tilt series (see Fig. 7.9). A landmark chain is allowed to have gaps (this means that the algorithm cannot find the landmark in a given projection, but it does in the projections before that image and after that image). The maximum gap length is normally selected by the user and frequently it is a number between 1 and 5 images; the larger the gap length, the higher the probability of tracking the wrong point. Each landmark chain is supposed to be related to a single (unknown) 3D landmark. This 3D landmark, when projected onto the different collected images, is located at different places. The coordinate of their projections depend as

$$\mathbf{p}_{ij} = A_{i,tiltAxis}\mathbf{r}_j + \mathbf{s}_i \tag{7.1}$$

That is, the coordinate of the *j*-th 3D landmark in image i,  $\mathbf{p}_{ij} \in \mathbb{R}^2$ , can be calculated using a matrix that depends on the orientation of the tilt axis in the *i*-th image and its tilt angle,  $A_{i,tiltAxis}$ , the 3D location of the landmark,  $\mathbf{r}_j \in \mathbb{R}^3$ , and a shift of the projection,  $\mathbf{s}_i \in \mathbb{R}^2$  (this shift should be ideally zero if the precentering was perfectly performed). This projection model is at the basis of a number of

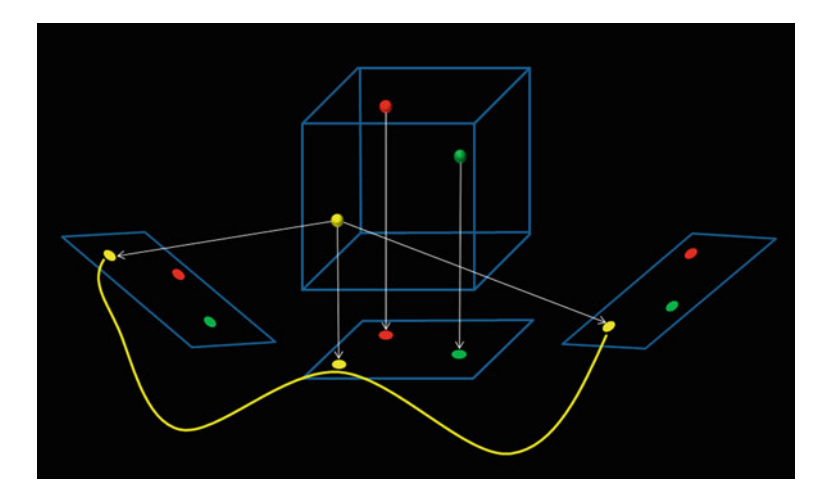


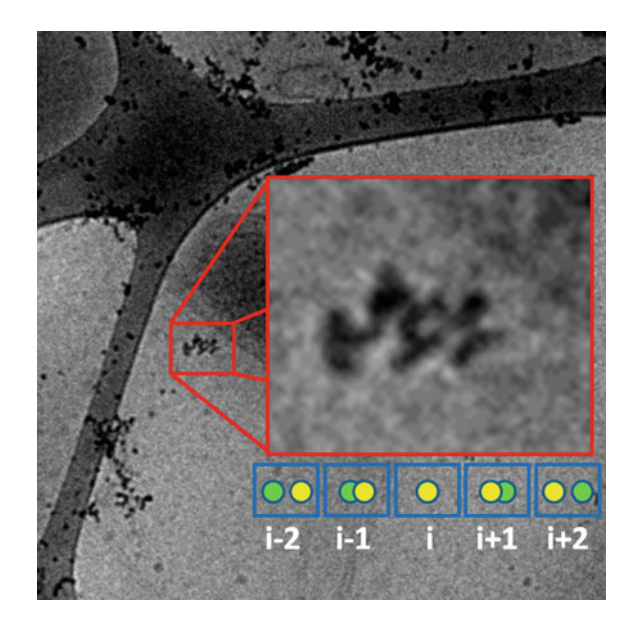
**Fig. 7.9** The 2D landmarks observed in each of the projections correspond to the projection of a 3D landmark (whose exact location has to be estimated). A landmark chain (like the yellow one highlighted in the figure) is formed by the set of 2D locations of the same 3D landmark projected at different tilt angles

works [10, 12–17]. A much more detailed description of the projection mathematics can be found at [18].

After having determined the landmark chains, it is possible to precisely compute the orientation of the tilt axis by finding the matrices  $A_{i,tiltAxis}$  and residual shifts  $\mathbf{s}_i$ . If there are  $N_{projections}$  in the tilt series, we need to estimate  $N_{projections}$  angles (the small rotations suffered by each projection),  $2N_{projections}$  shift parameters (x, y shifts)per image), and 2 parameters for the orientation of the tilt axis with respect to the electron beam. This makes a total of  $3N_{projections} + 2$  parameters. However, the process requires the estimation of the auxiliary variables  $\mathbf{r}_i$ . Thus, if we have an average of  $N_{chains}$  landmark chains per image, each with a (x, y, z) location, there would be a total of  $3N_{chains}N_{projections}$  extra parameters to estimate. Each point in the landmark chain brings 2 equations for an overdetermined equation system, and let us assume that on average the length of a chain is  $L_{chain}$ . Then, there are  $2N_{chains}N_{projections}L_{chain}$  equations and  $3N_{projections}(N_{chains}+1)+2$  unknowns. The ratio between the number of equations and the number of unknowns is approximately  $2/3L_{chain}$ . A typical value of  $L_{chain}$  is between 10 and 50, meaning that this is a highly overdetermined equation system. Therefore, this equation system can be easily solved by Least Squares [10, 12, 16], or by Least Squares combined with some statistically robust technique [14, 18].

An important problem of the construction of the landmark chains is the problem of landmark occlusion (illustrated in Fig. 7.10). When the projection of two landmarks overlaps, algorithms have difficulties in deciding which 2D landmarks go with which, and landmark chains are sometimes misconstrued mixing projections from several 3D landmarks. A robust resolution of the equation system at (7.1) tends to mitigate this effect.

Fig. 7.10 The projections of two 3D landmarks (green and yellow in the figure) may come close to each other as the tilt is increased. Eventually they overlap, and as the tilt keeps increasing they separate again. If instead of two 3D landmarks, the 3D landmarks tend to aggregate (as shown in the experimental image), then the problem is much more aggravated



Another source of problems during the alignment is the uneven distribution of landmarks along the tilt series. Normally at high tilts it is more difficult to distinguish 2D landmarks due to the thicker sample and resulting low contrast. Additionally, as the tilt increases, there are more chances of overlapping projections of different 3D landmarks resulting in a lack of reliable landmark chains covering high tilt angles. However, in spite of these difficulties, projection alignment and determination of the tilt-axis orientation is frequently feasible, but in some cases some advanced alignment methods are required.

# 7.3 Advanced Alignment Methods

In this section, we will explain and evaluate the interest of some improvements for image registration between two images suitable for the alignment of tilt series in electron tomography. Some of these improvements use global image information by applying a multiscale scheme associated to change in similarity measure. Others are based on registration of unique descriptors for points of interest.

# 7.3.1 Multiscale Registration

Most recent advances in image registration are based on multiscale scheme associated to gradient descent algorithms to determine the transformation between two

images. The main principle of multiscale scheme is to separate information in images at different scale. Coarse scales would then consist to main shapes and general features of the images while fine scales consist to details and noise. The decomposition allows a coarse-to-fine registration in which an initial transformation is found for the coarsest scales of the images and then it is refined using finer scales images. The use of this technique has many advantages:

- large transformations between two images can be found on coarser scales of images
- the signal-to-noise-ratio increases with coarser scales thus making it easier the finding of alignment
- as images at coarse level have less possible local minima, the robustness is increased
- part of the computation is done on smaller data and it need less time than computing everything on full size data

The multiscale decomposition can be done in several different ways. The simpler one is Gaussian pyramid where images size are reduced after applying a Gaussian filter in a pyramidal manner (Fig. 7.11). But other possibilities have also been proposed such as Laplacian pyramids [19], wavelets or BV,  $L^2$  decomposition [20].

The multiscale approach allows the use of different models for transformation: translation only, rigid transformation (translation and rotation), affine transformation (global deformations where straight lines stays straight) or non-rigid transformation (combination of global and local deformation). With translation only or rigid transformation the gain over classical cross-correlation is not so clear. The main interest is the increased robustness and by extension, a lower error propagation at the cost of higher computation time compared to Fourier calculations. However, translation, as aforementioned is not enough to correct most of deviation from the ideal projection geometry. The addition of deformation in the transformation could seem a good idea to correct deformations in projection geometry

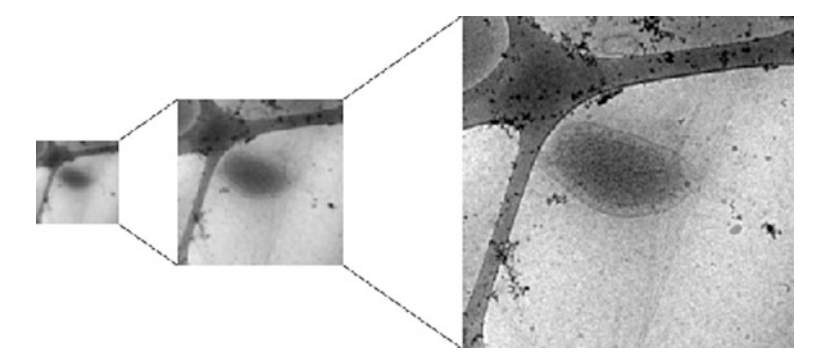


**Fig. 7.11** The gaussian pyramid is formed from original image (on the right), filtered with Gaussian filter and reduced in size to form coarser scale of image. The coarser scale is used first for correction of large transforms and then finer scale is used to further improve transform

(change in magnification or sample shrinkage for example). The problem arising is that images are easily aligned 2 by 2 without taking into account global projection geometry but then some deformations in images are due to change of tilt angle. It is then necessary to add some prior information such as tilt axis position and tilt angle of images to prevent some wrong correction in projection geometry. When information about tilt axis position and tilt angle is not known a priori, the possibility of deformation is unusable.

Once the type of transformation is fixed, the multiscale approach also allows different optimization techniques to find the best transformation. It can be brute force testing, where an exhaustive but limited set of possibilities is taken at each scale. It helps to stay around the local minima found at coarsest scale. Better optimization scheme involves the use of gradient descent algorithms, often powell or convex. The interests of these approaches were well debated in the medical imaging field [21–24] to register data in 2D and 3D from computer axial tomography (CAT), positron emission tomography (PET), magnetic resonance imaging (MRI) or ultrasound.

To estimate the better result of alignment, there is need of a metric. Many algorithms use mean (or sum) of square difference or correlation (see part 7.1 for more concise description), but other metrics exists such as mutual information. Mutual information was designed to allow the registration of images with very different contrasts [25, 26]. Formally, the mutual information of two discrete random variables X and Y can be defined as:

$$I(X;Y) = \sum_{x,y} p(x,y) log \frac{p(x,y)}{p(x)p(y)}$$

Where p(x,y) is the joint probability distribution function of X and Y, and p(x) and p(y) are the marginal probability distribution functions of X and Y respectively. In the case of 3D chemical mapping by EFTEM, mutual information was designed to align energy filtered images together between them or with zero-loss or plasmon images which represents the ultra-structural information. So, mutual information is needed to obtain better alignment between chemical and structural images (two modalities). Even if some studies demonstrated higher robustness and lesser sensitivity to noise [23], the higher computation cost over cross-correlation makes the use of mutual information approach questionable to align images coming from a single modality (ultra-structural tilt series from standard tomographic approach for example).

Multiscale registration allows to have sometimes a better alignment than cross-correlation methods but it does not compensate the fact that it is not sufficient as it will still align image two by two and so some propagation of errors will still occurs even if smaller. There is also need to take into account the fact that the information inside the image is a projection from a 3D sample and so the improvement is not competitive enough compared to feature-based registration. Therefore, multiscale registration is suitable for prealignment but it will frequently require further refinement based on landmarks.

# 7.3.2 Invariant Feature Recognition

A way to further improve alignment of tilt series is to optimize the detection of corresponding points in images of the tilt series. For this purpose, new approaches in object detection or panoramic stitching, based on the concept of Scale Invariant Feature Transform (SIFT), introduced by Lowe [27], have been proposed for alignment in electron tomography [28].

Feature-based alignment methods require several steps which are performed by separate algorithms. Here we will describe these steps which correspond to the common strategy used for image alignment using SIFT. Additionally to the emergence of this method many other algorithms appeared, providing alternatives for the different steps.

# • Detection of points of interest

First step is the detection of points of interest. To this purpose the algorithm has to choose points in the image which will be easy to locate in other images of the same sample. These points of interest are determined where the algorithm is able to recognize a feature which is based on mathematical properties, such as local extrema, and may not match physical features of the sample. This feature detection step is performed independently on all images of a series and leads to the creation of unique descriptors for each point of interest.

• Creation of a unique descriptor for each point of interest

With a set of point of interest on each image, alignment requires that they correspond to the same physical location on the feature to be matched. One way to achieve that is to rely on distinctive features. Most algorithms attach a single descriptor to each interest point for that purpose.

• Comparison of interest points between two or more images

The next step is to identify the matches in the sets of points of interest by comparing their descriptors. Once the point of interest, associated to the same feature, are grouped together they can be used to deduce the space transformation which occurred during the tilt-series acquisition.

#### 7.3.2.1 Methods to Detect the Points of Interest

Different mathematical methods can be used to perform the detection step which yields various shape of interest on the image: point, curve or area. The methods proposed in detection algorithms are essentially based on contours detection, i.e. the detection of variation of intensity levels on the area near the location of interest. In the case of the SIFT detection algorithm, each point of interest is identified by its location on the image (coordinates x, y), its gradient orientation, the scale factor and

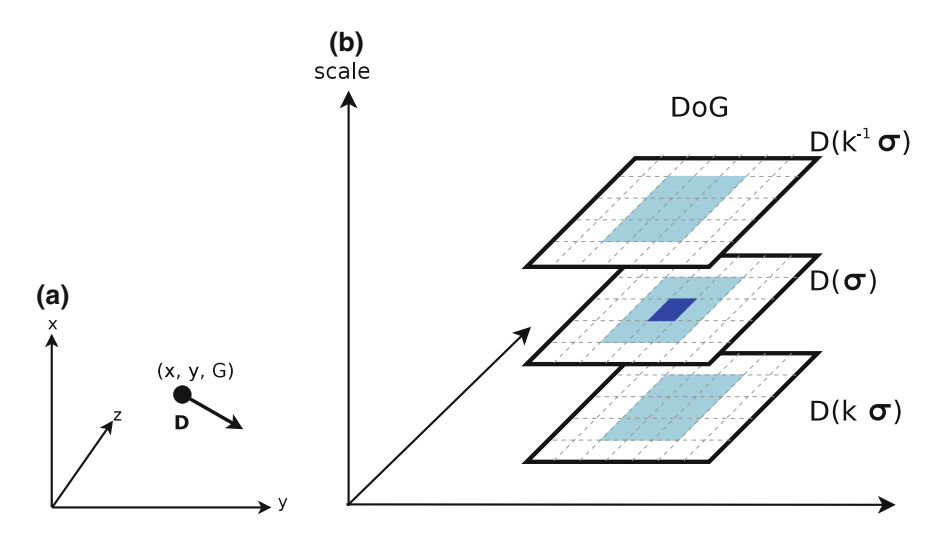


**Fig. 7.12** a An interest point is composed by its location, the gradient information and an unique descriptor noted D. b Diagram showing an example of the extremum detection during the computing of the difference of Gaussian for one point. The point of interest (dark blue) is evaluated from its neighborhood (light blue) between 3 different scales

finally a descriptor noted as D. The Fig. 7.12a is an example of the composition of an interest point.

In order to determine the location of the points of interest, the initial step is their detection at various image scales. For fulfilling this task, first the original image is reduced several times to obtain different scale levels, called octaves. For each image scale, a Gaussian blur is applied several times.

Second, in order to detect the local extrema, the computation of the Gaussian gradients is required at the same scale (Fig. 7.12b). Differences of Gaussians (DoG) are used on adjacent Gaussian in an octave. The different blur and octave can be represented as a pyramid of images as shown on Fig. 7.13.

Then, all local extrema are searched on all DoG at all scales. This defines the location of the interest points. It is stored along with the scale and convolution level that led to its detection. Afterwards, to obtain a position with a sub-pixel resolution it is possible to interpolate using a Taylor model. Moreover, the points with a low contrast or on an edge without curvature are eliminated.

Additionally to the location and scale, an orientation needs to be computed for each point of interest. This is obtained by filtering the gradients of multiple areas near the interest point. Once multiple gradients have been computed for some points of the neighborhood, an histogram is created. This histogram categorizes the orientations in a fixed number of classes which are weighted by the amplitude of gradients. At the end, the retained orientation of the point of interest is defined by the major orientation in the histogram (Fig. 7.14b).

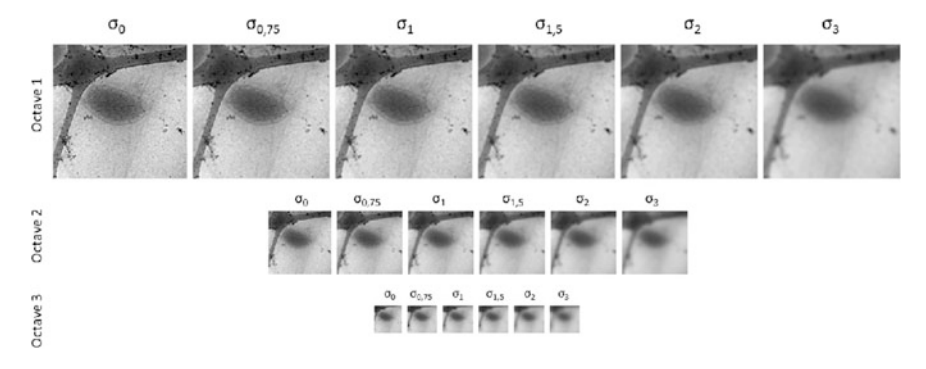
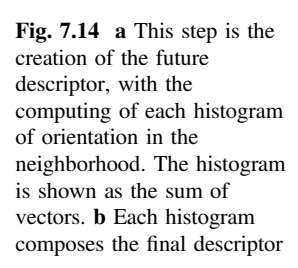
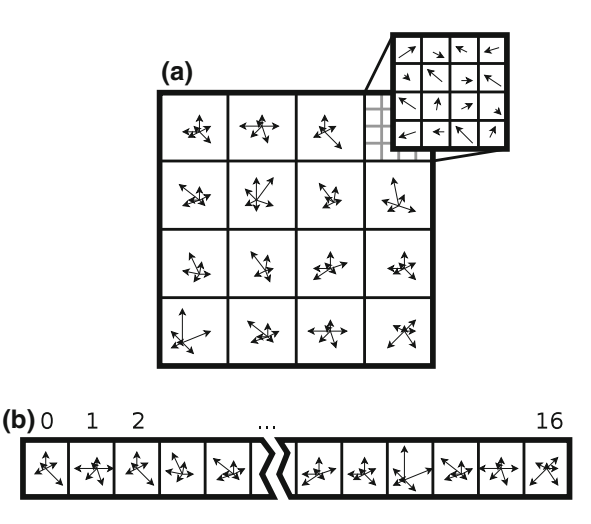


Fig. 7.13 This pyramid is obtained with a projection of *Pyrodictium abyssi* at several gaussian blurs and scales also called octave





There are several other alternate algorithms available for detection. Some are similar to the SIFT detection as they rely on the pyramid concept but using a differing convolution kernel. Here is a list of notable detection algorithms:

- Most blob detection methods are based on local differences in an image, as is the case for the search of local extrema. Several properties of the region of interest, like contrast and pixel intensity, are compared against surrounding regions. The difference of Gaussian presented previously is one of these methods. However, it is possible to use the Laplacian of Gaussian (LoG) or the difference of Hessian (DoH) instead.
- Some algorithms, like Harris corner and FAST (Features from Accelerated Segment Test [29]), are based on corners detection. They work by detecting corners which are the intersection of two edges on an image. This method is based on finding small patches in the image which are not similar to neighbor

A. Verguet et al.

patches. When a patch is located on a low contrast area, all close patches of a given size are similar. When the patch is located on a line or edge, close patches along the edge are similar too. This similarity is measured with the sum of squared differences of multiple patches being compared.

• Affine variants of the previous methods can be used to identify similar regions between images with scale change, rotation and shearing. Harris affine and Hessian affine are the most common.

#### 7.3.2.2 Construction of the Descriptor

Once interest points are detected, they must be made distinctive. To do so, one approach is to build a vector which depends on a small image patch near the interest point. There are two common methods used to compute a descriptor: SIFT and SURF. The SIFT descriptor is based on orientation histograms. The SURF (Speed-Up Robust Features) [30] descriptor is based on the sum of the Haar wavelet response around the point of interest.

In the SIFT algorithm, the calculation of the descriptor is similar to the last step of the detection process, but it is more computationally intensive. The descriptor is computed from an image area around the interest point, which is first transformed according to the scale and orientation computed during the detection phase. This ensures that the content of the descriptor is not sensitive to the image scaling and rotation. Thus, the descriptor only depends on the orientation and the amplitude of the gradient in multiple neighborhood areas of the point of interest. In order to create a descriptor having the aforementioned properties a common way to proceed is to determine the orientations in different  $4 \times 4$  pixels patches in the  $16 \times 16$  neighborhood of the interest point. Nevertheless, other patch sizes may be used. The Fig. 7.14 shows an example of gradient in each patch around an interest point. An histogram of orientations is then created for each patch. The final descriptor is composed by a vector containing values from all histograms.

The final size of the descriptor depends on the choice of patch size and the number of orientations classes in the histogram. For example, for a patch size of  $4 \times 4$  pixels and a number of orientation classes of 8, the histogram created will have a size of 36 like in the Fig. 7.14.

In this example, the values in each histogram of the 16 patches are organized according to 8 angles ( $0^{\circ}$ ,  $45^{\circ}$ ,  $90^{\circ}$ ,  $135^{\circ}$ ,  $180^{\circ}$ ,  $225^{\circ}$ ,  $270^{\circ}$ ,  $315^{\circ}$ ) for a final size vector of 128 values. Then the vector is normalized in sum unit to obtain contrast invariance. To be sure that the vector of the interest point will be invariant in front of the local affine transformations, each value is weighted in the histogram. The method allows having a descriptor more robust and unique for each interest point on the image.

As in the detection section, several other alternatives at the SIFT descriptor are available since some years. These alternatives are presented here as a non-exhaustive list:

• The ORB algorithm [31] is like SIFT divided in two major parts: the detection and the creation of a descriptor. ORB is based on the Features from Accelerated Segment Test (FAST) algorithm for the interest points detection and on the BRIEF algorithm [32] for the descriptor creation. The FAST algorithm relies on the corner detection method.

The BRIEF algorithm itself is based on the DAISY algorithm [33] which uses another type of descriptor which is a binary vector which created by following 3 steps:

- The research of a pattern around the interest point,
- The selection of several couple of points a
- The creation of the descriptor itself starting by a comparison of point intensity in each couple. If the value of the first point intensity is higher of the second, the value returned is 1, else it is 0. This way allows to obtain a binary chain whose the size is depending of the number of couples selected.

In the case of the binary descriptor, the pattern used can be different according to the algorithm.

- BRISK [34] is based on FAST algorithm for detection and inspired of BRIEF/DAISY for the descriptor creation, it used a concentric pattern to determined the neighborhood of the interest point.
- The Descriptor-Nets or D-net [35] is based on SIFT for detection, but guided random position are also proposed. The descriptor creation relies on paths connecting interest points in graph. Thus, it uses the information between nodes to create the descriptor instead of using neighborhood of interest points.

# 7.3.2.3 Comparison of Interest Points Between Two or More Image: Match and Alignment

Once the points of interest of two images are detected, the next step is to establish the match between the points of the first image with those of the second image.

This match between is determined by computing the Euclidian distance. The couple of interest points with the smallest distance is preserved. The difference between the two Euclidian distances of the interest points descriptor selected is then computed. The Fig. 7.15 is a diagram of the possible matches between three descriptors of three interest points.

The difference obtained is next compared with a user defined threshold and the match is considered strong when the difference computed is higher than the threshold. In this case, the point of interest of the first image and the best of the points selected in the second image are considered the same. This method of matching is considered as brute-force mechanism.

A. Verguet et al.

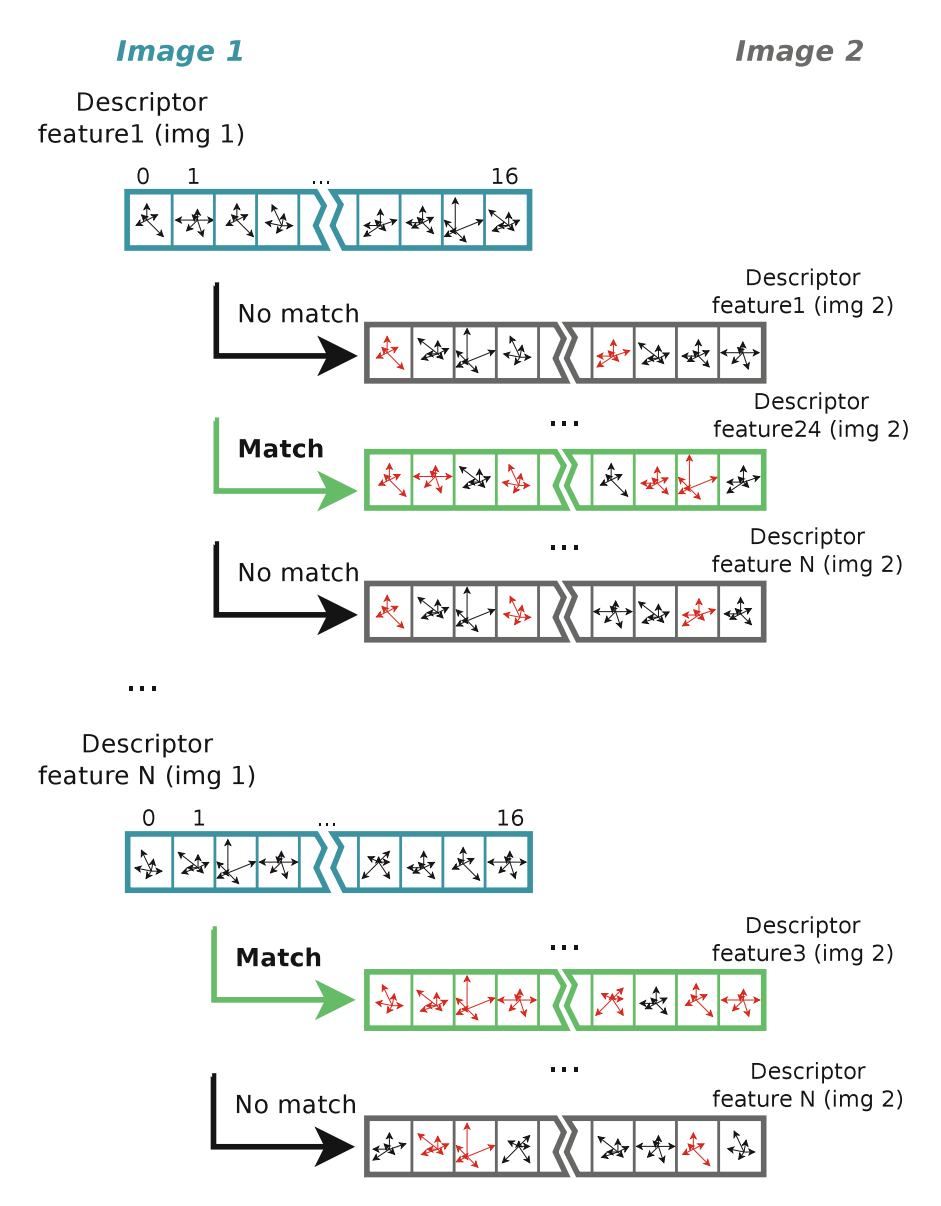


**Fig. 7.15** This diagram shows the research of the best match between each descriptor of the first image with each descriptor in the second image. In this example The red orientations are the cases of match between the descriptor of interest in the first image and each descriptor of the second

In the case of SIFT, the algorithm used to determine the parameters of the alignment of two images is the algorithm RANdom SAmple Consensus (RANSAC), an iterative algorithm proposed by Fischler and Bolles.

Summarizing, the algorithm SIFT is used to find common features between two images. These features are then used to find the parameters to align these two images. Since, tomography involves the alignment of a series of images acquired with different tilts angles, the detection step and the descriptor creation step must be performed for each image in the tilts series. The alignment step occurs once the matching of the descriptors associated to interest points have been determined for each couple of images in the tilts series. To align the images in the tilts series, an additional step of chain creation is needed. This mechanism consists in the tracking of each point of interest based on the results of the matching. The obtained chain can begin and end on any image. The chains of each point of interest along the sequence of images are used during the final alignment. The alignment model, allowing to determine the orientation of the tilt axis, that can be used in tomography is detailed in Sect. 2.2.

#### 7.4 Extension to Data Other than Tilt Series

#### 7.4.1 Data Alignment in Multiple-Axis Tomography

The impossibility to acquire a full 180° tilt series under the electron microscope generate a lack of information. To compensate this limitation two approaches are frequently used: N-axis tomography and sub-tomogram averaging. Both of then consist in combine reconstructed volumes in a single final reconstruction but they differ in the origin of data. In N-axis tomography several tomograms of a single object are combined whereas in sub-tomogram averaging tomograms of several objects are fused.

#### 7.4.1.1 N-Axis Tomography

N-axis tomography, allows to get back some of the missing information by acquiring multiple tilt series. The simplest approach is dual-axis tomography in which two tilt series are recorded with perpendicular tilt-axes [36, 37]. The use more than two axis has also been proposed [38, 39], but the higher dose and complexity of post-processing, compared to the gain of information is not valuable enough.

The reconstruction of data from N-axis tomography is performed by independent alignment and reconstruction of each tilt series followed by the determination of the geometric relationships between the different reconstructions. These relationships are computed using methods similar to those described in this chapter: correlation-based or landmarks-based approaches, but in three dimensions. Most of the time, software, such as imod [40], uses gold beads correspondences between the reconstructions to solve shifts, rotations and deformations such as shrinkage. Once aligned, tomograms

A. Verguet et al.

are combined in the Fourier space to take advantage of the precise positioning of the missing information in the Fourier transform. Thus, intensities for each frequency are generated by averaging non-null values, in the Fourier space, from tomograms to be combined.

#### 7.4.1.2 Sub-Tomogram Averaging

Sub-tomogram averaging consists in performing many independent reconstructions of biochemically identical or structurally similar objects (often macromolecular complexes) and then to average them to get a final reconstruction having higher resolution, less noise and without missing information artifacts [41]. To this purpose the objects are extracted from a single or from several tomograms. Since each one of the extracted object does not have the same orientation with respect to tilt axis, their missing information is different. Therefore, when combined, the lack of information of one extracted object is compensated by other objects. Such in N-axis tomography the information is combined in the Fourier space.

The computational process for sub-tomogram averaging is mainly adapted from single particle analysis approach [42]. This requires data alignment, classification and reconstruction averaging. Because of the missing information occurring in different orientation in each sub-tomogram, the major difficulty is the 3D alignment which need to consider this lack of information to compute the correlation functions in the Fourier space. Presently there are two main software devoted to sub-tomogram averaging: Dynamo [43] and Relion [44].

# 7.4.2 Serial Images Alignment

Nowadays an important effort is realized to get 3D information by other tomographic methods which are not based on the acquisition of tilt-series. In structural biology these methods are based on sample serial sectioning followed by image acquisition of each section. The most widespread methods are the serial block face (SBF) and dual-beam (FIB–SEM) in scanning electron microscopes and serial sectioning in transmission electron microscopy (ssTEM) or array tomography in scanning electron microscopes or light microscopy. The main differences between the first two methods and the latest ones are based on how sections are obtained. For SBF and FIB–SEM, resin embedded biological samples are directly sectioned and imaged in the electron microscope whereas in the other cases sections are produced before being deposited onto a support which is transferred to the microscope. Once serial images acquired, from the image processing point of view, the reconstruction process is identical independently of the acquisition method: images are superposed to produce a 3D reconstruction.

The limitation of this technique is associated to the anisotropy in the voxel size because X, Y dimensions depends on the electron microscope whereas Z dimension

relays on the sectioning system. In addition, the sectioning process lead to a rupture of the matter continuity in the sample and to deformations induced by sectioning forces when ultramicrotomes are used. Deformations and anisotropy should be taken in consideration to align images. Thus, a pre-alignment based on rigid alignment approaches is needed and, when deformations occur, it should be followed by elastic transformations computation to correct the deformations induced by sectioning. In both cases the methods used for axial-tomography described in previous sections of this chapter are valuable for both, rigid and elastic alignment. However, specific methods, based on squared difference [45, 46] or landmarks defined either manually or automatically using specific definition [47] or using SIFT [48], have been proposed for serial image alignment.

#### 7.5 Conclusion

Alignment of images in tomography is a crucial step to succeed in accurate reconstructions process. In spite that several methods and algorithms exist, while tomography trends towards new frontiers such as 3D chemical mapping, there is an active research on this field of image processing. Thus, from classical approaches, based on cross-correlation and on the use of gold-beads as fiducial markers, we move nowadays to more robust methods allowing the correction of image deformations or the automatic determination of inherent landmarks. Thus, it is expected that in near future, the advances in image alignment will contribute to the development of high-through flow tomography integrated in a multimodal and multiscale 3D imaging approach.

#### References

- B. Turoňová, L. Marsalek, P. Slusallek, On geometric artifacts in cryo electron tomography. Ultramicroscopy 163, 48–61 (2016)
- J. Frank, B.F. McEwen, M. Radermacher, J.N. Turner, C.L. Rieder, Three-dimensional tomographic reconstruction in high voltage electron microscopy. J. Electron Microsc. Tech. 6, 193–205 (1987)
- J. Frank, B.F. McEwen, Alignment by cross-correlation. Electron Tomogr (Springer Science, 1992), pp. 205–213
- 4. R. Guckenberger, Determination of a common origin in the micrographs of titl series in three-dimensional electron microscopy. Ultramicroscopy 9, 167–174 (1982)
- S. Brandt, J. Heikkonen, P. Engehardt, Automatic alignment of transmission electron microscope tilt series without fiducial markers. J. Struct. Biol. 136, 201–213 (2001)
- M. Cao, H.-B. Zhang, Y. Lu, R. Nishi, A. Takaoka, Formation and reduction of streak artefacts in electron tomography. J. Microsc. 239(1), 66–71 (2010)
- Y. Cong, J.A. Kovacs, W. Wriggers, 2D fast rotational matching for image processing of biophysical data. J. Struct. Biol. 144(1-2), 51-60 (2003)

A. Verguet et al.

8. X. Li, P. Mooney, S. Zheng, C.R. Booth, M.B. Braunfeld, S. Gubbens, D.A. Agard, Y. Cheng, Electron counting and beam-induced motion correction enable near-atomic-resolution single-particle cryo-EM. Nature Methods **10**(6), 584–590 (2013)

- 9. M. Petrou, C. Petrou, *Image processing: The Fundamentals*. (John Wiley & Sons, 2010)
- S. Brandt, J. Heikkonen, P. Engehardt, Multiphase method for automatic alignment of transmission electron microscope images using markers. J. Struct. Biol. 133, 10–22 (2001)
- 11. H. Winkler, K.A. Taylor, Accurate marker-free alignment with simultaneous geometry determination and reconstruction of tilt series in electron tomography. Ultramicroscopy **106** (3), 240–254 (2006)
- 12. S. Brandt, J. Heikkonen, Optimal method for the affine F-matrix and its uncertainty estimation in the sense of both noise and outliers. In *Proc. of the 8th IEEE Intl. Conf. on Computer Vision (ICCV)* (Vancouver, Canada, 2001), pp. 166–173
- F. Cantele, E. Paccagnini, G. Pigino, P. Lupetti, S. Lanzavecchia, Simultaneous alignment of dual-axis tilt series. J. Struct. Biol. 169(2), 192–199 (2010)
- D. Castaño-Díez, A. Al-Amoudi, A.M. Glynn, A. Seybert, A.S. Frangakis, Fiducial-less alignment of cryo-sections. J. Struct. Biol. 159(3), 413–423 (2007)
- D. Castaño-Díez, A. Seybert, A.S. Frangakis, Tilt-series and electron microscope alignment for the correction of the non-perpendicularity of beam and tilt-axis. J. Struct. Biol. 154, 195– 205 (2006)
- M.C. Lawrence, Least-squares method of alignment using markers. Electron tomogr. (Springer, 1992), pp. 197–204
- 17. P. Penczek, M. Marko, K. Buttle, J. Frank, Double-tilt electron tomography. Ultramicroscopy **60**(3), 393–410 (1995)
- C.O.S. Sorzano, C. Messaoudi, M. Eibauer, J.R. Bilbao-Castro, R. Hegerl, S. Nickell, S. Marco, J.M. Carazo, Marker-free image registration of electron tomography tilt-series. Bmc Bioinf. 10(1), 1 (2009)
- P.J. Burt, E.H. Adelson, The Laplacian pyramid as a compact image code. Commun. IEEE Trans. 31(4), 532–540 (1983)
- E. Tadmor, S. Nezzar, L. Vese, A multiscale image representation using hierarchical (BV, L 2) decompositions. Multiscale Model. Simul. 2(4), 554–579 (2004)
- S. Klein, M. Staring, J.P.W. Pluim, Evaluation of optimization methods for nonrigid medical image registration using mutual information and B-splines. Image Process. IEEE Trans. 16 (12), 2879–2890 (2007)
- 22. V.R.S. Mani, S. Arivazhagan, J.J. Braino, Multimodal image fusion using multiresolution techniques. Elixir Adv. Engg. Info. A. 55, 13160–13163 (2013)
- D.C. Paquin, D. Levy, E. Schreibmann, L. Xing, Multiscale image registration. Mathematics 5 (2006)
- P.J. Slomka, R.P. Baum, Multimodality image registration with software: state-of-the-art. Eur.
   J. Nucl. Med. Mol. Imaging 36(1), 44–55 (2009)
- A. Collignon, F. Maes, D. Delaere, D. Vandermeulen, P. Suetens, G. Marchal, Automated multi-modality image registration based on information theory. Inf. Process. Med. Imaging 263–274 (1995)
- W.M. Wells, P. Viola, H. Atsumi, S. Nakajima, R. Kikinis, Multi-modal volume registration by maximization of mutual information. Med. Image Anal. 1(1), 35–51 (1996)
- D.G. Lowe, Distinctive image features from scale-invariant keypoints. Int. J. Comput. Vis. 60

   (2), 91–110 (2004)
- 28. R. Han, F. Zhang, X. Wan, J.-J. Fernández, F. Sun, Z. Liu, A marker-free automatic alignment method based on scale-invariant features. J. Struct. Biol. **186**(1), 167–180 (2014)
- E. Rosten, T. Drummond, Machine learning for high-speed corner detection. Comput. Vision–ECCV 2006 (Springer, 2006), pp. 430–443
- H. Bay, T. Tuytelaars, L. Van Gool, Surf: speeded up robust features. Proc. Computer Vision-ECCV (2006)

- E. Rublee, V. Rabaud, K. Konolige, G. Bradski, ORB: an efficient alternative to SIFT or SURF. In Computer Vision (ICCV), 2011 IEEE International Conference on, pp. 2564–2571 (IEEE) (2011)
- M. Calonder, V. Lepetit, M. Ozuysal, T. Trzcinski, C. Strecha, Pascal Fua, BRIEF: computing a local binary descriptor very fast. IEEE Trans. Pattern Anal. Mach. Intell. 34, 1281–1298 (2012)
- 33. Engin Tola, Vincent Lepetit, Pascal Fua, Daisy: an efficient dense descriptor applied to wide-baseline stereo. Pattern Anal. Mach. Intell. IEEE Trans. 32(5), 815–830 (2010)
- S. Leutenegger, M. Chli, R.Y. Siegwart, BRISK: binary robust invariant scalable keypoints.
   In Computer Vision (ICCV), 2011 IEEE International Conference on, pp. 2548–2555 (IEEE) (2011)
- 35. F. Von Hundelshausen, R. Sukthankar, D-nets: beyond patch-based image descriptors. In *Computer Vision and Pattern Recognition (CVPR), 2012 IEEE Conference on*, pp. 2941–2948 (IEEE) (2012)
- S. Lanzavecchia, F. Cantele, P.L. Bellon, L. Zampighi, M. Kreman, E. Wright, G.A. Zampighi, Conical tomography of freeze-fracture replicas: a method for the study of integral membrane proteins inserted in phospholipid bilayers. J. Struct. Biol. 149(1), 87–98 (2005)
- D.N. Mastronarde, Dual-axis tomography: an approach with alignment methods that preserve resolution. J Struct. Biol. 120(3), 343–352 (1997)
- S. Hata, H. Miyazaki, S. Miyazaki, M. Mitsuhara, M. Tanaka, K. Kaneko, K. Higashida, K. Ikeda, H. Nakashima, S. Matsumura, and others, High-angle triple-axis specimen holder for three-dimensional diffraction contrast imaging in transmission electron microscopy. Ultramicroscopy. 111(8), 1168–1175 (2011)
- C. Messaoudi, N.Garreau Loubresse, T. Boudier, P. Dupuis-Williams, S. Marco, Multiple-axis tomography: applications to basal bodies from Paramecium tetraurelia. Biol. Cell 98(7), 415–425 (2006)
- 40. J.R. Kremer, D.N. Mastronarde, J.R. McIntosh, Computer visualization of three-dimensional image data using IMOD. J. Struct. Biol. 71–76 (1996)
- 41. J.A.G. Briggs, Structural biology in situ–the potential of subtomogram averaging. Curr. Opin. Struct. Biol. 23(2), 261–267 (2013)
- 42. J. Frank, Three-Dimensional Electron Microscopy of Macromolecular Assemblies: Visualization of Biological Molecules in Their Native State (Oxford Univ. Press, New York, USA, 2006)
- 43. D. Castaño-Dez, M. Kudryashev, M. Arheit, H. Stahlberg, Dynamo: a flexible, user-friendly development tool for subtomogram averaging of cryo-EM data in high-performance computing environments. J. Struct. Biol. **178**(2), 139–151 (2012)
- 44. A.M.B. Tanmay, J.R. Christophe, L. Jan, A.P. Lori, H.W.S. Sjors, Advances in single-particle electron cryomicroscopy structure determination applied to sub-tomogram averaging. Structure 23(9), 1743–1753 (2015)
- 45. I. Arganda-Carreras, C.O.S. Sorzano, J. Kybic, C. Ortiz de Solórzano, bUnwarpJ: consistent and Elastic Registration in ImageJ. Methods and Applications. *Proc. Conference Image J Users-Developers*, Luxembourg (2008)
- 46. C.O.S. Sorzano, P. Thévenaz, M. Unser, Elastic registration of biological images using vector-spline regularization. IEEE Trans. Biomed. Eng. **52**(4), 652–663 (2005)
- 47. C.-W. Wang, E.B. Gosno, Y.-S. Li, Fully automatic and robust 3D registration of serial-section microscopic images. Sci. R. 5 (2015)
- 48. S. Saalfeld, R. Fetter, A. Cardona, P. Tomancak, Elastic volume reconstruction from series of ultra-thin microscopy sections. Nat. Methods **9**(7), 717–720 (2012)

# Chapter 8 Tomographic Reconstruction from Electron Micrographs

#### J. Bernard Heymann

**Abstract** Reconstruction from a tilt series of electron micrographs is based on the assumption that each image represents a projection through the specimen, and that the 3D information can be recovered by "back-projecting" all the images in the correct geometry. We use algorithms that are integrative (back-projection or Fourier inversion) or iterative (algebraic or maximum entropy methods). In practical tomography, we can only record a finite set of images at a dose low enough to avoid radiation damage, yielding noisy tomograms with missing information. The quality of the tomograms depends on the algorithmic details, but also on the pre-processing of the tilt series images, and post-processing of the tomographic volume.

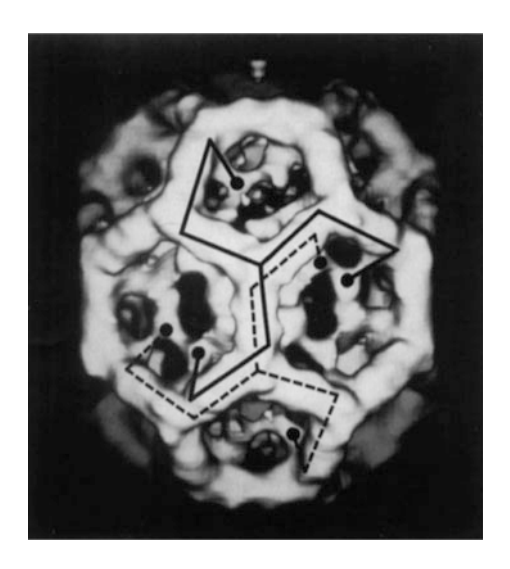
#### 8.1 Principles of Reconstruction

Any modality of imaging yields by nature a two-dimensional (2D) image of a three-dimensional (3D) object or scene. In the electron microscope (as in X-ray imaging), we treat the images as projections because of the large depth-of-focus [1]. The image is approximated to a good degree as an integration of the density along the beam direction. Radon [2, 3] showed that it is in principle possible to recover the 3D information from such images taken with different projection directions. Herman [4] reminded us that implementing such a mathematical operation is non-trivial, given that (i) we only have a finite number of images, (ii) there are inaccuracies in the measurements, and (iii) an efficient approach is required. de Rosier and Klug [1] formulated the first practical implementation of reconstruction from micrographs in frequency space (FSR or frequency space reconstruction). Around the same time, real space reconstruction algorithms were developed, including weighted back-projection (WBP) [5] and the algebraic reconstruction technique (ART) [6]. These algorithms form the basis of most subsequent

National Institute of Arthritis, Musculoskeletal and Skin Diseases, National Institutes of Health, 50 South Dr, Bethesda, MD 20892, USA e-mail: heymannb@mail.nih.gov

J. Bernard Heymann (⋈)

Fig. 8.1 The first electron tomographic reconstruction. Four clathrin cages with the same symmetry (D6) were reconstructed and averaged from a tilt series (-30° to 30° with a 6° step) of cryo-electron micrographs [7]



reconstruction approaches. de Rosier and Klug also mentioned the idea of a tilt series to determine individual 3D structures [1]. Vigers et al. [7] reported the first reconstruction (WBP) from an electron tomographic tilt series of clathrin cages. They averaged several cages with D6 symmetry to produce the first subtomogram application in electron microscopy (Fig. 8.1).

The principle of 3D reconstruction from 2D projection images is conceptually straightforward. The real space integration of the density through a 3D object in a particular direction is equivalent to a central section in the transform of the 3D volume (this is referred to as the projection-slice theorem, central section theorem or Fourier slice theorem [8]). These two representations therefore pose the two ways in which we do reconstructions: in real space, the projection is "back-projected" along the direction of the original projection; in frequency space (also called Fourier space or reciprocal space), the projection transform is added as a central section to the 3D frequency space volume in the correct orientation (see Sect. 8.2). A second class of algorithms aims at iteratively minimizing the difference between the original images and reprojections from the reconstruction (see Sect. 8.3). The practical issues that differentiate reconstruction algorithms are weighting schemes and interpolation, resulting in different levels of artifacts and noise. The weighting stems from the overlap of central sections in frequency space, leading to an overrepresentation of low-frequency information. The projection images are in most cases sampled on grids different from that of the reconstruction volume. This means that some interpolation is required in both real and frequency space. If all this is done correctly, the quality of the reconstruction is then a function of the number of contributing images, the signal-to-noise ratio (SNR) of the images, and the alignment accuracy (see Chap. 7—I assumed here that the images have been properly aligned).

While the actual production of a 3D volume from 2D images is the central operation in reconstruction, the quality of the result is strongly influenced by

pre-processing the images, as well as post-processing to facilitate interpretation. In real space, we typically normalize the original tilt series, remove high contrast features such as X-ray specks and fiducial markers, and do limited denoising (see Sect. 8.4). When we desire to recover high resolution information, we need to correct for the contrast transfer function (CTF) in frequency space (the equivalent of the point spread function in real space—see Sect. 8.5).

Post-processing is largely concerned with removing noise (see Sect. 8.6) and compensating for missing information. The low dose used in tomography (to avoid radiation damage) means a low SNR and noisy tomograms. The various reconstruction algorithms show differences in the noise level of the initially reconstructed tomogram, but there is almost always a need for further denoising. An integral second step in reconstruction is therefore to remove sufficient noise to allow proper interpretation (segmentation is very sensitive to noise—see Chap. 12). All denoising algorithms decrease detail in the tomograms (see Chap. 11). Therefore, the user determines the level of denoising with the aim of emphasizing the desired detailed structures with as little confusion attributed to noise as possible (see Sect. 8.6).

The limited tilt range in the electron microscope as well as a finite number of images give rise to missing information (i.e., poorly represented regions in frequency space—see Sect. 8.7). The result is highly anisotropic resolution, with apparent elongation of features in the beam direction and suppression of features perpendicular to the tilt axis. Dual and conical tilt acquisition schemes alleviate some of the loss, but to a limited extent. If we image a specimen with a repeating structure (such as isolated viruses), we can average such structures to decrease noise, fill in missing information and recover higher resolution information (see Sect. 8.8 and Chap. 9).

Numerous programs have been written to do 3D reconstructions (Table 8.1). While the basic concepts remain the same, the differences lie in the details of weighting and interpolation. Many denoising algorithms have been developed to deal with the typical low SNR in tomograms (Table 8.2). A more comprehensive list of software packages is available at <a href="https://en.wikibooks.org/wiki/Software\_Tools\_For\_Molecular\_Microscopy">https://en.wikibooks.org/wiki/Software\_Tools\_For\_Molecular\_Microscopy</a>.

# **8.2 Integrative Reconstruction**

The simplest reconstruction approach is to reverse the projection operation, either in real space or frequency space. The advantage of a straightforward integration algorithm is that it involves only the interpolation and weighting issues. Dealing with noise and missing information is done in subsequent steps.

Table 8.1 Software packages with tools for tomographic reconstruction (For more, see https://en.wikibooks.org/wiki/Software\_Tools\_For\_Molecular\_ Microscopy)

Package	Algorithm(s)	Remarks	Coding environment	Web site	References
ASTRA toolbox	WBP, SIRT, CGLS	Flexible plugins	CUDA/C++/ Matlab/python	http://visielab.uantwerpen.be/research/tomography	[87]
ATOM/ICON/FIRT	WBP, ART, SIRT, FIRT, ICON		С	http://feilab.ibp.ac.cn/LBEMSB	[67, 88, 89]
Bsoft	FSR	Simultaneous dual tilt reconstruction	C++/TcITk	http://bsoft.ws	[12]
ЕМЗБ	WBP	Defunct? (last 2011)	Java/C++ -	http://em3d.stanford.edu	[06]
Ettention	WBP, BIR, TF-ART, SIRT, SART	Integrated into eTomo	C++/Java	http://www.ettention.org	[91]
IMOD/ eTomo	WBP, GFSR, SIRT	Combining dual tilt and large volume tomograms	FORTRAN/C/Java	http://bio3d.colorado.edu/imod/	[27]
Protomo	WBP		FORTRAN/C/Python	http://www.electrontomography.org	[92]
PyTom	WBP, INFR		C++/Python	http://pytom.org	[73]
Tom toolbox	WBP		Matlab	http://www.biochem.mpg.de/tom/	[63]
Tomo3D	WBP, SIRT		C (threaded)	https://sites.google.com/site/3demimageprocessing/tomo3d	[94]
TomoJ	WBP, ART, SIRT	ImageJ plugin	Java	http://cmib.curie.fr/en/download/softwares/TomoJ	[95]
TxBR	WBP	Large volume reconstruction	Matlab	https://confluence.crbs.ucsd.edu/display/ncmir/TxBR	[96]
Xplore3D (FEI)	WBP, ART, SIRT	Proprietary	(Windows)	http://www.fei.com/life-sciences/	

WBP Weighted back-projection

GFSR Gridded frequency space reconstruction FSR Frequency space reconstruction

INFR Iterative non-uniform fast Fourier reconstruction

ART Algebraic reconstruction technique TF-ART Tilt-focal ART

ATOM Algebra TOMography package

FIRT Filtered iterative reconstruction technique

ICON Iterative compressed-sensing optimized non-uniform fast Fourier transform reconstruction SIRT Simultaneous iterative reconstruction technique

SART Simultaneous algebraic reconstruction technique

BIR Block-iterative reconstruction CGLS Krylov subspace least squares congruent gradients analytical solver

#### 8.2.1 Weighted Back-Projection (WBP)

This is by far the most common reconstruction algorithm used due to its simplicity (notice several implementations in Table 8.1). The back-projection algorithm (also called a direct method or direct summation method) is an effective reversal of the projection operation in real space [5, 9]. Each image is propagated ("smeared") into the direction of projection through the reconstruction volume. The result of back-projecting many images from different angles is that where these propagation lines agree, the signal is enhanced, and where they disagree, the signal is suppressed. The more the angular range is covered, the better the reconstruction gets.

The propagation algorithm requires an interpolation to calculate values at 3D grid points from 2D pixels. This is typically done by linear interpolation, assigning weights to neighboring voxels based on the distance between source pixels and destination voxels [10, 11].

One consequence of this process is that the large features (low frequencies) are emphasized compared to the detail (high frequencies), giving rise to a reconstruction with a decidedly low-pass filtered appearance. The cause is best understood as the overlap of central sections in frequency space. The reconstruction must be appropriately weighted, thus the term "weighted back-projection" [10]. In a single tilt tomographic series, the central sections all overlap along the tilt axis, but diverge perpendicular to the tilt axis. The appropriate filter is therefore a ramp function perpendicular to the tilt axis and proportional to the frequency (see Fig. 8.2a for an example). For more complicated view distributions (such as double or conical tilt series), the weighting function must be suitable to account for the distribution of views. If the view distribution has good coverage (usually not applicable to tomography), an isotropic ramp filter can be used (generally referred to as filtered back-projection [11].

# 8.2.2 Frequency Space Reconstruction (FSR)

The central section theorem [8] provides a basis for reconstruction in frequency space. The 2D Fourier transform of each micrograph is added to the 3D reconstruction volume as a central section in the correct orientation. The weight at each frequency space voxel is just the sum of the contributions from the micrographs, accounting for overlaps of the central sections. Once the summation is done, the complex value at each voxel is divided by the weight. This avoids the weighting complications encountered for WBP and produces fewer artifacts [12, 13].

The integration requires some form of interpolation, and several schemes have been devised [9]. The simplest is the nearest neighbor interpolation, where every pixel in the 2D image transform is assigned to the closest 3D frequency space voxel. This seems crude, but works reasonably well (see Fig. 8.2b for an example). It can be made more sophisticated by weighing each contribution by the distance between the source

pixel and the destination voxel. The source image can be padded in real space to increase the sampling in frequency space, thus decreasing the distance between source and destination grid points [12].

The natural interpolation in frequency space is of the Whittaker-Shannon type, based on sinc functions [9, 13, 14]. Exact interpolation (such as Whittaker-Shannon) implicitly assumes that the data is noise-less and that the continuous function can be reconstructed exactly up to Nyquest frequency. However, with significant noise present, the reconstruction with exact interpolation will emphasize the noise rather than the embedded signal. The smoothing effect of approximate interpolation methods such as nearest neighbor and bilinear interpolation has yielded acceptable results in the presence of noise.

Gridded-based interpolation is an approximation aimed at changing the sampling grid in frequency space. An intermediate sampling grid is often not rectangular, constructed through variations of fast Fourier transformation (FFT) called unequally spaced FFT (USFFT) [15] or non-uniform FFT (NUFFT) [16]. Several iterative forms of interpolation have been developed to improve accuracy [16–18]. It is not clear in practice that the slight increases in accuracy of gridded-based interpolation [42] is worth the more complicated implementation.

#### 8.3 Iterative Reconstruction

A different approach is to pose reconstruction as solving the integration problem. The back-projection algorithm propagates the 2D image through the 3D volume, adding each pixel to all the voxels along a projection line with the same contribution. Obviously, the values in the volume vary along the projection line and thus do not contribute equally to the projection result. However, each voxel in the volume should contribute the same value to all projections. This can be posed as a set of simultaneous equations, each representing the sum along a projection direction:

$$p_i = \sum_j w_{ij} f_j$$

where  $p_i$  is the projection value at pixel i,  $f_j$  is the volume value at voxel j, and  $w_{ij}$  is the weight assigned to the voxel j with respect to the pixel i. The weights are typically taken as the traversal distance of the projection line across a voxel. This system of equations can in principle be solved to determine the voxel values in the reconstruction volume. However, the resultant matrix is very large and is impractical to solve analytically. Several algorithms have been developed to find a solution through iteration.

In the original formulation the projection operation is viewed as following "rays" (projection lines) and some implementations attempt to calculate representative rays [6]. However, the effective process is the calculation of a projection from the

Table 6.2 Souwaic packa	wait pathages w	Tui toois foi delloit	sing (roi more, see imps.	ges with tools for uniforming (1 of more, see indps.//edi.wikibooks.org/wiki/software_1 ools_1 of _ivioleculaivitelescopy)	(Ada)
Package	Algorithm(s)	Remarks	Coding environment	Web site	References
Bsoft	IMF BLF		C++/TclTk	http://bsoft.ws	[12]
iMed	IMF	Integrated into pyCoAn	FORTRAN/C/Python http://coan.burnham.org	http://coan.bumham.org	[52]
IMOD	NAD		FORTRAN/C	http://bio3d.colorado.edu/imod/	[27]
TomoAND	NAD		C++	http://sites.google.com/site/3demimageprocessing/tomoand	[59]
TomoBFlow	BF		C++	http://sites.google.com/site/3demimageprocessing/tomobflow	[57]
XMSF	MSF	Integrated into C++	‡-2	https://sites.google.com/site/xmsfilter/	[55]
		Xmipp			

BF Beltrami flow

BLF Bilateral filter
IMF Iterative median filter
NAD Non-linear anisotropic filter
MSF Mean shift filter

current version of the reconstruction, calculation of the difference with the observed image, and adjusting the reconstruction values based on this difference. The key issues in such algorithms are (i) the starting volume, (ii) the way the projection is calculated, (iii) the way the reconstruction is updated, and (iv) the number of iterations (or stopping condition). The updating approach distinguishes the different techniques called ART (algebraic reconstruction technique) [19], SIRT (simultaneous iterative reconstruction technique) [20] and SART (simultaneous algebraic reconstruction technique) [21]. Alternative iterative methods include the maximum entropy method (MEM) [6], the progressive stochastic reconstruction technique (PSRT) [22], and frequency space methods [16, 17, 23]. The principle in the latter is the same as for real space methods, with each image compared with its corresponding central section and the volume updated to minimize the difference.

Gordon and Herman devised MEM at the same time as ART [6]. The aim is to obtain the least biased reconstruction with the entropy given as:

$$S = -\int p(\bar{x}) \ln \frac{p(\bar{x})}{m(\bar{x})} d^3 \bar{x}$$

where p(x) is the normalized density at voxel x and m(x) is a prior (initial) density [24–26].

Turonova et al. [22] implemented an iterative approach modeling density as Gaussian spheres (PSRT). The spheres are placed randomly within a volume and projections from this volume compared with the micrographs. Spheres that improve the comparison are retained, while those that don't are rejected. The spheres are reduced in size and increased in number over several iterations. Ultimately, the reconstruction is done when the spheres reach the size of the voxels.

# 8.3.1 The Starting Volume

The choices for a starting point for iterative reconstruction are either a homogenous feature-less volume, or an initial integrative reconstruction. The original ART implementation started with an empty volume [19]. In IMOD, the initial volume for the implementation of SIRT is an unweighted ("flat") or partially weighted back-projection [27]. The MEM approach can be adapted to include prior information limiting the possible reconstructions [24, 25, 28]. The PSRT method starts with a random placement of seed spheres in the tomographic volume [22].

# 8.3.2 Calculating the Projection Difference

The concept behind iterative methods is that the re-projection from the reconstruction should look the same as the corresponding micrograph. Therefore, at each

iteration k, a projection is calculated to compare with each micrograph image. The pixel  $p_i$  in the projection is the weighted sum of the voxels in the volume f:

$$p_i^{(k)} = \sum_j w_{ij} f_j^{(k)}$$

The weights  $w_{ij}$  are limited to a "ray" through the volume f. These are often referred to as basis functions related to the manner of interpolation in calculating the projection (see below). In the case of PSRT, the projection is a summation of Gaussian spheres in the current iteration [22].

The weighted difference between a projection  $p_i$  and the corresponding micrograph  $g_i$  is calculated for ART [19]:

$$\varepsilon_i^{(k)ART} = \frac{g_i - p_i^{(k)}}{\sum_j w_{ij}^2}$$

and SIRT [20]:

$$\varepsilon_i^{(k)SIRT} = \frac{g_i - p_i^{(k)}}{\sum_i w_{ij}}$$

and MEM [24]:

$$arepsilon_i^{(k)MEM} = \left(rac{g_i - p_i^{(k)}}{\sigma_i}
ight)^2$$

where  $\sigma_i$  is the standard deviation of the data at pixel i.

In the generation of the projection, the ray generally does not pass through sampled points in the Cartesian grid of the reconstruction. The interpolation is therefore a crucial determinant of the quality of a reconstruction. There is the so-called "pixel-basis", where the weight for each pixel contributing to a ray is taken as the traversal length across the pixel. In ART, this still results in the "salt and pepper" features, ascribed to a "discontinuous image representation" [21]. A solution to this is to use multiple rays going through the same voxels (supersampling) and average them [21, 29]. This however increases the computational burden.

A linear interpolation method was considered efficient and about as good as cubic spline interpolation [30]. A bilinear interpolation scheme was proposed with the SART algorithm [21]. A further improvement was reported using a Hamming window to suppress contributions from the beginnings and ends of rays. More complex basis functions with better properties can also be used [31].

# 8.3.3 Updating the 3D Map Volume

The original updating for ART was done per ray [19]:

$$f_j^{(k+1)} = f_j^{(k)} + \lambda \varepsilon_i^{(k)ART} w_{ij}$$

where  $\lambda$  is a damping or relaxation parameter (<1) to avoid instability. However, the updating did not account for the contributions from different micrographs, and tended to become chaotic, generating "salt and pepper" type artifacts. Gilbert [20] suggested that a better technique is to calculate a combined adjustment from all micrographs during each iteration, i.e., SIRT. The update now becomes:

$$f_j^{(k+1)} = f_j^{(k)} + \lambda \frac{\sum_i \varepsilon_i^{(k)SIRT} w_{ij}}{\sum_i w_{ij}}$$

where the summation is over all difference images. This results in increased computation and very slow convergence. Anderson and Kak proposed an algorithm intermediate between ART and SIRT, where the volume is updated with every difference image, i.e., SART [21]. Instead of difference images, Wolf et al. [32] updates the map at each iteration with appropriately weighted images (i.e., a WBP reconstruction).

A variant of these methods is DART (discrete algebraic reconstruction technique) [33], where the volume is segmented during each iteration into discrete levels. The application is appropriate where it is known that the different density values correspond to different elements or homogenous regions.

In MEM, various schemes have been devised to update the reconstruction [34]. A common technique is to update the volume based on the gradients of the entropy and the chi square metric of the difference between the calculated projection and micrograph [24, 26].

For PSRT, the addition of each Gaussian sphere is evaluated as to whether it improves the comparison with the micrographs or not. If the difference decreases, the sphere is accepted [22].

# 8.3.4 The Number of Iterations

It was noted in the original development of SIRT in synthetic test cases that an optimal correspondence is reach with the original map, after which it diverges [20]. It was reported that in ART the divergence is faster than SIRT. As an example, Fig. 8.2c shows part of a SIRT reconstruction after 10 iterations, and in Fig. 8.2d, after 50 iterations. Evidently the latter is dominated by noise. In this implementation of IMOD, the iterative process is started from a WBP reconstruction. The comparisons are not initially weighted, so that the low frequencies are amplified.

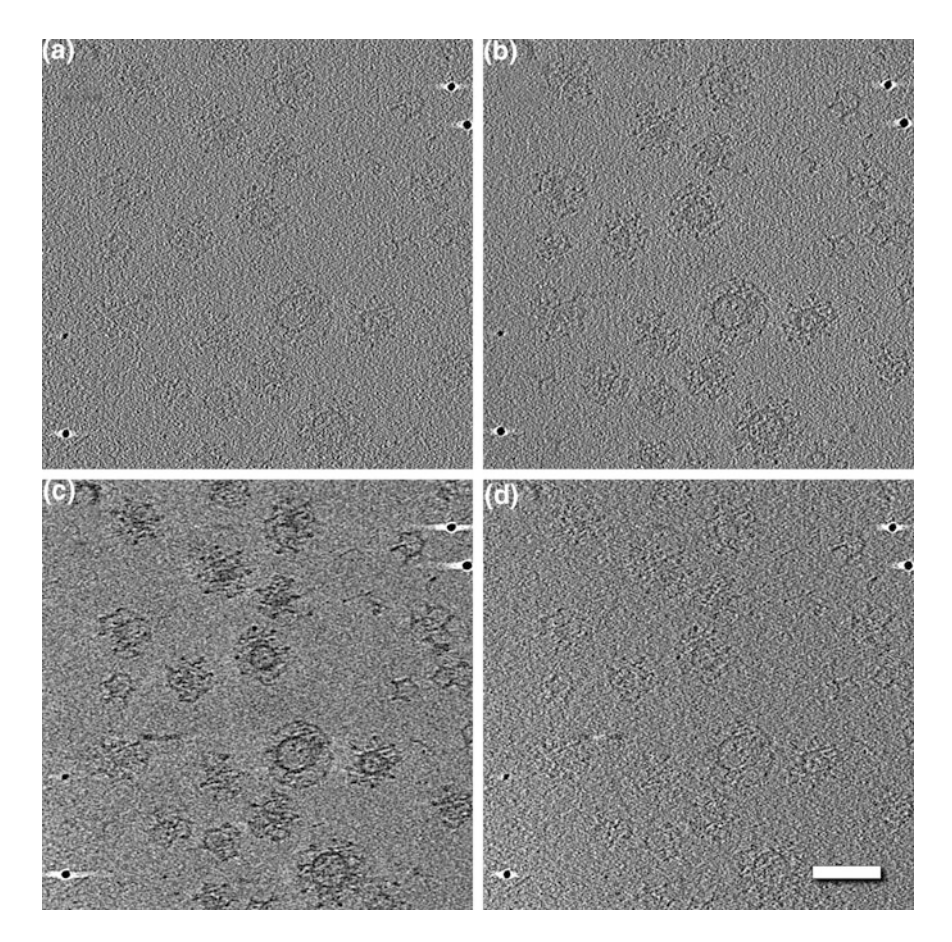


**Fig. 8.2** Examples of reconstruction from the same tilt series using three different algorithms. The specimen was isolated clathrin-coated vesicles from bovine brain [86]. a Weighted back-projection (IMOD [27]). b Fourier space nearest neighbor interpolation (Bsoft [12]). c SIRT after 10 iterations (IMOD [27). d SIRT after 50 iterations (IMOD). Scale bar: 1000 Å

Through successive iterations, the reconstruction is modified to increase the contribution of high frequency elements. This means that the map becomes noisier up to a point where it is actually similar to that obtained with WBP or FSR (Fig. 8.2).

# 8.4 Real Space Pre-processing

Micrographs often display features that complicate reconstruction. The typical descriptions for reconstruction algorithms do not mention how the micrographs are prepared. However, the interpretability of tomograms may suffer if appropriate

pre-processing is not done. Most of this is done in real space, while corrections for the contrast transfer function is done in frequency space (see next section).

#### 8.4.1 Normalizing Images

The tilting of the specimen means that the electron beam path through the specimen increases with tilt angle [12]:

$$I(\alpha) = I_0 e^{\frac{t_0}{\Lambda \cos(\alpha + \Delta \alpha)}}$$

where  $I_0$  is the incident beam intensity,  $t_0$  is the specimen thickness at zero-tilt, and  $\Lambda$  is the mean free path. The addition to the tilt angle,  $\Delta\alpha$ , accounts for the specimen being already tilted with respect to the specimen holder and perpendicular to the tilt axis. A common pre-processing step is to normalize the images to have a similar average and range [12, 26].

#### 8.4.2 Removing High Contrast Features

The electron microscope produces X-rays that are recorded in the micrographs as very high intensity (white) spots. These can influence alignment and reconstruction algorithms, and are therefore routinely removed [27, 35].

We typically add fiducial markers to the specimen to allow easy alignment of the tilt series. These however create high contrast objects with strong interference fringes in tomograms that may obscure elements of interest. These can be removed in the original images by erasure [12, 35], in-painting [36], or localized denoising [37].

# 8.4.3 Removing Extraneous Areas

The images obtained for highly tilted specimens include areas that do not fall within the reconstruction volume, but still contribute to it. This is called the "long object" problem [38]. Erasing the extraneous areas taking into account the thickness of the tomogram can minimize their contributions (implemented as an option in Bsoft [12]). Xu et al. [39] incorporated a scheme to weigh down these areas during SIRT. Turoňová et al. [40] suggested other ways of dealing with it, including larger reconstructions to include the additional areas, and appropriate weighting.

#### 8.4.4 Denoising

While denoising is typically done after reconstruction, removing noise in the source images could improve alignment and reconstructions. Maiorca et al. [41] implemented a non-linear anisotropic diffusion (NAD) algorithm to denoise the tilt series micrographs. They showed an improvement in segmentation results.

#### 8.5 Contrast Transfer Function (CTF) Correction

To obtain good contrast in micrographs, the electron microscope is typically defocused. This has the consequence of imposing an oscillating CTF on the image. In single particle analysis, the CTF is routinely corrected to obtain reconstructions at high resolution. In tomography, the tilting of the specimen means that there is a focus gradient across the image, complicating both parameter determination and correction. Nevertheless, to recover more detail, the micrographs need to be corrected for the CTF prior to reconstruction. Many reconstructions schemes incorporate this as part of the algorithm [24, 42].

#### 8.5.1 CTF Theory

The CTF equation most commonly used is:

$$CTF(s) = a \cos(\gamma(s)) - \sqrt{1 - a^2} \sin(\gamma(s))$$

where s is the spatial frequency (1/Å), a is the amplitude contrast fraction (typically about 0.07 for frozen specimens) and the phase shift due to defocus is:

$$\gamma(s) = \frac{\pi}{2} C_s \lambda^3 s^4 - \pi \lambda \Delta f s^2$$

where  $C_s$  is the spherical aberration (typically about 2 mm),  $\lambda$  is the electron wavelength (a function of the acceleration voltage), and  $\Delta f$  is the defocus. The latter is the complicated part of the CTF for tilted specimens, and is given by:

$$\Delta f(\xi, r, \zeta) = \Delta f_a + \Delta f_d \cos(2(\xi - \chi)) + r \sin(\beta - \zeta) \tan(\alpha)$$

The three terms are the average defocus,  $\Delta f_a$ , the astigmatism and the tilt compensation. The astigmatism term relates to frequency space, where  $\Delta f_d$  is the defocus deviation due to astigmatism, and  $\xi - \chi$  is the difference angle between the point in frequency space and the astigmatism angle. The tilt compensation term relates to real space, where r is the distance of the point from the tilt axis origin,  $\beta - \zeta$  is the difference angle between the point and the tilt axis angle and  $\alpha$  is the tilt

angle. The complication is that the defocus contains both these real and frequency space terms. Therefore, the convolution theorem cannot be used to simplify the calculation of the power spectrum or correcting for the CTF.

#### 8.5.2 Determining CTF Parameters

To determine the CTF parameters (defocus average, defocus deviation and astigmatism angle), a representative power spectrum must be calculated. This is commonly done by dividing the image into tiles and averaging the power spectra of the tiles (see Fig. 8.3a for an untilted specimen). Because of the focus gradient for a tilted specimen, a power spectrum calculated in this way decays quickly (Fig. 8.3b, d). One approach is to calculate separate power spectra for strips or tiles parallel to the tilt axis [43–45]. The array of defocus values is then assessed to obtain an average value at the tilt axis.

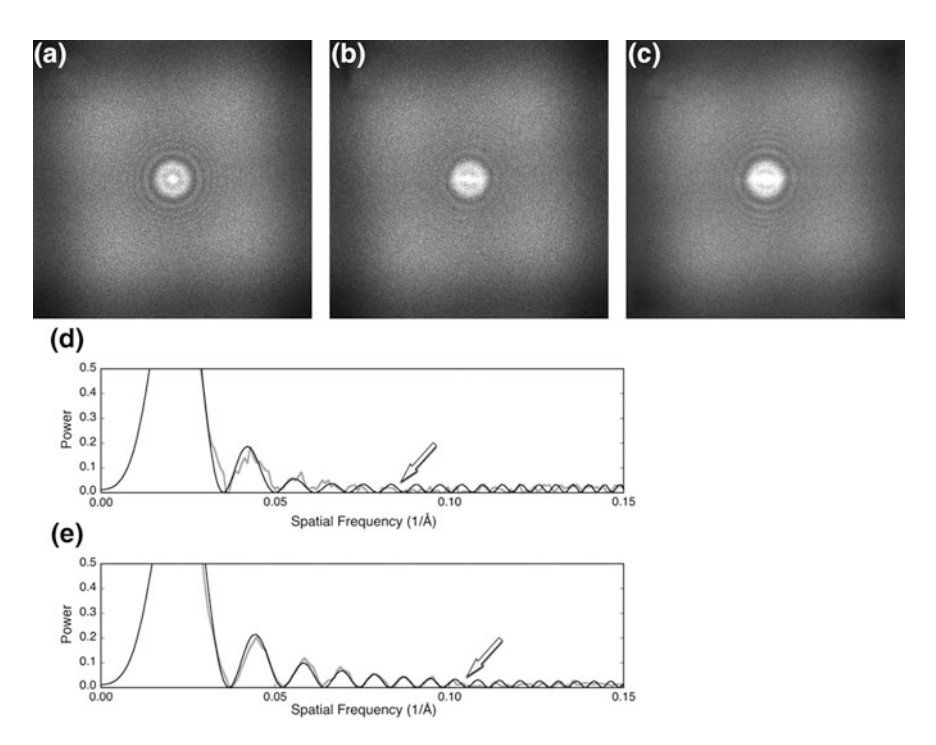


Fig. 8.3 Estimating the CTF. Tiled power spectra of:  $\bf a$  the  $0^{\circ}$  micrograph,  $\bf b$  the  $-60^{\circ}$  tilted micrograph without compensating for tilt, and  $\bf c$  with compensating for tilt. The curves show the fit of the CTF (black) to the radial power spectrum (gray) for:  $\bf d$  the power spectrum in  $\bf b$  and,  $\bf e$  the power spectrum in  $\bf c$ . The arrows indicate the information limits (i.e., the points where the fitted curves deviate from the radial power spectra). The micrographs are of ribosomes as provided from the EMPIAR site: https://www.ebi.ac.uk/pdbe/emdb/empiar/entry/10045/. All calculations were done in Bsoft [12]

If correctly calculated with compensation for the tilt, a better power spectrum can be calculated (Fig. 8.3c, e). Xiong et al. [46] describe an adjustment to the power spectra from tiles at different heights to compensate for the focal gradient. This is based on the reciprocal relationship between defocus and spatial frequency in the CTF equation:

$$\Delta f_1 s_1^2 = \Delta f_2 s_2^2$$

Figure 8.3c, e shows the result of using this equation to calculate a power spectrum from an image of a tilted specimen using all tiles (implemented in Bsoft [12]).

A different strategy is to forgo using the images of the tilt series as too low in SNR (which is less of a problem with direct detectors). During tilt series acquisition, two images along the tilt axis on either side of the area of interest are taken at high dose. These images are then used to determine the defocus [47]. The disadvantage is that data acquisition becomes more tedious and slow.

How accurate do the CTF parameters have to be? Schur et al. [48] examined the relationship between the level of detail that can be recovered from tomograms and the error in CTF correction. For detail in a structure to 8 Å, the defocus must be accurate on the order of  $0.1~\mu m$ . This includes error due to significant astigmatism.

#### 8.5.3 Correcting for the CTF

The most accurate correction for the CTF is per pixel, where a region around the pixel is extracted, Fourier transformed, a CTF function applied, back-transformed, and only the one resultant pixel value retained. This is obviously very inefficient. If the tilt series is appropriately oriented along a Cartesian axis, the correction can be done line-by line [43]. Xiong et al. [46] showed that correcting strips of about 128 pixels wide by phase-flipping showed very little error. The actual implementation in IMOD calculates overlapping strips with intervals of 20 pixels and interpolates between overlapping pixels. Winkler and Taylor [45] devised an iterative restoration algorithm applied line-by-line. The latter is conceptually attractive because the inverse CTF function is ill-behaved.

When the target is subvolume averaging, the CTF correction can be done per subvolume, compensating for the height of the subvolume within the larger tomographic reconstruction [49, 50].

# 8.6 Denoising

While denoising is treated here as a separate issue (and is covered in Chap. 11), it is an important part of the reconstruction process to obtain interpretable tomograms (it is often a prerequisite for segmentation—Chap. 12). As is evident from Fig. 8.2, some

reconstruction techniques can inherently produce maps with less noise (e.g., the IMOD SIRT implementation used in Fig. 8.2c). In particular, the integrative reconstruction algorithms incorporate sufficient noise to require subsequent denoising (Fig. 8.2a, b). Appropriate denoising can allow the analysis of the locations and copy numbers of individual proteins [51].

Tomograms from cryo-EM micrographs are typically very noisy due to the low dose used in data acquisition. The goal of denoising is to make desirable objects and features stand out from the background (e.g., when an isosurface is calculated). Denoising can even be done on the original tilt series, preceding 3D reconstruction [37, 41] (see Sect. 8.5). Any form of denoising is a smoothing operation limited to spatially defined kernels. Many algorithms are iterative, requiring the user to choose a stopping point. The typical parameters include the size of the kernel, some kernel weighting function and the number of iterations. In each case we have to judge when a denoising operation has removed enough noise (and artifacts) without degrading the details of interest. The algorithm and parameters chosen therefore reflects this subjectivity.

#### 8.6.1 Low-Pass Filter

The simplest filters remove high frequency noise. Two commonly used real-space filters are local averaging (moving window) and Gaussian smoothing. Both these constitute convolution with a local kernel where the size of the kernel and Gaussian width are user-selected parameters. In frequency space, a high-frequency limit with a hard or soft cutoff can be imposed. The frequency limit and the soft cutoff width are likewise user-selected.

#### 8.6.2 Iterative Median Filter

For a median filter, the middle-ranked value within a kernel is taken as the new value of a pixel. This is a particularly simple method to eliminate extreme pixel values (Fig. 8.4a). The user typically decides the size of the kernel and the number of iterations, both smoothing the map with larger values (2–3 iterations are typically sufficient). Excessive iterations may result in the loss of information as homogenous median blocks are expanding [52].

#### 8.6.3 Bilateral Filter

The bilateral filter calculates a value for a pixel integrating over a kernel with both distance and density difference functions (Fig. 8.4b) [53, 54].

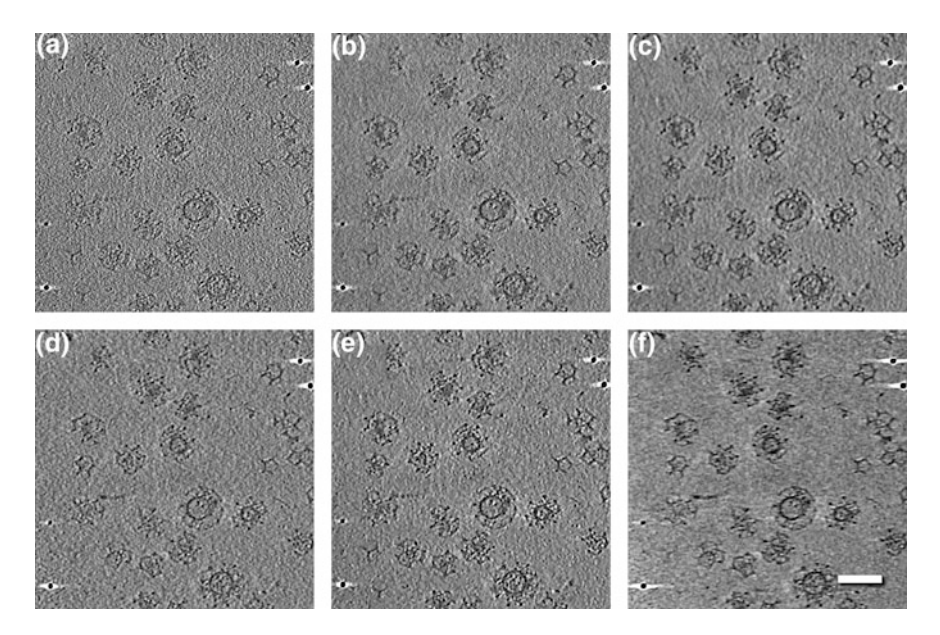


**Fig. 8.4** Examples of denoising. **a–c** Denoising algorithms starting with the FSR map from Fig. 8.2b: **a** Median filtering with a 3 × 3 × 3 kernel over 3 iterations (Bsoft [12]). **b** Bilateral filter with a spatial sigma of 3 and a range sigma 3 times the map standard deviation (Bsoft [12]). **c** Beltrami flow denoising over 30 iterations with edge enhancement (Tomobflow [57]). **d–f** Nonlinear anisotropic diffusion over 100 iterations starting with reconstructions shown in Fig. 8.2**a–c** (Bsoft [12]). Scale bar: 1000 Å

# 8.6.4 Mean Shift Filtering

Mean shift filtering is another kernel-based filtering technique. It is different in that the kernel moves until a stable "centroid" is found. Both distance and density-difference are included in the centroid calculation. The centroid is calculated using either uniform or Gaussian kernels for both distance and density. The sizes of these kernels are user-defined parameters [55].

#### 8.6.5 Non-local Means Filter

This filter is a type of texture filter. The similarity between two pixels is defined as a function of the difference between the pixel values within kernels surrounding the pixels. This therefore encodes both the spatial variation and orientation in the similarity measure. Because of the cost of a comparison of all possible kernels, the comparisons are limited to small kernels (few pixels:  $\sim 3$ ) and search regions (about twice the kernel size). The input parameters are therefore the kernel size, the search area size and a decay factor for the Gaussian weighting kernel [56].

#### 8.6.6 Beltrami Flow: Isotropic Diffusion

Beltrami flow is an isotropic diffusion algorithm where the rate of diffusion is dependent on the presence of edges. Fernandez [57] implemented it with an edge enhancement option (Fig. 8.4c).

#### 8.6.7 Non-linear Anistropic Diffusion (NAD)

NAD is intended to smooth the data (i.e., remove noise) in such a way that contiguous structures are preserved (Fig. 8.4d–f) [58]. The parameters can be tuned to favor needle-like or disc-like structures, depending on the specimen [59]. The diffusion process is essentially a simulation with a very small time step, so that many iterations are required to achieve a meaningful level of denoising. The kernels over which the structure and diffusion tensors are calculated are small ( $3 \times 3 \times 3$ ), but the computational cost is very high. While considered one of the best denoising algorithms, other methods that are computationally more efficient may be more appropriate.

NAD is typically done on the 3D map, but it can also be implemented ahead of reconstruction [37, 41]. Here the aim is to decrease the appearance of streaking artifacts in the reconstruction, resulting in easier interpretation.

# 8.7 Information Recovery

# 8.7.1 Missing Information

In the current tilt geometry of the microscopes, the grid cannot be tilted beyond 70°, leaving a significant gap in the sampled views. This is reflected in the reconstruction as missing information in frequency space: a missing wedge for single a single tilt series. Methods to reduce the missing wedge include doing double tilt [60–62] or conical tilt [63] series reconstructions. The effort involved in acquiring the data and dealing with dose and distortion issues make these approaches less attractive.

Missing information in the reconstruction means that the resolution will always be lower in the z direction. In addition, as the tilt angle increases, the planar specimen effectively becomes thicker. This decreases contrast and diminishes the information content further in high tilt images. At 60°, the effective thickness is twice that of the specimen thickness, and at 70°, it is almost three times!

The effects of missing information includes artifacts such streaks emanating from high density regions (e.g., gold particles) and the apparent elongation of structures in the z direction. Filtering to smooth the transitions between known and

missing regions in frequency space can suppress these artifacts to some extent [64, 65]. The difference observed between WBP and FSR in terms of these artifacts [12] is likely due to more appropriate weighting in these transition regions in the latter.

### 8.7.2 Recovering Missing Information

Information that is not recorded cannot be recovered. However, if we impose constraints on what the data should be, the relationships inherent in these constraints can be used to fill in some of the missing information. Carazo and Carrascoza [66] introduced the constraints-based method of projection onto convex sets (POCS) into the cryo-EM field. However, the results were disappointing and little progress has been made [11]. Deng et al. [67] developed a compressed sensing approach to fill in some of the missing information with promising results. Here the principle used is that most of the specimen is solvent, meaning that the matrix relating the reconstruction volume to the micrographs is largely sparse. The introduction of external information such as constraints is partially subjective and should be considered with care.

#### 8.7.3 Visual Assessment

The most common assessment of the quality of tomograms involves examining slices in the xy plane as shown in Figs. 8.2 and 8.4 (i.e., perpendicular to the electron beam for the 0° micrograph). Isosurface renderings of denoised tomograms reveal the anisotropy of details (Fig. 8.5). The densities are typically elongated in the z direction due to the missing wedge. Tubular structures in the xy plane perpendicular to the tilt axis are usually poorly represented.

The different reconstruction algorithms also result in tomograms with variable interpretability. Figure 8.5 shows three reconstructions of a clathrin basket oriented to show a hexagon in the front face. It is hard to make out the hexagon in the WBP map (Fig. 8.5a), while the FSR map (Fig. 8.5b) is easier to interpret with five of the hexagon sides visible. The SIRT map (Fig. 8.5c) seems to be relatively noise free, but only four sides of the hexagon is apparent.

#### 8.7.4 Resolution Estimation

While the quality of a tomographic reconstruction is often judged by eye, it is important to have a more objective measure of resolution (see Chap. 10). However, any measure reflects the anisotropy derived from the geometry of data acquisition. For a single tilt experiment, the resolution is the highest along the tilt axis as shown

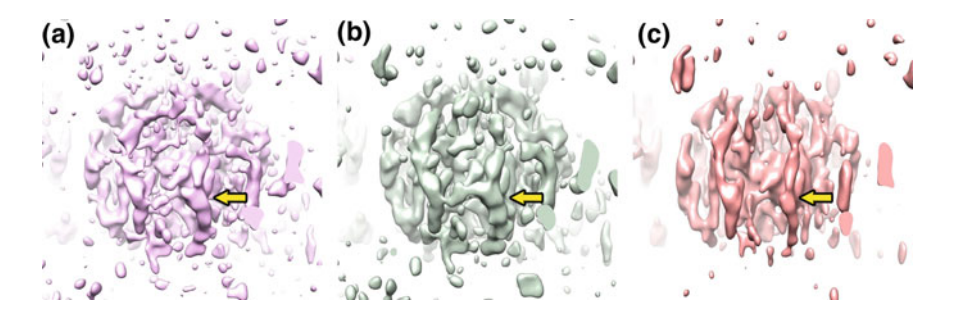


Fig. 8.5 Isosurface renderings of clathrin baskets from denoised reconstructions as shown in Fig. 8.4d–f. a Weighted back-projection (IMOD [27]). b Frequency space reconstruction (Bsoft [12]). c SIRT after 10 iterations (IMOD [27]). The front face features a hexagon that differs substantially between the reconstructions. The yellow arrow indicates the lower right vertex of the hexagon. The electron beam direction (z) for the  $0^{\circ}$  micrograph is vertical and the tilt axis is horizontal. All maps were isosurfaced at  $2.5\sigma$ 

with filamentous structures aligned with the axis [68]. Perpendicular to the tilt axis, the resolution is limited to the overlap of neighboring central sections in frequency space (see below). In the third direction, the limited tilt range results in a missing wedge. The latter is characterized by the apparent elongation or smearing of objections in the z direction (parallel to the electron beam). All of these factors decrease the value of a single resolution estimate for a tomogram.

Crowther et al. [13] made the original attempt to give an estimate of the resolution for a limited number of images. Given a tilt series with a constant step increment in the tilt angle, the number of images, m, required to achieve a desired resolution, d, for a particle of size D, was derived as:

$$m \approx \pi \frac{D}{d}$$

(this equation is also known as the Crowther criterion).

This equation can be derived in a different way that is more intuitive when considering Fourier reconstruction. Placing two adjacent central sections from a tilt series in frequency space is separated by the tilt step size,  $\Delta\alpha$ , so that the central sections overlap up to a point. At this point,  $k_r$ , the planes are separated by one voxel unit distance, so that:

$$\Delta \alpha k_r = 1$$

The resolution (inverse frequency) at this point is then:

$$d = \frac{D}{k_r} = D\Delta\alpha$$

To cover all tilt angles (180° or  $\pi$ ) with the given step size, the number of images required is:

$$m = \frac{\pi}{\Delta \alpha} = \pi \frac{D}{d}$$

Note that for a single tilt series, this equation only accounts for a limit on resolution perpendicular to the tilt axis. It also assumes noise-free images in perfect alignment. Noise and alignment errors will suppress the resolution. Targeting a particular number of images for a tilt series is in practice more a function of the total dose desired than the achievable resolution based on the Crowther criterion.

The most appropriate way of considering resolution in a full tomogram is to assess the recovery of information from each image in the tilt series. Cardone et al. [69] devised a method called noise-compensated leave-one-out (NLOO). The method calculates for each micrograph the ratio between two Fourier ring correlations (FRCs): the first an FRC between the micrograph and a projection from the full reconstruction with the micrograph left out, and the second an FRC between the micrograph and a projection from the full reconstruction. This is however only applicable to integrative methods (WBP and FSR), because the iterative methods incorporate a similar comparison already in the reconstruction.

The typical NLOO FRC curve reflect the anisotropy relative to the tilt axis, giving a ramp-like curve rather than the sigmoidal curve familiar in SPA (Fig. 8.6a). Figure 8.6b shows the resolution estimates obtained for all the images in a tilt series. This can be fitted to a curve accounting for the effective thickness of the specimen as it is tilted [12]. It is evident that the resolution is severely degraded in higher tilt micrographs, diminishing their value in the reconstruction (Fig. 8.6).

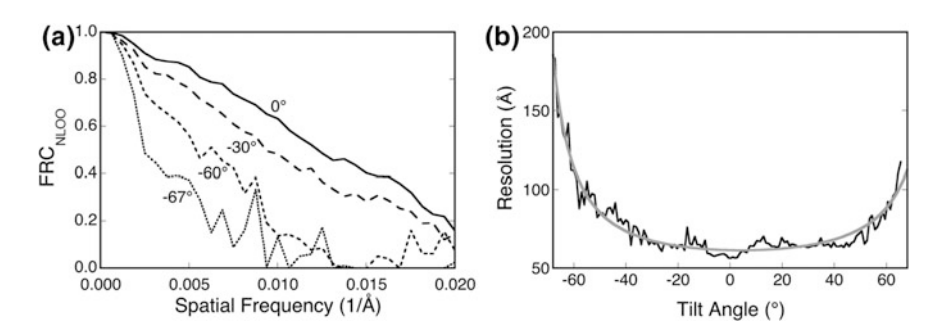


**Fig. 8.6** Examples of resolution estimates (for the same tomogram as in Figs. 8.2 and 8.4) based on the noise-compensated leave-one-out (NLOO) algorithm [69]. **a** Fourier ring correlation (FRC) curves for micrographs from the tilt series at different tilt angles. **b** Resolution estimates from the FRC curves at a cutoff of 0.3. The fit (gray line) is based on the equation given in [12]

with the following parameters:  $r = 10.1 + 29.8e^{1600\text{\AA}\cos(\alpha - 4.2^{\circ})}$ . All calculations were done in Bsoft [12]

### 8.8 Subtomogram Reconstruction

When a tomogram contains particles thought to be identical in structure, they can be averaged to decrease the noise. This can be done in multiple ways, each with its own complexities and limitations. Although it is covered in Chap. 9 in more detail, here it is treated as an extension of the original reconstruction approaches.

#### 8.8.1 3D Alignment and Averaging

The most common approach is to locate and pick 3D subvolumes from tomograms. These are then aligned with respect to a reference or template and averaged [48, 50, 70–82]. With the introduction of direct detectors, it is now possible to easily correct for the CTF (see Sect. 8.5) and achieve sub-nanometer resolutions [83].

Bharat et al. [84] developed a correction method that includes compensating for the accumulated dose, effectively low-pass filtering images taken later in the tilt series to avoid degradation of high resolution information in the earlier images. Lin et al. [85] classified individual subtomograms to reveal the dynamics of dynein in sea urchin sperm flagella.

## 8.8.2 2D Alignment, Reconstruction and Averaging

The large fields-of-view covered in tomography means that parts of the specimen might shift relative to other parts. One solution may be to do local alignments and do a distortion correction using a vector field (e.g., as is done in IMOD [27]). If the target is to extract subtomograms, the task becomes somewhat easier. The global alignment can be used to locate the 2D submicrographs, refine their individual alignments, and then do a subtomogram reconstruction (implemented in the current version of Bsoft [12]). This is effectively the same as single particle analysis, with the advantage of taking the orientational constraints of the tilt series into consideration.

# 8.8.3 Model-Based Averaging

Macromolecules are often arranged in defined locations and orientations. For example, the glycoproteins on the surface of an enveloped virus typically adopt a specific orientation with respect to the membrane. This can be used to select the glycoprotein densities with considerable orientation constraints to aid in alignment and averaging [74, 76]. The clathrin networks of coated vesicles can be modeled as

polyhedra, allowing averaging of the vertices to reduce noise and reveal substructure in a highly pleomorphic specimen [86]. Bharat et al. [83] modeled the lattice of helical tubes of the HIV capsid protein, locating and averaging individual unit cells to a resolution of 8 Å.

#### 8.9 Conclusion

Ultimately we would like to know what reconstruction approach is the best to use. The answer is complicated because it involves multiple issues that may be specific to a particular situation. For instance, if the data originates from a non-FEG microscope, it is likely resolution-limited to such an extent that CTF correction is not feasible, and that most reconstruction algorithms will yield reasonable tomograms. However, if the aim is to do subtomogram averaging to high resolution on data from an FEG microscope with a direct detector, then preprocessing (both real space and CTF correction), and appropriate reconstruction (including denoising) are required. What is appropriate depends to some extent on computational resources and the targeted interpretation. If the goal is to generate tomograms fast or in large numbers, the slow computation-intensive reconstruction algorithms are unsuitable. Because denoising removes high frequency information, any form of it (including iterative reconstruction techniques such as SIRT) may erode useful high resolution details that are desired in subtomogram averaging. For these reasons, we try to tailor the many different reconstruction methods to specific applications.

#### References

- D.J. De Rosier, A. Klug, Reconstruction of three dimensional structures from electron micrographs. Nature 217(5124), 130–134 (1968)
- J. Radon, On the determination of functions from their integral values along certain manifolds. IEEE Trans. Med. Imaging 5(4), 170–176 (1986). doi:10.1109/TMI.1986.4307775
- J. Radon {Ü}ber die {B}estimmung von {F}unktionen durch ihre {I}ntegralwerte l\u00e4ngs gewisser {M}annigfaltigkeiten. Akad Wiss 69, 262–277. doi:citeulike-article-id:7680709 (1917)
- 4. G.T. Herman, Fundamentals of Computerized Tomography: Image Reconstruction from Projections (Springer Publishing Company, Incorporated, 2009)
- P.F.C. Gilbert, The reconstruction of a three-dimensional structure from projections and its application to electron microscopy. II. Direct methods. Proc. R. Soc. Lond. B: Biol. Sci. 182 (1066), 89–102 (1972). doi:10.1098/rspb.1972.0068
- R. Gordon, G.T. Herman, Reconstruction of pictures from their projections. Commun. ACM 14(12), 759–768 (1971). doi:10.1145/362919.362925
- G.P. Vigers, R.A. Crowther, B.M. Pearse, Three-dimensional structure of clathrin cages in ice. EMBO J. 5(3), 529–534 (1986)
- R. Bracewell, Strip integration in radio astronomy. Aust. J. Phys. 9(2), 198–217 (1956). doi: http://dx.doi.org/10.1071/PH560198

- M. Radermacher, Three-dimensional reconstruction of single particles from random and nonrandom tilt series. J. Electron Microsc Tech. 9(4), 359–394 (1988). doi:10.1002/jemt. 1060090405
- M. Radermacher, Weighted back-projection methods, in *Electron Tomography: Methods for Three-Dimensional Visualization of Structures in the Cell*, ed. by J, Frank (Springer, New York, 2006), pp. 245–273. doi:10.1007/978-0-387-69008-7\_9
- J.-M. Carazo, G.T. Herman, C.O.S. Sorzano, R. Marabini, Algorithms for three-dimensional reconstruction from the imperfect projection data provided by electron microscopy. in *Electron Tomography: Methods for Three-Dimensional Visualization of Structures in the Cell* ed. by J. Frank (Springer, New York, 2006), pp. 217–243. doi:10.1007/978-0-387-69008-7\_8
- J.B. Heymann, G. Cardone, D.C. Winkler, A.C. Steven, Computational resources for cryo-electron tomography in Bsoft. J. Struct. Biol. 161(3), 232–242 (2008)
- 13. R.A. Crowther, D.J. De Rosier, A, Klug, The reconstruction of a three-dimensional structure from projections and its application to electron microscopy. Proc. R. Soc. Lond. 23 June 1970. Ser. A, Math. Phys. Sci. R. Soc. Lond., pp. 319–340
- C.E. Shannon, Communication in the presence of noise. Proc. IEEE 86(2), 447–457 (1998). doi:10.1109/JPROC.1998.659497
- K. Sandberg, D.N. Mastronarde, G. Beylkin, A fast reconstruction algorithm for electron microscope tomography. J. Struct. Biol. 144(1-2), 61-72 (2003)
- Y. Chen, F. Forster, Iterative reconstruction of cryo-electron tomograms using nonuniform fast Fourier transforms. J. Struct. Biol. 185(3), 309–316 (2014). doi:10.1016/j.jsb.2013.12. 001
- 17. J. Miao, F. Förster, O. Levi, Equally sloped tomography with oversampling reconstruction. Phys. Rev. B **72**(5), 052103 (2005)
- E. Lee, B.P. Fahimian, C.V. Iancu, C. Suloway, G.E. Murphy, E.R. Wright, D. Castano-Diez, G.J. Jensen, J. Miao, Radiation dose reduction and image enhancement in biological imaging through equally-sloped tomography. J. Struct. Biol. 164(2), 221–227 (2008). doi:10.1016/j. jsb.2008.07.011
- R. Gordon, R. Bender, G.T. Herman, Algebraic reconstruction techniques (ART) for threedimensional electron microscopy and x-ray photography. J. Theor. Biol. 29(3), 471–481 (1970)
- 20. P. Gilbert, Iterative methods for the three-dimensional reconstruction of an object from projections. J. Theor. Biol. **36**(1), 105–117 (1972)
- 21. A.H. Andersen, A.C. Kak, Simultaneous algebraic reconstruction technique (SART): a superior implementation of the art algorithm. Ultrason. Imaging 6(1), 81–94 (1984)
- B. Turonova, L. Marsalek, T. Davidovic, P. Slusallek, Progressive stochastic reconstruction technique (PSRT) for cryo electron tomography. J. Struct. Biol. 189(3), 195–206 (2015). doi:10.1016/j.jsb.2015.01.011
- 23. L. Wang, Y. Shkolnisky, A. Singer, in A Fourier-based Approach for Iterative 3D Reconstruction from Cryo-EM Images. ArXiv e-prints 1307 (2013)
- U. Skoglund, L.G. Ofverstedt, R.M. Burnett, G. Bricogne, Maximum-entropy three-dimensional reconstruction with deconvolution of the contrast transfer function: a test application with adenovirus. J. Struct. Biol. 117(3), 173–188 (1996). doi:10.1006/jsbi.1996.0081
- 25. S.F. Gull, T.J. Newton, Maximum entropy tomography. Appl. Opt. 25(1), 156 (1986)
- 26. M.C. Lawrence, M.A. Jaffer, B.T. Sewell, The application of the maximum entropy method to electron microscopic tomography. Ultramicr **31**(3), 285–301 (1989)
- J.R. Kremer, D.N. Mastronarde, J.R. McIntosh, Computer visualization of three-dimensional image data using IMOD. J. Struct. Biol. 116(1), 71–76 (1996)
- 28. P. Engelhardt, Electron tomography of chromosome structure, in *Encyclopedia of Analytical Chemistry* (Wiley, New York, 2006). doi:10.1002/9780470027318.a1405
- M. Kunz, A.S. Frangakis, Super-sampling SART with ordered subsets. J. Struct. Biol. 188(2), 107–115 (2014). doi:10.1016/j.jsb.2014.09.010
- 30. G.T. Herman, S.W. Rowland, Yau Mm, A comparative study of the use of linear and modified cubic spline interpolation for image reconstruction. IEEE Trans. Nucl. Sci. **26**(2), 2879–2894 (1979). doi:10.1109/TNS.1979.4330555

- 31. R. Marabini, G.T. Herman, J.M. Carazo, 3D reconstruction in electron microscopy using ART with smooth spherically symmetric volume elements (blobs). Ultramicr 72(1–2), 53–65 (1998)
- 32. D. Wolf, A. Lubk, H. Lichte, Weighted simultaneous iterative reconstruction technique for single-axis tomography. Ultramicr 136, 15–25 (2014). doi:10.1016/j.ultramic.2013.07.016
- K.J. Batenburg, J. Sijbers, DART: a practical reconstruction algorithm for discrete tomography. IEEE Trans. Image Process. 20(9), 2542–2553 (2011). doi:10.1109/TIP.2011. 2131661
- 34. J. Skilling, R.K. Bryan, Maximum entropy image reconstruction: general algorithm. Mon. Not. R. Astron. Soc. **211**(1), 111–124 (1984). doi:10.1093/mnras/211.1.111
- J. Cope, J. Heumann, A. Hoenger, Cryo-electron tomography for structural characterization of macromolecular complexes. Curr. Protoc. Protein Sci. Chapter 17(Unit17), 13 (2011). doi:10. 1002/0471140864.ps1713s65
- K. Song, L.R. Comolli, M. Horowitz, Removing high contrast artifacts via digital inpainting in cryo-electron tomography: an application of compressed sensing. J. Struct. Biol. 178(2), 108–120 (2012). doi:10.1016/j.jsb.2012.01.003
- 37. M. Maiorca, C. Millet, E. Hanssen, B. Abbey, E. Kazmierczak, L. Tilley, Local regularization of tilt projections reduces artifacts in electron tomography. J. Struct. Biol. **186**(1), 28–37 (2014). doi:10.1016/j.jsb.2014.03.009
- 38. M. Defrise, F. Noo, H. Kudo, A solution to the long-object problem in helical cone-beam tomography. Phys. Med. Biol. **45**(3), 623–643 (2000)
- W. Xu, F. Xu, M. Jones, B. Keszthelyi, J. Sedat, D. Agard, K. Mueller, High-performance iterative electron tomography reconstruction with long-object compensation using graphics processing units (GPUs). J. Struct. Biol. 171(2), 142–153 (2010). doi:10.1016/j.jsb.2010.03. 018
- 40. B. Turonova, L. Marsalek, P. Slusallek, On geometric artifacts in cryo electron tomography. Ultramicr 163, 48–61 (2016). doi:10.1016/j.ultramic.2016.01.002
- 41. M. Maiorca, E. Hanssen, E. Kazmierczak, B. Maco, M. Kudryashev, R. Hall, H. Quiney, L. Tilley, Improving the quality of electron tomography image volumes using pre-reconstruction filtering. J. Struct. Biol. **180**(1), 132–142 (2012). doi:10.1016/j.jsb.2012.05.019
- V. Abrishami, J.R. Bilbao-Castro, J. Vargas, R. Marabini, J.M. Carazo, C.O. Sorzano, A fast iterative convolution weighting approach for gridding-based direct Fourier three-dimensional reconstruction with correction for the contrast transfer function. Ultramicr 157, 79–87 (2015). doi:10.1016/j.ultramic.2015.05.018
- 43. J.J. Fernandez, S. Li, R.A. Crowther, CTF determination and correction in electron cryotomography. Ultramicr 106(7), 587–596 (2006). doi:10.1016/j.ultramic.2006.02.004
- 44. J.A. Mindell, N. Grigorieff, Accurate determination of local defocus and specimen tilt in electron microscopy. J. Struct. Biol. **142**(3), 334–347 (2003)
- 45. H. Winkler, K.A. Taylor, Focus gradient correction applied to tilt series image data used in electron tomography. J. Struct. Biol. **143**(1), 24–32 (2003)
- Q. Xiong, M.K. Morphew, C.L. Schwartz, A.H. Hoenger, D.N. Mastronarde, CTF determination and correction for low dose tomographic tilt series. J. Struct. Biol. 168(3), 378–387 (2009). doi:10.1016/j.jsb.2009.08.016
- M. Eibauer, C. Hoffmann, J.M. Plitzko, W. Baumeister, S. Nickell, H. Engelhardt, Unraveling the structure of membrane proteins in situ by transfer function corrected cryo-electron tomography. J. Struct. Biol. 180(3), 488–496 (2012). doi:10.1016/j.jsb.2012.09.008
- F.K. Schur, W.J. Hagen, A. de Marco, J.A. Briggs, Determination of protein structure at 8.5A resolution using cryo-electron tomography and sub-tomogram averaging. J. Struct. Biol. 184 (3), 394–400 (2013). doi:10.1016/j.jsb.2013.10.015
- A. Bartesaghi, F. Lecumberry, G. Sapiro, S. Subramaniam, Protein secondary structure determination by constrained single-particle cryo-electron tomography. Structure 20(12), 2003–2013 (2012). doi:10.1016/j.str.2012.10.016
- J.G. Galaz-Montoya, C.W. Hecksel, P.R. Baldwin, E. Wang, S.C. Weaver, M.F. Schmid,
   S.J. Ludtke, W. Chiu, Alignment algorithms and per-particle CTF correction for single

- particle cryo-electron tomography. J. Struct. Biol. **194**(3), 383–394 (2016). doi:10.1016/j.jsb. 2016.03.018
- D. Nemecek, J.B. Heymann, J. Qiao, L. Mindich, A.C. Steven, Cryo-electron tomography of bacteriophage φ6 procapsids shows random occupancy of the binding sites for RNA polymerase and packaging NTPase. J. Struct. Biol. 171(3), 389–396 (2010). doi:10.1016/j.jsb. 2010.06.005
- 52. P. van der Heide, X.P. Xu, B.J. Marsh, D. Hanein, N. Volkmann, Efficient automatic noise reduction of electron tomographic reconstructions based on iterative median filtering. J. Struct. Biol. **158**(2), 196–204 (2007). doi:10.1016/j.jsb.2006.10.030
- 53. W. Jiang, M.L. Baker, Q. Wu, C. Bajaj, W. Chiu, Applications of a bilateral denoising filter in biological electron microscopy. J. Struct. Biol. **144**(1–2), 114–122 (2003)
- R.A. Ali, M.J. Landsberg, E. Knauth, G.P. Morgan, B.J. Marsh, B. Hankamer, A 3D image filter for parameter-free segmentation of macromolecular structures from electron tomograms. PLoS ONE 7(3), e33697 (2012). doi:10.1371/journal.pone.0033697
- J.R. Bilbao-Castro, C.O. Sorzano, I. Garcia, J.J. Fernandez, XMSF: structure-preserving noise reduction and pre-segmentation in microscope tomography. Bioinformatics 26(21), 2786– 2787 (2010). doi:10.1093/bioinformatics/btq496
- D.Y. Wei, C.C. Yin, An optimized locally adaptive non-local means denoising filter for cryo-electron microscopy data. J. Struct. Biol. 172(3), 211–218 (2010). doi:10.1016/j.jsb. 2010.06.021
- 57. J.J. Fernandez, TOMOBFLOW: feature-preserving noise filtering for electron tomography. BMC Bioinform. 10, 178 (2009). doi:10.1186/1471-2105-10-178
- 58. A.S. Frangakis, R. Hegerl, Noise reduction in electron tomographic reconstructions using nonlinear anisotropic diffusion. J. Struct. Biol. **135**(3), 239–250 (2001)
- 59. J.J. Fernandez, S. Li, An improved algorithm for anisotropic nonlinear diffusion for denoising crvo-tomograms. J. Struct. Biol. **144**(1–2), 152–161 (2003)
- D.N. Mastronarde, Fiducial marker and hybrid alignment methods for single- and double-axis tomography, in *Electron Tomography: Methods for Three-Dimensional Visualization of Structures in the Cell* ed. by J. Frank. (Springer New York, 2006), pp. 163–185. doi:10.1007/ 978-0-387-69008-7
- C.V. Iancu, E.R. Wright, J. Benjamin, W.F. Tivol, D.P. Dias, G.E. Murphy, R.C. Morrison, J.B. Heymann, G.J. Jensen, A "flip-flop" rotation stage for routine dual-axis electron cryotomography. J. Struct. Biol. 151(3), 288–297 (2005)
- 62. J. Tong, I. Arslan, P. Midgley, A novel dual-axis iterative algorithm for electron tomography. J. Struct. Biol. 153(1), 55–63 (2006). doi:10.1016/j.jsb.2005.10.005
- 63. G.A. Zampighi, L. Zampighi, N. Fain, E.M. Wright, F. Cantele, S. Lanzavecchia, Conical tomography II: A method for the study of cellular organelles in thin sections. J. Struct. Biol. **151**(3), 263–274 (2005). doi:10.1016/j.jsb.2005.05.008
- L. Kovacik, S. Kereiche, P. Matula, I. Raska, Sub-volume averaging of repetitive structural features in angularly filtered electron tomographic reconstructions. Folia Biol. (Praha) 60 (Suppl 1), 66–70 (2014)
- L. Kovacik, S. Kereiche, J.L. Hoog, P. Juda, P. Matula, I. Raska, A simple Fourier filter for suppression of the missing wedge ray artefacts in single-axis electron tomographic reconstructions. J. Struct. Biol. 186(1), 141–152 (2014). doi:10.1016/j.jsb.2014.02.004
- J.M. Carazo, J.L. Carrascosa, Restoration of direct Fourier three-dimensional reconstructions of crystalline specimens by the method of convex projections. J. Microsc. 145(Pt 2), 159–177 (1987)
- 67. Y. Deng, Y. Chen, Y. Zhang, S. Wang, F. Zhang, F. Sun, ICON: 3D reconstruction with 'missing-information' restoration in biological electron tomography. J. Struct. Biol. **195**(1), 100–112 (2016). doi:10.1016/j.jsb.2016.04.004
- 68. D.N. Mastronarde, Dual-axis tomography: an approach with alignment methods that preserve resolution. J. Struct. Biol. **120**(3), 343–352 (1997). doi:10.1006/jsbi.1997.3919
- 69. G. Cardone, K. Grunewald, A.C. Steven, A resolution criterion for electron tomography based on cross-validation. J. Struct. Biol. **151**(2), 117–129 (2005)

- K. Grunewald, P. Desai, D.C. Winkler, J.B. Heymann, D.M. Belnap, W. Baumeister, A.C. Steven, Three-dimensional structure of herpes simplex virus from cryo-electron tomography. Science 302(5649), 1396–1398 (2003)
- Y. Chen, S. Pfeffer, J.J. Fernandez, C.O. Sorzano, F. Forster, Autofocused 3D classification of cryoelectron subtomograms. Structure (2014). doi:10.1016/j.str.2014.08.007
- 72. Y. Chen, S. Pfeffer, T. Hrabe, J.M. Schuller, F. Forster, Fast and accurate reference-free alignment of subtomograms. J. Struct. Biol. **182**(3), 235–245 (2013). doi:10.1016/j.jsb.2013. 03.002
- T. Hrabe, Y. Chen, S. Pfeffer, L.K. Cuellar, A.V. Mangold, F. Forster, PyTom: a python-based toolbox for localization of macromolecules in cryo-electron tomograms and subtomogram analysis. J. Struct. Biol. 178(2), 177–188 (2012). doi:10.1016/j.jsb.2011.12.003
- J.T. Huiskonen, M.L. Parsy, S. Li, D. Bitto, M. Renner, T.A. Bowden, Averaging of viral envelope glycoprotein spikes from electron cryotomography reconstructions using Jsubtomo. J. Vis. Exp. 92, e51714 (2014). doi:10.3791/51714
- L.M. Voortman, M. Vulovic, M. Maletta, A. Voigt, E.M. Franken, A. Simonetti, P.J. Peters, L.J. van Vliet, B. Rieger, Quantifying resolution limiting factors in subtomogram averaged cryo-electron tomography using simulations. J. Struct. Biol. 187(2), 103–111 (2014). doi:10. 1016/j.jsb.2014.06.007
- J. Fontana, G. Cardone, J.B. Heymann, D.C. Winkler, A.C. Steven, Structural changes in Influenza virus at low pH characterized by cryo-electron tomography. J. Virol. 86(6), 2919– 2929 (2012). doi:10.1128/JVI.06698-11
- 77. J.G. Galaz-Montoya, J. Flanagan, M.F. Schmid, S.J. Ludtke, Single particle tomography in EMAN2. J. Struct. Biol. **190**(3), 279–290 (2015). doi:10.1016/j.jsb.2015.04.016
- F.K. Schur, R.A. Dick, W.J. Hagen, V.M. Vogt, J.A. Briggs, The structure of immature virus-like Rous Sarcoma Virus Gag particles reveals a structural role for the p10 domain in assembly. J. Virol. 89(20), 10294–10302 (2015). doi:10.1128/JVI.01502-15
- 79. F.K. Schur, W.J. Hagen, M. Rumlova, T. Ruml, B. Muller, H.G. Krausslich, J.A. Briggs, Structure of the immature HIV-1 capsid in intact virus particles at 8.8 A resolution. Nature 517(7535), 505–508 (2015). doi:10.1038/nature13838
- 80. D. Nicastro, Cryo-electron microscope tomography to study axonemal organization. Methods Cell Biol. **91**, 1–39 (2009). doi:10.1016/S0091-679X(08)91001-3
- U.E. Maurer, T. Zeev-Ben-Mordehai, A.P. Pandurangan, T.M. Cairns, B.P. Hannah, J.C. Whitbeck, R.J. Eisenberg, G.H. Cohen, M. Topf, J.T. Huiskonen, K. Grunewald, The structure of herpesvirus fusion glycoprotein B-bilayer complex reveals the protein-membrane and lateral protein-protein interaction. Structure 21(8), 1396–1405 (2013). doi:10.1016/j.str. 2013.05.018
- J. Liu, A. Bartesaghi, M.J. Borgnia, G. Sapiro, S. Subramaniam, Molecular architecture of native HIV-1 gp120 trimers. Nature 455(7209), 109–113 (2008). doi:nature07159 [pii] 10. 1038/nature07159
- T.A. Bharat, N.E. Davey, P. Ulbrich, J.D. Riches, A. de Marco, M. Rumlova, C. Sachse, T. Ruml, J.A. Briggs, Structure of the immature retroviral capsid at 8 A resolution by cryo-electron microscopy. Nature 487(7407), 385–389 (2012). doi:10.1038/nature11169
- 84. T.A. Bharat, C.J. Russo, J. Lowe, L.A. Passmore, S.H. Scheres, Advances in single-particle electron cryomicroscopy structure determination applied to sub-tomogram averaging. Structure 23(9), 1743–1753 (2015). doi:10.1016/j.str.2015.06.026
- J. Lin, K. Okada, M. Raytchev, M.C. Smith, D. Nicastro, Structural mechanism of the dynein power stroke. Nat. Cell Biol. 16(5), 479–485 (2014). doi:10.1038/ncb2939
- J.B. Heymann, D.C. Winkler, Y.I. Yim, E. Eisenberg, L.E. Greene, A.C. Steven, Clathrin-coated vesicles from brain have small payloads: a cryo-electron tomographic study. J. Struct. Biol. 184(1), 43–51 (2013). doi:10.1016/j.jsb.2013.05.006
- 87. W. van Aarle, W.J. Palenstijn, J. De Beenhouwer, T. Altantzis, S. Bals, K.J. Batenburg, J. Sijbers, The ASTRA toolbox: a platform for advanced algorithm development in electron tomography. Ultramicr 157, 35–47 (2015). doi:10.1016/j.ultramic.2015.05.002

88. Q. Chu, K. Zhang, X. Wan, C. Zhang, Y. Zhang, G. Zhang, B. Shen, X. Lu, K. Zhao, X. Chu, F.F.S. Zhang, ATOM1.0 A GPU powered package for electron tomography reconstruction. Acta Biophys. Sin. 27(3), 231–241 (2011)

- 89. Y. Chen, Y. Zhang, K. Zhang, Y. Deng, S. Wang, F. Zhang, F. Sun, FIRT: filtered iterative reconstruction technique with information restoration. J. Struct. Biol. **195**(1), 49–61 (2016). doi:10.1016/j.jsb.2016.04.015
- D. Ress, M.L. Harlow, M. Schwarz, R.M. Marshall, U.J. McMahan, Automatic acquisition of fiducial markers and alignment of images in tilt series for electron tomography. J. Electron Microsc. 48(3), 277–287 (1999)
- T. Dahmen, L. Marsalek, N. Marniok, B. Turonova, S. Bogachev, P. Trampert, S. Nickels, P. Slusallek, The ettention software package. Ultramicr 161, 110–118 (2016). doi:10.1016/j. ultramic.2015.10.012
- H. Winkler, 3D reconstruction and processing of volumetric data in cryo-electron tomography.
   J. Struct. Biol. 157(1), 126–137 (2007)
- 93. S. Nickell, F. Forster, A. Linaroudis, W.D. Net, F. Beck, R. Hegerl, W. Baumeister, J.M. Plitzko, TOM software toolbox: acquisition and analysis for electron tomography. J. Struct. Biol. **149**(3), 227–234 (2005)
- 94. J.I. Agulleiro, J.J. Fernandez, Fast tomographic reconstruction on multicore computers. Bioinformatics 27(4), 582–583 (2011). doi:10.1093/bioinformatics/btq692
- C. Messaoudii, T. Boudier, C.O. Sanchez Sorzano, S. Marco, TomoJ: tomography software for three-dimensional reconstruction in transmission electron microscopy. BMC Bioinform. 8, 288 (2007). doi:10.1186/1471-2105-8-288
- S. Phan, A. Lawrence, T. Molina, J. Lanman, M. Berlanga, M. Terada, A. Kulungowski,
   J. Obayashi, M. Ellisman, TxBR montage reconstruction for large field electron tomography.
   J. Struct. Biol. 180(1), 154–164 (2012). doi:10.1016/j.jsb.2012.06.006

## Chapter 9 Structural Biology in Situ Using **Cryo-Electron Subtomogram Analysis**

Stefan Pfeffer and Friedrich Förster

**Abstract** Cryo-electron tomography (CET) provides three-dimensional (3D) views on the structure and organization of a wide range of frozen-hydrated specimens under near-to-native conditions. In combination with advanced image processing methods, the locations, orientations and structures of large macromolecular complexes can be mined from tomographic data.

#### 9.1 Introduction

CET and subtomogram analysis allow studying the structure and distribution of macromolecular complexes without isolation and purification, which is a major caveat in the structural analysis of large membrane-embedded or transiently associated complexes. CET often complements reductionist structural molecular biology approaches that aim at obtaining high-resolution structures of isolated components (X-ray crystallography, cryo-EM single particle analysis), putting them into a cellular context. In this sense CET bridges the traditionally largely separated disciplines of molecular and cellular structural biology. Here, we provide an overview of the computational methodology for subtomogram analysis and illustrate the use of these approaches for a set of tomograms depicting endoplasmic reticulum (ER)-derived vesicles. Using strategies for particle localization, subtomogram alignment and subtomogram classification, a subnanometer resolution

S. Pfeffer · F. Förster (⋈) Department of Molecular Structural Biology, Max-Planck Institute

of Biochemistry, Am Klopferspitz 18, 82152 Martinsried, Germany e-mail: f.g.forster@uu.nl

S. Pfeffer

e-mail: Pfeffer@biochem.mpg.de

F. Förster

Cryo-Electron Microscopy, Bijvoet Center for Biomolecular Research, Utrecht University, Padualaan 8, 3584 CH Utrecht, The Netherlands

subtomogram average of the mammalian ribosome bound to the protein-conducting channel in the native ER-membrane is obtained from these tomograms.

## 9.2 Increasing the Resolution of Volumetric Data by Averaging

The interpretation of tomographic data from frozen hydrated samples is a formidable challenge due to their low signal-to-noise ratio (SNR). The low SNR is a direct consequence of the high dose sensitivity of vitrified specimens, which must be hence imaged with very few electrons [1]. Typically, the cumulative electron dose used for acquisition of a tomogram should not exceed 100 e<sup>-</sup>/Å<sup>2</sup> to avoid specimen alteration and excessive structural damage. This electron dose ultimately limits the resolution of the raw tomogram. The SNR strongly decreases as a function of spatial frequency until it is too low to distinguish signal from the background. Depending on the sample and equipment used for imaging this frequency is somewhere in the range of 3-10 nm [2, 3]. However, by iterative alignment and averaging of subtomograms, each depicting the same macromolecular complex, the inherently low SNR can be increased and the higher resolution signal hidden in the raw tomogram can be retrieved. Assuming a perfect spatial alignment of subtomograms, the SNR scales linearly with the square of the number of subtomograms used for averaging. With an increasing number of structure factors rising above the significance (noise) level, the resolution of the subtomogram average improves.

#### 9.3 Particle Localization

Although the SNR is typically low in CET, it is possible to locate macromolecular structures of 500 kDa or more with acceptable specificity. This section introduces different concepts for particle localization, with an emphasis on cross-correlation based pattern recognition algorithms.

### 9.3.1 Template-Free Approaches

Template-free approaches for detection of macromolecules in tomograms rely on generic features of complexes. For example, the strong variation of the intensity at the boundaries can be used for detection in mean curvature motion (MCM) based particle localization [4]. More elaborate approaches first filter the tomogram according to objects of target sizes by convolution with a Gaussian and

subsequently focus on the candidates with strong curvature, as specified by the second derivative tensor [5]. Similarly, strong anisotropic diffusion, which also bases on the second derivative tensor, and subsequent thresholding for the prevailing features has been used for initial detection of candidates, which were afterwards filtered according to the volume of the objects [6]. Subsequently, the candidates were clustered according to efficiently computed, rotation-invariant properties in an entirely data-driven workflow.

#### 9.3.2 Template Matching

In many cases, however, structures of the complexes of interest are at least approximately known. Template-based identification and detection is then preferred because it is more specific and efficient. Cross-correlation based pattern recognition algorithms use a template structure ('template matching') [7] depicting the complex of interest for particle localization. In essence, the tomographic volume is screened for features that closely resemble the 3D template. For optimal performance, the provided template structure has to be adapted to the acquisition conditions. In particular, the average defocus modulating the phase contrast and the information loss due to the missing wedge has to be considered. To this end, the template structure is convoluted with a point-spread function (PSF), i.e., a function that describes how a point is deformed in the tomographic imaging.

In general, template matching provides a measure of the local similarity of the template and the tomogram. The most common similarity metric in image processing is cross-correlation. For this purpose, the template structure is shifted through the tomogram in all three spatial directions, voxel by voxel. This can be accomplished efficiently with the help of Fast Fourier Transforms (FFT) [7, 8]. In the cross correlation volume, the cross-correlation coefficient (CCC) of the template and the local tomogram is assigned to the respective central voxel. To account for the missing wedge and contrast variations within the tomogram, the CCC is constrained to commonly sampled segments in Fourier space and computed on volumes locally normalized within a tight mask [8, 9]. Because the macromolecular complexes of interest can be oriented arbitrarily in the tomogram, the voxel-wise cross-correlation is determined using a predefined set of 3D orientations for the template structure. To avoid excessive computational demands for template matching the angular sampling must not be too fine. The required sampling depends on the voxel size used for the search and on the diameter of the template. In many cases, the angular difference between two adjacent orientations is above 10°. From the computed cross correlation volumes only the highest CCC is typically retained for each voxel because the required storage space would be enormous otherwise. A list of peaks can be compiled from the resulting 3D correlation volume, indicating positions and corresponding orientations of candidate particles [7].

## 9.3.3 Peak Selection After Template Matching

Mostly due to the low SNR in the data, high CCCs are not exclusively obtained for the macromolecular complex of interest, but in certain cases also for other structures ('false positives'). To distinguish between true and false positive peaks of the cross-correlation volume, a variety of methods is available [7]. A pragmatic way of assessing the identity of a cross correlation peak is to manually inspect the corresponding position in the queried tomogram. The phenomenal performance of the human eye is then used to distinguish false from true positives in the context of the tomogram (Fig. 9.1a). Another option for roughly distinguishing between true and false positive peaks is to plot a histogram of correlation coefficients: for data with good quality, a Gaussian-like distribution of high correlation coefficients originating from 'true positives' will be mostly separated from an increasing number of low correlation coefficients originating from 'false positives' (Fig. 9.1b). Furthermore, repeating cross-correlation based pattern recognition with a structurally different decoy with comparable statistics as the template, most easily obtained by mirroring the reference structure [10], can help to discriminate true and false positives. For false positives, cross-correlation coefficients for the right- and wrong-handed reference are typically similar. In contrast, a markedly higher correlation coefficient can be expected for the right-handed reference structure in case of a true positive peak (Fig. 9.1c). Expanding the template matching approach to more than one single template and combining the scores for the different templates can also enhance the specificity of the approach [7, 11]. Finally, approaches to classification of subvolumes extracted from the tomogram at the corresponding positions are powerful to distinguish true and false positive peaks, in particular, if the subvolumes can be classified according to features that are not included in the reference structure (see below).

## 9.3.4 Example Dataset

In a representative tomogram of the example dataset depicting ER membrane-associated ribosomes used for illustration, peaks of the cross-correlation volume resulting from template matching in PyTom with a cryo-EM single particle reconstruction of the mammalian ribosome (EMD-5592) primarily correspond to cytosolic and membrane-bound ribosomes. However, also high-contrast features, such as gold beads used as fiducial markers for tilt image alignment, edges of the carbon support foil, or the membrane of ER-derived vesicles all yield high cross-correlation peaks due to their high SNRs and are thus frequently picked up as false positives (Fig. 9.2).

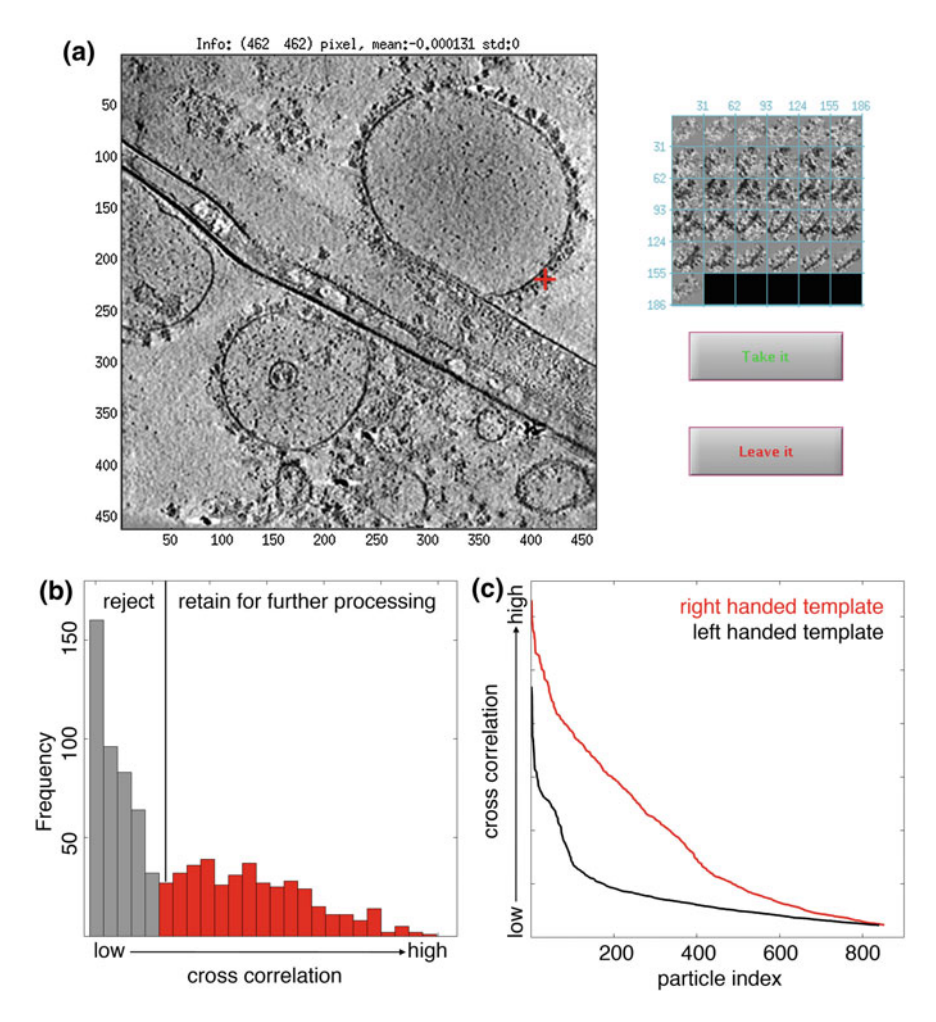


**Fig. 9.1** Approaches to peak selection after template matching. **a** Visual inspection of cross correlation peaks in context of the tomogram using the MATLAB function tom\_chooser.m. For each peak, the position in the tomogram (left) and a slice series through the local surroundings (right) are displayed. **b** Histogram of cross correlation values, showing a Gaussian-like distribution of high correlation coefficients originating from putative 'true positives' (red), mostly separated from an increasing number of low correlation coefficients originating from putative 'false positives' (grey). **c** Plot of cross correlation values from template matching using either a right-(red) or left-handed (black) template structure in descending order. A markedly higher correlation coefficient is obtained for the right-handed template structure for approximately 400 peaks

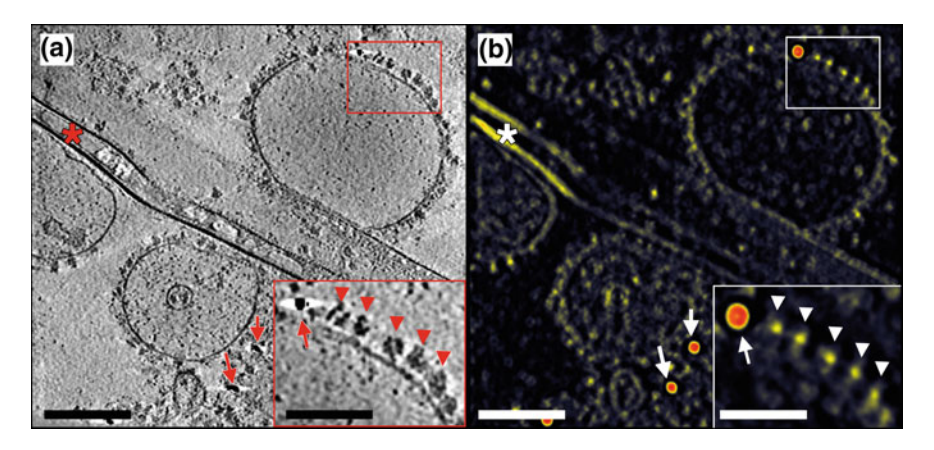


**Fig. 9.2** Example for template matching against the mammalian ribosome in PyTom. **a** Slice of a tomogram depicting canine ER-derived membrane vesicles populated with membrane-bound ribosomes. The insert shows a magnified region of the tomogram, in which ER-associated ribosomes can be clearly discerned (red arrow heads). The edge of the lacey carbon support film (red asterisk) and gold fiducials (red arrows) are highlighted. **b** Corresponding slice through the cross correlation volume after template matching against the mammalian ribosome. Very high (red), medium (yellow) and low (dark blue) cross correlation values are colour-coded. High cross correlation values are obtained not only for ribosomes (white arrow heads), but also for high contrast features, such as gold fiducials (white arrows) and the carbon edge (white asterisk). Scale bars in the full tomogram and the magnified region correspond to 200 nm and 100 nm, respectively

### 9.4 Subtomogram Alignment

By iterative alignment and averaging of subtomograms, all depicting the same macromolecular complex, the SNR and resolution of structural information can be increased [12]. This section introduces various concepts for subtomogram alignment, focusing on the different scoring and sampling strategies that are commonly used.

## 9.4.1 Scoring Strategies

The problem in subtomogram averaging is that the orientations and precise positions of particles in the subtomograms are not known. In mathematical terms, the orientations and positions are hidden variables. In subtomogram averaging one needs to find the values of these hidden parameters and the corresponding subtomogram average that explains the observed data best. An elegant approach to solve this problem is based on maximum likelihood (ML) principles [13, 14]. This methodology assigns a probability density distribution to each hidden variable. Importantly, this distribution function is continuous, i.e., a particle does not have a

single position or orientation, but rather a whole set with different probabilities. The assignments are initially fuzzy and become better defined during an iterative learning process, most commonly using an optimization algorithm called expectation maximization. This algorithm starts from an initial model for the 3D density underlying the tomograms. In the expectation step different rotations and translations of the model are sampled and compared with the subtomograms in order to approximate their probabilities. Taking into consideration the probabilities of the rotations and translations, subtomograms are averaged (maximization step) and the resulting structure is used as a reference for the next round of alignment. In addition to approximation of the hidden variables, the software RELION also uses an empirical Bayesian approach to correct for the CTF [15]. This approach is very successful in single particle analysis [16] and has recently been generalized to subtomogram averaging.

The above ML-based subtomogram averaging approach is computationally extremely demanding. To process large amounts of data in a reasonable timeframe a simpler quasi-expectation maximization algorithm is typically used. Instead of assigning a continuous probability density function to each hidden variable only a single value is assigned—the one with the highest probability. In mathematical terms the probability density function would be a delta function, i.e., non-zero only for a single value. This binary assignment greatly simplifies the alignment process, but the radius of convergence is typically decreased compared to ML-based alignment; the iterative optimization process is more prone to getting trapped in local minima. Nevertheless, this simpler algorithm is sufficient for accurate particle alignment in particular for large complexes and will be described in more detail in the following.

## 9.4.2 Sampling Strategies

Starting from an initial structural model, the iterative quasi-expectation maximization algorithm aims to approximate the values of experimentally undetermined translations and rotations of the respective subtomogram. In each iteration, different rotations and translations of subtomograms are sampled in order to estimate the expected rotations and translations (quasi-expectation step). These values are determined on the basis of a similarity score, commonly the cross-correlation coefficient (CCC) of the subtomogram with the iteratively updated reference. The computation of the CCC is typically constrained to commonly sampled regions in Fourier space ('constrained cross correlation') in order to compensate for the missing wedge effect [9]. Taking into consideration the rotations and translations yielding the maximum CCCs, subtomograms are averaged and the resulting structure is used as a reference for the next round of alignment (quasi-maximization step). This procedure is repeated until rotations and translations of subtomograms have converged.

In order to reduce the risk of aligning and enhancing noise ('overfitting') or getting caught in local minima during the alignment, an adaptive bandpass filter can be applied to the reference during the iterative alignment procedure. In the beginning of each iteration, this bandpass filter is set according to the resolution determined by Fourier Shell Correlation (FSC) of two halves of the data averaged according to the previous iteration [17]. A way to further reduce the influence of noise on subtomogram alignment is to split the dataset into two halves that are processed completely independently from each other ('gold standard alignment') [16, 18]. By determining the adaptive bandpass filter that is applied to the reference for alignment by FSC of the two completely independent halfsets of the data, the resolution can be approximated essentially without contribution of artificially correlated noise [19]. Note that both independent averages still contain artificially enhanced ('overfitted') noise, but it will not affect the FSC because these artefacts are different in both subtomogram averages.

Typically, the translational search is carried out in Fourier space using the convolution theorem, while rotational search can be performed either in real space [17] or in spherical harmonics space using a generalized convolution theorem [19]. The latter approach to rotational sampling is also known as Fast Rotational Matching (FRM). Since the rotational search using spherical harmonics is orders of magnitude faster than in real space, it provides the opportunity to sample rotations exhaustively in a sensible amount of time, while in real space, rotational search is usually restricted around a predetermined starting angle (e.g. from template matching). Sampling rotations globally allows a reference-free alignment approach, in which subtomograms are initially aligned to a featureless sphere, instead of an external reference structure. This strongly reduces template bias during the subtomogram alignment and allows determining the structure of unknown macromolecular complexes without using a reference.

## 9.4.3 Example Dataset

For demonstration purposes, we selected approximately 350 ribosome-containing subtomograms from the tomogram shown in Fig. 9.2b and aligned them without any prior knowledge about ribosome orientations using alternating translational and global rotational search in Fourier space using FRM in PyTom. The subtomogram average evolves from a featureless sphere to a defined ribosome within 10 alignment iterations (Fig. 9.3a). This approach can be chosen to minimize template bias during subtomogram alignment or to align subtomograms extracted from manually picked coordinates, if no prior structural knowledge about the macromolecule of interest is available. From the example dataset depicting ER membrane-associated ribosomes used for illustration, 17,500 subtomograms were selected and aligned using simultaneous translational and restricted rotational search in real space following either the 'conventional' or the 'gold standard' alignment approach implemented in PyTom. Both approaches yielded essentially identical densities

with an overall resolution of approximately 9 Å (Fig. 9.3b), as estimated by Fourier cross-resolution (FCR) and FSC of averages from two halves of the data. Rod-like densities co-localizing with alpha helices in a superposed atomic model of the ribosome as well as the presence of clearly resolved transmembrane helices for the protein translocon are consistent with the estimated overall resolution. Local resolution estimation reveals that the ribosome and membrane-embedded parts of the protein translocon are better resolved than segments protruding into the lumen of the ER (Fig. 9.3c). In line with this observation, subtomogram classification independently indicates that ribosome binding to the translocon is not entirely homogeneous. The translocon allows for minor tilting of the ribosome, which results in increasing alignment error of lumenal translocon segments.

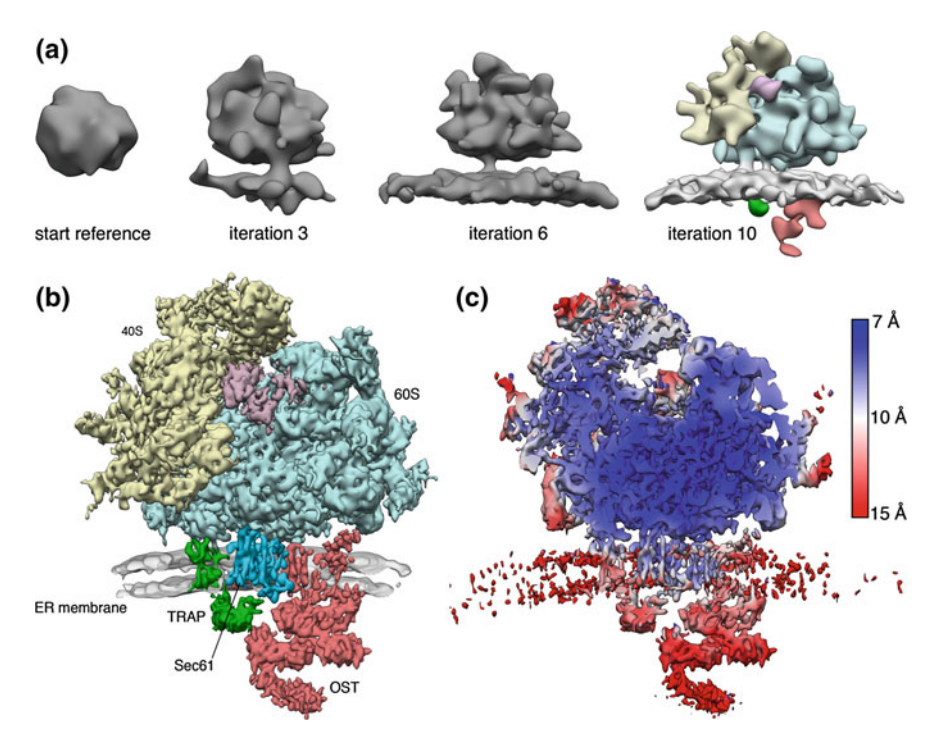


**Fig. 9.3** Examples for subtomogram averaging of the ER membrane-associated ribosome in PyTom. **a** 377 ribosome-containing subtomograms originating from one tomogram were aligned without prior knowledge using FRM. The subtomogram average evolves from a featureless sphere used as a starting reference (left) to a defined ribosome with density for the ER membrane within 10 alignment iterations (right). 40S subunit: yellow, 60S subunit: blue, translation elongation factors: magenta. **b** 17,500 subtomograms depicting ribosomes bound to the fully assembled protein translocon were aligned using simultaneous translational and restricted rotational search in real space, yielding a density with an overall resolution of 9 Å. Secondary structure elements are clearly resolved for the ribosome (Coloring as in **a**) and membrane-embedded parts of the protein translocon (Sec61: dark blue, TRAP: green, OST: red). **c** Local resolution estimation reveals that the ribosome and membrane-embedded parts of the protein translocon are better resolved than segments protruding into the lumen of the endoplasmic reticulum

#### 9.5 Subtomogram Classification

The purpose of classification approaches is to disentangle compositional and conformational heterogeneity of the macromolecular complex of interest. However, the incomplete spatial sampling originating from the missing wedge, the low SNR, the unknown number of classes and the often-unbalanced class occupation (i.e., relative abundances of conformers differ strongly) in tomographic data make a reliable classification of subtomograms challenging. In this section, various classification approaches are introduced that either rely on a prior, separate alignment of the subtomograms or allow simultaneous alignment and classification based on multiple references.

#### 9.5.1 Uncoupled Alignment and Classification

For classification by constrained principal-component analysis (CPCA), a matrix of constrained correlation coefficients is computed for all pairs of pre-aligned subtomograms and subsequently analysed by principal-component analysis (PCA) and k-means clustering [20, 21]. A major advantage of this approach is that it is conceptually easy and its independence from the alignment process allows straightforward focusing on specific areas of interest. Due to the pairwise cross-correlation, this approach is computationally very expensive and only applicable to medium-sized datasets (<10,000 subtomograms). However, in many instances the analysis can be performed in smaller subsets of the data and the subtomograms can often be downsampled ('binned') to distinguish their main distinctive features. In order to recover also small populations of structurally or conformationally distinct macromolecular complexes, the number of output classes typically strongly oversamples the number of expected distinct classes in the data. Redundant classes can then be merged to reduce the number of classes and increase the SNRs of the individual structures.

### 9.5.2 Simultaneous Alignment and Classification

Other commonly used methods base on simultaneous subtomogram alignment to different reference structures ('multi-reference procedures'). Classification is achieved by assigning the subtomogram to the reference class with the highest score [13, 14, 17]. Since the computational effort of simultaneous alignment to multiple references is much larger than for a single reference, acceleration of the alignment by FRM is strongly beneficial [22]. A further problem of multi-reference alignment is that the noise outside the area of structural variation can strongly decrease the classification accuracy. To overcome this limitation, multi-reference alignment has recently been extended to

automatically focus on the areas of major structural discrepancy between the references [22]. While these multi-reference approaches are computationally less expensive and can thus be applied to extended datasets of subtomograms, a high number of iterations are necessary for convergence of class assignments, if the initial references do not properly sample the structural and conformational landscape of the depicted macromolecular complexes.

#### 9.5.3 Example Dataset

Using CPCA and k-means clustering in PyTom to sort pre-aligned subtomograms extracted from one tomogram of the example dataset depicting ER membrane-associated ribosomes (shown in Fig. 9.2b), structural heterogeneity can be detected in various regions of the average. Several consecutive steps of classification separate 60S and 80S ribosomes (Fig. 9.4a), membrane- and non membrane-bound ribosomes (Fig. 9.4b), as well as fully and partially assembled translocon complexes (Fig. 9.4c). Eventually, a relatively pure set of 80S ribosomes bound to the fully assembled protein translocon can be obtained. Extensive classification of the set of 17,500 subtomograms depicting the protein translocon will allow detection of substoichiometric translocon components, essentially defining all long-lived states describing the compositional landscape of the translocon.

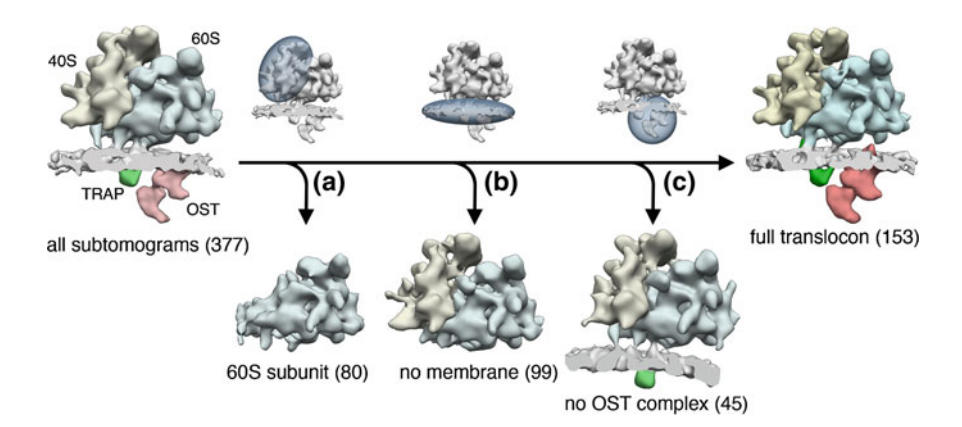


**Fig. 9.4** Example for subtomogram classification using CPCA and kmeans clustering in PyTom. Several consecutive steps of classification separate a set of 377 pre-aligned ribosome-containing subtomograms into 60S and 80S ribosomes (**a**), membrane- and non membrane-bound ribosomes (**b**), as well as fully and partially assembled translocon complexes (**c**). Masks used for the respective classification step are depicted in dark blue. Numbers of subtomograms for the respective class averages are given in brackets. Coloring as in Fig. 9.3

#### 9.6 Available Software

This section provides a (non-comprehensive) overview of the currently developed and/or maintained software packages for above-described subtomogram analysis.

Package	Tasks	Published applications
PyTom/av3	Localization, alignment, classification	Ribosome, ER-associated ribosome, NPC, viral proteins, Golgi protein array, COPI + II, proteasome
Dynamo	Localization, alignment, classification	Viral proteins, Serotonin 5-HT3 Receptor
PEET	Alignment, classification	Axoneme, secretion systems, viral proteins, IgG hexamers, flagellar motor, chemoreceptor arrays, ATP-synthase
Relion	Alignment, classification	Ribosome, viral proteins
EMAN2	Alignment, classification	TriC chaperone
protomo	Alignment, classification	Viral spikes, Chemotaxis receptor, flight muscles

## 9.7 Selected Recent Applications of Subtomogram Averaging

This section briefly highlights some successful case studies focusing on structural analysis of macromolecular complexes using CET and subtomogram analysis. In general, cryoelectron tomograms of vitrified samples represent a 3D snapshot of the native structures and interactions of all imaged macromolecules. Thus, in addition to plain structural information of single macromolecular complexes in their native environment, subtomogram analysis allows a detailed dissection of the 3D distribution and arrangement of these complexes with respect to each other and other cellular structures.

#### 9.7.1 Ribosomes

Cellular protein synthesis is carried out by the ribosome, a universally conserved RNA-protein complex of 3–4 MDa size. Due to its size and high contrast, the ribosome is excellently suited to be studied using CET and subtomogram analysis. It consists of two subunits: the small subunit facilitates decoding of the messenger

RNA, while the large subunit mediates formation of peptide bonds in the nascent protein [23]. An analysis of the relative positioning and orientation of ribosomes imaged using CET and localized using subtomogram analysis revealed the compact organization of bacterial and eukaryotic cytosolic polyribosomes [24–28]. In these studies, neighboring ribosomes exhibit preferred arrangements, resulting in pseudoplanar or pseudohelical organizations. While the transcript is sequestered on the inside of the polyribosome, polypeptide exit sites of individual ribosomes are well separated and face the cytosol, presumably to limit aggregation of nascent peptides and to promote productive folding. Another specific macromolecular arrangement that has been structurally characterized using CET and subtomogram analysis is the 100S ribosome pair that transiently forms in bacterial cells under nutritional stress [29]. The 3D configuration of these ribosome pairs is well preserved and results in close contact between the small ribosomal subunits.

CET and subtomogram analysis furthermore provided an unprecedented view on the structure and molecular architecture of the native ribosome-associated protein translocon in the ER membrane [30] and further studies allowed identification of the oligosaccharyl-transferase (OST) complex, the translocon associated protein complex (TRAP) and the protein-conducting channel Sec61 in a map at 20 Å resolution [31]. Subtomogram classification approaches furthermore uncovered compositional heterogeneity with respect to translocon constituents; TRAP is present on all ribosome-bound translocon complexes, while OST is highly substoichiometric and found on only 40–70% of translocon complexes. Recently, technical developments in the field of cryo-EM (direct detectors, acquisition and image processing software) enabled us to visualize the mammalian ribosome-bound translocon in a native membrane environment at subnanometer resolution [32]. Secondary structure elements were clearly resolved in the density for the ribosome and the directly associated Sec61 protein-conducting channel. The visibility of secondary structure elements allowed for a detailed analysis of the Sec61 conformational state in a native lipid environment. Finally, an analysis of the structure and supramolecular organization of mitochondrial ribosomes in intact yeast mitochondria complements the growing compendium of cellular translation machineries studied using CET and subtomogram analysis [33].

### 9.7.2 Other Cytosolic Complexes

A recent study imaged intact neuronal cells with CET and analysed the structure, variability and distribution of a central component of the cytosolic protein degradation machinery, the 26S proteasome, using subtomogram analysis [3]. Subtomogram classification approaches allowed separating populations of proteasomes with one or two regulatory 19S caps bound to the 20S core proteasomes, and visualized the regulatory caps in different functional states of substrate degradation that have been previously characterized using single particle cryo-EM analysis [34]. Based on the low abundance of the substrate processing state of the proteasome, the authors

concluded that the capacity of the proteasomal protein degradation system is by far not fully used in the absence of proteotoxic stress.

Another cytoplasmic macromolecular assembly that proved highly suitable for structural analysis using CET and subtomogram analysis is the axoneme cytoskeletal element in eukaryotic cilia and flagella. An axoneme typically consists of a ring of nine outer microtubule doublets with each an outer and inner dynein arm, connected to two central microtubule doublets via nine radial spokes. Subtomogram averages revealed nucleotide-induced global structural changes of the outer and inner dynein arms, which drive sliding motions of adjacent microtubules and explain axoneme bending [35, 36]. Further studies aimed at a detailed structural dissection of the molecular axoneme architecture, focusing on the radial spokes [37], the nexin-dynein regulatory complex that bridges outer microtubule doublets [38], the polarity and asymmetry in outer dynein arms [39, 40] and structural defects of axonemes arising from primary ciliary dyskinesia [41].

#### 9.7.3 Membrane Protein Complexes

CET and subtomogram analysis are particularly attractive for studying the structure of membrane-embedded and –associated complexes, because detergent solubilization is not required. Thus, destabilization of the complex as well as possible misinterpretation of the density of the detergent micelle surrounding a solubilized membrane protein are avoided. Structural analysis of the nuclear pore complex (NPC), the gateway for nucleo-cytoplasmic transport, has long remained an enormous challenge. The NPC is a highly dynamic, gigantic machinery of >100 MDa molecular weight, embedded into the two membranes constituting the nuclear envelope. CET and subtomogram analysis revealed that the ~30 different nucleoporins, constituting the NPC, assemble into distinct cytoplasmic and nuclear rings, associated to a scaffold [42, 43]. NPC structures from different organisms illuminated various aspects in regulation/gating of nucleo-cytoplasmic transport and led to increasingly detailed insights into the molecular architecture of the NPC [44–47].

Protein transport between organelles is mediated by trafficking vesicles that are formed by protein coats polymerizing as cages on the membrane surface. The variable size of trafficking vesicles and the highly dynamic nature of coat proteins precluded their analysis using conventional structural biology methods. Retrograde transport from the Golgi to the ER and within the Golgi compartments is mediated by coat protein complex (COP) I. Studies using CET and subtomogram analysis revealed a three-fold symmetrical arrangement of the COPI components on the vesicle membrane. COPI triads adopted alternative conformations to change the number of neighboring interacting triads to form vesicles with variable size [48]. Based on a higher resolution subtomogram average, the detailed molecular architecture of a single COPI triad could be determined [49]. Anterograde transport of newly synthesized proteins from the ER to the Golgi is mediated by COPII. A recent study using subtomogram analysis revealed, how the inner layer of the

COPII coat, which interacts with the cargo and the membrane, assembles with the cage-forming outer COPII layer [50].

Other macromolecular membrane protein assemblies that have been studied using CET and subtomogram analysis are immature retrovirus capsids that are heterogeneous in size and morphology, favoring CET for their structural analysis. These highly repetitive structures could be resolved to subnanometer resolution for three different retroviruses including HIV-1, revealing the tertiary and quaternary structural interactions mediating virus assembly [51, 52].

Another huge membrane-embedded structure extensively studied using CET and subtomogram analysis is the bacterial flagellar motor that drives locomotion using energy stored in a chemical gradient across the bacterial cell membrane. Subtomogram averages of the flagellar motor from various species revealed its basic molecular architecture [53], structural diversity [54] and sequential assembly [55]. Structurally closely related to the flagellar motor are bacterial secretion systems/injectisomes that are used to transfer virulence proteins into eukaryotic host cells. Studies using CET and subtomogram analysis illuminated the interaction between host and pathogen cells, providing insights into the extensive conformational changes of secretion systems that drive effector translocation upon host membrane contact [56, 57]. A size analysis of injectisome basal bodies in single subtomograms revealed significant variations in length, which is likely required for many proteins spanning two membranes to accommodate a range of variable intermembrane distances [58].

Finally, the structure of mitochondrial ATP synthases in the inner mitochondrial membrane was studied using CET and subtomogram analysis, revealing a conserved dimeric organization in various organisms, mediated by their peripheral stalks [59, 60]. Analysis of the long-range order of ATP synthase dimers revealed their distinct arrangement in long double rows along the cristae ridges, likely inducing their high membrane curvature.

This multitude of successful case studies demonstrates the potential of CET and subtomogram analysis for structural studies in situ. Recent advances in direct detector technology, data acquisition strategies and image processing software promise highly detailed insights into the structure and organization of macromolecules in a cellular context, which will advance our understanding of a cell's native molecular landscape significantly, in the future.

## 9.8 Practical Section: Step-by-Step Guide for Subtomogram Analysis Using av3 and PyTom

### 9.8.1 Template Matching and Peak Selection

This section explains how to set up a template matching job and how to select a number of cross-correlation peaks for further processing in av3/tom and PyTom.

Scripts from av3/tom are in MATLAB (ending:.m) and PyTom procedures in python (.py). The main steps are (I) preparing files for template matching, (II) running template matching on your local computing cluster, (III) extracting peaks from the cross-correlation volumes and (IV) selecting peaks for subtomogram reconstruction.

- (I) Preparation of files for template matching:
  - A template structure can be generated either from EM densities deposited in the EMDB or by simulating EM density based on an atomic structure deposited in the PDB (tom\_pdb2em.m). In order to recapitulate the imaging conditions used for acquisition of the tomography data, the density should be convoluted with a simulated CTF (tom\_create\_ctf.m). To reduce template bias, the template structure should be low-pass filtered to 5 nm resolution (tom\_bandpass.m), before being scaled to the appropriate voxel size (tom\_rescale.m). The resulting template structure can also be mirrored (tom\_mirror.m) to probe specificity of detections.
  - In addition to the template structure, a mask has to be prepared (tom\_spheremask.m). The mask must have the same dimensions as the template structure and should encompass the template tightly without cutting off density. The edges of the mask should be smoothened to reduce artifacts from masking.
  - A job file has to be prepared, in which the paths for the tomogram to be queried, the template structure and the mask are specified. Furthermore, the missing wedge of the tomogram, the type of scoring function to be used, and the angular sampling have to be specified. Templates for generating the job file can be downloaded from www.pytom.org.
- (II) Run template matching on your local computing cluster (localization.py). Template matching outputs two volumes in the starting directory:
  - scores.em, containing the constrained cross-correlation values for the best-matching orientation for each voxel.
  - angles.em, containing the orientation of the template structure that yielded the best cross-correlation for each voxel.
- (III) Extract peaks from the correlation volume into an av3/TOM motiflist (av3\_createmotl.m) or PyTom XML particle list. Particular attention should be paid to the radius of the sphere used to mask out the correlation volume around the respective peak. This radius should be chosen as big as possible, to avoid picking the same copy of your complex of interest several times, but without risking to mask out peaks of neighboring copies. Typically, the number of peaks being extracted should be considerably higher than the anticipated number of instances of your complex of interest.
- (IV) For selection of peaks for subtomogram reconstruction, three approaches are commonly used. Fast ways are to select peaks according to (A) the distribution of cross-correlation coefficients or (B) a comparison of cross-correlation

coefficients between right- and left-handed template structures. Theses approaches are fast and do not need much user input, but high-scoring false positives are retained and have to be sorted out later by classification approaches. A third approach is to (C) manually inspect peaks in the context of the tomogram to assign their identity (Fig. 9.1a). This typically yields a very pure set of subtomograms with few false positives, but is quite laborious.

- (A) Display a histogram of correlation coefficients for all extracted peaks (column 1 in TOM/av3 motiflists). For data with high quality, a Gaussian distribution of high correlation coefficients originating from 'true positives' will be visible and mostly separated from an increasing number of low correlation coefficients originating from 'false positives' (Fig. 9.1b). A cross-correlation threshold placed on the left-hand tail of the Gaussian distribution discriminates roughly between true and false positives.
- (B) If template matching has been performed for a right-handed and a left-handed template structure, selection of peaks can be based on a comparison of their correlation coefficients. Plot the correlation coefficients for the right and left-handed templates into the same figure. For true positive peaks, cross-correlation values for the right-handed template should be higher than for the left-handed template, while they should be similar for false positive peaks. Thus, the curve for the right-handed template should start clearly separated from the curve for the left-handed template in the region of the highest-scoring peaks, but both curves should converge for lower cross-correlation values, indicating the number of true positive peaks detected in the tomogram (Fig. 9.1c).
- (C) Peaks can be inspected visually in the context of the tomogram (tom\_chooser.m) and the motiflist can be filtered according to the assigned class labels (Fig. 9.1a).

## 9.8.2 Extraction and Alignment of Subtomograms

This section introduces how to extract and align subtomograms iteratively to increase resolution and signal-to-noise ratio. The main steps are (*I*) reconstruction of subtomograms at the selected coordinates and (*II*) running iterative subtomogram alignment using different approaches.

(I) After localization of particles, subtomograms are individually reconstructed from the unbinned aligned weighted projections at the selected coordinates provided in lines 8–10 (x,y,z) in TOM/av3 motiflists (av3\_fastrecparticles.m). Note that the particle coordinates must be provided with respect to the center

of the complete unbinned tomographic volume. Scaling factors originating from size reduction of the tomographic volume and offsets originating from cutting the volume have to be considered. Subtomograms should be large enough to easily include the macromolecules of interest, typically twice their size.

- (II) Three distinct approaches for *iterative alignment of subtomograms* are implemented in PyTom. For all three alignment approaches a reference structure for the first iteration, a mask and a PyTom XML particle list must be prepared:
  - A reference structure can be either generated from an external structure as
    described above (template matching, preparation of files) or it can be
    obtained by averaging the reconstructed subtomograms, using the orientations determined by template matching (av3 average exact.m).
  - A mask can be prepared as described above (template matching, preparation of files).
  - A PyTom XML particle list can be prepared from a TOM/av3 motiflist in PyTom (fromMOTL.py and toXMLFile.py).

In PyTom, subtomograms can be aligned using coupled translational and restricted rotational search in real space following either a 'conventional' (ExMaxAlignment.py) or a 'gold standard' alignment approach (GLocalJob.py). Alternatively, subtomograms can be aligned using alternating translational and rotational search in Fourier space using spherical (FRMAlignment.py). For each alignment approach, specific job files have to be prepared. In these job files, you have to specify the output folder, the number of alignment iterations, the paths for reference structure and mask, the voxel size, the bandpass filter and the angular increment of rotational search for the first iteration (not in FRM). Running 'conventional' alignment, the PyTom XML particle list generated for the selected peaks has to be inserted into the job file at the indicated position. Running 'gold standard' or FRM alignment, a path can specify the PyTom XML particle list. Templates for generating the job files, as well as further instructions for choosing appropriate alignment parameters can be downloaded from www.pytom.org.

## 9.8.3 Classification of Subtomograms Using CPCA and Kmeans Clustering

This section introduces how to sort out compositional and conformational heterogeneity in a set of pre-aligned subtomograms using constrained principal component analysis and k-means clustering in av3/PyTom. The main steps are (*I*) preparing files for classification, (*II*) computing a pairwise matrix of constrained

cross-correlation coefficients and (III) using this matrix for CPCA and kmeans clustering.

- (I) Preparation of files for subtomogram classification:
  - Subtomograms have to be pre-aligned to a common reference system to obtain an aligned PyTom XML particle list.
  - A mask has to be prepared (tom\_spheremask.m) that focuses on the feature of interest, but it should not be chosen too small.
  - A job file has to be prepared that specifies the paths for the aligned PyTom XML particle list and the mask, as well as the lowpass filter for used for classification. The lowpass filter should be set according to the size of the feature to be classified for. Since single subtomograms have a low SNR, higher frequencies should be generally excluded, but the feature of interest must not be compromised.
- (II) The pairwise matrix of constrained cross-correlation coefficients (output file: correlation\_matrix.csv) is computed using PyTom on your local computing cluster (calculate\_correlation\_matrix.py). Computational time will significantly increase with the number and size of subtomograms.
- (III) Principal component analysis and k-means clustering are performed in av3/TOM (pcacov.m, kmeans.m from the MATLAB statistics toolbox). The number of eigenvectors for CPCA, the number of classes for k-means clustering and the subtomogram path have to be specified. Typically, 5 eigenvectors are sufficient to represent the main features of the data and suppress the noise. The number of classes should be chosen as high as possible in order to be able to pick up also small populations of structurally distinct particles. For high quality data, 200 subtomograms per class usually yield sufficient SNR for subsequent visual assessment or further clustering using hierarchical classification, treating the class averages like subtomograms. Once sufficiently pure subsets of particles have been obtained, they can be averaged separately to increase the SNR for each distinct population.

#### References

- R. Henderson, The potential and limitations of neutrons, electrons and X-rays for atomic resolution microscopy of unstained biological molecules. Q. Rev. Biophys. 28(2), 171–193 (1995)
- K. Grunewald, P. Desai, D.C. Winkler, J.B. Heymann, D.M. Belnap, W. Baumeister, A.C. Steven, Three-dimensional structure of herpes simplex virus from cryo-electron tomography. Science 302(5649), 1396–1398 (2003). doi:10.1126/science.1090284
- S. Asano, Y. Fukuda, F. Beck, A. Aufderheide, F. Forster, R. Danev, W. Baumeister, Proteasomes. A molecular census of 26S proteasomes in intact neurons. Science 347(6220), 439–442 (2015). doi:10.1126/science.1261197

- J. Bohm, A.S. Frangakis, R. Hegerl, S. Nickell, D. Typke, W. Baumeister, Toward detecting and identifying macromolecules in a cellular context: template matching applied to electron tomograms. Proc. Natl. Acad. Sci. U.S.A. 97(26), 14245–14250 (2000). doi:10.1073/pnas. 230282097
- M. Xu, F. Alber, Automated target segmentation and real space fast alignment methods for high-throughput classification and averaging of crowded cryo-electron subtomograms. Bioinformatics 29(13), i274–282 (2013). doi:10.1093/bioinformatics/btt225
- X. Chen, Y. Chen, J.M. Schuller, N. Navab, F. Förster, Automatic particle picking and multi-class classification in cryo-electron tomograms. Paper presented at the IEEE 11th International Symposium on Biomedical Imaging, Beijing (2014)
- F. Forster, B.G. Han, M. Beck, Visual proteomics. Methods Enzymol. 483, 215–243 (2010). doi:10.1016/S0076-6879(10)83011-3
- A.S. Frangakis, J. Bohm, F. Forster, S. Nickell, D. Nicastro, D. Typke, R. Hegerl, W. Baumeister, Identification of macromolecular complexes in cryoelectron tomograms of phantom cells. Proc. Natl. Acad. Sci. U.S.A. 99(22), 14153–14158 (2002). doi:10.1073/pnas. 172520299
- F. Forster, O. Medalia, N. Zauberman, W. Baumeister, D. Fass, Retrovirus envelope protein complex structure in situ studied by cryo-electron tomography. Proc. Natl. Acad. Sci. U.S.A. 102(13), 4729–4734 (2005). doi:10.1073/pnas.0409178102
- J.O. Ortiz, F. Forster, J. Kurner, A.A. Linaroudis, W. Baumeister, Mapping 70S ribosomes in intact cells by cryoelectron tomography and pattern recognition. J. Struct. Biol. 156(2), 334–341 (2006). doi:10.1016/j.jsb.2006.04.014
- M. Beck, J.A. Malmstrom, V. Lange, A. Schmidt, E.W. Deutsch, R. Aebersold, Visual proteomics of the human pathogen Leptospira interrogans. Nat. Methods 6(11), 817–823 (2009). doi:10.1038/nmeth.1390
- J. Walz, D. Typke, M. Nitsch, A.J. Koster, R. Hegerl, W. Baumeister, Electron Tomography of single ice-embedded macromolecules: three-dimensional alignment and classification. J. Struct. Biol. 120(3), 387–395 (1997)
- S.H. Scheres, R. Melero, M. Valle, J.M. Carazo, Averaging of electron subtomograms and random conical tilt reconstructions through likelihood optimization. Structure 17(12), 1563–1572 (2009). doi:10.1016/j.str.2009.10.009
- M. Stolken, F. Beck, T. Haller, R. Hegerl, I. Gutsche, J.M. Carazo, W. Baumeister, S.H. Scheres, S. Nickell, Maximum likelihood based classification of electron tomographic data.
   J. Struct. Biol. 173(1), 77–85 (2011). doi:10.1016/j.jsb.2010.08.005
- T.A. Bharat, C.J. Russo, J. Lowe, L.A. Passmore, S.H. Scheres, Advances in single-particle electron cryomicroscopy structure determination applied to sub-tomogram averaging. Structure 23(9), 1743–1753 (2015). doi:10.1016/j.str.2015.06.026
- S.H. Scheres, RELION: implementation of a Bayesian approach to cryo-EM structure determination. J. Struct. Biol. 180(3), 519–530 (2012). doi:10.1016/j.jsb.2012.09.006
- T. Hrabe, Y. Chen, S. Pfeffer, L.K. Cuellar, A.V. Mangold, F. Forster, PyTom: a python-based toolbox for localization of macromolecules in cryo-electron tomograms and subtomogram analysis. J. Struct. Biol. 178(2), 177–188 (2012). doi:10.1016/j.jsb.2011.12.003
- N. Grigorieff, Resolution measurement in structures derived from single particles. Acta Crystallogr. D Biol. Crystallogr. 56(Pt 10), 1270–1277 (2000)
- 19. Y. Chen, S. Pfeffer, T. Hrabe, J.M. Schuller, F. Forster, Fast and accurate reference-free alignment of subtomograms. J. Struct. Biol. (2013). doi:10.1016/j.jsb.2013.03.002
- A. Bartesaghi, P. Sprechmann, J. Liu, G. Randall, G. Sapiro, S. Subramaniam, Classification and 3D averaging with missing wedge correction in biological electron tomography. J. Struct. Biol. 162(3), 436–450 (2008). doi:10.1016/j.jsb.2008.02.008
- F. Forster, S. Pruggnaller, A. Seybert, A.S. Frangakis, Classification of cryo-electron sub-tomograms using constrained correlation. J. Struct. Biol. 161(3), 276–286 (2008). doi:10. 1016/j.jsb.2007.07.006

- Y. Chen, S. Pfeffer, J.J. Fernandez, C.O. Sorzano, F. Forster, Autofocused 3D classification of cryoelectron subtomograms. Structure 22(10), 1528–1537 (2014). doi:10.1016/j.str.2014.08. 007
- T.A. Steitz, A structural understanding of the dynamic ribosome machine. Nat. Rev. Mol. Cell Biol. 9(3), 242–253 (2008). doi:10.1038/nrm2352
- F. Brandt, L.A. Carlson, F.U. Hartl, W. Baumeister, K. Grunewald, The three-dimensional organization of polyribosomes in intact human cells. Mol. Cell 39(4), 560–569 (2010). doi:10. 1016/j.molcel.2010.08.003
- F. Brandt, S.A. Etchells, J.O. Ortiz, A.H. Elcock, F.U. Hartl, W. Baumeister, The native 3D organization of bacterial polysomes. Cell 136(2), 261–271 (2009). doi:10.1016/j.cell.2008.11.
- A.G. Myasnikov, Z.A. Afonina, J.F. Menetret, V.A. Shirokov, A.S. Spirin, B.P. Klaholz, The molecular structure of the left-handed supra-molecular helix of eukaryotic polyribosomes. Nat. Commun. 5, 5294 (2014). doi:10.1038/ncomms6294
- Z.A. Afonina, A.G. Myasnikov, V.A. Shirokov, B.P. Klaholz, A.S. Spirin, Formation of circular polyribosomes on eukaryotic mRNA without cap-structure and poly(A)-tail: a cryo electron tomography study. Nucleic Acids Res. 42(14), 9461–9469 (2014). doi:10.1093/nar/ gku599
- Z.A. Afonina, A.G. Myasnikov, V.A. Shirokov, B.P. Klaholz, A.S. Spirin, Conformation transitions of eukaryotic polyribosomes during multi-round translation. Nucleic Acids Res. 43 (1), 618–628 (2015). doi:10.1093/nar/gku1270
- J.O. Ortiz, F. Brandt, V.R. Matias, L. Sennels, J. Rappsilber, S.H. Scheres, M. Eibauer, F.U. Hartl, W. Baumeister, Structure of hibernating ribosomes studied by cryoelectron tomography in vitro and in situ. J. Cell Biol. 190(4), 613–621 (2010). doi:10.1083/jcb.201005007
- S. Pfeffer, F. Brandt, T. Hrabe, S. Lang, M. Eibauer, R. Zimmermann, F. Forster, Structure and 3D arrangement of endoplasmic reticulum membrane-associated ribosomes. Structure 20 (9), 1508–1518 (2012). doi:10.1016/j.str.2012.06.010
- S. Pfeffer, J. Dudek, M. Gogala, S. Schorr, J. Linxweiler, S. Lang, T. Becker, R. Beckmann, R. Zimmermann, F. Forster, Structure of the mammalian oligosaccharyl-transferase complex in the native ER protein translocon. Nat. Commun. 5, 3072 (2014). doi:10.1038/ncomms4072
- 32. S. Pfeffer, L. Burbaum, P. Unverdorben, M. Pech, Y. Chen, R. Zimmermann, R. Beckmann, F. Forster, Structure of the native Sec61 protein-conducting channel. Nat. Commun. 6, 8403 (2015). doi:10.1038/ncomms9403
- S. Pfeffer, M.W. Woellhaf, J.M. Herrmann, F. Forster, Organization of the mitochondrial translation machinery studied in situ by cryoelectron tomography. Nat. Commun. 6, 6019 (2015). doi:10.1038/ncomms7019
- P. Unverdorben, F. Beck, P. Sledz, A. Schweitzer, G. Pfeifer, J.M. Plitzko, W. Baumeister,
   F. Forster, Deep classification of a large cryo-EM dataset defines the conformational landscape of the 26S proteasome. Proc. Natl. Acad. Sci. U.S.A. 111(15), 5544–5549 (2014). doi:10.1073/pnas.1403409111
- 35. T. Movassagh, K.H. Bui, H. Sakakibara, K. Oiwa, T. Ishikawa, Nucleotide-induced global conformational changes of flagellar dynein arms revealed by in situ analysis. Nat. Struct. Mol. Biol. 17(6), 761–767 (2010). doi:10.1038/nsmb.1832
- 36. J. Lin, K. Okada, M. Raytchev, M.C. Smith, D. Nicastro, Structural mechanism of the dynein power stroke. Nat. Cell Biol. 16(5), 479–485 (2014). doi:10.1038/ncb2939
- G. Pigino, K.H. Bui, A. Maheshwari, P. Lupetti, D. Diener, T. Ishikawa, Cryoelectron tomography of radial spokes in cilia and flagella. J. Cell Biol. 195(4), 673–687 (2011). doi:10. 1083/jcb.201106125
- T. Oda, H. Yanagisawa, M. Kikkawa, Detailed structural and biochemical characterization of the nexin-dynein regulatory complex. Mol. Biol. Cell 26(2), 294–304 (2015). doi:10.1091/ mbc.E14-09-1367

- 39. K.H. Bui, T. Yagi, R. Yamamoto, R. Kamiya, T. Ishikawa, Polarity and asymmetry in the arrangement of dynein and related structures in the Chlamydomonas axoneme. J. Cell Biol. 198(5), 913–925 (2012). doi:10.1083/jcb.201201120
- 40. T. Oda, T. Abe, H. Yanagisawa, M. Kikkawa, Structure and function of outer dynein arm intermediate and light chain complex. Mol. Biol. Cell (2016). doi:10.1091/mbc.E15-10-0723
- J. Lin, W. Yin, M.C. Smith, K. Song, M.W. Leigh, M.A. Zariwala, M.R. Knowles, L.E. Ostrowski, D. Nicastro, Cryo-electron tomography reveals ciliary defects underlying human RSPH1 primary ciliary dyskinesia. Nat. Commun. 5, 5727 (2014). doi:10.1038/ncomms6727
- 42. M. Beck, V. Lucic, F. Forster, W. Baumeister, O. Medalia, Snapshots of nuclear pore complexes in action captured by cryo-electron tomography. Nature **449**(7162), 611–615 (2007). doi:10.1038/nature06170
- M. Beck, F. Forster, M. Ecke, J.M. Plitzko, F. Melchior, G. Gerisch, W. Baumeister, O. Medalia, Nuclear pore complex structure and dynamics revealed by cryoelectron tomography. Science 306(5700), 1387–1390 (2004). doi:10.1126/science.1104808
- A. von Appen, J. Kosinski, L. Sparks, A. Ori, A.L. DiGuilio, B. Vollmer, M.T. Mackmull, N. Banterle, L. Parca, P. Kastritis, K. Buczak, S. Mosalaganti, W. Hagen, A. Andres-Pons, E.A. Lemke, P. Bork, W. Antonin, J.S. Glavy, K.H. Bui, M. Beck, In situ structural analysis of the human nuclear pore complex. Nature 526(7571), 140–143 (2015). doi:10.1038/nature15381
- M. Eibauer, M. Pellanda, Y. Turgay, A. Dubrovsky, A. Wild, O. Medalia, Structure and gating of the nuclear pore complex. Nat. Commun. 6, 7532 (2015). doi:10.1038/ncomms8532
- K.H. Bui, A. von Appen, A.L. DiGuilio, A. Ori, L. Sparks, M.T. Mackmull, T. Bock, W. Hagen, A. Andres-Pons, J.S. Glavy, M. Beck, Integrated structural analysis of the human nuclear pore complex scaffold. Cell 155(6), 1233–1243 (2013). doi:10.1016/j.cell.2013.10. 055
- 47. T. Maimon, N. Elad, I. Dahan, O. Medalia, The human nuclear pore complex as revealed by cryo-electron tomography. Structure **20**(6), 998–1006 (2012). doi:10.1016/j.str.2012.03.025
- 48. M. Faini, S. Prinz, R. Beck, M. Schorb, J.D. Riches, K. Bacia, B. Brugger, F.T. Wieland, J.A. Briggs, The structures of COPI-coated vesicles reveal alternate coatomer conformations and interactions. Science **336**(6087), 1451–1454 (2012). doi:10.1126/science.1221443
- S.O. Dodonova, P. Diestelkoetter-Bachert, A. von Appen, W.J. Hagen, R. Beck, M. Beck, F. Wieland, J.A. Briggs, VESICULAR TRANSPORT. A structure of the COPI coat and the role of coat proteins in membrane vesicle assembly. Science 349(6244), 195–198 (2015). doi:10. 1126/science.aab1121
- 50. G. Zanetti, S. Prinz, S. Daum, A. Meister, R. Schekman, K. Bacia, J.A. Briggs, The structure of the COPII transport-vesicle coat assembled on membranes. Elife **2**, e00951 (2013). doi:10. 7554/eLife.00951
- F.K. Schur, W.J. Hagen, M. Rumlova, T. Ruml, B. Muller, H.G. Krausslich, J.A. Briggs, Structure of the immature HIV-1 capsid in intact virus particles at 8.8 A resolution. Nature 517(7535), 505–508 (2015). doi:10.1038/nature13838
- 52. F.K. Schur, R.A. Dick, W.J. Hagen, V.M. Vogt, J.A. Briggs, The structure of immature virus-like rous sarcoma virus gag particles reveals a structural role for the p10 domain in assembly. J. Virol. 89(20), 10294–10302 (2015). doi:10.1128/JVI.01502-15
- G.E. Murphy, J.R. Leadbetter, G.J. Jensen, In situ structure of the complete Treponema primitia flagellar motor. Nature 442(7106), 1062–1064 (2006). doi:10.1038/nature05015
- S. Chen, M. Beeby, G.E. Murphy, J.R. Leadbetter, D.R. Hendrixson, A. Briegel, Z. Li, J. Shi, E.I. Tocheva, A. Muller, M.J. Dobro, G.J. Jensen, Structural diversity of bacterial flagellar motors. EMBO J. 30(14), 2972–2981 (2011). doi:10.1038/emboj.2011.186
- X. Zhao, K. Zhang, T. Boquoi, B. Hu, M.A. Motaleb, K.A. Miller, M.E. James, N.W. Charon, M.D. Manson, S.J. Norris, C. Li, J. Liu, Cryoelectron tomography reveals the sequential assembly of bacterial flagella in Borrelia burgdorferi. Proc. Natl. Acad. Sci. U.S.A. 110(35), 14390–14395 (2013). doi:10.1073/pnas.1308306110

- B. Hu, D.R. Morado, W. Margolin, J.R. Rohde, O. Arizmendi, W.L. Picking, W.D. Picking, J. Liu, Visualization of the type III secretion sorting platform of Shigella flexneri. Proc. Natl. Acad. Sci. U.S.A. 112(4), 1047–1052 (2015). doi:10.1073/pnas.1411610112
- A. Nans, M. Kudryashev, H.R. Saibil, R.D. Hayward, Structure of a bacterial type III secretion system in contact with a host membrane in situ. Nat. Commun. 6, 10114 (2015). doi:10.1038/ncomms10114
- M. Kudryashev, M. Stenta, S. Schmelz, M. Amstutz, U. Wiesand, D. Castano-Diez, M.T. Degiacomi, S. Munnich, C.K. Bleck, J. Kowal, A. Diepold, D.W. Heinz, M. Dal Peraro, G.R. Cornelis, H. Stahlberg, In situ structural analysis of the Yersinia enterocolitica injectisome. Elife 2, e00792 (2013). doi:10.7554/eLife.00792
- M. Strauss, G. Hofhaus, R.R. Schroder, W. Kuhlbrandt, Dimer ribbons of ATP synthase shape the inner mitochondrial membrane. EMBO J. 27(7), 1154–1160 (2008). doi:10.1038/ emboj.2008.35
- K.M. Davies, C. Anselmi, I. Wittig, J.D. Faraldo-Gomez, W. Kuhlbrandt, Structure of the yeast F1Fo-ATP synthase dimer and its role in shaping the mitochondrial cristae. Proc. Natl. Acad. Sci. U.S.A. 109(34), 13602–13607 (2012). doi:10.1073/pnas.1204593109

# **Chapter 10 Resolution in Electron Tomography**

Mikhail Kudryashev

**Abstract** Electron microscopes yield point resolution on the order of one angstrom, however the density maps from electron tomography typically have resolutions in the nanometre range. In this chapter I qualitatively discuss the typical limitations that occur in electron tomography of biological samples depending on the imaging modalities, with the focus on cryo electron tomography and subtomogram averaging.

#### 10.1 Introduction

In microscopy the term resolution defines the minimal distance between two point objects or features that allows distinguishing one from another. Higher resolution results in higher information content of the images; lower resolution corresponds to larger distances between resolvable points. In the case of bright field light microscopy the resolution is limited by the wavelength of the used light and measured by the Rayleigh criterion [1]

$$\mathbf{R} = 0.61 \frac{L}{n * \sin(beta)} = 0.61 \frac{L}{NA}$$
 (10.1)

Where **R** is the minimal resolvable distance, L is the wavelength, n is the refractive index of the media, and *beta* is the semi-aperture angle. NA is numerical aperture, which for optical microscopes is around 1. Typical values are in the order

M. Kudryashev (⊠)

Max Planck Institute for Biophysics, Max-von-Laue Strasse 3,

60348 Frankfurt am Main, Germany

e-mail: misha.kudryashev@biophys.mpg.de

M. Kudryashev

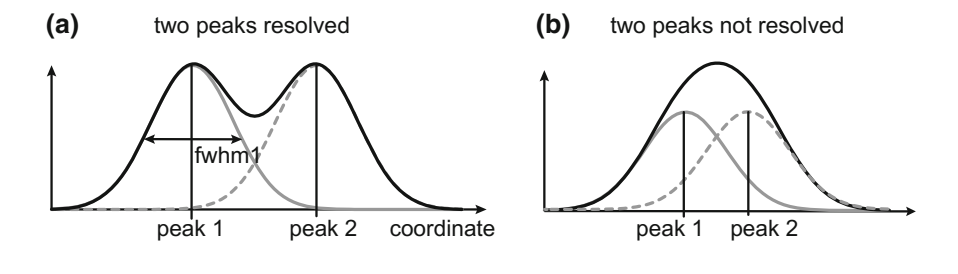
Buchmann Institute for Molecular Life Sciences, Goethe University of Frankfurt am Main, Max-von-Laue Strasse 17, 60348 Frankfurt am Main, Germany

262 M. Kudryashev

200 nm for light with the wavelength of 400 nm. Reduced numerical aperture may further degrade the resolution.

Wavelength of the electrons of the electron microscope is determined by L = h/p (Planck constant over the particle impulse) and is 0.039 Å for accelerating voltage 100 kV and 0.022 Å for 300 kV. Since the effective NA for light and electron microscopes differ, the R for 300 kV is in the order of 0.8 Å [2]. Typical point resolution of an electron microscope is in the order of 1 Angstrom. Single atoms in thin films may be routinely observed using modern microscopes [3], however this cannot be done routinely for the 3DEM modalities described in this book for a number of reasons described below in this chapter.

Limited signal to noise ratio (SNR) in the images may further degrade the resolution (Fig. 10.1). While additive Gaussian noise like in Fig. 10.1c may be partially removed, more complex noise will overlap with high-resolution features of the signal. In a more general case the resolution dependent signal-to-noise ratio is commonly used in electron microscopy [4] which may be expressed in a form of a phase residual [5], Fourier Ring Correlation [6, 7] or Fourier Shell Correlation [8]. FRC/FSC between two statistically independent datasets quantitatively represent the reproducibility of the corresponding datasets. The frequencies for which FSC is above the defined thresholds [9, 10] are reproducible, the highest of these frequencies if often referred to as resolution.



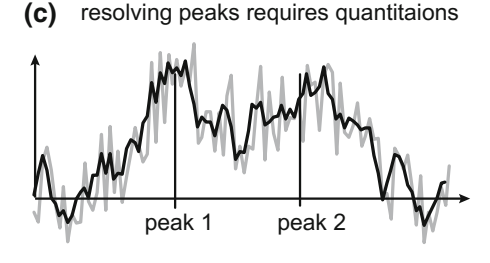


Fig. 10.1 Resolving two peaks **a** The peaks with the same full width at half maximum (fwhm) are further than R and are resolved; **b** closer then R and therefore not resolved; **c** two peaks as in A with white noise (SD = 1, grey line) therefore processing/quantitation is required. Black line is an average over 3 neighbouring data points

If during an imaging workflow several factors limit the resolution, then the final resolution will be worse than the worst of the limits:

$$R_{lim} > max(Lim_1, Lim_2, ... Lim_n)$$

Furthermore, it may be useful to separately consider the factor-by-factor decay of the signal that result from each of the distortions. This may be described by envelope functions that in EM typically suppress the higher frequencies. Each factor including microscope distortions, sample processing, image noise, DQE of the detector, and/or misalignments during processing result in an envelope function. The combined envelope function is at best a product of the contributing envelope functions (Fig. 10.2). It may be useful to estimate the relevant envelope functions at the stage of experimental design.

The practical limitations imposed by the processing steps are briefly discussed in part 2 of this chapter. Part 3 refers to the general geometrical limitations of electron tomography. In the fourth part I discuss the potential limitations that apply to the highest-resolution method from the tomographic family: subtomogram averaging (StA).

#### **10.2** Limits Imposed by Sample Preparation

Depending on the research question there is generally a compromise between the imaged area and the target resolution. For higher resolution cryo-preservation is used, while for imaging larger volumes samples are typically strongly processed. Chemical fixation and dehydration is used in a number of techniques to preserve the biological object before placing it to the vacuum of the electron microscope column. Addition of amorphous stain is needed to improve the contrast of the sample in the electron microscope. Such preparations provide high contrast and resolution on the order of tens of nanometres. Additionally, the "classical preparations" may significantly perturb the biological object of interest [11].

More delicate imaging methods include high pressure freezing, freeze substitution, staining and sectioning for semi-thick 200–400 nm sections for further tomographic analysis [12]. Optimal sample preparation conditions are sample-specific and have to be experimentally determined, however such preparations may preserve the biological details up to 35 Å [13].

## 10.2.1 Sectioning- and SEM-Based Methods

Serial thin sections, array tomography [14] and serial block face [15], and FIB-SEM [16–18] allows 3D analysis of large up-to-millimetre-scale volumes. A common target for these sectioning-based EM methods is visualization of ultrastructure of

264 M. Kudryashev

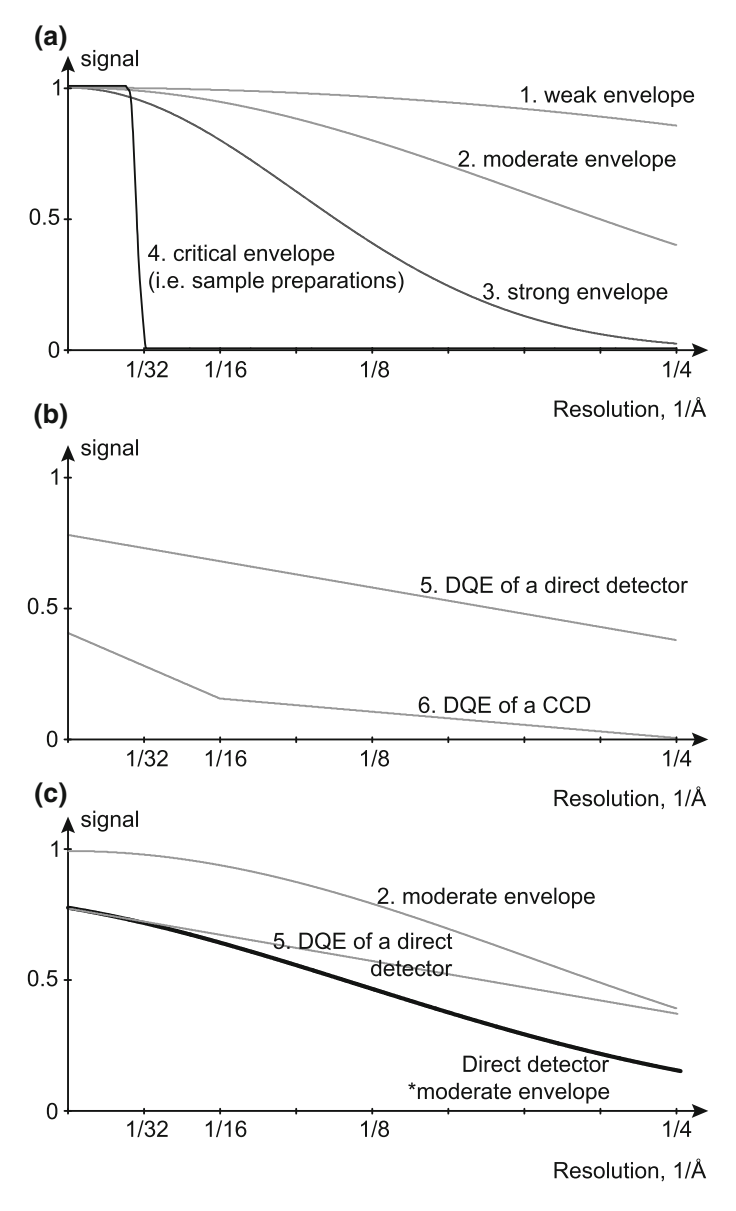


**Fig. 10.2** Envelope functions observed in electron microscopy. **a** Weak (1), moderate (2), strong (3) and critical (4) envelope functions. (4) Imposes a strong limit on resolution typical for a sample preparation by negative staining. Strong envelope function (3) is a combination of four applied moderate envelope functions (2). **b** Digital Quantum Efficiency of electron detectors may be considered as envelope functions. **c** Resulting envelope function is at best a product of all the applied envelope functions. It results in a lower signal transfer that is important to consider at the experimental design stage

tissues [19] or cultured cells [20]. Imaging the surface of a resin-embedded and typically osmium-stained block is imaged by a scanning electron microscope. Each successive surface is removed by a diamond knife ("serial block face", [15]) or a focused ion beam ("FIB-SEM", [16, 17]). The newly exposed surface is imaged and the recorded images are aligned in a 3D stack. Serial thin sections and array tomography is performed by TEM with the consecutive alignment of slices into the 3D-volumes.

The above mentioned methods, sometimes called tomography, allow for the creation of 3D volumes with anisotropic resolution, however the section-based methods are not generated by tomographic reconstruction [21] but by assembling the 3D volumes layer-by-layer. Array tomography, serial block face and FIB-SEM have a Z-resolution that is determined by the thickness of the section or by the thickness of the layer erased between the consecutive images. The X-Y resolution is typically limited by sampling (twice the pixel size) and sample preparation, which is also dependent on the electron dose per exposure and energy of the applied electrons.

#### 10.2.2 Imaging Cryo Preserved Samples

Cryo-fixation preserves biological features to atomic details [22] however the sample becomes radiation sensitive and degrades upon exposure in a dose-dependent manner [23, 24]. However, additionally to degradation the vitreous ice moves in a non-isotropic way and may diverge by as much as 6 Å over a distance of 300 nm and an exposure 35 e<sup>-</sup>/Å<sup>2</sup> [25]. This dose is 2–5 times smaller than is typically used for tomograms used for subtomogram averaging [26], application of higher dose further increases the anisotropic movement of density. The resulting tomograms are therefore not generated by imaging "rigid bodies" and may result in incoherent reconstructions.

The observed contrast between the electron scattering of buffer (mostly H and O atoms) and of proteins and lipids (mostly O, H, C, N, P) is weak, therefore the biological samples are called weak phase objects. Limited contrast is enhanced by defocusing the microscope's objective lens introducing a non-linear oscillating contrast transfer function (CTF, Fig. 3.3, Chap. 3).

$$CTF(s) = E(s) * sin(0.5 * Pi * Cs * L^3 * s^4 - Pi * L * dF * s^2)$$
 (10.2)

where Cs is a spherical lens aberration of the microscope; L—electron wavelength; s—spatial frequency, dF—applied defocus (negative for underfocus, in Angstroms). E(s) is an envelope function associated with high resolution information degradation as a result of increasing the defocus. CTF correction must be performed otherwise the resolution is limited by the frequency of the first zero of the CTF [26–28] which corresponds to a few to several nanometers.

Low frequencies may be recovered by phase plates introducing a phase shift to the CTF and recovering low resolution signal [29]. Phase shift of Pi/2 in the (10.2) changes the sine-function to a cosine amplifying low-resolution contrast. The increased low resolution contrast allows recording data close to focus, thereby minimizing the envelope function due to defocusing and avoiding errors in defocus determination (Sect. 10.3.2). Volta Phase plate (VPP) preserves the resolution at least to 3.2 Å as shown by a single particle cryo-EM reconstruction of 20S proteasome [30]. VPP was successfully used for cryo electron tomography [31] and subtomogram averaging [32]. However, the full potential of VPP for cryo electron tomography is still to be implemented.

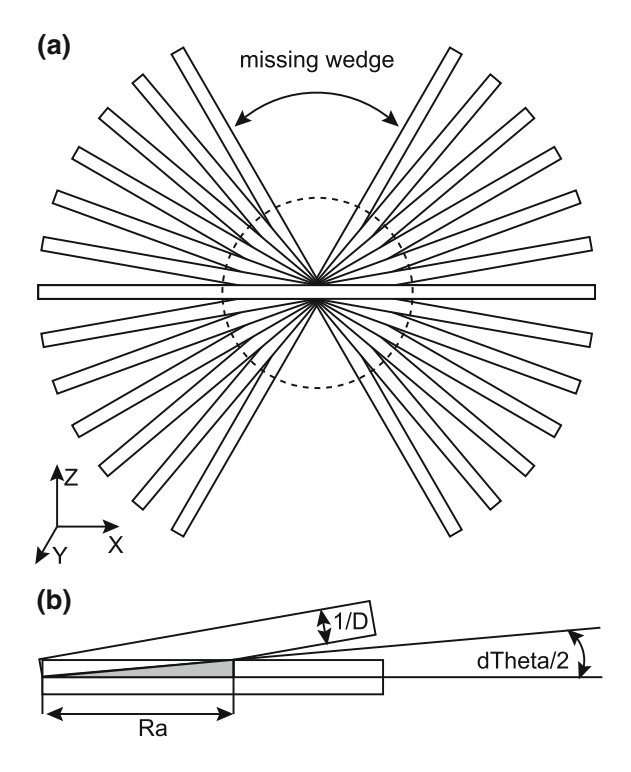
#### 10.3 Resolution of Tomographic Reconstructions

Electron tomography allows resolution on the order of nanometres and therefore is typically performed on well-preserved samples that have been high pressure frozen, freeze substituted, or otherwise cryo-preserved. Details of tomographic acquisition and reconstruction are discussed in Chap. 9 of this book. There are two types of resolution limits—defined by geometry of acquisition and by SNR of the actual data in the projections. Geometrical limits of tomographic reconstructions were quantitatively discussed previously [33, 34]. While the geometrical limits apply to all the types of sample preparation, the SNR considerations are particularly important for frozen hydrated samples where the resolution is not limited by sample preservation.

#### 10.3.1 Geometric Limits

Three-dimensional reconstruction from 2D projection is based on the central slice theorem: inserting a Fourier transform of each 2D image into the 3D Fourier space perpendicular to the projection direction followed by an inverse Fourier transform is equivalent to back-projecting the slice into the 3D volume (Chap. 9). For the most commonly used single-axis tomography around Y-axis this may be reduced to a series of independent reconstructions for the x-z slices, therefore only one slice may be considered in 2D (Fig. 10.3). The first geometric limitation of electron tomography is that the sample has non-negligible length in the direction perpendicular to the electron axis Z ("slab-geometry"), therefore with tilting by an angle *Theta* it becomes effectively thicker. The thickness increases as  $1/\cos(Theta)$  which is twofold for *Theta* = 60, threefold for *Theta* = 70, fourfold for *Theta* = 75.5. Higher sample thickness reduces the fraction of the elastically scattered electrons, degrades the image quality and in practical terms limits the maximal used tilting angle to  $60^{\circ}$ – $70^{\circ}$ . Missing information in Fourier space constitutes a "missing wedge", resulting in a resolution anisotropy in real space for a given tomogram.

Fig. 10.3 Fourier space sampling during tomography. a Illustration of the sampling of X-Z planes for single tilt tomography. Slices with thickness 1/D fill Fourier space up to a resolution of Ra (dashed circle), but not in the missing wedge area. Lower frequencies are located in the middle of the image, higher frequencies-outside. b Two slices are depicted for clarity; the data overlaps only up to Ra, which may be calculated as (10.3) from the triangle highlighted in grey



The effect is an apparent elongation of dense features along the electron axis and the apparent lack of horizontal features like cellular membranes.

In order to minimize the size of the missing wedge higher tilts may be collected. Dual-axis tomography minimizes the missing wedge to a smaller missing pyramid [35] by recording an additional tomogram with a tilting axis X perpendicular to the Y axis. Conical tomography [36, 37] involves tilting the sample to a high angle (40°–60°) along one axis and rotating by a small angular step around the own axis. Conical tomography results in an isotropic resolution in X-Y plane and a missing cone of information in Fourier space, however is rarely used due to technical reasons. Finally, specially designed holders in combination with FIB-milling of thin "needles" in principle allow "on axis tilt tomography" without the missing wedge [38]. This however may be achieved only for the samples that would form needles highly stable during tilt series acquisition.

The second geometrical limit at high resolution is the spacing between the slices in Fourier space. The thickness of a 2D slice in Fourier space is inversely proportional to the sample thickness; filling up the Fourier space up to high resolution requires multiple 2D slices corresponding to projections in different directions (Fig. 10.3). From trigonometry (Fig. 10.3b) the maximal sampled spatial frequency r is

268 M. Kudryashev

$$\mathbf{Ra} = \mathbf{1/r} = \mathbf{2D} * \mathbf{sin} \left( \frac{dTheta}{2} \right) \tag{10.3}$$

where dTheta is the angular step during the tomographic data collection. For small angular increments dThetas (less than  $10^{\circ}$ ) measured in radians

$$\sin\left(\frac{dTheta}{2}\right) \approx \frac{dTheta}{2}$$
 (10.4)

using that dTheta = Pi/N we get

$$\mathbf{Ra} = \frac{\mathbf{P}i * \mathbf{D}}{\mathbf{N}} \tag{10.5}$$

With Ra being an angular resolution, N—number of projections, D—linear size of the object in the direction of the electron beam in pixels. For electron microscopy this relation is called the Crowther's criterion [39]. For sampling the frequencies up to the Nyqyist limit Ra = 2 pixels and using (3–5) we get the required angular step

$$dTheta = \frac{2}{D} \tag{10.6a}$$

in radians or

$$dTheta = \frac{Pi}{D * 90} \tag{10.6b}$$

in degrees.

When the thickness of the sample is not negligible compared to the mean free path of an electron ( $\sim 350$  nm in vitreous ice at 300 kV accelerating voltage), the thickness D effectively increases as  $D/\cos(Theta)$  making the slice in the Fourier space thinner. The angular resolution is therefore also different in different viewing directions

$$Ra(Theta) = \frac{Pi * D}{N * \cos(Theta)}$$
 (10.7)

For optimal sampling of the tomogram it was therefore suggested to record the tilt series with smaller angular increments at higher tilting angles [40]. Typical data acquisition schemes also involve applying higher electron dose for higher tilts.

Resolution anisotropy may be expressed in terms of a point spread function [34]. Resolution along the Y-direction is the resolution of the micrograph. Resolution in the X-direction is the angular resolution resulting from the Crowther criterion, (10.5). Elongation of a point along the Z-direction is

$$Exz = \sqrt{\frac{\alpha + \sin(\alpha) * \cos(\alpha)}{\alpha - \sin(\alpha) * \cos(\alpha)}}$$
(10.8)

where  $\alpha$  is the highest tilt in radians and Exz = 1.55 for  $\alpha = Pi/3$ , deduction are in [34].

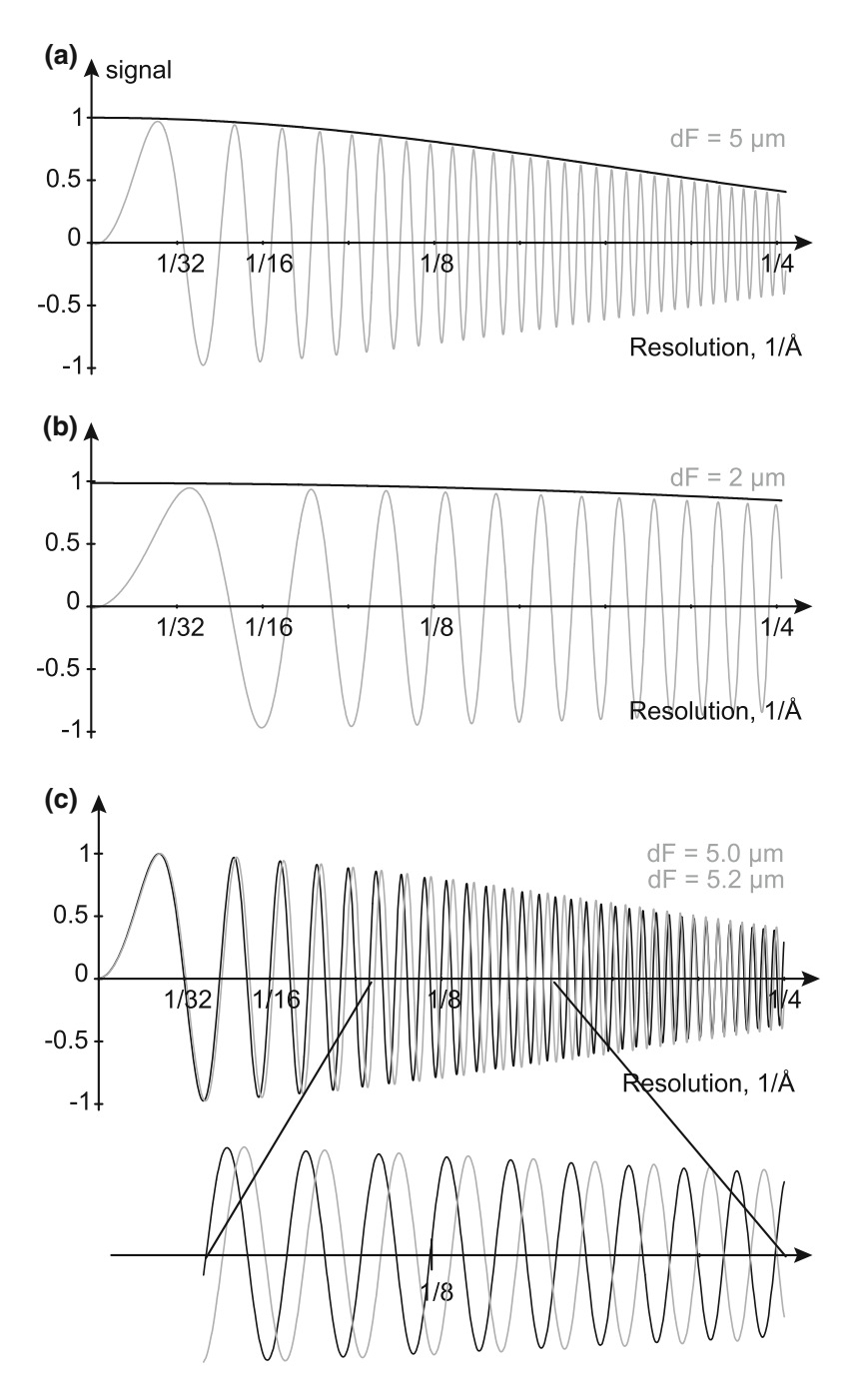
In summary, in order to obtain the highest-quality tomogram it is recommended to use small angular increments, try to record as many high-tilt images as possible with smaller angular steps at high tilts and with a higher electron dose used at high tilts to compensate for the signal quality. Ideally it should be a double-tilt tomogram. However, fulfilling the geometric constraints is a necessary but not a sufficient condition for having high-resolution information in the tomograms. Limited signal, distortions of the imaging system, sample thickness, sub-optimal imaging conditions, and sub-optimal alignment of tilt series or moving of the sample during data collection may degrade the resolution.

External information may be used to "fill" the missing wedge in some cases. Discrete algebraic reconstruction technique (DART reconstruction) method requires density segmentation and assumes discrete values for the density values [41]. Given enough signal DART fills the missing wedge and the gaps between the neighbouring projections in the Fourier space at high resolution (overcoming the Crowther criterion). "Missing cone" present in cryo electron crystallography was demonstrated to be filled by the use of external constraints [42]. Combination of algebraic reconstruction and filtering by nonlinear diffusion was recently used on synthetic datasets and tomograms of stained samples to successfully to fill the missing wedge and the high-resolution gaps in the Fourier space [43] of tomograms recorded on plastic sections. Application of compressed sensing ("ICON" reconstruction) to tomographic reconstructions of ice-embedded samples recently allowed restoration of a significant signal in the missing areas of the Fourier space [44]. This also improved the resolution of subtomogram averaging originating from these tomograms. High noise is one of the limiting factors for filling the missing areas of Fourier space; use of phase plates for tomography will improve some of the approaches.

### 10.3.2 TEM Electron Optical Limits

All limits imposed by high-resolution TEM imaging also apply for tomography. However, the ice/sample thickness during tomography is typically larger than for single particle data collection. Zhang and Zhou reviewed that among the factors limiting the resolution, two are thickness-dependent [45]. First, CTF correction requires precise determination of the applied defocus (Fig. 10.4), otherwise an additional envelope function is applied to the signal and the resolution is limited to

270 M. Kudryashev



**<Fig. 10.4** Effects of CTF on high frequencies. **a−b** CTF (grey lines) and envelope function (black lines) of a 300 kV microscope with a Cs = 2 mm and 2 Å per pixel magnification. The applied defocus is −2 μm for (**a**) and −5 μm for (**b**) resulting in a stronger envelope function at higher resolution. **c** Effect of an error of 200 nm for defocus determination with −5 μm defocus applied (orange graph). While at lower frequencies the error is relatively small, at 7 Å there is a complete loss of signal (phase error of 180°), at 11 Å there is a 90° phase error

$$Dm = \sqrt{2 * dFE * L} \tag{10.9}$$

where Dm is the maximal achievable resolution and dFE is the error in defocus determination. For 300 kV electrons Dm = 20 Å is achieved for dFE = 1016 nm, 10 Å at dFE = 250 nm, 5 Å at dFE = 63 nm, 3 Å at 23 nm. The error in defocus determination is combined from not knowing the applied defocus precisely and the difference between the defocus at different Z-heights in the tomogram. The later may be approximated by half of the sample thickness; as mentioned earlier, the thickness effect increases at high tilting angles. Knowing the coordinates of the particles inside the tomographic volume it is possible to estimate the local defocus of the particle and to compensate for this during StA.

Several strategies are suggested for the precise determination of the applied defocus. First–detecting Thon rings from the single projections individually or over the entire tilt-series [27, 46]. While intuitive this method suffers from a limited electron dose applied per projection (1–3 e<sup>-</sup>/Å<sup>2</sup>) and therefore may have a limited precision. Another strategy is to focus as close to the area of interest as close as possible and to repeat the autofocusing routine several times till stabilization [47]. Third strategy is to use the extended acquisition scheme including recording of two high-exposure images of carbon on the tilting axis, detecting defocus there and interpolate the defocus value to the sample area [48]. Images on carbon allow getting much more reliable Thon rings therefore improving the defocus determination accuracy. This extended acquisition scheme was further complemented by acquiring two additional off-axis images [49] without the notable improvement in the defocus estimation for a flat specimen.

The second thickness-dependent distortion is multiple (dynamic) scattering of electrons. Multiple scattering applies an addition modulation function [45, 50] having multiple zeroes

$$\mathbf{DTF} = \frac{\sin(0.5 * \mathbf{Pi} * \mathbf{L} * s^2 * \mathbf{D})}{0.5 * \mathbf{Pi}^2 * s^2}$$
(10.10)

With D being the sample dimension along the electron beam direction. DTF imposes an envelope function and, unless DTF correction is performed, limits the signal to the first zero of the DTF.

$$\mathbf{Dm} = \sqrt{L * D} \tag{10.11}$$

Dm = 4.44 Å for D = 200 nm; Dm = 3.14 Å for D = 100 nm and Dm = 2.22 Å for D = 50 nm. DTF may play a role for resolution better than 4.5 Å

272 M. Kudryashev

and 100 nm samples when they are highly tilted. The mentioned limit is less deteriorative than the limit associated to defocus determination.

#### 10.3.3 STEM Tomography

Atomic resolution of 2.4 Å was obtained for tomograms of a  $\sim$  10 nm thick gold nanoparticle [51]. It was recorded in ADF-STEM modality with a maximum tilt angle of 72.6° and up to 69 images per tilt series, pixel size 0.42 Å and a total electron dose of 7.6  $\times$  10e6 e<sup>-</sup>/Å<sup>2</sup>. Tilt series were aligned using centres of mass; tomographic reconstruction was generated with equally sloped tomography [52]. As described in Chap. 2 of this book, STEM tomography may also be applied to cryo-preserved samples. The maximal tolerable electron dose that may be applied on a cryo sample preserving near atomic resolution is  $\sim$  200,000 times lower. This will result in noisier tomograms however may be compensated for using subtomogram averaging. In case of the ideally aligned particles  $\sim$  200,000 asymmetric units could be enough, however in practice much more particles may be needed.

STEM imaging gives an advantage over TEM in obtaining higher resolution for cryo-samples thicker than 500 nm (using 300 kV electrons) [53]. One of the limitations during recording STEM tomograms of radiation sensitive samples is to have the sample thickness at high tilts match the depth of field. For a 1-micron thick sample the effective probe size is 3–4 nm [53] and a sampling limit for resolution of 6–8 nm. It is not clear if STEM tomography in combination with StA is beneficial in terms of obtainable resolution over TEM tomography for thin cryo-preserved samples.

## 10.3.4 Measuring the Resolution of Tomograms

As discussed earlier in this chapter several factors limit the resolution of electron tomograms; therefore, additionally to the theoretical estimates several practical ways to measure the resolution were suggested. Knowing the resolution is useful for interpretation and visualization of the data—band pass or other filters may be designed based on the maximum resolution. Additionally, it is important for subtomogram averaging (below) to understand up to which resolution the particles have reliable signal. An intuitive way to estimate the resolution is to see the defined features inside the tomograms—resolving a lipid bilayer means that the resolution of a tomogram is at least 4 nm.

Two quantitative criteria have been proposed based on signal-to-noise levels of the tomogram [54]: the first method includes splitting the tilt series into even and odd projections, generating two tomograms and calculating Fourier shell correlation between them, which has the downside of losing half of the signal during FSC calculation and depending on interpolated Fourier voxels. Second approach is to compare the original projection images and the corresponding re-projections of the tomogram lacking the given projections. The advantage of the second method is the

possibility to measure the resolution for each micrograph based on the tilting angle. Finally, if some protein complex with the known structure in the tomogram may be unambiguously identified, FSC may be calculated between this structure and its instance in the tomogram, assuming that CTF correction have been carried out. Analysis of tomograms from HSV particles recorded on a CCD demonstrated resolution ~7 nm with low tilts corresponding to 5.5 nm and high tilts—10 nm. Higher resolution in tomograms was observed closer to the tilting axis [54]. More recent tomograms recorded with a Volta phase plate, a direct detector and an energy filter were evaluated by a similarity of the 26S proteasome particles from the tomograms and the average structure of the proteasome. The best subtomograms had resolutions up to 3.5 nm [32].

Resolution anisotropy present in tomograms and sometimes in the average structures from StA may be quantitatively estimated using FSC in the conical segments of the Fourier space [55]. The median resolution of single- and dual-axis cryo TEM tomograms recorded on CCD was  $\sim 6$  nm [56]. The highest resolution for single tilt tomograms of  $\sim 3$  nm was measured along the tilting axis due to oversampling of the projection information of all the micrographs; the resolution of dual-axis tomograms was more isotropic as of single-axis tomograms [56].

Another quantitative resolution criterion was proposed based on the edge quality of gold particles [57] which are used as fiducial markers for alignment of tilt series. The intensity decay of the edges can be quantitatively assessed in three directions and be used to monitor the convergence of SIRT reconstructions. The STEM tomograms had resolution of 1.2–2.8 nm in different directions for gold particles [57]. The method in principle may be used for defocused TEM tomography taking CTF into account.

## 10.4 Limits of Subtomogram Averaging

StA described in the Chap. 9 of this book improves the signal to noise ratio of the subtomograms containing repeating elements, located in cryo electron tomograms. If the particles in subtomograms do not have preferential orientation to the electron beam StA fills the missing and the Crowther criterion does not apply. Otherwise all the aspects from imaging cryo-sample preparation, microscope alignments and tomographic reconstruction apply for the resolution limits. Recently several groups obtained reconstructions at sub-nanometer resolution including the structure of the HIV protein GAG at an atomic resolution (Table 10.1). At the resolution protein secondary structure may be seen and atomic structures may be fit by flexible fitting with molecular dynamics [58]. The structures of the GAG protein in the intact HIV virions [59] and of ribosomes on the ER membranes [60] directly implement the in situ structural approach analysing the structure the molecular complex of interest in the native context.

Several StA-specific parameters affect the resolution of the final maps.

Table 10.1 Summary of the selected high-resolution structures determined by StA

Object	Microscope	Camera	Tilt range and	Pixel	Number of	Underfocus	Electron	Resolution,	Reference
			step	size	asym units	range, microns	dose, e <sup>-</sup> /Å <sup>2</sup>	Å	
Isolated GroEL	FEI Titan Krios	4 k CCD @ 80 kV	-45:2:56	1.74	~ 70,000	23	106	8.4	[61]
GAG, tubular crystal	FEI Titan Krios	2 k CCD @200 kV + GIF	-45:3:60	2.44	~ 243,000	1.53.3	40	8.5	[47]
GAG in native HIV virions	FEI Titan Krios	2 k CCD @200 kV + GIF	-45:3:60	2	~ 200,000	1.24	40	8.8	[59]
GAG in RSV virions	FEI Titan Krios	2kCCD @200 kV + GIF	-45:3:45 or -30:3:30	1	~ 50,000	1.55	2436	7.7	[62]
HBV capsid	FEI Titan Krios	K2 Summit + GIF	-60:3:60	2.17	~ 68,000	3.35.6	09	8.1	[63]
Ribosome-sec61	FEI Titan Krios	K2 Summit	-60:2:60	2.62	17,600	34	90100*	6	[09]
Ion channel 5HT-3 in lipid vesicles	FEI Titan Krios	K2 Summit	-60:3:60	1.67	~ 65,000	2.5 4	41	12	[64]
Tobacco Mosaic Virus	FEI Titan Krios	K2 Summit + GIF	-60:3:60	1.1	3625	2	80	8.5	[65]
GAG in native HIV virions	FEI Titan Krios	K2 Summit + GIF	0,-3, 3, 6, -6, 1.3 -9 [66]	1.3	~ 600,000	1.5 5	90150	3.9	[67]

## 10.4.1 Alignment of Subtomograms to the Average

Precision of rotational and translational alignment of the particles to the average is a critical factor particularly for small or membrane associated protein complexes. Estimation of envelope functions has shown that in order to retain 90% of the signal at the resolution of 7 Å for a 1-MDa particle the translational error has to be less than 0.5 Å and the rotational error has to be less than 0.5° for any given particle [68]. Importantly, for a reliable alignment the signal inside the alignment mask has to be sufficient to dominate the alignment. Different views of the same particle or particles recorded at different defocus will have different signal-to-noise ratio; the mask for particle alignment has to be designed to enable the reliable alignment of the most particles from the dataset.

Sample movement during image acquisition may be recorded using "movie mode" recording several consecutive low-dose images with their further aligning and compensation for drift [25]. Precision of the movie frame alignment affects the data quality [69], however the current methods of movie alignment seem sub-optimal for cryo-ET. Fractionating the total dose of 1–3 e<sup>-</sup>/Å<sup>2</sup> per projection can be done only to a few movie frames having close-range correlated noise from the detector. These neighbouring frames are excluded from alignment for higher dose single particle acquisition, which is not possible if only few frames are present [25]. Adjustment of processing methods for sub-frame alignment would further improve the StA data quality.

Non-perfect alignment of tilt series prior to the generation of tomogram is an important limiting factor. Simulations with the parameters reasonable for cryo-conditions and perfectly aligned subtomograms resulted with the resolution of 12 Å [49] with a median angular error in particle alignment of 0.5°. Upon introduction of a misalignment error to the alignment of tilt series with a standard deviation of 3 Å, the resolution drops to 15 Å; misalignment of 7 Å results in the resolution drop to 22 Å. One of the consequences of the tilt series misalignment is reduced to 1-degree precision for the particle alignment to the average. For pseudo-crystalline arrangements the lack of signal may be compensated by including more than one copy of the molecule of interest to contribute to the alignment. Schur and colleagues used 7 copies of the 50 kDa GAG in the final structure which resulted in atomic resolution [67]. In another study, a  $\sim 250$  kDa ion channel 5HT-3 in lipid vesicles did not allow precise alignment; therefore four neighbouring protein copies were used for alignment. However, the mutual arrangement of the protein copies was not fixed and classification into multiple classes had to be performed in order to minimize heterogeneity for given classes [64].

As aligned particles share the information to the reference only to a certain resolution, the conservative part of this resolution range should be used for alignment. As discussed earlier in the Sect. 10.3.1 the tomograms only contain reliable resolution up to 3–6 nm. The use of higher frequencies results in a higher alignment precision, however if there is not enough signal it will lead to overfitting similar to

the situation in single particle cryo-EM [70]. Threshold constrained cross correlation [71] estimates the reliable set of Fourier components to compute cross correlation for each subtomogram which results in better alignment of particles to the average and a slightly higher resolution. The commonly used empirical approach is to separate the dataset into two parts, process them separately, and at each iteration calculate to which resolution the two structures from the independent datasets aligned to each other mach. Then this resolution is used as the resolution limit for the following iteration. This scheme is implemented in multiple processing packages, including Dynamo [72], EMAN2 [73], and Relion [63]. Both approaches described here deal with overfitting of noise.

The presence of dense cellular background or membranes inside the mask for alignment may influence or dominate the alignment of particles to the template. The use of sharp alignment masks with local cross-correlation was adjusted for particle picking in single-particle EM in 2D [74] and for subtomogram averaging in 3D [72]. Use of local cross-correlation minimizes the influence of the context on the particle alignment and is beneficial for in situ structural analysis of protein complexes in crowded cellular environments or membrane proteins embedded into membranes.

### 10.4.2 Limited Number of Particles

More particles increase the signal to noise ratio in single particle cryo-EM [10] with a close-to-linear relation between the logarithm of particle number and the inverse resolution [75]. In StA after reaching a certain number of particles and resolution the other factors could come into the play and saturate the resolution [26]. The currently reported structures at subnanometer resolution mostly included over 50,000 asymmetric subunits recorded on direct detectors. The particles that align well to the average or have higher signal-to-noise ratio saturate the resolution faster, as a result less particles are required for a given target resolution. Each of the high-contrast particles recorded with the use of the Volta Phase Plate had resolutions from 35 to 50 Å while an average of 339 particles resulted in resolution of 31 Å, another conformation with 1367 particles had a resolution of 27 Å [32]. Subtomograms with large ribosome particles on the ER membranes recorded with higher defocus have been shown to align very accurately, which helped in obtaining subnanometer resolution with less particles [60]. However when the data is very high quality and the molecule of interest is very structurally homogeneous large number of particles may lead to atomic resolution [67]. In order to "pick" enough particles from the tomograms manual, semi-automatic [76] and automatic [77] methods have been suggested.

### 10.4.3 Structural Heterogeneity

Averaging over different conformational states of one particle will result in a non-coherent average with a reduced overall resolution. Heterogeneity may be compositional or conformational and both may be analysed by the subtomogram classification pipelines described in Chap. 9 of this book. Compositional heterogeneity with a limited number of classes may represent bound interaction partners and is well analysed by principal component-based statistics (Forster et al. 2008). The multi-reference alignment (MRA) family of algorithms combines iterative alignment of each particle to several references [78] which may efficiently sample broad conformational spectrums of molecules. However, the resolution of each of the classes may be limited by the number of particles contributing to it, therefore defining the number of classes is a sensitive parameter for the final resolution. The repeating elements from different classes may be mutually aligned and further summed increasing the resolution [64]. Conformational heterogeneity is one of the key challenges in both StA and in single particle cryo-EM; it should be addressed in the following years.

### 10.4.4 Data Collection Strategy

Movement and dose-dependent feature degradation of cryo-preserved samples [79] suggests a different approach to data collection rather than for getting a good point spread function. Best data come from lowly tilted micrographs and from the first electrons that expose the sample. It is possible to use the entire angular range for alignment of the particles to the average and then only incorporate the first exposures corresponding to i.e. 0°-30° for the final average [64]. Pfeiffer and colleagues recorded data starting from -20° going up to +60, then recording [-22:-2:-60] and used only the data from -20 to 20 for the final reconstruction [60]. The low-tilt consideration has been incorporated into an empirically derived kernel for convolution of particles and templates in Fourer space [63]. In this approach high-resolution information is down-weighted with applied electron dose and higher tilting angles; this was found beneficial and improved the resolution of StA. The concept of recording the low-tilt micrographs first in the tilt series was implemented by Hagen and colleagues as a "dose-symmetric tilt scheme" [66]. It's advantages are: (1) better distribution of electron dose and a more smooth effect of beam-induced density motion on the reconstruction quality, therefore (2) ability to apply higher electron dose per tomogram; (3) possibility to discard the information from the highly tilted images easily and (4) higher optical stability which is important while using phase plates. This data collection strategy was used to obtain the highest resolution StA structure to date [67].

Finally, the angular coverage of tomograms needs to be enough to precisely align the particles to the average but not more. Schur and colleagues used tomograms 278 M. Kudryashev

recorded from -45 to 45 or from -30 to 30 degrees to obtain a 7.7 Å resolution structure [62]. There also seem to be no reason to use higher dose for higher tilts or record dual tilt tomograms for subtomogram averaging if no preferred orientation of particles is present.

## 10.4.5 Image Processing

Image rotation is followed by interpolation of noisy image values, which degrades the high-resolution details. Tomographic reconstruction involves one or two interpolations (depending on the used software), subtomogram averaging introduces an additional interpolation step when the particles are rotated for averaging. Bartesaghi and colleagues introduced a hybrid method going back to the original tilt series during StA [61]. This elegant approach allows performing only one interpolation when bringing the patch of the micrograph with the particle to the final average. It also allowed evaluating the phase residuals for each of the tilting angle and potentially for different imaging conditions. The data recorded on CCD allowed obtaining an 8.4 Å structure after the processing [61].

#### 10.5 Conclusion and Overview

Electron tomography is a powerful modality that permits structural analysis of unique objects. For thin material science objects it can reveal atomic resolution using STEM imaging at a resolution of up to 2.4 Å. The wider use of the available advanced instrumentation and careful processing with the available algorithms will reveal new structures at atomic resolution. For cryo-ET the quality of the tomograms will be greatly improved by the common use of phase pates in combination with the new detectors and energy filters. This will improve the resolution of tomograms to  $\sim 2-4$  nm depending on the sample thickness, which will be very useful for cell biological applications. For subtomogram averaging the future will be in the use of the mentioned instrumentation, however the more important role will be dedicated to data processing. Correction of the distortions mentioned in this chapter will be limited by noise, however more structures at near-atomic resolution will be obtained for some samples.

**Acknowledgements** I thank Alex Noble, Andrea Nans, Mikhail Eltsov and Daniel Castano-Diez for valuable discussions and comments on the text. The author is funded by the Sofja Kovalevstaja Award from the Alexander von Humboldt Foundation and acknowledges support from the Max Planck Society.

#### References

- Lord Rayleigh, "XXXI. Investigations in optics, with special reference to the spectroscope," Philos. Mag. Ser. 5, 8(49), 261–274 (1879)
- 2. D.B. Williams, C.B. Carter, "The Transmission Electron Microscope," in *Transmission Electron Microscopy* (Springer, New York, USA, 2009), pp. 3–22
- K.W. Urban, Studying atomic structures by aberration-corrected transmission electron microscopy. Science 321(5888), 506–510 (2008)
- 4. M. Unser, B.L. Trus, A.C. Steven, A new resolution criterion based on spectral signal-to-noise ratios. Ultramicroscopy 23(1), 39–51 (1987)
- J. Frank, A. Verschoor, M. Boublik, Computer averaging of electron micrographs of 40S ribosomal subunits. Science 214(4527), 1353–1355 (1981)
- W.O. Saxton, W. Baumeister, The correlation averaging of a regularly arranged bacterial cell envelope protein. J. Microsc. 127(2), 127–138 (1982)
- 7. M. Van Heel, W. Keegstra, W. Schutter, E.J.F. Van Bruggen, Arthropod hemocyanin structures studied by image analysis. Life Chem. Rep. Suppl 1, 69–73 (1982)
- 8. G. Harauz, M. van Heel, Exact filters for general geometry three dimensional reconstruction. Optik **73**(4), 146–156 (1986)
- M. van Heel, M. Schatz, Fourier shell correlation threshold criteria. J. Struct. Biol. 151(3), 250–262 (2005)
- P.B. Rosenthal, R. Henderson, Optimal determination of particle orientation, absolute hand, and contrast loss in single-particle electron cryomicroscopy. J. Mol. Biol. 333(4), 721–745 (2003)
- C.k.e. Bleck et al., "Comparison of different methods for thin section EM analysis of Mycobacterium smegmatis," J. Microsc. 237(1), 23–38 (2010)
- A. Hoenger, C. Bouchet-Marquis, Cellular tomography. Adv. Protein Chem. Struct. Biol. 82, 67–90 (2011)
- 13. S. Wu, J. Liu, M.C. Reedy, H. Winkler, M.K. Reedy, K.A. Taylor, Methods for identifying and averaging variable molecular conformations in tomograms of actively contracting insect flight muscle. J. Struct. Biol. **168**(3), 485–502 (2009)
- 14. I. Wacker, R.R. Schroeder, Array tomography. J. Microsc. 252(2), 93–99 (2013)
- 15. W. Denk, H. Horstmann, Serial block-face scanning electron microscopy to reconstruct three-dimensional tissue nanostructure. PLoS Biol. 2(11), e329 (2004)
- G. Knott, H. Marchman, D. Wall, B. Lich, Serial section scanning electron microscopy of adult brain tissue using focused ion beam milling. J. Neurosci. 28(12), 2959–2964 (2008)
- 17. J.A.W. Heymann, M. Hayles, I. Gestmann, L.A. Giannuzzi, B. Lich, S. Subramaniam, Site-specific 3D imaging of cells and tissues with a dual beam microscope. J. Struct. Biol. **155** (1), 63–73 (2006)
- C. Villinger et al., FIB/SEM tomography with TEM-like resolution for 3D imaging of high-pressure frozen cells. Histochem. Cell Biol. 138(4), 549–556 (2012)
- 19. E. Wisse et al., Fixation methods for electron microscopy of human and other liver. World J. Gastroenterol. **16**(23), 2851–2866 (2010)
- P.C. Hawes, Preparation of cultured cells using high-pressure freezing and freeze substitution for subsequent 2D or 3D visualization in the transmission electron microscope. Methods Mol. Biol. Clifton NJ 1282, 271–282 (2015)
- 21. G.T. Herman, Fundamentals of Computerized Tomography (Springer, London, 2009)
- T. Gonen et al., Lipid-protein interactions in double-layered two-dimensional AQP0 crystals. Nature 438(7068), 633–638 (2005)
- 23. M. Allegretti, D.J. Mills, G. McMullan, W. Kühlbrandt, J. Vonck, "Atomic model of the F420-reducing [NiFe] hydrogenase by electron cryo-microscopy using a direct electron detector," *eLife*, **3** (2014)
- 24. T. Grant, N. Grigorieff, "Measuring the optimal exposure for single particle cryo-EM using a 2.6 Å reconstruction of rotavirus VP6," *eLife* **4**, e06980 (2015)

280 M. Kudryashev

25. X. Li et al., Electron counting and beam-induced motion correction enable near-atomic-resolution single-particle cryo-EM. Nat. Methods 10(6), 584–590 (2013)

- 26. M. Kudryashev, D. Castaño-Díez, H. Stahlberg, Limiting factors in single particle cryo electron tomography. Comput. Struct. Biotechnol. J. 1(2), 1–6 (2012)
- 27. J.J. Fernández, S. Li, R.A. Crowther, CTF determination and correction in electron cryotomography. Ultramicroscopy **106**(7), 587–596 (2006)
- 28. H. Winkler, K.A. Taylor, Focus gradient correction applied to tilt series image data used in electron tomography. J. Struct. Biol. **143**(1), 24–32 (2003)
- R. Danev, B. Buijsse, M. Khoshouei, J.M. Plitzko, W. Baumeister, Volta potential phase plate for in-focus phase contrast transmission electron microscopy. Proc. Natl. Acad. Sci. U. S. A. 111(44), 15635–15640 (2014)
- R. Danev, W. Baumeister, "Cryo-EM single particle analysis with the Volta phase plate," eLife 5 (2016)
- 31. M. Khoshouei, S. Pfeffer, W. Baumeister, F. Förster, R. Danev, "Subtomogram analysis using the Volta phase plate," *J. Struct. Biol.* (2016)
- 32. S. Asano et al., A molecular census of 26S proteasomes in intact neurons. Science **347**(6220), 439–442 (2015)
- 33. P.A. Penczek, J. Frank, "Resolution in Electron Tomography," in *Electron Tomography*, ed. by J. Frank (Springer, New York, 2007), pp. 307–330
- 34. M. Radermacher, Three-Dimensional reconstruction of single particles from random and nonrandom tilt series. J. Electron Microsc. Tech. **9**(4), 359–394 (1988)
- 35. P. Penczek, M. Marko, K. Buttle, J. Frank, Double-tilt electron tomography. Ultramicroscopy **60**(3), 393–410 (1995)
- W. Hoppe, D. Typke, "Three-Dimensional Reconstruction of Aperiodic Objects in Electron Microscopy," in *Unconventional Electron Microscopy for Molecular Structure Determination*, ed. by W. Hoppe, R. Mason (Vieweg+Teubner Verlag, 1979), pp. 137–190
- S. Lanzavecchia et al., Conical tomography of freeze-fracture replicas: a method for the study of integral membrane proteins inserted in phospholipid bilayers. J. Struct. Biol. 149(1), 87–98 (2005)
- 38. N. Kawase, M. Kato, H. Nishioka, H. Jinnai, Transmission electron microtomography without the 'missing wedge' for quantitative structural analysis. Ultramicroscopy **107**(1), 8–15 (2007)
- 39. R.A. Crowther, L.A. Amos, J.T. Finch, D.J. De Rosier, A. Klug, Three dimensional reconstructions of spherical viruses by fourier synthesis from electron micrographs. Nature **226**(5244), 421–425 (1970)
- 40. W.O. Saxton, W. Baumeister, M. Hahn, Three-dimensional reconstruction of imperfect two-dimensional crystals. Ultramicroscopy 13(1-2), 57-70 (1984)
- 41. K.J. Batenburg et al., 3D imaging of nanomaterials by discrete tomography. Ultramicroscopy **109**(6), 730–740 (2009)
- B.R. Gipson, D.J. Masiel, N.D. Browning, J. Spence, K. Mitsuoka, H. Stahlberg, "Automatic recovery of missing amplitudes and phases in tilt-limited electron crystallography of two-dimensional crystals," *Phys. Rev. E Stat. Nonlin. Soft Matter Phys.* 84(1, Pt 1), 11916 (2011)
- Y. Chen et al., FIRT: Filtered iterative reconstruction technique with information restoration.
   J. Struct. Biol. 195(1), 49–61 (2016)
- 44. Y. Deng, Y. Chen, Y. Zhang, S. Wang, F. Zhang, F. Sun, ICON: 3D reconstruction with 'missing-information' restoration in biological electron tomography. J. Struct. Biol. **195**(1), 100–112 (2016)
- 45. X. Zhang, Z. Hong, Zhou, "Limiting factors in atomic resolution cryo electron microscopy: No simple tricks". J. Struct. Biol. 175(3), 253–263 (2011)
- 46. J.G. Galaz-Montoya et al., "Alignment algorithms and per-particle CTF correction for single particle cryo-electron tomography," *J. Struct. Biol*
- 47. F.K.M. Schur, W.J.H. Hagen, A. de Marco, J.A.G. Briggs, Determination of protein structure at 8.5 Å resolution using cryo-electron tomography and sub-tomogram averaging. J. Struct. Biol. **184**(3), 394–400 (2013)

- 48. M. Eibauer, C. Hoffmann, J.M. Plitzko, W. Baumeister, S. Nickell, H. Engelhardt, Unraveling the structure of membrane proteins in situ by transfer function corrected cryo-electron tomography. J. Struct. Biol. **180**(3), 488–496 (2012)
- 49. L.M. Voortman et al., Quantifying resolution limiting factors in subtomogram averaged cryo-electron tomography using simulations. J. Struct. Biol. 187(2), 103–111 (2014)
- 50. Q. Yang, Y. Wang, Q. Liu, X. Yan, An accurate analytical approach to electron crystallography. Ultramicroscopy **87**(4), 177–186 (2001)
- 51. M.C. Scott et al., Electron tomography at 2.4-ångström resolution. Nature **483**(7390), 444–447 (2012)
- J. Miao, F. Förster, O. Levi, Equally sloped tomography with oversampling reconstruction. Phys. Rev. B 72(5), 52103 (2005)
- S.G. Wolf, L. Houben, M. Elbaum, Cryo-scanning transmission electron tomography of vitrified cells. Nat. Methods 11(4), 423–428 (2014)
- G. Cardone, K. Grünewald, A.C. Steven, A resolution criterion for electron tomography based on cross-validation. J. Struct. Biol. 151(2), 117–129 (2005)
- N.V. Dudkina, M. Kudryashev, H. Stahlberg, E.J. Boekema, Interaction of complexes I, III, and IV within the bovine respirasome by single particle cryoelectron tomography. Proc. Natl. Acad. Sci. U. S. A. 108(37), 15196–15200 (2011)
- C.A. Diebolder, F.G.A. Faas, A.J. Koster, R.I. Koning, Conical Fourier shell correlation applied to electron tomograms. J. Struct. Biol. 190(2), 215–223 (2015)
- H. Heidari Mezerji, W. Van den Broek, S. Bals, A practical method to determine the effective resolution in incoherent experimental electron tomography. Ultramicroscopy 111(5), 330–336 (2011)
- L.G. Trabuco, E. Villa, K. Mitra, J. Frank, K. Schulten, "Flexible fitting of atomic structures into electron microscopy maps using molecular dynamics," *Struct. Lond. Engl.* 1993 16(5), 673–683 (2008)
- F.K.M. Schur et al., Structure of the immature HIV-1 capsid in intact virus particles at 8.8 Å resolution. Nature 517(7535), 505–508 (2015)
- S. Pfeffer et al., Structure of the native Sec61 protein-conducting channel. Nat. Commun. 6, 8403 (2015)
- A. Bartesaghi, F. Lecumberry, G. Sapiro, S. Subramaniam, "Protein secondary structure determination by constrained single-particle cryo-electron tomography," *Struct. Lond. Engl.* 1993 20(12), 2003–2013 (2012)
- F.K.M. Schur, R.A. Dick, W.J.H. Hagen, V.M. Vogt, J.A.G. Briggs, The Structure of Immature Virus-Like Rous Sarcoma Virus Gag Particles Reveals a Structural Role for the p10 Domain in Assembly. J. Virol. 89(20), 10294–10302 (2015)
- T.A.M. Bharat, C.J. Russo, J. Löwe, L.A. Passmore, S.H.W. Scheres, "Advances in Single-Particle Electron Cryomicroscopy Structure Determination applied to Sub-tomogram Averaging," Struct. Lond. Engl. 1993 23(9), 1743–1753 (2015)
- 64. M. Kudryashev et al., "The Structure of the Mouse Serotonin 5-HT3 Receptor in Lipid Vesicles," Struct. Lond. Engl. 1993 24(1), 165–170 (2016)
- 65. M. Kunz, A.S. Frangakis, "Three-dimensional CTF correction improves the resolution of electron tomograms," *J. Struct. Biol.* (2016)
- 66. W.J.H. Hagen, W. Wan, J.A.G. Briggs, "Implementation of a cryo-electron tomography tilt-scheme optimized for high resolution subtomogram averaging," *J. Struct. Biol.* (2016)
- 67. F.K.M. Schur et al., An atomic model of HIV-1 capsid-SP1 reveals structures regulating assembly and maturation. Science **353**(6298), 506–508 (2016)
- 68. G.J. Jensen, Alignment error envelopes for single particle analysis. J. Struct. Biol. **133**(2–3), 143–155 (2001)
- J.M. Spear, A.J. Noble, Q. Xie, D.R. Sousa, M.S. Chapman, S.M. Stagg, The influence of frame alignment with dose compensation on the quality of single particle reconstructions. J. Struct. Biol. 192(2), 196–203 (2015)
- S.H.W. Scheres, S. Chen, Prevention of overfitting in cryo-EM structure determination. Nat. Methods 9(9), 853–854 (2012)

282 M. Kudryashev

 F. Amat, L.R. Comolli, F. Moussavi, J. Smit, K.H. Downing, M. Horowitz, Subtomogram alignment by adaptive Fourier coefficient thresholding. J. Struct. Biol. 171(3), 332–344 (2010)

- 72. D. Castaño-Díez, M. Kudryashev, M. Arheit, H. Stahlberg, Dynamo: a flexible, user-friendly development tool for subtomogram averaging of cryo-EM data in high-performance computing environments. J. Struct. Biol. 178(2), 139–151 (2012)
- 73. J.G. Galaz-Montoya, J. Flanagan, M.F. Schmid, S.J. Ludtke, Single particle tomography in EMAN2. J. Struct. Biol. **190**(3), 279–290 (2015)
- 74. A.M. Roseman, Particle finding in electron micrographs using a fast local correlation algorithm. Ultramicroscopy **94**(3–4), 225–236 (2003)
- 75. S.M. Stagg, A.J. Noble, M. Spilman, M. Chapman, ResLog plots as an empirical metric of the quality of cryo-EM reconstructions. J. Struct. Biol. **185**(3), 418–426 (2014)
- D. Castaño-Díez, M. Kudryashev, H. Stahlberg, "Dynamo Catalogue: Geometrical tools and data management for particle picking in subtomogram averaging of cryo-electron tomograms," J. Struct. Biol. (2016)
- 77. F. Förster, B.-G. Han, M. Beck, Visual proteomics. Methods Enzymol. 483, 215–243 (2010)
- M. Stölken et al., Maximum likelihood based classification of electron tomographic data.
   J. Struct. Biol. 173(1), 77–85 (2011)
- 79. M.G. Campbell et al., "Movies of ice-embedded particles enhance resolution in electron cryo-microscopy," *Struct. Lond. Engl. 1993* **20**(11), 1823–1828 (2012)

# Chapter 11 Signal Optimization in Electron Tomography

Mauro Maiorca and Peter B. Rosenthal

**Abstract** Signal optimization is essential for the reliable recognition and interpretation of structural features in volumes obtained by electron tomography. Optimization may be achieved through image processing algorithms that minimize noise and artefacts in either raw or reconstructed image signal. Procedures for signal optimization may be performed in real or Fourier space. We survey procedures and applications with an emphasis on cryotomography of frozen-hydrated biological specimens.

#### 11.1 Introduction

Three-dimensional structures of biological specimens from the molecular to cellular scale may be obtained through volumetric reconstruction from projection images recorded in the electron microscope. Frozen-hydrated, unstained specimen preparations preserve high-resolution structural features but are sensitive to radiation damage by the electron beam, requiring minimal electron exposure (low dose) methods during image acquisition. The projection images therefore have low contrast and a low signal-to-noise ratio (SNR).

SNR may be increased by image averaging, as exploited in single particle reconstruction, which requires the identification of randomly oriented particles followed by coherent averaging. In recent years, atomic structures have been determined from single particles that are of comparable resolution to those obtained by X-ray crystallography. However, many specimens are pleomorphic and no two identical examples of the specimen exist, so that image averaging is not possible. For three-dimensional reconstruction from projection images, many views must be recorded of a single, unique example of the specimen, usually by tilting the specimen

M. Maiorca (⋈) · P. B. Rosenthal (⋈)

Francis Crick Institute, 1 Midland Road, London NW1 1AT, UK

e-mail: mauromaiorca@gmail.com

P. B. Rosenthal

e-mail: Peter.Rosenthal@crick.ac.uk

holder in the microscope (a tilt series). Electron cryotomography is the unique approach to determine the architecture of pleomorphic biological specimens. Radiation damage imposes a limit on the number of low-dose images that may be recorded in a tilt-series of a frozen-hydrated specimen. The acquired tilt-series thus possesses a low SNR. In addition, there is usually a restriction on the range of views that may be obtained of the specimen, resulting in a "missing wedge" of data.

In electron tomography, the final volume (tomogram) is obtained through reconstruction from angular tilt projections of the specimen, typically from  $-70^{\circ}$  to  $+70^{\circ}$ , with  $2^{\circ}$  to  $4^{\circ}$  increments. The tomographic reconstruction has been referred to as a "severely ill-posed" inverse problem because of the limited range of angular projections and the limited sampling rate in the image acquisition protocol [10, 11, 37]. Computational procedures that reduce this ill-posedness are termed "regularization". The ill-posedness can be reduced by collecting additional information from the sample. In electron tomography this can be achieved by modifying the acquisition geometry, for example, by collecting a dual tilt series [19] or by obtaining better images, such as with direct detector devices that have recently become available. Even so, the missing data still produces artefacts, and computational regularization may be necessary.

A common application of cryotomography is the imaging of thick specimens that present additional problems of multiple scattering causing further degradation of the signal available in the images. Specimen thickness increases with increasing tilt angle. Electrons that are inelastically scattered contribute only noise to the image that may be removed by energy filtration, and in the future thicker specimens may also benefit from chromatic aberration correction [16].

Another type of problem results from the use of gold nanoparticles as fiducial markers in specimens for alignment or as immunolabels to identify molecules in the images and tomograms. Such particles are electron dense and are located proximal to regions of low density [7, 30]. These grayscale irregularities in tilt projections result in edge-gradient effects that obscure surrounding features in reconstructed volumes [6, 29]. Those artefacts are streak-shaped in filtered back projection (FBP) reconstruction [6, 9] and can be reduced by pre-reconstruction signal optimization approaches [28].

In practice, the low SNR of reconstructed data combined with missing data makes the identification and analysis of biological features in 3D tomograms challenging [32]. Signal optimization is essential for visualization as well computational segmentation of features in low contrast, noisy tomograms.

This chapter describes signal optimization procedures for cryotomograms. Many have analogues as filters for 2D image analysis and may be linear or non-linear, and the effect on voxel densities may be isotropic or anisotropic. Sections 11.2 and 11.3 discuss signal optimization in Fourier and real space respectively.

Several approaches have been described for using post-reconstruction diffusion-based methods to aid the interpretability of electron tomograms through local regularization [21, 32]. Within the last decade, Non-linear Anisotropic Diffusion (NAD) became the state of the art method for denoising reconstructed data [12, 13, 15, 38, 40]. Many of the procedures described for post-reconstruction

signal optimization may be applied successfully pre-reconstruction for signal optimization and regularization, as described in Sect. 11.4.

In general, the choice of a signal optimization method depends on the particular specimen, the goal of the experiment, the image acquisition protocol, and the reconstruction method used. There must be an awareness of when image reconstruction or signal optimization methods may introduce artefacts.

For simplicity of notation, the mathematical expressions are sometimes presented for the 2D case, but the 3D case is conceptually analogous.

## 11.2 Signal Optimisation in the Fourier Domain

Signal optimization in Fourier space is useful for the processing and analysis of overall features in the whole tomogram or in a given region of interest. We begin with a preamble on Fourier Transforms (Sect. 11.2.1), then we introduce bandpass filters (Sect. 11.2.2) and Gaussian filters (Sect. 11.2.3).

### 11.2.1 Fourier Transforms

Fourier analysis was introduced by the French mathematician Jean Baptiste Joseph Fourier (1768–1830) in his studies of heat conduction. Fourier's original context of heat conduction is related to diffusion, which also serves as an image processing technique as described in Sect. 11.3.2. In this section we give a brief overview of *Fourier transforms*, a fundamental mathematical tool for understanding image formation, processing, and analysis in electron tomography.

In image analysis, Fourier transforms can be used for a reversible conversion of an image into its spatial-frequencies [18]. Specifically, if we have a continuously sampled image I, its Fourier transformed image F is

$$F(u,v) = \mathscr{F}\{I(x,y)\} = \int_{-\infty}^{\infty} \int_{-\infty}^{\infty} I(x,y)e^{-i2\pi(ux+vy)}dxdy$$
 (11.1)

where u and v are the spatial frequencies in x and y, respectively, and F(u,v) is the 2D Fourier spectrum of I(x,y). Inverse Fourier transformation can be applied to obtain the spatial image I(x,y) through the linear combination of *complex exponentials*  $e^{i2\pi(ux+vy)}$  and *weights* F(u,v),

$$I(x,y) = \mathscr{F}^{-1}\{F(u,v)\} = \int_{-\infty}^{\infty} \int_{-\infty}^{\infty} F(u,v)e^{i2\pi(ux+vy)}dudv \qquad (11.2)$$

The above expressions refer to continuous functions. In practical image analysis problems, however, the input image is discretely sampled, and a discrete spectrum is recorded. In image processing and analysis, the discrete Fourier transform (DFT) is considered [18]. Specifically, given the natural numbers k, l and u, v, the discrete Fourier transform F of the image I is

$$F(k,l) \equiv \frac{1}{MN} \sum_{v=0}^{N-1} \sum_{u=0}^{M-1} I(u,v) e^{-i2\pi \left(\frac{uK}{M} + \frac{vl}{N}\right)}$$
(11.3)

The inverse discrete Fourier transform becomes:

$$I(u,v) \equiv \frac{1}{MN} \sum_{l=0}^{N-1} \sum_{k=0}^{M-1} F(k,l) e^{i2\pi \left(\frac{uK}{M} + \frac{vl}{N}\right)}$$
(11.4)

Fast computations of the DFT can be achieved using a method called the *Fast Fourier Transform* (FFT) [4].

An important application of the FFT is the efficient solution of the convolution problem. Using 3-D generalization, the convolution of two image volumes  $I_1(x, y, z)$  and  $I_2(x, y, z)$  is known to be a computationally onerous problem in real space [23]. In the frequency domain it can be solved by a computationally inexpensive multiplication [34], by application of the well-known convolution theorem which states that convolution in real space is equivalent to a multiplication in the Fourier domain

$$I_1(x, y, z) * I_2(x, y, z) = \mathscr{F}^{-1} \{ \mathscr{F} \{ I_1(x, y, z) \} \mathscr{F} \{ I_2(x, y, z) \} \}$$
 (11.5)

where \* is the convolution operator.

## 11.2.2 Bandpass Filters

In the Fourier spectrum of an image, coarse features are associated with low spatial frequency signal, while fine features are associated with high spatial frequency. Noise may predominate over signal at high spatial frequency, impairing the interpretation of both coarse and fine features. Denoising can be obtained by filtering specific frequency bands associated with noise. Specifically, filtering high spatial frequencies may reduce the contribution of high resolution noise. Filtering is achieved by weighting functions that vary from crude frequency truncation to strictly monotonic functions, with the choice designed to avoid the creation of spurious detail in the image.

An example of crude noise reduction by removing high frequency information is shown for a cryo-tomogram of frozen-hydrated influenza virus in Fig. 11.1. Images in a tilt series were acquired from  $-60^{\circ}$  to  $+60^{\circ}$ ,  $3^{\circ}$  increment, and reconstructed

using the Filtered Back Projections (FBP) method [5]. Figure 11.1a shows a section of the unprocessed reconstruction. From the original image (Fig. 11.1a) it is possible to appreciate the amount of high frequency noise obscuring overall features of the image. In fact, it is almost impossible to identify the virus membrane (green arrow) and the membrane glycoproteins (red arrows). Although the high frequency information may be important for some applications (i.e. subtomogram averaging), it impairs coarse assessment of the content. A Fourier Transform of the original image is shown in Fig. 11.1b, with the coordinate origin located in the middle of the image, which corresponds to the point of lowest spatial frequency. A darker vertical region is due to the missing wedge in the data (yellow arrow). Figure 11.1c represents the low pass filtered Fourier transform, obtained by setting high frequencies (black area) to zero, while leaving low frequencies unchanged (gray area). The effect of the low pass filter on the image is obtained by the inverse Fourier transform of the low pass filtered Fourier transform (Fig. 11.1c) and is shown in Fig. 11.1d. From Fig. 11.1d it is possible to identify gross features of the original image, such as virus membrane (green arrow) and membrane glycoproteins (red arrows) not visible in Fig. 11.1a. However, high-spatial frequency related fine details are no longer present in Fig. 11.1d, but they may be recovered from FBP with other methods that enhance higher frequency-related features explored within this chapter. The example in Fig. 11.1 uses frequency truncation for simplicity, however, the filter limit may be softened by a gentler filter, such as a Gaussian.

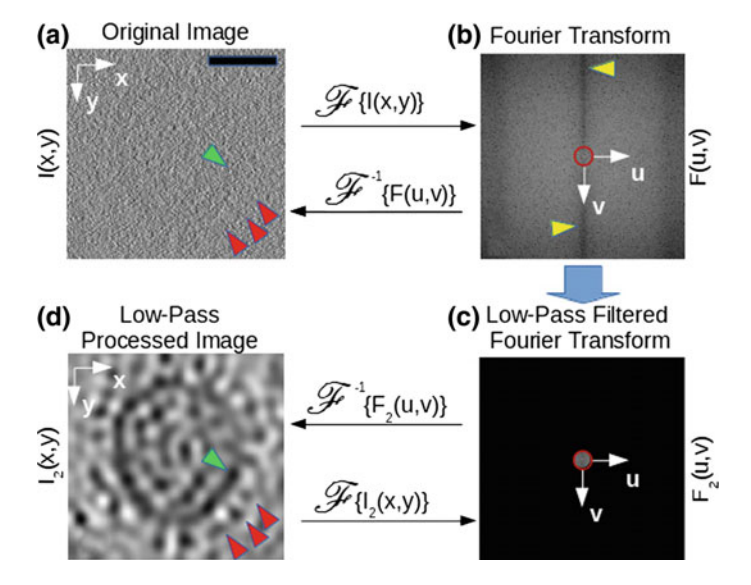


**Fig. 11.1** Example of coarse noise reduction in electron cryo-tomography using high frequency truncation. **a** Tomogram of frozen-hydrated influenza virus obtained by filtered back projection reconstruction method. **b** Fourier transform of the original tomogram, the red circle includes area of low frequencies. **c** Low-pass filtered Fourier transform, where all the high frequencies (outside the red circle) have been truncated. **d** Final processed image, obtained by performing inverse Fourier transform of the low-pass filtered Fourier transform. Scale Bar 50 nm

#### 11.2.3 Gaussian Filter

The Gaussian function is arguably the most used spatial frequency weighting function, due to its *scale-space* property of not introducing spurious details in the processed image (see paragraph 3.2). Furthermore, Gaussian spatial frequency weighting is usually included in any image processing toolkit, and can be implemented in both Fourier space and real space. In the 2D case this can be obtained by convoluting the original image I(x, y) with the 2D Gaussian function

$$G_{\sigma}(x,y) = \frac{1}{2\sigma^2 \pi} \exp\left(-\frac{x^2 + y^2}{2\sigma}\right)$$
 (11.6)

In Fourier space, this convolution can be obtained with (11.5) by performing a multiplication between the Fourier transform of the original image,  $\mathcal{F}\{I(x,y)\}$ , with the Fourier transform of the Gaussian function,

$$\mathscr{F}\left\{G_{\sigma}(x,y)\right\} = \frac{1}{2\sigma^{2}\pi} \exp\left(-\frac{\sigma^{2}}{2}\left(u^{2}+v^{2}\right)\right),\tag{11.7}$$

which is also a Gaussian. The challenge of using Gaussian filters for signal optimization is to select the optimal value of the parameter  $\sigma$  able to minimize the signal loss, while maximising noise loss. Larger  $\sigma$  increases contrast in the processed image.

An example of a cryo-ET volume processed with a Gaussian diffusion filter is shown in Fig. 11.2. Influenza A virus was imaged as described in Sect. 11.2.2. The original FBP tomogram is shown in Fig. 11.2a. The original tomogram blurred with  $\sigma=1$ ,  $\sigma=2$ , and  $\sigma=4$  are shown in Fig. 11.2b–d (respectively). Larger  $\sigma$  (i.e.  $\sigma=4$ ) produces stronger contrast images (see Fig. 11.2d). In Fig. 11.2d it is possible to identify the structures not visible in the unprocessed image (Fig. 11.2a), for example the ribonucleoprotein particles (RNPs) that package the genome segments in the virus interior (white arrows in Fig. 11.2a–d). High frequency data loss in the filtering process can be assessed using Fourier Shell Correlation (FSC), a frequency-by-frequency agreement measure between two images that has value 1 when the two images are in full agreement [20, 21]. The FSC between Gaussian filter processed and unprocessed data (Fig. 11.2e) shows that the increase of  $\sigma$  results in a decrease of FSC between the processed and unprocessed image [21].

## 11.3 Signal Optimization in Real Space

Real space signal optimization is used to enhance local spatial features by managing gray value fluctuations within a neighbourhood of each image point.

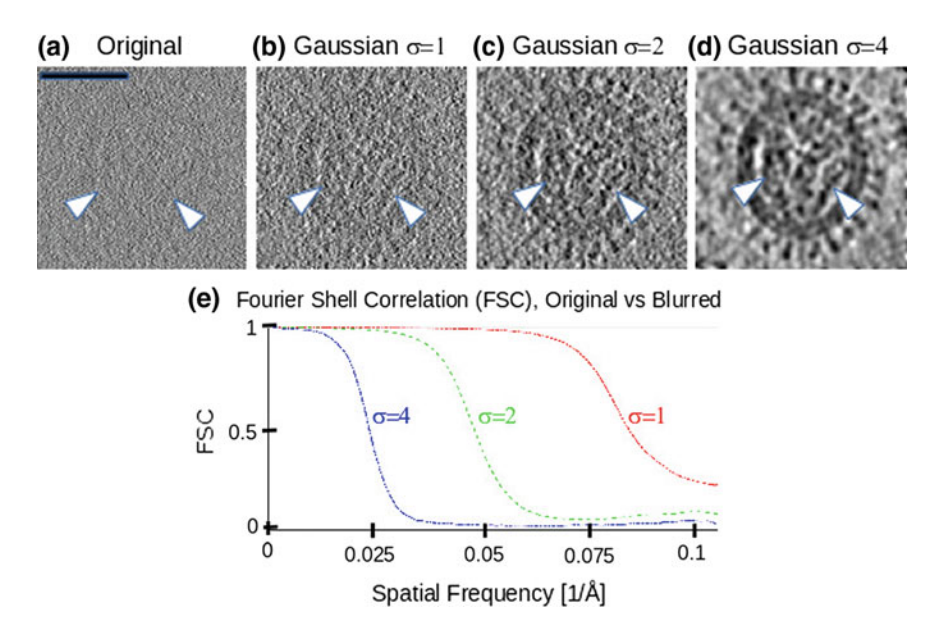


**Fig. 11.2** Example of cryo-ET volume processed with a Gaussian diffusion: visual appearance and Fourier Shell Correlation analysis. **a** Original image obtained by filtered back projection reconstruction. **b** Image blurred with Gaussian  $\sigma$  of 1 pixel. **c** Image blurred with Gaussian  $\sigma$  of 2 pixels. **d** Image blurred with Gaussian  $\sigma$  of 4 pixels. **e** Fourier shell correlation of blurred image against the original image. The larger the  $\sigma$  the highest the Fourier Shell Correlation distance from the original image, which suggests data lost in the process. Scale Bar 50 nm

In Sect. 11.3.1 we examine the median filter. In Sect. 11.3.2 we discuss signal optimization based on diffusion. In Sect. 11.3.3 we examine the case of non-linear diffusion filters. In Sect. 11.3.4 we discuss the Edge Enhancing Diffusion (EED) filter. In Sect. 11.3.5 we discuss the bilateral filter.

#### 11.3.1 Median Filter

The median filter is a non-linear filter for noise reduction. In its classical implementation, each single pixel is replaced with the median value of its neighbouring pixels. The median filter is particularly useful for removing impulse-type real space noise (for example, "salt and pepper" noise). Furthermore, it is easy to use, as the only parameter choice required is the neighbourhood size.

The median filter itself does not have any mechanism for identifying edges, in contrast to the approaches described in the next sections. However, directional weighted median computations may aid edge preservation [8]. Also, iterative application of the median filter has been found useful in the denoising of electron tomogrography volumes [22].

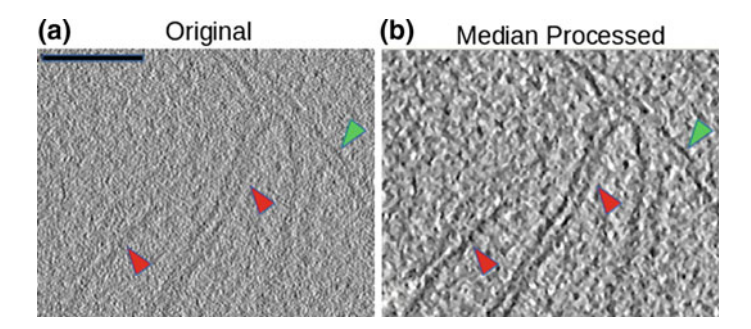


**Fig. 11.3** Application of median filter on tomogram of a mitochondrion in a frozen-hydrated cell. **a** Original tomogram reconstructed using the filtered back projection method. **b** Median filtered tomogram. Green arrow points to the outer membrane; red arrow points to folds in the inner membrane (cristae). Median filtering delineated membranes of mitochondrion, and the overall contrast of the processed tomogram. Image collected by Dr. Pauline McIntosh, The Francis Crick Institute, London (UK). Scale Bar 200 nm

An example of 3D median filter application to frozen-hydrated cells is provided in Fig. 11.3, showing a mitochondrion from canine cocker spaniel kidney (CCSK) cells which have been snap frozen and imaged. The original tomogram reconstructed using the filtered back projection method is shown in Fig. 11.3a, and the median filtered tomogram is shown in Fig. 11.3b. The median filtered image has been obtained by iteratively applying a 3D median filter of 1 pixel radius, and 3 iterations. The processed image (3.B) helped delineate the mitochondrion membranes, including the folds in the inner membrane known as cristae (red arrows). The outer membrane is also enhanced (green arrow).

## 11.3.2 Physical Model of Linear Diffusion

Practical use of Gaussian filters in electron tomography is described in Sect. 11.2.3. However, the use of Gaussian filters is linked with physical models of linear diffusion, which provide a powerful framework for the processing and analysis of data (in general) and signal optimization (in particular). Theoretical foundations for justifying the use of diffusion in electron tomography signal optimization are given by *scale space* theory [14, 25, 33, 43].

In scale space theory, the grayscale image of the specimen is regarded as a density that is redistributed by a conservative diffusive process. The equilibration of intensity due to its inhomogeneity is determined by Fick's law of diffusion, so the time-evolution of the grayscale image I, namely  $I_t$ , is obtained by solving the diffusion equation

$$\frac{\partial I}{\partial t} = \nabla \cdot (c\nabla I) \tag{11.8}$$

with t a diffusion process time and c a constant parameter. In real space, when the stop diffusion process occurs at the time  $t = T_{\sigma} = \sigma^2/2$ , the solution  $I_{\sigma}(x, y)$  of the diffusion (11.8) is informally referred to as *Gaussian blurring* and is obtained by convoluting I(x, y) with a Gaussian function  $G_{\sigma}$ 

$$I_{\sigma}(x,y) = (I * G_{\sigma})(x,y) \tag{11.9}$$

where, in the two dimensional case,  $G_{\sigma}$  is

$$G_{\sigma}(x,y) = \frac{1}{2\sigma^2 \pi} \exp\left(-\frac{x^2 + y^2}{2\sigma}\right)$$
 (11.10)

Due to the linear and isotropic nature of Gaussian diffusion, Gaussian blurring is also referred to as *linear isotropic diffusion*. A direct consequence of linearity is the *non-enhancement of local extrema* (known as the *causality criterion*), which guarantees that no spurious details may be created while applying Gaussian blurring [25, 43].

However, as shown in Sect. 11.2.3, the trade-off for using Gaussian blurring is a significant loss in resolution and feature-edge delineation. In the rest of this chapter we show variations of the simple Gaussian filter that enhance contrast while preserving feature-edge delineation.

### 11.3.3 Non-Linear Diffusion

Non-linear diffusion approaches aim to smooth an image and to simultaneously enhance relevant features that otherwise become blurred when filters such as the Gaussian are applied to edges. The diffusion process is driven by the derivative analysis of the evolving image. In non-linear diffusion, the Gaussian diffusion causality criterion is no longer guaranteed, thus non-linear filters have the potential of creating spurious details from random noise and artefacts. However, careful filter design, investigator technical awareness, and problem-specific filter selection may greatly reduce the likelihood of this happening.

In Non-Linear diffusion, equilibration of intensity is determined by Fick's law of diffusion, analogously to linear diffusion (11.8). The non-linear diffusion time-evolution of I is obtained by solving the diffusion equation

$$\frac{\partial I}{\partial t} = \nabla \cdot (D\nabla I) \tag{11.11}$$

where D is the diffusion tensor, a matrix used to control the local diffusive flux of intensity values to be redistributed, which replaces the constant c of linear diffusion (11.8). If the diffusion tensor D is constant over the entire domain of I, the diffusion process is defined as homogeneous [43]. Otherwise, diffusion is defined as

inhomogeneous if *D* varies with pixel position. If the local diffusive flux does not privilege any specific direction, the diffusion is called *isotropic*, which is the case of Gaussian diffusion (Sects. 11.3.2 and 11.2.3). Otherwise it is called *anisotropic*.

The non-linear diffusion filter proposed by [36] employed an isotropic model of the form  $D = g(\nabla I \cdot \nabla I)I$ , where g describes the scalar-valued, edge-driven, diffusivity flux  $g(s^2) = (1 + s^2/\mu^2)^{-1}$  in which  $\mu$  is a real, positive, normalization parameter.

The diffusion tensor D enables the diffusive flux to locally privilege specific directions, leading to the case of non-linear anisotropic diffusion (NAD). Thus, NAD allows directional diffusion to be coherent with structural features of the image, under the assumption of local structural continuity. Structural details of a 3-dimensional image are inferred from local grayscale intensity variations (using eigen-analysis). Structural details are encoded in components of the diffusion tensor D together with the diffusivity parameters  $\lambda_1, \lambda_2$ , and  $\lambda_3$  that control the diffusive flux ratio along the three major orthogonal axes of local intensity variation. Different characterizations of diffusivity parameters  $\lambda_1, \lambda_2, ..., \lambda_N$  define different NAD approaches. A 3-dimensional example of a NAD approach, Edge Enhancing Diffusion (EED), is explained in Sect. 11.3.4.

## 11.3.4 Edge Enhancing Diffusion (EED)

Edge Enhancing Diffusion (EED) is a non-linear anisotropic diffusive (NAD) inhomogeneous approach, previously described by [44] as an anisotropic version of the Perona-Malik model (described in Sect. 11.3.3). EED was introduced in electron tomography by [15], combined with another NAD filter, Coherence Enhancing Diffusion (CED), first described by [45]. However, current post-reconstruction NAD-processing methods do not take into account unavoidable reconstruction artefacts due to incomplete, irregular sampling. An implementation of EED is included in several software packages, used by the EM community, e.g. IMOD [26] and SPIDER [39].

In its 3D implementation, EED varies from other NAD approaches primarily in its definitions of diffusivity parameters  $\lambda_1$ ,  $\lambda_2$ , and  $\lambda_3$ . EED has an isotropic behavior when  $\lambda_1 \approx 1$  (no edge is detected), and anisotropic behavior when  $\lambda_1 \approx 0$  (when an edge is detected). Specifically,  $\lambda_1$ ,  $\lambda_2$ , and  $\lambda_3$  are defined as

$$\lambda_{1} = \begin{cases} 1 & \text{if } G(\sigma) = 0, \\ 1 - \exp\left[-C\frac{G(\sigma)^{4}}{\lambda_{e}}\right] & \text{if } G(\sigma) > 0. \end{cases}$$

$$\lambda_{2} = 1$$

$$\lambda_{3} = 1$$

$$(11.12)$$

where  $G(\sigma) = \nabla I_{\sigma} \cdot \nabla I_{\sigma}$  is the edge discriminator, C = 3.31488 is a threshold parameter [31] and  $\lambda_e$  is a user defined normalization parameter (typical value is  $\lambda_e = 30$ ) [44, 45].

The ability of the algorithm to detect edges is thus driven by (11.12), and mainly depends on how  $\lambda_e$  and  $\sigma$  are set. Large  $\lambda_e$  forces the algorithm to have an overall isotropic behavior, while small  $\lambda_e$  encourages an overall anisotropic behavior of the filter. Large  $\sigma$  makes the algorithm less sensitive to noise, but may blur out features.

In comparison to other NAD filters, including CED, EED has less potential for inducing spurious details in the image due to noise, mainly due to the gentle anisotropic behavior of the filter (because  $\lambda_2 = \lambda_3 = 1$ ). However, due to the inhomogeneous nature of EED, weak edges may be blurred out. This is especially true when aggressive parameters are used, i.e. large  $\lambda_e$ , large  $\sigma$ , and a large number of iterations.

An example of EED filtering is shown in Fig. 11.4. A tilt series of frozen-hydrated influenza virus was acquired and reconstructed using the filtered back projection method (Fig. 11.4a and detail a'), the resulting tomogram processed by EED

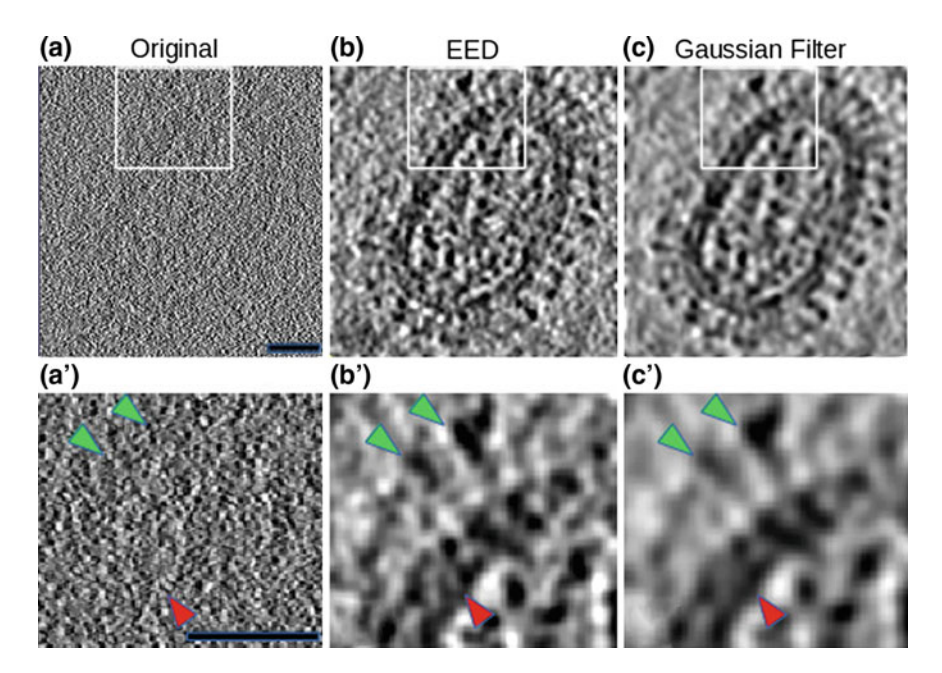


**Fig. 11.4** Frozen-hydrated influenza virus processed by Edge Enhancement Diffusion (EED) and Gaussian Filtering: visual outcome and analysis. **a** and detail **a'** Original reconstructed volume using the filtered back projection method. **b** and detail **b'** EED of the original image **c** and detail **c'** Gaussian filtered image and detail. Parameters for EED were  $\sigma = 6$  pixels,  $\lambda_e = 30$ , 45 iterations, see (11.12). Parameters for Gaussian blurring,  $\sigma = 4$  pixels. In the EED image details of the biological structures are more definite compared to the Gaussian blurred image. Green arrows point to glycoproteins, red points to the inner matrix layer. Original data from [5]. Scale bar 25 nm

(Fig. 11.4b and detail b') or Gaussian filtered (Fig. 11.4c and detail c'). Both the EED and Gaussian filtered images show an increased contrast. However, EED filtering better preserves small details blurred out by Gaussian filtering, for example glycoproteins (green arrows) and the inner matrix layer (red arrows).

### 11.3.5 Bilateral Filter

The bilateral filter was first introduced by [42], aiming to combine Gaussian diffusion with the elimination of noise-related small pixel intensity variations. The bilateral filter was adapted for electron tomography by [24] and implemented in EMAN2 [41].

In practice, the intensity value at each pixel in an image is replaced by a Gaussian-weighted average of intensity values from pixels within a neighbourhood  $\xi$ . The weights depend on Euclidean distance of pixels, and on the intensity value differences. Using notation from [24],

$$I_{out}(\overrightarrow{r}) = \int \exp\left\{-\frac{|\overrightarrow{\xi} - \overrightarrow{r}|^2}{2\sigma_1^2}\right\} \exp\left\{-\frac{|I(\overrightarrow{\xi}) - I(\overrightarrow{r})|^2}{2\sigma_2^2}\right\} \times I(\overrightarrow{\xi})d\overrightarrow{\xi} \quad (11.13)$$

 $I(\overrightarrow{r})$  is the input image,  $exp(|\overrightarrow{\xi}-\overrightarrow{r}|^2)/(2\sigma_1^2)$  is the Euclidean distance contribution, and  $exp(|I(\overrightarrow{\xi})-I(\overrightarrow{r})|^2)/(2\sigma_2^2)$  is the intensity value difference. Furthermore, variations of the bilateral filter can include an edge detection paradigm [35]

The parameter  $\sigma_1$  controls the extent of the Gaussian diffusion, and a larger  $\sigma_1$  causes severe smoothing.  $\sigma_2$  controls the discrimination of intensity value differences. Larger pixel intensity value variations are mainly from true features and smaller pixel intensity value variations are contributed by noise. This filter has the property of removing isolated pixels, without the need of aggressive Gaussian diffusion.

An example of bilateral filtering is shown in Fig. 11.5. Tilt series of images of frozen-hydrated filopodia were acquired and reconstructed using the filtered back projection method (Fig. 11.5a and detail a'), and processed by bilateral filtering (Fig. 11.5b and detail b'). Bilateral filtering preserved both outer membrane (green arrow) and actin filament (red arrow) integrity, aiding their visual tracking, and increasing the overall image contrast.

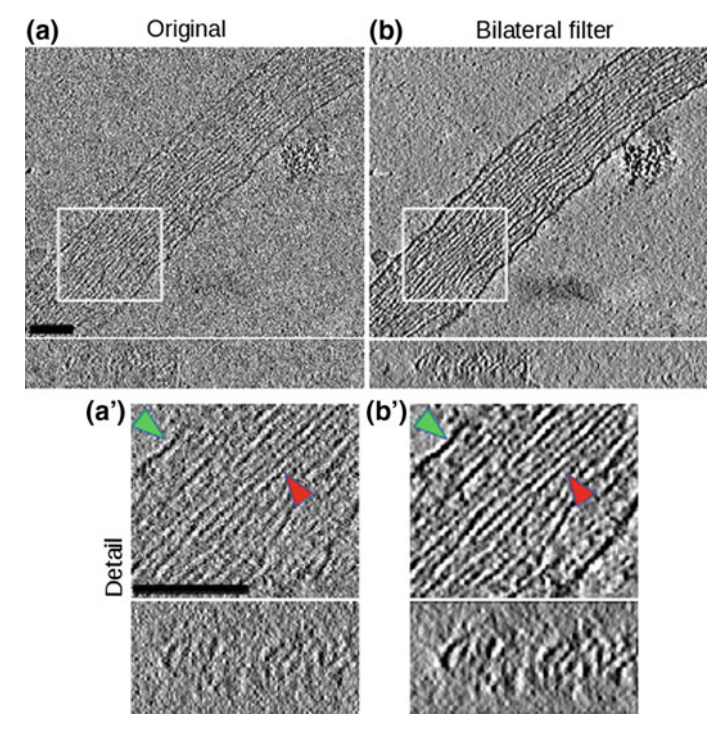


**Fig. 11.5** Demonstration of Bilateral Filter processing on filopodia (a) Original (b) Bilateral filter reconstruction, Parameters are  $\sigma_1 = 2$  pixels,  $\sigma_2 = 2000$  intensity values, half width = 5, and 5 iterations, see (11.13). Green arrow shows filopodial membrane, Red arrow shows filopodial actin with other filaments. Bilateral filtering preserved both outer membrane and actin filament continuity, aiding their visual tracking, and increasing the overall image contrast. Scalebar 50 nm

## 11.4 Pre-Reconstruction Approaches

Computational approaches to signal optimization, including many of those already described for post-reconstruction optimization, may be applied to image tilt series prior to calculating a 3D reconstruction. Pre-reconstruction approaches may help overcome the ill-posedness of reconstruction algorithms and reduce artefacts due to the limited range of angular projections and the limited sampling rate.

A popular approach is to reduce the size of each tilt projection, by binning pixels in the aligned tilt projection stack (while at the same time reducing noise). The greater the bin size, the clearer is the output image, but at the expense of substantial image resolution loss.

An alternative approach is to apply a 2D Gaussian filter to each tilt projection in the stack. The pre-reconstruction application of a Gaussian filter may be preferred over applying a 3D Gaussian blurring to the reconstructed images, for two reasons: (1) it requires a smaller  $\sigma$  than 3D smoothing, and (2) it is possible to apply different  $\sigma$  values as a function of tilt angle, as suggested by [27].

In solving the inverse problem of reconstruction, extra free variables are required to analytically account for irregularities in local grayscale value fluctuations as well as missing data [2]. Thus, a recovery from ill-posedness (namely, regularization of the inverse problem) is desirable for reducing reconstruction artefact. The discrete algebraic reconstruction technique (DART) approaches the problem by drastically reducing the possible range of intensity values in the whole reconstructed image [2, 3]. Although this approach effectively reduces artefacts, it drastically contracts the intensity grayscale values of the reconstructed volume to a small set of discrete values, which may cause problems in the interpretation of complex biological structures. Compressive sensing approaches to the regularization of the inverse problem of reconstruction have recently been described. Reference [17] presented a reconstruction algorithm that uses total variation minimization (TVM) regularization for reducing the overall range of intensity values. This method can produce a reconstructed volume with a larger set of discrete grayscale values than DART. However, the grayscale value impairment affects the whole image, which is not desirable when only selected objects in the tomogram are causing the artefacts.

Pre-reconstruction Nonlinear Anisotropic diffusion (pre-NAD) may be used for contrast enhancement. For pre-NAD [27], the magnitude of  $\sigma$  determines the spatial interval over which the structure tensor is calculated [1, 25, 33]. Small values of  $\sigma$  cause negligible smoothing of the image. Large values of  $\sigma$  reduce noise but may obscure significant features, such as edges and discontinuities. Pre-NAD compensates for the variable projected depth through the sample by using a specific smoothing parameter  $\sigma(\phi) = \sigma cos(\phi)$  for each tilt projection acquired at an angle  $\phi$ .

For pre-NAD, an analysis of the intensity variations across the tomogram is presented in Fig. 11.6 for a sample embedded with epoxy resin. In the original tomogram, (Fig. 11.6, column a) it is not possible to distinguish the boundary between the two organelles ( $R_1$  and  $R_2$ ), as an electron lucent region (c) that separates two electron-dense regions. Each of the processed tomograms (columns b-d) displays a clear electron-dense edge (low gray values) at the boundary of rhoptry  $R_1$ , which is less well defined in the unprocessed tomogram (a). Also, the unprocessed tomogram contains an artefactual feature (arrow e). This artefactual feature is partially removed by post-reconstruction NAD processing (b) and more effectively removed when pre-reconstruction NAD processing is applied (c and d). Also, the pre-NAD processed tomograms (c and d) represent more faithfully the adjacent rhoptry  $R_2$  (arrow e) than the post-NAD processed tomogram (b).

The re-equilibration of grayscale irregularities in regions corresponding to gold particles in tilt projection images using pre-reconstruction Non-Linear Isotropic Diffusion (pre-NAD) may reduce the streak artefacts in the reconstructed tomogram [28]. Figure 11.7 shows the application of pre-reconstruction Non-Linear Isotropic Diffusion (pre-NID) processing to a tomogram of a frozen-hydrated *P. falciparum* gametocyte sample. In the unprocessed tomograms, streak artefacts were evident around the gold particle in the field of view. These artefacts are substantially

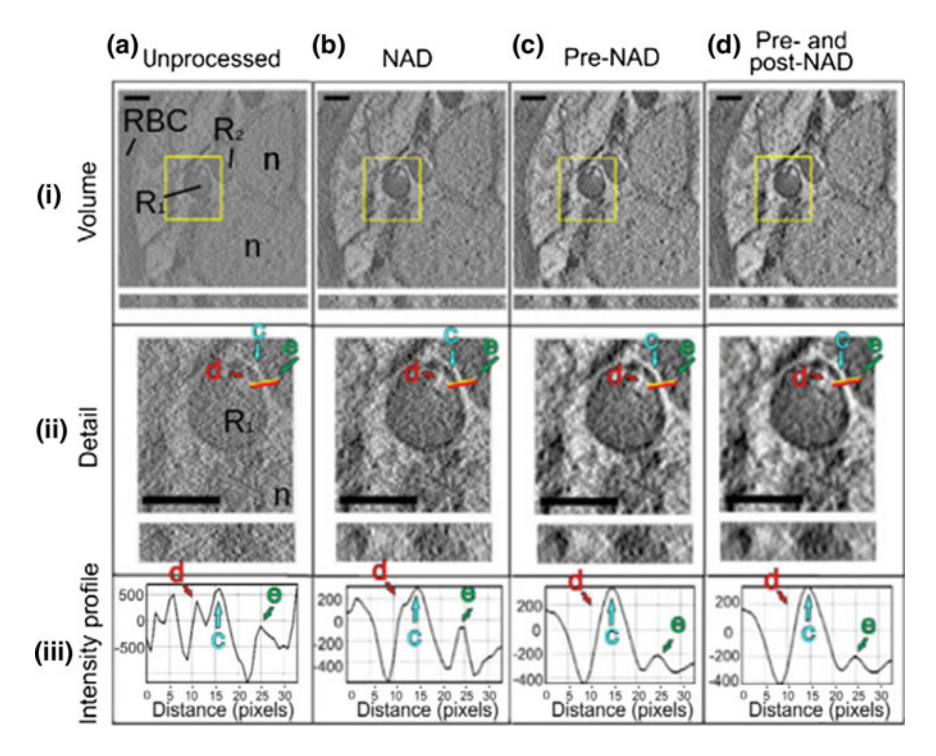
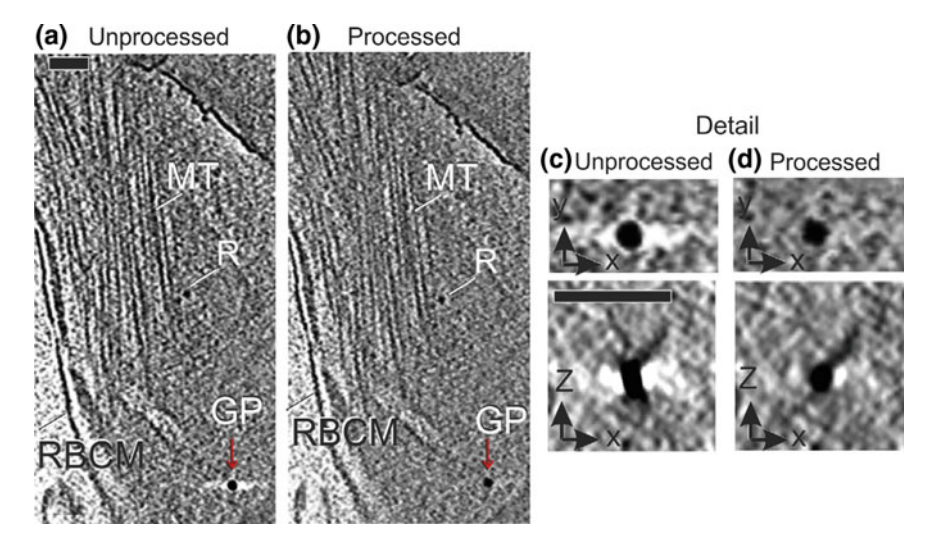


Fig. 11.6 Improvement in electron tomogram interpretation following application of pre-NAD filtering to a limited angle data set. **a** Low exposure tomogram views of *P.falciparum*-infected red blood cell (RBC). **b** Views of processed tomogram, filtered using the IMOD post-reconstruction NAD filter [15], or **c** filtered with the pre-NAD algorithm [27] or **d** processed with both pre- and post-NAD filtering. The RBC cytoplasm, the peripheries of two nuclei (n), and two rhoptry organelles (R1 and R2) are indicated. Row (i) shows a view of the tomogram, row (ii) shows a detailed view of a rhoptry organelle. The intensity-profile graphs in row (iii) show analyses of the intensity variations across the data in the region of the line (red/yellow). A low electron-density region between the rhoptries (indicated by the aqua arrow, c), a region at the edge of  $R_1$  (marked with red arrow, d) and region within  $R_2$  (marked with green arrow, e) are indicated. Pre-NAD filtered reconstructions seem to represent more faithfully the boundary between the two rhoptry organelles. Image adapted from [27] and reproduced with permission. Scale bars: 200 nm

reduced in the pre-NID-processed tomograms (Fig. 11.7 red arrows, and panels c and d). By contrast, other features such as microtubules (MT) and ribosomes (R) that do not have the sharp gradient differential characteristic of gold particles, do not seem to be affected by the pre-NID processing.



**Fig. 11.7** Application of pre-reconstruction Nonlinear Isotropic diffusion (pre-NID) on cryo electron tomography, data for microtubules in a frozen-hydrated *P. falciparum* gametocyte. Panel **a** shows an unprocessed view of *xy* section of the tomogram, unveiling ribosomes (R), microtubules (MT), the red blood cell membrane (RBCM), a colloidal gold particle (GP) surrounded by streak-shaped artefacts. Panel **b** shows a view of the processed tomogram, streak-shaped artefacts around to the gold particle seem to be reduced. Panels **c** and **d** provide *xy* and *xz* details of unprocessed and processed tomogram. The streak-shaped artefacts surrounding the gold are significantly reduced in the pre-NID processed tomogram, while the rest of the image is unaltered. Original data from Dr. Eric Hanssen, image adapted from [28] and reproduced with permission. Scale bars: 50 nm

#### 11.5 Conclusion

In principle, signal optimization is a goal in all aspects of the experimental design as well as in the reconstruction methods used to calculate volumes from the tilt-series of projection images. However, interpretation of the tomogram often benefits from signal optimization or filtering post-reconstruction. The need arises because of the low contrast and noise of the reconstruction in the absence of possibilities for image or volume averaging as in single particle reconstruction or sub-tomogram averaging. The choice of procedure may depend on the specific structural problem or the scale of its features. In many cases a Fourier or real space filter may be sufficient to remove high-resolution noise, such as those that are subject to artefactual interpretation. However, the signal-optimization procedure should not introduce artefacts. An objective procedure for discriminating real features from artefacts is an important goal for which at present there is no general recipe. In real space, blurring with a Gaussian is considered the safest method as it will not create spurious "extrema" in the image or tomogram, but of course results in the loss of high-resolution features. Optimal combination of pre-and post processing filters for each reconstruction method is a continuing area of research.

#### References

- J. Babaud, A. Witkin, M. Baudin, R. Duda, Uniqueness of the Gaussian kernel for scale-space filtering. IEEE Trans. Pattern Anal. Machine Intell. 8(1), 26–33 (1986)
- K. Batenburg, S. Bals, J. Sijbers, C. Kübel, P. Midgley, J. Hernandez, U. Kaiser, E. Encina, E. Coronado, G.V. Tendeloo, 3D imaging of nanomaterials by discrete tomography. Ultramicroscopy 109, 730–740 (2009)
- 3. K. Batenburg, J. Sijbers, Dart: a practical reconstruction algorithm for discrete tomography. IEEE Trans. Image Process. **20**, 2542–2553 (2011)
- 4. E. Brigham, The Fast Fourier Transform and Its Applications (Prentice-Hall, UK, 1988)
- L. Calder, S. Wasilewski, J. Berriman, P. Rosenthal, Structural organization of a filamentous influenza A virus. PNAS 107(10), 685–690 (2010)
- M. Cao, H. Zhang, Y. Lu, R. Nishi, A. Takaoka, Formation and reduction of streak artefacts in electron tomography. J. Microsc. 239, 66–71 (2010)
- H. Chapman, C. Jacobsen, S. Williams, A characterisation of dark-field imaging of colloidal gold labels in a scanning transmission x-ray microscope. Ultramicroscopy 62(3), 191–213 (1996)
- 8. Y. Dong, S. Xu, A new directional weighted median filter for removal of random-valued impulse noise. IEEE Signal Process. Lett. **14**(3), 193–196 (2007)
- A. Duerinckx, A. Macovski, Polychromatic streak artifacts in computed tomography images.
   J. Comput. Assist. Tomogr. 2, 481–487 (1978)
- H. Engl, M. Hanke, A. Neubauer, Regularization of Inverse Prob. (Springer, Berlin, 2000) (31 Mar 200)
- 11. D. Fanelli, O. Öktem, Electron tomography: a short overview with an emphasis on the absorption potential model for the forward problem. Inverse Prob. **24**(1), 1–51 (1997)
- 12. J. Fernández, S. Li, An improved algorithm for anisotropic nonlinear diffusion for denoising cryo-tomograms. J. Struct. Biol. **144**(1–2), 152–161 (2003)
- J. Fernandez, S. Li, Anisotropic nonlinear filtering of cellular structures in cryoelectron tomography. Comput. Sci. Eng. 7(5), 54–61 (2005)
- L. Florack, R. Duits, J. Bierkens, Tikhonov regularization versus scale space: A new result. ICIP (2004) pp. 271–274
- A. Frangakis, R. Hegerl, Noise reduction in electron tomographic reconstructions using nonlinear anisotropic diffusion. J. Struct. Biol. 135(3), 239–250 (2001)
- J. Frank, Introduction: Principles of electron tomography, in *Electron Tomography*, 2nd edn. (Springer, New York, 2006)
- B. Goris, W.V. den Broek, K. Batenburg, H.H. Mezerji, S. Bals, Electron tomography based on a total variation minimization reconstruction technique. Ultramicroscopy 113, 120–130 (2012)
- 18. R. Gray, J. Goodman, Fourier Transforms (Kluwer, Alphen aan den Rijn, 1995)
- A. Guesdon, S. Blestel, C. Kervrann, D. Chretien, Single versus dual-axis cryo-electron tomography of microtubules assembled in vitro: limits and perspectives. J. Struct. Biol. 181, 169–178 (2013)
- G. Harauz, M. van Heel, Exact filters for general geometry three-dimensional reconstruction. Optik 73, 146–156 (1986)
- 21. R. Hegerl, A. Frangakis, Denoising of electron tomograms, in *Electron Tomography*, vol. 2006, 2nd edn. (Springer, New York, 2006), pp. 331–352
- P. van der Heide, X. Xu, B. Marsh, D. Hanein, N. Volkmann, Efficient automatic noise reduction of electron tomographic reconstructions based on iterative median filtering. J. Struct. Biol. 158(2), 196–204 (2007)
- P. Henrici, Applied and Computational Complex Analysis, Discrete Fourier Analysis, Cauchy Integrals, Construction of Conformal Maps, Univalent Functions (Wiley, Hoboken, 1993)
- W. Jiang, M. Baker, Q. Wu, C. Bajaj, W. Chiu, Applications of a bilateral denoising filter in biological electron microscopy. J. Struct. Biol. 144, 114–122 (2003)

- 25. J. Koenderink, The structure of images. Biol. Cybern. **50**(5), 363–370 (1984)
- J. Kremer, D. Mastronarde, J. McIntosh, Computer visualization of three-dimensional image data using imod. J. Struct. Biol. 116(1), 71–76 (1996)
- M. Maiorca, E. Hanssen, E. Kazmierczak, B. Maco, M. Kudryashev, R. Hall, H. Quiney, L. Tilley, Improving the quality of electron tomography image volumes using pre-reconstruction filtering. J. Struct. Biol. 180(1), 132–142 (2012)
- M. Maiorca, C. Millet, E. Hanssen, B. Abbey, E. Kazmierczak, L. Tilley, Local regularization of tilt projections reduces artifacts in electron tomography. J. Struct. Biol. 186(1), 28–37 (2014)
- 29. D. Mastronarde, Dual-axis tomography: An approach with alignment methods that preserve resolution. J. Struct. Biol. **120**(3), 343–352 (1997)
- P. McMillan, C. Millet, S. Batinovic, M. Maiorca, E. Hanssen, S. Kenny, R. Muhle, M. Melcher, D. Fidock, J. Smith, M. Dixon, L. Tilley, Spatial and temporal mapping of the pfemp1 export pathway in *Plasmodium falciparum*. Cell. Microbiol. 15(8), 1401–1418 (2013)
- A. Mendrik, E. Vonken, A. Rutten, M. Viergever, B. van Ginneken, Noise reduction in computed tomography scans using 3d anisotropic hybrid diffusion with continuous switch. IEEE Trans. Med. Imag. 28, 1585–1594 (2009)
- 32. R. Narasimha, I. Agani, A. Bennett, M. Borgnia, D. Zabransky, G. Sapiro, S. McLaughlin, J. Milne, S. Subramania, Evaluation of denoising algorithms for biological electron tomography. J. Struct. Biol. **164**(1), 7–17 (2008)
- M. Nielsen, L.M.J. Florack, R. Deriche, Regularization, scale space, and edge detection Iters.
   J. Math. Imaging Vis. 7(4), 291–307 (1997)
- 34. H. Ozaktas, O.A. Ankan, G.B. Kutay, Digital computation of the fractional fourier transform. IEEE Trans. Sig. Process. **44**(9), 2141–2150 (1996)
- 35. R. Pantelic, G. Ericksson, N. Hamilton, B. Hankamer, Bilateral edge filter: photometrically weighted, discontinuity based edge detection. J. Struct. Biol. **160**(1), 93–102 (2007)
- 36. P. Perona, J. Malik, Scale-space and edge detection using anisotropic diffusion. IEEE Trans. Pattern Anal. Mach. Intell. **12**(7), 629–639 (1990)
- H. Rullgård, O. Öktem, U. Skoglund, A component-wise iterated relative entropy regularization method with updated prior and regularization parameter. Inverse Prob. 23, 2121–2139 (2007)
- 38. R. Salzer, Biomedical Imaging: Principles and Applications (Wiley, Hoboken, 2010)
- T. Shaikh, H. Gao, W. Baxter, F. Asturias, N. Boisset, A. Leith, J. Frank, Spider image processing for single-particle reconstruction of biological macromolecules from electron micrographs. Nat. Protoc. 3, 1941–1974 (2008)
- J. Spence, High-Resolution Electron Microscopy, (Oxford University Press, Oxford, 2013) 12
   Sep 2013–Science
- 41. G. Tang, L. Peng, P. Baldwin, D. Mann, W. Jiang, I. Rees, S. Ludtke, Eman2: an extensible image processing suite for electron microscopy. J. Struct. Biol. 157, 38–46 (2007)
- 42. C. Tomasi, R. Manduchi, Bilateral filtering for gray and colour images. Proceedings of the 1998 IEEE Intern. Conference on Comp, (Vision, Bombay, India, 1998) pp. 839–846
- J. Weickert, Anisotropic Diffusion in Image Processing, ECMI (Teubner-Verlag, Stuttgart, Germany, 1996)
- 44. J. Weickert, Anisotropic diffusion in image processing. Ph.D. thesis, University of Kaiserslautern (1996)
- 45. J. Weickert, Coherence-enhancing diffusion filtering. Int. J. Comput. Vision 31(2–3) (1999)

# Chapter 12 Segmentation of Features in Electron Tomographic Reconstructions

Niels Volkmann

**Abstract** Electron tomography is the most widely applicable method for obtaining three-dimensional information from biological samples by electron microscopy. However, owing to the complexity and low signal-to-noise ratio of the reconstructions, direct interpretation of their three-dimensional content is not straight forward. This chapter describes computational approaches designed to extract the most accurate information possible from biological electron tomograms.

#### 12.1 Introduction

Modern biology has now advanced to a stage where structural information about isolated macromolecules and assemblies must be integrated to define higher-order cellular functions. Electron tomography is the most widely applicable method for obtaining three-dimensional information by electron microscopy and has become a powerful tool for revealing the molecular architecture of biological cells and tissues [1–3]. The achievable resolution (3–6 nm) is intermediate between that achievable by light microscopy and X-ray crystallography or high-resolution single-particle electron cryo-microscopy, thus capable of bridging the gap between live-cell imaging and atomic resolution structures. In the field of biology it has been realized that electron tomography, in particular its cryo variant, is capable of providing a complete, molecular resolution three-dimensional mapping of entire proteoms, at least in principle [4, 5]. However, to realize this goal, the relevant information needs to be extracted from the tomograms by means of segmentation. This task is complicated by several factors:

N. Volkmann

1. The damaging effect of the electron beam limits the amount of electrons available for image formation. As a consequence, electron tomograms tend to exhibit very high noise levels and low contrast.

- 2. The noise in electron tomographic reconstructions is the result of a complex combination of different sources including signal-dependent shot noise due to the quantum nature of the electrons, digitization noise of the detection device, and additional structured noise due to the presence of support and embedding media [6]. The noise is highly correlated in space, and is corrupted by the contrast transfer function [7] and the missing wedge. Thus, it is hard to define adequate noise models to take advantage of algorithms that explicitly take noise characteristics into account.
- 3. The geometry of the electron tomography sample holders does not allow tilting of the sample by more then 60°-70°. This restriction severely affects the completeness of the projection data necessary for three-dimensional reconstruction, which is best visualized as a "missing wedge" in Fourier space. This issue can be alleviated experimentally by taking a second data set after rotation of the sample by 90° around the optical axis [8–10], but some of the data space remains inaccessible and some missing data artifacts will still remain.
- 4. Aberrations of the optics of the electron microscope give rise to a point-spread function best described in Fourier space by its Fourier transform, the contrast transfer function. This function depends primarily on the amount of defocus used for imaging and modifies both amplitudes and phases of the signal. The contrast transfer function of the microscope is not very well defined in an electron tomography setting, especially for thick specimens where there tends to be a significant variance in focus. In addition, the tilting introduces a focus gradient, further obstructing the underlying signal.

Cryo preservation allows imaging of biological samples with the electron microscope in their native environment without any staining, chemical fixation, or drying [11]. The quality of cryo-tomographic reconstructions can be correlated with the electron dose. A total dose of 50–300 e<sup>-</sup>/Å<sup>2</sup> tends to be a good compromise with a sweet spot around 120 e<sup>-</sup>/Å<sup>2</sup> [12]. This dose needs to be spread over the whole data set. For a  $\pm 60^{\circ}$  double tilt series with a  $2^{\circ}$  increment, the dose available for a single image is thus only 1 e<sup>-</sup>/Å<sup>2</sup>, which gives rise to extremely high noise levels in the individual images. The signal in the resulting three-dimensional reconstructions is improved by the dose fractionation effect [13] and can be further enhanced by using new technologies such as direct electron detectors [14] or Volta phase plates [15], but the signal-to-noise ratio for these tomograms is still well below 1 (often only 0.1 or less). Owing to the technical difficulties of cryo-sample sectioning [16] or cryo-milling approaches [17], conventional electron tomography, which involves staining and plastic embedding, is often preferred in practice for samples that require sectioning [18]. While the signal-to-noise ratio is improved in these samples as compared to cryo-samples, the resulting images and reconstructions still tend to be quite noisy with signal-to-noise ratios usually well below five. Furthermore, these types of samples can suffer additional problems such as uneven staining and other sample preparation artifacts that may complicate subsequent analysis.

Because of the low signal-to-noise ratio and the other factors mentioned above, reconstructions obtained by electron tomography are difficult to interpret. This difficulty is further aggravated in highly complex, crowded cellular systems [19]. As a consequence of these factors, image and signal processing methods developed for other imaging domains are not straightforward to apply to electron tomography data. While there have been substantial efforts during the last few years which specifically address segmentation of features from electron tomograms, progress has been much slower than in related imaging fields. In fact, the relative lack of adequate tools for automatic and objective extraction of information has been recognized as a critical barrier to progress in the field of electron tomography [20–23] and the task is often carried out manually, using programs that allow tracing within slices to create iso-contour models of the features of interest [24, 25]. This type of hand tracing tends to be time consuming, tedious, and subjective. The remainder of this chapter describes computational approaches specifically targeted to segmentation of electron tomograms with special emphasis on electron cryo-tomography.

## 12.2 Membrane Segmentation

Membranes tend to be relatively easily identifiable by eye in tomogram sections perpendicular to the electron beam direction. This includes cell membranes as well as membrane compartments or vesicles in cells. Many computational segmentation approaches specifically developed for electron tomography target improvement of manual segmentation using various types of surface or curve fitting approaches. These methods include simple spatial gradient optimization in two dimensions [26], three-dimensional geodesic active contours [27], and full-fledged dynamic level-set based approaches [28, 29]. All these methods are based on some form of energy-minimization, thus having tendencies to get trapped in local optima and being subject to scalability issues. These complications result in the requirement for reasonably good starting models as well as careful fine-tuning of the algorithm parameters to ensure correct convergence.

Other edged-based methods that do not rely on manual pre-segmentation include a bilateral edge-detection algorithm [30], a method based on orientation fields and line segment detection [31], a dual-contour fast marching method with automated seed selection [32], and an approach based on differential geometry and use of the Hessian tensor [33]. The latter was improved at a later stage by including the ability to classify the detected membrane structures [34]. These membrane detectors do a good job in enhancing the membrane signal but can suffer a number of drawbacks. For example, gaps that can appear in membrane delineations due to experimental imaging conditions may not be properly filled or structures that protrude from the membrane may be segmented as part of the membrane. Also, because these detectors are primarily sensitive to line-like features, they tend to be problematic in cases

N. Volkmann

where a membrane compartment appears like a solid object with dense material inside. A method that is still based on edge information and tries to overcome these issues is based on anisotropic propagation of local structural information using a tensor-voting algorithm [35]. The initial membrane detection step is based on the Hessian for line-like membranes [33] and the Structure tensor [36] for membranes delineating solid-like membrane compartments. The results are fed into a tensor voting algorithm that enhances the membrane structures further and is capable to bridge gaps in the membrane efficiently. The method performs well in low signal-to-noise ratio situations typically found in cryo-tomography.

An alternative to edge-based boundary detection algorithms is the use of region-based approaches where contiguous regions such as membrane compartments or the inside/outside of the cell are identified by some characteristic such as texture or intensity (Fig. 12.1). The boundary of the regions then becomes the output of the segmentation. For example, the immersion based watershed algorithm [37, 38] has been adapted specifically for electron tomography [39]. The method can be understood as an analogy with a step-wise flooding of a topological relief, with dams being built where independent flows meet. The approach is capable of fully automatic segmentation but, in practice, it is more appropriate to use it in a semi-automatic fashion, optimizing the few operating parameters. Because the speed of the algorithm allows interactive refinement of these parameters it has been implemented in the popular graphics packages Amira [25, 40] and Chimera [41, 42] for interactive use. Other region-based segmentation approaches that showed promise with electron tomograms are based on fuzzy set theory [43] or on normalized graph cut methods and eigenvector analysis [44].

There are three principal sources of information that can be used to guide membrane segmentation algorithms: (i) features that define the outside or inside of a region; (ii) features that define a boundary point; and (iii) shape information about the object to be segmented. The segmentation approaches described above use only one of these information sources at a time. A strength of energy-based methods is their ability to incorporate shape information in a straight forward manner. This is the case for strong constraints such as adherence to an absolute shape as well as weak constraints such as boundary smoothness. While the actual shape of a general membrane structure is not generally predictable, some distinct geometric properties are known that can be exploited. For example, template-based iterative boundary detection combined with elliptic shape models was used to generate high fidelity segmentations of *Caulobacter crescentus* cell membranes [46]. The downside of model-based methods is that the models tend to be highly case specific and need to be modified for each new application.

Shape information is not as easily incorporated into region-based approaches as it can be incorporated into energy-based algorithms. Weak constraints such as boundary smoothness can be imposed into region-based approaches [39, 42], but the direct inclusion of sophisticated shape models cannot easily be done. An exception is the watersnake method [47], which combines watershed transforms with active contours (snakes) into a region growing approach that responds to an energy function, thus allowing inclusion of shape information. The watersnake approach was

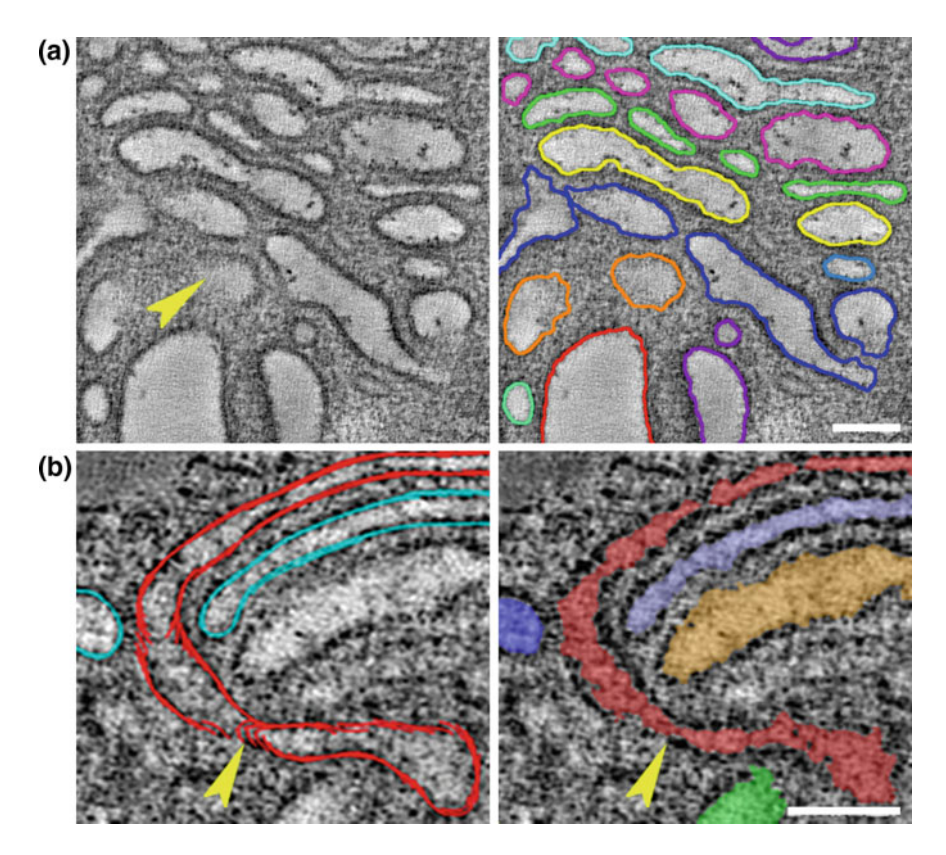


Fig. 12.1 Region-based membrane segmentation. a In region-based membrane segmentation, the difference between the interior and the exterior of membrane compartments is used to delineate them by detecting the entire compartment rather than its boundary directly. The figure shows example slices through electron tomography reconstructions from the Golgi region of high-pressure frozen, freeze-substituted pancreatic mouse beta cells [45]. While the difference between interior and exterior is quite clear for the most part, some of the Golgi membranes are oblique to the section (see for example at yellow arrowhead on the left), making it hard to determine where the actual boundary is. Applying the watershed transform [39] allows not only faithful tracing of the visible membranes (colored lines on the right) but also determining the boundaries that are unclear in the section. Membranes drawn with the same color are connected in three dimensions. b The fact that human operators using manual tracing approaches by drawing contour lines within sections can lead to unexpected artifacts. In the oblique view shown here, which is slightly tilted in respect to the sections used for drawing contours, the lines add up in a way that eliminates a thin connection at the yellow arrowhead (left). Because the watershed transform operates in three dimensions, these types of artifacts are avoided efficiently (right). The bars correspond to 200 nm

used to generate convincing segmentation results for several types of membranes [48]. However, the current implementation requires a rough manual segmentation in the form of manually traced slices to define the shape model and has only been applied to situations with relatively high signal-to-noise ratios. Approaches based on

N. Volkmann

models alone have also been used with encouraging results. Templates for different types of membranes have allowed to distinguish between coated and uncoated membrane patches [49, 50]. So far, these studies were limited to stained, plastic embedded sections and may be less effective in low signal-to-noise ratio situations as encountered in cryo-tomograms.

Because of the missing wedge, membranes perpendicular to the electron beam essentially become invisible. Edge-based methods will not be able to retrieve those parts of the membrane because there is no edge present. Region-based methods can fare somewhat better but because the boundary is not well defined, segmentation tends to be inaccurate in those regions. Methods that include shape information in the segmentation process can give a good approximation for the invisible membrane portions [46] but that will depend on the quality and validity of the shape information. A recent membrane tracing strategy addresses these issues by using sparse representations of the cell interior to delineate all cell membranes [51]. The approach is independent of external shape information and is based on detecting the boundary between the exterior and the interior of the cell by first performing a sparse segmentation of features inside the cell followed by calculating convex hulls of slices parallel to the direction of the electron beam. Finally, a thin-plate spline is calculated using the points of the convex hulls as anchor points to retrieve the cell boundary. Tests with simulated data and experimental cryo-tomograms of fibroblast cells indicate excellent performance of the method (Fig. 12.2).

## 12.3 Segmentation of Large Macromolecular Assemblies

The segmentation approaches described in the last section can detect, identify, and extract features like membranes or vesicles, but compact macromolecular assemblies are less accessible by these methods and are generally addressed in a more direct fashion. One way is through labeling the assembly to be identified with

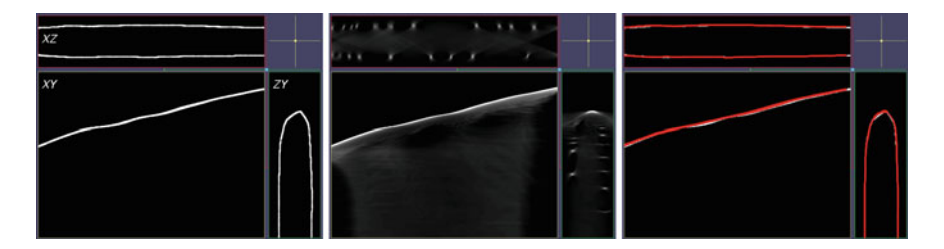


Fig. 12.2 Missing wedge effect on membrane appearance in tomographic reconstructions. When the model membrane on the left is reconstructed from simulated reconstructions at tilt angles between  $\pm 60^{\circ}$  with 1° increments around the Y-axis, membranes perpendicular to the XY plane become essentially invisible (center panel). The entire membrane can be recovered with high fidelity using convex hulls of sparse cell interior representations [51]. The red lines (right panel) correspond to the recovered membrane, overlaid with the original model membrane (white)

electron dense material such as gold labels. Another possibility is the use of correlative imaging where a fluorescence signal from light microscopy is overlaid with the electron tomogram to pin-point features or macromolecular assemblies of interest [52]. Localization accuracy is currently in the range of 50–100 nm [53, 54] and correlative imaging techniques using super-resolution light microscopy with potentially higher localization accuracy are also under development [55]. However, both techniques will only give access to a small subset of assemblies and can introduce perturbations into the cellular system.

A more general and possibly more attractive way of detection is through computational methods where some model of the assembly is used as a template to find copies of that assembly in the tomographic reconstructions. The first feasibility test for this sort of approach was done using correlation-based template matching with tomograms of reconstituted systems containing purified thermosomes, 20S proteasomes, and GroEL respectively [56]. While the results were encouraging with very high detection fidelity, the conditions of the specimen were idealized and not very close to the situation in cells, which are highly crowded with many different constituents and interacting partners. Slightly more realistic follow-up tests with liposomes filled with 20S proteasomes, thermosomes, or both [44] showed somewhat less convincing results, but were still encouraging.

This type of correlation-based template matching uses a 'matched filter' in terms of detection theory [57]. A matched filter can be shown to minimize the probability of identification errors, as long as the template and the target are nearly identical and the noise is independent and identically distributed, additive, and Gaussian [58, 59]. These conditions are not very well met for reconstructions done by electron tomography. The noise in these reconstructions is spatially correlated and the tails of the noise distribution are often quite heavy, especially in stained samples [60]. These issues generate a noise distribution that is distinctly non-Gaussian. In addition, the potential mix of conformations, potential inaccuracies in the magnification estimate, and/or the presence of stain make it difficult to obtain accurate templates. As a consequence, correlation-based template matching tends to generate false hits in areas of high density such as membranes or vesicles when used with cellular tomograms [61–63]. The method generally performs better when the signal-to-noise ratio is high [64] and the use of the new Volta phase plate technology [15, 65] has led to very encouraging results when correlation-based template matching was used in full cellular environments for assemblies such as proteasomes [66] or ribosomes [67].

Several recent studies address the shortcomings of the matched filter approach by introducing new ways of scoring or defining templates. One set of studies uses a measure in real space, somewhat analogous to the R-free value in X-ray crystallography [68, 69]. In this approach a mask is used to outline the area of the template without modification of the template itself. The mask is then split into a working and a testing area. The working area is used for the calculation of the correlation during the template-matching search. The information from both areas is used to calculate a score (M-free) that measures how strongly the template influences the correlation signal in each position. The M-free score gives a significantly better distinction between true and false hits in the test cases presented [69]. While the

308 N. Volkmann

results may somewhat depend on the definition of the mask in the general case, mask-independent scores can be obtained for certain classes of template-matching problems [68].

Another recent approach employs reduced representation templates [70]. Instead of using a search model based on the entire density of the template, this approach reduces the search model to a small number of anchor points that are used to calculate the scoring function (Fig. 12.3). Advantages include a speed-up in calculations [71], efficient ways to account for conformational variations, and flexibility of defining scoring functions and constraints in real space. Test calculations indicate that a reduction of false positive hits of about 50% with matched-filter approaches to below 5% with the reduced representation approach can be achieved in the full cellular environment [70].

## 12.4 Segmentation of Filamentous Structures

The third distinct type of features in biological tomograms at the nanometer scale are filaments. This includes line-like features (actin and intermediate or extra cellular filaments) as well as tubular features (microtubules). Extraction of filament traces is an active research subject in fluorescence microscopy where the filaments can be selectively observed through specific fluorescence tags. Many approaches that have shown promising results for the extraction of filament or bundle center lines from fluorescence data involve two separate steps of binarization and skeletonization. The simplest way to binarize an image is by applying a threshold value to assign all voxels that are brighter than the threshold to be part of a filament. This method almost inevitably leads to binarized images with many artifacts, which need to be either suppressed by filtering the input or corrected in a subsequent step. The skeletonization requires thinning of the broadened binarized filaments to a representation of one voxel diameter. To achieve a good skeleton representation, tracing along the ridges of Euclidean distance maps [75, 76], Hessian-based enhancement filters [77], constrained diffusion-based methods [78], image decomposition [79], medial axis determination by distance-ordered homotopic thinning [80], orientation fields [81], and iterative tensor voting [82], have all been used. Some of these methods were successfully employed for skeletonization of images [83] and tomographic reconstructions [84] from scanning electron microscopy, but the contrast and signal-to-noise ratio in those is much higher than (cryo-)tomograms from transmission electron microscopy of biological material can provide. For the latter type of data, methods based on binarization by any type of thresholding tend to fail [85].

An alternative strategy uses open active contours to segment filaments from three-dimensional fluorescence data [86, 87]. This approach works well for fluorescence data and approaches based on active contours have also been applied successfully for tracing of microtubules in stained electron tomograms [88, 89]. Because filaments appear line-like or, in the case of microtubules, as two adjacent lines, very

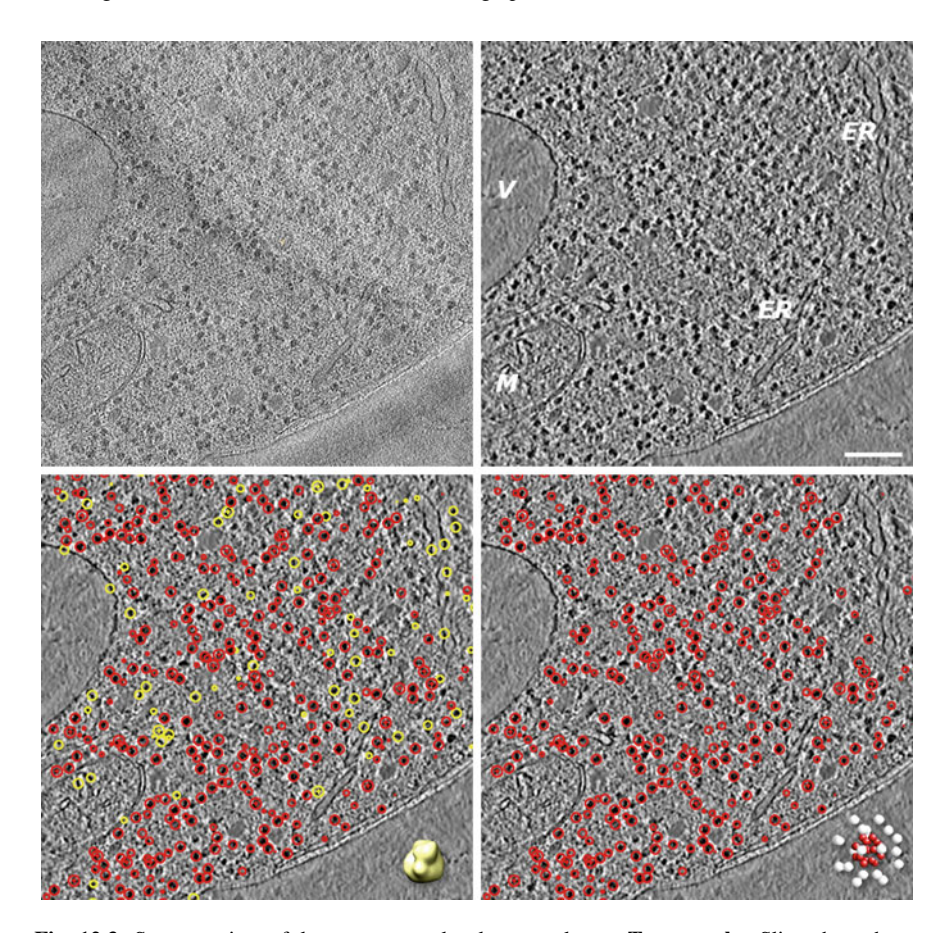
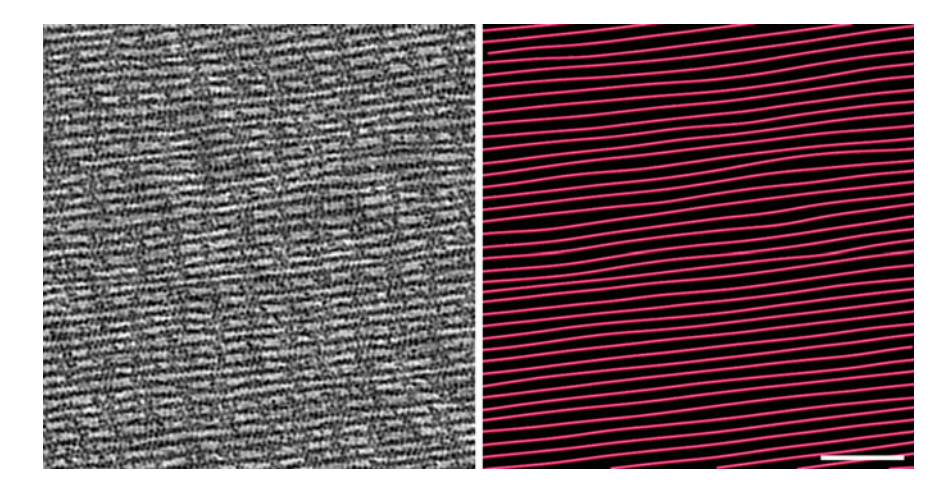


Fig. 12.3 Segmentation of large macromolecular complexes. Top panels: Slice through an electron cryo-tomogram of a vitrious section through a Saccharomyces cerevisiae cell [72]. The left panel shows the unprocessed data; the right panel shows the same slice after processing with a non-local means filter to suppress the noise and increase the contrast [73]. A large vacuole (V), a mitochondrion (M) and endoplasmic reticulum (ER) are visible. Large macromolecular complexes are visible as dark dots. The bar corresponds to 100 nm. **Bottom panels:** Detection of tentative 80S ribosomes using template-matching approaches. The algorithms were run on the unprocessed data. The left panel shows results from a correlation-based matched filter approach [62] using a low-pass filtered high-resolution single-particle reconstruction [74] as a template (yellow surface representation on left panel). Many of the yellow hits are clearly false positives on the high intensity membrane sections of the vacuole, the mitochondrion and the endoplasmic reticulum. The right panel shows the results of the reduced representation template-matching approach [70]. The reduced representation template is depicted at the right bottom corner and consists of a sphere of 20 inside anchor points (red) surrounded by a shell of 18 outside anchor points (white). False positives are greatly reduced in comparison to the matched-filter approach without significant addition of false negatives

similar to the appearance of membranes in sections, algorithms that respond to line-like appearance of membranes in sections are also applicable to filament detection [31, 90]. The use of localized radon transforms has also been proposed [91].

The general approach for filament tracing that gained the most traction in the electron tomography field, especially for cryo-tomograms, is template matching, possibly triggered by the successes in detection of large macromolecular complexes. For filament tracing, a cylindrical or tubular template of defined length and width matching the filament system of interest is used to scan the volume with standard template matching approaches to extract the filament center lines [50, 92, 93]. The templates are generally modified to account for imaging artifacts such as the missing wedge. This approach has been shown to have high potential and is now incorporated in the commercial graphical environment Amira [92, 94]. Stochastic template-based searches combining a genetic algorithm and a bidirectional expansion strategy have also been proposed [95]. Like template matching for locating large assemblies, template matching for filament tracing can benefit from the use of reduced representation templates [70]. For cylinder-like filaments such as actin or intermediate filaments, the template is reduced to a number of anchor points along the centerline, surrounded by a cylindrical shell of anchor points that define the outside of the filament (Fig. 12.4). One advantage of the reduced representation



**Fig. 12.4** Detection of filaments in tomographic reconstructions. Filaments in the cell can be very densely packed with many cross-linking molecules bridging between them. It is important that filament tracing algorithms can account for these situations appropriately and do not generate gaps or link up filaments that are separate. The left panel shows a slice through an electron tomogram of actin filaments on a lipid monolayer cross-linked by aldolase [96, 97]. This is a good test case because the two-dimensional nature of the tomogram makes it feasible to follow the filaments accurately by eye for performance evaluation and the imperfect order and heavy presence of cross-linking molecules make it a challenging filament detection task for tracing algorithms. The right panel shows the results after using the reduced-representation template-matching approach [70]. The bar corresponds to 100 nm

approach is that it enables easy imposition of real-space constraints such as penalizing solutions that have large intensity variations along the centerline, which can significantly improve performance [70].

## 12.5 Outlook and Conclusions

Many promising computational approaches for segmentation have become available in recent years and it is likely that more such algorithms, taking advantage of the recent hardware developments [14, 65], will emerge in the near future. However, many of these algorithms are relatively complex to use, are only applicable to subsets of electron tomographic reconstructions, often need tweaking of parameters to yield optimal performance, and tend to require careful examination and adjustments by expert users. As a consequence, accurate segmentation still relies heavily on human intervention.

One possibility to reduce workload and increase throughput is the use of crowdsourcing analogous to what was done in the serial block face scanning electron microscopy community. An example is the EyeWire project [98]. Anyone can register on the EyeWire website and-after a brief training session-can segment neurons in three-dimensional serial block face scanning electron microscopy reconstructions through the interface of an online game. Currently an impressive number of over 200,000 individuals from 145 countries are part of the project [99]. While the EyeWire project relies on people volunteering their time, the use of commercial services like the Amazon Turk can also be a viable solution [100]. However, block face scanning electron microscopy reconstructions have very high contrast if compared to biological electron (cryo-)tomography data. Even in stained biological electron tomograms, variations between expert-user segmentation results are not negligible [43, 48]. To generate an interface that is amenable for crowdsourced non-expert segmentation with tolerable error rate is challenging. Three-dimensional landscapes at the nanometer resolution of electron (cryo-) tomograms are unfamiliar to the human eye and even in the absence of noise they would likely appear quite chaotic owing to the dense crowding of macromolecules in cells [19]. Another complication is that humans are susceptible to all sorts of biases when evaluating visual cues, especially in the presence of high noise levels [101–103]. A striking example is an experiment where participants were presented with images containing random noise and were made to believe that 50% of those images contain faces [104]. Not only did the participants believe to see faces in over 30% of the images containing nothing but random noise, fMRI measurements showed activity in regions of the brain that are known to be associated with face processing whenever a participant believed to see a face. While individual subjectivity could possibly be averaged out in segmentation tasks by averaging over many individuals, it is doubtful that these species-dependent biases can be adequately addressed by averaging. Whether crowdsourcing is used or not, some

independent objective validation criteria are needed to ensure that segmentations are not subject to bias.

Another possibility to improve performance and throughput is the use of machine learning. Machine learning has been used with some success in single-particle electron cryo-microscopy data processing in the context of particle picking [105–109] and has also been used for segmentation tests on tomograms of silicon pillars obtained by scanning transmission electron microscopy [110]. Applications to biological (cryo-)tomograms are lacking. One reason is that conventional machine-learning approaches do not process data in their raw form but require careful engineering and considerable expertise to design feature extractors that convert raw voxel values into an internal representation suitable as input for learning algorithms [111]. However, a new class of machine learning approaches termed deep learning have recently been introduced that simplify this task [112]. The underlying learning methods are fed with raw data and automatically discover the representations needed for detection or classification. The deep learning approach uses multiple levels of representations, each at a slightly more abstract level than the previous one. The layers of representations are not designed by human operators but are learned through the general purpose representation learning algorithm. These types of deep learning approaches were shown to be spectacularly successful in some application domains. In particular, deep convolutional neural networks have done exceedingly well in image recognition tasks. Before 2012 no computer algorithm was able to surpass the 25% mark in error rates for the ImageNet competition, which concerns classifying and locating different objects in a large set of natural images [113]. With the introduction of deep convolutional neural networks in 2012, this rate dropped to 16% [114] and, after additional improvements, is now reduced to a few percent [115–117]. Applications of deep learning approaches are already appearing for particle picking tasks in single-particle electron cryo-microscopy [118-120] and neuron tracing in block face scanning electron microscopy reconstructions [121] but have not penetrated the field of electron (cryo-)tomography yet. One downside of deep convolutional networks is the need for a sufficient amount of 'ground-truth' training data that are hard to obtain, especially for electron cryo-tomograms. Another issue is that poorly defined training and test data can lead to significant bias [122]. Deep reinforcement learning approaches, which might remedy both issues, are under development and show some promise [123–125] but are not well enough matured yet to be useful in the electron (cryo-)tomography context. Perhaps a combination of supervised deep learning and carefully designed crowdsourcing will present the next step forward.

**Acknowledgements** Writing of this article was made possible by support from the National Institutes of Health (grant numbers P01-GM121203 and R01-GM119948).

## References

- A. Leis, B. Rockel, L. Andrees, W. Baumeister, Visualizing cells at the nanoscale. Trends Biochem. Sci. 34, 60–70 (2009)
- E.I. Tocheva, Z. Li, G.J. Jensen, Electron cryotomography. Cold Spring Harb. Perspect. Biol. 2, a003442 (2010)
- C.V. Robinson, A. Sali, W. Baumeister, The molecular sociology of the cell. Nature 450, 973–982 (2007)
- S. Nickell, C. Kofler, A.P. Leis, W. Baumeister, A visual approach to proteomics. Nat. Rev. Mol. Cell Biol. 7, 225–230 (2006)
- 5. S. Asano, B.D. Engel, W. Baumeister, In situ cryo-electron tomography: a post-reductionist approach to structural biology. J. Mol. Biol. **428**, 332–343 (2015)
- W.T. Baxter, R.A. Grassucci, H. Gao, J. Frank, Determination of signal-to-noise ratios and spectral SNRs in cryo-EM low-dose imaging of molecules. J. Struct. Biol. 166, 126–132 (2009)
- S.H. Scheres, H. Gao, M. Valle, G.T. Herman, P.P. Eggermont, J. Frank, J.M. Carazo, Disentangling conformational states of macromolecules in 3D-EM through likelihood optimization. Nat. Methods 4, 27–29 (2007)
- 8. P. Penczek, M. Marko, K. Buttle, J. Frank, Double-tilt electron tomography. Ultramicroscopy **60**, 393–410 (1995)
- 9. D.N. Mastronarde, Dual-axis tomography: an approach with alignment methods that preserve resolution. J. Struct. Biol. 120, 343–352 (1997)
- S. Nickell, R. Hegerl, W. Baumeister, R. Rachel, Pyrodictium cannulae enter the periplasmic space but do not enter the cytoplasm, as revealed by cryo-electron tomography. J. Struct. Biol. 141, 34–42 (2003)
- J. Dubochet, M. Adrian, J.-J. Chang, J.-C. Homo, J. Lepault, A.W. McDowall, P. Schultz, Cryo-electron microscopy of vitrified specimens. Q. Rev. Biophys. 21, 129–228 (1988)
- 12. C.V. Iancu, E.R. Wright, J.B. Heymann, G.J. Jensen, A comparison of liquid nitrogen and liquid helium as cryogens for electron cryotomography. J. Struct. Biol. 153, 231–240 (2006)
- 13. B.F. McEwen, K.H. Downing, R.M. Glaeser, The relevance of dose-fractionation in tomography of radiation-sensitive specimens. Ultramicroscopy **60**, 357–373 (1995)
- 14. N. Grigorieff, Direct detection pays off for electron cryo-microscopy. Elife 2, e00573 (2013)
- Y. Fukuda, U. Laugks, V. Lučić, W. Baumeister, R. Danev, Electron cryotomography of vitrified cells with a Volta phase plate. J. Struct. Biol. 190, 143–154 (2015)
- A. Al-Amoudi, L.P. Norlen, J. Dubochet, Cryo-electron microscopy of vitreous sections of native biological cells and tissues. J. Struct. Biol. 148, 131–135 (2004)
- A. Rigort, F.J. Bäuerlein, E. Villa, M. Eibauer, T. Laugks, W. Baumeister, J.M. Plitzko, Focused ion beam micromachining of eukaryotic cells for cryoelectron tomography. Proc. Natl. Acad. Sci. U. S. A. 109, 4449–4454 (2012)
- B.F. McEwen, M. Marko, The emergence of electron tomography as an important tool for investigating cellular ultrastructure. J. Histochem. Cytochem. 49, 553–564 (2001)
- K. Grünewald, O. Medalia, A. Gross, A.C. Steven, W. Baumeister, Prospects of electron cryotomography to visualize macromolecular complexes inside cellular compartments: implications of crowding. Biophys. Chem. 100, 577–591 (2003)
- B.J. Marsh, Lessons from tomographic studies of the mammalian Golgi. Biochim. Biophys. Acta 1744, 273–292 (2005)
- T.G. Frey, G.A. Perkins, M.H. Ellisman, Electron tomography of membrane-bound cellular organelles. Annu. Rev. Biophys. Biomol. Struct. 35, 199–224 (2006)
- R.I. Koning, A.J. Koster, Cryo-electron tomography in biology and medicine. Ann Anat. 191, 427–445 (2009)
- 23. K. Ben-Harush, T. Maimon, I. Patla, E. Villa, O. Medalia, Visualizing cellular processes at the molecular level by cryo-electron tomography. J. Cell Sci. 123, 7–12 (2010)

 J.R. Kremer, D.N. Mastronarde, J.R. McIntosh, Computer visualization of three-dimensional image data using IMOD. J. Struct. Biol. 116, 71–76 (1996)

- 25. D. Stalling, H. Hege, M. Westerhoff, Amira—a highly interactive system for visual data analysis. In *Visualization Handbook* ed. by C.R. Johnson, C.D. Hansen (Academic Press, Cambridge, 2004)
- D.B. Ress, M.L. Harlow, R.M. Marshall, U.J. McMahan, Methods for generating high-resolution structural models from electron microscope tomography data. Structure 12, 1763–1774 (2004)
- A. Bartesaghi, G. Sapiro, S. Subramaniam, An energy-based three-dimensional segmentation approach for the quantitative interpretation of electron tomograms. IEEE Trans. Image Proc. 14, 1314–1323 (2005)
- 28. R.T. Whitaker, V. Elangovan, A direct approach to estimating surfaces in tomographic data. Med. Image Anal. 6, 235–249 (2002)
- S. Osher, J.A. Sethian, Fronts propagating wirh curvature dependent speed: algorithms based on Hamilton-Jacobi formulations. J. Comp. Phys. 79, 12–49 (1988)
- R.A. Ali, M.J. Landsberg, E. Knauth, G.P. Morgan, B.J. Marsh, B. Hankamer, A 3D image filter for parameter-free segmentation of macromolecular structures from electron tomograms. PLoS ONE 7, e33697 (2012)
- K. Sandberg, M. Brega, Segmentation of thin structures in electron micrographs using orientation fields. J. Struct. Biol. 157, 403

  –415 (2007)
- 32. C. Bajaj, Z.Y. Yu, M. Auer, Volumetric feature extraction and visualization of tomographic molecular imaging. J. Struct. Biol. **144**, 132–143 (2003)
- A. Martinez-Sanchez, I. Garcia, J.J. Fernandez, A differential structure approach to membrane segmentation in electron tomography. J. Struct. Biol. 175, 372–383 (2011)
- A. Martinez-Sanchez, I. Garcia, J.J. Fernandez, A ridge-based framework for segmentation of 3D electron microscopy datasets. J. Struct. Biol. 181, 61–70 (2013)
- A. Martinez-Sanchez, I. Garcia, S. Asano, V. Lucic, J.J. Fernandez, Robust membrane detection based on tensor voting for electron tomography. J. Struct. Biol. 186, 49–61 (2014)
- J. Bigun, Optimal orientation detection of linear symmetry. IEEE 1st Int. Conf. Comp. Vis. 1 (1987)
- 37. S. Beucher, F. Meyer, The morphological approach to segmentation: the watershed transformation, in *Mathematical morphology in image processing*, ed. by E.R. Dougherty (Marcel Dekker, New York, 1993), pp. 433–481
- 38. L. Vincent, P. Soille, Watersheds in digital space: an efficient algorithm based on immersion simulations. IEEE Trans. Pattern Anal. Mach. Intell. 13, 583–598 (1991)
- N. Volkmann, A novel three-dimensional variant of the watershed transform for segmentation of electron density maps. J. Struct. Biol. 138, 123–129 (2002)
- S. Pruggnaller, M. Mayr, A.S. Frangakis, A visualization and segmentation toolbox for electron microscopy. J. Struct. Biol. 164, 161–165 (2008)
- T.D. Goddard, C.C. Huang, T.E. Ferrin, Visualizing density maps with UCSF Chimera.
   J. Struct. Biol. 157, 281–287 (2007)
- G. Pintilie, J. Zhang, W. Chiu, D. Gossard, Identifying components in 3D density maps of protein nanomachines by multi-scale segmentation. IEEE NIH Life Sci. Syst. Appl. Workshop. 2009, 44–47 (2009)
- 43. E. Garduño, M. Wong-Barnum, N. Volkmann, M.H. Ellisman, Segmentation of electron tomographic data sets using fuzzy set theory principles. J. Struct. Biol. 162, 368–379 (2008)
- 44. A.S. Frangakis, R. Hegerl, Segmentation of two- and three-dimensional data from electron microscopy using eigenvector analysis. J. Struct. Biol. 138, 105–113 (2002)
- B.J. Marsh, N. Volkmann, J.R. McIntosh, K.E. Howell, Direct continuities between cisternae at different levels of the Golgi complex in glucose-stimulated mouse islet beta cells. Proc. Natl. Acad. Sci. U. S. A. 101, 5565–5570 (2004)
- F. Moussavi, G. Heitz, F. Amat, L.R. Comolli, D. Koller, M. Horowitz, 3D segmentation of cell boundaries from whole cell cryogenic electron tomography volumes. J. Struct. Biol. 170, 134–145 (2010)

- 47. H.T. Nguyen, M. Worring, R. van den Boomgaard, Watersnakes: Energy-driven watershed segmentation. IEEE Trans. Pattern Anal. Mach. Intell. **25**, 330–342 (2003)
- 48. H. Nguyen, Q. Ji, Shape-driven three-dimensional watersnake segmentation of biological membranes in electron tomography. IEEE Trans. Med. Imaging 27, 616–628 (2008)
- M.N. Lebbink, N. Jimenez, K. Vocking, L.H. Hekking, A.J. Verkleij, J.A. Post, Spiral coating of the endothelial caveolar membranes as revealed by electron tomography and template matching. Traffic 11, 138–150 (2010)
- M.N. Lebbink, W.J. Geerts, T.P. van der Krift, M. Bouwhuis, L.O. Hertzberger, A.J. Verkleij, A.J. Koster, Template matching as a tool for annotation of tomograms of stained biological structures. J. Struct. Biol. 158, 327–335 (2007)
- 51. C. Page, D. Hanein, N. Volkmann, Accurate membrane tracing in three-dimensional reconstructions from electron cryotomography data. Ultramicroscopy 155, 20–26 (2015)
- 52. A. Briegel, S. Chen, A.J. Koster, J.M. Plitzko, C.L. Schwartz, G.J. Jensen, Correlated light and electron cryo-microscopy. Methods Enzymol. **481**, 317–341 (2010)
- P. Schellenberger, R. Kaufmann, C.A. Siebert, C. Hagen, H. Wodrich, K. Grünewald, High-precision correlative fluorescence and electron cryo microscopy using two independent alignment markers. Ultramicroscopy 143, 41–51 (2014)
- 54. M. Schorb, J.A. Briggs, Correlated cryo-fluorescence and cryo-electron microscopy with high spatial precision and improved sensitivity. Ultramicroscopy **143**, 24–32 (2014)
- 55. G. Wolff, C. Hagen, K. Grünewald, R. Kaufmann, Towards correlative super-resolution fluorescence and electron cryo-microscopy. Biol. Cell 108, 245–258 (2016)
- J. Böhm, A.S. Frangakis, R. Hegerl, S. Nickell, D. Typke, W. Baumeister, From the cover: toward detecting and identifying macromolecules in a cellular context: template matching applied to electron tomograms. Proc. Natl. Acad. Sci. U. S. A. 97, 14245–14250 (2000)
- 57. G. Turin, An introduction to matched filters. IRE Trans. Inf. Theory 3, 311-329 (1960)
- H.L. Van Trees, Classical detection and estimation theory, *Detection, Estimation, and Modulation Theory: Detection, Estimation, and Linear Modulation Theory* (Wiley, New York, 1968), pp. 19–165
- F.J. Sigworth, Classical detection theory and the cryo-EM particle selection problem.
   J. Struct. Biol. 145, 111–122 (2004)
- P. van der Heide, X.P. Xu, B.J. Marsh, D. Hanein, N. Volkmann, Efficient automatic noise reduction of electron tomographic reconstructions based on iterative median filtering. J. Struct. Biol. 158, 196–204 (2007)
- J.O. Ortiz, F. Forster, J. Kurner, A.A. Linaroudis, W. Baumeister, Mapping 70S ribosomes in intact cells by cryoelectron tomography and pattern recognition. J. Struct. Biol. 156, 334– 341 (2006)
- B.K. Rath, R. Hegerl, A. Leith, T.R. Shaikh, T. Wagenknecht, J. Frank, Fast 3D motif search of EM density maps using a locally normalized cross-correlation function. J. Struct. Biol. 144, 95–103 (2003)
- 63. Z. Yu, A.S. Frangakis, Classification of electron sub-tomograms with neural networks and its application to template-matching. J Struc Biol. **174**, 494–504 (2011)
- T. Hrabe, Y. Chen, S. Pfeffer, L.K. Cuellar, A.V. Mangold, F. Förster, PyTom: a python-based toolbox for localization of macromolecules in cryo-electron tomograms and subtomogram analysis. J. Struct. Biol. 178, 177–188 (2012)
- R. Danev, B. Buijsse, M. Khoshouei, J.M. Plitzko, W. Baumeister, Volta potential phase plate for in-focus phase contrast transmission electron microscopy. Proc. Natl. Acad. Sci. U. S. A. 111, 15635–15640 (2014)
- S. Asano, Y. Fukuda, F. Beck, A. Aufderheide, F. Förster, R. Danev, W. Baumeister, Proteasomes. A molecular census of 26S proteasomes in intact neurons. Science 347, 439– 442 (2015)
- J. Mahamid, S. Pfeffer, M. Schaffer, E. Villa, R. Danev, L.K. Cuellar, F. Förster, A.A. Hyman, J.M. Plitzko, W. Baumeister, Visualizing the molecular sociology at the HeLa cell nuclear periphery. Science 351, 969–972 (2016)

68. M. Kunz, Z. Yu, A.S. Frangakis, M-free: mask-independent scoring of the reference bias. J. Struct. Biol. **192**, 307–311 (2015)

- 69. Z. Yu, A.S. Frangakis, M-free: scoring the reference bias in sub-tomogram averaging and template matching. J. Struct. Biol. **187**, 10–19 (2014)
- X.P. Xu, C. Page, N. Volkmann, Efficient extraction of macromolecular complexes from electron tomograms based on reduced representation templates. Lect. Notes Comput. Sci. 9256, 423–431 (2015)
- N. Volkmann, An approach to automated particle picking from electron micrographs based on reduced representation templates. J. Struct. Biol. 145, 152–156 (2004)
- 72. J. Pierson, M. Vos, J.R. McIntosh, P.J. Peters, Perspectives on electron cryo-tomography of vitreous cryo-sections. J. Electron. Microsc. (Tokyo) 60(Suppl 1), S93–S100 (2011)
- 73. A. Buades, B. Coll, J.-M. Morel, A non-local algorithm for image denoising. IEEE Comput. Soc. Conf. Comp. Vis. Pattern Recog. **2**, 60–65 (2005)
- C.M. Spahn, E. Jan, A. Mulder, R.A. Grassucci, P. Sarnow, J. Frank, Cryo-EM visualization of a viral internal ribosome entry site bound to human ribosomes: the IRES functions as an RNA-based translation factor. Cell 118, 465–475 (2004)
- J. Wu, B. Rajwa, D.L. Filmer, C.M. Hoffmann, B. Yuan, C. Chiang, J. Sturgis, J.P. Robinson, Automated quantification and reconstruction of collagen matrix from 3D confocal datasets. J. Microsc. 210, 158–165 (2003)
- A.M. Stein, D.A. Vader, L.M. Jawerth, D.A. Weitz, L.M. Sander, An algorithm for extracting the network geometry of three-dimensional collagen gels. J. Microsc. 232, 463– 475 (2008)
- 77. G. Herberich, R. Windoffer, R. Leube, T. Aach, 3D segmentation of keratin intermediate filaments in confocal laser scanning microscopy, in *Proceedings of Annual International Conference of the IEEE EMBS* (2011) pp. 7751–7754
- S. Basu, C. Liu, G.K. Rohde, Localizing and extracting filament distributions from microscopy images. J. Microsc. 258, 13–23 (2015)
- M. Alioscha-Perez, C. Benadiba, K. Goossens, S. Kasas, G. Dietler, R. Willaert, H. Sahli, A robust actin filaments image analysis framework. PLoS Comput. Biol. 12, e1005063 (2016)
- W. Mickel, S. Münster, L.M. Jawerth, D.A. Vader, D.A. Weitz, A.P. Sheppard, K. Mecke,
   B. Fabry, G.E. Schröder-Turk, Robust pore size analysis of filamentous networks from three-dimensional confocal microscopy. Biophys. J. 95, 6072–6080 (2008)
- B. Eltzner, C. Wollnik, C. Gottschlich, S. Huckemann, F. Rehfeldt, The filament sensor for near real-time detection of cytoskeletal fiber structures. PLoS ONE 10, e0126346 (2015)
- 82. L.A. Loss, G. Bebis, B. Parvin, Iterative tensor voting for perceptual grouping of ill-defined curvilinear structures. IEEE Trans. Med. Imaging 30, 1503–1513 (2011)
- M. Beil, H. Braxmeier, F. Fleischer, V. Schmidt, P. Walther, Quantitative analysis of keratin filament networks in scanning electron microscopy images of cancer cells. J. Microsc. 220, 84–95 (2005)
- S. Lück, M. Sailer, V. Schmidt, P. Walther, Three-dimensional analysis of intermediate filament networks using SEM tomography. J. Microsc. 239, 1–16 (2010)
- D. Mayerich, J. Keyser, Hardware accelerated segmentation of complex volumetric filament networks. IEEE Trans. Vis. Comput. Graph. 15, 670–681 (2009)
- 86. T. Xu, D. Vavylonis, X. Huang, 3D actin network centerline extraction with multiple active contours. Med. Image Anal. 18, 272–284 (2014)
- 87. T. Xu, D. Vavylonis, F.C. Tsai, G.H. Koenderink, W. Nie, E. Yusuf, I-Ju Lee, J.Q. Wu, X. Huang, SOAX: a software for quantification of 3D biopolymer networks. Sci. Rep. 5, 9081 (2015)
- 88. M. Jiang, Q. Ji, B.F. McEwen, Model-based automated extraction of microtubules from electron tomography volume. IEEE Trans. Inf. Technol. Biomed. 10, 608–617 (2006)
- 89. D. Nurgaliev, T. Gatanov, D.J. Needleman, Automated identification of microtubules in cellular electron tomography. Methods Cell Biol. **97**, 475–495 (2010)
- K. Sandberg, Methods for image segmentation in cellular tomography. Methods Cell Biol. 79, 769–798 (2007)

- 91. C. Winkler, M. Vinzenz, J.V. Small, C. Schmeiser, Actin filament tracking in electron tomograms of negatively stained lamellipodia using the localized radon transform. J. Struct. Biol. 178, 19–28 (2012)
- A. Rigort, D. Günther, R. Hegerl, D. Baum, B. Weber, S. Prohaska, O. Medalia,
   W. Baumeister, H.C. Hege, Automated segmentation of electron tomograms for a quantitative description of actin filament networks. J. Struct. Biol. 177, 135–144 (2012)
- B. Weber, G. Greenan, S. Prohaska, D. Baum, H.C. Hege, T. Müller-Reichert, A.A. Hyman, J.M. Verbavatz, Automated tracing of microtubules in electron tomograms of plastic embedded samples of Caenorhabditis elegans embryos. J. Struct. Biol. 178, 129–138 (2011)
- S. Redemann, B. Weber, M. Möller, J.M. Verbavatz, A.A. Hyman, D. Baum, S. Prohaska, T. Müller-Reichert, The segmentation of microtubules in electron tomograms using Amira. Methods Mol. Biol. 1136, 261–278 (2014)
- M. Rusu, Z. Starosolski, M. Wahle, A. Rigort, W. Wriggers, Automated tracing of filaments in 3D electron tomography reconstructions using Sculptor and Situs. J. Struct. Biol. 178, 121–128 (2012)
- K.A. Taylor, D.W. Taylor, Formation of two-dimensional complexes of F-actin and crosslinking proteins on lipid monolayers: demostration of unipolar a-actinin F-actin crosslinking. Biophys. J. 67, 1976–1983 (1994)
- C. Sukow, D.J. DeRosier, Order, disorder, and perturbations in actin-aldolase rafts. Biophys. J. 85, 525–536 (2003)
- J.S. Kim, M.J. Greene, A. Zlateski, K. Lee, M. Richardson, S.C. Turaga, M. Purcaro, M. Balkam, A. Robinson, B.F. Behabadi, M. Campos, W. Denk, H.S. Seung, EyeWirers, Space-time wiring specificity supports direction selectivity in the retina. Nature 509, 331– 336 (2014)
- 99. S. Borrett, L. Hughes, Reporting methods for processing and analysis of data from serial block face scanning electron microscopy. J. Microsc. **263**, 3–9 (2016)
- R.J. Giuly, K.Y. Kim, M.H. Ellisman, DP2: distributed 3D image segmentation using micro-labor workforce. Bioinformatics 29, 1359–1360 (2013)
- E.M. Harley, K.A. Carlsen, G.R. Loftus, The "saw-it-all-along" effect: demonstrations of visual hindsight bias. J. Exp. Psychol. Learn. Mem. Cogn. 30, 960–968 (2004)
- 102. L. Zhaoping, L. Jingling, Filling-in and suppression of visual perception from context: a Bayesian account of perceptual biases by contextual influences. PLoS Comput. Biol. 4, e14 (2008)
- L.T. Maloney, M.F. Dal Martello, C. Sahm, L. Spillmann, Past trials influence perception of ambiguous motion quartets through pattern completion. Proc. Natl. Acad. Sci. U. S. A. 102, 3164–3169 (2005)
- J. Liu, J. Li, L. Feng, L. Li, J. Tian, K. Lee, Seeing Jesus in toast: neural and behavioral correlates of face pareidolia. Cortex 53, 60–77 (2014)
- R. Norousi, S. Wickles, C. Leidig, T. Becker, V.J. Schmid, R. Beckmann, A. Tresch, Automatic post-picking using MAPPOS improves particle image detection from cryo-EM micrographs. J. Struct. Biol. 182, 59–66 (2013)
- R. Langlois, J. Pallesen, J. Frank, Reference-free particle selection enhanced with semi-supervised machine learning for cryo-electron microscopy. J. Struct. Biol. 175, 353– 361 (2011)
- C.O.S. Sorzano, E. Recarte, M. Alcorlo, J.R. Bilbao-Castro, C. San-Martin, R. Marabini, J.M. Carazo, Automatic particle selection from electron micrographs using machine learning techniques. J. Struct. Biol. 167, 252–260 (2009)
- P. Arbeláez, B.G. Han, D. Typke, J. Lim, R.M. Glaeser, J. Malik, Experimental evaluation of support vector machine-based and correlation-based approaches to automatic particle selection. J. Struct. Biol. 175, 319–328 (2011)
- R. Langlois, J. Pallesen, J.T. Ash, D.N. Ho, J.L. Rubinstein, J. Frank, Automated particle picking for low-contrast macromolecules in cryo-electron microscopy. J. Struct. Biol. 186, 1–7 (2014)

110. L. Staniewicz, P.A. Midgley, Machine learning as a tool for classifying electron tomographic reconstructions. Adv. Struct. Chem. Imaging 1, 9–23 (2015)

- 111. C.M. Bishop, Pattern recognition and machine learning (Springer, New York, 2006)
- 112. Y. LeCun, Y. Bengio, G. Hinton, Deep learning. Nature **521**, 436–444 (2015)
- 113. J. Deng, W. Dong, R. Socher, L.-J. Li, K. Li, L. Fei-Fei, ImageNet: a large-scale hierarchical image database, in *Proceedings of IEEE Conference on Computer Vision and Pattern Recognition* (2009), pp. 248–255
- A. Krizhevsky, I. Sutskever, G.E. Hinton, ImageNet classification with deep convolutional neural networks. Proc. Adv. Neural Inf. Process. Syst. 25, 1097–1105 (2012)
- O. Russakovsky, J. Deng, H. Su, J. Krause, S. Satheesh, S. Ma, Z. Huang, A. Karpathy, A. Khosla, M. Bernstein, ImageNet large scale visual recognition challenge. Int. J. Comput. Vis. 115, 211–252 (2015)
- C. Szegedy, W. Liu, Y. Jia, P. Sermanet, S. Reed, D. Anguelov, D. Erhan, V. Vanhoucke,
   A. Rabinovich, Going deeper with convolutions, in *Proceedings of IEEE Conference on Computer Vision and Pattern Recognition* (2015), pp. 1–9
- K. He, X. Zhang, S. Ren, J. Sun, Deep residual learning for image recognition. Preprint arXiv:1512.03385 (2015)
- 118. F. Wang, H. Gong, G. liu, M. Li, C. Yan, T. Xia, X. Li, J. Zeng, DeepPicker: a Deep Learning Approach for Fully Automated Particle Picking in Cryo-EM. Preprint arXiv:1605.01838 (2016)
- 119. Y. Zhu, Q. Ouyang, Y. Mao, A deep learning approach to single-particle recognition in cryo-electron microscopy. Preprint arXiv:1605.05543 (2016)
- 120. M. Chen, M.L. Baker, S.J. Ludtke, Application of deep learning to CryoEM heterogeneity analysis. Biophys. J. 110, 158a (2016)
- M. Helmstaedter, K.L. Briggman, S.C. Turaga, V. Jain, H.S. Seung, W. Denk, Connectomic reconstruction of the inner plexiform layer in the mouse retina. Nature 500, 168–174 (2013)
- 122. M. Hardt, E. Price, N. Srebro, Equality of Opportunity in Supervised Learning. Preprint arXiv:1610.02413 (2016)
- 123. V. Mnih, K. Kavukcuoglu, D. Silver, A.A. Rusu, J. Veness, M.G. Bellemare, A. Graves, M. Riedmiller, A.K. Fidjeland, G. Ostrovski, S. Petersen, C. Beattie, A. Sadik, I. Antonoglou, H. King, D. Kumaran, D. Wierstra, S. Legg, D. Hassabis, Human-level control through deep reinforcement learning. Nature 518, 529–533 (2015)
- T.P. Lillicrap, J.J. Hunt, A. Pritzel, N. Heess, T. Erez, Y. Tassa, D. Silver, D. Wierstra, Continuous control with deep reinforcement learning. Preprint arXiv:1509.02971 (2015)
- 125. J. Ba, V. Mnih, K. Kavukcuoglu, Multiple object recognition with visual attention. Preprint arXiv:1412.7755 (2014)

A	Blotting, 66
Active contours, 308	Bright-Field (BF), 34
After cryo-FIB milling, 84	Bright Field (BF) detector, 39, 41
Algebraic reconstruction technique, 16, 209,	
216	C
Alignment algorithms, 80	Carbon, 174
Alignment and reconstruction, 77	Causality criterion, 291
Alignment of tilt series, 275	Cell shape, 82
Alignment precision, 275	Cellular systems, 303
Align subtomograms, 253	Central section theorem, 210, 213
Amplitude contrast, 19	CET reconstructions, 47
Angular range, 24	Characteristic scattering angle, 36, 37
Angular variations, 40	Classical preparations, 263
Anisotropic, 11	Classification, 275
Anisotropy, 227	Classification approaches, 246
Annular Dark-Field (ADF), 34, 38	CLEM, 81
Antibodies, 158	Coat proteins, 250
Antibody elution, 158	Coherence Enhancing Diffusion (CED), 292,
Antigenicity, 151	293
Applications, 248	Coherent, 69
Array tomography, 150, 153	Colloidal gold, 14
Atomic resolution, 272	Compressed sensing, 227
ATP synthases, 251	Computational molecular phenotyping, 150
Automated TEM (ATEM), 150	Concept, 7
Automatically, 71	Confocal microscopy, 1
Avoid excessive damage, 73	Conical tilt, 226
Axoneme, 250	Conical tomography, 267
	Consecutive steps of classification, 247
В	Constrained cross correlation, 243
Bacterial cytoskeletal proteins, 84	Constrained principal-component analysis,
Bandpass filter, 286	246, 254
Beam cross-section, 11	Constraints-based method, 227
Beltrami flow-isotropic diffusion, 226	Contextualize results from more reductionist
Better processing, 85	approaches, 84
BF contrast, 46	Contrast transfer function, 64, 211, 221, 265,
Bidirectional schemes, 76	302
Bilateral filter, 224, 294, 295	Convex hulls, 306
Biochemical reductionist approach, 4	Correlative imaging, 307
Biological material, 64	Correlative methods, 52
,	,

© Springer International Publishing AG 2018
E. Hanssen (ed.), *Cellular Imaging*, Biological and Medical Physics, Biomedical Engineering, https://doi.org/10.1007/978-3-319-68997-5

Counting mode, 70	Eigenvectors, 255
Cross-correlation, 15, 77	Elastic scattering, 35
Cross correlation volume, 239	Electron diffraction, 13
Crowdsourcing, 311	Electron Energy-Loss Spectrometer (EELS), 42
Crowther criterion, 17, 75, 228, 268	Electron exposure, 64
Cryocartridge, 68	Electron-sample interactions, 35
Cryo-correlative microscopy, 25	Electron-specimen interaction, 36
Cryo-electron tomography, 3	Electron tomography, 1
Cryo-preservation, 263	Electrostatic Coulomb forces, 35
Cryo-preserved, 46, 61	Elemental analysis, 42, 47
Cryo-preserved specimens, 39	Elemental analysis of eukaryotic cells, 48
Cryo-sectioning, 67	Elemental mapping using EDS or EELS, 44
Cryo-STEM, 46	Elongation, 228
Cryo-STEM images, 50	Endoplasmic reticulum, 49
Cryo-STEM tomography (CSTET), 46	Energy filter, 70
Cryo-TEM, 46	Energy-minimization, 303
CryoTEM Tomography (CET), 47	Envelope function, 263
CSTET on eukaryotic cells, 48	Equally sloped tomography, 272
CSTET reconstructions, 49	Error in defocus determination, 271
CTF correction, 74, 78	Expectation maximization, 243
Cumulative electron dose, 9, 73	Exposure filtering, 78
cumulative election dose, y, ve	Extended acquisition scheme, 271
D	Extract peaks, 252
Deep learning, 312	Entract peans, 202
Defocus, 74, 221, 265	F
Denoising, 18, 80, 211, 223	Falciparum, P., 296–298
Detective Quantum Efficiency, 69	False positives, 240
Devitrification temperature, 8	Fast Rotational Matching, 244
DF detector, 42	Feature-tracking, 14
Differential inelastic cross-sections, 37	FIB-SEM, 265
Differential scattering cross-section, 36, 37, 39	Fiducial locations, 77
Diffusion tensor, 291, 292	Fiducial markers, 14, 51, 220
Diffusive flux, 291, 292	Field emission guns, 69
Direct electron detectors, 21	Filaments, 308
Discrete Algebraic Reconstruction Technique	Filopodia, 294, 295
(DART), 218, 269	Filters, 79
Divergence, 45	First projection image, 76
Dose fractionation, 24, 47	Flagellar motor, 251
Dose fractionation theorem, 10	Flexible control of semi-convergence angle and
Dose symmetric scheme, 76	probe size, 51
Dose tolerance of vitrified specimens, 46	Focal gradient, 223
Double tilt, 226	Focused ion beam, 8, 67
3-D structure, 64	Focus gradient, 24
Dual-axis acquisition, 11	Fourier ring correlations, 229
Dual-axis tilt series, 75	Fourier Shell Correlation (FSC), 80, 288
Dual-axis tomography, 47, 267	Fourier space, 4, 283, 285, 288, 298
Dynamic focusing, 35, 45	Fourier transforms, 65, 285
Dynamic focusing, 55, 45	Free software options, 71
E	Freeze-substitution, 7, 152, 156
Edged-based methods, 303	Frequency space reconstruction, 209, 213
Edge Enhancing Diffusion (EED), 292, 293	Frequency truncation, 286, 287
Edge quality, 273	Frozen-hydrated, 4
EDS analysis, 50	Fully automated, 86
Eigenvector analysis, 304	Fuzzy set theory, 304
LIEUTYCUI AHAIYSIS, JUT	1 ULLY SEL LICULY, JUT

J
Job file, 252, 254, 255
L
Light elements, 39
Limit of sample thickness, 38
Linear diffusion, 290, 291
Lipid droplets, 49
Liquid cryogen, 66
Liquid nitrogen, 67
Loading, 68
Load specimen, 88
Local cross-correlation, 276
Localization accuracy, 307
Local resolution, 245
Longitudinal beam profiles, 40
Low atomic number Z, 46
Low dose, 71
Lowicryl HM20, 152, 156
Low-pass filter, 224
Low signal-to-noise, 64
Lung fibroblast cells, 49
M
Machine learning, 312
Marker-free alignment, 14
Mask, 252
Masking, 78
Mass density variation, 46
Mass loss, 11
Mass measurements, 44
Mass/thickness contrast, 39
Matched filter, 307
Maximum entropy method, 216
Maximum likelihood, 242
Mean Free Path (MFP), 38
Mean shift filtering, 225
Mechanistic insights, 82
Median filter, 289, 290
MFP for inelastic scattering by vitreous ice, 38
M-free score, 307
Microtrabecular lattice, 7
Microtubule, 49, 250
Missing information, 211, 226
Missing pyramid, 24
Missing wedge, 24, 65, 75, 266, 302
Mitochondria, 49
Mitochondrion, 290
Model-based averaging, 230
Model-based methods, 304

Modulation Transfer Function, 69	Power spectrum, 222
Molecular function in situ, 85	Practical thickness limit, 38
More data, 85	Precision, 275
MosaicPlanner, 159	Pre-reconstructionNon-Linear Anisotropic
Movie mode, 275	Diffusion (Pre-NAD), 296, 297
MRA, 277	Pre-reconstructionNon-Linear Isotropic
Multiple scattering events, 7	Diffusion (Pre-NID), 297, 298
Multiplex-immunolabeling, 51	Preset magnifications, 71
Multi-reference procedures, 246	Probe size, 45
Multi-ring annular detector, 53	Projection difference, 216
Myelinated axons, 162	Projection onto convex sets, 227
•	Protein translocon, 245, 247
N	
Nanofabrication, 24	R
Nanometer-resolution, 41	Radiation damage, 38
Native context, 273	Radiation sensitivity, 11
Near-atomic resolution, 278	Radiation tolerance of the specimen, 73
Near-native, 62	Radon transform, 16
Noise, 302	Ratio of MFP for elastic to inelastic scattering
Noise-compensatedleave-one-out, 229	38
Noise ratio (SNR), 262	Rayleigh, 261
Non-linear Anistropic Diffusion (NAD), 226	Real space, 4, 288, 289, 291, 298
Non-linear diffusion, 291, 292	Real-space constraints, 311
Non-local means filter, 225	Reconstruct, 88
Normalizing images, 220	Reconstruction, 15
Nuclear pore complex, 250	Reduced representation templates, 308
Number of iterations, 218	Region-based approaches, 304
Nyquist frequency, 17, 65, 74	Relation between the inelastic and elastic
	scattering cross-section, 38
0	Relative orientations, The, 77
Of intact vitrified cells, 53	Reliable production of grids, 86
Optimal specimen, 87	Resolution, 17, 79, 227, 238, 261
Optimize vitrification, 87	Resolution anisotropy, 273
Optimizing the signal-to-noise ratio, 72	Resolution in STEM, 41
Overfitting, 244, 275	Resolution of a STEM image, 40
	Retrovirus capsids, 251
P	Ribosomes, 240, 245, 247
Pairwise matrix, 255	Role of the microscope optics in STEM, 34
Parameters, 72	
Particle coordinates, 253	S
Particle list, 254	Sample geometry, 23
Particle localization, 238	Scale space, 290
Peak selection, 241	Scan generators, 53
Phage attack on an E coli cell, 49	Scanning electron microscope, 155
Phase contrast, 19, 70	Scanning Transmission Electron Microscope
Phase plates, 21, 70, 266	(STEM), 2, 33
Photobleaching, 25	Secretion systems, 251
Pixel size, 74	Segmentation, 18, 79, 301, 303
Plastic sections, 39	Selection of peaks, 252
Pleomorphic specimens, 6	Semi-convergence angles, 40
Point spread function, 268, 302	Serial block face, 265
Polyribosomes, 249	Serial block-face imaging, 3
Post-process, 88	Serial block-face scanning electron
Poststaining, 178	microscopy, 12

Serial sections, 156	Thick biological samples, 40
Shape information, 304	Thick biological sections, 44
Shrinkage, 11	Thicker biological sections, 50
Side-entry cryoholder, 68	Thick sample, 45
Signal-to-noise, 272	Thin-plate spline, 306
Signal-to-noise ratio, 39, 210, 302	Thin specimen limit, 36
Simultaneous algebraic reconstruction	Thresholding, 308
technique, 216	Throughput, 86
Simultaneous Iterative Reconstruction	Tilt compensation, 221
Technique (SIRT), 16, 216	Tilt increment, 75
Single-axis tomography, 266	Tilt range, 75
Single-particle analysis, 3	Tilt series, 13
Single-scattering approximation, 36	Time-resolved electron tomography, 26
SIRT, 78	Tomographic experiments, 41
Skeletonization, 308	Tomography applications, 39
Small semi-convergence angle, 45	Total elastic scattering, 37
Sodium azide, 167	Total elastic scattering cross-section, 36
Sodium pentobarbital, 167	Total inelastic scattering, 37
Software packages, 71, 248	Translocon, 249
Soft X-ray tomography, 1	Transmission Electron Microscope (TEM), 2
Span cellular and structural biology, 81	True positives, 240, 253
Spatial frequencies, 79	
Specimen charging, 13, 69	U
Specimen movement, 69	Ultra-small gold labels, 51
26S proteasome, 249	Ultra-stable supports, 85
Stained samples, 39	Ultrathin sectioning, 174
Starting volume, 216	Unique insights into biological systems, 87
STEM biological imaging, 44	Unstained biological specimens, 46
STEM contrast of biological samples, 38	Updating the 3D map volume, 218
STEM detector, 40	
STEM image formation, 35	V
STEM imaging, 33	Visual proteomics, 5, 20, 80
STEM tomography, 41, 43, 44, 46, 50	Vitreous ice, 65
Stereological techniques, 25	Vitrification, 6, 66
Stochastic variability, 6	Vitrified human cells, 52
Stopping condition, 216	Vitrified samples, 51
Stopping point, 224	Volta phase plate, 22, 273, 302
Subframe alignment, 69	Volume rendering, 79
Subjectivity, 311	Volumetric rendering, 49
Sub-nanometer resolution, 273	, , , , , , , , , , , , , , , , , , , ,
Subtomogram, 210	$\mathbf{W}$
Subtomogram alignment, 242	Watershed algorithm, 304
Subtomogram averaging, 79	Watersnake method, 304
Subtomogram reconstruction, 230	Weighted back-projection, 16, 78, 209, 213
Synapse, 151, 161	Weighting function, 213
~JF,, 101	e.gg randon, 210
T	X
Template bias, 244	X-rays, 220
Template matching, 18, 80, 239, 242, 251, 307	• /
Template structure, 252	